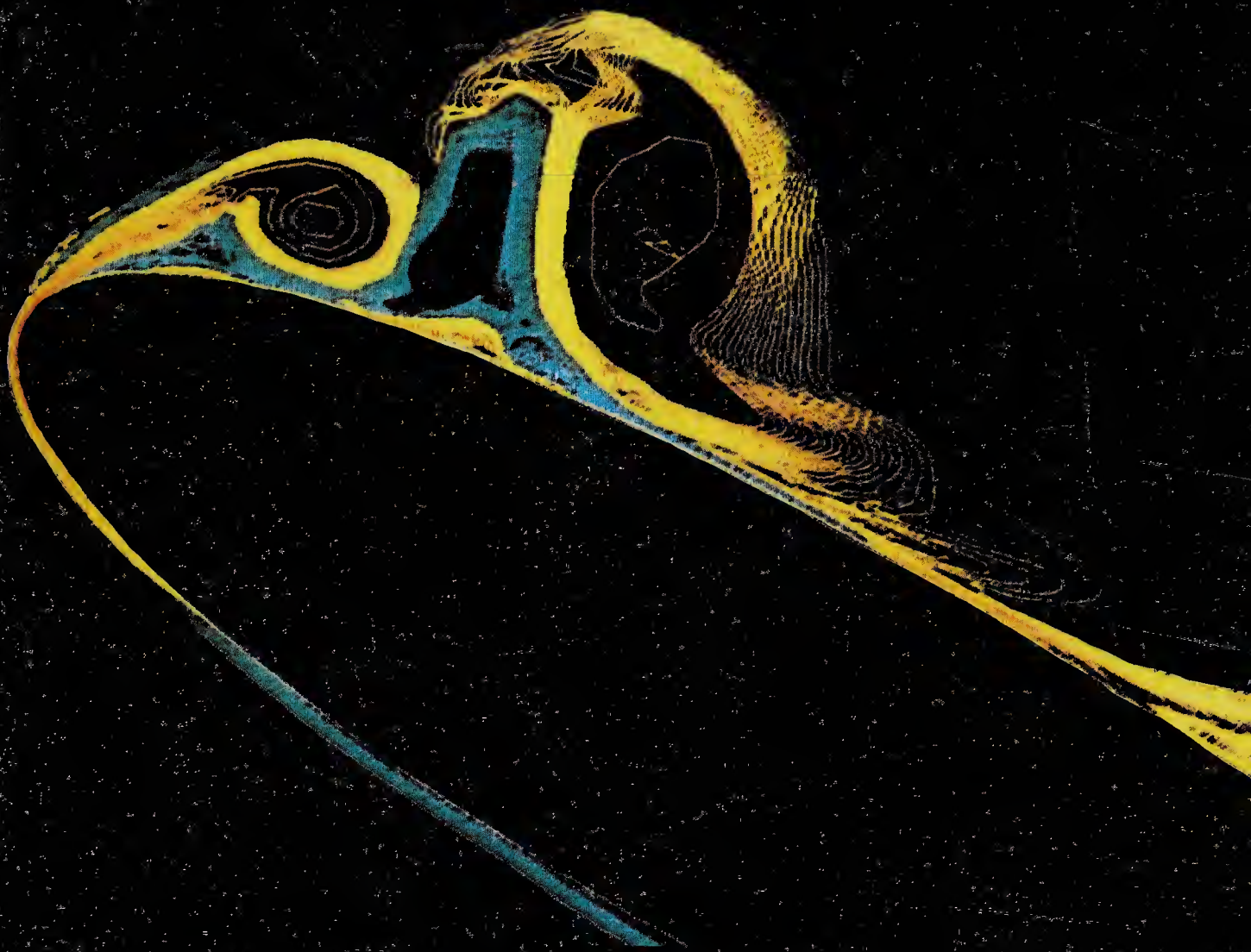

SURVEYS IN FLUID MECHANICS
III

Edited by
R NARASIMHA

INDIAN ACADEMY OF SCIENCES
Bangalore 560 080

SURVEYS IN FLUID MECHANICS
III

Edited by

R NARASIMHA
Jawaharlal Nehru Centre
for Advanced Scientific Research and
Indian Institute of Science, Bangalore

1993

INDIAN ACADEMY OF SCIENCES
Bangalore 560 080

Eruption of a secondary vortex during dynamic stall of an aerofoil in constant-rate pitch-up motion. The picture shows contours of equal vorticity of an NACA 0015 aerofoil at an instantaneous angle of attack of 28·56°, as computed by an unsteady Navier–Stokes code (see Ghia *et al*, pp. 207–268).

© 1993 by the Indian Academy of Sciences

Reprinted from *Sādhanā* – Academy Proceedings in Engineering sciences
Volume 18, pp. 365–728, 1993

Edited by R Narasimha, phototypeset at Thomson Press (India) Ltd., New Delhi and printed at
Printek Printers, Bangalore 560 079 for the Indian Academy of Sciences

CONTENTS

Foreword v

FUJIHIKO SAKAO: Modelling aerodynamic sound in the airways of a human body: A possible diagnostic tool 1

P K SEN: Some recent developments in the theory of boundary layer instability 19

S M DESHPANDE: Boltzmann schemes for continuum gas dynamics 37

H DAIGUJI and B R SHIN: Some numerical schemes using curvilinear coordinate grids for incompressible and compressible Navier–Stokes equations 63

FAZLE HUSSAIN, DAVINDER VIRK and MOGENS V MELANDER: New studies in vortex dynamics: Incompressible and compressible vortex reconnection, core dynamics and coupling between large and small scales 109

M KIYA: Simulating three-dimensional vortex motion by a vortex blob method 163

V C PATEL: Three-dimensional flow separation 185

K N GHIA, J YANG, U GHIA and G A OSSWALD: Analysis and control of dynamic stall phenomena using Navier–Stokes formulation involving vorticity, stream function and circulation 207

T J CHUNG: Turbulence/shock wave interactions in chemically reacting flows 269

CLIVE A J FLETCHER: Gas particle industrial flow simulation using RANSTAD 289

GUOCAN LING: Numerical study of bluff body flow structures 315

KAZUYOSHI TAKAYAMA and GABI BEN-DOR: State-of-the-art in research on Mach reflection of shock waves 327

P N SHANKAR: The fluid mechanics of phase change 343

BING-GANG TONG, LI-XIAN ZHUANG and JIAN-YU CHENG: The hydrodynamic analysis of fish propulsion performance and its morphological adaptation 351

Author Index 361

Subject Index 365

Surveys in fluid mechanics–III

Foreword

This book is the third in the series of Surveys in Fluid Mechanics that have been published by the Academy (the first appeared in 1982, and the second in 1988, collected in a volume titled *Recent Developments in Fluid Mechanics and Space Technology*). As on the previous occasions, the Surveys are extended versions of invited lectures given at the Asian Congress of Fluid Mechanics; the present volume contains those presented at the 5th Congress in the series, held in Taejon, Korea during 10–14 August 1992.

We begin with the text of the Tani Memorial Lecture, given at Taejon by Fujihiko Sakao (Higashihiroshima). He investigates (at the request of a medical doctor) the familiar method of examining a patient with a stethoscope: is it possible to obtain more information from this kind of instrument using sophisticated data-processing methods? From analysing the sound field outside a soft tube in which the vocal cords and "obstacles" are simulated, the author concludes that there are new diagnostic possibilities, and perhaps even potential for improvements in the common stethoscope.

P K Sen (Delhi) reviews recent developments in the stability of spatially growing boundary layers, which is still the subject of some controversy. The new treatment he proposes here produces better agreement with experimental data.

A series of papers on computational fluid dynamics follows. S M Deshpande (Bangalore) pursues the intriguing possibilities of setting up numerical schemes for solving the (continuum) Navier–Stokes equations that exploit a connection with the Boltzmann equation of the kinetic theory of gasses. A variety of applications of such "kinetic" schemes are described, including an Euler code for hypersonic flows. Daiguji (Tohoku) and Shin (Daejeon, Korea) describe other numerical schemes that use curvilinear grids, especially for handling turbomachinery flows. Both compressible and incompressible flows are included, and a $K\varepsilon$ turbulence model with low Reynolds number corrections can be incorporated.

Hussain, Virk and Melander (Houston, Texas) describe two new studies in vortex dynamics inspired by the need to understand coherent structures in turbulent flows. These developments enable distinct advances in the "structural" approach to turbulence, which as the authors point out has brought fluid mechanics back into what had become a branch of statistical physics. Direct numerical simulations, along with the powerful tool of helical wave decomposition, provide new and fundamental insights into the physical processes that are at the heart of the problem of turbulent flows.

Kiya (Hokkaido) also uses vortex methods to study several interesting flows, including jets from elliptic nozzles, unsteady flow past a disk at angles of attack, and a collection of vortex rings whose interaction leads approximately to the Kolmogorov spectrum. Kiya uses vortex blobs to compute these flows: as he points out, vortex methods have several advantages: they do not need complex grid systems, computation is confined to only vortical regions in the fluid, and high Reynolds number flows are not unmanageable (as they are in say finite difference approaches to direct numerical solutions of turbulent flows).

V C Patel (Iowa) presents a comprehensive review of three-dimensional flow separation, which is actually much more common in real life than the more intensely studied two-dimensional problem. Both kinematic and dynamic complications of three-dimensional flows are formidable, so the phenomenon is still beyond the reach of definitive theoretical or numerical analyses, as well as of comprehensive measurement. Drawing on both experimental and computational results, Patel summarises work on a prolate spheroid and a wing intersecting a plane, both over a wide range of incidences, and points out that laminar flow separation offers a much richer topological variation than turbulent flow does.

The Ghias, with Yang and Osswald (Cincinnati), are also concerned with separated flows, – in particular unsteady ones of the kind that are important for "super-manœuvrable" aircraft operating in post-stall flight regimes, as well as for compressor, helicopter and windmill blades. They tackle these problems of dynamic stall by solving the unsteady Navier–Stokes equations and show not only favourable comparisons with experiment, but also possibilities for active control of the flow.

T J Chung (Alabama at Huntsville) continues with CFD, this time adopting finite element methods for handling flows that occur in supersonic combustion, involving in particular shock/turbulence interactions and chemical reactions.

Clive Fletcher (New South Wales) reports on the simulation of a complex industrial flow, namely that in a coal classifier. This involves the use of an algebraic stress model for turbulent flow in a two-phase (gas–particle in this case) medium. Fletcher, who views the study as an exercise in computational engineering, shows how design changes may be suggested by such simulations.

Another class of problems in engineering fluid mechanics is bluff-body flows: buildings, bridge piers, offshore platforms etc. Guocan Ling (Beijing) looks at some idealized problems in this class, such as oscillating plates and cylinders, with particular attention given to the effect of unsteadiness and the vortical structure of the wake.

Takayama (Tohoku) and Ben-Dor (Beer Sheva) provide some experimental relief by reviewing the transition from Mach to regular reflection in supersonic flow over wedges. A wealth of flow visualizations using holographic interferometry techniques in a shock tube illustrate the numerous types of reflection possible.

P N Shankar (Bangalore) sees evaporation and condensation as problems in fluid mechanics. Strange phenomena, such as temperature jumps and anomalous gradients, have been predicted by kinetic-theory treatments of the problem in the pure vapour phase. Shankar reviews recent work on the problem, with some surprising results but with much that still remains to be understood.

The present collection ends (as it began) with bio-fluid dynamics: this time on fish propulsion. Analysis of performance from this viewpoint, by Tong, Zhuang and Cheng (Anhui, China), leads to a tentative understanding of the morphological adaptation of fish propulsion modes in biological evolution.

The Taejon Congress deliberately emphasized computational fluid dynamics, so it is no surprise that more than half of the present collection is concerned with that subject. Even otherwise, however, comparison with the first volume in this series shows beyond doubt the vastly greater role that computation now plays in fluid mechanics. I hope that this volume, like previous ones, will provide readers with a stimulating collection of surveys of recent developments that show the rich variety of fluid-dynamical problems that are still demanding investigation and solution, and incidentally also present a cross-section of the best Asian work in fluid mechanics.

August 1993

R NARASIMHA
Guest Editor

Digitized by the Internet Archive
in 2018 with funding from
Public.Resource.Org

https://archive.org/details/surveysinfluidme03unse

Modelling aerodynamic sound in the airways of a human body: A possible diagnostic tool

FUJIHIKO SAKAO

Faculty of Engineering (at Higashihiroshima), Kinki University, Takaya-Umenobe, Higashihiroshima, Japan 729-17

Abstract. The sound generated aerodynamically by a pillow-like body simulating an obstacle in the human airway is observed through a soft wall from outside the duct. It is intended to provide a physical basis for an attempted medical diagnostic technique for detecting an obstacle by observing the sound during breathing. So far at least two kinds of sound have been identified: One is sound of the half-jet flow formed downstream of the obstacle, and the other is sound due to unsteady motion of the separation point on the curved surface of the obstacle. For simulating the flow condition downstream of the vocal cords during inhalation, cases with an obstacle at various positions relative to a jet flow are also examined. In this case, the sound due to the downstream obstacle exhibits a complicated dependence on the geometry and flow parameters. Nevertheless, increase in the sound, or more correctly, deformation in the sound power spectrum, due to the presence of an obstacle is detectable from outside, opening up possibilities of its use as a diagnostic aid.

Keywords. Aerodynamic sound; soft wall; diagnostics.

1. Foreword and introduction

It is a great pleasure and honour for the author to be asked to present the Tani Memorial Lecture. Before starting the lecture, the author would like to take this opportunity to say a few words about Professor Tani and the work presented here.

Professor Tani liked to study new areas in fluid mechanics. He encouraged his students or colleagues to engage themselves in research in new branches. He himself did some work in the then-quite-new branch of magneto-hydrodynamics, though in the later phase of his life he concentrated on the field of turbulence and boundary layers in which he had acquired world-wide fame. When the author started research on aerodynamic sound generation, he was pleased about it, and encouraged and gave the author very valuable help. Hence, it is certain that he would be pleased to know that the author and Professor Sato (both his students) are engaged in work such as is presented here.

Dedicated to the late Professor Itiro Tani on the occasion of 5ACFM, Taejon, Korea

And some further words about Professor Itiro Tani. In his favourite office at ISAS (Inst. Space Aeronaut. Sci., Tokyo University, then), on a wall above his desk, there was a portrait of one of his old and respected friends, namely Dr. Th von Karman. We heard, however, Professor Tani say that his genuine teacher, whose influence on him was the most and the best, was Professor L Prandtl. Professor Tani died on May 28, 1990. On the next Sunday, June 6, a lecture by him had been scheduled. The title was to be "Prandtl's mind", or it might be better to say, 'Spirit of L Prandtl'. Professor Tani was very eager to give that lecture almost to the very end of his life, so we heard. What he wanted to tell his students in that lecture cannot be known now. We can infer, however, from what he said on different occasions, the intention of his lecture to some extent. As many others do, the author supposes that he wanted to make us give importance to getting physical insight into the essential mechanism underlying a phenomenon, rather than merely getting one solution for a problem, or getting a heap of raw data, through experiments or numerical investigations.

From such point of view, the author is quite anxious whether Prof. Tani would be content with our achievement so far in the present work, but we are making effort to go along that line of progress.

To start with, it should be remarked that this work is done in cooperation with Professor Hiroshi Sato, and results are usually reported with both as co-authors.

Among physicians there is expectation and/or desire for methods for detecting obstacles in human airways by observing the sound of breathing from outside the body. Such a method, if at all possible, would enjoy the advantage of being totally non-intrusive, free from any pain for the patient. For diagnosing, all that the patient 'suffers' is being examined with a stethoscope, which is quite familiar to any one. The only difference from the usual process will be that here the sound is not just heard by the doctor but is also analysed through rather sophisticated processes to give, for instance, a spectrum. This does not inflict any additional pain or inconvenience on the patient if, for example, a rapid recording process is utilized. The work presented here is aimed at providing a physical basis to such methods of diagnosis. It should be remarked that the work has been stimulated by a physician's request.

There are many different kinds of mechanisms by which sound is generated in the human airway by breathing, though we cannot name or identify all of them. Some of them are related to vibrations of muscles or other tissues, or even mucus ("viscous fluid"). The present work concentrates on sound generated aerodynamically, not influenced by vibrations of solid or solid-like materials. Sounds of such kind are not only easy to define and reproduce in a model experiment, but are also very important in practice.

The sound by an obstacle in a section of airways is generated inside a tube, and heard through the wall of the tube. Up to now, aerodynamic sound generation has been investigated intensely, after Lighthill's (1952) classic work. Most of the investigations so far, however, have been either on sound of a flow field in an open space, or otherwise, on sound generated inside a tube and emitted through an opening after travelling along the tube. For the present purpose, investigation is necessary on sound generated inside a tube and observed through the tube wall at a nearby location, with essentially no openings in the tube. As the performance of a "voice tube" (although it is rather rarely seen today) reveals, a hard-walled tube quite effectively inhibits the sound pressure inside it from emerging outside. That inhibition is chiefly by the action of the elasticity, and not the inertia of the tube wall. The two effects become the same at the resonance frequency of the wall of the relevant mode, and usually, the frequency

is anyway very high, especially for the fundamental, uniform dilatation mode. Sound generated inside a hard-wall tube has no way other than travelling along the tube until it finds an opening to exit.

Hence we need a tube with a soft wall to simulate, to any extent, the sound heard outside a human body. We thus started experiments with a set-up as described in the next section.

2. Experimental set-up

The most characteristic part of the present set-up is the "tube" in which an obstacle is set and generates sound which can be heard outside. Since a "soft wall" tube is not easy to realise with sufficient accuracy and reproducibility, a "sufficiently soft" wall is adopted, namely, a sheet of thin paper. Inevitably, a square cross-section is chosen, 2 cm by 2 cm (inner dimensions). Of the four side walls, three are made of acrylic resin, and the other is of a sheet of paper, with surface density 0·01 to 0·02 g/cm^2. Observation of sound is made through this wall with a microphone. Up to now, the obstacle was set always on the wall opposite to the paper wall, for the maximum sensitivity. An outline of the set-up is illustrated in figure 1.

The flow in the tube is up to about 100 mm Aq in terms of the dynamic pressure (corresponding to approximately 45 m/s) at the highest velocity point. This is within realistic range for the human airway. No flutter of the paper wall has been observed. Too much caution was not paid to make the inlet flow uniform and disturbance free. The inlet flow is under rather humble conditions with a simple honeycomb in the settling chamber and a bell-mouth inlet for conditioning the flow. The wall boundary

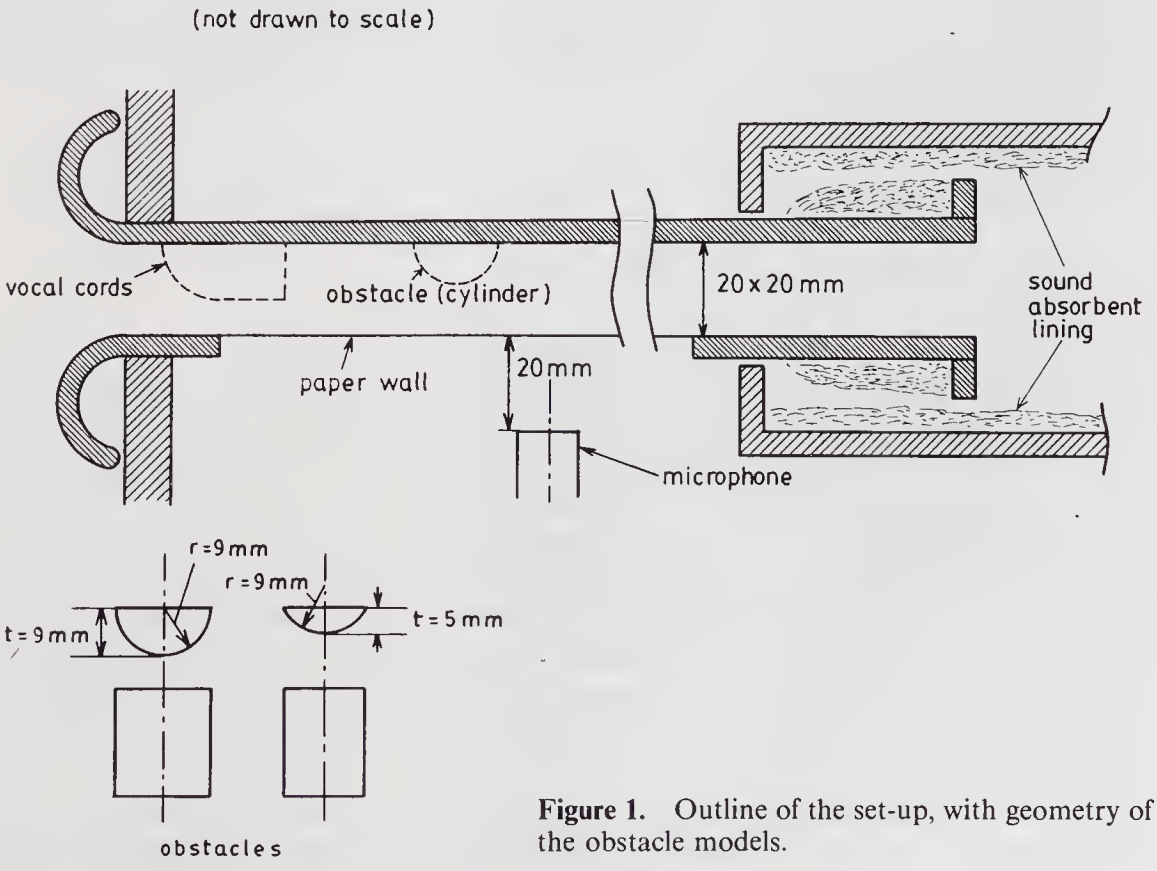

Figure 1. Outline of the set-up, with geometry of the obstacle models.

layer seems about to make transition to turbulence at around 100 mm downstream of the inlet when there is no obstacle. With an obstacle, flow is accelerated there, and transition is postponed.

For the purpose of the present investigation, control of noise from the airflow facility is essential. A centrifugal fan is concealed in a sound-shielding box with sound absorbent liner, and placed outside the anechoic chamber in which the main test section is set. The airflow passes through a flexible hose, then a muffler section, and finally reaches the settling chamber.

The model obstacle to be set in the tube is of nominally two-dimensional shape (though with rather limited aspect ratio), with the axis normal to the duct axis (hence, to the flow as well). The back surface is flat and attached to the wall opposite to the paper wall. The surface facing the flow is usually a smooth convex one, being a part of a circular cylinder with radius 9 mm. The thickness (or height) is either 5 or 9 mm. Cross-sections of two typical models are shown in figure 1.

A condenser microphone (13 mm nominal diameter) is set outside the tube, facing the paper wall. While its axial position is varied, the distance from the paper wall is fixed at 20 mm. This position is inside the "near field" for most of the relevant frequencies of the obstacle as the sound source. However, in an actual situation with a stethoscope, the sensor can be no further than this. The signal from the microphone is processed, in most cases in the form of a 1/3 octave band power spectrum.

So far, only a limited number of hot-wire anemometer surveys of the flow field inside the duct have been made.

In the human airway, the airflow may be regarded as rather uniform during exhalation. This situation can be modelled by a smoothly contracted air flow into the duct. During inhalation, on the contrary, the airflow may be made into a jet between the vocal cords. In experiments simulating this condition, a half nozzle is set at the inlet section of the duct to form a half jet flowing through half of the tube cross-section. The obstacle downstream is set at different positions and attitudes relative to the nozzle (or "vocal cords").

3. Results and discussion

3.1 *Obstacle in a quasi-uniform flow*

First, an obstacle is set in the duct, as described above, in a nominally uniform duct flow (that is, with no nozzle or like object that positively causes flow non-uniformity). Sound (or quasi-sound) observed outside the paper wall is increased by the presence of the obstacle. There is some ambiguity in this comparison: Due to the presence of the obstacle, the flow passing its side is accelerated. If the velocity there is kept the same as quasi-uniform velocity in the duct without the obstacle, then the flow rate with obstacle becomes much lower, hence the flow velocity in most of the duct is reduced as well. The sound generated by the duct itself (other than the obstacle) would also be reduced greatly. Nevertheless, in the present investigation, comparison is made on the basis of the same maximum velocity. This proves to be useful for clarifying the cause of the sound or the mechanism of its production by the obstacle, as presented below.

Figure 2 illustrates some examples of 1/3 octave band power spectra of the microphone output. They are "hard copies" of the output diagram of the signal analyser

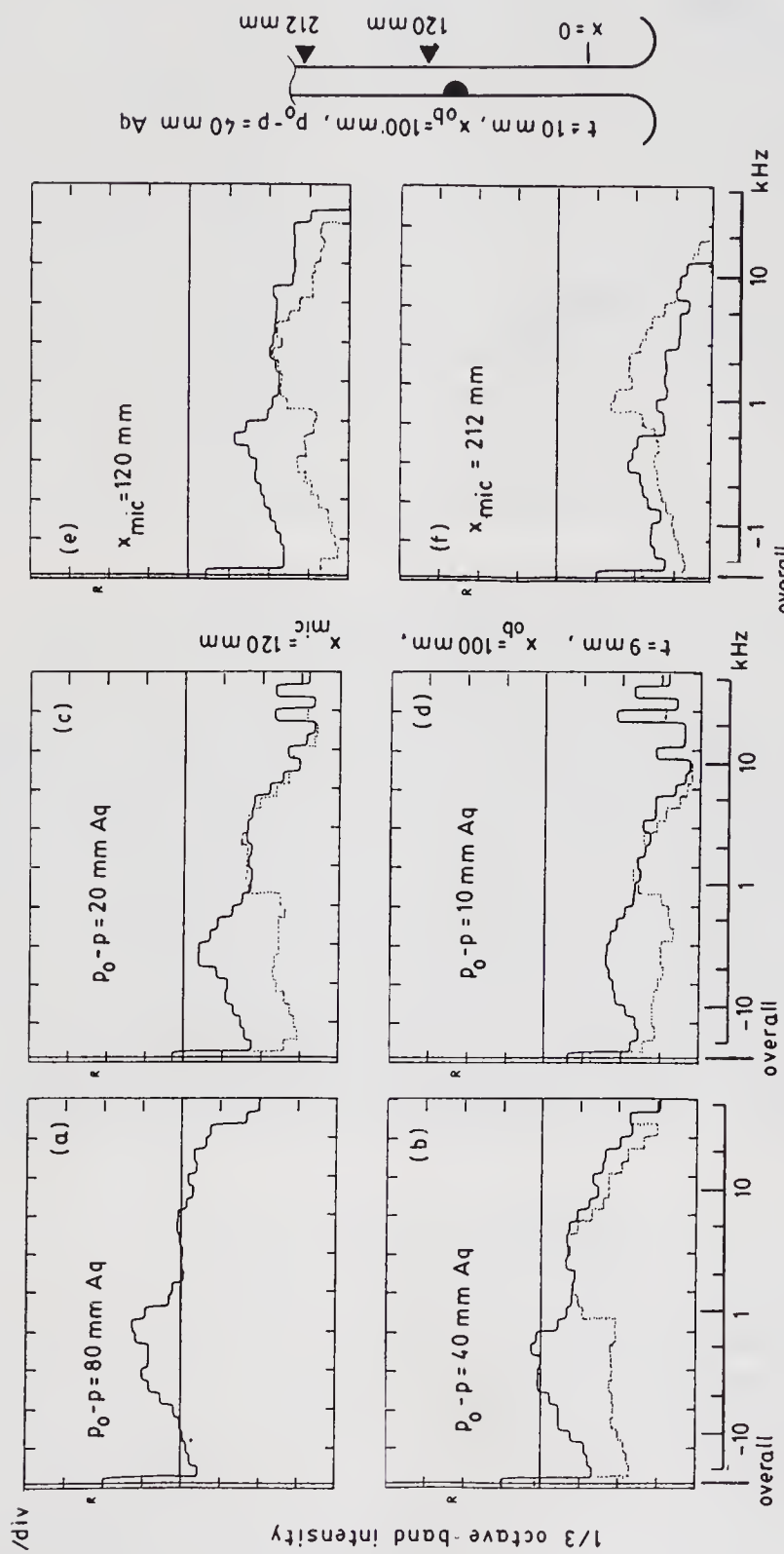

Figure 2. Examples of 1/3 octave band power spectra of the microphone output, adapted from "hardcopies" of the diagram displayed on the signal analyser screen. Obstacles are in a usual duct flow. In (**a**) to (**d**), the obstacle is 9 mm thick, and in (**e**) and (**f**) 10 mm thick. Control data not available in (a).)

The ordinate scale is 10 dB/div. The abscissa is band-centre frequency. The extreme-left band is the overall level. The broken lines indicate the level without obstacles. They are taken from the corresponding figures by manual tracing.

displayed on the screen, with some hand-written notes on them. The ordinate scale is 10 dB/div, and the abscissa is band-centre frequency, usually ranging from 50 Hz to 50 kHz. The band at extreme left is the overall level. These settings are the same for all similar diagrams of the spectrum throughout this paper. The flow velocity at the side of the obstacle is given in terms of dynamic pressure there (in mm Aq). X_{ob}, and X_{mic} denote respectively the axial positions of the obstacle (at its centre) and the microphone. The origin of the coordinate is arbitrarily set at the beginning of the paper wall, which is near the beginning of the parallel portion of the duct walls. The thickness (or height) of the model obstacles used to obtain the results shown in figure 2 was mostly 9 mm, with two exceptional cases of 10 mm (figures 2e and f). In the figures, sound with and without the obstacle is indicated by solid and broken lines, respectively; the solid lines are original ones while the broken lines have been taken from the corresponding diagrams by manual tracing. Apparently, the sound due to the obstacle is over a wide range of frequency, and this may be divided into two: One around several hundred hertz and the other around a few kilohertz and above. Of the two, the former, that is, the lower frequency components, seem to be far more important, both in the extent of deformation of the spectral shape and the amount of sound produced.

Figure 3 illustrates sample data for dependence of the peak spectral levels of the lower and higher frequency parts of the power spectra on the flow velocity at the side of the obstacle, U. The lower frequency components shown by solid circles are in fairly good agreement with U^6-dependence. The higher frequency data shown by open circles do not deny the U^8-dependence. From these observations, the higher frequency components may be regarded as "jet noise" of the half jet formed downstream of the obstacle. The U-dependence, the shape of the spectrum and the frequency range all support the suggestion. The U^6-dependence of the lower frequency components suggests the influence of a solid body. Since they have frequencies quite different from the supposed jet noise, they cannot be jet noise simply influenced by the solid body. There is a frequency gap between them and the suspected jet noise. There should be a different mechanism causing relatively slow variations of flow, or vortices.

The present author has experience on aerodynamic sound similar to this. With a round, convex-to-stream nozzle lip, a jet emitted very remarkable extra sound under some conditions (Sakao & Hiramoto 1983; Sakao 1984). By detailed investigation of

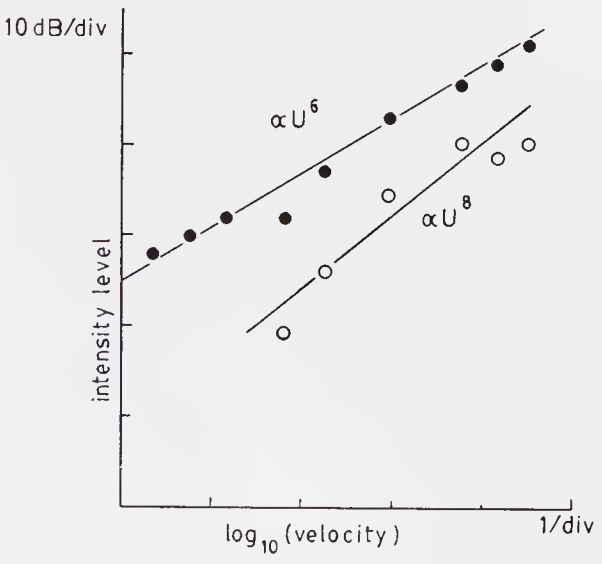

Figure 3. Example of dependence of the peak spectral level of the lower (●) and higher (○) frequency parts of the power spectra on the flow velocity at the side of the obstacle, U. Other details as in figure 2.

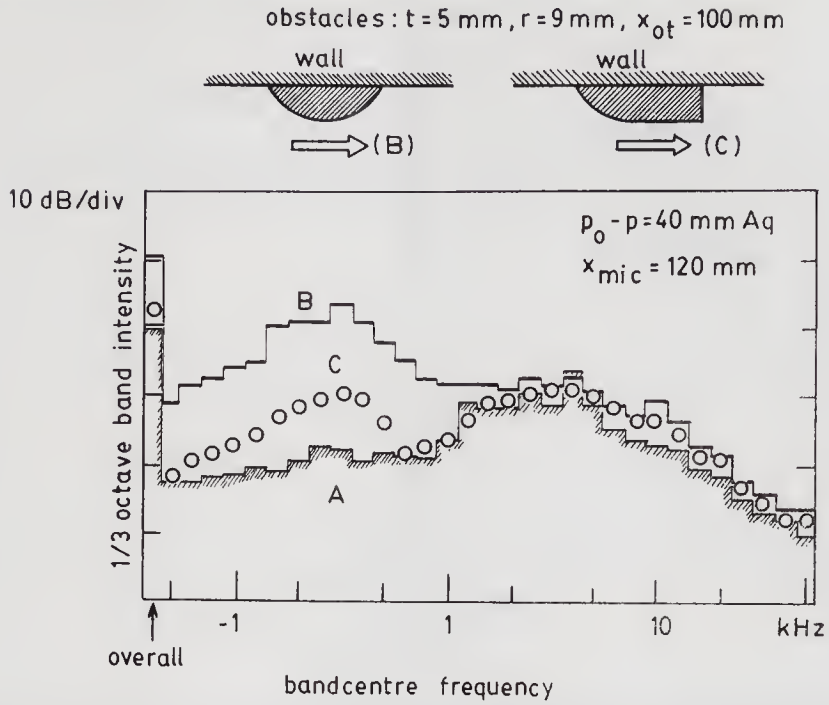

Figure 4. Most of the lower frequency components of the increased sound disappears for an obstacle with a sharp rear edge. Other details as in figure 2.

fluctuations in flow and wall pressure in conjunction with the sound, it has been concluded that the sound is caused by unsteady fluctuations of the separating point of the boundary layer on the surface. That experience immediately told the author that the lower frequency part of the increased sound that is proportional to U^6 should be due to unsteady separation of the flow on the round surface of the obstacle. Although detailed investigation of the flow field or surface pressure fluctuations have not been performed yet because of technical difficulties, this conjecture is supported by the fact that if the geometry of the obstacle is changed at its downstream portion to have a sharp edge as shown in figure 4, the lower frequency components of the increased sound virtually disappear. Thus it would be safe to say that the lower and higher frequency components are mainly due to unsteady separation and jet noise, respectively, though some smaller contribution from unsteady reattachment sound could be present.

Investigations have been made also on the effect of the axial location of the microphone. Some data related to this point are illustrated in figures 2e and f. It is found that for the lower frequency components the location of the microphone relative to the obstacle has rather little effect on the observed sound, while for the higher frequency components the microphone output is rapidly decreased as the distance between them is increased (compare figures 2e and f). From the point of view of practical application, it might be said that the former can be used to detect existence, and the latter to identify the location of the obstacle though the magnitude is usually very small.

Although experiments under this condition are mostly with obstacles of thickness 9 mm, it has been verified that moderate variation in thickness has little effect on the sound generated. That is, a 5 mm thick obstacle generates sound that is essentially the same as that generated by a 9 mm thick one. This is quite plausible if the sound-generating mechanisms conjectured above are correct: Both of them are essentially independent of the thickness within a certain limit.

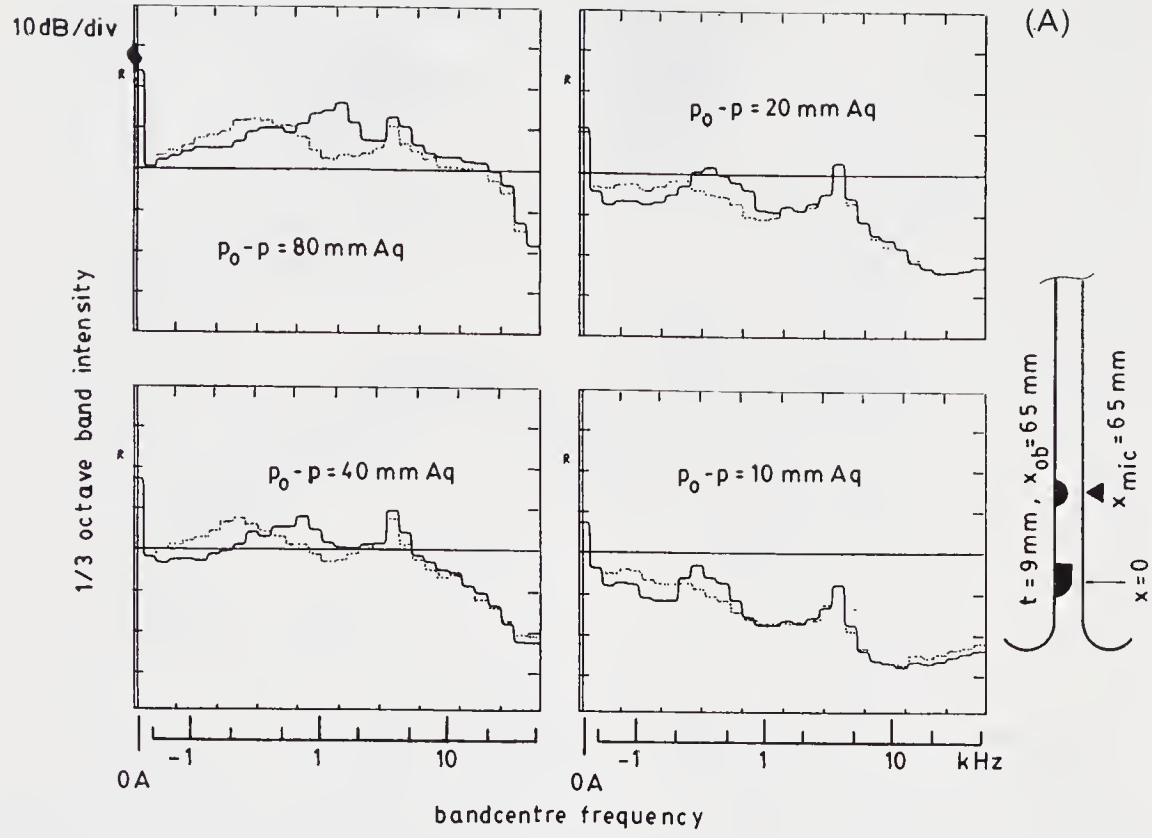

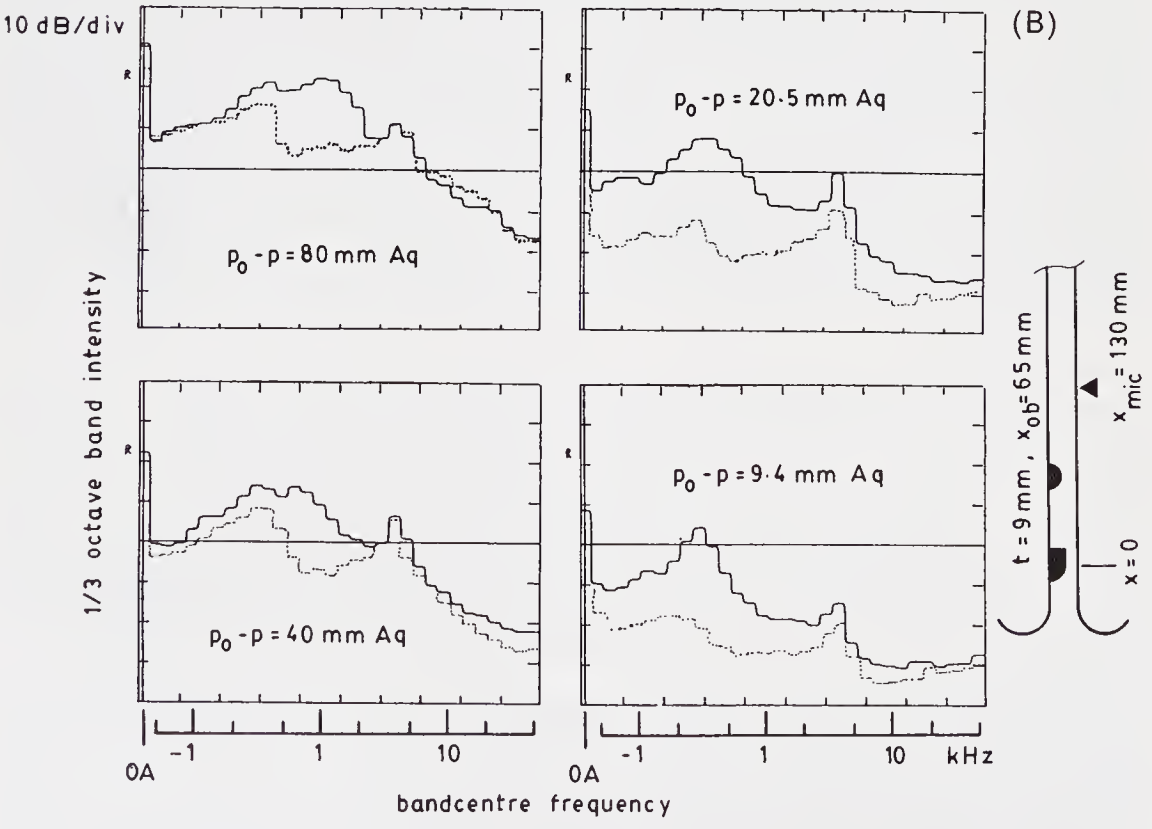

Figure 5A & B (continued)

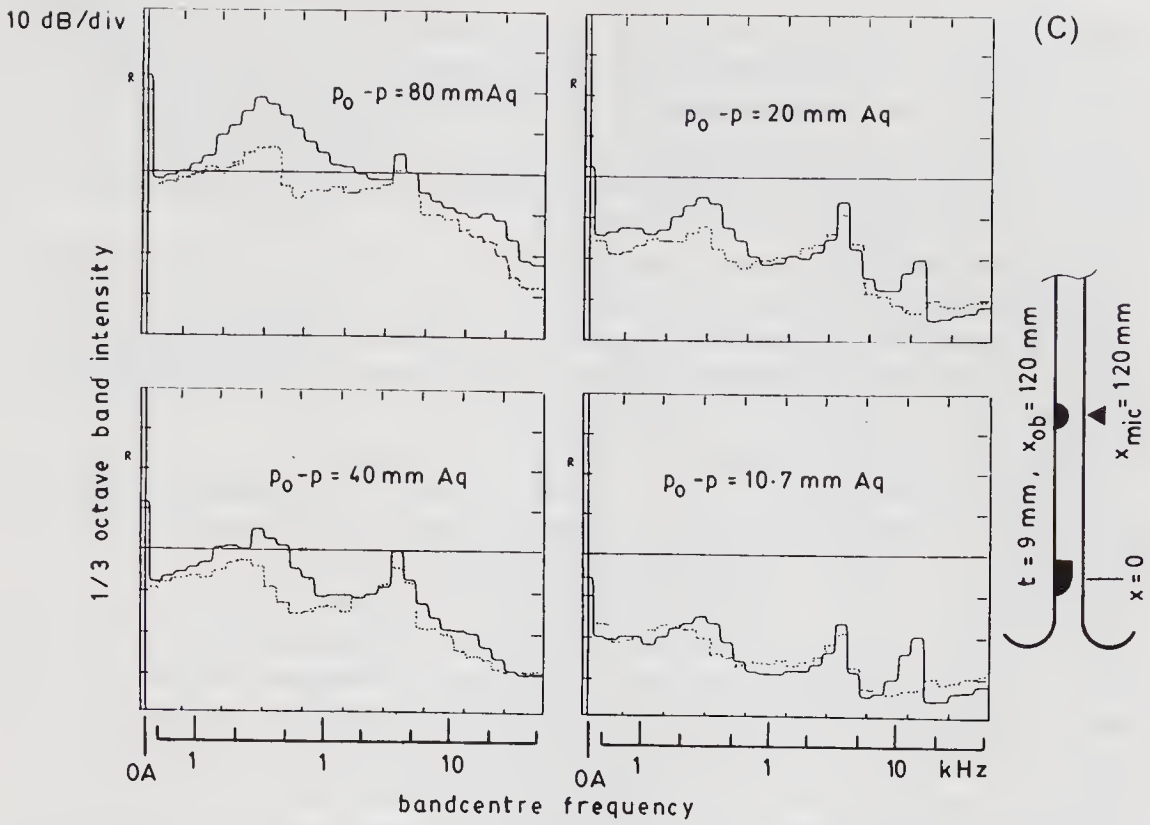
10 dB/div
(C)
P_0 -p = 80 mmAq
P_0 -p = 20 mm Aq
P_0 -p = 40 mm Aq
P_0 -p = 10·7 mm Aq
1/3 octave band intensity
t = 9 mm, x_{ob} = 120 mm
x_{mic} = 120 mm
x = 0
OA 1 1 10 kHz
OA 1 1 10 kHz
bandcentre frequency

Figure 5. Examples of 1/3 octave band power spectra of the microphone output for 9 mm thick obstacle in the wake-side of the vocal cord jet. The figures of group **A** are for the obstacle 51 mm downstream of the nozzle exit with the microphone at its side. Figures in group **B** are for the microphone set far downstream, group **C** is for the obstacle further downstream, with the microphone at the side. Other details as in figure 2.

3.2 *Simulation for the inhalation phase*

During inhalation, a jet flow is formed at the vocal cords. An obstacle immersed in the jet may generate sound different from that in a uniform flow. In order to simulate this situation, a half nozzle is set at the inlet of the duct to make a half jet (it can hardly be expected that a jet in the human airway be positioned at the centre-line, without attachment to a side wall). An obstacle, as shown in figure 1, with thickness 5 mm or 9 mm, is set downstream. The obstacle is always set on the wall opposite the paper wall. The position of the obstacle relative to the nozzle (or equivalently, the jet flow) is changed by changing the location of the obstacle and attitude of the nozzle (vocal cords) on various walls. Results show that the dependence of the sound increment on the flow parameters is often different, even qualitatively, from that in the usual duct flow. Investigations on these cases are still going on. Several remarkable results are presented below. In the various configurations investigated, the level of spectral components at the "lower" frequencies (as referred to in the previous section) varies generally as U^6, though with varying amounts of scatter.

3.2a *Downstream obstacle on the same side as the half nozzle*: Figure 5 presents examples of 1/3 octave band power spectra of the microphone output for a 9 mm thick obstacle in the wake-side of the vocal-cord jet. Note that the nozzle block has a thickness of 12 mm, and the obstacle is in the wake of the nozzle. The figures of

group A (figure 5A) are for the obstacle 51 mm downstream of the nozzle exit with the microphone at its side. The sound is indeed increased by the introduction of the downstream obstacle, but the increase in this case is not so remarkable. The increase is remarkable only at the higher end of the velocity (U) range, and then only in a rather narrow frequency range. With the microphone set far downstream (figure 5B), increase in sound is by far more remarkable.

If the obstacle is shifted further downstream to 106 mm from the nozzle exit, increase in sound becomes more than in the case of A, as shown in figure 5C. The increase is more remarkable at higher flow velocities. In this case, with the obstacle further downstream, the increase in the microphone output is greater near the obstacle; hence the sound in this configuration remains less than that in the case B. The peak sound level after increase approximately scales as U^6 in this case too.

In the above results, in some cases, a greater increase in sound due to the obstacle is observed with the microphone far downstream. This fact may suggest the presence of sound due to unsteady reattachment of the flow on the wall.

Next, the downstream obstacle with thickness (or height) of 5 mm is tested. In this case, its axial location is of further importance. When it is placed 51 mm downstream of the nozzle exit, its presence causes a hardly detectable increase in the sound, as shown in figure 6A. This is easy to understand because the thin obstacle would be well out of the jet flow, in the dead-water region of the nozzle which is 12 mm thick. When the 5 mm thick obstacle is located 106 mm downstream of the nozzle exit, however, the sound increase is quite remarkable over a very wide range of frequency despite its small thickness, as shown in figure 6B. The extent of increase due to the obstacle seems to be a little more for higher flow velocities. The possible causes of such remarkable increase, will be discussed later.

3.2b *Downstream obstacle on the opposite side of the half nozzle*: In this configuration, the jet flow made by the simulated vocal cords (the half nozzle) directly impinges on the downstream obstacle model. Typical results are presented in figure 7. With a 9 mm thick obstacle (the thicker one), sound is virtually always increased by the introduction of an obstacle. For the 51 mm thick obstacle downstream the nozzle exit and the microphone near the obstacle, as shown in figure 7A, the increase is similar for high and low flow velocity U values. This is essentially the same for the microphone 90 mm downstream of the obstacle, as shown in figure 7B. However, it may be noted that in the latter the highest U results in the least amount of relative increase, while in the former the highest U results in the greatest increase.

With the 9 mm thick obstacle set further downstream, namely at 106 mm downstream of the nozzle exit, the sound due to the obstacle is usually rather remarkable. The relative increase is in all cases smaller for larger U, as revealed by examining figures 7C and D, for the microphone at the side or far downstream of the obstacle.

With the thinner, 5 mm thick obstacle set 51 mm downstream of the half nozzle exit, the increase in sound is small. More important from the practical point of view, the deformation in the spectral pattern is difficult to detect, as seen in figures 8A. For the thin obstacle set for (106 mm) downstream of the nozzle exit shown in figures 8B, increase in sound becomes detectable at *lower velocities*, while being negligible at high velocities. Unlike in some of the foregoing cases (e.g. figure 7), the dependence on U is the same in this case for both the near and far downstream microphone positions.

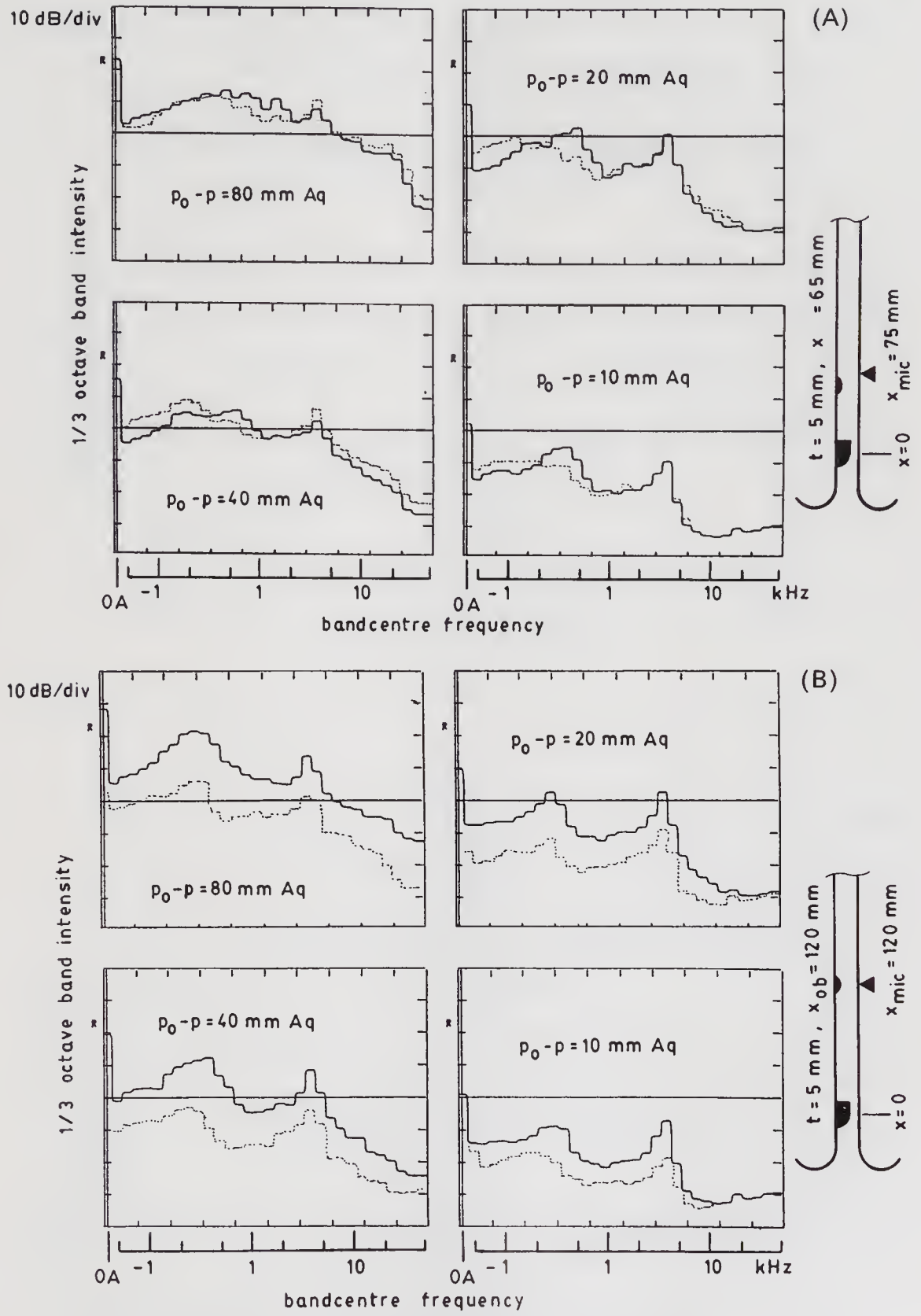
10 dB/div
(A)
p_0-p = 20 mm Aq
p_0 -p = 80 mm Aq
p_0 -p = 10 mm Aq
p_0 -p = 40 mm Aq
1/3 octave band intensity
t = 5 mm, x = 65 mm
x_{mic} = 75 mm
x = 0
0A -1 1 10 kHz
bandcentre frequency
10 dB/div
(B)
p_0 -p = 20 mm Aq
p_0-p = 80 mm Aq
p_0-p = 40 mm Aq
p_0 -p = 10 mm Aq
1/3 octave band intensity
t = 5 mm, x_{ob} = 120 mm
x_{mic} = 120 mm
x = 0
0A -1 1 10 kHz
bandcentre frequency

Figure 6. Examples of 1/3 octave band power spectra of the microphone output for 5 mm thick obstacle in the wake-side of the vocal cord jet. The figures of group **A** are for the obstacle 51 mm downstream of the nozzle exit with the microphone near its side. Group **B** is for the obstacle further downstream, with the microphone near the side.

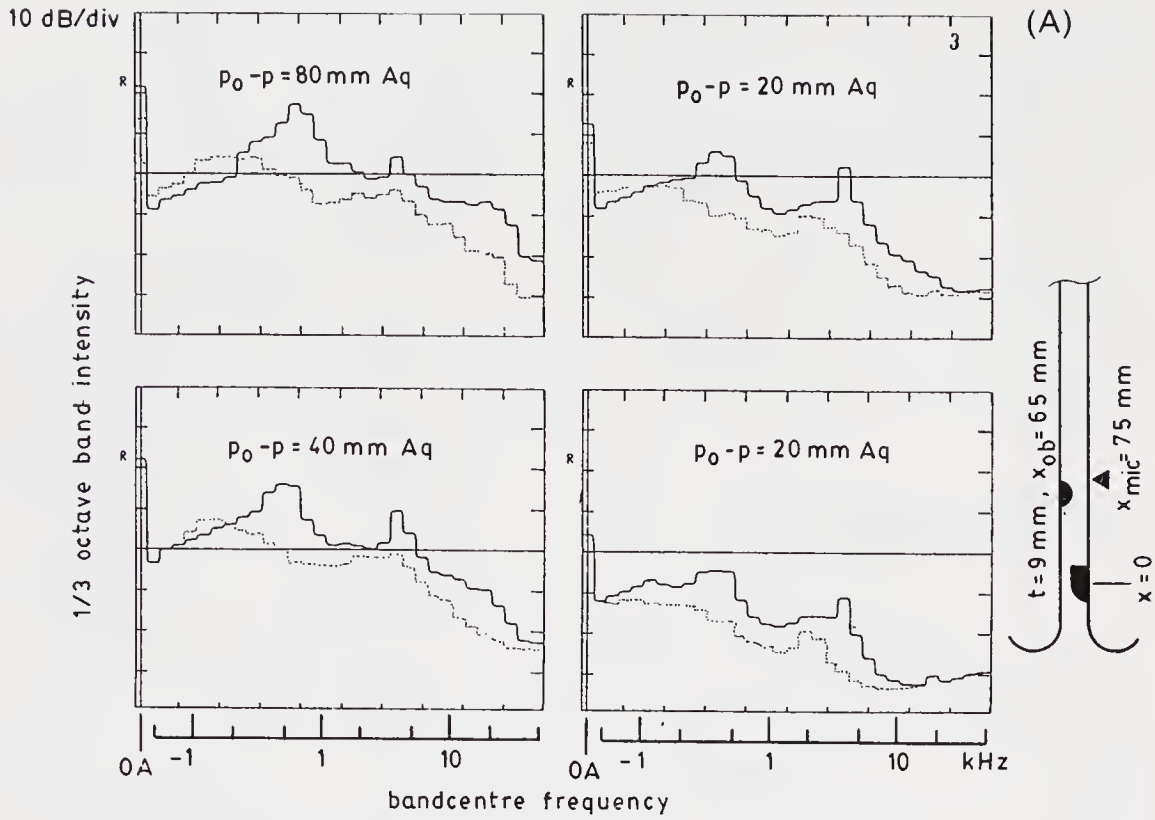
10 dB/div
(A)
3
P_0 -p = 80 mm Aq
P_0 -p = 20 mm Aq
P_0 -p = 40 mm Aq
P_0 -p = 20 mm Aq
1/3 octave band intensity
t = 9 mm, x_{ob} = 65 mm
x_{mic} = 75 mm
x = 0
0A -1 1 10 kHz
bandcentre frequency

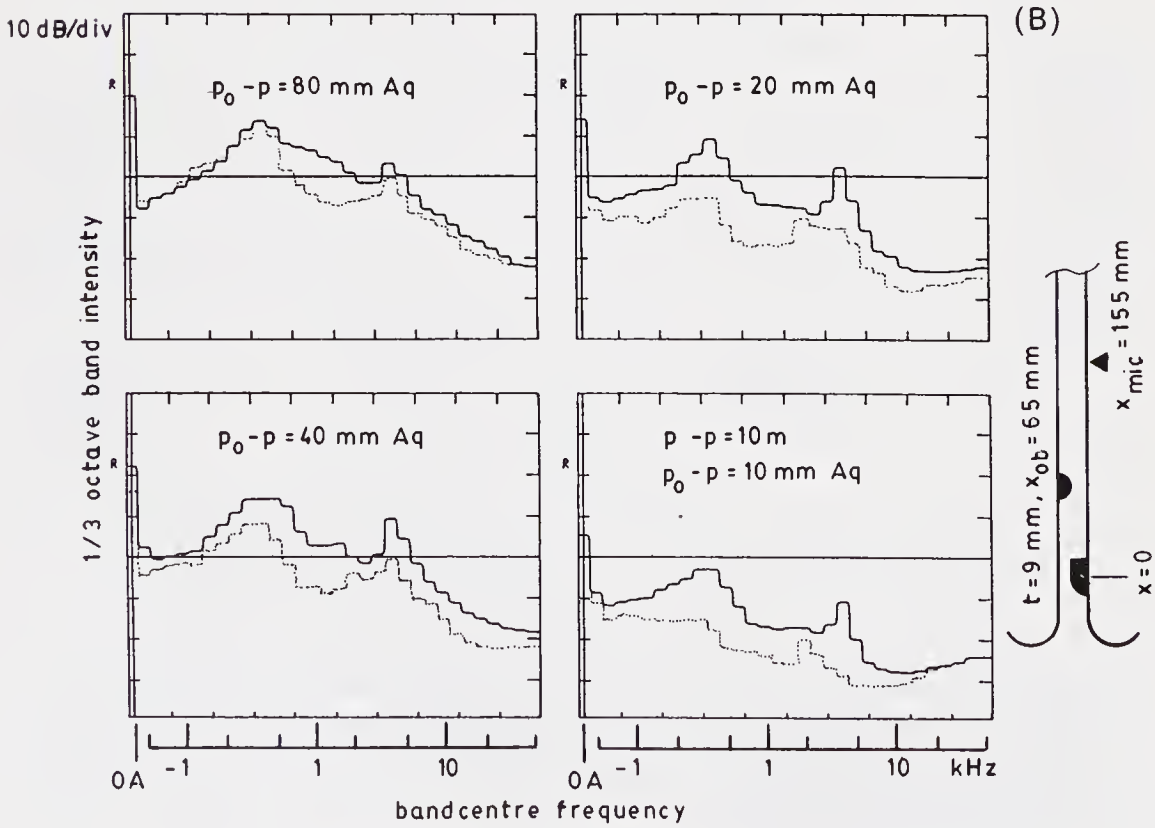
10 dB/div
(B)
P_0 -p = 80 mm Aq
P_0 -p = 20 mm Aq
P_0 -p = 40 mm Aq
p -p = 10 m
P_0 -p = 10 mm Aq
1/3 octave band intensity
t = 9 mm, x_{ob} = 65 mm
x_{mic} = 155 mm
x = 0
0A -1 1 10 kHz
bandcentre frequency

Figure 7A & B (continued)

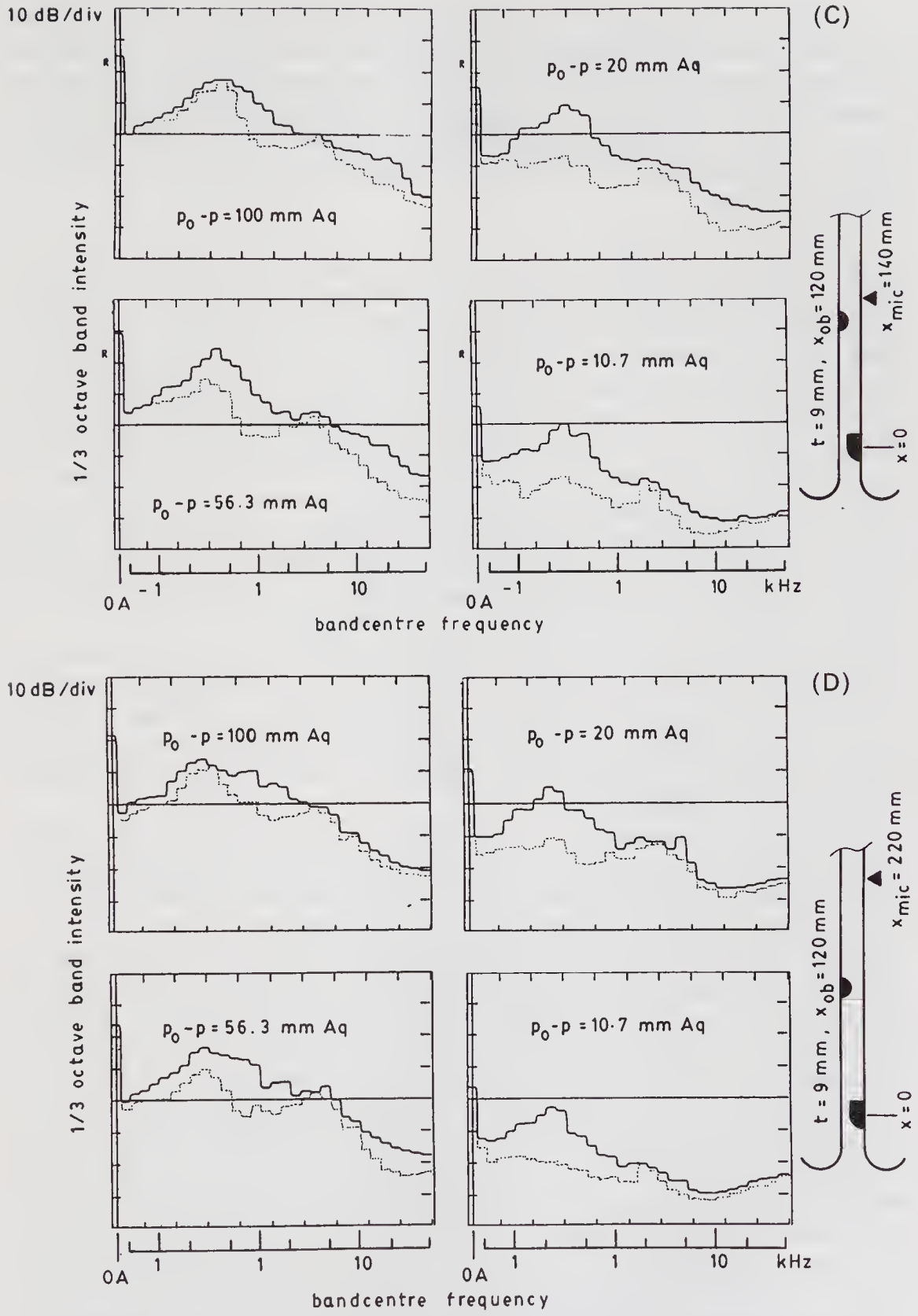

Figure 7. Examples of 1/3 octave band power spectra of the microphone output for 9 mm thick obstacle in the jet from the vocal cords. The figures of group **A** are for the obstacle 51 mm downstream of the nozzle exit with the microphone near its side, while those in group **B** are for the microphone far downstream.

The group **C** figures are for the 9 mm thick obstacle at the far downstream position, with the microphone near the side. The group **D** figures are for the microphone further downstream.

3.2c *Downstream obstacle on the wall adjacent to the half nozzle*: When the half nozzle and the downstream obstacle have axes crossing each other, that is, the former is set laterally while the latter is set vertically, a little less than half of the obstacle is immersed in the jet flow. In this configuration, although there is certainly some increase of sound by the downstream obstacle, a distinct feature to be contrasted with the other cases has not been identified yet, partly because the analysis of results is still not complete.

3.2d *Sensitivity of separation and reattachment to flow disturbances*: As shown in the § 3.1 (by figure 4), the main part of the sound increment due to an obstacle is caused by unsteady separation of flow on the round convex surface of the obstacle, with possible supplementation by unsteady reattachment of flow on the downstream wall. This should be essentially valid in the case of obstacles in a non-uniform flow also. Unlike in the former case, where sound increment depends on flow velocity and other parameters in a rather simple way, in this case the (relative) increment of sound often shows peculiar dependence on flow parameters and microphone position.

Although the spectral level after increase scales roughly as U^6 in all the cases, the relative amount of increment often varies unexpectedly. In the following, possible explanations for it will be given. Here the author should confess that although they are based on his previous experimental observations, they still might belong to the realm of speculations; efforts to verify them are still going on.

First, when a greater increase in the sound is observed with the microphone at a position farther downstream, the increment is likely to be due to unsteady reattachment of the flow separating at the obstacle, though direct evidence for this is not yet obtained. This conjecture may explain the results in figures 5B in comparison with figures 5A. Dependence of sound on flow velocity may be interpreted in the same way as that of unsteady separation.

According to the author's experiences in previous experimental investigations on related situations, the unsteadiness of the separation of flow (boundary layer) on a convex wall very critically depends on the on-coming flow disturbances under certain situations. The resulting sound should vary in the same way, of course.

A purely laminar boundary layer separates itself quite calmly, making virtually no additional sound (except the jet mixing noise). A fully turbulent boundary layer does separate itself unsteadily, and causes remarkable increase in the sound generated. However, under some conditions, which were later determined by the author and his co-worker as intermittent turbulent boundary layers (Ouwa *et al* 1989, 1991) very violent swinging of the separation and very greatly increased generation of sound take place (Sakao & Hiramoto 1983; Sakao 1984). The increase in sound power amounts up to 15 dB over the case of a developed turbulent boundary layer, in the frequency range where the level is highest. The amount of sound depends on the disturbances in the flow, especially in the boundary layer. In the present experiment too, a similar situation can be present. Then, it is possible that increased jet velocity results in increased (or decreased, possibly) turbulence levels, and steadier separation behaviour, and hence in reduced (on a relative scale) sound generation, as well as the reverse variation. Such a change should explain the variations shown in figures 7B, C, and 8B, while figures 6B and 7A may be examples of the "reverse" variation above. If a similar situation should occur for reattachment after separation, then the results in figures 7D seem plausible. The disturbance level naturally also depends on the distance from the "vocal cords" nozzle as well as on the velocity, and a larger

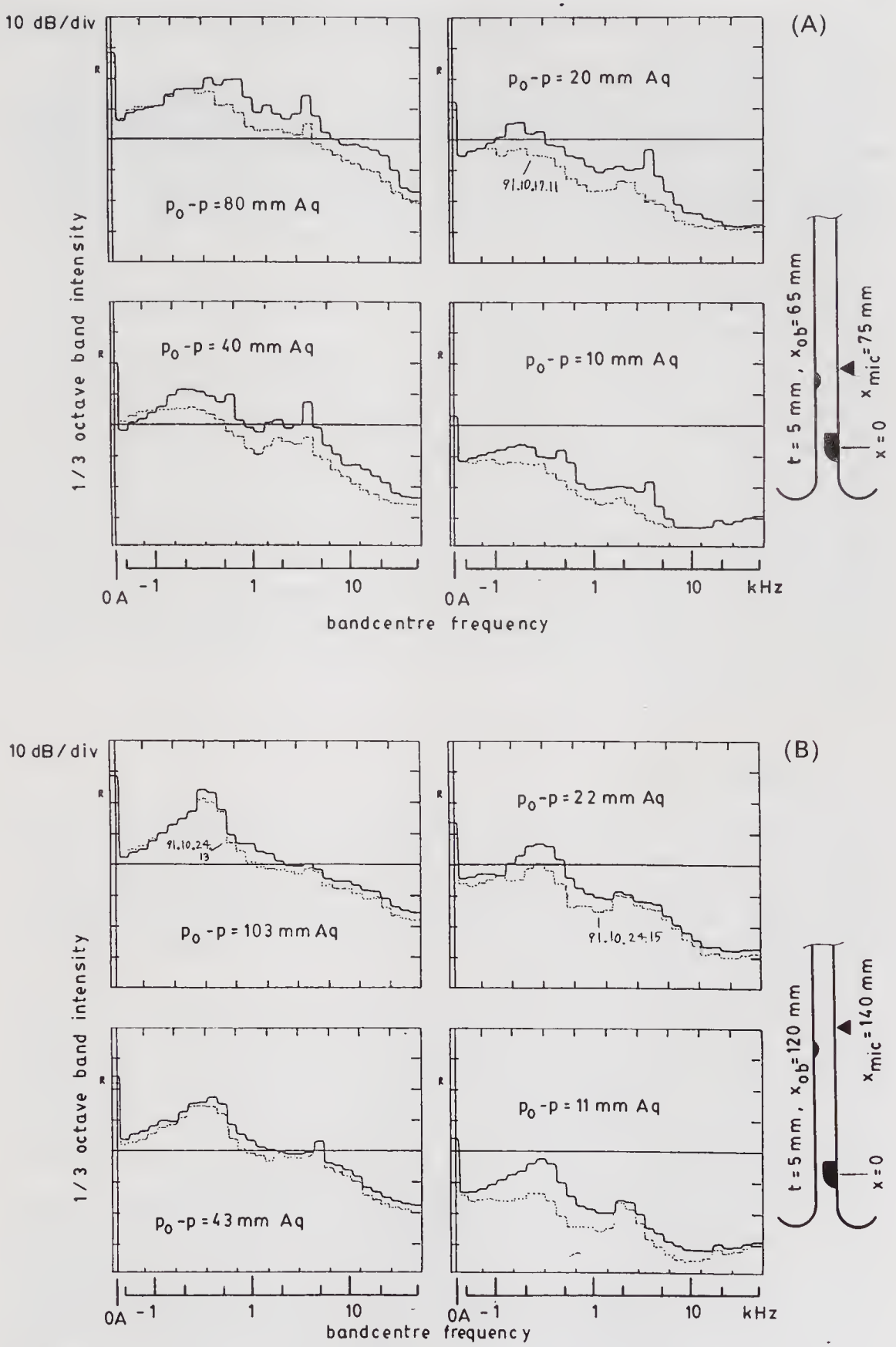

Figure 8. Examples of 1/3 octave band power spectra of the microphone output for a 5 mm thick obstacle in the jet from the vocal cords. The figures of group **A** are for the obstacle 51 mm downstream of the nozzle exit with the microphone near its side, while those in group **B** are for the obstacle far downstream.

increase in sound at the downstream position of the obstacle, as in figures 5C, 6B, and 8B, is also possible.

Since the unsteadiness of separation or reattachment and the resulting sound are not necessarily less for the thinner obstacle, the fact that the thinner obstacle causes quite a remarkable increase in sound, as seen in figure 6B, does not cause surprise.

Summarising, unsteady separation and reattachment of flow on convex obstacle surface and wall may explain the seemingly peculiar behaviour of the incremental sound, though further investigations are necessary to confirm it.

4. Some remarks on the stethoscope

Doctors use a stethoscope to examine a human body through sound. The usual stethoscope has long tubings connecting a vessel, like a shallow cup, and the ears. Such tubings result in very poor acoustic characteristics of the stethoscope, as may easily be conceived. According to the author's test (though of preliminary nature) it exhibits strong resonance and anti-resonance (peaks and valleys) alternately. Thus the doctors seem to be accustomed not to hear, or get information from, the high frequency part of sound, even through microphones and data-processing machines. There are some attempts to improve the situation (Pastercamp *et al* 1992), and even standardise the sound-sensing apparatus for a human body. The author, with Professor Sato and Doctor M Mori of the Tokyo National Chest Hospital, is engaged in one such attempt now.

5. Concluding remarks

Sound related with an obstacle in the human airway can be detected from outside through the soft tissues, as is a well-known fact. Our experiments reveal that sound signals easily detectable from outside may be generated aerodynamically, inside a human airway, at least in the larger tube, by the presence of a rather small obstacle there. Though it still needs intense effort to bring such a diagnostic method into practical use, the prospect does exist.

So far, in the model experiments, it is easy to compare absolute levels of observed sound (or quasi-sound). In practical applications, however, variation of conditions which are out of control (for instance, the fat layer thickness) would make the absolute level of sound almost meaningless. Even in such a case, the spectral (or similar) pattern would give important information, allowing some compensation for the frequency characteristics of body tissues. In this lecture, the author deliberately concentrated on the spectral pattern, based on such considerations.

The work presented here has been supported by Mr H Honda, President of Honda Manufacturing Company, Ltd. It is very gratefully acknowledged that the investigation was triggered by a question from Dr M Mori (Tokyo National Chest Hospital) to Prof H Sato, and started at the initiative of the latter, who has given invaluable and continuous help. Thanks are extended to members of the Breath Flow Research Group (presided over by Prof Sato), whose vivid discussions have been sources of pleasant stimulation. The use of a paper sheet as the wall material was suggested by Dr Mori during discussions.

References

Lighthill M J 1952 On sound generated aerodynamically I. General theory. *Proc. R. Soc. London* A211: 564–587

Ouwa Y, Sakao F, Matsuoka Y 1989 Unsteady separation of boundary layers on a two-dimensional convex wall as influenced by flow disturbances. *Proc. 4 Asian Congress on Fluid Mechanics* (Hongkong) 2: A252–255, also Ouwa *et al* 1991 *Nagare* 10: 240 (in Japanese)

Pasterkamp H, DeFrain P D, Kraman S S, Wodicka G R 1992 Performance of air-coupled and contact sensors in lung sound measurements. *Prep. 17th Int Conf. Lung Sounds, Helsinki* pp. 35–55

Sakao F 1984 Noise of jets from modified nozzle geometry – Dependence of unsteady behaviour of separating flow along a convex wall on disturbances in the flow. *Nagare* 3: 51–68 (in Japanese)

Sakao F, Hiramoto M 1983 Some effects of nozzle-lip geometry on jet noise. *Proc. 2nd Asian Congress on Fluid Mechanics* (Beijing: Science Press) pp. 874–879

Some recent developments in the theory of boundary layer instability

P K SEN

Department of Applied Mechanics, Indian Institute of Technology, Delhi, Hauz Khas, New Delhi 110016, India

Abstract. The stability of boundary-layer flow over a flat-plate is investigated after taking into account the effects of boundary-layer growth. A critical review and analysis of earlier work is presented, mainly for those works that use an inhomogeneous Orr–Sommerfeld equation and a solvability condition to obtain corrections for the growth-rate based on the quasi-parallel (QP) approximation. During the course of this review and analysis an important result is proven; viz., for a ray, the basic spatial periodicity of the disturbance wave is in *dimensional* space. Thereafter the energy integral equation is invoked, and an optimal monitorable property is found that has the same growth-rate as given by the eigensolution of the associated homogeneous problem. This also leads to the optimal normalisation of the eigenfunction at different downstream stations along the plate. A surprising result found is that the past non-parallel results can be virtually totally reproduced based on the QP-approximation and using the present methodology. And, by using the present methodology for the full non-parallel problem, the results obtained are in very much better agreement with past experimental results, and with the results of Smith based on the triple-deck theory.

Keywords. Stability; flat-plate; boundary-layer; non-parallel effects.

1. Introduction

This paper will be confined to the case of boundary layer flow over a flat plate, and will address itself to the non-parallel effects.

Past work on the above can be broadly divided into four categories.

Category I is based on the triple-deck theory developed by Smith (1979), followed by many subsequent developments of this theory. The theory is mathematically proper, but perhaps too elaborate to be of immediate practical value, for instance for e^n-calculations.

Category II is based on the direct numerical simulations of the Navier–Stokes equations, mainly contributed to by Fasel (1976) and Fasel & Konzelmann (1990). The elegant methodology developed can be used to cross-check results based on other analytical theories.

Category III works have an inhomogeneous Orr–Sommerfield equation, and the solvability condition determines the correction to the eigenvalue or growth-rate. Studies in this category were pioneered by Bouthier (1972, 1973) and Gaster (1974), followed by many others, important among these being the works of Saric & Nayfeh (1975, 1977), Van Stijn & Van de Vooren (1983), Bridges & Morris (1987) and Bertolotti *et al* (1992). In this category the results of Gaster (1974) have now come to be looked upon as standard, and all subsequent workers have eventually reproduced Gaster's results. Theoretical interest mainly centres around the studies in category III, and these are given due consideration in the present work.

Category IV works are attempts to modify the Orr–Sommerfeld equation itself. The pioneering effort was by Barry & Ross (1970). Efforts thereafter are far and few except by Dey *et al* (1990) and Sen & Vashist (1987; details given in Vashist 1988).

The first experiments were carried out by Schubauer & Skramstad (1947), and later by Ross *et al* (1970), followed by a good many others like Babenko & Kozlov (1973), Kachanov *et al* (1977) and Strazisar *et al* (1975). The conclusion is that the results of Ross *et al* (1970) are amply supported by subsequent experiments, and therefore may be considered as standard results.

The unresolved dilemma in the entire exercise is that the theoretical results of Gaster (1974) are quite at variance with the experimental results of Ross *et al* (1970) (which are again standard results for experiments). And, to add to the fray, the numerical simulations of Fasel & Konzelmann (1990) seem to support the results of Gaster. It is in the backdrop of this dilemma that the present work was taken up.

2. The quasi-parallel approximation

To understand the details of the full non-parallel problem, we have to look carefully at the quasi-parallel (QP) approximation. Classically, the disturbance stream-function ψ is expressed as

$$\psi = \phi(y)\exp[\imath(\alpha x - \beta t)], \tag{1}$$

which leads to the well-known Orr–Sommerfeld (OS) equation:

$$(\bar{u} - \beta/\alpha)(\phi'' - \alpha^2\phi) - \bar{u}''\phi + (\imath/\alpha \mathrm{R})(\phi'''' - 2\alpha^2\phi'' + \alpha^4\phi) = 0, \tag{2}$$

where $\bar{u}$ is the mean velocity, R is the Reynolds number given as $\mathrm{R} = U_\infty \delta/\nu$, $\delta = 5(\nu X/U_\infty)^{1/2}$, U_∞ is the freestream speed, and primes ($'$) denote differentiation with respect to y. Also used later is the Reynolds number R* based on the displacement thickness δ^*. Morever, α is the spatial wavenumber, β is the temporal frequency, and, the complex phase speed is given as $c = \beta/\alpha$.

The coordinate system is shown in figure 1. There is no length scale in the problem

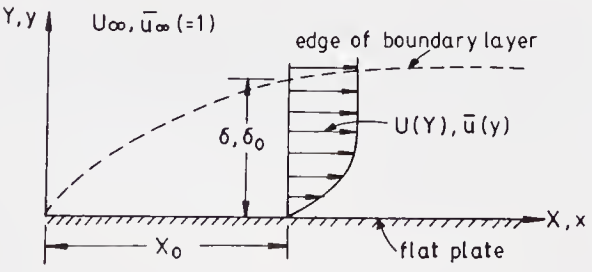

Figure 1. Sketch showing the coordinate system.

because $\delta \sim X^{1/2}$, and X is a coordinate. It is due to the genius of Prandtl that he was able to extract a length scale δ as a physical measure of the boundary-layer thickness, where apparently no length scale exists. Along with δ, also defined is δ_0 which numerically equals δ at a given station $X = X_0$; but δ_0 is assumed to have no X-dependence. Dimensional and non-dimensional quantities are written respectively in capital and lower case, while U_∞ is the velocity scale and δ or δ_0 is used as the length scale.

We next look at the OS-equation (2). There is one non-parallel correction already there because $\bar{u}$ is the Blasius mean-velocity. Further, in the form of the exponent $\exp[\imath(\alpha x - \beta t)]$ how is x to be interpreted? Is it as $x = X/\delta$, or as $x = X/\delta_0$? In case of the former, periodicity will be in similarity space, but in case of the latter, periodicity will be in dimensional space. This important question is ignored in the QP-approximation. Next, in the function $\phi(y)$, y could be interpreted as $y = Y/\delta$ or as $y = Y/\delta_0$; in the former case y becomes the Blasius similarity variable, and in the latter case y is like the dimensional variable. A look at (2) shows that as the disturbance moves downstream, $\mathrm{R} = U_\infty \delta/\nu$ increases because δ increases. Therefore, at every local station, the local value of δ becomes the length scale, and thus, in the function $\phi(y)$, the natural interpretation for y is $y = Y/\delta$, i.e. as the similarity variable.

The boundary conditions for (2) are $\phi, \phi' = 0$ at $y = 0$, and $\phi, \phi' = 0$ at $y = \infty$. The second set for $y = \infty$ is replaced by the behaviour of $\phi(y)$ at the edge of the boundary layer; viz. $\phi \sim \exp[-\alpha y]$ for $y \geqslant 1$. The OS-equation (2) and the boundary conditions give an eigenvalue problem, the characteristic equation becoming $\mathscr{F}(\alpha, \beta, \mathrm{R}) = 0$. In the spatial problem considered herein, β and R are chosen real and α is determined as an eigenvalue, i.e. $\alpha = \alpha_r + \imath\alpha_i$, and $-\alpha_i$ gives the spatial growth rate. Further, for a ray, i.e. for a disturbance wave moving downstream at a fixed temporal physical frequency (i.e. $F = \beta/\mathrm{R} \times 10^6$ is constant), β is known at every station in X as $\beta = F \times \mathrm{R} \times 10^{-6}$. Thus the eigenvalue problem reduces to $\mathscr{F}(\alpha, \beta(\mathrm{R}), \mathrm{R}) = 0$ or $\mathscr{F}(\alpha, \mathrm{R}) = 0$. Now, at every different station in X, R is different and we therefore have a different eigenvalue for α at every different X. Note that R and X become synonymous in the sense that $\mathrm{R} \sim X^{1/2}$. Also at every X we have a new eigenfunction $\phi(y)$. The conclusion, therefore, is that as a disturbance ray moves downstream, R increases, and different values of α and different $\phi(y)$ are obtained for each different value of R.

Keeping this in view, the original form of (1) may be improved:

$$\psi = \phi(y, x)\exp[\imath(\int \alpha \mathrm{d}x - \beta t)]. \tag{3}$$

The above form may be substituted in the QP-primitive which is given next. We consider the quantities u, v as decomposed into mean (with an overbar) and fluctuating (with a prime) parts. Also the fluctuating stream-function is ψ and the fluctuating vorticity is ω'. This gives

$$u = \bar{u} + u', \quad v = \bar{v} + v', \quad p = \bar{p} + p', \quad \omega' = [(\partial v'/\partial x) - (\partial u'/\partial y)] = -\nabla^2 \psi. \tag{4}$$

The equations for u' and v' after linearising and ignoring $\bar{v}$ and $\partial\bar{u}/\partial x$ are given below:

$$\frac{\partial u'}{\partial t} + \bar{u}\frac{\partial u'}{\partial x} + v'\frac{\partial \bar{u}}{\partial y} = -\frac{\partial p'}{\partial x} + \frac{1}{\mathrm{R}}\left(\frac{\partial^2 u'}{\partial x^2} + \frac{\partial^2 u'}{\partial y^2}\right), \tag{5}$$

$$\frac{\partial v'}{\partial t} + \bar{u}\frac{\partial v'}{\partial x} = -\frac{\partial p'}{\partial y} + \frac{1}{\mathrm{R}}\left(\frac{\partial^2 v'}{\partial x^2} + \frac{\partial^2 v'}{\partial y^2}\right). \tag{6}$$

Also the continuity equation for the disturbances is

$$\frac{\partial u'}{\partial x} + \frac{\partial v'}{\partial y} = 0. \tag{7}$$

Further, the equation for $\nabla^2\psi = -\omega'$ is given as

$$\frac{\partial}{\partial t}(\nabla^2\psi) + \bar{u}\frac{\partial}{\partial x}(\nabla^2\psi) - \frac{\partial\psi}{\partial x}\frac{\partial^2\bar{u}}{\partial y^2} - \frac{1}{\mathrm{R}}\nabla^4\psi = 0. \tag{8}$$

The set of equations (4)–(8) above are called QP-primitive, the terms neglected being $\bar{v}$ and $\partial\bar{u}/\partial x$. Also, in deriving the original OS-equation (2), the implicit derivative $(\partial\phi/\partial x)_{\mathrm{IM}} = (\partial\phi/\partial y)\cdot(\partial y/\partial x)$ is neglected, and so is the explicit derivative $(\partial\phi/\partial x)_y$. Also neglected is $\partial\alpha/\partial x$.

Now, remembering (3), we retain the explicit derivative $(\partial\phi/\partial x)_y$ (hereafter referred to as $\partial\phi/\partial x$), and we also retain $\partial\alpha/\partial x$. The other terms, viz. $\bar{v}$, $\partial\bar{u}/\partial x$, and $(\partial\phi/\partial x)_{\mathrm{IM}}$ continue to be neglected. Also $\partial^n\alpha/\partial x^n$, $\partial^n\phi/\partial x^n$, for $n \geqslant 2$, are neglected as these are small. The resulting differential equation is of the form

$$L\phi = P_1\frac{\partial\phi}{\partial x} + P_2\frac{\partial\alpha}{\partial x}, \tag{9}$$

where L is the OS operator (see (2)), P_1 is a known operator and P_2 is a known expression. One way of solving (9) is to express $\phi = \phi_0 + \varepsilon\phi_1$, $\alpha = \alpha_0 + \varepsilon\alpha_1$, where ε is a small parameter $O(\mathrm{R}^{-1})$. This gives

$$L\phi_0 = 0, \tag{10a}$$

$$\varepsilon L\phi = P_1(\partial\phi_0/\partial x) + P_2(\partial\alpha_0/\partial x) + P_3\alpha_1. \tag{10b}$$

To solve (10b), we need to know $\partial\alpha_0/\partial x$ and $\partial\phi_0/\partial x$. For this purpose, one of the techniques is to differentiate the OS-equation (10a). Remembering that $x = X/\delta \sim X^{1/2}$ and $\mathrm{R} \sim X^{1/2}$, we find that $(\partial/\partial x) \sim (\partial/\partial\mathrm{R})$. So we put $\chi = \partial\phi_0/\partial\mathrm{R}$ and obtain $(\partial/\partial\mathrm{R})[L\phi_0]$ keeping in mind that $L\phi_0 = 0$. This gives

$$\begin{aligned} L\chi &+ \left[\left(-\frac{1}{\alpha}\frac{\partial\beta}{\partial\mathrm{R}} + \frac{\beta}{\alpha^2}\frac{\partial\alpha}{\partial\mathrm{R}}\right)(\phi'' - \alpha^2\phi)\right] - \left[(\bar{u} - \beta/\alpha)\cdot 2\alpha\frac{\partial\alpha}{\partial\mathrm{R}}\phi\right] \\ &- \left[\frac{\imath(\alpha + \mathrm{R}(\partial\alpha/\partial\mathrm{R}))}{(\alpha\mathrm{R})^2}(\phi'''' - 2\alpha^2\phi'' + \alpha^4\phi)\right] \\ &- \left[\frac{\imath 4\alpha(\partial\alpha/\partial\mathrm{R})}{\alpha\mathrm{R}}(\phi'' - \alpha^2\phi)\right] = 0, \end{aligned} \tag{11}$$

where, in (11), the subscript '0' has been dropped from α_0 and ϕ_0. Written in operator form, (11) becomes

$$L\chi + T_1 - T_2 - T_3 - T_4 = 0. \tag{12}$$

It can be proved that

$$\int_0^\infty \theta(T_1 - T_2 - T_3 - T_4)\mathrm{d}y = 0, \tag{13}$$

where, θ is the adjoint eigenfunction. This is because

$$\int_0^\infty \theta L(\chi)\mathrm{d}y = B(\theta,\chi)|_0^\infty + \int_0^\infty \chi \bar{L}(\theta)\mathrm{d}y, \tag{14}$$

where $B(\theta,\chi)|_0^\infty$ is the bilinear concomitant, and $\bar{L}(\theta)=0$, because it is the adjoint OS equation. Since $\theta,\theta',\chi,\chi'=0$ both at $y=0$ and at $y=\infty$, $B(\theta,\chi)|_0^\infty=0$. This proves (13). Note that $L\chi\neq 0$, because the outer boundary condition of χ is different from ϕ_0; viz. $\phi_0\sim\exp[-\alpha y]$, $\chi\sim y\exp[-\alpha y]$ for $y\geqslant 1$.

Equation (13) enables one to determine $\partial\alpha/\partial x$. Nevertheless, $\partial\alpha/\partial x$ could also have been determined as $\Delta\alpha/\Delta x$, i.e. by numerically differentiating the eigenvalues α at different stations in x.

Next, we examine the orders of magnitude of the various terms that appear in (11)–(13). We remember that $\phi''\sim\theta$, and, we may anticipate that $\partial\alpha/\partial\mathrm{R}\sim O(\mathrm{R}^{-1})$. Also, the scale of the viscous critical layer gives the nth derivative of ϕ as $\phi^{(n)}\sim O(\mathrm{R}^{n/3})$ in the critical layer, and $\phi^{(n)}\sim O(1)$ everywhere else. Thus $T_4\sim o(\mathrm{R}^{-1})$ (i.e. $<O(\mathrm{R}^{-1})$) everywhere. Further, since $\phi''''/\mathrm{R}\sim(u-c)\phi''\sim\phi$ inside the *critical layer only*, $T_3\sim O(\mathrm{R}^{-1})$ inside the critical layer and $T_3\sim O(\mathrm{R}^{-2})$ elsewhere. Hence the lowest order in T_2, T_3, T_4 is $O(\mathrm{R}^{-1})$ with $T_2\geqslant T_3>T_4$.

Next we examine the terms given by the integrals $V_i=\int_0^\infty\theta T_i\mathrm{d}y$, $i=1,2,3,4$, with reference to (13). Corresponding to V_1 and V_4, there appears in these terms the integral $\int_0^\infty\theta(\phi''-\alpha^2\phi)\mathrm{d}y$, which is seen to have order $O(\mathrm{R})$. And, in the term corresponding to V_2, there appears the integral $\int_0^\infty(\bar{u}-c)\phi\theta\mathrm{d}y$ which is $O(1)$; thus, $V_2=\int_0^\infty T_2\theta\mathrm{d}y\sim O(\mathrm{R}^{-1})$. It may be further deduced that $V_3=\int_0^\infty T_3\theta\mathrm{d}y\sim O(\mathrm{R}^{-2/3})$, and $V_4=\int_0^\infty T_4\theta\mathrm{d}y\sim O(\mathrm{R}^{-1})$. Thus we have $V_3>V_2,V_4$. Finally therefore we see from (13) that we must have

$$\int_0^\infty T_1\theta\mathrm{d}y\sim\int_0^\infty T_3\theta\mathrm{d}y\sim O(1/\mathrm{R}^{2/3}). \tag{15}$$

Remembering that $\int_0^\infty(\phi''-\alpha^2\phi)\theta\mathrm{d}y\sim O(\mathrm{R})$ in the term corresponding to V_1, we find that (15) can only be valid when, in the term T_1, we have the following satisfied:

$$\left(-\frac{1}{\alpha}\frac{\partial\beta}{\partial\mathrm{R}}+\frac{\beta}{\alpha^2}\frac{\partial\alpha}{\partial\mathrm{R}}\right)\sim O\left(\frac{1}{\mathrm{R}^{5/3}}\right)\sim o\left(\frac{1}{\mathrm{R}}\right). \tag{16}$$

Now for a ray $\partial\beta/\partial\mathrm{R}=\beta/\mathrm{R}$ and $\beta/\alpha=c$. Therefore, it is seen from (16) that

$$\frac{\partial\alpha}{\partial\mathrm{R}}=\frac{\alpha}{\mathrm{R}}+o\left(\frac{1}{\mathrm{R}}\right). \tag{17}$$

The above equation (17) formally proves that $\partial\alpha/\partial\mathrm{R}\sim O(1/\mathrm{R})$. Moreover, if one remembers that β is real, then it follows that

$$\frac{\partial\alpha}{\partial\mathrm{R}}=\frac{\alpha}{\mathrm{R}}+O\left(\frac{\varepsilon}{\mathrm{R}}\right), \tag{18}$$

where $\varepsilon\sim O(\alpha_i)\sim O(\mathrm{R}\cdot\partial\alpha_i\partial\mathrm{R})$. Thus (18) proves the following theorem:

Theorem 1. *For a ray, that is for a disturbance with a fixed temporal frequency, travelling downstream, the dimensional wavenumber α^+ is approximately constant so*

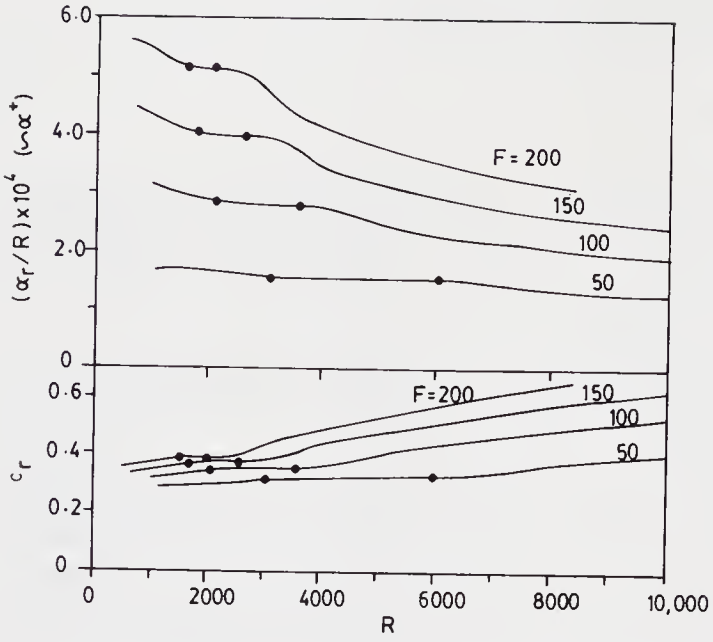

Figure 2. Illustration of approximate constancy of α^+ and c_r, for a fixed F, in the region inside, and outside neighbourhood, of the neutral-curve. Results based on the spatial OS-equation. Also $(\alpha_r/R) \sim \alpha^+$, $c_r = (F \times R)/\alpha_r \times 10^{-6}$, $R = U_\infty \delta/\nu$, and ● denotes neutral points.

long as α_i is small; in other words, the basic periodicity of the waveform is in dimensional space.

Figure 2 shows numerical evidence of the constancy of α^+ and of c_r, within and immediately outside the neutral-curve, i.e. for small values of $|\alpha_i|$. Note that with F constant and $\alpha^+ \sim \alpha/R$ approximately constant, the phase speed c_r will also be approximately constant. Moreover, upon plotting α_r versus R for constant F, it is seen that α_r obeys an equation of the form $\alpha_r = nR + \varepsilon$, in the range $|\alpha_i|$ small, i.e. in the range in which the viscous critical layer theory for near-neutral disturbances is valid. The value of n depends on F (e.g. $n = 4{\cdot}95 \times 10^{-4}$, for $F = 200$), and $\varepsilon \simeq 0{\cdot}035$ for a large range of F, i.e. for $50 \leqslant F \leqslant 200$.

Next we concentrate on the solution for χ. The solution for χ may be obtained from (12), in the following asymptotic form:

$$\chi = \chi_0 + \chi_1, \tag{19}$$

where $\chi_1/\chi_0 = O(R^{-1})$. Thus (11) and (19) give

$$L\chi_0 = 0, \tag{20}$$

$$L\chi_1 = -(T_1 - T_2 - T_3 - T_4), \tag{21}$$

where the right-hand side of (21) is subject to (13), and the outer form of χ_1 is $\chi_1 \sim y\exp[-\alpha y]\, y \geqslant 1$. It is evident that the solution for χ_0 is $\chi_0 = \lambda\phi_0$ where λ is arbitrary and the solution for χ_1 that is obtained from (21) is orthogonal to ϕ_0. Hence $\chi = \lambda\phi_0 + \chi_1$.

One is now in a position to determine the correction α_1 to the eigenvalue α_0 from (10b). This is done by applying the solvability condition

$$\int_0^\infty \theta[P_1(\partial\phi_0/\partial x) + P_2(\partial\alpha_0/\partial x) + P_3\alpha_1]\,dy = 0. \tag{22}$$

The arbitrary constant λ is determined from the choice of the particular property being monitored; like the inner or outer maximum of u', i.e. respectively $|u'|_{im}$ and

$|u'|_{om}$, or the kinetic energy integral (cf. Gaster 1974) $\int_0^\infty \{(|u'|^2 + |v'|^2)/2\} \mathrm{d}Y$. Thus, corresponding to each different monitored property a different α_i is obtained, and thus the neutral-curve corresponding to each monitored property is different.

The method detailed above, for solving for $\partial\alpha_0/\partial x$, $\partial\phi_0/\partial x$ and α_1, is lengthy and laborious. But the procedure brings out many important and interesting facets of the problem. So the procedure remains as the background theoretical information for other solution procedures, and for the problem in general.

An alternative and equivalent way of solving (9) is by using Gaster's (1974) method. Here a notional amplitude $A(x)$ is used to qualify (3), viz.,

$$\psi = A(x)\phi(y, x)\exp(\imath[\int \alpha \mathrm{d}x - \beta t]). \tag{23}$$

After expressing ϕ as $\phi = \phi_0 + \varepsilon\phi_1$, one gets

$$L\phi_0 = 0, \tag{24a}$$

$$\varepsilon L\phi_1 = P_4 + (1/A)(\mathrm{d}A/\mathrm{d}x)P_5, \tag{24b}$$

where, in (24b), P_4 and P_5 are known expressions containing the $\partial\alpha/\partial x$ and $\partial\phi_0/\partial x$ terms. The solvability condition,

$$\int_0^\infty \theta[P_4 + (1/A)(\mathrm{d}A/\mathrm{d}x)P_5]\mathrm{d}y = 0, \tag{25}$$

gives $(1/A)(\mathrm{d}A/\mathrm{d}x)$. And $\partial\alpha/\partial x$ and $\partial\phi_0/\partial x$ are respectively determined as $\Delta\alpha/\Delta x$ and $\Delta\phi_0/\Delta x$, i.e. by direct numerical differentiation of the solutions of the OS-equation at neighbouring stations in x. Whereas $\Delta\alpha/\Delta x$ can be uniquely determined, $\Delta\phi_0/\Delta x$ depends on the manner in which ϕ_0 has been normalised at each station in x. As illustration, figure 3 shows contiguous eigenfunctions normalised with the maximum kinetic energy norm $k_m = [(\overline{u'^2} + \overline{v'^2})^{1/2}]_{max}$. The steps necessary, therefore, in Gaster's method are as follows. Let P be any monitored property like $|u'|_{im}$, $|u'|_{om}$, etc. Then P may be expressed as $P = A\exp[-\alpha_i x]\bar{p}$, where $\bar{p} = \bar{p}(\phi, \tilde{\phi})$, i.e. a quadratic form of ϕ and its complex conjugate $\tilde{\phi}$. For example, $|u'|_{om} = A\exp[-\alpha_i x]\{\phi'\tilde{\phi}'\}_{om}^{1/2} = A\exp[-\alpha_i x]|\phi'|_{om}$. Hence the growth rate of P is given as

$$(1/P)(\mathrm{d}P/\mathrm{d}x) = -\alpha_i + [(1/A)(\mathrm{d}A/\mathrm{d}x) + (1/\bar{p})(\mathrm{d}\bar{p}/\mathrm{d}x)]. \tag{26}$$

Now ϕ is normalised at each station in x using *any* consistent norm. For instance,

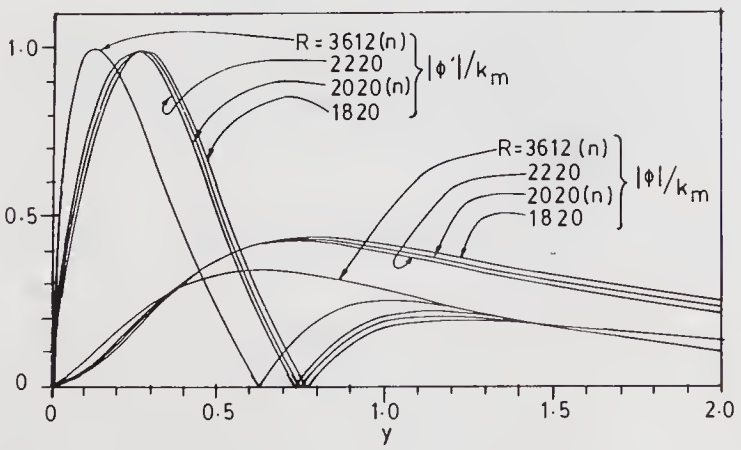

Figure 3. Illustration of local similarity. $|\phi'|/k_m$ and $|\phi|/k_m$ versus y, for $F = 100$ and different values of R. Also, (n) indicates neutral point, and, k_m is the maximum value of k in the range $0 \leqslant y \leqslant \infty$, where $k = (|\phi'|^2 + \alpha^2|\phi|^2)^{1/2}$ is the kinetic energy function. Results based on the modified OS-equation.

putting $\phi = 1 + 0i$ at $y = 1$ is a consistent normalisation. Thereafter $(1/\bar{p})(\mathrm{d}\bar{p}/\mathrm{d}x)$ is determined by numerically differentiating the neighbouring values of $\bar{p}$ with respect to x. Finally $(1/A)(\mathrm{d}A/\mathrm{d}x)$ is determined from (25). Gaster (1974) has shown that the final answer for $(1/P)(\mathrm{d}P/\mathrm{d}x)$ is unique, and is independent of the manner in which ϕ has been normalised. Thus in (26) there is only an exchange between the terms $(1/A)(\mathrm{d}A/\mathrm{d}x)$ and $(1/\bar{p})(\mathrm{d}p/\mathrm{d}x)$, with different norms for the normalisation of ϕ, the sum of the two being independent of the normalisation of ϕ. Using formulae like (26), Gaster (1974) was thus able to construct different neutral curves for different monitorable properties.

At this stage we enquire whether it is possible to find an *optimal monitorable property* P_0, the growth rate of which is just $-\alpha_i$, that is as given from the solution of the OS-equation. Thus, if P_0 is expressed as $P_0 = A\exp[-\alpha_i x]\bar{p}_0$, then, since $(1/P_0)(\mathrm{d}P_0/\mathrm{d}x) = -\alpha_i$, it follows from (26) that

$$(1/A)(\mathrm{d}A/\mathrm{d}x) + (1/\bar{p}_0)(\mathrm{d}\bar{p}_0/\mathrm{d}x) = 0. \tag{27}$$

Equation (27) also shows the way for an *optimal normalisation* of ϕ at every station in x. Remembering that $\bar{p}_0 = \bar{p}_0(\phi, \tilde{\phi})$, we note that the optimal normalisation of ϕ would be so as to keep $\mathrm{d}\bar{p}_0/\mathrm{d}x = 0$, or $\bar{p}_0$ as constant at every station in x. Such an optimal normalisation would render $\mathrm{d}A/\mathrm{d}x = 0$. Thus, with reference to (26), the growth rate of any other property $P(P \neq P_0)$ would be given as:

$$(1/P)(\mathrm{d}P/\mathrm{d}x) = -\alpha_i + (1/\bar{p})(\mathrm{d}\bar{p}/\mathrm{d}x). \tag{28}$$

In other words, the step given by (25) would be circumvented. Also, in (25), we have $\int_0^\infty \theta P_4 \mathrm{d}y = 0$. That is P_4 would become naturally orthogonal to ϕ_0. Moreover, $\partial\phi/\partial x$, calculated as $\Delta\phi/\Delta x$ using the optimally normalised ϕ_0, would be orthogonal to ϕ_0. Or $\partial\phi/\partial x$ will be like χ_1 and will not contain $\chi_0 = \lambda\phi_0$ (see (19)). One very important consequence of the orthogonality of χ_1 or $\partial\phi/\partial x$ to ϕ_0 is that $\partial\phi/\partial x$ does not have any influence on the eigenvalue problem or the associated homogeneous problem (see (10a) or (24a)). This being so, the eigenfunction ϕ_0 of the associated homogeneous equation may be assumed to be *locally similar* for the purposes of the eigenvalue problem because the explicit derivative $\partial\phi/\partial x$ does not appear in the eigenvalue problem, i.e. in the equation for the associated homogeneous problem. Actually numerical evidence for the local similarity of the eigenfunction may be seen in figure 3.

Reverting to the question of the optimal monitorable property, we note that such an optimal property P_0 has been lying hidden in the integral energy equation for stability given by Stuart (1957). This equation may be obtained by multiplying (5) and (6) respectively by u' and v', adding the two and averaging (either over one wavelength in x for the temporal problem or over one time period t for the spatial problem), and after carrying out some further algebra. The equation for the temporal problem was derived by Stuart (1957). For the spatial problem, this has been done in the present work (see Verma 1992). These are respectively given below:

$$\frac{\partial}{\partial t}\left[\int_0^\infty \left(\frac{\overline{u'^2} + \overline{v'^2}}{2}\right)\mathrm{d}y\right] = -\int_0^\infty \overline{u'v'}\frac{\partial\bar{u}}{\partial y}\mathrm{d}y - \frac{1}{\mathrm{R}}\int_0^\infty \overline{\omega'^2}\mathrm{d}y, \tag{29}$$

$$\frac{\partial}{\partial x}\left[\int_0^\infty \bar{u}\left(\frac{\overline{u'^2} + \overline{v'^2}}{2}\right)\mathrm{d}y + \int_0^\infty \overline{u'p'}\mathrm{d}y - \frac{1}{\mathrm{R}}\int_0^\infty \overline{u'\omega'}\mathrm{d}y\right]$$

$$= -\int_0^\infty \overline{u'v'}\frac{\partial\bar{u}}{\partial y}\mathrm{d}y - \frac{1}{\mathrm{R}}\int_0^\infty \overline{\omega'^2}\mathrm{d}y, \tag{30}$$

where, in (29) and (30), overbar means averaged quantity. The two terms on the right hand sides of (29) and (30) are respectively the production and dissipation integrals. The integral on the left of (29) is the kinetic energy integral. The three integrals on the left of (30), taken together, may be called the extended energy integral E^*, consisting of the kinetic energy integral weighted by $\bar{u}$, the u', p' correlation integral, and, the v', ω' correlation integral. The integrals in (30) may be expressed in terms of the Orr–Sommerfeld solution for the spatial problem, in the following manner:

$$(\mathrm{d}/\mathrm{d}x)[(I_1 + I_2 + I_3)\exp(-2\alpha_i x)] = (I_4 - I_5)\exp(-2\alpha_i x), \tag{31}$$

where, after putting $p' = p\exp[\imath(\alpha x - \beta t)]$ and $\omega' = \Omega\exp[\imath(\alpha x - \beta t)]$, one obtains the integrals I_n as follows:

$$I_1 = \int_0^\infty \bar{u}(|\phi'|^2 + |\alpha|^2|\phi|^2)\mathrm{d}y; \quad I_2 = \int_0^\infty (\phi'\tilde{p} + \tilde{\phi}'p)\mathrm{d}y; \tag{32a, b}$$

$$p = \frac{\mathrm{d}\bar{u}}{\mathrm{d}y}\phi - (\bar{u} - c)\phi' + \frac{1}{\imath\alpha\mathrm{R}}(\phi''' - \alpha^2\phi'); \quad I_3 = -\frac{1}{\mathrm{R}}\int_0^\infty \imath(\alpha\phi\tilde{\Omega} - \tilde{\alpha}\tilde{\phi}\Omega)\mathrm{d}y; \tag{32c, d}$$

$$\Omega = \phi'' - \alpha^2\phi; \quad I_4 = \int_0^\infty \imath(\alpha\phi\tilde{\phi}' - \tilde{\alpha}\tilde{\phi}\phi')\frac{\mathrm{d}\bar{u}}{\mathrm{d}y}\mathrm{d}y; \tag{32e, f}$$

$$I_5 = \frac{1}{\mathrm{R}}\int_0^\infty [|\phi''|^2 - (\tilde{\alpha}^2\tilde{\phi}\phi'' + \alpha^2\phi\tilde{\phi}'') + |\alpha|^4|\phi|^4]\mathrm{d}y = \frac{1}{\mathrm{R}}\int_0^\infty 2|\Omega|^2\mathrm{d}y; \tag{32g}$$

where, in (32a–g), primes ($'$) denote differentiation with respect to y and tilde ($\tilde{}$) denotes the complex conjugate. Let us now define $e^* = I_1 + I_2 + I_3$, so that from (30)–(31) we have the extended energy integral $E^* = e^*\exp(-2\alpha_i x)$. Hence from (31)–(32) we have

$$(1/E^*)(\mathrm{d}E^*/\mathrm{d}x) = -2\alpha_i = (I_4 - I_5)/e^*, \tag{33}$$

and, from the definition of $E^* = e^*\exp(-2\alpha_i x)$, we have

$$(1/E^*)(\mathrm{d}E^*/\mathrm{d}x) = -2\alpha_i + (1/e^*)(\mathrm{d}e^*/\mathrm{d}x). \tag{34}$$

In view of (33) and (34), two important results are arrived at. First it is seen that the "optimal property" P_0 that we have been seeking is in fact the extended energy integral E^* (ignoring the factor 2 in $-2\alpha_i$, which appears because E^* is a quadratic form). The second result we state in the form of the following theorem.

Theorem 2. *The optimal normalisation of ϕ, at every station in x, is that e^* be the same at each station in x, i.e. $de^*/dx = 0$.*

We next look at some of the results. First, the truth of (33) was verified. A sample result is given below for $F = 140$, $\mathrm{R} = 1600$.

(i) From the OS-equation solution, $\alpha_i = 0{\cdot}01244681$;
(ii) From (33),

$$\alpha_i = -\frac{1}{2}\left(\frac{I_4 - I_5}{I_1 + I_2 + I_3}\right)$$

$$= -\frac{1}{2}\left(\frac{0{\cdot}03739 - 0{\cdot}24044}{5{\cdot}9871 + 2{\cdot}16968 + 9{\cdot}3 \times 10^{-5}}\right) = 0{\cdot}01244683.$$

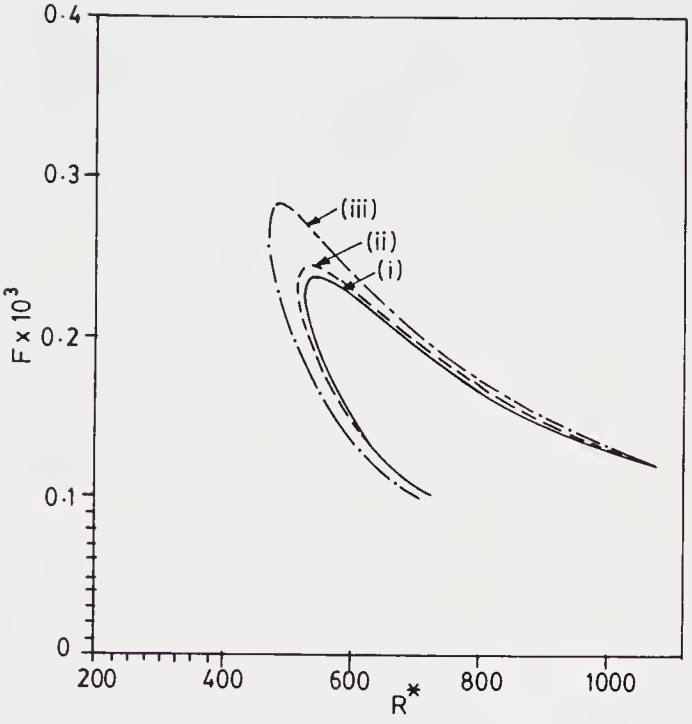

Figure 4. Various neutral-curves for the QP problem. (i) is the OS neutral-curve. This curve also coincides with the neutral-curve based on $\bar{p} = \int_0^\infty (\overline{u'^2} + \overline{v'^2})\mathrm{d}y$, serving as a cross-check for numerical work. (ii) is based on $\bar{p} = \int_0^\infty |u'|\mathrm{d}y$. (iii) is based on $\bar{p} = \int_0^\infty (\overline{u'^2} + \overline{v'^2})\mathrm{d}Y$. Compare with Gaster (1974).

Next, after using the optimal normalisation of ϕ, the growth rates of various different monitorable properties were calculated according to the formula in (28). Also, in (28), in view of the optimal normalisation of ϕ, $\mathrm{d}\bar{p}/\mathrm{d}x$ was simply, and also uniquely, calculated as $\Delta\bar{p}/\Delta x$, i.e. by direct numerical differentiation. The results, corresponding to the different monitorable properties considered by Gaster (1974), are shown in figures 4–6. There are two kinetic energy integrals considered, viz.,

$$ke = \int_0^\infty \left(\frac{\overline{u'^2} + \overline{v'^2}}{2}\right)\mathrm{d}y, \tag{35}$$

$$ke_g = \int_0^\infty \left(\frac{\overline{u'^2} + \overline{v'^2}}{2}\right)\mathrm{d}Y = \delta \int_0^\infty \left(\frac{\overline{u'^2} + \overline{v'^2}}{2}\right)\mathrm{d}y. \tag{36}$$

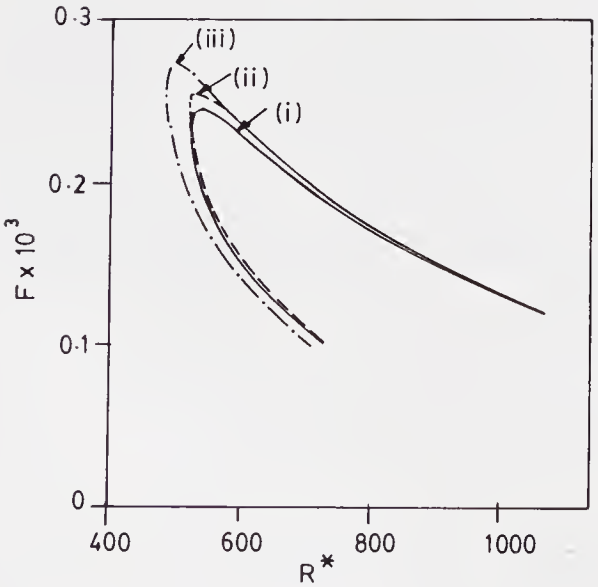

Figure 5. Various neutral-curves for the QP problem. (i) is the OS neutral-curve. (ii) is based on $\bar{p} = |u'|_{\mathrm{im}}$, i.e. inner maximum of u'. (iii) is based on $\bar{p} = |u'|_{\mathrm{om}}$, i.e. outer maximum of u'. Compare with Gaster (1974).

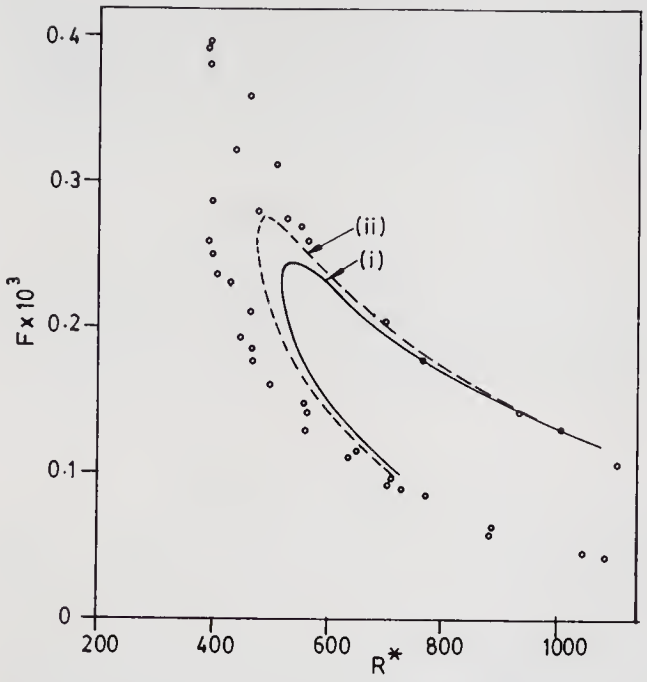

Figure 6. Various neutral-curves for the QP problem. (i) is the OS neutral-curve. (ii) is based on $\bar{p} = |u'|_{y=0\cdot15}$. (○) are the experimental neutral points of Ross *et al* (1970) based on $|u'|_{y=0\cdot15}$. Compare with Gaster (1974).

The integral ke_g was considered by Gaster. Also, it may be seen from (29), i.e. from the associated temporal problem, that the neutral-curve corresponding to ke (i.e., (35)) should be the same as that for $\alpha_i = 0$. This was indeed found to be the case.

The neutral-curves shown in figures 4–6 revealed a very interesting, and initially a very baffling feature. These curves, which are based on the QP-approximation and the QP-primitive, are found to be *virtually the same* as Gaster's (1974) neutral-curves which are based on the *full* non-parallel problem. And, it is to be remembered that all subsequent works in category III (defined in the beginning) eventually reproduced Gaster's (1974) results. To seek a satisfactory resolution we focus attention on the full non-parallel problem, going through the formulation of Sen & Vashist (1987) as an intermediate step.

3. The non-parallel problem

Sen & Vashist (1987; details given in Vashist 1988) started from the dimensional Navier–Stokes equations in vorticity form:

$$\frac{\partial}{\partial T}(\nabla_+^2 \Psi^+) + \frac{\partial \Psi^+}{\partial Y}\frac{\partial}{\partial X}(\nabla_+^2 \Psi^+) - \frac{\partial \Psi^+}{\partial X}\frac{\partial}{\partial Y}(\nabla_+^2 \Psi^+) - \nu \nabla_+^4 \Psi^+ = 0, \quad (37a)$$

$$\nabla_+^2 = \left(\frac{\partial^2}{\partial X^2} + \frac{\partial^2}{\partial Y^2}\right), \quad \text{and } \nabla_+^4 = \nabla_+^2(\nabla_+^2), \quad (37b)$$

where superscript plus (+) on Greek letters depicts dimensional quantities. Further they used the following transforms:

$$x = (X/\delta_0); \quad y = (Y/\delta); \quad \text{and,} \quad t = (TU_\infty/\delta_0). \quad (38)$$

Also, Ψ^+ was decomposed into a mean part $\bar{\phi}$ and a fluctuating part $\hat{\phi}$ as follows:

$$\Psi^+ = U_\infty \delta \bar{\phi}(y) + U_\infty \delta_0 \hat{\phi}(y, X, T), \quad (39)$$

$$\hat{\phi}(y, X, T) = \phi(y)\exp\{\imath(\alpha^+ X - \beta^+ T)\}; \quad \beta^+/\alpha^+ = C. \quad (40)$$

For a ray, the form of (40) assumes constancy of α^+ and local similarity of ϕ. Both these assumptions are justified in the light of earlier discussions. Using (37)–(40), and neglecting $O(R^{-2})$ terms, the following modified form of the Orr–Sommerfeld equation was derived:

$$L\phi - N\phi = 0; \quad \text{or } L_m\phi = 0, \quad \text{where } L_m = L - N; \quad \text{and,}$$

$$N\phi = \frac{25}{\iota\alpha R}\left[-\alpha^2\phi' y(\bar{u} - c) + \bar{u}\phi'' + \frac{1}{2}\frac{d\bar{u}}{dy}\phi' + \frac{1}{2}\bar{\phi}(\phi''' - \alpha^2\phi')\right]. \quad (41)$$

The boundary conditions of (41) were derived as follows:

$$\phi, \phi' = 0; \quad y = 0$$

$$\phi \sim \exp[-\alpha(1 + \varepsilon^*\mu + \varepsilon^*\lambda y)y], \quad \text{for } y \geqslant 1 \text{ with } \varepsilon^* y \sim O(1),$$

with

$$\varepsilon^* = -(1/\iota\alpha R); \quad \mu = -(25/4)[(3 - c)/(1 - c)]; \quad \text{and, } \lambda = -(25/4)\alpha. \quad (42)$$

Note that $(\partial\phi/\partial x)_y$ was neglected in (41) based on the local similarity assumption; the justification being that this term would appear on the right side of (21) (see (9)), and, this term being orthogonal to ϕ would not contribute to the eigenvalue problem or the associated homogeneous problem. However, (41) does include the terms neglected in the QP-approximation, viz. $\bar{v}$, $\partial\bar{u}/\partial x$ and $(\partial\phi/\partial x)_{IM}$.

The neutral-curve based on the eigenvalue problem defined by (41)–(42) is shown in figure 7. It is seen that this neutral-curve is fuller in extent than the OS neutral-curve, with the upper tip extending to values of F upto $F_u = 300$ and the critical R* going as low as $R^*_{cr} = 444$. The corresponding values for the OS neutral-curve are $F_u = 244$ and $R^*_{cr} = 519$.

Along with (41) we look at the *full* non-parallel equation of Gaster (1974), which is an extension of (23)–(24). Specifically, (24b) becomes

$$L\phi = P_4 + (1/A)(dA/dx)P_5 + P_6, \quad (43)$$

where P_6 is the contribution due to $\bar{v}$, $\partial\bar{u}/\partial x$ and $(\partial\phi/\partial x)_{IM}$ (see Gaster 1974, (8) and

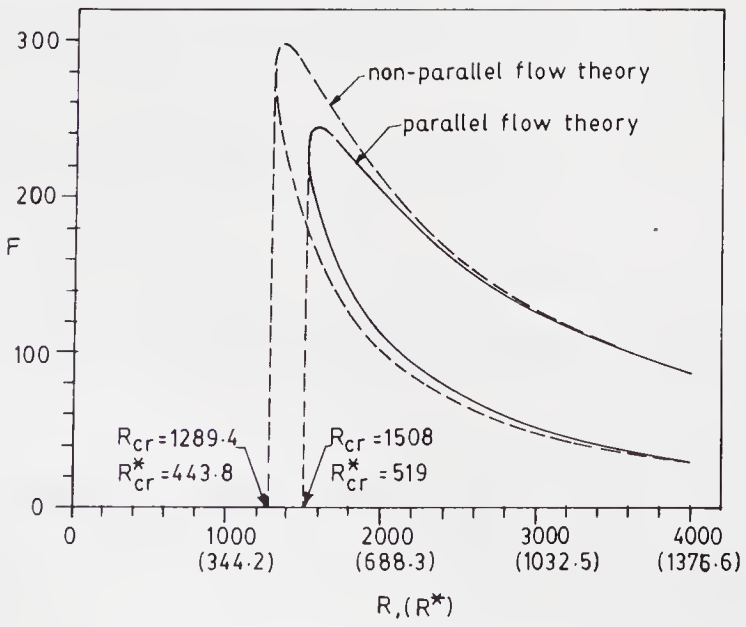

Figure 7. Neutral-curves for the OS-equation (solid line), and for the modified OS-equation of Sen & Vashist (1987) (broken line).

(A6), for full details of (43) herein). It can be seen that P_6 in (43) corresponds to $N\phi$ in (41).

Let us now attempt to solve (41), not as an eigenvalue problem with boundary conditions given by (42), but according to Gaster's approach. Thus, let $\phi = \phi_0 + \varepsilon\phi_1$ and $\alpha = \alpha_0 + \varepsilon\alpha_1$. From (41) we obtain

$$L\phi_0 = 0, \tag{44a}$$

$$\varepsilon L\phi_1 = N\phi_0 + \varepsilon P\alpha_1, \tag{44b}$$

where (44a) is the OS-equation and ϕ_0 has the boundary conditions ϕ_0, $\phi_0' = 0$ at $y = 0$ and $\phi_0 \sim \exp[-\alpha y]$ for $y \geqslant 1$. Further, P is a known expression in (44b). The solvability condition for (44b) gives

$$\int_0^\infty \theta[N\phi_0 + \varepsilon P\alpha_1]\mathrm{d}y = 0. \tag{45}$$

It is at this stage that the fallacy of the procedure becomes apparent. Inspection of the terms in $N\phi$ in (41) reveals that $N\phi_0 \sim y\exp[-\alpha y]$ for $y \geqslant 1$ as against $\phi_0 \sim \exp[-\alpha y]$ for $y \geqslant 1$. We already know from consideration of χ_1 in the earlier section that, if $N\phi_0 \sim y\exp[-\alpha y]$ for $y \geqslant 1$, then it will tend to be naturally orthogonal to ϕ_0. In other words $\int_0^\infty \theta[N\phi_0]\mathrm{d}y \simeq 0$. In which case it is seen from (45) that $\alpha_1 \simeq 0$. In other words no correction to the eigenvalue is obtained.

Now we turn our attention to (43), i.e. the full non-parallel problem of Gaster (1974). The term P_6 plays the same role as $N\phi$, and, because P_6 is kept on the *right-hand side* of (43), no additional correction to α_0 is obtained in this case also. Thus, Gaster's results also do not elicit more information on non-parallel effects over what may be gleaned from the QP-approximation. It may further be added that all works belonging to category III, subsequent to Gaster's, have kept the P_6 term on the right-hand side. Thus these studies also have, on the one hand, repeated Gaster's results, and, on the other hand, are subject to the same limitations as Gaster's work. The other limitation of the studies in category III is that in these the zeroth order or base equation is kept as the OS-equation (e.g. as in (44a)), with the same boundary conditions as for the OS-equation. Whereas, in the non-parallel problem, the correct base equation should be (41) with boundary conditions given by (42). This new base equation gives different (and improved) eigenvalues for α, as compared to the OS-equation. Because, not only is (41) different from the OS-equation, the boundary conditions, (42), are also different from those for the OS-equation.

In conclusion, it may be said that the Orr–Sommerfeld equation, which has been somewhat obsessively retained as the zeroth order or base equation for the problem, is *not* the correct base equation for the problem. The correct base equation for the problem is (41) with boundary conditions given by (42).

It now remains to extend the non-parallel problem given by (41)–(42) on lines similar to the QP-problem discussed earlier, so that the growth rates of individual monitorable properties can be obtained. As before, this requires finding an optimal property and also the optimal normalisation of ϕ. Again, this is done by considering the energy integral equation for stability for the non-parallel problem. Details of the subsequent analysis are given in Verma (1992).

Before considering the energy integral equation, it is necessary to define some pseudo quantities like pseudo velocities and pressure. These pseudo quantities are written with a caret ($\hat{}$) on top. We thus define the following:

$$u' = (\delta_0/\delta)\hat{u}'; \quad v' = \hat{v}' + (25/2\mathrm{R})(\partial\hat{\phi}/\partial y)y; \quad p' = (\delta/\delta_0)\hat{p}'. \tag{46}$$

Thus from (41) and (46) we have further that

$$\hat{u}' = (\partial\hat{\phi}/\partial y); \quad \hat{v}' = -(\partial\hat{\phi}/\partial x). \tag{47}$$

One may now obtain the integral energy equation for stability for the full non-parallel problem. This is done starting from the two-dimensional linearised disturbance equations in *dimensional* form (similar to (5)–(6) without making the QP-approximation), using (37)–(39) and (46)–(47), and using a procedure similar to the quasi-parallel case. The resulting equations are given below, for the temporal and spatial problem respectively:

$$\frac{\partial}{\partial t}\left[\int_0^\infty \left\{\overline{\hat{q}'^2} + \frac{a}{2}y(\overline{\hat{u}'\hat{v}'})\right\}\mathrm{d}y\right]$$
$$= -\int_0^\infty \overline{\hat{u}'\hat{v}'}\frac{\partial\bar{u}}{\partial y}\mathrm{d}y - \frac{1}{\mathrm{R}}\int_0^\infty \overline{\hat{\omega}'^2}\mathrm{d}y - \frac{a}{2}\int_0^\infty \left\{\frac{\partial\bar{u}}{\partial y}y\overline{\hat{v}'^2} - \frac{1}{2}(\overline{\hat{u}'^2} - \overline{\hat{v}'^2}) + \overline{\hat{u}'\hat{p}'}\right\}\mathrm{d}y, \tag{48}$$

$$\frac{\partial}{\partial x}\left[\int_0^\infty \bar{u}\left\{\overline{\hat{q}'^2} + \frac{a}{2}y(\overline{\hat{u}'\hat{v}'})\right\}\mathrm{d}y + \int_0^\infty \overline{\hat{u}'\hat{p}'}\mathrm{d}y - \frac{1}{\mathrm{R}}\int_0^\infty \overline{\hat{v}'\hat{\omega}'}\mathrm{d}y\right]$$
$$= -\int_0^\infty \overline{\hat{u}'\hat{v}'}\frac{\partial\bar{u}}{\partial y}\mathrm{d}y - \frac{1}{\mathrm{R}}\int_0^\infty \overline{\hat{\omega}'^2}\mathrm{d}y - \frac{a}{2}\int_0^\infty \left\{\frac{\partial\bar{u}}{\partial y}y\overline{\hat{v}'^2} - \frac{1}{2}(\overline{\hat{u}'^2} - \overline{\hat{v}'^2}) + \overline{\hat{u}'\hat{p}'}\right\}\mathrm{d}y, \tag{49}$$

where, in (48)–(49)

$$a = 25/\mathrm{R}; \quad \overline{\hat{q}'^2} = (\overline{\hat{u}'^2} + \overline{\hat{v}'^2})/2, \quad \text{and } \hat{\omega}' = [(\partial\hat{v}'/\partial x) - (\partial\hat{u}'/\partial y)]. \tag{50}$$

The next step is to express (49) in terms of the solution of the modified Orr–Sommerfeld equation, i.e. (41) with boundary conditions given by (42). This gives, similar to (31), the following equation:

$$(\mathrm{d}/\mathrm{d}x)[(I_1 + I_2 + I_3)\exp[-2\alpha_i x] = (I_4 - I_5 - I_6)\exp[-2\alpha_i x], \tag{51}$$

where, again after putting $\hat{p}' = p\exp[\imath(\alpha x - \beta t)]$ and $\hat{\omega}' = \Omega\exp[\imath(\alpha x - \beta t)]$, one obtains the integrals I_n as follows:

$$I_1 = \int_0^\infty \bar{u}[(|\phi'|^2 + |\alpha|^2|\phi|^2) + (a/2)y\{\imath(\alpha\phi\tilde{\phi}' - \tilde{\alpha}\tilde{\phi}\phi')\}]\mathrm{d}y; \tag{52a}$$

$$I_2 = \int_0^\infty (\phi'\tilde{p} + \tilde{\phi}'p)\mathrm{d}y; \tag{52b}$$

$$p = [(\partial\bar{u}/\partial y)\phi - (\bar{u} - c)\phi' + (1/\imath\alpha\mathrm{R})(\phi''' - \alpha^2\phi') + (25/2\imath\alpha\mathrm{R})$$
$$\times \{\bar{\phi}\phi'' + \bar{u}\phi' - \alpha^2 y(\bar{u} - c)\}]/(1 + 25/2\imath\alpha\mathrm{R}); \tag{52c}$$

$$I_6 = (a/2)\int_0^\infty [(\partial\bar{u}/\partial y)y|\alpha|^2|\phi|^2 - \bar{u}(|\phi'|^2 - |\alpha|^2|\phi|^2) + (\phi'\tilde{p} + \tilde{\phi}'p)]\mathrm{d}y. \tag{52d}$$

In addition, the integrals I_3, I_4 and I_5 have the same forms as those given by the quasi-parallel case, i.e. by (32c–g).

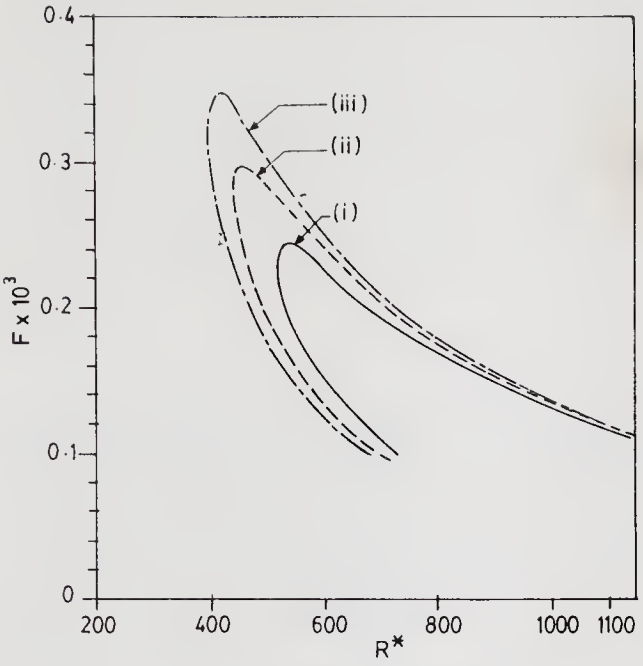

Figure 8. Various neutral-curves for the non-parallel problem. (i) is the OS neutral-curve. (ii) is based on $\bar{p} = \int_0^\infty (\overline{u'^2} + \overline{v'^2})\mathrm{d}y$. (iii) is based on $\bar{p} = \int_0^\infty (\overline{u'^2} + \overline{v'^2})\mathrm{d}Y$.

As before, the optimal property is the augmented energy integral E^* defined as $E^* = e^* \exp(-2\alpha_i x)$ where $e^* = I_1 + I_2 + I_3$, and

$$(1/E^*)(\mathrm{d}E^*/\mathrm{d}x) = -2\alpha_i = (I_4 - I_5 - I_6)/e^*. \tag{53}$$

Thus, again with reference to (34), we find that the optimal normalisation would be the same as that given by theorem 2 earlier. Further, a sample cross-check for (53), for $F = 140$ and $R = 1600$, shows that $\alpha_i = 0{\cdot}006439$ from the solution of the modified OS-equation, (41–42), and $\alpha_i = 0{\cdot}006432$ by (53); and, in general, the agreement is good upto five decimal places.

The detailed results for the non-parallel problem are shown in figures 8–10. As

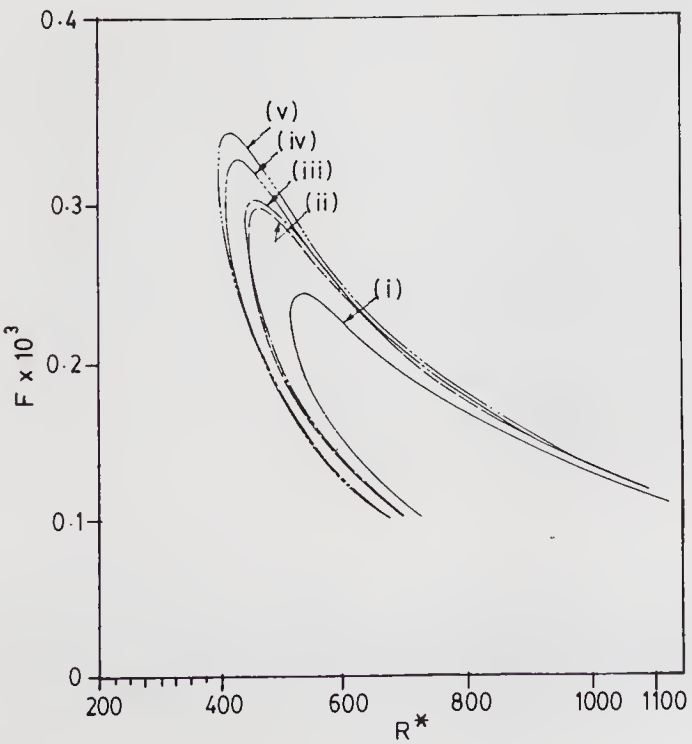

Figure 9. Various neutral-curves for the non-parallel problem. (i) is the OS neutral-curve. (ii) is based on the modified OS-equation of Sen & Vashist (1987). (iii) is based on $\bar{p} = |u'|_{\mathrm{im}}$, i.e. inner maximum of u'. (iv) is based on $\bar{p} = |u'^2|_{\mathrm{om}}$, i.e. outer maximum of u'. (v) is based on $\bar{p} = \int_0^\infty (\overline{u'^2} + \overline{v'^2})\mathrm{d}Y$.

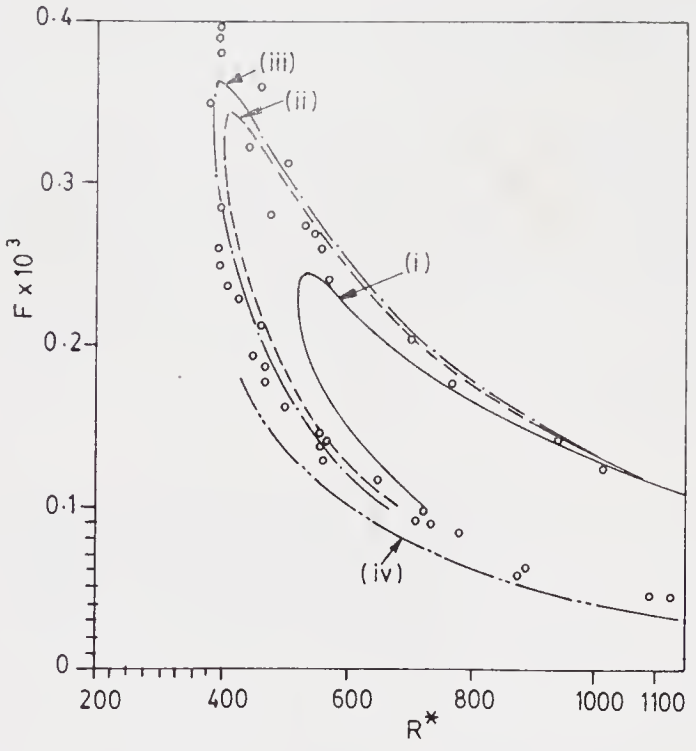

Figure 10. Various neutral-curves for the non-parallel problem. (i) is the OS neutral-curve. (ii) is based on $\bar{p} = |u'|_{y=0\cdot15}$. (iii) is based on the maximum of v'. (iv) is based on the triple-deck theory for the lower-branch as given by Smith (1979). (○) are the experimental neutral points of Ross *et al* (1970) based on $|u'|_{y=0\cdot15}$.

before, growth rates corresponding to different monitorable properties were calculated based on (28) after using the optimal normalisation of ϕ. Thereafter different neutral-curves were obtained, as shown in the figures. The results in figure 10 show very good agreement with the experimental results of Ross *et al* (1970), and with the results of Smith (1979) based on the triple-deck theory. Of particular interest in the results is the good agreement in the neutral-curve for $|u'|$ at $y = 0\cdot15$ from the present theory, and the corresponding measurements of Ross *et al* (1970).

Finally, we consider the results of Fasel & Konzelmann (1990). Although these results seem to verify Gaster's (1974) results, the growth-rates seem to be consistently, though only marginally, higher than Gaster's. Further, the outer boundary conditions used by them is based on $\exp(-\alpha y)$ decay, with α given from the *local* solution of the OS-equation. An incorrect value of α, particularly if the *sign* of α_i is incorrect, can cause subtle changes in the imaginary part of ϕ. This in turn can cause change in the sign of the Reynolds stress and therefore in the production integral (see (30) and (32f)), thereby upsetting the delicate balance between the production and dissipation integrals. This, in turn, can give incorrect answers for the values of the growth-rates. Thus there seems to be scope to further improve upon the simulation studies of Fasel & Konzelmann (1990), before definite conclusions can be drawn. We refrain from discussing here the work of Bertolotti *et al* (1992), but this will be done in a future paper.

The students and co-workers who have worked on this problem are Dr T K Vashist and Ms R Verma. Thanks are due to Professors J T Stuart, M Gaster, P W Carpenter and R Narasimha for helpful discussions, and to Ms R Govindrajan for helpful criticisms.

References

Babenko V V, Kozlov L F 1973 Experimental investigation of hydrodynamic stability on rigid and elastic-damping surfaces. *Izv. Akad. Nauk. SSSR. Mekh. Zhid. Gaza* (1): 122–127

Barry M D J, Ross M A S 1970 The flat plate boundary layer. Part 2. The effect of increasing boundary layer thickness on stability. *J. Fluid Mech.* 43: 813–818

Bertolotti F P, Herbert Th, Spalart P R 1992 Linear and non-linear stability of the Blasius boundary layer. *J. Fluid Mech.* 242: 441–474

Bouthier M 1972 Stabilité linéaire des écoulements presque parallèles. (Part I) *J. Mécanique* 11: 599–621

Bouthier M 1973 Stabilité linéaire des écoulements presque parallèles. Part II. La couche limite de Blasius. *J. Mécanique* 12: 75–95

Bridges T J, Morris P J 1987 Boundary layer stability calculations. *Phys. Fluids* 30: 3351–3358

Dey J, Prabhu A, Tumen D 1990 On the non-parallel effect in linear stability of Blasius boundary layer. Rep. No. 90 FM 4, Indian Inst. Sci. Bangalore

Fasel H 1976 Investigation of the stability of boundary layers by a finite-difference model of the Navier–Stokes equations. *J. Fluid Mech.* 78: 355–383

Fasel H, Konzelmann U 1990 Non-parallel stability of a flat-plate boundary layer using the complete Navier–Stokes equations. *J. Fluid Mech.* 221: 311–347

Gaster M 1974 On the effects of boudary-layer growth on flow stability. *J. Fluid Mech.* 66: 465–480

Kachanov Yu S, Kozlov V V, Levchenko V Ya 1977 Non-linear development of a wave in a boundary layer. *Fluid Dyn.* 3: 383–390

Ross J A, Barnes F H, Burns J C, Ross M A 1970 The flat plate boundary layer. Part 3. Comparison of theory with experiment. *J. Fluid Mech.* 43: 819–832

Saric W S, Nayfeh A H 1975 Nonparallel stability of boudary layer flows. *Phys. Fluids* 18: 945–950

Saric W S, Nayfeh A H 1977 Nonparallel stability of boundary layers with pressure gradient and suction. In *Laminar-turbulent transition.* AGARD CP-224, pp. 6/1–21

Schubauer G B, Skramstad H K 1947 Laminar boundary-layer oscillations and transition on a flat plate. *J. Res. Natl. Bur. Stand.* 38: 251–292

Sen P K, Vashist T K 1987 On the stability of boundary-layer flow over a flat plate, considering non-parallel effects. *Euromech 228 Colloquium on Boundary Layer Stability and Transition* (Exeter, UK)

Smith F T 1979 On the nonparallel flow stability of the Blasius boundary layer. *Proc. R. Soc. London* A366: 91–109

Strazisar A J, Prahl J M, Reshotko E 1975 Experimental study of the stability of heated laminar boundary layers in water. Case Western Univ., Dept. Fluid Therm. Aerosp. Sci., FTAS/TR-75–113

Stuart J T 1957 On the non-linear mechanics of hydrodynamic stability. *J. Fluid Mech.* 4: 1–21

Van Stijn Th L, Van de Vooren A I 1983 On the stability of almost parallel boundary layer flows. *Comput. Fluids* 10: 223–241

Vashist T K 1988 *Stability of boundary layer flow over a flat plate*, Ph D thesis, Dept. Appl. Mech., Indian Inst. Technol., Delhi

Verma R 1992 *Linear and non-linear stability of boundary layer flow over a flat-plate, considering non-parallel effects*, Ph D thesis (submitted), Dept. Appl. Mech., Indian Inst. Technol., Delhi

Note added in proof

Recent work by Sen and Thomas (1993, being sent to *J. Fluid Mech.*) shows that the contention $\int_0^\infty \theta[N\phi_0]\mathrm{d}y \simeq 0$, is incorrect. In fact, by use of (45), the correction α_1 retrieves the eigenvalue for the modified OS-equation (41).

The error in the earlier works is most probably due to the following reason. At different stations in X, the basic Orr–Sommerfeld equation has different length scales due to change in δ with X. This feature has to be taken proper cognisance of while numerically evaluating the term corresponding to $\partial\phi/\partial x$. The matter is being investigated further.

Boltzmann schemes for continuum gas dynamics

S M DESHPANDE

Computational Fluid Dynamics Laboratory, Department of Aerospace Engineering, Indian Institute of Science, Bangalore 560012, India

Abstract. Many problems arising in the aerodynamic design of aerospace vehicles require the numerical solution of the Euler equations of gas dynamics. These are nonlinear partial differential equations admitting weak solutions such as shock waves and constructing robust numerical schemes for these equations is a challenging task. A new line of research called Boltzmann or kinetic schemes discussed in the present paper exploits the connection between the Boltzmann equation of the kinetic theory of gases and the Euler equations for inviscid compressible flows. Because of this connection, a suitable moment of a numerical scheme for the Boltzmann equation yields a numerical scheme for the Euler equations. This idea called the "moment method strategy" turns out to be an extremely rich methodology for developing robust numerical schemes for the Euler equations. The richness is demonstrated by developing a variety of kinetic schemes such as kinetic numerical method, kinetic flux vector splitting method, thermal velocity based splitting, multidirectional upwind method and least squares weak upwind scheme.

A 3-D time-marching Euler code called BHEEMA based on the kinetic flux vector splitting method and its variants involving equilibrium chemistry have been developed for computing hypersonic reentry flows. The results obtained from the code BHEEMA demonstrate the robustness and the utility of the kinetic flux vector splitting method as a design tool in aerodynamics.

Keywords. Boltzmann equation; kinetic schemes for Euler equation; gas dynamics; computational fluid dynamics; robust numerical schemes.

1. Introduction

Many problems arising in the aerodynamic design of aerospace vehicles require the numerical solution of the Euler equations of gas dynamics. Some notable examples are flow past delta wings, flow through ramjet type intakes of missiles, external supersonic flow around launch vehicles and missiles, and hypersonic re-entry flow. Generally any flow which is nearly attached (that is, not involving separation of the thin viscous layer from the body surface) needs the solution of the Euler equations of motion. These equations also need to be solved in cases of flow problems where

viscous effects are approximately taken into account by solving the famous boundary layer equations which again require the inviscid solution. Such problems involve weak viscid-inviscid coupling. Therefore, constructing numerical schemes for solving these equations has been one of the principal subjects of research among the CFD community for the last decade. The Euler equations are nonlinear vector conservation equations and, further, are hyperbolic. These equations are known to admit shocks, which are known as weak solutions from the mathematical point of view. At the Euler level, shocks are gas dynamic discontinuities across which the physical variables density, pressure and temperature, undergo sudden jumps. The challenge in constructing numerical schemes for solving the Euler equations then lies in correctly and accurately computing the weak solutions within the framework of the inviscid approximation. It is therefore highly desirable from the point of view of accuracy and robustness to design numerical schemes which are conservative and upwind, that is, which respect hyperbolicity.

Before the advent of the Boltzmann or kinetic schemes, upwinding has been enforced via flux-vector splitting (see, for example, Van Leer 1982) or via flux-difference splitting (Roe 1981). In the former approach, the flux-vector G is split into two flux-vectors G^+ and G^-, so that the flux-Jacobians (the Jacobians of G^+ and G^- with respect to the conserved vector U) have all-positive and all-negative eigenvalues. In the flux-difference splitting approach, the domain is divided into cells in each of which the state is assumed constant. The fluid variables will, in general, be discontinuous across the cell interfaces. Local 1-D Riemann problems are then solved exactly or approximately and the solutions of these are used to obtain the numerical solution of the Euler equations. Both these approaches have to grapple with the nonlinearity of the Euler equations. The third line of approach employed in constructing conservative upwind schemes is based on what Deshpande (1986c) calls the moment method strategy which is based on the fact that the Euler equations are suitable moments of the Boltzmann equation of the kinetic theory of gases. In some sense, the Boltzmann equation is more fundamental than the Navier–Stokes equations of fluid dynamics because the latter follow from the former when the mean free path of the molecules is much smaller than the characteristic length of the body. In this case, the velocity distribution function is the well-known Chapman–Enskog distribution. The Chapman–Enskog theory is intimately connected with the Navier–Stokes equations. If, on the other hand, the velocity distribution is taken as the Maxwellian distribution, then the suitable moments of the Boltzmann equation yield the Euler equations. Several other workers have also exploited this connection between the Boltzmann and the Euler equations for constructing the Boltzmann schemes (see Pullin 1980, Rietz 1981, Elizarova & Chetverushkin 1985, Kaniel 1988, Perthame 1990, Croisille & Delorme 1991, and Crosille & Villedieu 1992). One of the major advantages of dealing with the Boltzmann equation is that it reduces to a linear partial differential equation (PDE) in the Euler limit (as the collision term vanishes for the Maxwellian distribution). Designing an upwind scheme for this linear PDE is very much simpler than for the Euler equations which, as noted earlier, are nonlinear vector conservation equations. The principal subject matter of the present paper is to survey several Boltzmann schemes developed by the author and his coworkers and point out some promising future directions of research into the rapidly growing area of Boltzmann (also called kinetic) schemes.

2. Basic theory of Boltzmann schemes

Let us illustrate the basic idea with reference to 1-D unsteady Euler equations

$$(\partial U/\partial t) + (\partial G/\partial x) = 0, \tag{1}$$

where U is the vector of conserved variables, G is the flux-vector and are given by

$$U = \begin{bmatrix} \rho \\ \rho u \\ \rho e \end{bmatrix}, \tag{2}$$

$$G = \begin{bmatrix} \rho u \\ p + \rho u^2 \\ (\rho e + p)u \end{bmatrix}. \tag{3}$$

Here ρ = mass density, u = fluid velocity, p = pressure, e = total energy per unit mass $= p/[\rho(\gamma - 1)] + (1/2)u^2$. Equation (1) can be obtained as the Ψ-moment of the 1-D Boltzmann equation (without the collision term)

$$(\partial F/\partial t) + v(\partial F/\partial x) = 0, \tag{4}$$

where F is the Maxwellian velocity distribution given by

$$F = (\rho/I_0)(\beta/\pi)^{\frac{1}{2}} \exp[-\beta(v-u)^2 - (I/I_0)] \tag{5}$$

$\beta = 1/(2RT)$, R = gas constant per unit mass, v = molecular velocity, I = internal energy variable corresponding to nontranslational degrees of freedom, and

$$I_0 = (3-\gamma)/[4(\gamma-1)\beta]. \tag{6}$$

The moment function vector is defined by

$$\Psi = [1, v, I + (v^2/2)]^T. \tag{7}$$

The Euler equations (1) can then be cast in the compact form

$$(\Psi, (\partial F/\partial t) + v(\partial F/\partial x)) = 0, \tag{8}$$

where the scalar product (Ψ, f) is defined by

$$(\Psi, f) = \int_0^\infty dI \int_{-\infty}^{\infty} dv \Psi f(v). \tag{9}$$

2.1 *KFLIC method*

Equation (8) is the basis of many kinetic schemes. One of the earliest schemes called kinetic-fluid-in-cell (KFLIC) method due to Deshpande & Raul (1982) exploits the above connection between the Euler equations and the Boltzmann equation. To obtain the state update formulae for the scheme let us consider 1-D interval $a \leqslant x \leqslant b$ which is assumed to be divided into cells. If a particle moves from $x \in C_i$ to $x' \in C_j$

during time interval Δt, then this particle will have molecular velocity $v = (x' - x)/\Delta t$. Hence the mass, momentum and energy transfer from cell C_i to C_j during Δt are given by

$$Ma(C_i \to C_j) = \int_{C_i} dx \int_{C_j} dx' [F(x, x')/\Delta t], \tag{10}$$

$$Mo(C_i \to C_j) = \int_{C_i} dx \int_{C_j} dx' [(x' - x)/\Delta t][F(x, x')/\Delta t], \tag{11}$$

$$En(C_i \to C_j) = \int_{C_i} dx \int_{C_j} dx' \{I_0 + [(x' - x)^2/2\Delta t^2]\}[F(x, x')/\Delta t], \tag{12}$$

where

$$F(x, x') = \rho(x)[\beta(x)/\pi]^{\frac{1}{2}} \exp\{-\beta(x)[((x' - x)/\Delta t) - u(x)]^2\}. \tag{13}$$

At the end of the transport of mass, momentum and energy from all cells C_i to the cell C_j, we have

$$Ma(C_j) = \sum_{\text{all } i} Ma(C_i \to C_j), \quad Mo(C_j) = \sum_{\text{all } i} Mo(C_i \to C_j),$$

$$En(C_j) = \sum_{\text{all } i} En(C_i \to C_j), \tag{14}$$

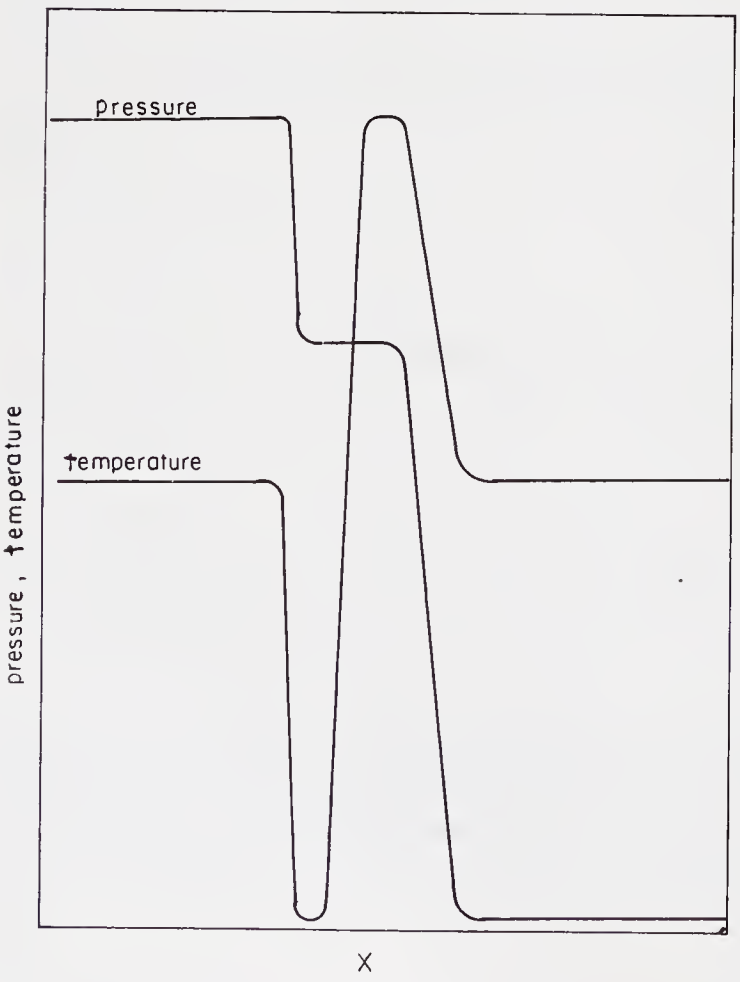

Figure 1. Application of KFLIC to 1-D shock propagation problem, no. of cells = 500 and $\Delta t = 10$.

which are the state update formulae for the method. Deshpande & Raul (1982) have used the KFLIC method for the 1-D shock propagation problem and the results are shown in figure 1. A large number of mesh points (500) were required for crisp shock. The KFLIC method is explicit, unconditionally stable, and first-order accurate in space and time. It can be regarded as a forerunner of Morton's characteristic Galerkin approach (Morton 1985). The method involves double integrals which have to be computed numerically and, hence, the method is computationally very expensive. Also, extension to multidimensions involves some problems in dealing with boundary conditions and keeping track of several possibilities as a particle moves from any cell to any other cell. Therefore this line of approach is not followed hereafter.

2.2 *Kinetic numerical method*

A faster version of the KFLIC method is the kinetic numerical method (KNM) which has the simple state update formula,

$$U_j^{n+1} = (\Psi, F^n(x_j - v\Delta t, v, I)), \tag{15}$$

where $F^n(x_j, v, I)$ is the local Maxwellian at the grid point x_j and time level n. Rietz (1981) was the first one who developed this KNM and applied it to the 1-D shock problem. Deshpande (1986a) has shown that the KNM satisfies the entropy condition, upwinding property and has TVD (total variation diminishing) property. For the purpose of proving that the entropy condition is satisfied, Deshpande (1986a) has used a slightly modified H function and flux-function H_v,

$$H = \int\int \{F \ln F + [(5-3\gamma)/2(\gamma-1)] F \ln \beta\} \, \mathrm{d}v \, \mathrm{d}I,$$

$$H_v = \int\int v\{F \ln F + [(5-3\gamma)/2(\gamma-1)] F \ln \beta\} \, \mathrm{d}v \, \mathrm{d}I, \tag{16}$$

and has further shown that these functions satisfy the entropy conservation

$$(\partial H/\partial t) + (\partial H_v/\partial x) = 0.$$

Developing higher order accurate versions of KNM is not straightforward. The difficulty arises due to the fact that the governing equations are (8) and not (4), hence it is not possible to construct higher order schemes for (8) by taking moments of higher order schemes of (4). We emphasize that $(\partial F/\partial t) + v(\partial F/\partial x) \neq 0$; in fact

$$\frac{\partial F}{\partial t} + v\frac{\partial F}{\partial x} = \left(\frac{\partial \rho}{\partial t} + v\frac{\partial \rho}{\partial x}\right)\frac{\partial F}{\partial \rho} + \left(\frac{\partial u}{\partial t} + v\frac{\partial u}{\partial x}\right)\frac{\partial F}{\partial u} + \left(\frac{\partial \beta}{\partial t} + v\frac{\partial \beta}{\partial x}\right)\frac{\partial F}{\partial \beta}. \tag{17}$$

The right-hand side of (17) is very characteristic of the Chapman–Enskog theory. Replacing the time derivatives of ρ, u, β above in terms of space derivatives using the Euler equations we get

$$(\partial F/\partial t) + v(\partial F/\partial x) = P_{CE}F, \tag{18}$$

where P_{CE} is a polynomial similar to the Chapman–Enskog polynomial and is given by*

*This polynomial is exactly the same as the polynomial that appears when Chapman–Enskog analysis is applied to the one-dimensional BGK model of the Boltzmann equation.

$$P_{CE} = (\partial u/\partial x)P_\tau + (\partial \beta/\partial x)P_q, \tag{19}$$

$$P_\tau = [(3\gamma - 5)/2] + (3 - \gamma)[(v - u)^2/2RT] - [4(\gamma - 1)^2/(3 - \gamma)](I/2RT), \tag{20}$$

$$P_q = 5RT(v - u) - [4(\gamma - 1)/(3 - \gamma)]I(v - u) - (v - u)^3. \tag{21}$$

The polynomial P_{CE} has the interesting property

$$(\Psi, P_{CE}F) = 0. \tag{22}$$

We are now ready to construct the second-order accurate KNM of Deshpande (1986a, b). Start with

$$U^{n+1} = (\Psi, F^{n+1}) = (\Psi, F^n) + \Delta t[\Psi, (\partial F^n/\partial t)] + (\Delta t^2/2)[\Psi, (\partial^2 F^n/\partial t^2)] + \cdots.$$

Using (17) we obtain

$$U^{n+1} = (\Psi, F^n) - \Delta t[\Psi, v(\partial F^n/\partial x)] + \Delta t^2[\Psi, (\partial^2 F^n/\partial t^2)] + \cdots, \tag{23}$$

where we have used (18) and (22). For the second derivative $\partial^2 F/\partial t^2$ we have

$$\begin{aligned}(\partial^2 F/\partial t^2) &= -v(\partial/\partial x)(\partial F/\partial t) + (\partial/\partial t)(P_{CE}F) \\ &= v^2(\partial^2 F/\partial x^2) - v(\partial/\partial x)(P_{CE}F) + (\partial/\partial t)(P_{CE}F).\end{aligned}$$

Substituting the above expression for the second derivative of F with respect to time in (23) and rearranging we get

$$U^{n+1} = (\Psi, F^n(x - v\Delta t)) - (\Delta t^2/2)[\Psi, v(\partial/\partial x)P_{CE}F] + O(\Delta t^3), \tag{24}$$

which shows that in addition to the $F^n(x - v\Delta t)$ term we have one more term containing the polynomial P_{CE}. Hence the Maxwellian distribution alone will not yield a second-order accurate KNM. Defining

$$f_{CE} = F[1 + (\Delta t/2)P_{CE}], \tag{25}$$

(24) can also be recast as

$$U^{n+1} = [\Psi, f^n_{CE}(x - v\Delta t)] + O(\Delta t^3). \tag{26}$$

When (25) is compared with the usual Chapman–Enskog distribution,

$$f_{CE} = F[1 - (\tau/p)P_\tau - (q\beta^{\frac{1}{2}}/p)P_q],$$

we observe that the distribution (25) is antidiffusive showing that such antidiffusive terms are necessary to achieve second-order accuracy. The first-order accurate KNM given by (15) is very diffusive as many first-order upwind methods are. The antidiffusive terms cancel this hefty amount of numerical diffusion to achieve second-order accuracy. Figure 2 shows the density and velocity plots for 1-D shock propagation problems solved by using the state update formula (26). Slope limiters have been used to suppress wiggles (Deshpande 1986a). It is observed that the method yields accurate results with high resolution.

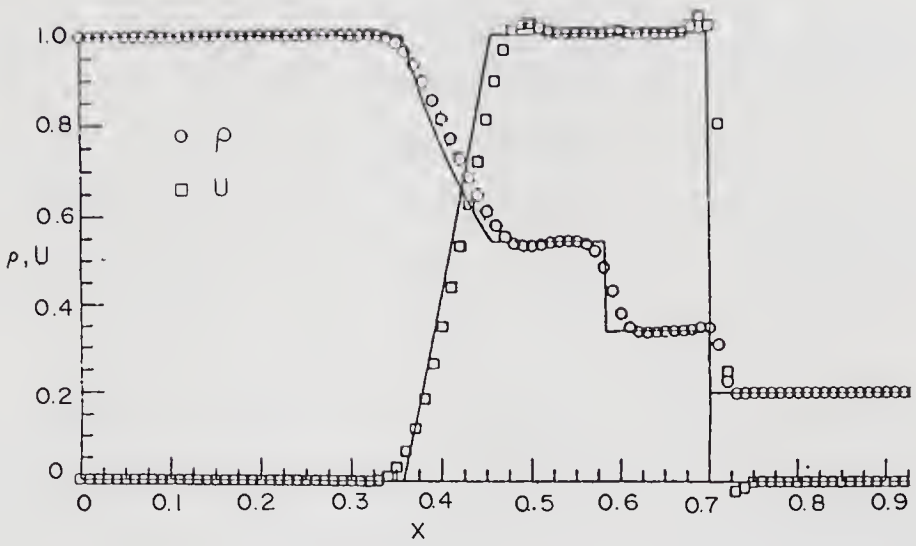

Figure 2. Computed and exact ρ and U profiles for shock tube problem with the antidiffusive Chapman–Enskog ansatz with TVD modification. $J = 101$, $t_A = 0{\cdot}00041$ s.

3. The kinetic flux vector splitting scheme

The KNM involves only one numerical integration with respect to the space variable and is therefore faster than the KFLIC method. It is tempting to enhance the speed further by modifying the KNM, and this can be accomplished by reducing its support. This brings us to the kinetic flux vector splitting (KFVS) scheme of Deshpande (1986b) and Mandal & Deshpande (1988). The KFVS method is obtained by splitting the Maxwellian into two parts corresponding to $v > 0$ and $v < 0$. The flux-vector G therefore splits as

$$G^+ = [\Psi, (v + |v|)/2F] \text{ and } G^- = [\Psi, (v - |v|)/2F]. \tag{27}$$

The split flux-vectors G^+ and G^- are integrals of $vF\Psi$ over positive and negative half spaces in velocity v. They can be evaluated in closed form in terms of error functions as

$$G^{\pm} = \begin{bmatrix} \rho u A^{\pm} \pm [\rho/2(\pi\beta)^{\frac{1}{2}}]B \\ (p + \rho u^2)A^{\pm} \pm [\rho u/2(\pi\beta)^{\frac{1}{2}}]B \\ (pu + \rho ue)A^{\pm} \pm [(p/2) + \rho e][B/2(\pi\beta)^{\frac{1}{2}}] \end{bmatrix}, \tag{28}$$

where

$$A^{\pm} = (1 \pm erfs)/2, \quad B = \exp[-s^2] \text{ and } s = \text{speed ratio} = u\beta^{\frac{1}{2}}.$$

In terms of the split fluxes the Euler equations become

$$(\partial U/\partial t) + (\partial G^+/\partial x) + (\partial G^-/\partial x) = 0. \tag{29}$$

Upwind differencing the split-flux terms in (29) we obtain the first order KFVS scheme

$$(\partial U/\partial t)_j^n + [(G_j^{+n} - G_{j-1}^{+n})/\Delta x] + [(G_{j+1}^{-n} - G_j^{-n}/\Delta x] = 0. \tag{30}$$

Substituting for U, G^+ and G^- in terms of F we get

$$(\partial/\partial t)(\Psi, F_j^n) + (1/\Delta x)[\Psi, (v + |v|)/2(F_j^n - F_{j-1}^n)] + (1/\Delta x)[\Psi, (v - |v|)/2(F_{j+1}^n - F_j^n)] = 0,$$

which is obviously the Ψ-moment of the Courant–Isaacson–Rees (CIR) differenced Boltzmann equation

$$(\partial F/\partial t)_j^n + [(v + |v|)/2][(F_j^n - F_{j-1}^n)/\Delta x] + [(v - |v|)/2][(F_{j+1}^n - F_j^n)/\Delta x] = 0. \tag{31}$$

Now an interesting question arises whether the KFVS scheme (30) which is obtained from (31) remains an upwind scheme after moments are taken. In order to demonstrate that the scheme (30) obtained by differencing (29) is an upwind scheme, it is necessary to transform (29) to a symmetric hyperbolic form. Deshpande (1986c) has shown that (29) can be transformed to

$$P(\partial q/\partial t) + B^+(\partial q/\partial x) + B^-(\partial q/\partial x) = 0, \tag{32}$$

where q is the transformed vector given by

$$q = [\ln \rho + [\ln \beta/(\gamma - 1)] - \beta u^2, 2\beta u, -2\beta]^T,$$

P is a positive symmetric matrix, and B^+, B^- are positive and negative symmetric matrices respectively. It then follows that $P^{-1}B^+$ and $P^{-1}B^-$ have real positive and real negative eigenvalues, respectively, thus justifying the backward differencing of $B^+(\partial q/\partial x)$ and forward differencing of $B^-(\partial q/\partial x)$. It has been found that the eigenvalues of $P^{-1}B^+$ and $P^{-1}B^-$ are smooth functions of the Mach number (Mandal 1989).

Mandal & Deshpande (1988) have shown that the above KFVS scheme can be made higher order accurate by following the analysis of Chakravarthy & Osher (1983). For this purpose we difference (29) as

$$(\partial U/\partial t)_j^n + [(G_{j+\frac{1}{2}}^n - G_{j-\frac{1}{2}}^n)/\Delta x] = 0. \tag{33}$$

The first-order KFVS given by (30) is obtained by choosing

$$G_{j+\frac{1}{2}} = [(G_j + G_{j+1})/2] + [DG_{j+\frac{1}{2}}^- - DG_{j+\frac{1}{2}}^+)/2], \tag{34}$$

where the flux differences $DG_{j+\frac{1}{2}}^{\pm}$ are defined by

$$DG_{j+\frac{1}{2}}^{\pm} = \{\Psi, [(v \pm |v|)/2](F_{j+1} - F_j)\} = (G_{j+1}^{\pm} - G_j^{\pm})/2. \tag{35}$$

Equations (33) and (34) express the KFVS scheme in a flux-difference splitting format implying that the KFVS scheme can also be looked upon as a flux-difference splitting scheme. Higher order schemes can now be obtained by modifying the formulae for $G_{j+\frac{1}{2}}$ as

$$G_{j+\frac{1}{2}} = \text{EFS} + (1/4)[(1 + \phi)(DG_{j+\frac{1}{2}}^+ - DG_{j+\frac{1}{2}}^-) + (1 - \phi)(DG_{j-\frac{1}{2}}^+ - DG_{j+\frac{3}{2}}^-)], \tag{36}$$

where the expression for the first order scheme (EFS) is the right-hand side of (34). The parameter ϕ takes on respectively the values -1 and $1/3$ for the second- and

third-order upwind schemes. In order to suppress the spurious wiggles in the solution it is necessary to introduce the modified differences

$$\tilde{D}G^{\pm}_{j+\frac{1}{2}} = \text{minmod}[DG^{\pm}_{j+\frac{1}{2}}, \tilde{R} \times DG^{\pm}_{j-\frac{1}{2}}] \tag{37}$$

$$\tilde{\tilde{D}}G^{\pm}_{j+\frac{1}{2}} = \text{minmod}[DG^{\pm}_{j+\frac{1}{2}}, \tilde{R} \times DG^{\pm}_{j+\frac{3}{2}}] \tag{38}$$

where $\tilde{R}$ is a limiter with $0 \leqslant \tilde{R} \leqslant (3-\phi)/(1-\phi)$ and

$$\text{minmod}[a,b] = [(\text{sgn}(a) + \text{sgn}(b))/2]\min[|a|,|b|], \tag{39}$$

$$\text{sgn}(a) = +1, \text{ if } a > 0, \; -1 \text{ if } a < 0, \; 0{\cdot}0 \text{ if } a = 0{\cdot}0. \tag{40}$$

With these modified differences the formula (36) becomes

$$G_{j+\frac{1}{2}} = \text{EFS} + (1/4)[(1+\phi)(\tilde{D}G^{+}_{j+\frac{1}{2}} - \tilde{\tilde{D}}G^{-}_{j+\frac{1}{2}}) + (1-\phi)(\tilde{\tilde{D}}G^{+}_{j-\frac{1}{2}} - \tilde{\tilde{D}}G^{-}_{j+\frac{3}{2}})]. \tag{41}$$

Figure 3 shows the computed density and fluid velocity profiles using the first-order, second-order and third-order KFVS schemes for which $G_{j+\frac{1}{2}}$ given by (34) and (41) are used. The accuracy of the results and the crispness of the shock are evident.

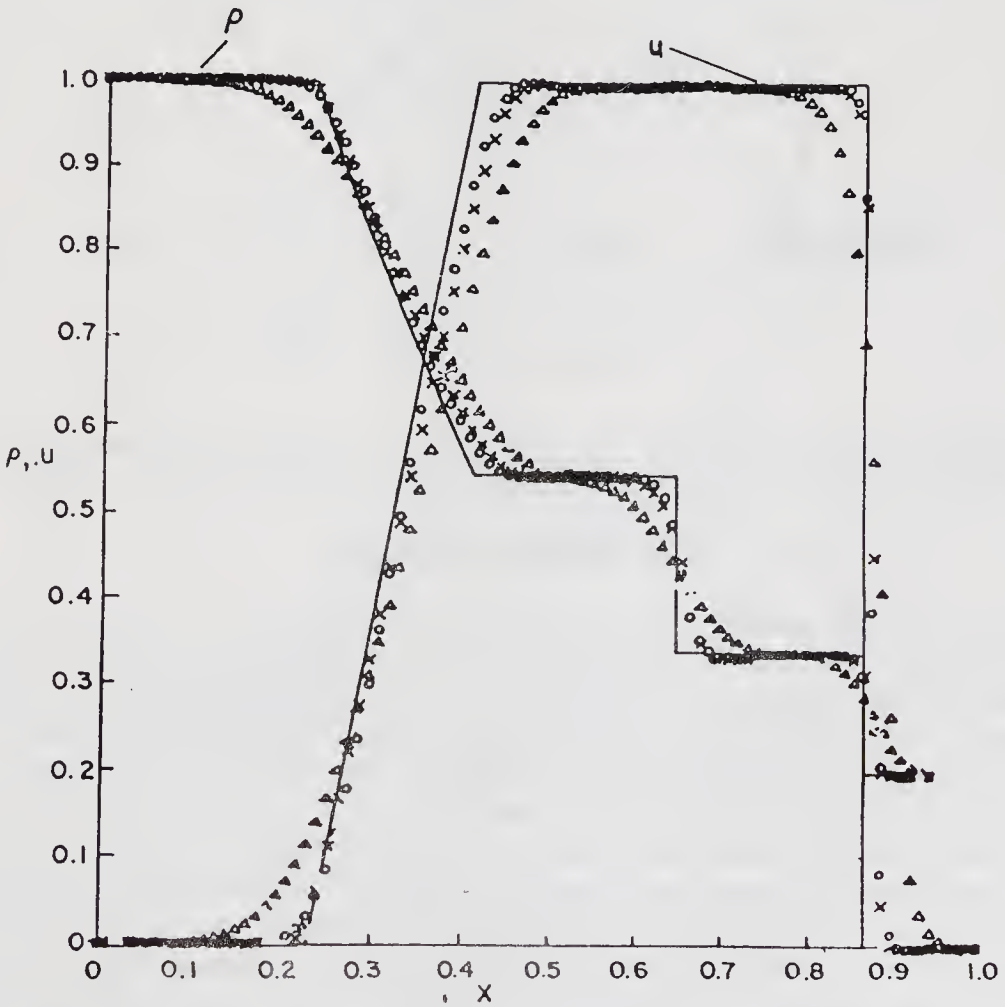

Figure 3. Computed ρ, u and exact (——) profiles for shock tube problems for KFVS. First order (△), second order (×) and third order (○).

4. KFVS applied to multidimensional flows

After having proved the capability of the KFVS method for a 1-D test case it is necessary to find out how it performs on 2-D and 3-D flows for low subsonic to hypersonic Mach numbers. Mandal (1989) has applied the high resolution finite volume KFVS method to the standard test cases of shock reflection and bump-in-a-channel problems. Figures 4 to 9 show the pressure contours and residue history for these problems. Mathur & Weatherill (1992) have applied the first order as well as high resolution KFVS schemes to a variety of 2-D problems with structured and unstructured meshes. They have used the cell-centred finite volume KFVS method. In order to use the high resolution KFVS method (which is a must in transonic regime) on a triangular mesh it is necessary to obtain the fluxes on the edges of a cell using extrapolation. Consider for example, a cell centre P of a triangular cell whose edges are shown hatched in I. The problem is to determine the flux on the edge AB in

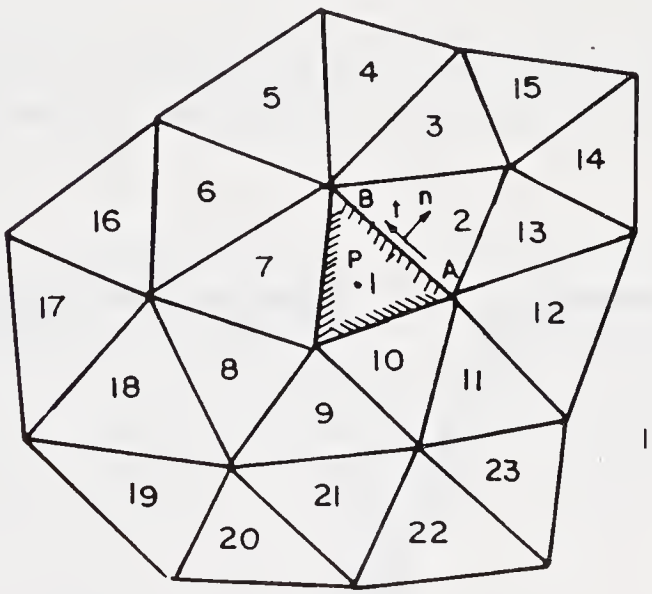

I

conformity with the upwinding principle. Let n be the outward normal to AB and t the tangent to the edge. Then applying the usual upwinding criterion we get

$$G_{AB} = G^+(u_{n1}, u_{t1}) + G^-(u_{n2}, u_{t2}). \tag{42}$$

Here we have suppressed the dependence of G^+ and G^- on density and temperature. In obtaining G_{AB} as above we have used only the data at cell centres 1 and 2. In order to obtain high resolution KFVS it is necessary to use the data at other neighbouring cell centres. Mathur & Weatherill (1992) consider the cell centres 13, 14, 15 and 3 and select that cell centre of this set which is closest to the straight line joining the centres 1 and 2. Assuming that this centre is 15, the flux G^-_{AB} is then obtained by extrapolation based on G^-_2 and G^-_{15}. By using the same criterion G^+_{AB} can also be obtained. Obviously to suppress the wiggles minmod operators as explained before need to be used again. Figures 10 and 11 show typical results obtained by Mathur & Weatherill (1992) for the flow past an airfoil and flow through a ramp in a channel. They have made extensive comparisons between the results obtained by KFVS and Jameson's methods and concluded that the results obtained using the KFVS method generally compare favourably with those obtained using the Jameson scheme.

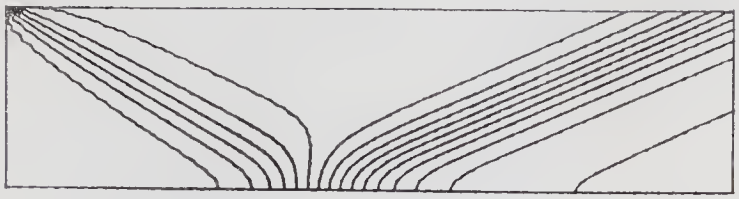

Figure 4. Pressure contours from 0·9 to 4·1 with an interval of 0·2 for shock reflection problem at supersonic Mach number ($M_\infty = 2{\cdot}9$, oblique shock angle = 29°) obtained using first-order time-marching finite difference KFVS scheme.

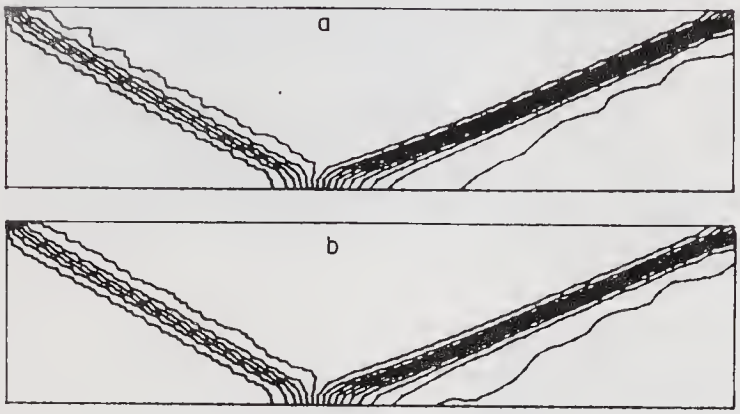

Figure 5. Pressure contours from 0·9 to 4·1 with an interval of 0·2 for shock reflection problem at supersonic Mach number ($M = 2{\cdot}9$, oblique shock angle = 29°) obtained using (**a**) second-order, and (**b**) third-order time-marching finite difference KFVS scheme.

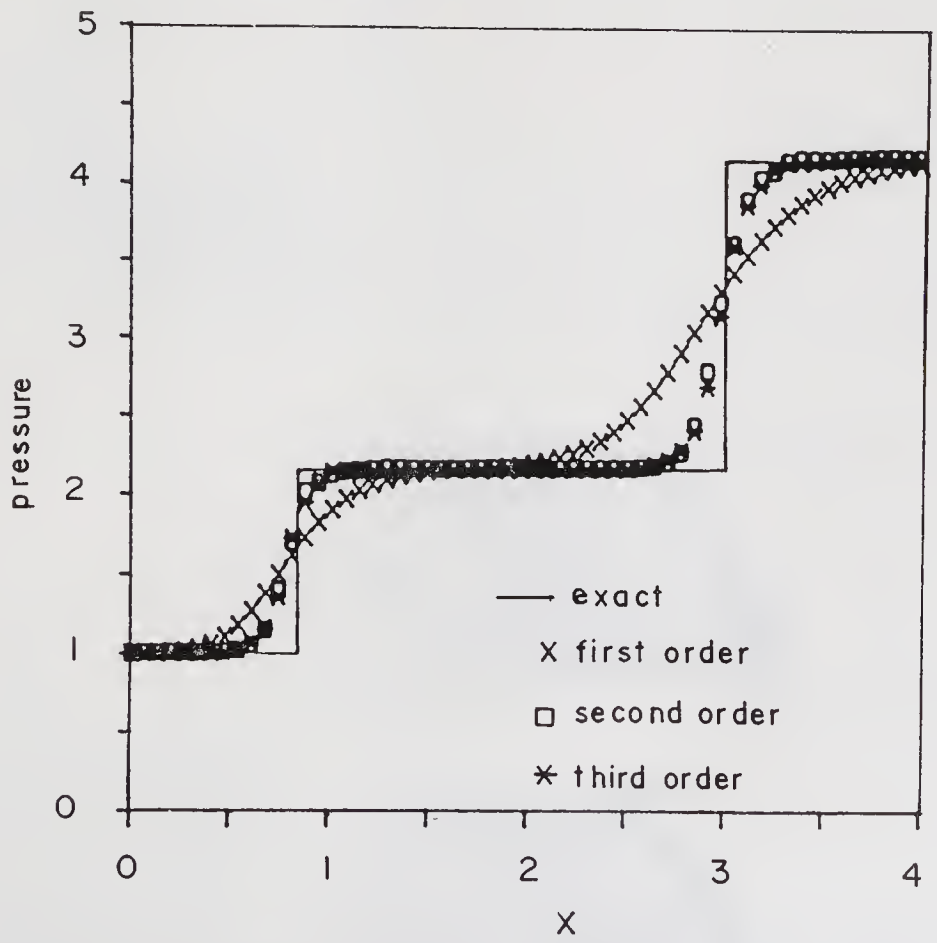

Figure 6. Pressure distribution at $y = 0{\cdot}5$ computed using first, second and third-order time-marching finite difference KFVS schemes.

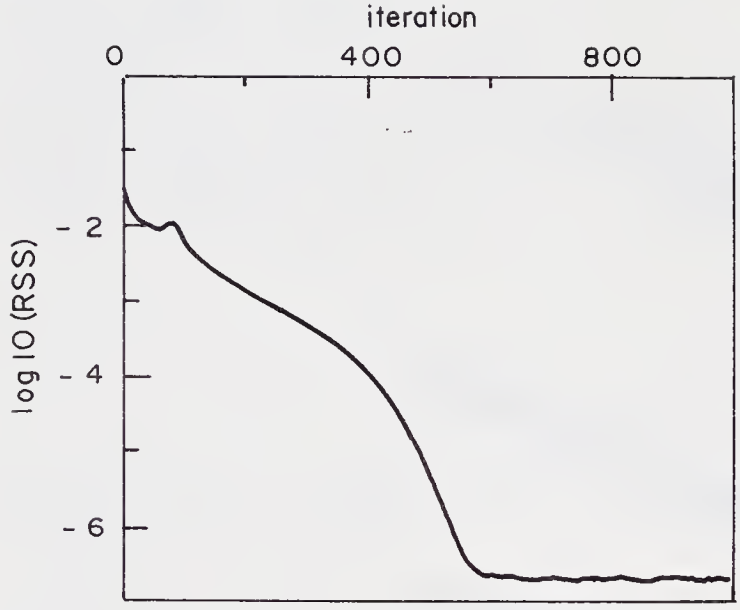

Figure 7. Convergence history for the shock reflection problem at supersonic Mach number using first-order time-marching finite difference KFVS scheme.

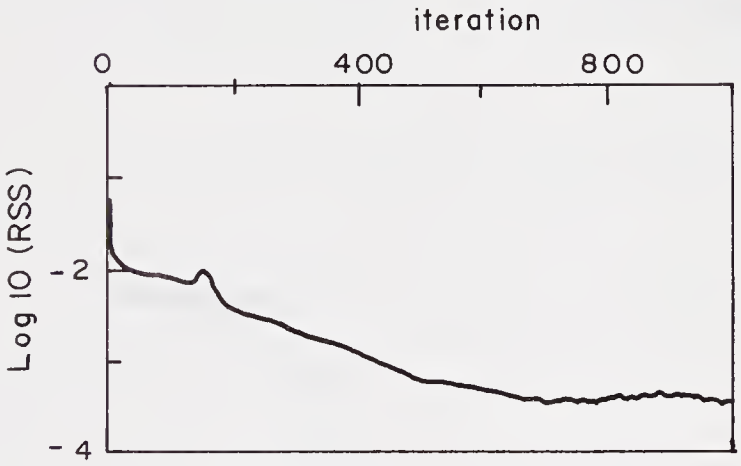

Figure 8. Convergence history for the shock reflection problem at supersonic Mach number using second-order time-marching finite difference KFVS scheme.

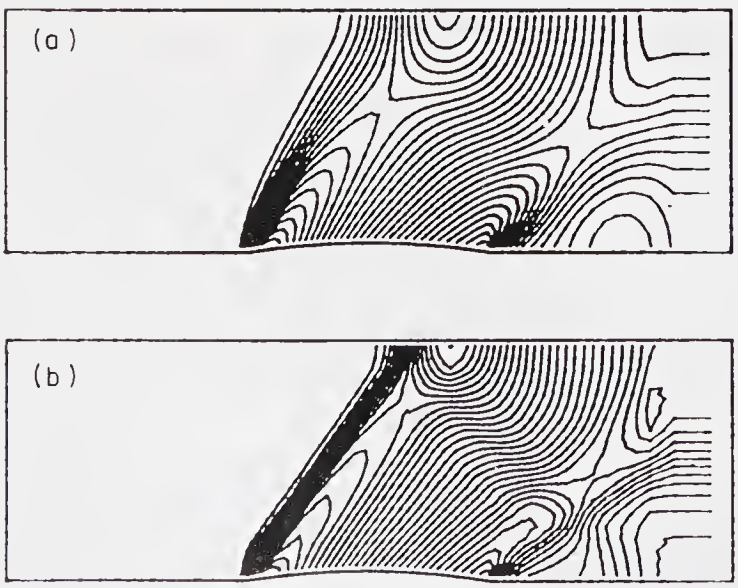

Figure 9. Pressure contours, from 0·65 to 1·45, with an interval of 0·025, for supersonic flow ($M_\infty = 1{\cdot}4$) over a 4% thick circular arc bump in a channel obtained using (**a**) first-order, and (**b**) high-resolution time-marching finite volume KFVS schemes.

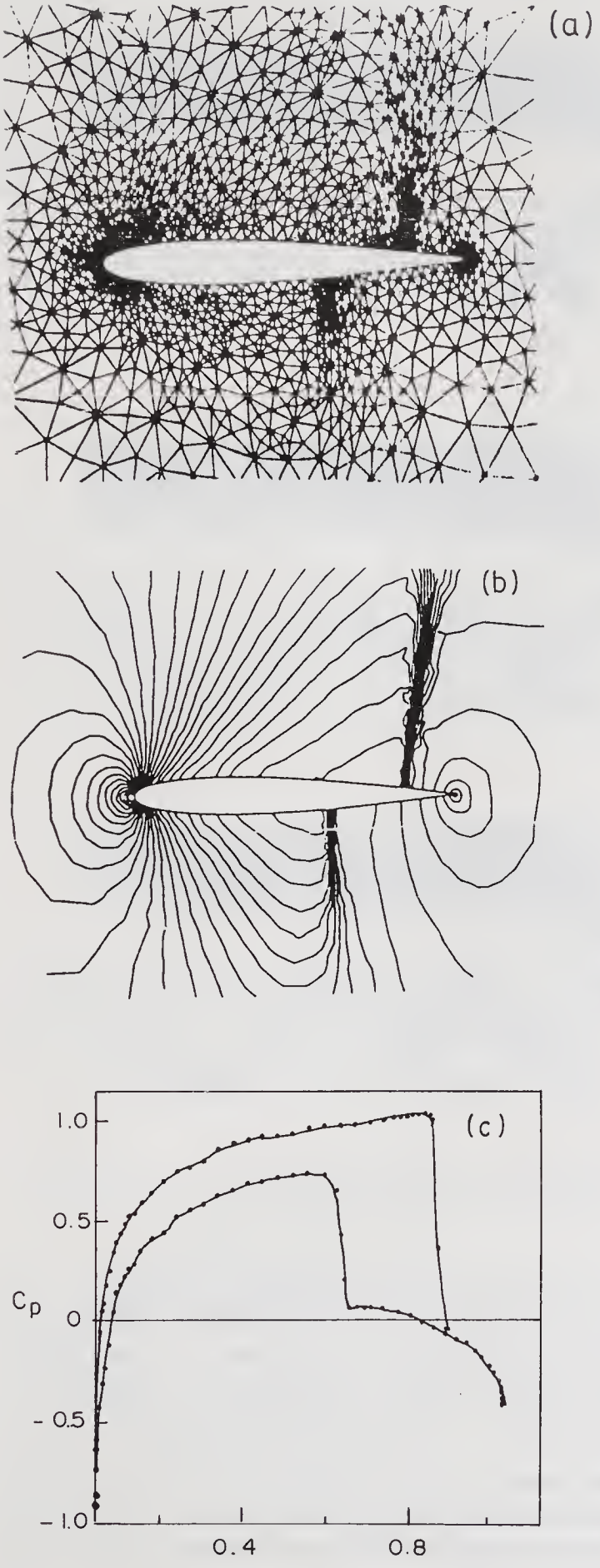

Figure 10. (**a**) Refined mesh, NACA 0012 airfoil. (**b**) Contours of pressure, refined mesh, KFVS. (**c**) C_p refined mesh, KFVS.

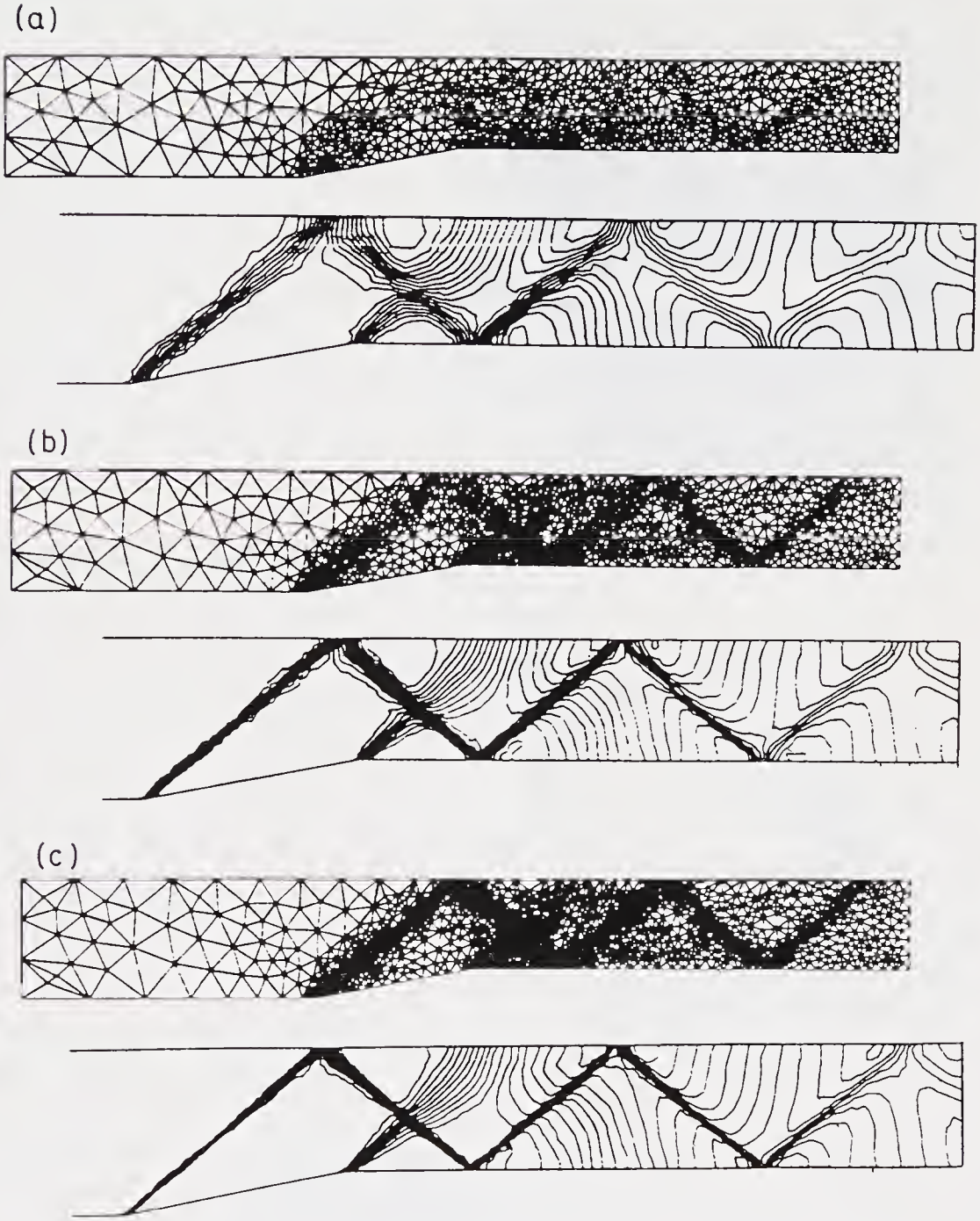

Figure 11. First (**a**), second (**b**), and third (**c**) refined meshes and contours of density.

Recently Deshpande *et al* (1992) have developed a 3-D time-marching Euler code (called BHEEMA) using the KFVS method for computing high speed flows around hypersonic re-entry configurations consisting of cone-cylinder-flares and control surfaces. This code uses finite volume method and operates on a hexahedral mesh generated by using stacked grids. Figures 12 and 13 show the pressure contours for axisymmetric configuration at $M = 4$ and $\alpha = 2°$, and a plot of the pressure coefficient for the re-entry configuration with wings at $M = 4$ and $\alpha = 0°$. Based on an elaborate comparison of the aerodynamic coefficients (C_A, C_N, C_M etc.) obtained from BHEEMA with the wind-tunnel results, they conclude that the time-marching 3-D Euler code

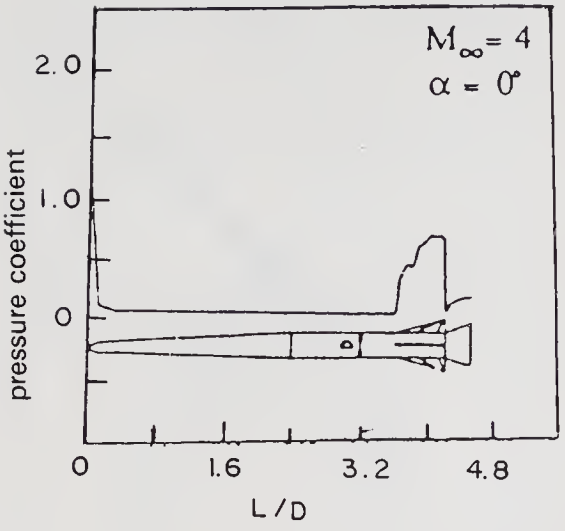

Figure 12. Pressure distribution along blunt cone-cylinder-flare (with lifting surfaces).

BHEEMA is a reliable design tool for predicting aerodynamic coefficients within 15%. Recently Deshpande & Dass (1992) have successfully used the convergence acceleration device called general minimum residual (GMRES) algorithm in combination with KFVS for obtaining faster convergence.

As a last example of the application of KFVS, mention may be made of the work of Theerthamalai & Deshpande (1992) who computed hypersonic reacting flow over a hemisphere using the KFVS method and an equilibrium chemistry model. For this purpose they considered 5 species (O, N, NO, O_2, N_2) and 3 reaction models

$$R_1\colon\ O_2 + M \rightleftharpoons 2O + M,$$

$$R_2\colon\ N_2 + M \rightleftharpoons 2N + M,$$

$$R_3\colon\ N_2 + O_2 \rightleftharpoons 2NO.$$

Here M stands for any one of the 5 species. For a specified γ the Euler equations were solved by BHEEMA for computing density, fluid velocity and temperature, everywhere in the flow field. Then the chemistry module was used to compute mass fractions, temperature and γ, everywhere in the flow field. The results of the computations reveal that the drag coefficient for Mach 10, 15, 20 was within 2% of that obtained by using

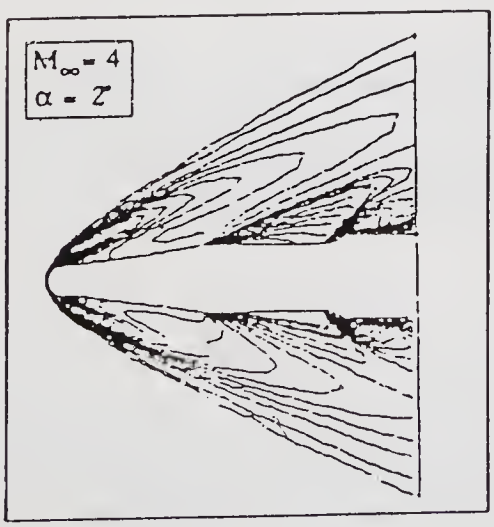

Figure 13. Iso-pressure contours for the configuration without lifting surfaces.

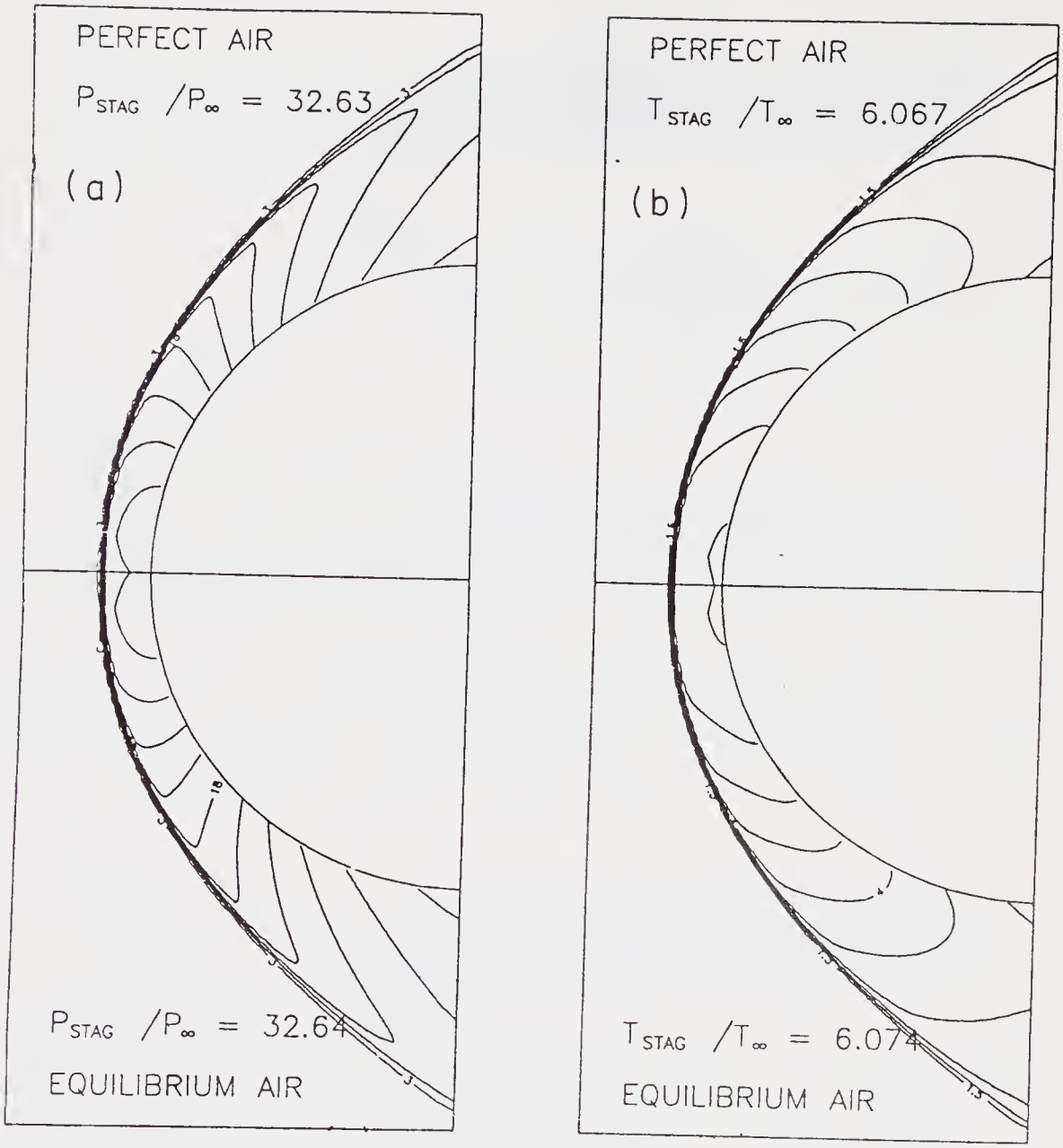

Figure 14. Pressure (**a**), and temperature (**b**) contours for reacting flow past a sphere (M = 5).

the nonreacting perfect gas model. However, the temperature differs substantially. Figures 14 and 15 show the temperature and pressure contours for $M_\infty = 5, 15$.

It is therefore reasonable to conclude that the KFVS method has travelled a long way since its modest beginning in 1982 and is now a fully tested and validated kinetic upwind method capable of computing inviscid compressible flows past any configuration.

5. Promising future directions

The search is continuously on for the elusive best method for obtaining numerical solutions of the Euler equations. The two guiding principles for developing new methods are that the method be less dissipative as compared to the existing ones

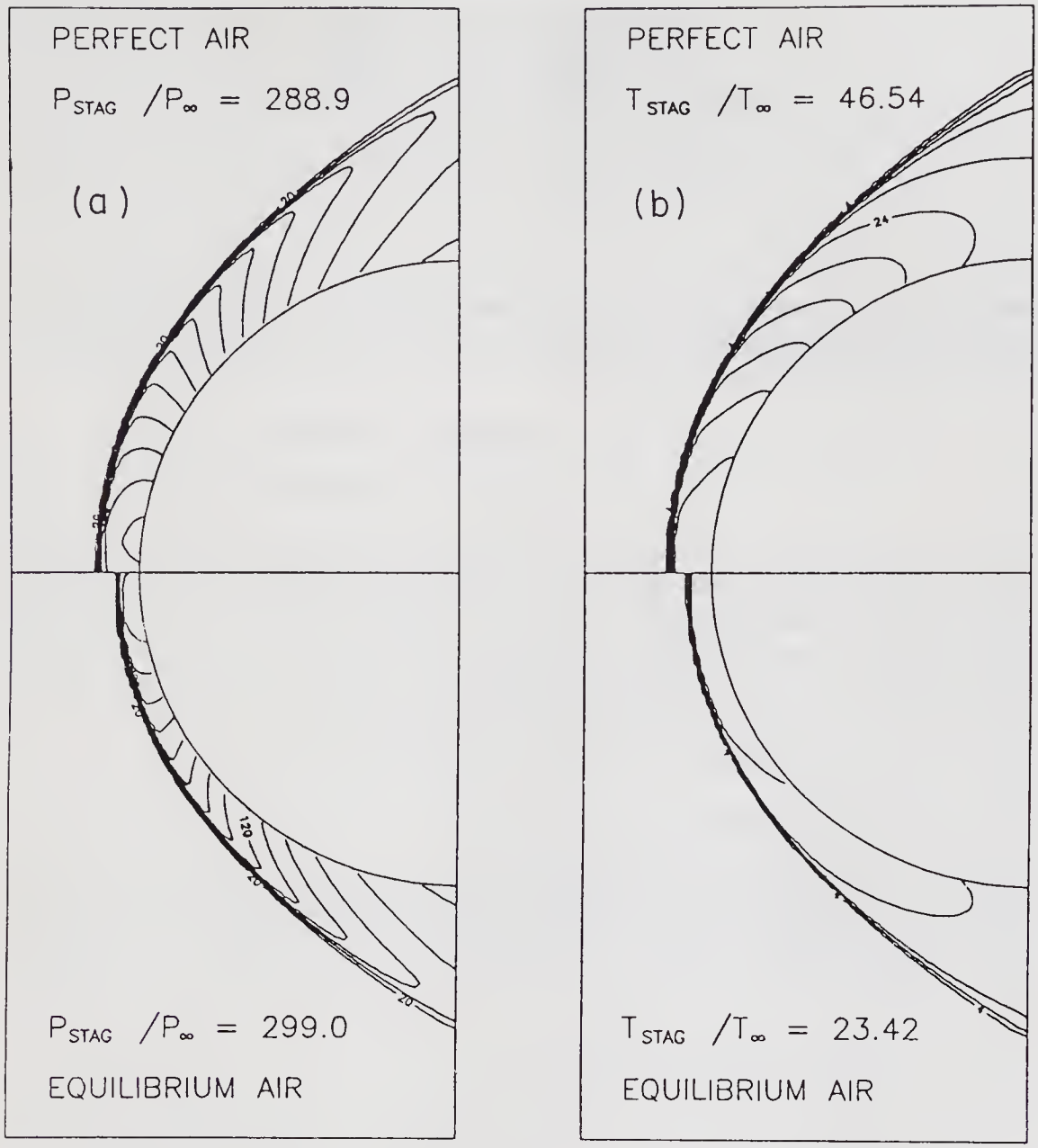

Figure 15. Pressure (**a**), and temperature (**b**) contours for reacting flow past a sphere (M = 15).

and further that it should mimic the physics of the flow as closely as possible. The development of upwind schemes is a consequence of following the second principle. We discuss briefly here four new ideas for developing upwind schemes exploiting the connection between the Boltzmann equation and the Euler equations.

5.1 *Use of exponential switch*

Considering the 1-D problem again for the sake of demonstrating the idea, we observe that KFVS is equivalent to assuming that the flux at the boundary B of a cell (see II) is given by

$$f_B = [(F_R + F_L)/2] - [(F_R - F_L)/2]\mathrm{sgn}(v). \tag{43}$$

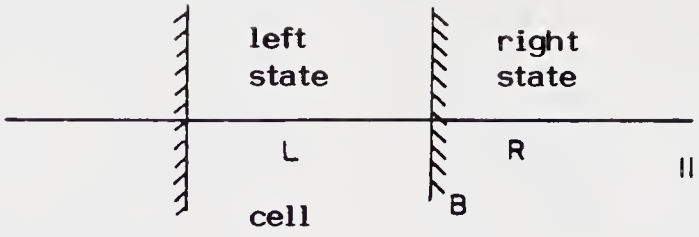

Here F_R and F_L are the Maxwellians corresponding to the right and left states, respectively, and sgn(v) is the usual sign function. We now replace the sign function by the exponential function giving

$$f_B = [(F_R + F_L)/2] - [(F_R - F_L)/2]\exp(-(\alpha|v|\Delta t)/\Delta x), \quad \text{for } v \geqslant 0,$$
$$f_B = [(F_R + F_L)/2] + [(F_R - F_L)/2]\exp(-(\alpha|v|\Delta t)/\Delta x), \quad \text{for } v \leqslant 0, \qquad (44)$$

where α is a nonnegative real number. When the controlling parameter α is zero we get the standard KFVS scheme, and when α is infinity we obtain the central difference scheme which has zero diffusion. Thus by continuously varying α we can control the numerical diffusion in the scheme. Raghurama Rao & Deshpande (1991a) have applied the above scheme to the 1-D shock tube problem. The results are shown in figure 16 from which it is obvious that the above modification does reduce the diffusion in the scheme. Further investigation is essential to develop the idea even more.

5.2 *Kinetic splitting based on thermal velocity*

One of the criticisms that may be raised against the KFVS is that the method assumes the existence of the rest frame as the splitting of the flux requires the division of velocity space into two halves $v \geqslant 0$ and $v \leqslant 0$. As the rest frame is physically

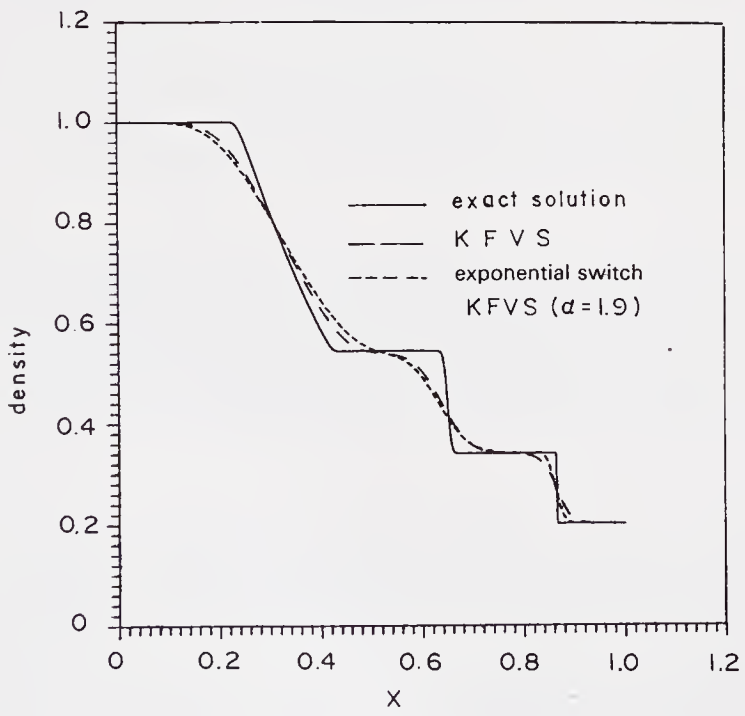

Figure 16. Results (KFVS) for 1-D shock tube problem.

meaningless it may be a good idea to do the splitting without assuming the existence of a rest frame. One possibility is to do the splitting based on the thermal (or what is also called peculiar) velocity. The thermal velocity **c** appears in the formulae for pressure, temperature and stress tensors of the kinetic theory of gases, and is thus physically more meaningful than the variable **v**. The motion of a molecule can be thought of as consisting of a random movement with velocity c superimposed on an orderly motion with velocity u. The random variable c is a Gaussian-distributed variable if we are dealing with inviscid gas dynamics. It may therefore be rewarding if a numerical scheme is constructed exploiting the above ideas. For the present we do splitting based on c. Towards this end we write the Boltzmann equation (without the collision term) in the form

$$(\partial F/\partial t) + u(\partial F/\partial x) + c(\partial F/\partial x) = 0. \tag{45}$$

Taking the moments we obtain

$$(\partial U/\partial t) + (\partial G^t/\partial x) + (\partial G^a/\partial x) = 0, \tag{46}$$

where

$$G^t = (u\Psi, F) = \begin{bmatrix} \rho u \\ \rho u^2 \\ \rho e u \end{bmatrix}, \quad \text{and } G^a = (c\Psi, F) = \begin{bmatrix} 0 \\ p \\ pu \end{bmatrix} \tag{47}$$

The eigenvalues of the flux Jacobian $(\partial G^t/\partial U)$ are all u, u, u showing that $(\partial G^t/\partial x)$ corresponds to the transport of fluid with velocity u. The eigenvalues of $(\partial G^a/\partial U)$ on the other hand are $0, \pm a[(\gamma-1)/\gamma]^{1/2}$ where a is the local sonic velocity. The dynamics of the fluid can therefore be considered as being influenced partly by the particle motion (movement with velocity u) and partly by the wave motion (random movement or movement of waves with velocity $0, \pm a[(\gamma-1)/\gamma]^{1/2}$). Loosely speaking the fluid motion can be considered partly particle-like and partly wave-like. Balakrishnan & Deshpande (1991, 1992) were the first ones who experimented with numerical schemes exploiting the wave–particle behaviour of fluid motion. Here we attack the problem from a different angle, namely, the construction of the Boltzmann scheme by treating the u and c terms differently. Following Raghurama Rao & Deshpande (1991a, 1992) we split G^a into G^{a+} and G^{a-}, defined by

$$G^{a+} = \{\Psi, [(c + |c|)/2]F\} \text{ and } G^{a-} = \{\Psi, [(c - |c|)/2]F\}, \tag{48}$$

which can be simplified as

$$G^{a\pm} = \begin{bmatrix} \pm \rho/2(\pi\beta)^{\frac{1}{2}} \\ (p/2) \pm [\rho u/2(\pi\beta)^{\frac{1}{2}}] \\ (pu/2) \pm [1/2(\pi\beta)^{\frac{1}{2}}][(p/2) + \rho e] \end{bmatrix} \tag{49}$$

Raghurama Rao & Deshpande (1991a, 1992) have solved the 1-D shock tube problem and 2-D shock reflection problem using the above upwind method (which they term the peculiar velocity based upwind (PVU) method). Figures 17 and 18 show the results obtained. The PVU method is found to be much less expensive compared to the KFVS method. The basic idea of treating uf_x and cf_x terms in a different fashion seems quite sound and definitely needs much more study and testing on a variety of multidimensional problems.

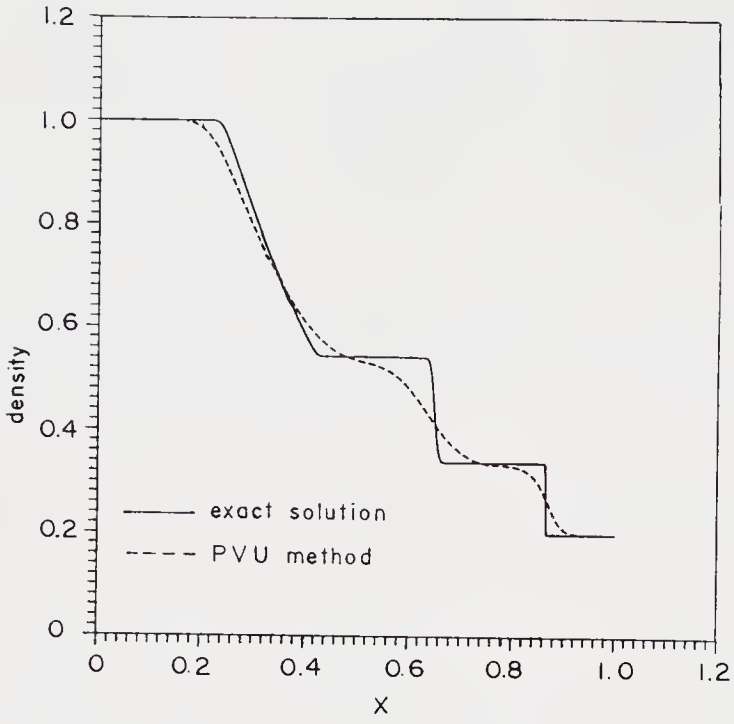

Figure 17. Results (PVU) for 1-D shock tube problem.

5.3 *Multidirectional Boltzmann schemes*

Many multidimensional upwind schemes advance the solution through a sequence of one-dimensional operators. The underlying physical model therefore involves wave propagation only along coordinate directions while the physical situation is that the

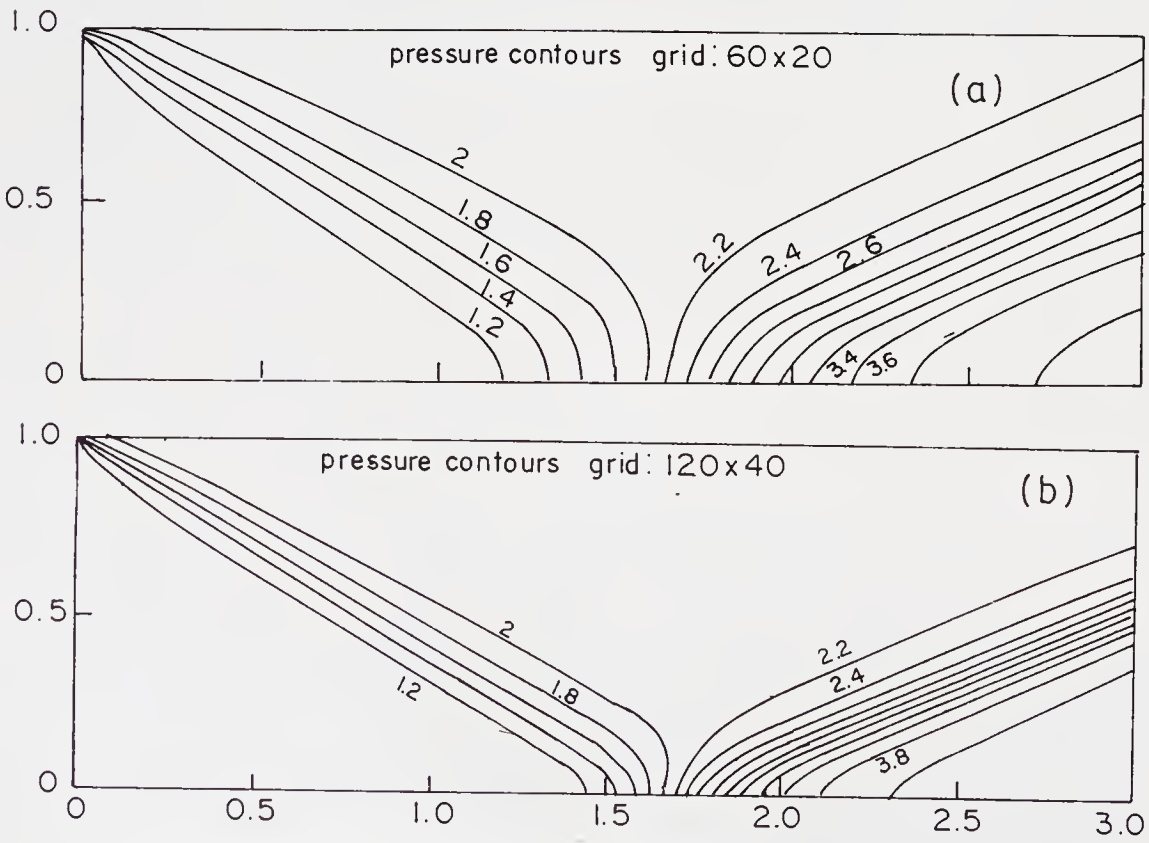

Figure 18. (**a**) & (**b**). Shock reflections with PVU method.

waves can propagate along all possible directions. Powell & Van Leer (1989) have observed that the inability to take the physics properly into account leads to a strong coupling between numerical schemes mentioned above and the grid on which they operate. Thus there is a need to design grid independent numerical schemes. Raghurama Rao & Deshpande (1991b) (see also Deshpande & Raghurama Rao 1992) have developed a genuinely multidimensional upwind Boltzmann scheme. Following the recent terminology this method can also be called the multidirectional upwind Boltzmann scheme.

Consider the Boltzmann equation without the collision term

$$(\partial f/\partial t) + \mathbf{v}\cdot(\partial f/\partial \mathbf{x}) = 0. \tag{50}$$

Considering a 2-D flow, the central problem in developing a multidirectional upwind scheme for the Euler equations (via the moment method strategy) is to develop a suitable discrete approximation to $v_1(\partial f/\partial x) + v_2(\partial f/\partial x)$ on the quadrilateral mesh, a portion of which is shown in III.

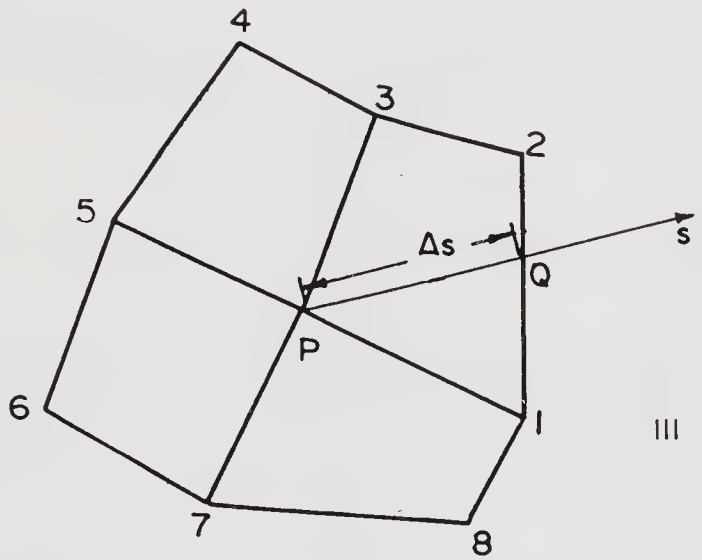

III

The mesh point P is surrounded by eight other mesh points. Particles arrive at P from all directions and *not* just along coordinate directions x and y since the molecular velocities v_1, v_2 vary from $-\infty$ to $+\infty$. The problem then boils down to obtaining a finite difference approximation to $\mathbf{v}\cdot grad\ f$ for each $\mathbf{v}$. Keeping in mind that $\mathbf{v}\cdot grad\ f = v(\partial f/\partial s)$, where s = coordinate along $\mathbf{v}$, we can obtain the first-order finite difference approximation as

$$v(\partial f/\partial s) = v[(f_P - f_Q)/\Delta s], \tag{51}$$

where Δs = distance between the points P and Q. We notice that on the right hand side of (51) the difference $f_P - f_Q$ appears instead of $f_Q - f_P$ because particles having velocity antiparallel to direction s send information to P. A slight rearrangement of (51) yields

$$v(\partial f/\partial s) = [v(\Delta n/\Delta s)][(f_P - f_Q)/\Delta n] = v_n[(f_P - f_Q)/\Delta n], \tag{52}$$

where Δn is the perpendicular distance of P from the segment 12. The next problem is to calculate f_Q from the data at the nodes $1, 2, \ldots, 8$. The position of the donor

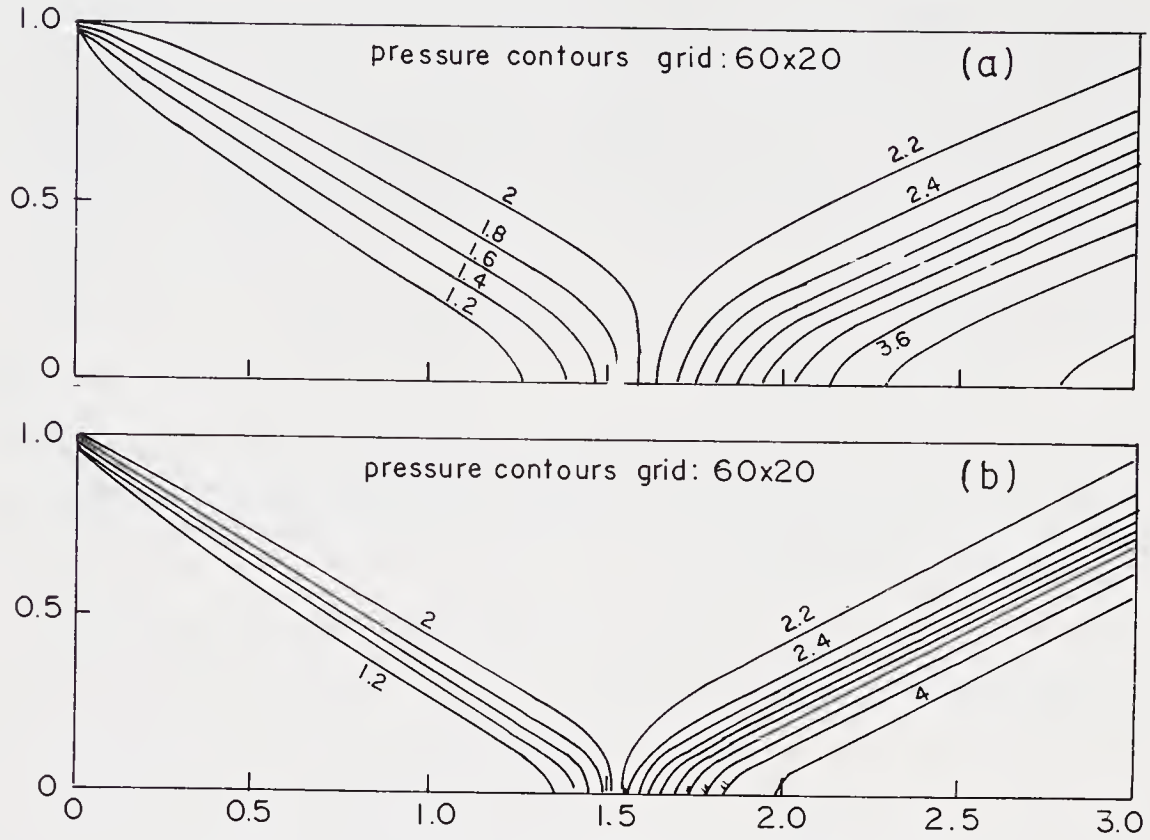

Figure 19. Shock reflections with KFVS (**a**) and GMBU (**b**) schemes.

point Q depends on the velocities (v_1, v_2) and could be anywhere on any of the eight segments $12, 23, \ldots, 81$. Consider the segment 12. Assuming linear variation between the nodes 1 and 2 the distribution function f_Q can be computed easily. Raghurama Rao & Deshpande (1991b) have given all the details involved in interpolation, obtaining appropriate limits of integration with respect to v_1, v_2. Of the two integrations they have been able to perform one, while the other one has to be performed numerically. Integrations with respect to velocities v_1, v_2 appear in the formulation when we pass from (51) to the Euler equations via the moment method strategy. As the resultant scheme takes into account all possible directions it is aptly called a multidirectional upwind Boltzmann scheme. They have applied this scheme to the standard shock reflection problem and the results are shown in figure 19 where the pressure contours from this scheme are compared with those from the usual KFVS scheme. It is obvious that the multidirectional scheme has much less smearing. Unfortunately, this scheme is very expensive and further research is necessary to improve it. Constructing a new multidirectional scheme using the thermal velocity is an attractive idea.

5.4 *Least squares weak upwind scheme*

Presently development of Euler solvers on unstructured meshes is mostly limited to finite element and finite volume based methods. The use of finite difference formulation on an unstructured grid is still a challenging task. Recently Deshpande *et al* (1988, 1989) have tackled this problem from a completely different point of view. At the heart of this formulation is the least squares discrete approximation to the derivatives f_x and f_y of any function f which in the present case is the Maxwellian velocity

distribution

$$f = F = [\rho/2\pi RT]\exp\{-[(v_1 - u_1)^2/2RT] - [(v_1 - u_1)^2/2RT] - [I/I_0]\}. \tag{53}$$

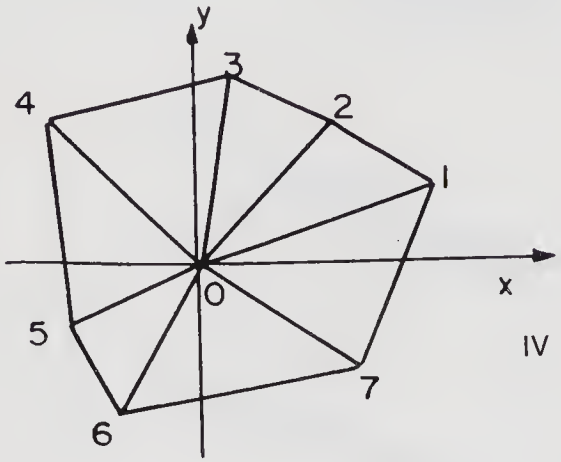

Let us consider a part of the triangular mesh shown in IV where the node O is surrounded by nodes 1, 2, 3, ... and let x_i, y_i be the coordinates of the node i. Introduce the notation

$$\Delta f_i = f_i - f_o, \quad \Delta x_i = x_i - x_o, \quad \Delta y_i = y_i - y_o.$$

The Taylor expansion gives

$$\Delta f_i = f_{xo}\Delta x_i + f_{yo}\Delta y_i, \quad i = 1, 2, \ldots, n. \tag{54}$$

Thus we have two unknowns f_{xo} and f_{yo} and n linear equations. By minimizing the square of the error

$$e = \sum_{i=1}^{n} (\Delta f_i - f_{xo}\Delta x_i - f_{yo}\Delta y_i)^2, \tag{55}$$

we get the least squares approximation

$$f_{xo} = \frac{\|\Delta y\|^2(\Delta x, \Delta f) - (\Delta x, \Delta y)(\Delta y, \Delta f)}{\|\Delta x\|^2\|\Delta y\|^2 - (\Delta x_1 \Delta y)^2}, \tag{56}$$

$$f_{yo} = \frac{\|\Delta y\|^2(\Delta y, \Delta f) - (\Delta x, \Delta y)(\Delta x, \Delta f)}{\|\Delta x\|^2\|\Delta y\|^2 - (\Delta x_1 \Delta y)^2}, \tag{57}$$

where

$$\|\Delta x\|^2 = \sum_{i=1}^{n} \Delta x_i^2, \quad \|\Delta y\|^2 = \sum_{i=1}^{n} \Delta y_i^2,$$

$$(\Delta x, \Delta f) = \sum_{i=1}^{n} \Delta x_i \Delta f_i, \quad (\Delta y, \Delta f) = \sum_{i=1}^{n} \Delta y_i \Delta f_i. \tag{58}$$

The formulae (56) and (57) are only first-order accurate. The second-order accurate approximations are obtained by replacing Δf_i in (56) and (57) by $\Delta \tilde{f}_i$ defined by

$$\Delta \tilde{f}_i = \Delta f_i - \tfrac{1}{2}\Delta x_i \Delta f_{xi} - \tfrac{1}{2}\Delta y_i \Delta f_{yi}, \quad \Delta f_{xi} = f_{xo} - f_{xi}, \quad \Delta f_{yi} = f_{yo} - f_{yi}. \tag{59}$$

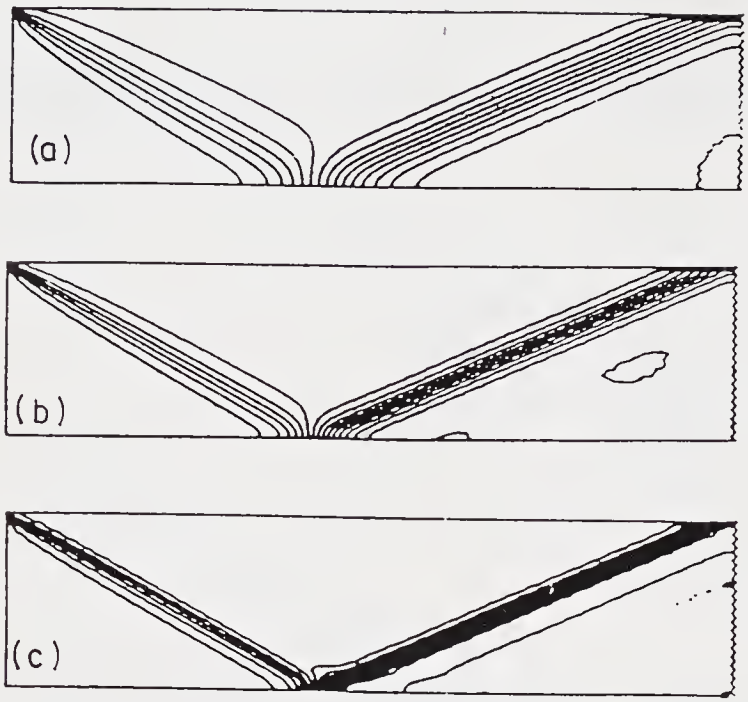

Figure 20. Pressure contours for shock reflection problem using least squares upwind method: first order without (**a**) and with (**b**) rotation; second order with rotation (**c**). (Contour levels 0·9 to 4·1 at intervals of 0·2.)

An upwind scheme for the solution of the 2-D Boltzmann equation

$$(\partial f/\partial t) + v_1(\partial f/\partial x) + v_2(\partial f/\partial y) = 0, \tag{60}$$

can now be constructed using the discrete approximation (56) and (57). For $v_1 > 0$ and for obtaining discrete upwind approximation to f_{xo} we take the stencil to the left of the y-axis, and for $v_1 < 0$ we take the stencil to its right. A similar approach can be used for obtaining the discrete upwind approximation to f_{yo}. We term this approach x–y splitting. It is important to note that we can locally rotate the coordinate system as (56) and (57) are valid for any arbitrary frame. It is possible to reduce the numerical diffusion in the scheme by locally rotating the x, y frame to x', y' such that the x'-axis is parallel to the local streamline and the y'-axis is normal to the streamline. We then do the upwinding for $f_{x'_o}$ along the x'-axis and take all the nodes around O for obtaining $f_{y'_o}$. Once (60) is upwind differenced the least squares weak upwind scheme for the Euler equations can be obtained by the moment method strategy. The capability of the method has been demonstrated on a 2-D shock reflection problem. The first-order scheme without rotation (x–y splitting in global frame) and with rotation (x–y splitting in local frame) and the second-order accurate scheme with rotation have been applied to this problem. The pressure contours are shown in figure 20. These plots show that the scheme with rotation even though of first order captures the shock crisply. The second-order scheme captures the shock even more crisply.

6. Concluding remarks

In this paper, an attempt has been made to survey the tremendous development that has taken place over the last ten years in kinetic schemes. We have concentrated on the work done in the field by the author and several of his coworkers; for lack of time and space, the contributions of other researchers have been only passingly

referred to. The KFVS scheme and its other variants have made steady progress over the years from its modest beginning in the early eighties to a mature numerical method for computing 3-D flows. The richness of the *moment method strategy* has been amply demonstrated by considering many possible directions such as wave-particle splitting, least squares upwinding and multidirectional upwinding.

The work presented in this paper is based on the research work done by several graduate students at our laboratory and collaborators from research and development organizations within the country. The author is specially thankful to J C Mandal, S V Raghurama Rao, A K Ghosh, A K Dass, M Nagarathinam, S Sekar, R Krishnamurthy, P K Sinha and P S Kulkarni. Financial support obtained from the Indo-Soviet Integrated Long Term Programme of Coordination in Science and Technology and the Indo-French Centre for the Promotion of Advanced Research (IFCPAR)/Centre Franco-Indien pour la Promotion de la Recherche Advancé (CFIPRA) is gratefully acknowledged.

References

Balakrishnan N, Deshpande S M 1991 New upwind schemes with wave–particle splitting for inviscid compressible flows. 91 FM 12, Fluid Mechanics Report, Department of Aerospace Engineering, Indian Institute of Science, Bangalore

Balakrishnan N, Deshpande S M 1992 New upwind methods exploiting the wave–particle behaviour of fluid flow. Presented at IMACS *International Symposium on Mathematical Modelling and Scientific Computing* (Calcutta: Int. J. Services)

Chakravarthy S R, Osher S 1983 High resolution applications of the Osher upwind scheme for the Euler equations. AIAA Paper no. 83–1943

Croisille J P, Delorme P 1991 Kinetic symmetrizations and pressure laws for the Euler equations. Report 91-67, Universite de Paris – Sud, France

Croisille J P, Villedieu 1992 Kinetic flux splitting schemes for hypersonic flows. *Proceedings 13th International Conference on Numerical Methods in Fluid Dynamics* (Berlin: Springer-Verlag)

Deshpande S M 1986a A second order accurate kinetic theory based method for inviscid compressible flows. NASA Technical Paper 2613

Deshpande S M 1986b Kinetic theory based new upwind methods for inviscid compressible flows. AIAA Paper 86–0275

Deshpande S M 1986c On the Maxwellian distribution, symmetric form, and energy conservation for the Euler equations. NASA Technical Paper 2583

Deshpande S M, Dass A K 1992 GMRES acceleration of kinetic flux vector split Euler code. *Proceedings of the First European Conference on Computational Fluid Dynamics*, Brussels

Deshpande S M, Ghosh A K, Mandal J C 1989 Least squares weak upwind method for Euler equations. 89 FM 4, Fluid Mechanics Report, Department of Aerospace Engineering, Indian Institute of Science, Bangalore

Deshpande S M, Mandal J C, Ghosh A K 1988 Kinetic upwind method for inviscid gas dynamics. *Proceedings Commonwealth Advisory Aeronautical Research Council (CAARC) Specialists Meeting on CFD*, National Aeronautical Laboratory, Bangalore

Deshpande S M, Raghurama Rao S V 1992 A genuinely multi-dimensional upwind scheme based on kinetic theory for Euler equations. Presented at *IMACS International Symposium on Mathematical Modelling and Scientific Computing* (Calcutta: Int. J. Services)

Deshpande S M, Raul R 1982 Kinetic theory based fluid-in-cell method for Eulerian fluid dynamics. 82 FM 14, Fluid Mechanics Report, Department of Aerospace Engineering, Indian Institute of Science, Bangalore

Deshpande S M, Sekar S, Nagarathinam M, Krishnamurthy R, Sinha P K, Kulkarni P S 1992 A 3-dimensional upwind Euler solver using kinetic flux vector splitting method. *Proceedings 13th International Conference on Numerical Methods in Fluid Dynamics, Lecture notes in Physics.* (Berlin: Springer-Verlag) 414:

Elizarova T G, Chetverushkin B N 1985 Kinetic algorithms for calculating gas dynamic flows. *J. Comput. Math., Math. Phys.* 25: 1526–1533

Kaniel S 1988 A kinetic model for the compressible flow equations. *Indiana Univ. Math. J.* 37: 537–563

Mandal J C 1989 *Kinetic upwind method for inviscid compressible flows*, Ph D thesis, Department of Aerospace Engineering, Indian Institute of Science, Bangalore

Mandal J C, Deshpande S M 1988 Higher order accurate kinetic flux vector splitting method for Euler equations. *Proceedings of the Second International Conference on Nonlinear Hyperbolic Problems* (Aachen FRG) (Braunschweig: Vieweg) Also (1989) *Notes Numer. Fluid Mech* 24: 384–392

Mathur J S, Weatherill N P 1992 The simulation of inviscid compressible flows using an upwind kinetic method on unstructured grids. *Int. J. Numer. Methods Fluids* 15: 59–82

Morton K W 1985 Generalized Galerkin methods for nonlinear hyperbolic problems. *Comput. Methods Appl. Mech. Eng.* 52: 835–859

Perthame B 1990 Boltzmann type schemes for gas dynamics and the entropy property. *SIAM J. Numer. Anal.* 27: 1405–1421

Powell K G, Van Leer B 1989 A genuinely multidimensional upwind cell-vertex scheme for the Euler equations. AIAA Paper 89–0095

Pullin D I 1980 Direct simulation methods for compressible inviscid ideal gas flows. *J. Comput. Phys.* 34: 231–244

Raghurama Rao S V, Deshpande S M 1991a A class of efficient kinetic upwind schemes for compressible flows. 91 FM 11, Fluid Mechanics Report, Department of Aerospace Engineering, Indian Institute of Science, Bangalore

Raghurama Rao S V, Deshpande S M 1991b A genuinely multi dimensional upwind Boltzmann scheme for Euler equations. 91 FM 6, Fluid Mechanics Report, Department of Aerospace Engineering, Indian Institute of Science, Bangalore

Raghurama Rao S V, Deshpande S M 1992 New upwind methods for Euler equations using thermal velocity based flux splitting. Presented at *IMACS International Symposium on Mathematical Modelling and Scientific Computing* (Calcutta: Int. J. Services)

Rietz R D 1981 One-dimensional compressible gas dynamics calculations using the Boltzmann equation. *J. Comput. Phys.* 42: 108–123

Roe P L 1981 Approximate Riemann solvers, parameter vectors and difference schemes. *J. Comput. Phys.* 43: 357–372

Theerthamalai P, Deshpande S M 1992 Computation of hypersonic flows over a sphere using kinetic flux vector splitting scheme with equilibrium chemistry. *Proceedings 6th National Conference on Aerodynamics*, Aeronautical Development Establishment, Bangalore

Van Leer B 1982 Flux vector splitting for the Euler equations. *Lecture Notes in Physics* (Berlin: Springer Verlag) 170: 507–512

Some numerical schemes using curvilinear coordinate grids for incompressible and compressible Navier–Stokes equations

H DAIGUJI and B R SHIN*

Department of Aeronautics and Space Engineering, Faculty of Engineering, Tohoku University, Sendai 980, Japan
* Present address: Department of Mechanical Design Engineering, College of Engineering, Chungnam National University, Daejeon 305-764, Korea

Abstract. In this review paper some numerical schemes recently developed by the authors and their coworkers for analysing the cascade flows of turbomachinery are described. These schemes use the curvilinear coordinate grid and solve the momentum equations of contravariant velocities (volume flux). The compressible flow schemes are based on the delta-form approximate-factorization finite-difference scheme, and are improved by using the diagonalization, the flux difference splitting and the TVD schemes to save computational effort and to increase stability and resolvability. Furthermore, using higher-order compact TVD MUSCL schemes, we can capture not only shock waves but also contact surfaces very sharply. On the other hand, the incompressible flow schemes are based on the well-known SMAC scheme, and are extended to the curvilinear coordinate grid and further to the implicit scheme to reduce computations. These schemes, like the SMAC scheme, satisfy the continuity condition identically, and suppress the occurrence of spurious errors. In both the compressible and incompressible schemes, for the turbulent flow the k–ε turbulence model with the law of the wall or considering the low Reynolds number effects is employed, and for the unsteady flow the Crank–Nicholson method is employed and the solution at each time step is obtained by the Newton iteration. Use of the volume flux instead of the physical velocity is inevitable for the MAC type schemes, and makes it easy to impose boundary conditions. Finally, some calculated results using the present schemes are shown.

Keywords. Navier–Stokes equations; computational fluid dynamics; numerical schemes; curvilinear coordinates; incompressible flow; compressible flow.

1. Introduction

Of late, available computer facilities are making rapid progress as shown in figure 1, and it has been possible to solve the Navier–Stokes equations practically. We here explain some Euler and Navier–Stokes codes which have been developed in our

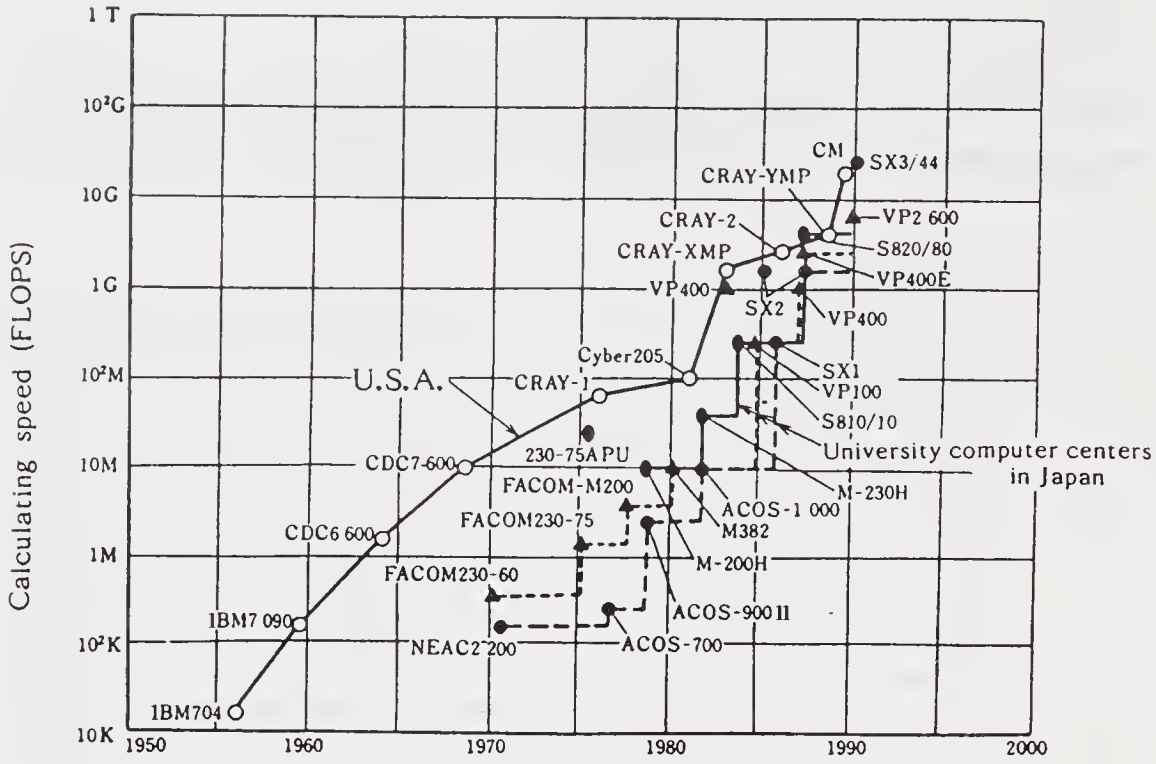

Figure 1. Progress in calculating speeds of large scale computers.

laboratory, Department of Aeronautics and Space Engineering, Tohoku University, during the past five years. These codes consist of the main parts for incompressible and compressible flows and pre- and post-processors, and have a number of versions for turbulent flows and unsteady flows. By employing these codes, many internal flow problems, especially cascade flows of turbomachinery, were computed.

We will first describe an outline of the numerical schemes for the compressible Euler and Navier–Stokes equations. In the 1970's the explicit MacCormack (1969) scheme was widely used, and Denton's (1974) explicit finite volume scheme was also used frequently for the cascade flow problems. However, since the beginning of the 1980's, the Beam–Warming (1978) delta-form approximate-factorization finite-difference scheme began to be used, because in such implicit schemes a large Courant number can be taken, that is, the computer time is saved. The MacCormack (1982) scheme was extended to an implicit scheme, and the Denton (1983) scheme was also improved considerably. Among these schemes the Beam–Warming (1978) scheme is the most flexible, and has been modified by various kinds of newly developed numerical techniques.

The unsteady one-dimensional Euler equations can be transformed into equations of waves propagating along a path line and two sound waves by applying the theory of characteristics. The flux vector splitting by Steger–Warming (1981) is an upwind method in which the flux vector is split into two subvectors according to signs of phase velocities of these waves, and the upwind differences are taken for these subvectors separately. The total variation diminishing (TVD) schemes proposed by Harten (1983) are those which contain a required artificial viscosity only in a restricted region. This artificial viscosity is added automatically by means of a nonlinear limiter function so as to stabilize the solution. These numerical techniques made possible the computation of high Reynolds number flow with discontinuities.

For the steady flow, the implicit Euler method is widely used in the time integration

for the TVD stability. On the left hand side, the first-order upwind scheme can be used, the viscous term is considered partially, and in order to save computer time the diagonalization (Pulliam & Chaussee 1981) or the LU factored scheme (Anderson *et al* 1988; Yokota & Caughey 1988) with the multigrid method is employed. On the right hand side, the flux vector (difference) splitting with more than the second-order TVD scheme (Chakravarthy & Osher 1985; Yee & Harten 1985) satisfying the entropy condition is used, and the viscous term must be contained completely. In order to capture the interface and the shock crossing the computational grid diagonally, it is necessary to use the accurate high resolution scheme (Tamura & Fujii 1991; Yamamoto & Daiguji 1991a). The ENO/SR scheme (Harten 1989) is an excellent high resolution scheme for the one-dimensional scalar equation, but the extension to the multi-dimensional Navier–Stokes equations has not been accomplished yet. For the unsteady flow, the Crank–Nicholson method is widely used, and the resultant equations are solved by the Newton iteration or the various kinds of relaxation methods.

In the schemes developed in our laboratory, the volume fluxes are used as dependent variables. For the equations of volume fluxes, it is easy to impose the boundary conditions. For example, although the Euler solutions of flow past a wing by different schemes are in general largely scattered due to incomplete treatments of the solid wall boundary condition, the trouble can be solved by using the present scheme (Daiguji *et al* 1987). And the treatments of the periodic condition in the three-dimensional rotor flow become very simple (Daiguji & Yamamoto 1988; Yamamoto & Daiguji 1991b). In the present schemes, the diagonalization, the flux difference splitting and some higher-order TVD schemes are used. The k–ε turbulence model is employed for the calculation of turbulent flows, and the Crank–Nicholson method and the Newton iteration for the unsteady flows. The details of the present schemes will be described in §§ 2.2 and 3.2.

We will next describe an outline of the numerical schemes for the incompressible Navier–Stokes equations. These schemes are classified according to the dependent variables, that is,

(i) primitive variable methods,
(ii) stream function methods,
(iii) others.

In the primitive variable (velocity $\mathbf{u}$ and pressure p) methods, there are

(ia) MAC type scheme,
(ib) pseudo- (artificial) compressibility method,
(ic) penalty function FEM,
(id) FEM using solenoidal weighting function.

These schemes are applicable to three-dimensional and turbulent flows. Next, though the stream function (ψ) methods can be extended to the third dimension by introducing the vector potential $\boldsymbol{\Psi}$, these methods are usually applied only to the two-dimensional laminar flow.

(iia) Method solving the fourth-order equation of ψ,
(iib) method using the vorticity transport equation and the Poisson equation of ψ.

As the other method, there is,

(iiia) method using the vorticity transport equation and calculating $\mathbf{u}$ from the Biot–Savart law directly.

Among these the methods most widely used for the calculation of turbulent flow are the MAC type schemes and the pseudo-compressibility methods.

The MAC scheme (Harlow & Welch 1965) is an epoch-making method in which the continuity condition is satisfied identically and the spurious error, that is checkerboard like oscillation of pressure, is removed completely by introducing a staggered grid. Then, the method was improved to the fractional step method (Chorin 1968; Kim & Moin 1985), the simplified MAC (SMAC) scheme (Amsden & Harlow 1970; Dodge 1977), the SIMPLE (Patankar 1980), and so on. Recently, these MAC type schemes were also extended to the curvilinear coordinate grid. The quantities to be defined at the each cell side centre must be the contravariant velocities (Shyy *et al* 1985; Nakamura & Takemoto 1985), the volume fluxes (Shin *et al* 1988; Rosenfeld *et al* 1991), the contravariant physical velocity components (Demirdzic *et al* 1987), or the covariant physical velocity components (Karki & Patankar 1988). To use these physical components is effective for removing defects due to the nonsmooth grid.

The pseudo-compressibility methods (Chorin 1967; Chang *et al* 1988; Hartwich & Hsu 1988) are time-marching methods modified to apply to the incompressible flow, and have been used only for the steady state flow. Because, while the incompressible flow has a elliptic character, such as a disturbance at one point in the flow field spreads throughout the field instantaneously, the pseudo-compressibility method based on the compressible flow scheme has a hyperbolic character, so the disturbance spreads only inside a limited region. However, recently the method has been extended to unsteady flow (Rogers *et al* 1991). In these methods, many excellent techniques developed for the compressible flow schemes can be utilized directly.

The steady and unsteady incompressible flow schemes (Ikohagi & Shin 1991; Shin *et al* 1992a) developed in our laboratory are SMAC schemes modified to be applicable to the curvilinear coordinate grid and further extended to the implicit scheme. The details of these schemes shall be explained in §§ 2.3 and 3.3.

2. Fundamental equations

2.1 *Coordinate transformation*

In the transformation between cartesian coordinates $\mathbf{x}=(x,y,z)$ and general curvilinear coordinates $\boldsymbol{\xi}=(\xi,\eta,\zeta)$, the relations between matrics $x_\xi, x_\eta, \cdots$ and $\xi_x, \xi_y, \cdots$ are

$$\begin{bmatrix} x_\xi & x_\eta & x_\zeta \\ y_\xi & y_\eta & y_\zeta \\ z_\xi & z_\eta & z_\zeta \end{bmatrix} \begin{bmatrix} \xi_x & \xi_y & \xi_z \\ \eta_x & \eta_y & \eta_z \\ \zeta_x & \zeta_y & \zeta_z \end{bmatrix} = \begin{bmatrix} 1 & 0 & 0 \\ 0 & 1 & 0 \\ 0 & 0 & 1 \end{bmatrix}, \tag{1}$$

and the Jacobian J is defined as

$$J = \frac{\partial(x,y,z)}{\partial(\xi,\eta,\zeta)} = \begin{vmatrix} x_\xi & x_\eta & x_\zeta \\ y_\xi & y_\eta & y_\zeta \\ z_\xi & z_\eta & z_\zeta \end{vmatrix}. \tag{2}$$

The derivatives with respect to x, y and z are rewritten to the derivatives with respect

to ξ, η and ζ as

$$(\partial/\partial x_i) = (\partial \xi_j/\partial x_i)(\partial/\partial \xi_j), \quad \nabla = (\nabla \xi_j)(\partial/\partial \xi_j), \tag{3}$$

$\partial(J\nabla\xi_i)/\partial\xi_i = 0$, therefore

$$J\nabla\phi = (\partial/\partial\xi_i)J(\nabla\xi_i)\phi, \quad J\nabla^2 = (\partial/\partial\xi_i)[Jg_{ij}(\partial/\partial\xi_j)], \tag{4}$$

$$u_i(\partial/\partial x_i) = U_i(\partial/\partial\xi_i), \tag{5}$$

and using (1), yields

$$\nabla\xi_l \cdot \nabla \times \mathbf{a} = \nabla\xi_l \times \nabla \cdot \mathbf{a} = \varepsilon_{ijk}\frac{\partial\xi_l}{\partial x_j}\frac{\partial a_i}{\partial x_k} = \varepsilon_{ijk}\frac{\partial\xi_l}{\partial x_j}\frac{\partial\xi_m}{\partial x_k}\frac{\partial a_i}{\partial\xi_m}$$

$$= \frac{1}{J}\varepsilon_{lmn}\frac{\partial x_i}{\partial\xi_n}\frac{\partial a_i}{\partial\xi_m} = \frac{1}{J}\varepsilon_{lmn}\frac{\partial}{\partial\xi_m}\left(\frac{\partial x}{\partial\xi_n}\cdot\mathbf{a}\right), \tag{6}$$

where ε_{ijk} is the permutation tensor, and the relation $\varepsilon_{lmn}\partial^2\mathbf{x}/\partial\xi_m\partial\xi_n = 0$ is used. If $\mathbf{a} = \mathbf{u}$, then

$$\nabla\xi_l \cdot \nabla \times \mathbf{u} = (1/J)\varepsilon_{lmn}(\partial/\partial\xi_m)(h_{nj}U_j), \tag{7}$$

where the metric tensor components g_{ij} and h_{ij} are

$$g_{ij} = \nabla\xi_i \cdot \nabla\xi_j, \quad h_{ij} = (\partial\mathbf{x}/\partial\xi_i)\cdot(\partial\mathbf{x}/\partial\xi_i), \tag{8}$$

and the relations between the physical velocity $\mathbf{u} = (u, v, w)$ in $\mathbf{x}$ space and the contravariant velocity $\mathbf{U} = (U, V, W)$ in $\boldsymbol{\xi}$ space are

$$U_j = (\partial\xi_j/\partial x_i)u_i, \quad u_i = (\partial x_i/\partial\xi_j)U_j. \tag{9}$$

Using the equations so far mentioned, we can rewrite the fundamental equations in cartesian coordinates into the equations in general curvilinear coordinates.

The flows through an impeller of turbomachinery are usually calculated under the assumptions of irrotational absolute flow and steady relative flow. Between the absolute velocity $\mathbf{v}$ and the relative velocity $\mathbf{w}$, the relation

$$\mathbf{v} = \mathbf{w} + \boldsymbol{\omega} \times \mathbf{r} \tag{10}$$

holds, where $\boldsymbol{\omega} \times \mathbf{r}$ is the circumferential velocity and $\boldsymbol{\omega}$ is the angular velocity of impeller. And for an arbitrary scalar a or vector $\mathbf{a}$, the relations

$$a_t + \mathbf{v}\cdot\nabla a = a_t + \mathbf{w}\cdot\nabla a,$$

$$\mathbf{a}_t + \mathbf{v}\cdot\nabla\mathbf{a} = \mathbf{a}_t + \mathbf{w}\cdot\nabla\mathbf{a} + \boldsymbol{\omega} \times \mathbf{a}, \tag{11}$$

hold, where the left and right hand sides show the substantial derivatives in the absolute and relative flows, respectively. Using (10) and (11), we can rewrite the fundamental equations for the absolute flow into the equations for the relative flows.

2.2 *Fundamental equations of compressible flows*

The fundamental equations of compressible viscous flows are the conservation laws of mass, momentum and energy, and can be written in general curvilinear coordinates

as

$$(\partial\hat{q}/\partial t) + \hat{L}(\hat{q}) \equiv (\partial\hat{q}/\partial t) + (\partial\hat{F}_j/\partial\xi_j) + \hat{S} + \hat{H} = 0, \tag{12}$$

where

$$\hat{q} = J\begin{bmatrix} \rho \\ \rho u \\ \rho v \\ \rho w \\ e \end{bmatrix}, \quad \hat{F}_j = J\begin{bmatrix} \rho U_j \\ \rho u U_j + (\xi_j)_x p \\ \rho v U_j + (\xi_j)_y p \\ \rho w U_j + (\xi_j)_z p \\ (e+p)U_j \end{bmatrix}, \quad (j = 1, 2, 3), \tag{13}$$

$$\hat{S} = -J\frac{\partial\xi_j}{\partial x_k}\frac{\partial}{\partial\xi_j}\begin{bmatrix} 0 \\ \tau_{1k} \\ \tau_{2k} \\ \tau_{3k} \\ \tau_{ik}u_i \end{bmatrix} - \frac{\partial}{\partial\xi_j}\tilde{g}_{jk}k\frac{\partial T}{\partial\xi_k}\begin{bmatrix} 0 \\ 0 \\ 0 \\ 0 \\ 1 \end{bmatrix},$$

where $\tilde{g}_{ij} = Jg_{ij}$, ρ, p and T are the static density, pressure and temperature, respectively, $e = \rho(\varepsilon + \mathbf{u}^2/2)$ is the total internal energy per unit volume, and τ_{ij} are the cartesian components of viscous stress tensor.

$$\tau_{ij} = \mu[(\partial u_i/\partial x_j) + (\partial u_j/\partial x_i) - (2/3)\delta_{ij}\nabla\cdot\mathbf{u}], \quad (i, j = 1, 2, 3). \tag{14}$$

The values of flux vector $\hat{F}_j$ can be evaluated from the values of dependent variable vector $\hat{q}$ using the equation of state as

$$p = \rho RT = (\gamma - 1)(e - \rho\mathbf{u}^2/2). \tag{15}$$

In the case of the relative flow through an impeller, we must take

$$\mathbf{u} = \mathbf{w},$$
$$e = \rho(\varepsilon + v^2/2 - \omega r v_u), \tag{16}$$

in (13), where v_u is the circumferential component of absolute velocity $\mathbf{v}$, and consider the centrifugal and coriolis forces, that is,

$$\hat{H} = J\rho\begin{bmatrix} 0 \\ 0 \\ -\omega^2 x_2 - 2\omega w_3 \\ -\omega^2 x_3 + 2\omega w_2 \\ 0 \end{bmatrix}. \tag{17}$$

The physical velocity $\mathbf{u}$ is essentially independent of the computational grid, but the contravariant velocity $\mathbf{U}$ depends on the grid.

$$(JU)_{i,j,k} = (\mathbf{u}\cdot\mathbf{x}_\eta \times \mathbf{x}_\zeta)_{i,j,k}$$
$$= \frac{1}{4\Delta\eta\Delta\zeta}\begin{vmatrix} u & v & w \\ x_{i,j+1,k} - x_{i,j-1,k} & y_{i,j+1,k} - y_{i,j-1,k} & z_{i,j+1,k} - z_{i,j-1,k} \\ x_{i,j,k+1} - x_{i,j,k-1} & y_{i,j,k+1} - y_{i,j,k-1} & z_{i,j,k+1} - z_{i,j,k-1} \end{vmatrix}.$$

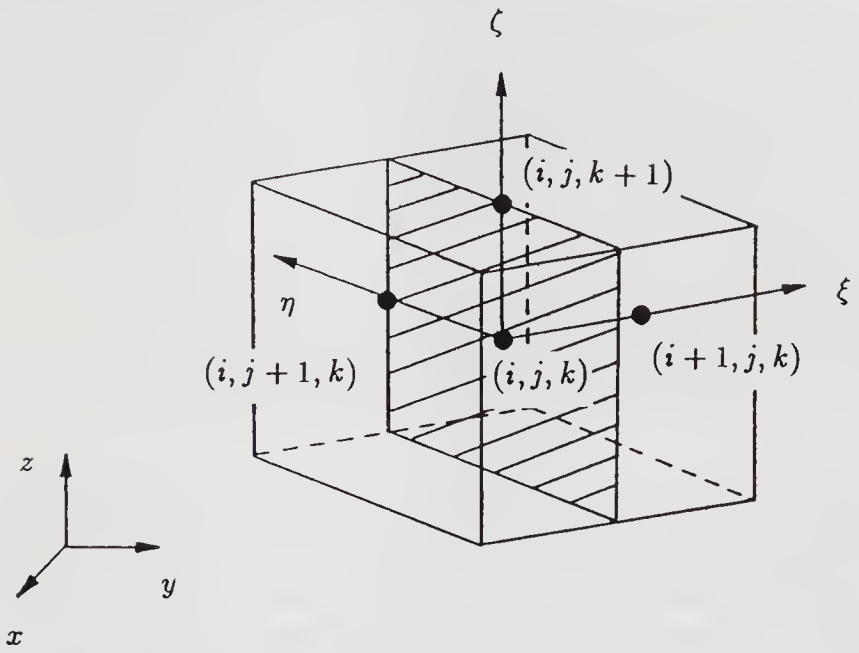

Figure 2. Curvilinear coordinate grid and volume flux.

Therefore, JU is the flow rate through ξ-const. surface, that is volume flux, as shown in figure 2. Since $\Delta\xi$, $\Delta\eta$ and $\Delta\zeta$ are usually taken constant, JU is independent of the grid spacing in the ξ-direction, but in proportion to the grid spaces in the η- and ζ-directions. The above-mentioned fundamental equations (12) and (13) contain the physical velocities and only the derivatives of JU, JV and JW with respect to ξ, η and ζ, respectively. Therefore, these equations are relatively insensitive to the smoothness of the computational grid. Furthermore, the Jacobian J means the volume of figure 2 divided by $8\Delta\xi\Delta\eta\Delta\zeta$. Therefore, the contravariant velocity U varies inversely as the grid space of ξ-direction and is nearly independent of the grid spaces of η- and ζ-directions.

By operating the matrix

$$B=\begin{bmatrix} 1 & 0 & 0 & 0 & 0 \\ 0 & \xi_x & \xi_y & \xi_z & 0 \\ 0 & \eta_x & \eta_y & \eta_z & 0 \\ 0 & \zeta_x & \zeta_y & \zeta_z & 0 \\ 0 & 0 & 0 & 0 & 1 \end{bmatrix}, \tag{18}$$

to (12), we get an alternating form of fundamental equations which contain the momentum equations of contravariant velocities.

$$\frac{\partial\tilde{q}}{\partial t}+\tilde{L}(\tilde{q})=B\left[\frac{\partial\hat{q}}{\partial t}+\hat{L}(\hat{q})\right]\equiv\frac{\partial\tilde{q}}{\partial t}+\frac{\partial\tilde{F}_j}{\partial\xi_j}+\tilde{R}+\tilde{S}+\tilde{H}=0, \tag{19}$$

where

$$\tilde{q}=J\begin{bmatrix}\rho\\ \rho U\\ \rho V\\ \rho W\\ e\end{bmatrix},\quad \tilde{F}_j=\begin{bmatrix}\rho JU_j\\ \rho JUU_j+\tilde{g}_{1j}p\\ \rho JVU_j+\tilde{g}_{2j}p\\ \rho JWU_j+\tilde{g}_{3j}p\\ (e+p)JU_j\end{bmatrix},\quad (j=1,2,3)$$

$$\tilde{R} = -J(\rho \mathbf{u} U_j + p\nabla\xi_j)\cdot\frac{\partial}{\partial\xi_j}\begin{bmatrix} 0 \\ \nabla\xi \\ \nabla\eta \\ \nabla\zeta \\ 0 \end{bmatrix}, \tag{20}$$

$$\tilde{S} = -J\frac{\partial\xi_j}{\partial x_k}\frac{\partial}{\partial\xi_j}\tau_{ik}\begin{bmatrix} 0 \\ (\partial\xi/\partial x_i)_0 \\ (\partial\eta/\partial x_i)_0 \\ (\partial\zeta/\partial x_i)_0 \\ u_i \end{bmatrix} - \frac{\partial}{\partial\xi_j}\tilde{g}_{jk}k\frac{\partial T}{\partial\xi_k}\begin{bmatrix} 0 \\ 0 \\ 0 \\ 0 \\ 1 \end{bmatrix}.$$

$\tilde{R}$ is an additional term introduced to express the convection term in divergence form.

The contravariant velocities U, V and W are the ξ, η and ζ components of transformed space velocity, respectively, and their momentum equations correspond to the equations of flow through each cell side. Therefore, for the usual curvilinear coordinate grid which is generated so as to fit to the boundaries, the boundary conditions of (19) can be imposed very easily. On the other hand, according to the above-mentioned matters, JUV does not always depend on the smoothness of grid spacings in the η- and ζ-directions, but JU^2 highly depends on the smoothness in the ξ-direction and inversely as the grid space. Therefore, (19) should be used for relatively smooth grids. In the actual numerical methods for (19), the right hand side is expressed as a linear combination of (12), while the left hand side is derived from (19) without the additional and diffusion terms. In fact, the time-increments of the additional term for the smooth grid are sufficiently small compared to the remaining terms, and the accuracy of our numerical methods does not depend on the left hand side operators for both of the steady and unsteady flows.

2.3 *Fundamental equations of incompressible flows*

The fundamental equations of incompressible viscous flows are the Navier–Stokes equations and the continuity equation. In the widely used MAC type schemes in curvilinear coordinates, the momentum equations of contravariant velocities are used in order to satisfy the continuity condition. Here, the following equations of the volume flux $J\mathbf{U}$ are employed.

$$\frac{\partial}{\partial t}(JU_l) + \frac{\partial}{\partial\xi_j}(JU_jU_l) - JU_j\mathbf{u}\cdot\frac{\partial}{\partial\xi_j}\nabla\xi_l = -\tilde{g}_{lj}\frac{\partial p}{\partial\xi_j} + J\frac{\partial\xi_l}{\partial x_i}\frac{\partial\tau_{ij}}{\partial x_j}, \quad (l = 1, 2, 3), \tag{21}$$

$$\frac{\partial}{\partial\xi_j}(JU_j) = 0. \tag{22}$$

These equations correspond to the compressible flow equations (19) and (20). The convection term is written in conservative form by introducing an additional term, but the pressure term is in nonconservative form. The final term of (21) is a viscous term written as

$$(Vis)_l = J\frac{\partial\xi_l}{\partial x_i}\frac{\partial}{\partial x_j}\nu\left(\frac{\partial u_i}{\partial x_j} + \frac{\partial u_j}{\partial x_i}\right). \tag{23}$$

Rewriting into curvilinear coordinates,

$$(Vis)_l = \frac{\partial \xi_l}{\partial x_i}\frac{\partial}{\partial \xi_j}\left(\nu \tilde{g}_{jk}\frac{\partial u_i}{\partial \xi_k}\right) + \frac{\partial \xi_i}{\partial x_j}\frac{\partial \nu}{\partial \xi_i}\tilde{g}_{lk}\frac{\partial u_j}{\partial \xi_k}, \quad (l = 1, 2, 3). \tag{24}$$

Further, rewriting this using the contravariant velocities,

$$(Vis)_l = \frac{\partial}{\partial \xi_j}\left\{\nu\left(\tilde{g}_{jk}\frac{\partial U_l}{\partial \xi_k} + \tilde{g}_{lk}\frac{\partial U_j}{\partial \xi_k}\right)\right\} - \frac{\partial}{\partial \xi_j}\left(\nu J\frac{\partial g_{jl}}{\partial \xi_k}U_k\right) - 2\nu J\frac{\partial^2 \xi_l}{\partial x_k \partial x_i}\frac{\partial u_k}{\partial x_i}.$$

If ν is constant throughout the flow field

$$\begin{aligned}(Vis)_l &= \nu\frac{\partial \xi_l}{\partial x_i}\frac{\partial}{\partial \xi_j}\tilde{g}_{jk}\frac{\partial u_i}{\partial \xi_k} \\ &= \nu\left[\frac{\partial}{\partial \xi_j}\tilde{g}_{jk}\frac{\partial U_l}{\partial \xi_k} - \frac{\partial}{\partial \xi_j}\left\{J\frac{\partial \xi_j}{\partial x_i}\frac{\partial}{\partial \xi_k}\left(\frac{\partial \xi_l}{\partial x_i}\right)U_k\right\} - J\frac{\partial^2 \xi_l}{\partial x_k \partial x_i}\frac{\partial u_k}{\partial x_i}\right],\end{aligned} \tag{25}$$

where $\partial u_k/\partial x_i = (\partial \xi_j/\partial x_i)\partial(U_m \partial x_k/\partial \xi_m)/\partial \xi_j$.

On the other hand, introducing the vorticity $\zeta = \nabla \times \mathbf{u}$, and using (6)

$$(Vis)_l = -\nu J \nabla \xi_l \cdot \nabla \times \zeta = -\nu \varepsilon_{lmn}\frac{\partial}{\partial \xi_m}\left(\frac{\partial \mathbf{x}}{\partial \xi_n}\cdot \zeta\right). \tag{26}$$

Further, introducing the contravariant vorticity defined as

$$Z_j = \frac{\partial \xi_j}{\partial x_i}\zeta_i, \quad \zeta_i = \frac{\partial x_i}{\partial \xi_j}Z_j, \tag{27}$$

we get

$$(Vis)_l = -\nu \varepsilon_{lmn}(\partial/\partial \xi_m)(h_{nj}Z_j), \quad (l = 1, 2, 3). \tag{28}$$

Using (7), the contravariant vorticities are

$$Z_j = (1/J)\varepsilon_{jkl}(\partial/\partial \xi_k)(h_{lm}U_m), \quad (l = 1, 2, 3). \tag{29}$$

Equation (24) is used in the case of turbulent flow, and (28) and (29) in the case of laminar flow and in the calculation of the direct numerical simulation (DNS).

2.4 *Turbulence model*

In the calculation of turbulent flow, the $k-\varepsilon$ turbulence model considering the low Reynolds number effects developed by Launder & Spalding (1974) and extended to curvilinear coordinates by Chien (1981) is employed. This model contains the transport of turbulence and wall effects, but has an assumption of eddy viscosity,

$$\tau_{ij} - \rho\overline{u_i' u_j'} = (\mu + \mu_t)\left(\frac{\partial u_i}{\partial x_j} + \frac{\partial u_j}{\partial x_i} - \frac{2}{3}\delta_{ij}\frac{\partial u_k}{\partial x_k}\right) - \frac{2}{3}\delta_{ij}\rho k, \quad (i, j = 1, 2, 3). \tag{30}$$

That is, anisotropic components of Reynolds stress $-\rho\overline{u_i' u_j'}$ are in proportion to anisotropic components of rate of strain.

The eddy viscosity μ_t is expressed as

$$\mu_t = C_\mu \rho k^2/\varepsilon, \tag{31}$$

where k is the turbulent kinetic energy and ε the dissipation rate of k. These turbulence quantities are obtained from their transport equations

$$\frac{\partial}{\partial t}J\begin{bmatrix}\rho k\\ \rho\varepsilon\end{bmatrix}+\frac{\partial}{\partial\xi_j}J\begin{bmatrix}\rho kU_j\\ \rho\varepsilon U_j\end{bmatrix}=J\begin{bmatrix}P\\ C_1\varepsilon P/k\end{bmatrix}+\frac{\partial}{\partial\xi_j}\begin{bmatrix}(\mu+\mu_t/\sigma_k)\tilde{g}_{jk}\partial k/\partial\xi_k\\ (\mu+\mu_t/\sigma_\varepsilon)\tilde{g}_{jk}\partial\varepsilon/\partial\xi_k\end{bmatrix}$$
$$-J\begin{bmatrix}\rho\varepsilon\\ C_2\rho\varepsilon^2/k\end{bmatrix}-J\begin{bmatrix}2\mu k/d^2\\ 2C_3\mu\varepsilon/d^2\end{bmatrix}, \tag{32}$$

where the kinetic energy production P is

$$P=-\rho\overline{u_i'u_j'}(\partial u_i/\partial x_j), \tag{33}$$

and the empirical constants and functions are

$$C_\mu=0{\cdot}09[1-\exp(-0{\cdot}0115y^+)],$$
$$C_1=1{\cdot}44,$$
$$C_2=1{\cdot}92[1-0{\cdot}3\exp(-R_{et}^2)],$$
$$C_3=\exp(-0{\cdot}5y^+),$$
$$\sigma_k=1{\cdot}0,\quad \sigma_\varepsilon=1{\cdot}3,$$
$$\mathrm{Re}_t=\rho k^2/\mu\varepsilon,\quad y^+=\rho_w u_\tau d/\mu_w,\quad u_\tau=(\tau_w/\rho_w)^{1/2}, \tag{34}$$

d is the normal distance from the wall, Re_t the turbulent Reynolds number, u_τ the friction velocity and τ_w the shear stress on the wall.

3. Numerical methods

3.1 *TVD upwind-difference schemes*

We here consider the simple one-dimensional scalar equation

$$(\partial u/\partial t)+(\partial f(a,u)/\partial x)=0, \tag{35}$$

where $a=\partial f/\partial u$ is the characteristic speed. The finite-difference equation of (35) can be generally written in the conservation form

$$u_i^{n+1}+(\Delta t/\Delta x)\theta(\hat{f}_{i+1/2}-\hat{f}_{i-1/2})^{n+1}=u_i^n-(\Delta t/\Delta x)(1-\theta)(\hat{f}_{i+1/2}-\hat{f}_{i-1/2})^n, \tag{36}$$

where $0\leqslant\theta\leqslant 1$, and $\hat{f}$ is the numerical flux function.

The second-order accurate upsteam- and central-difference schemes are

$$(f_x)_i=\begin{cases}(f_{i-2}-4f_{i-1}+3f_i)/2\Delta x, & (c\geqslant 0),\\ (-3f_i+4f_{i+1}-f_{i+2})/2\Delta x, & (c<0),\end{cases} \tag{37}$$

$$(f_x)_i=(f_{i+1}-f_{i-1})/2\Delta x. \tag{38}$$

In the total variation diminishing (TVD) scheme, these first-order difference schemes

are first expressed as a sum of the first-order upsteam-difference scheme and the remaining correction term, and then the correction term is modified locally by a limiter in order to stabilize the solution. The numerical flux of the second-order TVD upstream-difference scheme is

$$\left.\begin{aligned}\hat{f}_{i+1/2} = (1/2)(f_i + f_{i+1}) - (1/2)(Df^+_{i+1/2} - Df^-_{i+1/2})\end{aligned}\right] \text{first-order upstream-difference,}$$

$$\left.\begin{aligned}&+ (1/2)\text{minmod}[Df^+_{i-1/2}, bDf^+_{i+1/2}]\\ &- (1/2)\text{minmod}[Df^-_{i+3/2}, bDf^-_{i+1/2}]\end{aligned}\right] \text{correction.} \tag{39}$$

Similarly, the numerical flux of the second-order TVD central-difference scheme is

$$\begin{aligned}\hat{f}_{i+1/2} = {} & (1/2)(f_i + f_{i+1}) - (1/2)(Df^+_{i+1/2} - Df^-_{i+1/2})\\ & + (1/2)\text{minmod}[Df^+_{i+1/2}, bDf^+_{i-1/2}]\\ & - (1/2)\text{minmod}[Df^-_{i+1/2}, bDf^-_{i+3/2}],\end{aligned} \tag{40}$$

where, $Df^{\pm}_{j+1/2} = a^{\pm}_{i+1/2}\Delta u_{j+1/2}$, $a^{\pm} = (a \pm |a|)/2$, $\Delta u_{j+1/2} = u_{j+1} - u_j$, and here the minmod function

$$\text{minmod}[x, y] = \text{sign}(x)\max[0, \min\{|x|, y\,\text{sign}(x)\}],$$

which controls the slope of flux was used, $1 \leqslant b \leqslant 2$. As b is larger, the region where the limiter function acts becomes narrower.

Taking a linear combination of the TVD schemes, (39) and (40), using a parameter κ, we get (Chakravarthy & Osher 1985),

$$\begin{aligned}\hat{f}_{i+1/2} = {} & (1/2)(f_i + f_{i+1}) - (1/2)(Df^+_{i+1/2} - Df^-_{i+1/2})\\ & + [(1-\kappa)/4]\text{minmod}[Df^+_{i-1/2}, bDf^+_{i+1/2}]\\ & + [(1+\kappa)/4]\text{minmod}[Df^+_{i+1/2}, bDf^+_{i-1/2}]\\ & - [(1-\kappa)/4]\text{minmod}[Df^-_{i+3/2}, bDf^-_{i+1/2}]\\ & - [(1+\kappa)/4]\text{minmod}[Df^-_{i+1/2}, bDf^-_{i+3/2}],\end{aligned} \tag{41}$$

where $-1 \leqslant \kappa \leqslant 1$. In this case, $1 \leqslant b \leqslant (3-\kappa)/(1-\kappa)$. Particularly, if $\kappa = 1/3$, then (41) becomes the third-order accurate TVD upstream-difference scheme as

$$\begin{aligned}\hat{f}_{i+1/2} = {} & (1/2)(f_i + f_{i+1}) - (1/2)(Df^+_{i+1/2} - Df^-_{i+1/2})\\ & + (1/6)\text{minmod}[Df^+_{i-1/2}, bDf^+_{i+1/2}]\\ & + (1/3)\text{minmod}[Df^+_{i+1/2}, bDf^+_{i-1/2}]\\ & - (1/6)\text{minmod}[Df^-_{i+3/2}, bDf^-_{i+1/2}]\\ & - (1/3)\text{minmod}[Df^-_{i+1/2}, bDf^-_{i+3/2}].\end{aligned} \tag{42}$$

Further, when the limiters are removed, (42) is reduced to the usual four-point upstream difference form,

$$(f_x)_i = \begin{cases}(f_{i-2} - 6f_{i-1} + 3f_i + 2f_{i+1})/6\Delta x, & (a \geqslant 0),\\ (-2f_{i-1} - 3f_i + 6f_{i+1} - f_{i+2})/6\Delta x, & (a < 0).\end{cases}$$

The fourth-order accurate upstream- and central-difference schemes are

$$(f_x)_i = \begin{cases} (-f_{i-3} + 6f_{i-2} - 18f_{i-1} + 10f_i + 3f_{i+1})/12\Delta x, & (a \geqslant 0), \\ (-3f_{i-1} - 10f_i + 18f_{i+1} - 6f_{i+2} + f_{i+3})/12\Delta x, & (a < 0), \end{cases} \tag{43}$$

$$(f_x)_i = (f_{i-2} - 8f_{i-1} + 8f_{i+1} - f_{i+2})/12\Delta x. \tag{44}$$

The numerical fluxes of these difference schemes are

$$\begin{aligned} \hat{f}_{i+1/2} &= (1/2)(f_i + f_{i+1}) - (1/2)(Df^+_{i+1/2} - Df^-_{i+1/2}) \\ &\quad + (1/12)(-Df^+_{i-3/2} + 4Df^+_{i-1/2} + 3Df^+_{i+1/2}) \\ &\quad - (1/12)(3Df^-_{i+1/2} + 4Df^-_{i+3/2} - Df^-_{i+5/2}), \end{aligned} \tag{45}$$

$$\begin{aligned} \hat{f}_{i+1/2} &= (1/2)(f_i + f_{i+1}) - (1/2)(Df^+_{i+1/2} - Df^-_{i+1/2}) \\ &\quad + (1/12)(Df^+_{i-1/2} + 6Df^+_{i+1/2} - Df^+_{i+3/2}) \\ &\quad - (1/12)(-Df^-_{i-1/2} + 6Df^-_{i+1/2} + Df^-_{i+3/2}). \end{aligned} \tag{46}$$

Taking a linear combination of these fourth-order schemes with a parameter ϕ, we get

$$\begin{aligned} \hat{f}_{i+1/2} &= (1/2)(f_i + f_{i+1}) - (1/2)(Df^+_{i+1/2} - Df^-_{i+1/2}) \\ &\quad + [(1-\phi)/24](-Df^+_{i-3/2} + 4Df^+_{i-1/2} + 3Df^+_{i+1/2}) \\ &\quad + [(1+\phi)/24](Df^+_{i-1/2} + 6Df^+_{i+1/2} - Df^+_{i+3/2}) \\ &\quad - [(1-\phi)/24](3Df^-_{i+1/2} + 4Df^-_{i+3/2} - Df^-_{i+5/2}) \\ &\quad - [(1+\phi)/24](-Df^-_{i-1/2} + 6Df^-_{i+1/2} + Df^-_{i+3/2}). \end{aligned}$$

Further, by taking out the third-order upstream-difference scheme ahead of the form, yields

$$\begin{aligned} \hat{f}_{i+1/2} &= \left.\begin{aligned} &(1/2)(f_i + f_{i+1}) - (1/2)(Df^+_{i+1/2} - Df^-_{i+1/2}) \\ &+ (1/6)(Df^+_{i-1/2} + 2Df^+_{i+1/2}) \\ &- (1/6)(Df^-_{i+3/2} + 2Df^-_{i+1/2}) \end{aligned}\right] \text{third-order upstream-difference,} \\ &\quad \left.\begin{aligned} &- [(1-\phi)/24]D^3 f^+_{i-1/2} - [(1+\phi)/24]D^3 f^+_{i+1/2} \\ &+ [(1-\phi)/24]D^3 f^-_{i+3/2} + [(1+\phi)/24]D^3 f^-_{i+1/2} \end{aligned}\right] \text{correction,} \end{aligned} \tag{47}$$

where $D^3 f_{i+1/2} = Df_{i-1/2} - 2Df_{i+1/2} + Df_{i+3/2}$, and $-1 \leqslant \phi \leqslant 1$. Equation (47) has, in general, fourth-order accuracy, but for $\phi = 1/5$, it becomes the fifth-order upstream-difference scheme as

$$(f_x)_i = \begin{cases} (-2f_{i-3} + 15f_{i-2} - 60f_{i-1} + 20f_i + 30f_{i+1} - 3f_{i+2})/60\Delta x, & (a \geqslant 0), \\ (3f_{i-2} - 30f_{i-1} - 20f_i + 60f_{i+1} - 15f_{i+2} + 2f_{i+3})/60\Delta x, & (a < 0). \end{cases}$$

Finally, rewriting (47) into the TVD scheme, we get a compact TVD scheme

$$\begin{aligned} \hat{f}_{i+1/2} &= (1/2)(f_i + f_{i+1}) - (1/2)(Df^+_{i+1/2} - Df^-_{i+1/2}) \\ &\quad + (1/6)\text{minmod}[\tilde{D}f^+_{i-1/2}, b\tilde{D}f^+_{i+1/2}] \end{aligned}$$

$$+(1/3)\text{minmod}[\tilde{D}f^{+}_{i+1/2}, b\tilde{D}f^{+}_{i-1/2}]$$
$$-(1/6)\text{minmod}[\tilde{D}f^{-}_{i+3/2}, b\tilde{D}f^{-}_{i+1/2}]$$
$$-(1/3)\text{minmod}[\tilde{D}f^{-}_{i+1/2}, b\tilde{D}f^{-}_{i+3/2}], \tag{48}$$

where

$$\tilde{D}f^{+}_{i-1/2} = Df^{+}_{i-1/2} - [(1-\phi)/4]\bar{D}^3 f^{+}_{i-1/2},$$
$$\tilde{D}f^{+}_{i+1/2} = Df^{+}_{i+1/2} - [(1+\phi)/8]\bar{D}^3 f^{+}_{i+1/2},$$
$$\tilde{D}f^{-}_{i+3/2} = Df^{-}_{i+3/2} - [(1-\phi)/4]\bar{D}^3 f^{-}_{i+3/2},$$
$$\tilde{D}f^{-}_{i+1/2} = Df^{-}_{i+1/2} - [(1+\phi)/8]\bar{D}^3 f^{-}_{i+1/2}. \tag{49}$$
$$\bar{D}^3 f_{i+1/2} = \bar{D}f_{i-1/2} - 2\bar{D}f_{i+1/2} + \bar{D}f_{i+3/2},$$
$$\bar{D}f_{i-1/2} = \text{minmod}(Df_{i-1/2}, b_1 Df_{i+1/2}, b_1 Df_{i+3/2}),$$
$$\bar{D}f_{i+1/2} = \text{minmod}(Df_{i+1/2}, b_1 Df_{i+3/2}, b_1 Df_{i-1/2}),$$
$$\bar{D}f_{i+3/2} = \text{minmod}(Df_{i+3/2}, b_1 Df_{i-1/2}, b_1 Df_{i+1/2}),$$

and it is suitable to take $b = 4$ and $b_1 = 2$. Equation (48) is formally the same as the third-order TVD upstream-difference scheme of (42). Though the accuracy of this equation is fifth-order only for $\phi = 1/5$, the accuracy of the solution should gradually vary with the value of ϕ. By taking $\phi = 1/3$, (49) can be unificatively written as

$$\tilde{D}f^{\pm}_{j+1/2} = Df^{\pm}_{j+1/2} - (1/6)\bar{D}^3 f^{\pm}_{j+1/2}. \tag{50}$$

Therefore, the existing code using (42) can be easily improved to the fourth-order by using $\tilde{D}f^{\pm}$ of (50) in place of $Df^{\pm}$ in the minmod functions.

In the difference schemes mentioned so far, a common eigenvalue $a^{\pm}_{i+1/2}$ was used in a numerical flux $\hat{f}_{i+1/2}$, that is, $Df^{\pm}_{j+1/2} = a^{\pm}_{i+1/2}\Delta u_{j+1/2}$. Therefore, the accuracy of these schemes is not always attained, unless $a^{\pm}(x) = \text{const}$. Nevertheless, use of these higher-order compact schemes is very effective to capture discontinuities, especially of the contact or slip surface. In order to keep the accuracy of the higher-order compact schemes for the case where $a^{\pm}(x)$ is not constant, we must take

$$Df^{\pm}_{j+1/2} = \text{sign}|a^{\pm}_{i+1/2}|\Delta f_{j+1/2}.$$

The above higher-order compact TVD schemes can be easily extended to the schemes based on the MUSCL approach. The numerical flux is

$$\hat{f}_{i+1/2} = f^{+}(u^{L}_{i+1/2}) + f^{-}(u^{R}_{i+1/2}), \tag{51}$$

where

$$u^{L}_{i+1/2} = u_i + (1/6)\text{minmod}[\tilde{D}u_{i-1/2}, b\tilde{D}u_{i+1/2}]$$
$$+(1/3)\text{minmod}[\tilde{D}u_{i+1/2}, b\tilde{D}u_{i-1/2}],$$
$$u^{R}_{i+1/2} = u_{i+1} - (1/6)\text{minmod}[\tilde{D}u_{i+3/2}, b\tilde{D}u_{i+1/2}]$$
$$-(1/3)\text{minmod}[\tilde{D}u_{i+1/2}, b\tilde{D}u_{i+3/2}]. \tag{52}$$

$\tilde{D}u_{i-1/2}$, $\tilde{D}u_{i+1/2}$ and $\tilde{D}u_{i+3/2}$ are defined similar to (49) and (50) for the fifth- and fourth-order compact TVD MUSCL schemes, respectively.

3.2 *Numerical schemes of the compressible Navier–Stokes equations*

The Euler equations in general curvilinear coordinates, in which the diffusion terms in (12) are omitted, are

$$(\partial \hat{q}/\partial t) + (\partial \hat{F}_j/\partial \xi_j) = 0. \tag{53}$$

Taking a product of (53) by the matrix

$$C = \begin{bmatrix} 1 & 0 & 0 & 0 & 0 \\ -u & 1 & 0 & 0 & 0 \\ -v & 0 & 1 & 0 & 0 \\ -w & 0 & 0 & 1 & 0 \\ \phi^2 & -\tilde{\gamma}u & -\tilde{\gamma}v & -\tilde{\gamma}w & \tilde{\gamma} \end{bmatrix}, \tag{54}$$

we get the Euler equations in nonconservative form as

$$(\partial U/\partial t) + \hat{C}_j(\partial U/\partial \xi_j) = 0, \tag{55}$$

where

$$U = \begin{bmatrix} \rho \\ \rho_0 u \\ \rho_0 v \\ \rho_0 w \\ p \end{bmatrix}, \quad \hat{C}_j = \begin{bmatrix} U_j & (\xi_j)_x & (\xi_j)_y & (\xi_j)_z & 0 \\ 0 & U_j & 0 & 0 & (\xi_j)_x \\ 0 & 0 & U_j & 0 & (\xi_j)_y \\ 0 & 0 & 0 & U_j & (\xi_j)_z \\ 0 & (\xi_j)_x c^2 & (\xi_j)_y c^2 & (\xi_j)_z c^2 & U_j \end{bmatrix}, \quad (j = 1, 2, 3). \tag{56}$$

$\phi^2 = \tilde{\gamma}\mathbf{u}^2/2$, $\tilde{\gamma} = \gamma - 1$, c is the speed of sound, and subscript '0' means that the quantity is not differentiated, for example $\partial(\rho_0 u)/\partial x = \rho u_x$.

Similarly, the Euler equations of contravariant velocities in general curvilinear coordinates are expressed as

$$(\partial \tilde{q}/\partial t) + (\partial \tilde{F}_j/\partial \xi_j) + \tilde{R} = 0, \tag{57}$$

using the notations of (19). Taking a product of (57) by the matrix

$$\tilde{C} = \begin{bmatrix} 1 & 0 & 0 & 0 & 0 \\ -U & 1 & 0 & 0 & 0 \\ -V & 0 & 1 & 0 & 0 \\ -W & 0 & 0 & 1 & 0 \\ \phi^2 & -\alpha_1 & -\alpha_2 & -\alpha_3 & \tilde{\gamma} \end{bmatrix}, \tag{58}$$

we get the Euler equations of contravariant velocities in nonconservative form as

$$(\partial \tilde{U}/\partial t) + \tilde{C}_j(\partial \tilde{U}/\partial \xi_j) + \tilde{R}_1 = 0, \tag{59}$$

where

$$\tilde{U} = \begin{bmatrix} J_0 \rho \\ J\rho_0 U \\ J\rho_0 V \\ J\rho_0 W \\ J_0 p \end{bmatrix}, \quad \tilde{C}_j = \begin{bmatrix} U_j & \delta_{1j} & \delta_{2j} & \delta_{3j} & 0 \\ 0 & U_j & 0 & 0 & g_{1j} \\ 0 & 0 & U_j & 0 & g_{2j} \\ 0 & 0 & 0 & U_j & g_{3j} \\ 0 & \delta_{1j} c^2 & \delta_{2j} c^2 & \delta_{3j} c^2 & U_j \end{bmatrix}, \quad (j = 1, 2, 3), \tag{60}$$

$\alpha_i = \tilde{\gamma} u_k \partial x_k/\partial \xi_i$, $(i = 1, 2, 3)$.

First, we consider the Euler equations in general curvilinear coordinates, (53). From Euler's homogeneity relation, we get

$$\hat{F}_j = \hat{A}_j \hat{q}, \quad (j = 1, 2, 3), \tag{61}$$

where

$$\hat{A}_j = \partial \hat{F}_j / \partial \hat{q}$$

$$= \begin{bmatrix} 0 & (\xi_j)_x & (\xi_j)_y & (\xi_j)_z & 0 \\ -uU_j + \phi^2(\xi_j)_x & U_j + (1-\tilde{\gamma})u(\xi_j)_x & u(\xi_j)_y - \tilde{\gamma}v(\xi_j)_x & u(\xi_j)_z - \tilde{\gamma}w(\xi_j)_x & \tilde{\gamma}(\xi_j)_x \\ -vU_j + \phi^2(\xi_j)_y & v(\xi_j)_x - \tilde{\gamma}u(\xi_j)_y & U_j + (1-\tilde{\gamma})v(\xi_j)_y & v(\xi_j)_z - \tilde{\gamma}w(\xi_j)_y & \tilde{\gamma}(\xi_j)_y \\ -wU_j + \phi^2(\xi_j)_z & w(\xi_j)_x - \tilde{\gamma}u(\xi_j)_z & w(\xi_j)_y - \tilde{\gamma}v(\xi_j)_z & U_j + (1-\tilde{\gamma})w(\xi_j)_z & \tilde{\gamma}(\xi_j)_z \\ -HU_j + \phi^2 U_j & H(\xi_j)_x - \tilde{\gamma}uU_j & H(\xi_j)_y - \tilde{\gamma}vU_j & H(\xi_j)_z - \tilde{\gamma}wU_j & \gamma U_j \end{bmatrix},$$

$$(j = 1, 2, 3). \tag{62}$$

$H = (e + p)/\rho = (c^2 + \phi^2)/\tilde{\gamma}$ is the stagnation enthalpy. In this case, $\hat{F}_j$ depend not only on $\hat{q}$ but also on metrics $(\xi_j)_x, \cdots$. Therefore, the linearizations

$$(\partial \hat{F}_j / \partial \xi_j) \approx (\partial \hat{F}_j / \partial \hat{q})(\partial \hat{q} / \partial \xi_j) = \hat{A}_j (\partial \hat{q} / \partial \xi_j), \quad (j = 1, 2, 3), \tag{63}$$

are satisfied only approximately.

Eigenvalues and eigenvectors of $\hat{A}_j$ can be directly calculated from (62), but the calculation is considerably complicated. Therefore, we here use an alternative technique. By a comparison between (53) and (55), and using (54), (56) and (63), we get relations

$$C \hat{A}_j C^{-1} = \hat{C}_j, \quad (j = 1, 2, 3). \tag{64}$$

Therefore, the eigenvalues λ_{jk} of the matrices A_j can be easily obtained as eigenvalues of the simple form matrices $\hat{C}_j$

$$|C(\hat{A}_j - \lambda I)C^{-1}| = |\hat{C}_j - \lambda I| = 0. \tag{65}$$

From this, the eigenvalues $\lambda_{jk} = U_j$ (triple root), $U_j \pm c\sqrt{g_{jj}}$. And the left eigenvectors d_{jk} of $\hat{C}_j$ can also be easily obtained.

$$\hat{C}_j = \hat{D}_j^{-1} \hat{\Lambda}_j \hat{D}_j, \quad (j = 1, 2, 3), \tag{66}$$

where $\hat{\Lambda}_j$ is the diagonal matrix of eigenvalues λ_{jk} of the matrix $\hat{A}_j$

$$\hat{\Lambda}_j = \begin{bmatrix} U_j & 0 & 0 & 0 & 0 \\ 0 & U_j + c\sqrt{g_{11}}\delta_{1j} & 0 & 0 & 0 \\ 0 & 0 & U_j + c\sqrt{g_{22}}\delta_{2j} & 0 & 0 \\ 0 & 0 & 0 & U_j + c\sqrt{g_{33}}\delta_{3j} & 0 \\ 0 & 0 & 0 & 0 & U_j - c\sqrt{g_{jj}} \end{bmatrix}, \tag{67}$$

and $\hat{D}_j$ is the matrix composed of left eigenvectors d_{jk} of the matrix $\hat{C}_j$

$$\hat{D}_j = \begin{bmatrix} 1 & 0 & 0 & 0 & -1/c^2 \\ 0 & \partial\xi_j/\partial x_j & \xi_y\delta_{1j} - \eta_x\delta_{2j} & \xi_z\delta_{1j} - \zeta_x\delta_{3j} & (\sqrt{g_{11}}/c)\delta_{1j} \\ 0 & \eta_x\delta_{2j} - \xi_y\delta_{1j} & \partial\xi_j/\partial x_j & \eta_z\delta_{2j} - \zeta_y\delta_{3j} & (\sqrt{g_{22}}/c)\delta_{2j} \\ 0 & \zeta_x\delta_{3j} - \xi_x\delta_{1j} & \zeta_y\delta_{3j} - \eta_x\delta_{2j} & \partial\xi_j/\partial x_j & (\sqrt{g_{33}}/c)\delta_{3j} \\ 0 & \partial\xi_j/\partial x & \partial\xi_j/\partial y & \partial\xi_j/\partial z & -\sqrt{g_{jj}}/c \end{bmatrix},$$

$$(j = 1, 2, 3). \tag{68}$$

Finally, Jacobian matrices $\hat{A}_j$ can be diagonalized from (64) and (66) as

$$\hat{A}_j = \hat{L}_j^{-1}\hat{\Lambda}_j\hat{L}_j = C^{-1}\hat{D}_j^{-1}\hat{\Lambda}_j\hat{D}_j C, \quad (j=1,2,3). \tag{69}$$

We next consider the modified Euler equations in general curvilinear coordinates, (57). From Euler's homogeneity relation, we also get

$$\tilde{F}_j = \tilde{A}_j\tilde{q}, \quad (j=1,2,3), \tag{70}$$

where

$$\tilde{A}_j = \partial\tilde{F}_j/\partial\tilde{q}$$

$$= \begin{bmatrix} 0 & \delta_{1j} & \delta_{2j} & \delta_{3j} & 0 \\ -UU_j+\phi^2 g_{1j} & U_j+U\delta_{1j}-\alpha_1 g_{1j} & U\delta_{2j}-\alpha_2 g_{1j} & U\delta_{3j}-\alpha_3 g_{1j} & \tilde{\gamma}g_{1j} \\ -VU_j+\phi^2 g_{2j} & V\delta_{1j}-\alpha_1 g_{2j} & U_j+V\delta_{2j}-\alpha_2 g_{2j} & V\delta_{3j}-\alpha_3 g_{2j} & \tilde{\gamma}g_{2j} \\ -WU_j+\phi^2 g_{3j} & W\delta_{1j}-\alpha_1 g_{3j} & W\delta_{2j}-\alpha_2 g_{3j} & U_j+W\delta_{3j}-\alpha_3 g_{3j} & \tilde{\gamma}g_{3j} \\ -HU_j+\phi^2 U_j & H\delta_{1j}-\alpha_1 U_j & H\delta_{2j}-\alpha_2 U_j & H\delta_{3j}-\alpha_3 U_j & \gamma U_j \end{bmatrix}$$

$$(j=1,2,3) \tag{71}$$

Also in this case, since, $\tilde{F}_j$ are functions not only of $\tilde{q}$, the linearizations

$$(\partial\tilde{F}_j/\partial\xi_j) = \tilde{A}_j(\partial\tilde{q}/\partial\xi_j), \quad (j=1,2,3), \tag{72}$$

are performed approximately. And using

$$\tilde{C}\tilde{A}_j\tilde{C}^{-1} = \tilde{C}_j, \quad (j=1,2,3), \tag{73}$$

the following relation can be easily obtained,

$$\tilde{A}_j = \tilde{L}_j^{-1}\tilde{\Lambda}_j\tilde{L}_j = \tilde{C}^{-1}\tilde{D}_j^{-1}\tilde{\Lambda}_j\tilde{D}_j\tilde{C}, \quad (j=1,2,3), \tag{74}$$

where $\tilde{\Lambda}_j$ is the diagonal matrix of eigenvalues of the matrix $\tilde{A}_j$

$$\tilde{\Lambda}_j = \hat{\Lambda}_j, \tag{75}$$

and $\tilde{D}_j$ is the matrix composed of eigenvectors of the matrix $\tilde{C}_j$

$$\tilde{D}_j = \begin{bmatrix} 1 & 0 & 0 & 0 & -1/c^2 \\ 0 & 1 & -G_{12}\delta_{2j} & -G_{13}\delta_{3j} & (\sqrt{g_{11}}/c)\delta_{1j} \\ 0 & -G_{21}\delta_{1j} & 1 & -G_{23}\delta_{3j} & (\sqrt{g_{22}}/c)\delta_{2j} \\ 0 & -G_{31}\delta_{1j} & -G_{32}\delta_{2j} & 1 & (\sqrt{g_{33}}/c)\delta_{3j} \\ 0 & \delta_{1j} & \delta_{2j} & \delta_{3j} & -\sqrt{g_{jj}}/c \end{bmatrix},$$

$$(j=1,2,3), \tag{76}$$

$G_{ij} = g_{ij}/g_{jj}$.

Summarizing the matters mentioned so far, the flux vectors $\hat{F}_j$ and $\tilde{F}_j$ are

$$\hat{F}_j = \hat{A}_j\hat{q}, \quad \hat{A}_j = \hat{L}_j^{-1}\hat{\Lambda}_j\hat{L}_j, \quad \hat{L}_j = \hat{D}_j\hat{C},$$
$$\tilde{F}_j = \tilde{A}_j\tilde{q}, \quad \tilde{A}_j = \tilde{L}_j^{-1}\hat{\Lambda}_j\tilde{L}_j, \quad \tilde{L}_j = \tilde{D}_j\tilde{C}, \quad (j=1,2,3).$$

The matrix $\hat{\Lambda}_j$ can be split into the matrix $\hat{\Lambda}_j^+$ having only positive eigenvalues $\lambda_{jk}^+ =$

$(\lambda_{jk} + |\lambda_{jk}|)/2$ and the matrix $\hat{\Lambda}_j^-$ having only negative eigenvalues $\lambda_{jk}^- = (\lambda_{jk} - |\lambda_{jk}|)/2$,

$$\hat{\Lambda}_j = \hat{\Lambda}_j^+ + \hat{\Lambda}_j^-, \quad (j = 1, 2, 3). \tag{77}$$

Furthermore, using the relations

$$\hat{L}_j^{-1} \hat{\Lambda}_j^{\pm} \hat{L}_j = \hat{A}_j^{\pm}, \quad \hat{A}_j^{\pm} \hat{q} = \hat{F}_j^{\pm},$$
$$\tilde{L}_j^{-1} \hat{\Lambda}_j^{\pm} \tilde{L}_j = \tilde{A}_j^{\pm}, \quad \tilde{A}_j^{\pm} \tilde{q} = \tilde{F}_j^{\pm},$$

we get

$$\hat{A}_j = \hat{A}_j^+ + \hat{A}_j^-, \quad \hat{F}_j = \hat{F}_j^+ + \hat{F}_j^-,$$
$$\tilde{A}_j = \tilde{A}_j^+ + \tilde{A}_j^-, \quad \tilde{F}_j = \tilde{F}_j^+ + \tilde{F}_j^-, \quad (j = 1, 2, 3). \tag{78}$$

In the explicit scheme, especially for the compressible Navier–Stokes equations, the Courant number C, i.e., Δt is severely restricted. The usual explicit scheme demands $C = \lambda \Delta t / \Delta y < 1$. At the solid wall boundary, since $\lambda \approx c$ and the order of magnitude of $y^+ = u_\tau \Delta y \mathrm{Re}/\mu$ is $O(10)$, the value of Δt must be taken to be very small. On the other hand, the implicit scheme allows taking large values of Δt. For example, while the value of C in the main flow is $O(1)$, the value of C on the solid wall becomes $O(10^2)$. Applying the trapezoidal law to the modified Navier–Stokes equations in general curvilinear coordinates, we get

$$\Delta \tilde{q}^n = -\Delta t[(1-\theta)\tilde{L}(\tilde{q})^n + \theta \tilde{L}(\tilde{q})^{n+1}], \tag{79}$$

where $\Delta \tilde{q}^n = \tilde{q}^{n+1} - \tilde{q}^n$, $0 \leqslant \theta \leqslant 1$. Equation (79) becomes the Euler forward difference method for $\theta = 0$, the Crank–Nicholson method for $\theta = 1/2$ and the fully implicit method for $\theta = 1$.

The stability of (79) has been examined for a one-dimensional scalar model equation using the first-order upstream-difference scheme

$$u_j^{n+1} + \theta(C_{j-1/2}^+ \Delta u_{j-1/2} + C_{j+1/2}^- \Delta u_{j+1/2})^{n+1}$$
$$= u_j^n - (1-\theta)(C_{j-1/2}^+ \Delta u_{j-1/2} + C_{j+1/2}^- \Delta u_{j+1/2})^n, \tag{80}$$

where $\Delta u_{j+1/2} = u_{j+1} - u_j$. According to the stability analysis by von Neumann, the stability condition of (80) is

$$(1 - 2\theta)|\mathrm{C}| \leqslant 1.$$

Therefore if $\theta \geqslant 1/2$, then (80) is unconditionally stable. However, we often found that the Crank–Nicholson method leads to unstable solutions. The conditions of the TVD scheme for (80) are

$$C^+ \geqslant 0, \quad C^- \leqslant 0, \quad (1-\theta)|\mathrm{C}| \leqslant 1. \tag{81}$$

Therefore, if $\theta \geqslant 1$, then (80) becomes TVD stable inspite of the value of C. For the high-order TVD scheme using the limiter, similar conditions corresponding to (81) are also obtained. On the other hand, for the multi-dimensional nonlinear system (79), the TVD conditions have not been made clear. But in order to obtain the stable solution, the fully implicit method for $\theta = 1$ should be employed.

The widely-used compressible flow schemes are based on the time-marching schemes for the unsteady Euler equations. This system of equations is hyperbolic, and can be

reduced to a system of ordinary differential equations by the theory of characteristics. These ordinary differential equations mean waves propagating along characteristics, that is, sound waves and waves along path line. Recently, strong stabilization has been achieved by means of the upstreaming according to sign of phase velocity of each wave, and of the TVD scheme. At the same time, to reduce to ordinary differential equations can save the computational efforts. The steady flow is also calculated using the time-marching scheme, and the solution is obtained as an asymptotically converged solution at sufficiently large time steps. The unsteady Navier–Stokes equations are parabolic, and different from the Euler equations without the diffusion terms. However, since the diffusion effects are, in general, weak for the compressible flow, the Navier–Stokes equations are also solved by the unsteady Euler scheme considering the diffusion terms.

The nonlinear system of equations, (79) can be directly solved by the explicit methods, but must be linearized for the implicit methods. For the linearization, we use the Taylor expansion

$$\begin{aligned}\tilde{F}_j^{n+1} &\approx \tilde{F}_j^n + \Delta t(\partial \tilde{F}_j/\partial t)^n = \tilde{F}_j^n + \Delta t \tilde{A}_j^n(\partial \tilde{q}/\partial t)^n \\ &\approx \tilde{F}_j^n + \tilde{A}_j^n \Delta \tilde{q}^n.\end{aligned}$$

Treating the additional, diffusion and body force terms at time step t^n approximately, we get

$$\tilde{L}(\tilde{q})^{n+1} \approx \tilde{L}(\tilde{q})^n + (\partial/\partial \xi_j)(\tilde{A}_j^n \Delta \tilde{q}^n).$$

Therefore, (79) can be linearized as

$$[I + \Delta t\theta(\partial/\partial \xi_j)\tilde{A}_j^n]\Delta \tilde{q}^n = -\Delta t \tilde{L}(\tilde{q})^n \equiv \text{RHS}^n. \tag{82}$$

Here we first consider about the schemes for steady flow. Since RHS of (82) becomes zero when the solution converges, in the calculating process RHS regards as a residual and $\Delta \tilde{q}^n$ as a correction. If the residual tends to zero, then the correction also tends to zero, and the solution converges. The accuracy of the solution depends only on RHS, but is independent of the operator of left hand side. Hence, RHS must be treated accurately and completely. On the other hand, the left hand side operator is required to reduce the computational efforts and to accelerate the convergency. To this end, solving the left hand side operator of (82) into factors by applying the approximate-factorization method by Yanenko (1961), we get

$$[I + \Delta t\theta(\partial/\partial \xi)\tilde{A}_1^n][I + \Delta t\theta(\partial/\partial \eta)\tilde{A}_2^n][I + \Delta t\theta(\partial/\partial \zeta)\tilde{A}_3^n]\Delta \tilde{q}^n = \text{RHS}^n. \tag{83}$$

Here, the cross derivative terms $\Delta t^2\theta^2(\partial/\partial \xi_j)\tilde{A}_j^n(\partial/\partial \xi_k)\tilde{A}_k^n, \cdots$ are neglected. $\Delta t\theta \tilde{A}_j^n/\Delta \xi_j$ are not always small and the order of the Courant number. However, if we assume linearly varying flow field, then these cross derivative terms close to zero. Therefore, the error due to the factorization seems to be not so large, even though the Courant number is large. Equation (83) can be solved dividing into the following three steps.

$$[I + \Delta t\theta(\partial/\partial \xi)\tilde{A}_1^n]\Delta q^1 = \text{RHS}^n,$$

$$[I + \Delta t\theta(\partial/\partial \eta)\tilde{A}_2^n]\Delta q^2 = \Delta q^1,$$

$$[I + \Delta t\theta(\partial/\partial \zeta)\tilde{A}_3^n]\Delta \tilde{q}^n = \Delta q^2.$$

If the first-order upstream-difference scheme is used in the left hand side, then each step becomes the problem in which simultaneous linear equations with 5×5 block tri-diagonal matrix are solved.

Further applying the diagonalization by Pulliam–Chaussee (1981) to (83), and using (74), we get

$$[\tilde{L}_1^{-1}\{I + \Delta t\theta\hat{\Lambda}_1(\partial/\partial\xi)\}\tilde{M}_1^{-1}\{I + \Delta t\theta\hat{\Lambda}_2(\partial/\partial\eta)\}_{\mathrm{II}} \times \tilde{M}_2^{-1}\{I + \Delta t\theta\hat{\Lambda}_3(\partial/\partial\zeta)\,\tilde{L}_3\}]^n\Delta\tilde{q}^n = \mathrm{RHS}^n \tag{84}$$

where $\tilde{M}_1 = \tilde{L}_2\tilde{L}_1^{-1}$, $\tilde{M}_2 = \tilde{L}_3\tilde{L}_2^{-1}$. Equation (84) can be solved dividing into the following seven steps.

$$\begin{aligned}
&\text{(I)} && \Delta q^1 = \tilde{L}_1^n\,\mathrm{RHS}^n;\\
&\text{(II)} && [I + \Delta t\theta\hat{\Lambda}_1^n(\partial/\partial\xi)]\Delta q^2 = \Delta q^1;\\
&\text{(III)} && \Delta q^3 = \tilde{M}_1\Delta q^2;\\
&\text{(IV)} && [I + \Delta t\theta\hat{\Lambda}_2^n(\partial/\partial\eta)]\Delta q^4 = \Delta q^3;\\
&\text{(V)} && \Delta q^5 = \tilde{M}_2\Delta q^4;\\
&\text{(VI)} && [I + \Delta t\theta\hat{\Lambda}_3^n(\partial/\partial\zeta)]\Delta q^6 = \Delta q^5;\\
&\text{(VII)} && \Delta\tilde{q}^n = \tilde{L}_3^{n-1}\Delta q^6.
\end{aligned} \tag{85}$$

The odd steps are products of vector by matrix at each grid point, and the even steps are computations of five sets of linear equations with a scalar tri-diagonal matrix. The forms of $\tilde{M}_1$, $\tilde{M}_2$ and $\tilde{L}_3^{-1}$ which are necessary for the programming are

$$\tilde{M}_1 = \tilde{L}_2\tilde{L}_1^{-1} = \tilde{D}_2\tilde{D}_1^{-1}$$

$$= \begin{bmatrix}
1 & 0 & 0 & 0 & 0\\
0 & (1-G_{12}G_{21})/2 & -G_{12} & 0 & (1-G_{12}G_{21})/2\\
0 & (G_{21}+RG_{21})/2 & 1 & 0 & (G_{21}-RG_{21})/2\\
0 & (G_{31}-G_{32}G_{21})/2 & -G_{32} & 1 & (G_{31}-G_{32}G_{21})/2\\
0 & (G_{21}-RG_{21})/2 & 1 & 0 & (G_{21}+RG_{21})/2
\end{bmatrix},$$

$$\tilde{M}_2 = \tilde{L}_3\tilde{L}_2^{-1} = \tilde{D}_3\tilde{D}_2^{-1}$$

$$= \begin{bmatrix}
1 & 0 & 0 & 0 & 0\\
0 & 1 & (G_{12}-G_{13}G_{32})/2 & -G_{13} & (G_{12}G_{13}G_{32})/2\\
0 & 0 & (1-G_{23}G_{32})/2 & -G_{23} & (-G_{23}G_{32})/2\\
0 & 0 & (G_{32}RG_{32})/2 & 1 & (G_{32}-RG_{32})/2\\
0 & 0 & (G_{32}-RG_{32})/2 & 1 & (G_{32}+RG_{32})/2
\end{bmatrix}, \tag{86}$$

$$\tilde{L}_3^{-1} = \tilde{\tilde{C}}^{-1}\tilde{D}_3^{-1}$$

$$= \begin{bmatrix}
1 & 0 & 0 & 0 & 0\\
U & 1 & 0 & 0 & 0\\
V & 0 & 1 & 0 & 0\\
W & 0 & 0 & 1 & 0\\
\phi^2/\tilde{\gamma} & \alpha_1/\tilde{\gamma} & \alpha_2/\tilde{\gamma} & \alpha_3/\tilde{\gamma} & 1/\tilde{\gamma}
\end{bmatrix}
\begin{bmatrix}
1 & 0 & 0 & 1/2c\sqrt{g_{33}} & -1/2c\sqrt{g_{33}}\\
0 & 1 & 0 & G_{13}/2 & G_{13}/2\\
0 & 0 & 1 & G_{23}/2 & G_{23}/2\\
0 & 0 & 0 & 1/2 & 1/2\\
0 & 0 & 0 & c/2\sqrt{g_{33}} & -c/2\sqrt{g_{33}}
\end{bmatrix},$$

where $G_{ij}=g_{ij}/g_{jj}$, and $RG_{ij}=(g_{ii}/g_{jj})$. The matrices $\tilde{M}_1$ and $\tilde{M}_2$ are seen to depend only on the metrics.

As mentioned before, $\tilde{C}$ of (58) is the transformation matrix which rewrites the Euler equations in conservative form into a simpler nonconservative form. And $\tilde{D}_j$ of (76) is the transformation matrix which rewrites the Euler equations in nonconservative form into a system of ordinary differential equations by the theory of characteristics. After all, in the present implicit scheme (84), the three-dimensional problem is first solved as one-dimensional problems by the delta-form approximate-factorization method, and then each one-dimensional equation is integrated successively by the transformation into the system of ordinary differential equations by the diagonalization. Step (I) of (85) is the transformation into the system of ordinary differential equations with respect to ξ, step (II) is the integration along characteristics on ξt plane, and step (III) is the inverse transformation into the Euler equations and the transformation into the system of ordinary differential equations with respect to η.

The right hand side of (84) is calculated by applying the flux vector splitting by Steger–Warming (1981) to $B\hat{L}(\hat{q})$ and using the higher-order TVD upstream-difference scheme mentioned in the foregoing paragraph. Because, $\hat{L}(\hat{q})$ is a relatively simple form, and is not seriously affected by the smoothness of grid since $\hat{F}_j$ contains only the physical velocity **u** and the derivatives of JU_j with respect to ξ_j. From (12), (19) and (82)

$$\text{RHS}=-\Delta t\tilde{L}(\tilde{q})=-\Delta tB[(\partial\hat{F}_j/\partial\xi_j)+\hat{S}+\hat{H}], \tag{87}$$

and from (13), (54), (67), (68) and (78),

$$\begin{aligned}\hat{F}_j^{\pm}&=C^{-1}\hat{D}_j^{-1}\hat{\Lambda}_j^{\pm}\hat{D}_jC\hat{q}\\&=\frac{J\rho}{2\gamma}\begin{bmatrix}2\tilde{\gamma}\lambda_{j1}^{\pm}+\lambda_{j4}^{\pm}+\lambda_{j5}^{\pm}\\2\tilde{\gamma}u\lambda_{j1}^{\pm}+\left(u+\dfrac{c(\xi_j)_x}{\sqrt{g_{jj}}}\right)\lambda_{j4}^{\pm}+\left(u-\dfrac{c(\xi_j)_x}{\sqrt{g_{jj}}}\right)\lambda_{j5}^{\pm}\\2\tilde{\gamma}v\lambda_{j1}^{\pm}+\left(v+\dfrac{c(\xi_j)_y}{\sqrt{g_{jj}}}\right)\lambda_{j4}^{\pm}+\left(v-\dfrac{c(\xi_j)_y}{\sqrt{g_{jj}}}\right)\lambda_{j5}^{\pm}\\2\tilde{\gamma}w\lambda_{j1}^{\pm}+\left(w+\dfrac{c(\xi_j)_z}{\sqrt{g_{jj}}}\right)\lambda_{j4}^{\pm}+\left(w-\dfrac{c(\xi_j)_z}{\sqrt{g_{jj}}}\right)\lambda_{j5}^{\pm}\\2\phi^2\lambda_{j1}^{\pm}+\left(H+\dfrac{cU_j}{\sqrt{g_{jj}}}\right)\lambda_{j4}^{\pm}+\left(H-\dfrac{cU_j}{\sqrt{g_{jj}}}\right)\lambda_{j5}^{\pm}\end{bmatrix}\\&=J\lambda_{j1}^{\pm}q+J\lambda_{ja}^{\pm}M_jq_{aj}+J\lambda_{jb}^{\pm}q_b,\end{aligned} \tag{88}$$

where

$$q=\begin{bmatrix}\rho\\\rho u\\\rho v\\\rho w\\e\end{bmatrix},\quad q_{aj}=\frac{\rho c}{\gamma}\begin{bmatrix}0\\1\\1\\1\\U_j\end{bmatrix},\quad q_b=\frac{\rho}{\gamma}\begin{bmatrix}1\\u\\v\\w\\H\end{bmatrix},$$

$$M_j=\frac{1}{\sqrt{g_{jj}}}\begin{bmatrix}0&&&&0\\&(\xi_j)_x&&&\\&&(\xi_j)_y&&\\&&&(\xi_j)_z&\\0&&&&1\end{bmatrix}.$$

$\lambda_{j1} = U_j$, $\lambda_{j4} = U_j + c\sqrt{g_{jj}}$, $\lambda_{j5} = U_j - c\sqrt{g_{jj}}$, $\lambda_{ja}^{\pm} = (\lambda_{j4}^{\pm} - \lambda_{j5}^{\pm})/2$, $\lambda_{jb}^{\pm} = (\lambda_{j4}^{\pm} + \lambda_{j5}^{\pm})/2 - \lambda_{j1}^{\pm}$, $\lambda_{jk}^{\pm} = (\lambda_{jk} \pm |\lambda_{jk}|)/2$, $(k = 1, 4, 5)$. In the calculation of

$$(\partial \hat{F}_j/\partial \xi_j)_i = [(\hat{F}_j)_{i+1/2} - (\hat{F}_j)_{i-1/2}]/\Delta\xi_j,$$

the flux difference in $(\hat{F}_j)_{i+1/2}$ is

$$\begin{aligned}(D\hat{F}^{\pm})_{k+1/2} = {} & (J\lambda_{j1}^{\pm})_{i+1/2}(q_{k+1} - q_k) \\ & + (J\lambda_{ja}^{\pm} M_j)_{i+1/2}\{(q_{aj})_{k+1} - (q_{aj})_k\} \\ & + (J\lambda_{jb}^{\pm})_{i+1/2}\{(q_b)_{k+1} - (q_b)_k\}. \end{aligned} \tag{89}$$

The left hand side of (84) here is calculated using the first-order upstream-difference scheme, and considering the viscous term partially,

$$\hat{\Lambda}_j(\partial/\partial\xi_j) \approx \hat{\Lambda}_j^{+}\nabla_j + \hat{\Lambda}_j^{-}\Delta_j,$$

where ∇_j and Δ_j are the backward- and forward-difference operators with respect to ξ_j, respectively. In the present schemes the accuracy of the solution does not depend on the left hand side operators. However, to consider the viscous term in these operators leads always to the reasonable solution and accelerates the convergence of the flows including the separation zone. The viscous terms of the lth momentum equation are

$$-J(\partial\xi_j/\partial x_k)(\partial\tau_{lk}/\partial\xi_j) \approx J2\mu g_{jj}(1/\Delta\xi_j^2)\{(u_{li} - u_{li-1}) - (u_{li+1} - u_{li})\},$$

and the convection terms are

$$\lambda_{jl}(\partial/\partial\xi_j)J\rho u_l \approx J\rho(1/\Delta\xi_j)\{\lambda_{jl}^{+}(u_{li} - u_{li-1}) + \lambda_{jl}^{-}(u_{li+1} - u_{li})\}.$$

From a comparison of these forms, it is found that the main part of the viscous term to be added in the left hand side is

$$\lambda_{jl}^{\pm} \Rightarrow \lambda_{jl}^{\pm} \pm 2\nu g_{jj}/\Delta\xi_j. \tag{90}$$

The calculation of the turbulent flow is carried out using the low Reynolds number type $k-\varepsilon$ turbulence model. When (19) and (32) are solved simultaneously, good stability is obtained. In this calculation, B, $\tilde{q}$ and $\tilde{F}_j$ in (19) are

$$B = \begin{bmatrix} 1 & 0 & 0 & 0 & 0 & 0 & 0 \\ 0 & \xi_x & \xi_y & \xi_z & 0 & 0 & 0 \\ 0 & \eta_x & \eta_y & \eta_z & 0 & 0 & 0 \\ 0 & \zeta_x & \zeta_y & \zeta_z & 0 & 0 & 0 \\ 0 & 0 & 0 & 0 & 1 & 0 & 0 \\ 0 & 0 & 0 & 0 & 0 & 1 & 0 \\ 0 & 0 & 0 & 0 & 0 & 0 & 1 \end{bmatrix}, \tag{91}$$

$$\tilde{q} = J\begin{bmatrix} \rho \\ \rho U \\ \rho V \\ \rho W \\ e \\ \rho k \\ \rho\varepsilon \end{bmatrix}, \quad \tilde{F}_j = J\begin{bmatrix} \rho U_j \\ \rho U U_j + g_{1j}p \\ \rho V U_j + g_{2j}p \\ \rho W U_j + g_{3j}p \\ (e+p)U_j \\ \rho k U_j \\ \rho\varepsilon U_j \end{bmatrix}, \quad (j = 1, 2, 3). \tag{92}$$

And the Jacobian matrix in (17) is replaced by

$$\tilde{A}_j = \begin{bmatrix} 0 & \delta_{1j} & \delta_{2j} & \delta_{3j} & 0 & 0 & 0 \\ -UU_j+\phi^2 g_{1j} & U_j+U\delta_{1j}-\alpha_1 g_{1j} & U\delta_{2j}-\alpha_2 g_{1j} & U\delta_{3j}-\alpha_3 g_{1j} & \tilde{\gamma} g_{1j} & 0 & 0 \\ -VU_j+\phi^2 g_{2j} & V\delta_{1j}-\alpha_1 g_{2j} & U_j+V\delta_{3j}-\alpha_3 g_{2j} & V\delta_{3j}-\alpha_3 g_{2j} & \tilde{\gamma} g_{2j} & 0 & 0 \\ -WU_j+\phi^2 g_{3j} & W\delta_{1j}-\alpha_1 g_{3j} & W\delta_{2j}-\alpha_2 g_{3j} & U_j+W\delta_{3j}-\alpha_3 g_{3j} & \tilde{\gamma} g_{3j} & 0 & 0 \\ -HU_j+\phi^2 U_j & H\delta_{1j}-\alpha_1 U_j & H\delta_{2j}-\alpha_2 U_j & H\delta_{3j}-\alpha_3 U & \gamma U_j & 0 & 0 \\ 0 & 0 & 0 & 0 & 0 & 0 & 0 \\ 0 & 0 & 0 & 0 & 0 & 0 & 1 \end{bmatrix},$$

$(j = 1, 2, 3).$ (93)

The quantities which are needed for the programming are

$$\tilde{C} = \begin{bmatrix} 1 & 0 & 0 & 0 & 0 & 0 & 0 \\ -U & 1 & 0 & 0 & 0 & 0 & 0 \\ -V & 0 & 1 & 0 & 0 & 0 & 0 \\ -W & 0 & 0 & 1 & 0 & 0 & 0 \\ \phi^2 & -\alpha_1 & -\alpha_2 & -\alpha_3 & \tilde{\gamma} & 0 & 0 \\ 0 & 0 & 0 & 0 & 0 & 1 & 0 \\ 0 & 0 & 0 & 0 & 0 & 0 & 1 \end{bmatrix},$$

$$\tilde{D}_1 = \begin{bmatrix} 1 & 0 & 0 & 0 & -1/c^2 & 0 & 0 \\ 0 & 1 & 0 & 0 & \sqrt{g_{11}}/c & 0 & 0 \\ 0 & -G_{21} & 1 & 0 & 0 & 0 & 0 \\ 0 & -G_{31} & 0 & 1 & 0 & 0 & 0 \\ 0 & 1 & 0 & 0 & -\sqrt{g_{11}}/c & 0 & 0 \\ 0 & 0 & 0 & 0 & 0 & 1 & 0 \\ 0 & 0 & 0 & 0 & 0 & 0 & 1 \end{bmatrix},$$

$$\tilde{M}_1 = \begin{bmatrix} 1 & 0 & 0 & 0 & 0 & 0 & 0 \\ 0 & (1-G_{12}G_{21})/2 & -G_{12} & 0 & (1-G_{12}G_{21})/2 & 0 & 0 \\ 0 & (G_{21}+RG_{21})/2 & 1 & 0 & (G_{21}-RG_{21})/2 & 0 & 0 \\ 0 & (G_{31}-G_{32}G_{21})/2 & -G_{32} & 1 & (G_{31}-G_{32}G_{21})/2 & 0 & 0 \\ 0 & (G_{21}-RG_{21})/2 & 1 & 0 & (G_{21}+RG_{21})/2 & 0 & 0 \\ 0 & 0 & 0 & 0 & 0 & 1 & 0 \\ 0 & 0 & 0 & 0 & 0 & 0 & 1 \end{bmatrix},$$

$$\tilde{M}_2 = \begin{bmatrix} 1 & 0 & 0 & 0 & 0 & 0 & 0 \\ 0 & 1 & (G_{12}-G_{13}G_{32})/2 & -G_{13} & (G_{12}-G_{13}G_{32})/2 & 0 & 0 \\ 0 & 0 & (1-G_{23}G_{32})/2 & -G_{23} & (1-G_{23}G_{32})/2 & 0 & 0 \\ 0 & 0 & (G_{32}+RG_{32})/2 & 1 & (G_{32}-RG_{32})/2 & 0 & 0 \\ 0 & 0 & (G_{32}-RG_{32})/2 & 1 & (G_{32}+RG_{32})/2 & 0 & 0 \\ 0 & 0 & 0 & 0 & 0 & 1 & 0 \\ 0 & 0 & 0 & 0 & 0 & 0 & 1 \end{bmatrix},$$

(94)

$$\tilde{D}_3^{-1} = \begin{bmatrix} 1 & 0 & 0 & 1/2c\sqrt{g_{33}} & -1/2c\sqrt{g_{33}} & 0 & 0 \\ 0 & 1 & 0 & G_{13}/2 & G_{13}/2 & 0 & 0 \\ 0 & 0 & 1 & G_{23}/2 & G_{23}/2 & 0 & 0 \\ 0 & 0 & 0 & 1/2 & 1/2 & 0 & 0 \\ 0 & 0 & 0 & c/2\sqrt{g_{33}} & -c/2\sqrt{g_{33}} & 0 & 0 \\ 0 & 0 & 0 & 0 & 0 & 1 & 0 \\ 0 & 0 & 0 & 0 & 0 & 0 & 1 \end{bmatrix},$$

$$\tilde{C}^{-1} = \begin{bmatrix} 1 & 0 & 0 & 0 & 0 & 0 & 0 \\ U & 1 & 0 & 0 & 0 & 0 & 0 \\ V & 0 & 1 & 0 & 0 & 0 & 0 \\ W & 0 & 0 & 1 & 0 & 0 & 0 \\ \phi^2/\tilde{\gamma} & \alpha_1/\tilde{\gamma} & \alpha_2/\tilde{\gamma} & \alpha_3/\tilde{\gamma} & 1/\tilde{\gamma} & 0 & 0 \\ 0 & 0 & 0 & 0 & 0 & 1 & 0 \\ 0 & 0 & 0 & 0 & 0 & 0 & 1 \end{bmatrix},$$

$$\hat{\Lambda}_j = \begin{bmatrix} U_j & & & & & & 0 \\ & U_j + c\sqrt{g_{11}}\delta_{1j} & & & & & \\ & & U_j + c\sqrt{g_{22}}\delta_{2j} & & & & \\ & & & U_j + c\sqrt{g_{33}}\delta_{3j} & & & \\ & & & & U_j - c\sqrt{g_{jj}} & & \\ & & & & & U_j & \\ 0 & & & & & & U_j \end{bmatrix}, \quad (j = 1, 2, 3)$$

$$\hat{F}_j^{\pm} = J\lambda_{j1}^{\pm} \begin{bmatrix} \rho \\ \rho u \\ \rho v \\ \rho w \\ e \\ \rho k \\ \rho \varepsilon \end{bmatrix} + \frac{J\lambda_{ja}^{\pm}}{\sqrt{g_{jj}}} \begin{bmatrix} 0 & & & & & & 0 \\ & (\xi_j)_x & & & & & \\ & & (\xi_j)_y & & & & \\ & & & (\xi_j)_z & & & \\ & & & & 1 & & \\ & & & & & 0 & \\ 0 & & & & & & 0 \end{bmatrix} \frac{\rho c}{\gamma} \begin{bmatrix} 0 \\ 1 \\ 1 \\ 1 \\ U_j \\ 0 \\ 0 \end{bmatrix},$$

$$+ J\lambda_{jb}^{\pm} \frac{\rho}{\gamma} \begin{bmatrix} 1 \\ u \\ v \\ w \\ H \\ 0 \\ 0 \end{bmatrix}, \quad (j = 1, 2, 3).$$

The viscous terms consist of the viscous stress and the Reynolds stress as in (30), and the value of eddy viscosity μ_t is obtained from (31) using the values of k and ε at the former time step.

The unsteady flow problem can be solved by a number of explicit schemes. However, this problem can be solved more efficiently by the implicit schemes. In the present

scheme, the second-order accurate Crank–Nicholson method is used in the time integration, and the resultant equation is solved by the Newton iteration. Using the Crank–Nicholson method, we get

$$\tilde{q}^{(m)} - \tilde{q}^n = -\Delta t \tilde{L}[(\tilde{q}^n + \tilde{q}^{(m)})/2] \tag{95}$$

where $\tilde{q}^{(m)}$ is the mth approximation of $\tilde{q}^{n+1}$.

$$\tilde{q}^{(m)} = \tilde{q}^{(m-1)} + \Delta\tilde{q}^{(m)}.$$

Regarding $\tilde{L}$ as a linear operator,

$$\tilde{L}[(\tilde{q}^n + \tilde{q}^{(m)})/2] = \tilde{L}[(\tilde{q}^n + \tilde{q}^{(m-1)})/2] + (1/2)\,\tilde{L}(\Delta\tilde{q}^{(m)}).$$

Substituting these relations into (95), and applying the approximate-factorization scheme and the diagonalization, we get

$$\begin{aligned}\{\tilde{L}_1^{-1}[I + \Delta t\theta\hat{\Lambda}_1(\partial/\partial\xi)]\tilde{M}_1^{-1}[I + \Delta t\theta\hat{\Lambda}_2(\partial/\partial\eta)] \\ \times \tilde{M}_2^{-1}[I + \Delta t\theta\hat{\Lambda}_3(\partial/\partial\zeta)]\,\tilde{L}_3\}^n\Delta\tilde{q}^{(m)} \\ = -(\tilde{q}^{(m-1)} - \tilde{q}^n) - \Delta t\hat{BL}[(\hat{q}^n + \hat{q}^{(m-1)}/2].\end{aligned} \tag{96}$$

If $m = 1$, then $\tilde{q}^{(0)} = \tilde{q}^n$. And if $m \Rightarrow \infty$, then $\Delta\tilde{q}^{(m)} \Rightarrow 0$, $\tilde{q}^{(m)} \Rightarrow \tilde{q}^{n+1}$, and the solution converges. Usually, $\theta = 1$, in order to increase the TVD stability. The convergent solution at each time step can be obtained within a few iterations.

3.3 *Numerical schemes of the incompressible Navier–Stokes equations*

The fundamental equations of the incompressible flow are the Navier–Stokes equations and the continuity equation expressed in the vector forms,

$$(\partial\mathbf{u}/\partial t) + \nabla\cdot\mathbf{uu} = -\nabla p + \nu\nabla^2\mathbf{u}, \tag{97}$$

$$\nabla\cdot\mathbf{u} = 0. \tag{98}$$

The dependent variables of these equations are $\mathbf{u}$ and p, and the advanced value of $\mathbf{u}$ can be determined from the Cauchy problem of (97). However, the remaining variable p cannot be determined from the remaining (98). Taking the divergence of (97) and using (98), we can derive the Poisson equation of pressure

$$\nabla^2 p = -\nabla\cdot(\nabla\cdot\mathbf{uu}). \tag{99}$$

The values of p are usually determined from the boundary value problem of (99). However, the value of $\mathbf{u}$ determined in this way does not generally satisfy the continuity condition (98). The MAC scheme by Harlow & Welch (1965) and the simplified MAC scheme by Amsden & Harlow (1970) are those which completely solve this difficulty.

The fundamental equations of the SMAC scheme can be written as

$$\mathbf{u}^* = \mathbf{u}^n - \Delta t(\nabla p^n + \nabla\cdot\mathbf{uu} - \nu\nabla^2\mathbf{u})^n, \tag{100}$$

$$\nabla^2\phi^n = (1/\Delta t)\nabla\cdot\mathbf{u}^*, \tag{101}$$

$$\mathbf{u}^{n+1} = \mathbf{u}^* - \Delta t\nabla\phi^n, \tag{102}$$

$$p^{n+1} = p^n + \phi^n.$$

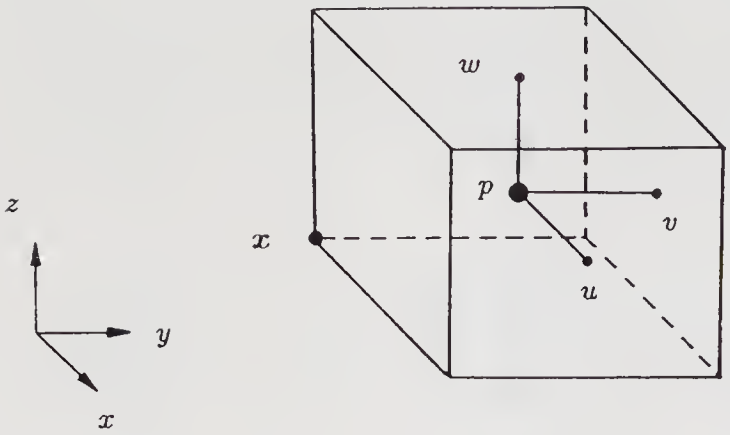

Figure 3. Staggered grid in Cartesian coordinates.

In this scheme, the Navier–Stokes equations, (97), are divided into (100) and (102) applying the time-splitting method. The Euler forward difference scheme is used for the convection and viscous terms, and the fully implicit scheme for the pressure term. The Poisson equation (101) of the pressure increment ϕ is derived by taking a divergence of (102) and using the continuity condition $\nabla\cdot\mathbf{u}^{n+1}=0$. However, in this equation $\nabla\cdot\mathbf{u}^{n}$ which is not always zero is contained through (100). Therefore, the advanced value $\mathbf{u}^{n+1}$ calculated in this way satisfies the continuity condition (98).

In the computation of the SMAC scheme, the staggered grid as shown in figure 3 is utilized, and the following equations which are discretized using the central-differences in (100) to (102) are employed. For two-dimensional (2-D) flow,

$$u^*_{ij}=u_{ij}-\Delta t\left(\frac{p_{ij}-p_{i-1j}}{\Delta x}+\frac{(u^2)_{ij}-(u^2)_{i-1j}}{\Delta x}+\frac{(uv)_{ij+1}-(uv)_{ij}}{\Delta y}-\nu\Lambda u_{ij}\right), \tag{103}$$

$$v^*_{ij}=v_{ij}-\Delta t\left(\frac{p_{ij}-p_{ij-1}}{\Delta y}+\frac{(uv)_{i+1j}-(uv)_{ij}}{\Delta x}+\frac{(v^2)_{ij}-(v^2)_{ij-1}}{\Delta y}-\nu\Lambda v_{ij}\right),$$

$$\Lambda\phi_{ij}=\frac{1}{\Delta t}\left(\frac{u^*_{i+1j}-u^*_{ij}}{\Delta x}+\frac{v^*_{ij+1}-v^*_{ij}}{\Delta y}\right), \tag{104}$$

$$u^{n+1}_{ij}=u^*_{ij}-(\Delta t/\Delta x)(\phi_{ij}-\phi_{i-1j}),$$

$$v^{n+1}_{ij}=v^*_{ij}-(\Delta t/\Delta y)(\phi_{ij}-\phi_{ij-1}), \tag{105}$$

where

$$\Lambda u_{ij}=(u_{i-1j}-2u_{ij}+u_{i+1j})/\Delta x^2+(u_{ij-1}-2u_{ij}+u_{ij+1})/\Delta y^2,$$

$$(u^2)_{ij}=(1/4)(u_{ij}+u_{i+1j})^2,\quad (uv)_{ij}=(1/4)(u_{ij-1}+u_{ij})(v_{i-1j}+v_{ij}),$$

and the superscript n is omitted here. The values of $\mathbf{u}^*$, ϕ and $\mathbf{u}^{n+1}$ are determined in order from (103), (104) and (105). The simultaneous linear equations (104) can be solved efficiently by the multi-grid method.

The continuity difference equations and the pressure difference equations which satisfy the continuity difference equations of $\nabla\cdot\mathbf{u}^{n+1}=0$ are as shown in figure 4. For grids A and B, since the values of p at neighbouring points are calculated separately, the spurious error, that is checker-board-like oscillation of pressure occurs. On the other hand, for the staggered MAC type grid, the pressure difference equation becomes compact, and this oscillation is completely removed.

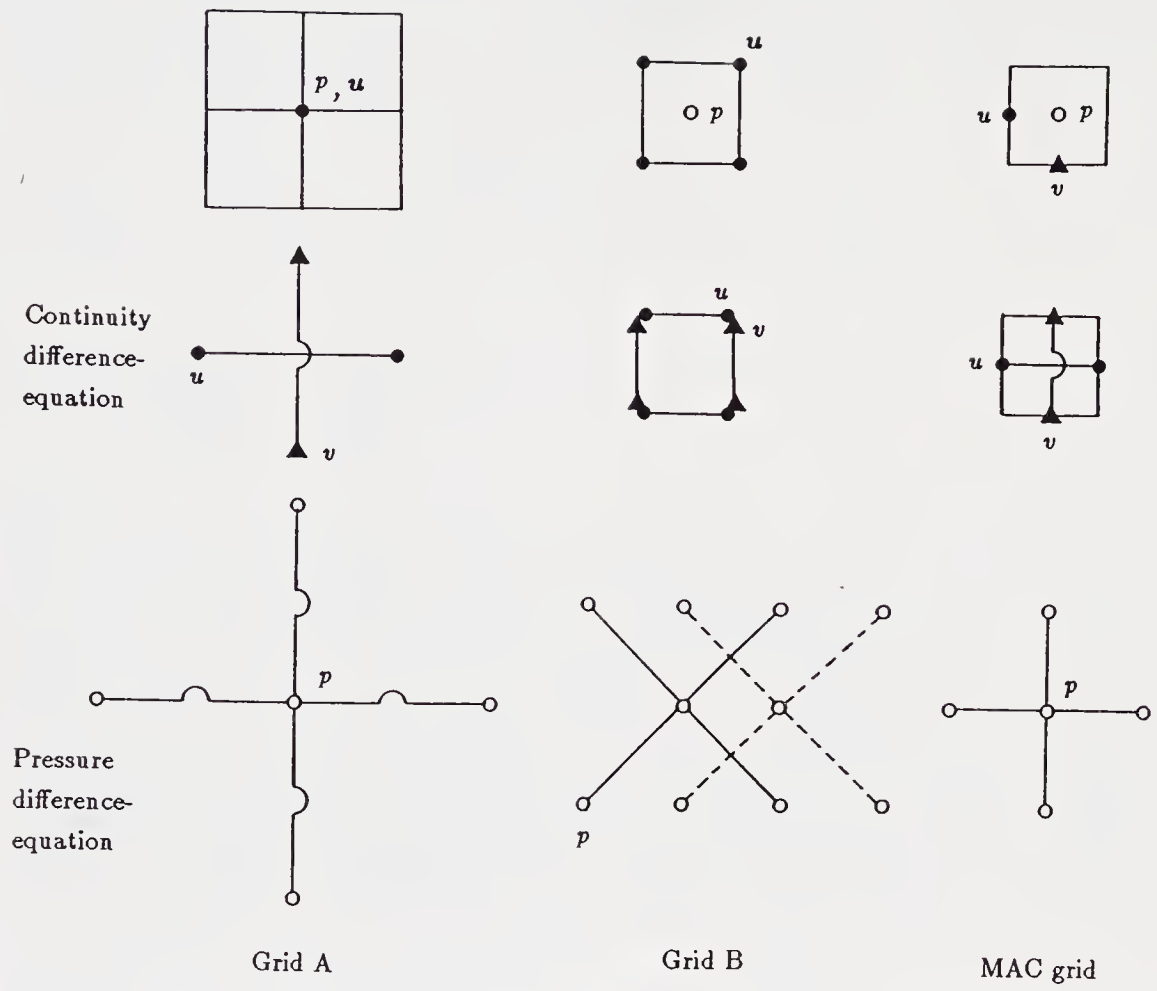

Figure 4. Continuity and pressure difference-equations for different grids.

We here explain about implicit SMAC schemes with curvilinear coordinate grids. In the MAC type scheme, the normal components of velocity are defined at each cell side centre, and the continuity difference-equation is made compact. For the curvilinear coordinate grid, at each cell side centre, the contravariant or covariant velocity components must be defined instead of the physical velocity components. Here the components of volume flux $J\mathbf{U}$ are used as shown in figure 5. The fundamental equations of the SMAC scheme using the curvilinear coordinate grid can be written as

$$JU_l^* = JU_l^n - \Delta t\left[\frac{\partial}{\partial \xi_j}(JU_jU_l) - JU_j\mathbf{u}\cdot\frac{\partial}{\partial \xi_j}\nabla\xi_l + \tilde{g}_{lj}\frac{\partial p}{\partial \xi_j} + \nu\varepsilon_{lmn}\frac{\partial}{\partial \xi_m}(\tilde{h}_{nj}JZ_j)\right]^n, \quad (l=1,2,3), \tag{106}$$

$$(\partial/\partial\xi_l)[\tilde{g}_{lj}(\partial\phi/\partial\xi_j)] = (1/\Delta t)(\partial/\partial\xi_l)(JU_l^*), \tag{107}$$

$$JU_l^{n+1} = JU_l^* - \Delta t\tilde{g}_{lj}(\partial\phi/\partial\xi_j), \quad (l=1,2,3) \tag{108}$$

$$p^{n+1} = p^n + \phi,$$

$$JZ_j = \varepsilon_{jkl}(\partial/\partial\xi_k)(\tilde{h}_{lm}JU_m), \quad (j=1,2,3) \tag{29 bis}$$

where $g_{ij} = \nabla\xi_i\cdot\nabla\xi_j$, $\tilde{g}_{ij} = Jg_{ij}$, $h_{ij} = \partial\mathbf{x}/\partial\xi_i\cdot\partial\mathbf{x}/\partial\xi_j$, $\tilde{h}_{ij} = h_{ij}/J$. Equations (106) and (108) are derived from (21), using the viscous term in (28) by applying the time-splitting

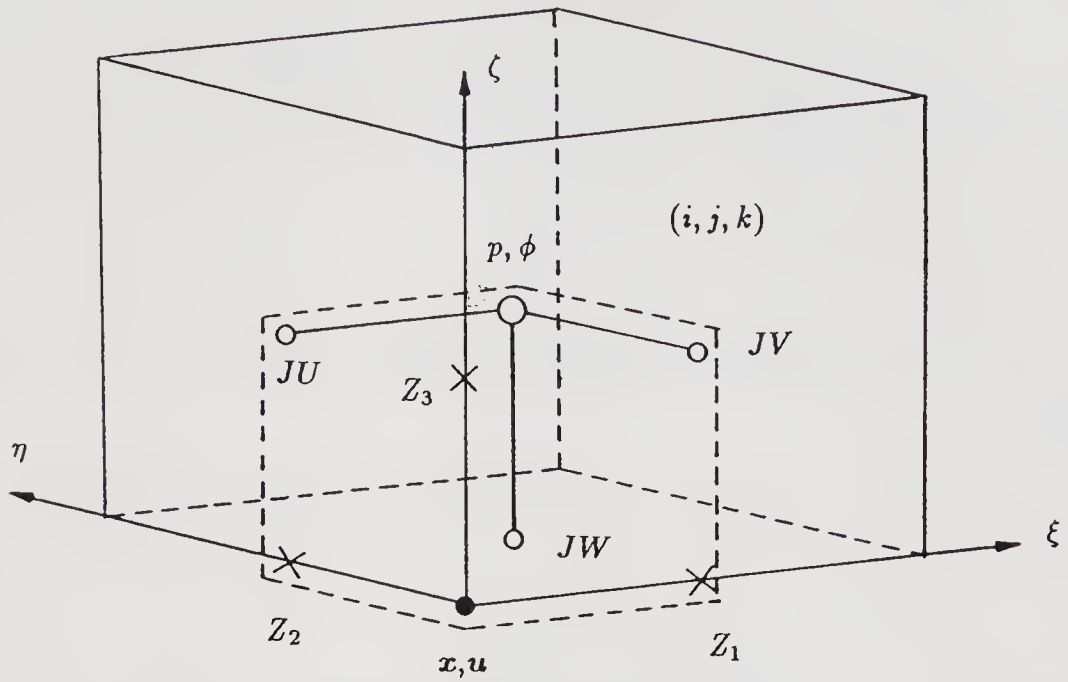

Figure 5. Staggered grid in 3-D space.

method. And the elliptic equation (107) of the pressure increment ϕ is derived by substituting (108) into the continuity condition (22). It is convenient to define the contravariant vorticities Z_j at the centre of the cell edges.

We next extend (106) to an implicit form by applying the delta-form approximate-factorization method and partially include the viscous term in the left hand side. Supposing that h_{ii} is greater than h_{ij} $(i \neq j)$, the viscous term is

$$(Vis)_1 \approx \nu\left[\frac{\partial}{\partial\eta}\tilde{h}_{33}\left(\frac{\partial}{\partial\xi}\tilde{h}_{22}JV - \frac{\partial}{\partial\eta}\tilde{h}_{11}JU\right) - \frac{\partial}{\partial\zeta}\tilde{h}_{22}\left(\frac{\partial}{\partial\zeta}\tilde{h}_{11}JU - \frac{\partial}{\partial\xi}\tilde{h}_{33}JW\right)\right].$$

Further, using the continuity equation (22) roughly,

$$(Vis)_1 \approx \nu\left(\frac{\partial}{\partial\xi}\tilde{h}_{22}\tilde{h}_{33}\frac{\partial}{\partial\xi} + \frac{\partial}{\partial\eta}\tilde{h}_{33}\frac{\partial}{\partial\eta}\tilde{h}_{11} + \frac{\partial}{\partial\zeta}\tilde{h}_{22}\frac{\partial}{\partial\zeta}\tilde{h}_{11}\right)JU.$$

Therefore, the fundamental equations of the present implicit SMAC scheme are

$$\left[1 + \Delta t\theta\left(\frac{\partial}{\partial\xi}U^n - \nu\frac{\partial}{\partial\xi}\tilde{h}_{22}\tilde{h}_{33}\frac{\partial}{\partial\xi}\right)\right].$$

$$\left[1 + \Delta t\theta\left(\frac{\partial}{\partial\eta}V^n - \nu\frac{\partial}{\partial\eta}\tilde{h}_{33}\frac{\partial}{\partial\eta}\tilde{h}_{11}\right)\right].$$

$$\left[1 + \Delta t\theta\left(\frac{\partial}{\partial\zeta}W^n - \nu\frac{\partial}{\partial\zeta}\tilde{h}_{22}\frac{\partial}{\partial\zeta}\tilde{h}_{11}\right)\right]\Delta JU^* = \mathrm{RHS}_1^n,$$

$$\left[1 + \Delta t\theta\left(\frac{\partial}{\partial\xi}U^n - \nu\frac{\partial}{\partial\xi}\tilde{h}_{33}\frac{\partial}{\partial\xi}\tilde{h}_{22}\right)\right].$$

$$\left[1 + \Delta t\theta\left(\frac{\partial}{\partial\eta}V^n - \nu\frac{\partial}{\partial\eta}\tilde{h}_{33}\tilde{h}_{11}\frac{\partial}{\partial\eta}\right)\right].$$

$$\left[1+\Delta t\theta\left(\frac{\partial}{\partial\zeta}W^n-\nu\frac{\partial}{\partial\zeta}\tilde{h}_{11}\frac{\partial}{\partial\zeta}\tilde{h}_{22}\right)\right]\Delta JV^*=\mathrm{RHS}_2^n,$$

$$\left[1+\Delta t\theta\left(\frac{\partial}{\partial\xi}U^n-\nu\frac{\partial}{\partial\xi}\tilde{h}_{22}\frac{\partial}{\partial\xi}\tilde{h}_{33}\right)\right].$$

$$\left[1+\Delta t\theta\left(\frac{\partial}{\partial\eta}V^n-\nu\frac{\partial}{\partial\eta}\tilde{h}_{11}\frac{\partial}{\partial\eta}\tilde{h}_{33}\right)\right].$$

$$\left[1+\Delta t\theta\left(\frac{\partial}{\partial\zeta}W^n-\nu\frac{\partial}{\partial\zeta}\tilde{h}_{11}\tilde{h}_{22}\frac{\partial}{\partial\zeta}\right)\right]\Delta JW^*=\mathrm{RHS}_3^n, \tag{109}$$

where

$$\mathrm{RHS}_l=-\Delta t\left[\frac{\partial}{\partial\xi_j}(JU_jU_l)-JU_j\mathbf{u}\cdot\frac{\partial}{\partial\xi_j}\nabla\xi_l+\tilde{g}_{lj}\frac{\partial p}{\partial\xi_j}+\nu\varepsilon_{lmn}\frac{\partial}{\partial\xi_m}(\tilde{h}_{nj}JZ_j)\right],$$

$$(l=1,2,3), \tag{110}$$

$$JU_l^*=JU_l^n+\Delta JU_l^*, \quad (l=1,2,3),$$

$0\leqslant\theta\leqslant 1$. Equation (109) becomes the explicit SMAC scheme for $\theta=0$, and is the most stable for $\theta=1$. As mentioned before, for calculating steady flow the RHS means the residual and ΔJU_l^* the correction. Therefore, the RHS of (110) must be calculated accurately, for example, using the third-order upstream-difference scheme with the third-order Lagrangian interpolation

$$\begin{aligned}(\partial JU^2/\partial\xi)_{ijk}=(1/6\Delta\xi)[&(JU^+)_{ijkP}(-U_{i-1jk}+5U_{ijk}+2U_{i+1jk})\\&-(JU^+)_{i-1jkP}(-U_{i-2jk}+5U_{i-1jk}+2U_{ijk})\\&+(JU^-)_{ijkP}(2U_{ijk}+5U_{i+1jk}-U_{i+2jk})\\&-(JU^-)_{i-1jkP}(2U_{i-1jk}+5U_{ijk}-U_{i+1jk})],\end{aligned}$$

where the subscript P shows the point where p is defined. On the other hand, the left hand side allows to calculate approximately, using the first-order upstream-difference scheme

$$\begin{aligned}[(\partial/\partial\xi)U\Delta JU^*]_{ijk}=(1/\Delta\xi)[&-U^+_{i-1jk}(\Delta JU^*)_{i-1jk}\\&+|U_{ijk}|(\Delta JU^*)_{ijk}+U^-_{i+1jk}(\Delta JU^*)_{i+1jk}.\end{aligned}$$

The computational procedure for obtaining the steady-state solution is summarized as follows.

(I) Compute grid, metrics and metric tensor components;
(II) Estimate starting values of JU_l, and p;
(III) Compute $\mathbf{u}$ and JZ_l from (9) and (29);
(IV) Compute JU_l^* from (109) and (110);
(V) Solve simultaneous equations of ϕ, (107), by an iterative method;
(VI) Compute JU_l^{n+1} from (108);
(VII) Repeat the steps (III) to (VI), until the solution converges.

Equation (109) can be solved by dividing into three steps, each step being problem solving the simultaneous linear equations with a tri-diagonal matrix by the Gaussian elimination. The simultaneous linear equations (107) are here solved by the

Tschebyscheff SLOR method alternating sweep directions like the ADI method, which is suitable in supercomputing.

We next explain an implicit SMAC scheme for unsteady flow. In the same manner as the compressible flow, rewriting the equations so far mentioned into the equations of the second-order Crank–Nicholson method, we get for the 2-D flow

$$\begin{aligned}
&\left\{1+\Delta t\theta\left(\frac{\partial}{\partial\xi}U^n-\nu\frac{\partial}{\partial\xi}\frac{1}{J}\frac{\partial}{\partial\xi}\tilde{h}_{22}\right)\right\}\cdot\\
&\left\{1+\Delta t\theta\left(\frac{\partial}{\partial\eta}V^n-\nu\frac{\partial}{\partial\eta}\frac{1}{J}\frac{\partial}{\partial\eta}\tilde{h}_{11}\right)\right\}\Delta JU^{*(m)}=\mathrm{RHS}_1^{(m-1)},\\
&\left\{1+\Delta t\theta\left(\frac{\partial}{\partial\xi}U^n-\nu\frac{\partial}{\partial\xi}\frac{1}{J}\frac{\partial}{\partial\xi}\tilde{h}_{22}\right)\right\}\cdot\\
&\left\{1+\Delta t\theta\left(\frac{\partial}{\partial\eta}V^n-\nu\frac{\partial}{\partial\eta}\frac{1}{J}\frac{\partial}{\partial\eta}\tilde{h}_{11}\right)\right\}\Delta JV^{*(m)}=\mathrm{RHS}_2^{(m-1)},
\end{aligned}\tag{111}$$

where

$$\begin{aligned}
\mathrm{RHS}_l^{(0)}&=-\Delta t\{F_l-\mathbf{u}\cdot[JU(\partial/\partial\xi)+JV(\partial/\partial\eta)]\nabla\xi_l\}^n,\\
\mathrm{RHS}_l^{(m)}&=\mathrm{RHS}_l^{(m-1)}+\Delta\mathrm{RHS}_l^{(m)},\\
\Delta\mathrm{RHS}_l^{(m)}&=-(JU_l^{(m)}-JU_l^{(m-1)})-(1/2)\Delta t(F_l^{(m)}-F_l^{(m-1)}),\\
&\qquad(l=1,2,\ m\geqslant 1),
\end{aligned}\tag{112}$$

$$\begin{aligned}
F_1&=(\partial/\partial\xi)JU^2+(\partial/\partial\eta)JUV+\nu\zeta_\eta+\tilde{g}_{11}p_\xi+\tilde{g}_{12}p_\eta,\\
F_2&=(\partial/\partial\xi)JUV+(\partial/\partial\eta)JV^2-\nu\zeta_\xi+\tilde{g}_{21}p_\xi+\tilde{g}_{22}p_\eta,
\end{aligned}$$

$$JU_l^{*(m)}=JU_l^{m-1}+\Delta JU_l^{*(m)},\quad(l=1,2),$$

$$\frac{\partial}{\partial\xi}(\tilde{g}_{11}\phi_\xi^{(m)}+\tilde{g}_{12}\phi_\eta^{(m)})+\frac{\partial}{\partial\eta}(\tilde{g}_{21}\phi_\xi^{(m)}+\tilde{g}_{22}\phi_\eta^{(m)})=\frac{2}{\Delta t}\left(\frac{\partial}{\partial\xi}JU^{*(m)}+\frac{\partial}{\partial\eta}JV^{*(m)}\right),\tag{113}$$

$$JU_l^{(m)}=JU_l^{*(m)}-(1/2)\Delta t(\tilde{g}_{l1}\phi_\xi^{(m)}+\tilde{g}_{l2}\phi_\eta^{(m)}),\quad(l=1,2),\tag{114}$$

$$p^{(m)}=p^{(m-1)}+\phi^{(m)},$$

$$\zeta=(1/J)\{(\partial/\partial\xi)(\tilde{h}_{21}JU+\tilde{h}_{22}JV)-(\partial/\partial\eta)(\tilde{h}_{11}JU+\tilde{h}_{12}JV)\}.\tag{115}$$

In these equations, the Navier–Stokes equations are split into (111) and (114) applying the time-splitting method. In the left hand sides of (111), the delta-form approximate-factorization method is applied. The viscous terms are contained completely in the right hand side, but partially in the left hand side. And the additional terms are taken only as values at time t^n, because these terms do not change as much in time as the other terms. The elliptic equation of pressure increment ϕ is derived by taking the divergence of (114) and considering the continuity condition

$$(\partial JU^{(m)}/\partial\xi)+(\partial JV^{(m)}/\partial\eta)=0.$$

The advanced values of JU_l^{n+1} and p^{n+1} are obtained by solving (111) to (115) by the Newton iteration. If both $\Delta JU_l^{*(m)}$ and $\phi^{(m)}$ tend to zero, then $JU_l^{*(m)}, JU_l^{(m)}\Rightarrow JU_l^{n+1}$, $p^{(m)}\Rightarrow p^{n+1}$, and the solution converges.

The computational procedure of the present implicit SMAC scheme for the unsteady flow is as follows.

(I) $n = n + 1$, $m = 0$,
Compute $\text{RHS}_l^{(0)}$ using (112).
(II) $m = m + 1$.
(III) Compute $\Delta JU_l^{*(m)}$ from (111) using the Gaussian elimination.
Determine $JU_l^{*(m)}$.
(IV) Compute $\phi^{(m)}$ from (113) using the Tschebyscheff SLOR method. Determine $p^{(m)}$.
(V) Compute $JU_l^{(m)}$ from (114).
(VI) Compute ζ from (115).
If $\Delta JU_l^{*(m)}$ and $\phi^{(m)}$ are sufficiently small, GO TO I.
(VII) Compute $\text{RHS}_l^{(m)}$ using (112).
GO TO II.

The solution at each time t^n usually converges within a few subiterations.

In these implicit SMAC schemes using the curvilinear coordinate staggered grid, the volume fluxes corresponding to the flow rate through each cell side are defined at the centres of these cell sides. The volume fluxes JU_l^{n+1} obtained from the difference equations of (108) or (114) are made to satisfy the difference equation of continuity condition (22) identically, when the difference equations of (107) or (113) are satisfied sufficiently. Since the principal part of these difference equations of pressure is expressed in compact form, no spurious error occurs in the computation.

4. Numerical examples

Several numerical calculations were carried out for the compressible and incompressible flow problems using the methods described so far. These problems include the steady and unsteady flows through two- and three-dimensional (3-D) cascades, and the unsteady flows in a 2-D channel and over a 3-D backward-facing stepped duct. The H-shaped grid generated algebraically was generally used in the cascade flow. The Poisson equation is partly used in the generation of 3-D stepped duct domain. The grid was concentrated near the solid wall boundaries according to the Reynolds number in the viscous flow problems. The k–ε turbulent model with low Reynolds number effect or the law of the wall is applied to solve the turbulent flow problems. A number of numerical examples and a brief discussion are presented.

4.1 *Compressible flow problems*

First the calculated results of a 2-D flow through a supersonic compressor cascade studied by Tweedt *et al* (1988) are shown. The feature of the cascade flow is that the inlet Mach number, M_1, and the static pressure ratio, p_2/p_1, at the design point are 1·612 and 2·15, respectively. The blade chord Reynolds number is specified as $1{\cdot}1 \times 10^6$. 141×61 grid points are used. Figures 6a and b show the Mach number contours and isentropic Mach number distributions on the blade surface by the steady calculation (Yamamoto & Daiguji 1991c). The consistency between the present and the experimental data is quite good on the suction surface, but is not always good on the pressure surface. And then we show another result of 2-D transonic turbulent flows through a turbine cascade. The turbine cascade has a high loaded nozzle guide vane configuration (Baines *et al* 1986). The computational grid is shown in figure 7 with

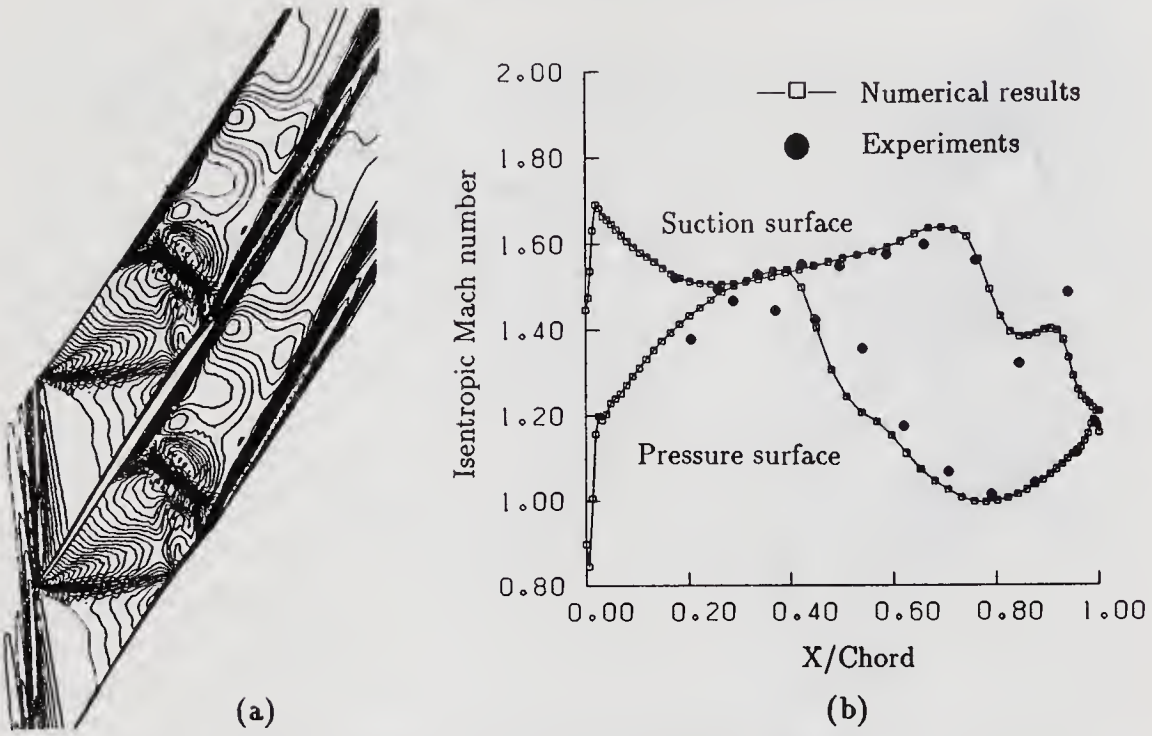

Figure 6. (**a**) Mach number contours and (**b**) isentropic Mach number distributions.

91 × 41 grid points. Figures 8a and b show the calculated Mach number contours and the isentropic Mach number distributions on the blade surfaces compared with the experiments, respectively (Yamamoto & Daiguji 1992). In spite of the relatively coarse grid, the results are in good agreement with the experimental data.

Next, we show some results calculated by the N–S direct simulation of 3-D flows through an axial-flow transonic compressor rotor with or without tip clearance. The

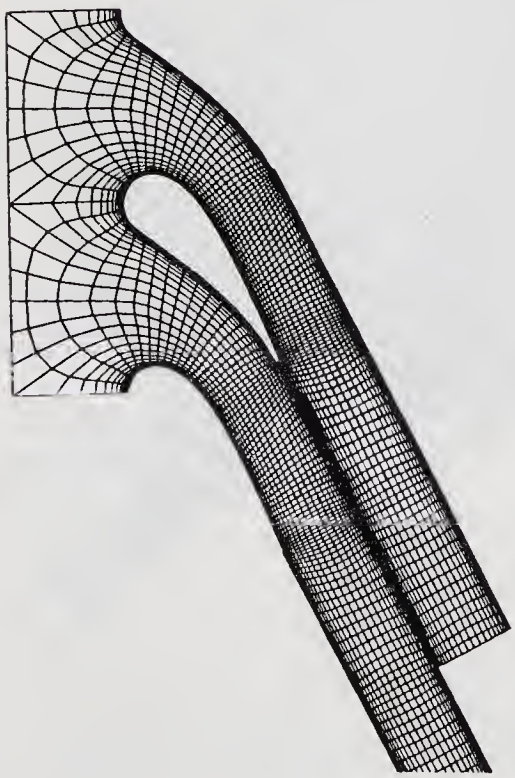

Figure 7. Computational grid for the nozzle guide vanes (91 × 41 grid points).

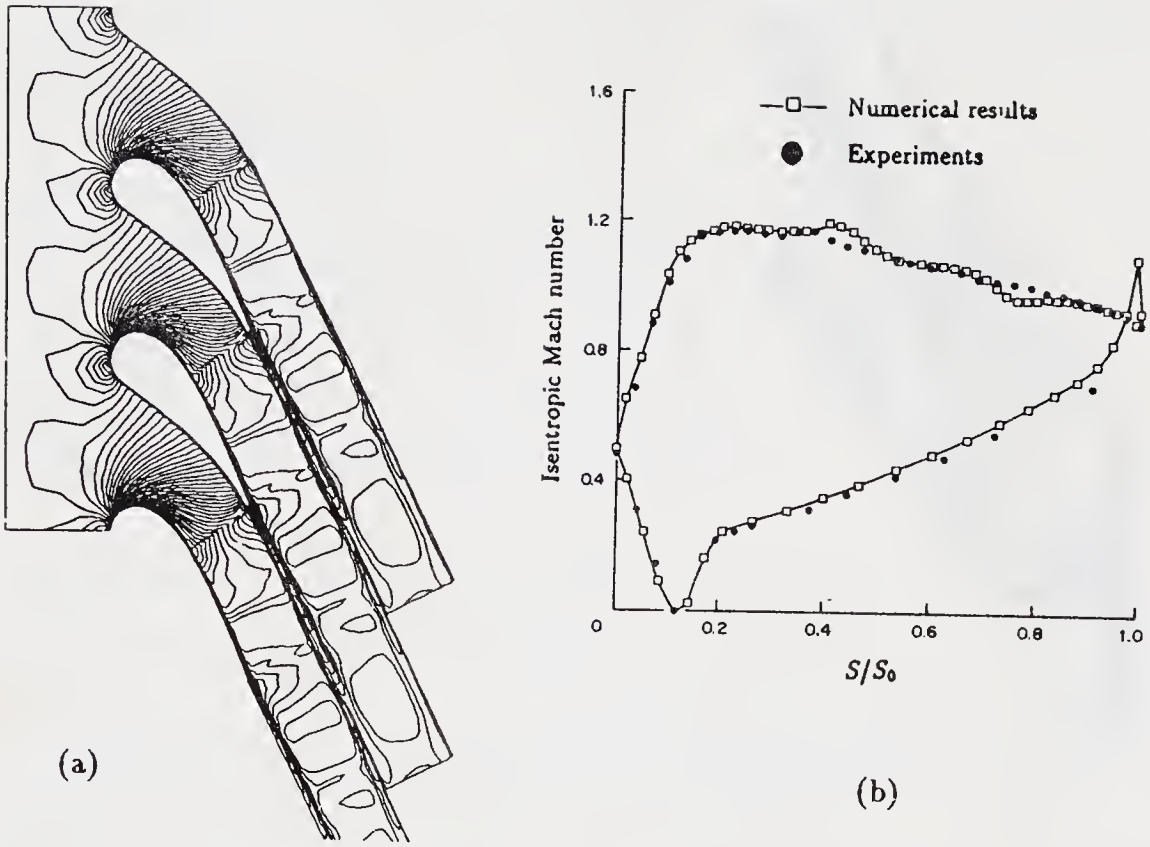

Figure 8. (**a**) Calculated Mach number contours, and (**b**) surface isentropic Mach number distributions.

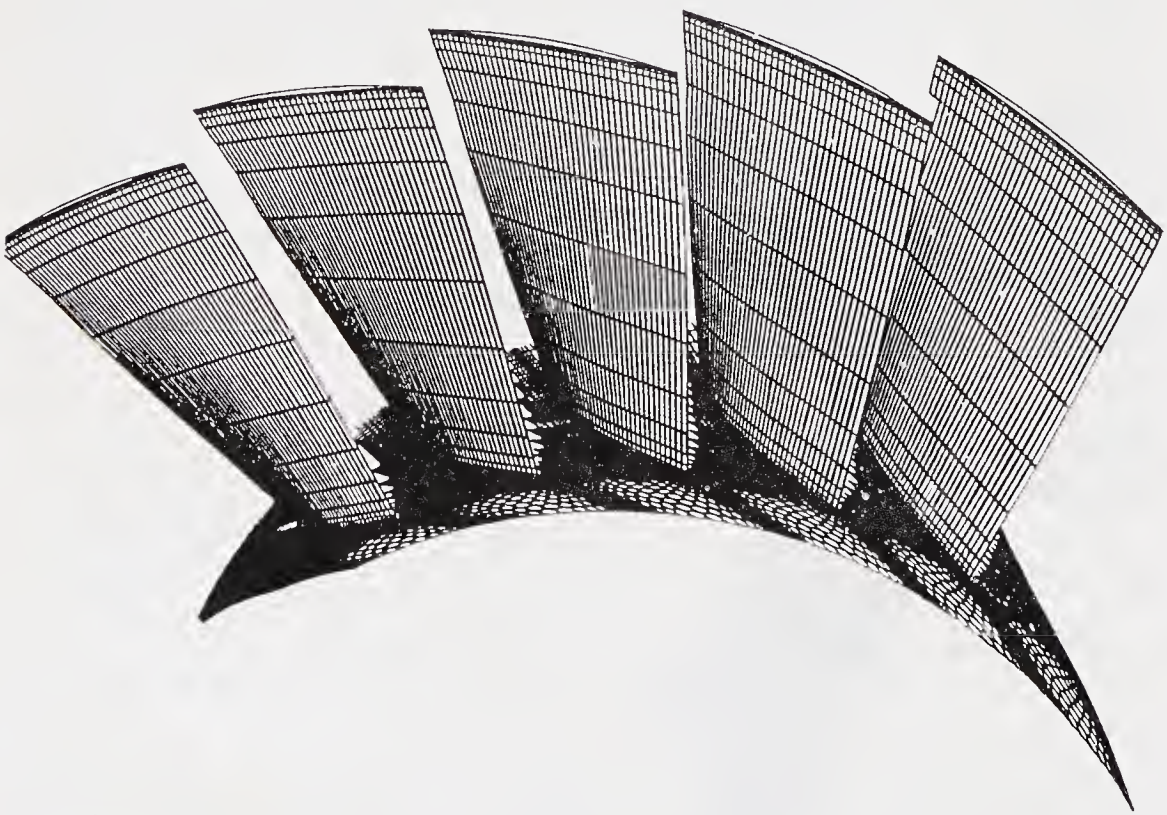

Figure 9. Computational grid for the axial-flow compressor rotor (81 × 25 × 25 grid points).

computational grid is shown in figure 9 with $81 \times 25 \times 21$ grid points. The hub-tip ratio $= 0{\cdot}680$, number of blades $= 24$, tip clearance $= 1{\cdot}5\%$ span, static pressure ratio $= 1{\cdot}5$ and $\mathrm{Re} = 1{\cdot}0 \times 10^6$. Figures 10a and b show the calculated Mach number contours on the several constant surfaces. These figures show that strong passage shocks and weak bow shocks are well captured in spite of the relatively coarse grid. In particular, it seems that figure 10b indicates the existence of leakage vortices at the tip regions. Figure 11 shows the pressure distributions on the suction surface in the case with tip clearance (Yamamoto & Daiguji 1991b). And figures 12a and b show different views of the same leakage vortex which are visualized using streamlines emanating from the tip clearance. This leakage vortex originates in clearance with strong vorticity, and this clearance flow grows to a leakage vortex only if the suction corner flow is stagnant or reversed.

As an unsteady flow problem, the calculated results of a 2-D unsteady turbulent flow through a transonic axial-flow turbine stator-rotor are shown. The computational grid is shown in figure 13 and it has $71 \times 41(\times 2)$ and $91 \times 41(\times 3)$ grid points at stator and rotor, respectively, in which the stator/rotor blade ratio is 2:3. Figures 14a and b show the Mach number contours at 0 and 0·2 cycles, respectively (Yamamoto & Daiguji 1989). From these results we know that the effect of the stator wakes on the rotor passage flow is clearly simulated and the unsteady shocks occurring at the trailing edge of the rotor can be sharply captured.

Figures 15a and b are the results of 2-D unsteady inviscid flows through a supersonic duct (Yamamoto & Daiguji 1991a). The computational grid used here has 241×81 grid points. The inlet Mach number is 1.6. Then, as time increases, unsteady complex shock patterens are observed. The numerical results of instantaneous Mach number contours are compared with the results of the present third-order and fourth-order

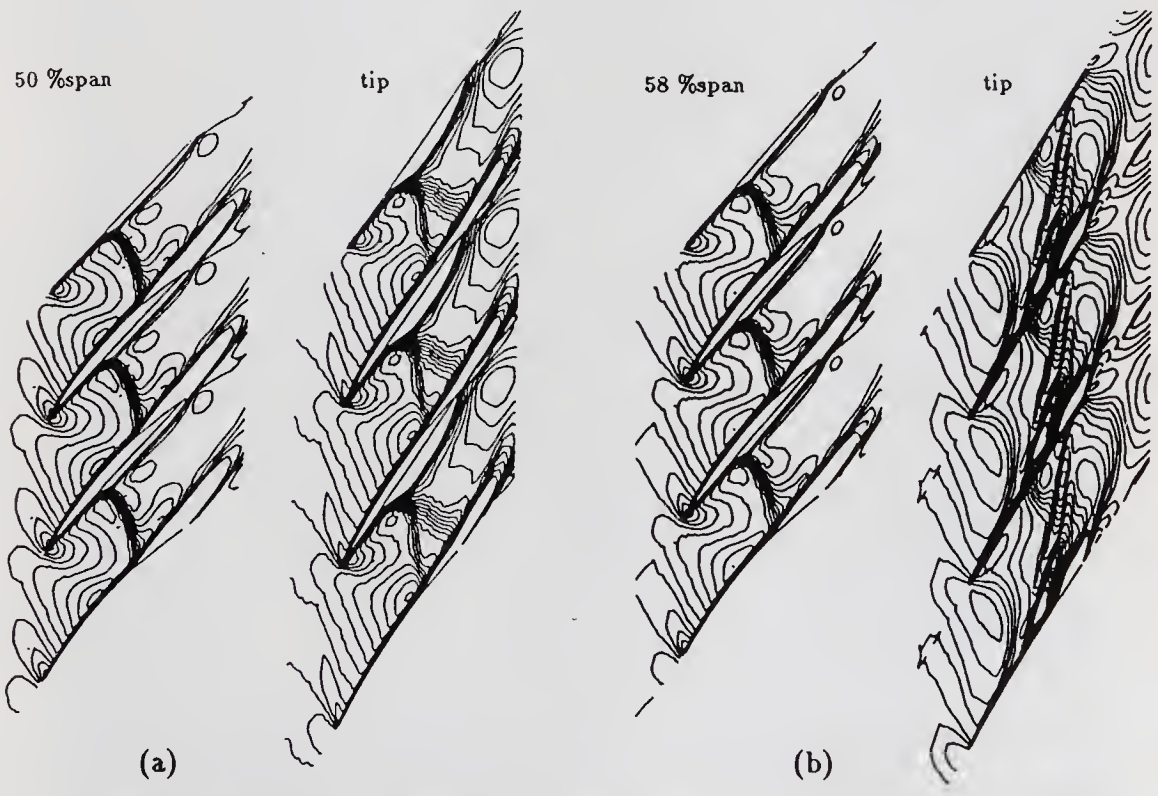

Figure 10. Calculated Mach number contours on the constant span surfaces: (**a**) without tip clearance and (**b**) with tip clearance.

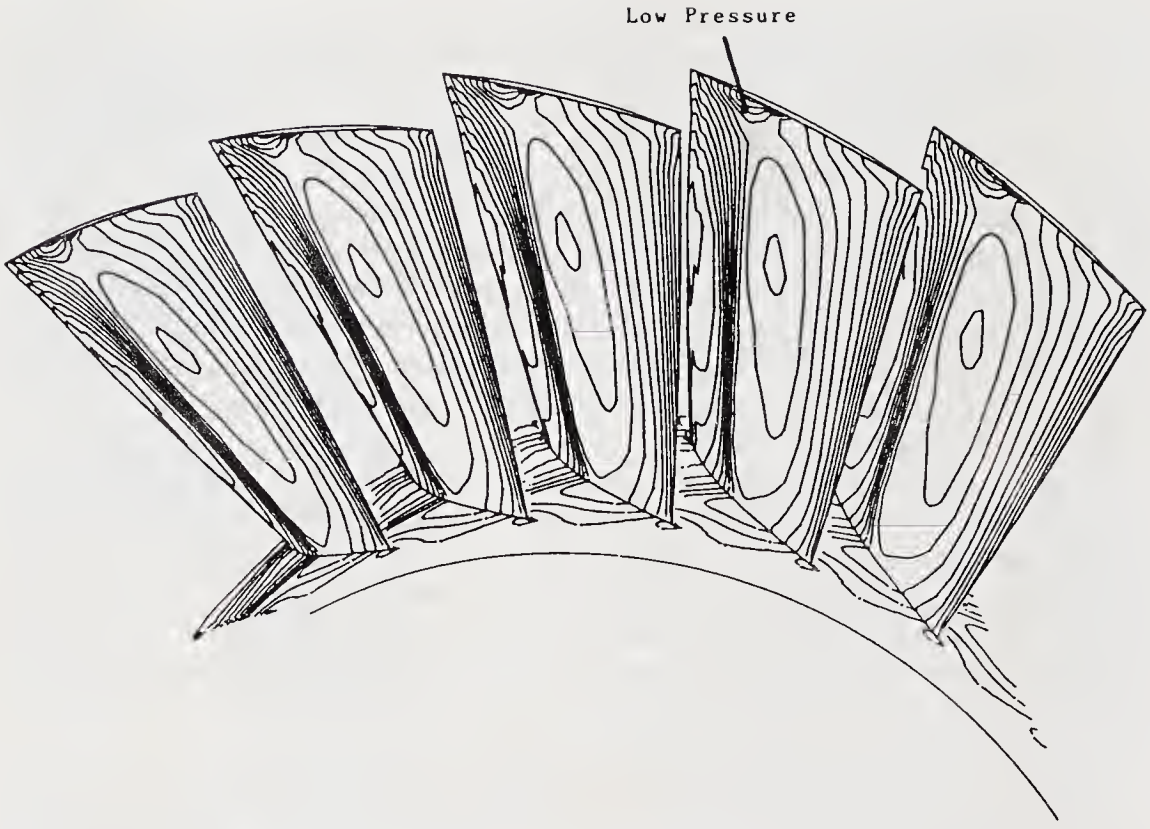

Figure 11. Pressure distributions on the suction surfaces.

MUSCL TVD scheme at some nondimensional times. From the comparison with these figures, the shock pattern and the sharpness show almost the same results as each other. The superiority of the fourth-order scheme appears at the resolution of a slip line. The high-order scheme can completely simulate the discontinuity through the whole flow field, that is, it is greatly effective to obtain the weak discontinuities such as slip lines or contract discontinuities.

4.2 *Incompressible flow problems*

Numerical calculations were performed for steady and unsteady incompressible cascade flows and over a backward-facing step using the present incompressible flow schemes. The modified QUICK upwind-difference scheme is generally applied for the space derivatives of the convection terms in the RHS of (109). A staggered grid is used and the definition points of unknown variables are as shown in figure 5.

Figure 16 shows the time evolution of velocity vectors and the surface pressure distribution in an unsteady 2-D decelerating cascade flow for $\mathrm{Re} = 10{,}000$ with the angle of attack (angle between flow direction and blade chord) $\alpha = 14{\cdot}5°$ (Shin *et al* 1992a). The cascade consists of a blade section of NACA 65(12)10, whose pitch-chord ratio and inlet flow angle are 0·667 and 45°, respectively. An H-shaped grid with 121×45 points for a single passage as in figure 17 was used. In this Re, the cascade flow becomes unsteady as indicated in the figure. A vortex generated by rolling-up at the trailing edge at the dimensionless time $T = 0$ causes a sharp pressure drop near the trailing edge. After the vortex sheds from the trailing edge, the pressure on the rear part of the blade tends to increase. As a result, a periodic fluctuating flow similar to the Kármán vortex street is formed in the wake. The shedding vortices into the

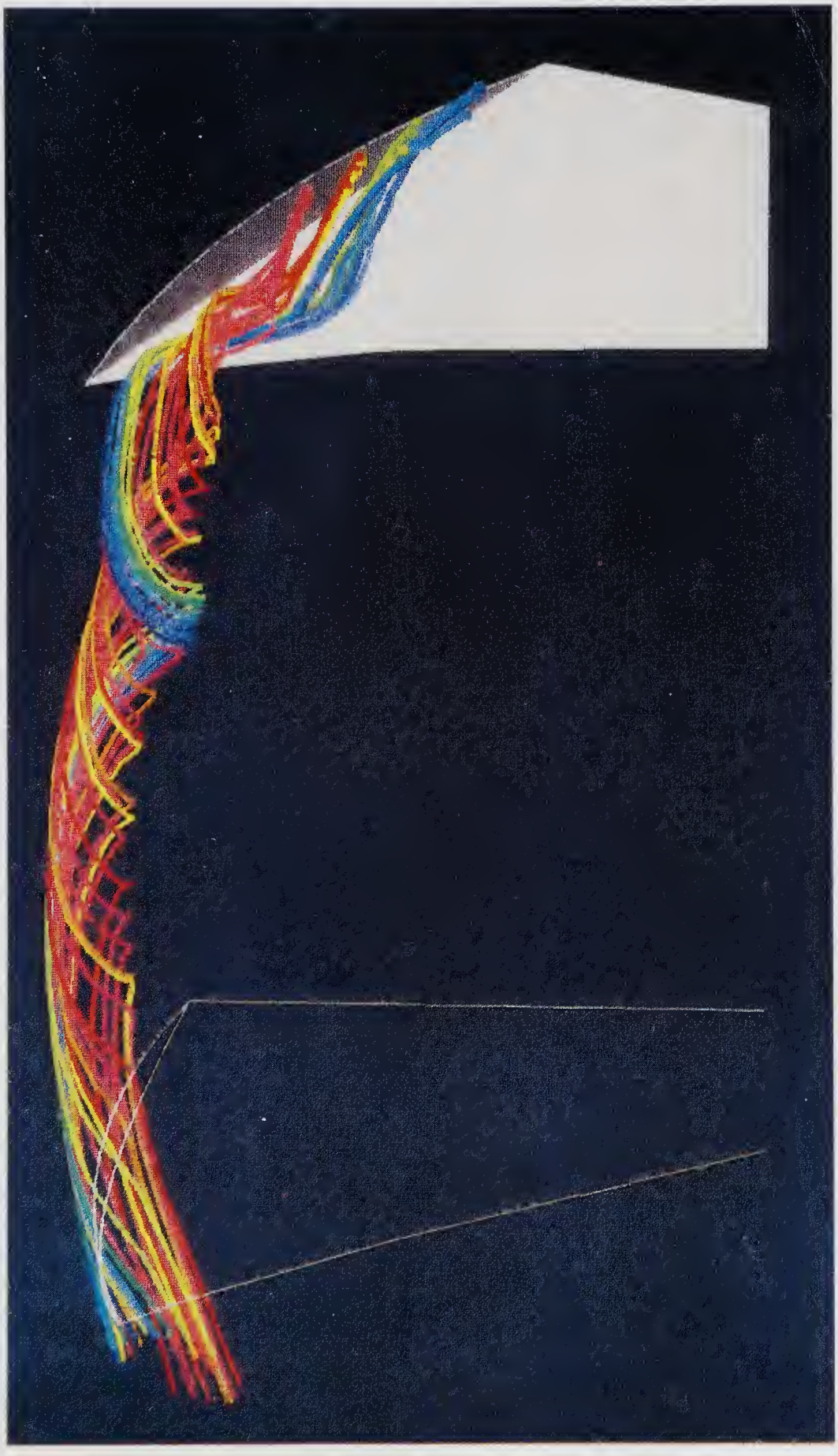

Figure 12(a). (Caption on next page.)

Figure 12. Flow visualization of the leakage vortex generating from the tip clearance (particle paths): **(a)** view from the inlet and **(b)** view from the casing.

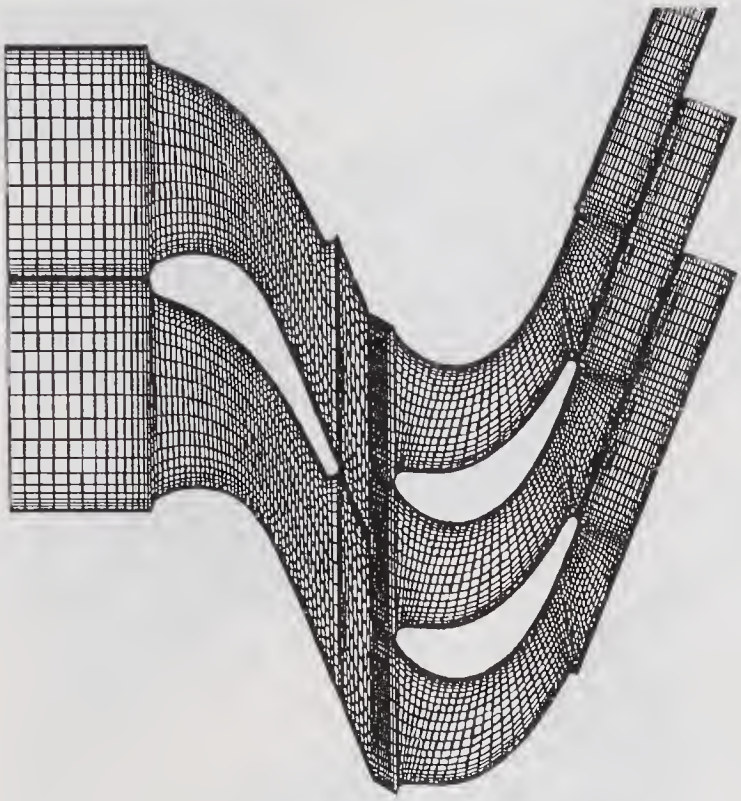

Figure 13. Computational grid for a transonic axial-flow turbine rotor-stator (stator: 71×41, rotor: 91×41 grid points).

wake have been simulated well at the downstream region. Figure 18 shows another numerical result of time-averaged pressure distributions in the cascade flow for $\mathrm{Re} = 2{\cdot}45 \times 10^5$ at $\alpha = 27{\cdot}6°$ (Shin *et al* 1991). The 255×55 grid points were used to simulate the boundary layer and the wake flows accurately. The cascade flow at this high Reynolds number indicated the unsteady flow characteristics in both simulations of the laminar and turbulent flow. Agreement of the present results with the experiment (Emery *et al* 1958) seems satisfactory. As far as the surface pressure distribution is concerned, the time-averaged laminar result shows little difference from the turbulent

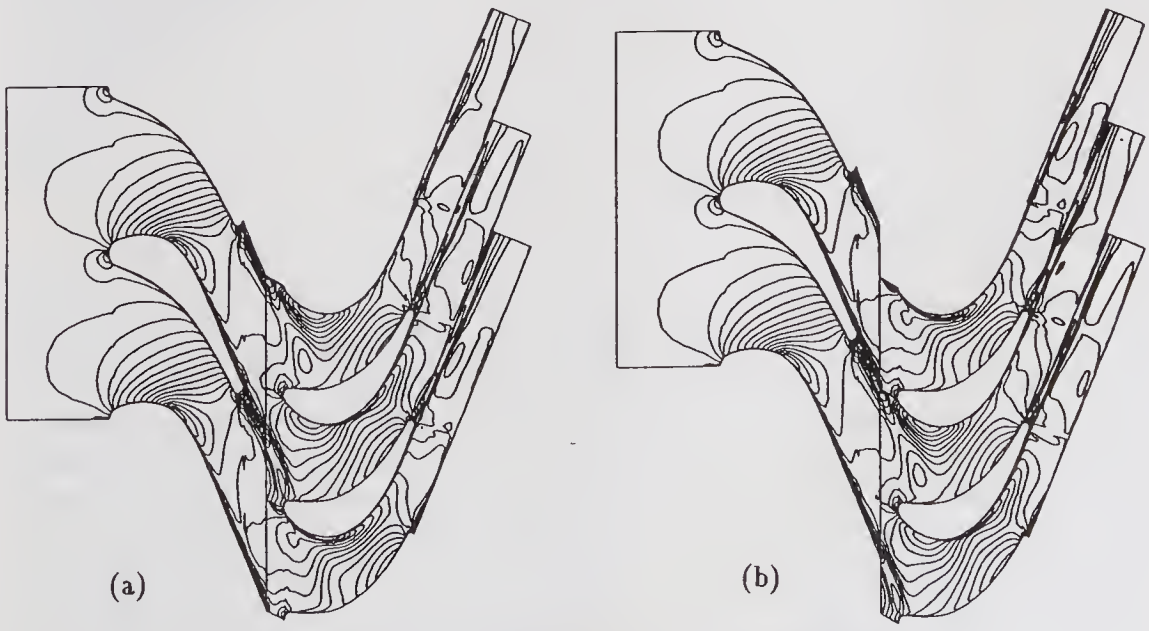

Figure 14. Mach number contours: (**a**) 0 cycle and (**b**) 0·2 cycle.

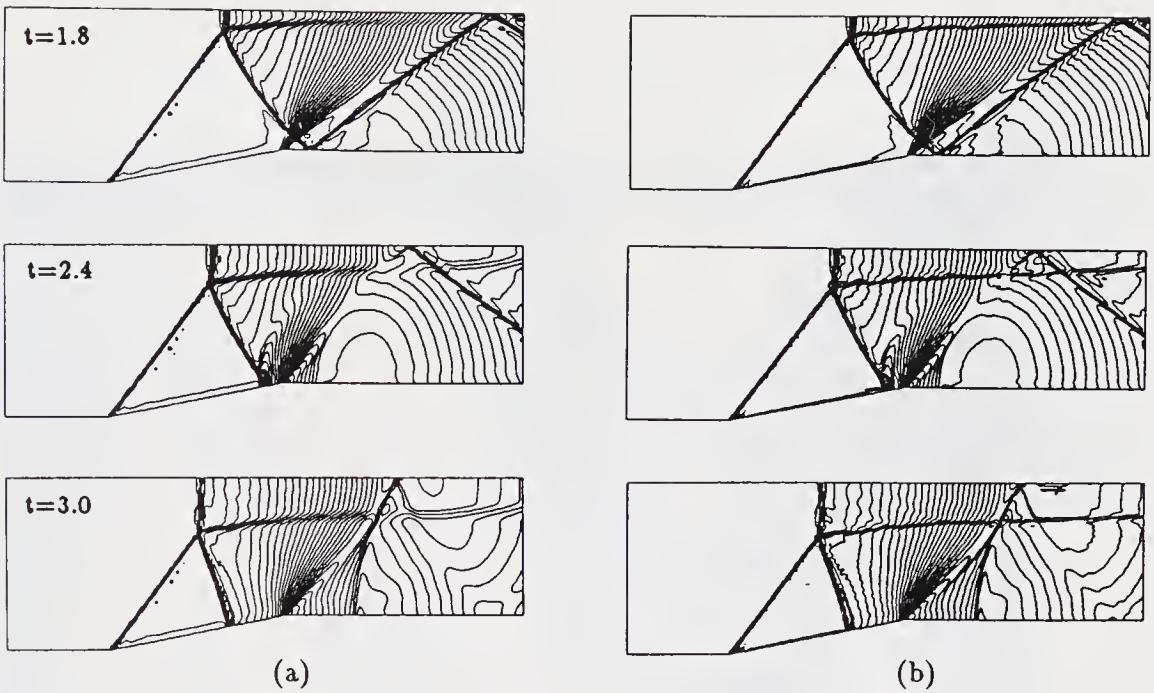

Figure 15. Mach number contours by (**a**) the third-order MUSCL TVD scheme, and (**b**) the fourth-order compact MUSCL TVD scheme.

one, indicating the validity of the unsteady laminar flow calculations. Figure 19 shows contour plots of instantaneous eddy-viscosity ν_t. It is clear that ν_t concentrates considerably on the turbulent boundary layer and the following wake with a wavy pattern.

Next, we applied the present incompressible flow schemes to practical flows in 3-D complex geometry, such as turbomachinery and stepped ducts. For example, a numerical calculation was carried out for the viscous flow through an impeller of an axial-flow turboblower. The grid has $61 \times 25 \times 25$ nodes for $\mathrm{Re} = 1000$. The impeller geometry consists of a double circular-arc type profile with a stagger angle 40·3° and a pitch-chord ratio 1·33 at mid-span, and a hub-to-tip ratio of 0·6. The velocity vectors for relative flow and the corresponding pressure contours in the hub-to-casing surface and the streamwise section at several locations are shown in figures 20 and 21, respectively (Ikohagi *et al* 1990). These figures indicate that strong radial inward flows occur along the blade wakes and cause a stagnant spot of high pressure on the hub surface behind the trailing edge. However, these flows may be somewhat strengthened because of no-tip-clearance geometry. Figure 22 shows the pressure distribution by 3-D colour graphics.

The direct numerical simulation of a 3-D turbulent flow over a backward-facing stepped-duct was also calculated. This is often selected as the standard test problem for numerical schemes. A computational grid having $211 \times 87 \times 55$ grid points is used. The expansion ratio is 1·5 and the aspect ratio based on the step height (h) is 16. Figures 23a and b show the instantaneous velocity vectors on the mid-span plane and near the side wall, respectively, for $\mathrm{Re} = 45{,}000$. The TVD upwind scheme (Chakravarthy & Osher 1985) is applied in this 3-D separated duct flow computation. At this Re, the flow is essentially unsteady, accompanying the secondary separated region on the no-stepped wall as well as the primary separated region behind the step (Armaly *et al* 1983; Kondoh & Nagano 1989), although the steady-state solution was obtained at a lower $\mathrm{Re} = 1000$ (Ikohagi *et al* 1992). Their reattachment lengths vary slightly with

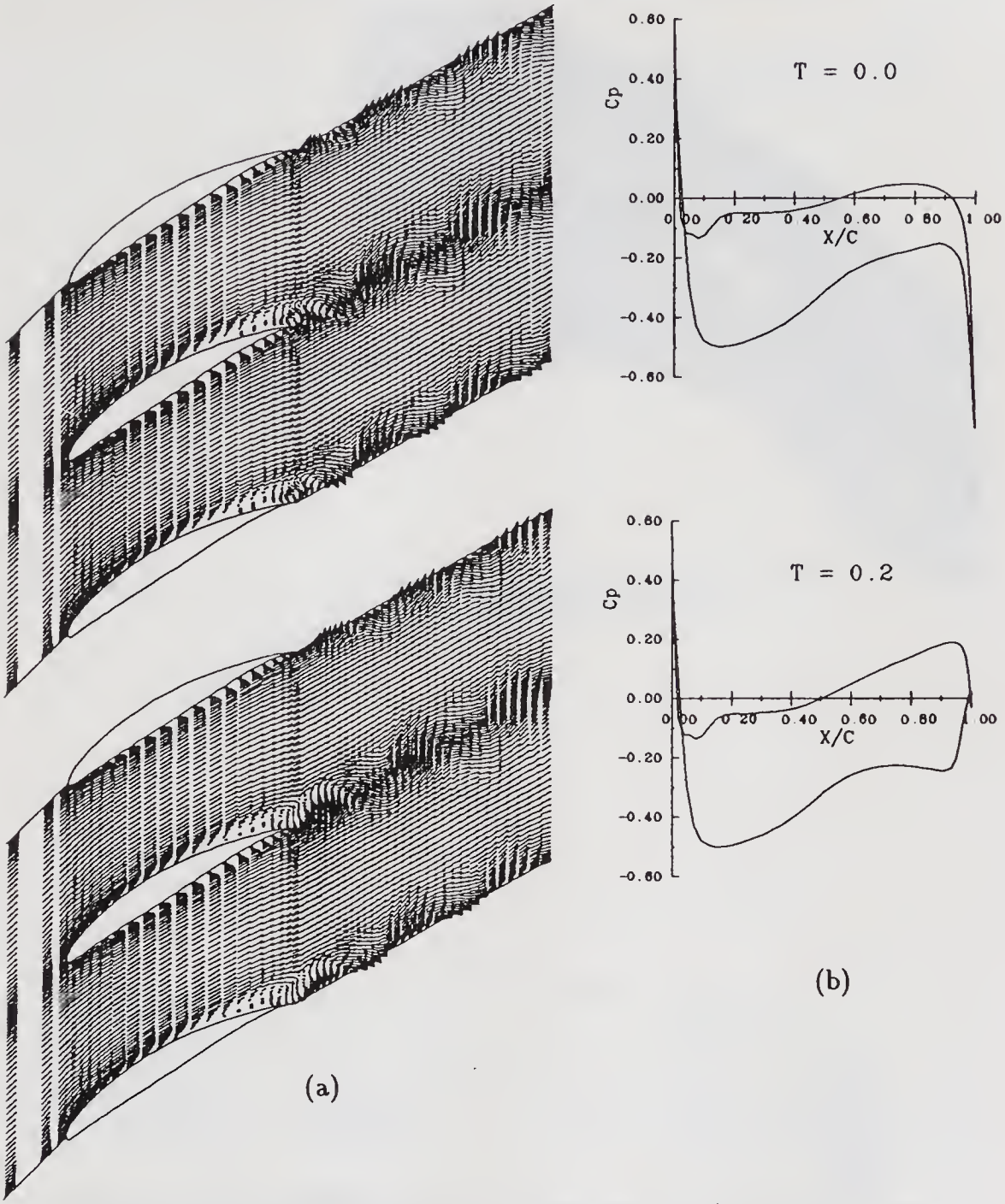

Figure 16. Unsteady decelerating cascade flow for $\mathrm{Re} = 10^4$: (**a**) time evolution of velocity vector, and (**b**) surface pressure distribution.

time, and very complicated forward and backward flows are found mainly near the wall. The reattachment length was estimated to be about $7{\cdot}3h$ when the time-averaged results were taken as the mean of the instantaneous flow data over the dimensionless time interval from $T = 50$ to $T = 64$. This value is in good agreement with the experimental one of 7 ± 1 (Kim *et al* 1980). Figure 24 is a plot of the mean velocity profiles compared with experiment at the several downstream locations on the mid-span plane. In the recirculation region, the present computations underpredict the experiments and the reverse flow is shown to be a little faster than that of Kim *et al* (1980). The velocity profile shown, however, is in general good agreement with

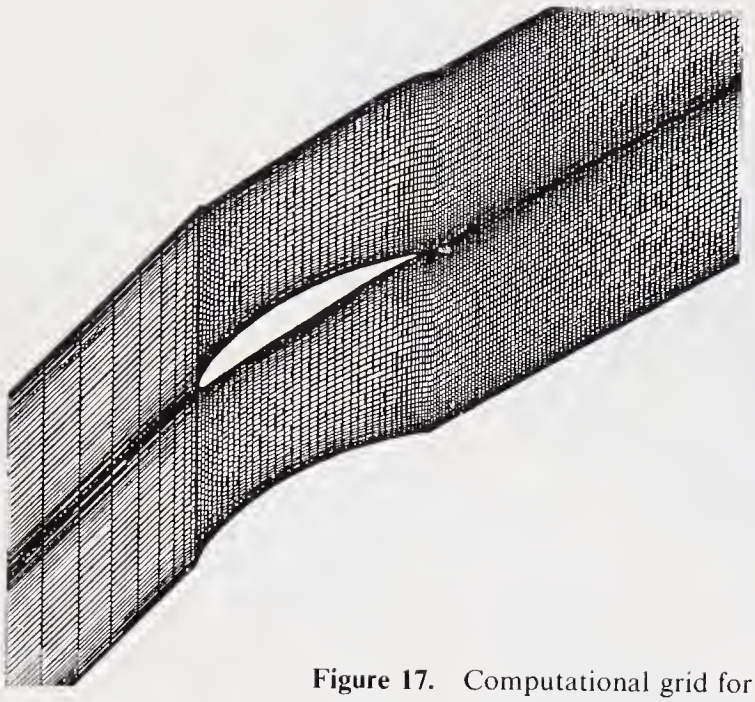

Figure 17. Computational grid for $Re = 10^4$ (121 × 45 grid points).

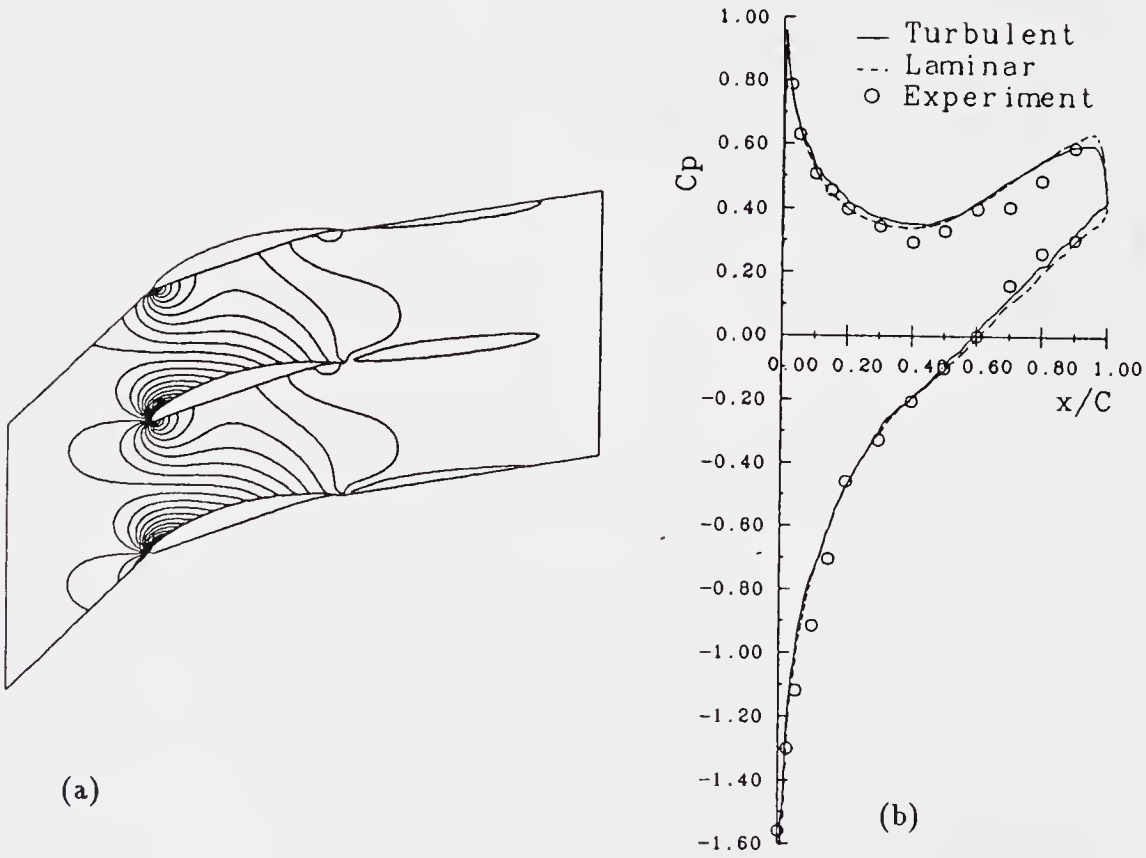

Figure 18. Unsteady 2-D cascade flow at $Re = 2{\cdot}45 \times 10^5$: (**a**) time-averaged pressure contours, and (**b**) surface pressure distribution.

Figure 19. Contour plots of instantaneous eddy-viscosity.

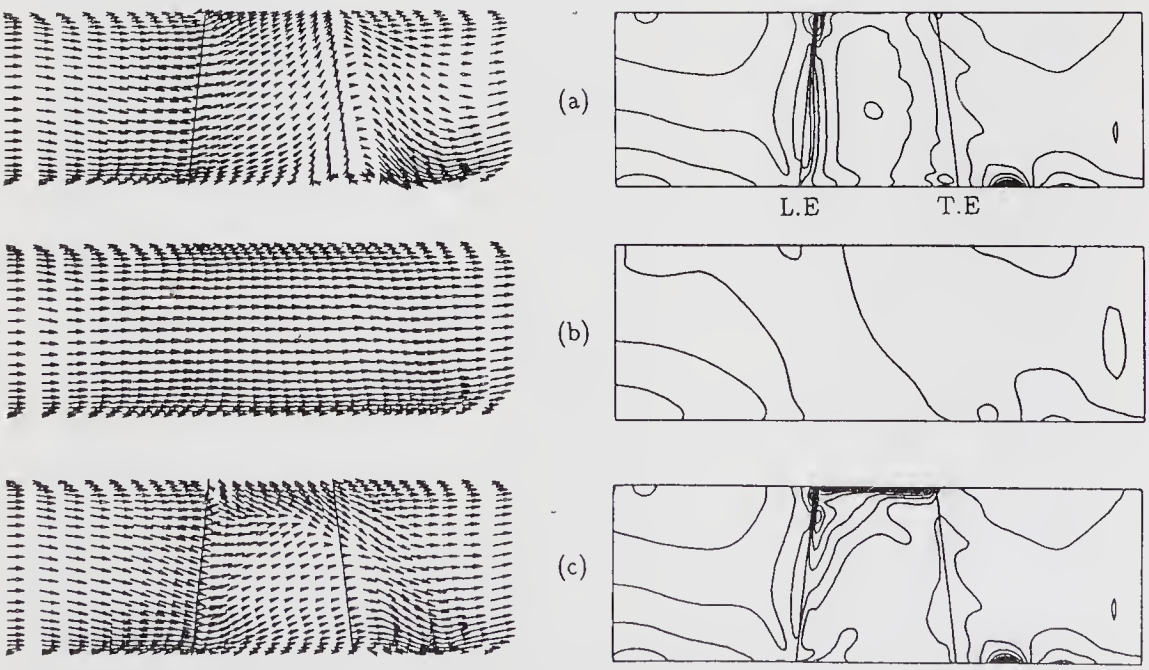

Figure 20. Velocity vectors and pressure contours in hub-to-casing surfaces: (**a**) near the suction surface, (**b**) at mid-passage, and (**c**) near the pressure surface.

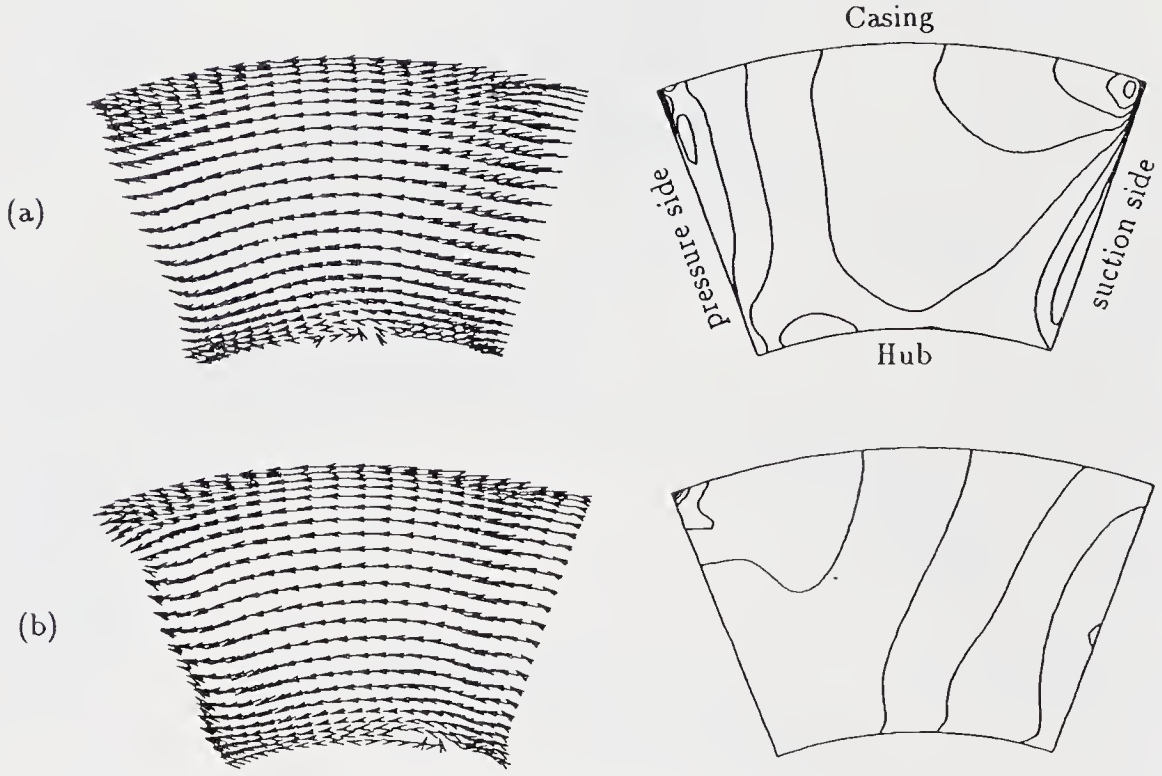

Figure 21. Velocity vectors and pressure contours in the streamwise sections at (**a**) the leading edge, and (**b**) the mid-chord.

the experiments. Figure 25 displays a surface of the instantaneous enstrophy field of $|\zeta|^2 = 15$ by 3-D computer graphics (Shin *et al* 1992b). The shear layer can be clearly discriminated and vorticity fluctuations of turbulent flows are observed in this figure.

5. Concluding remarks

Some numerical schemes for analysing incompressible and compressible flow problems developed by the authors and their coworkers were introduced. The fundamental equations of these schemes are the Navier–Stokes equations of contravariant velocities (volume fluxes), which make it easy to impose the boundary conditions, in general, the curvilinear coordinates. These equations are solved by implicit time-marching finite-difference schemes using the delta-form approximate-factorization and TVD schemes. Also, the compressible flow schemes are improved by using the diagonalization, the flux difference splitting and higher-order TVD MUSCL schemes to reduce the computational efforts, and increase the stability and the resolvability. The incompressible SMAC schemes satisfy the continuity condition identically, and suppress the occurrence of spurious errors by using the staggered grid. Unsteady flows are calculated using the Crank–Nicholson method and the Newton iteration. The k–ε two-equation turbulence model is employed for calculating the turbulent flows. The reliability of the present schemes is confirmed by comparison with available experimental data and existing numerical results.

Figure 22. Pressure distribution at mid-span plane (view from the inlet).

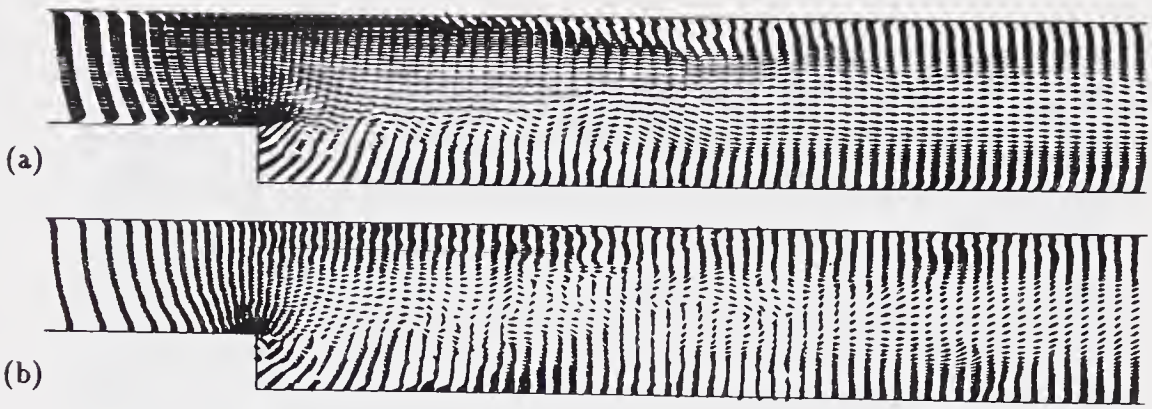

Figure 23. Instantaneous velocity vectors (**a**) on the mid-span plane, and (**b**) near the side wall.

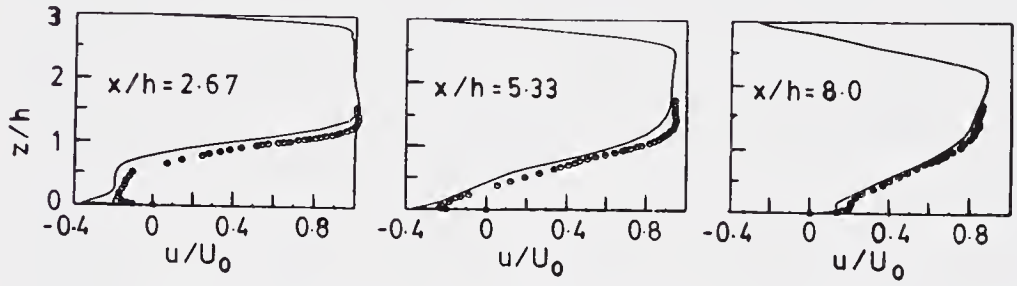

Figure 24. Mean velocity profiles on the mid-span planes.

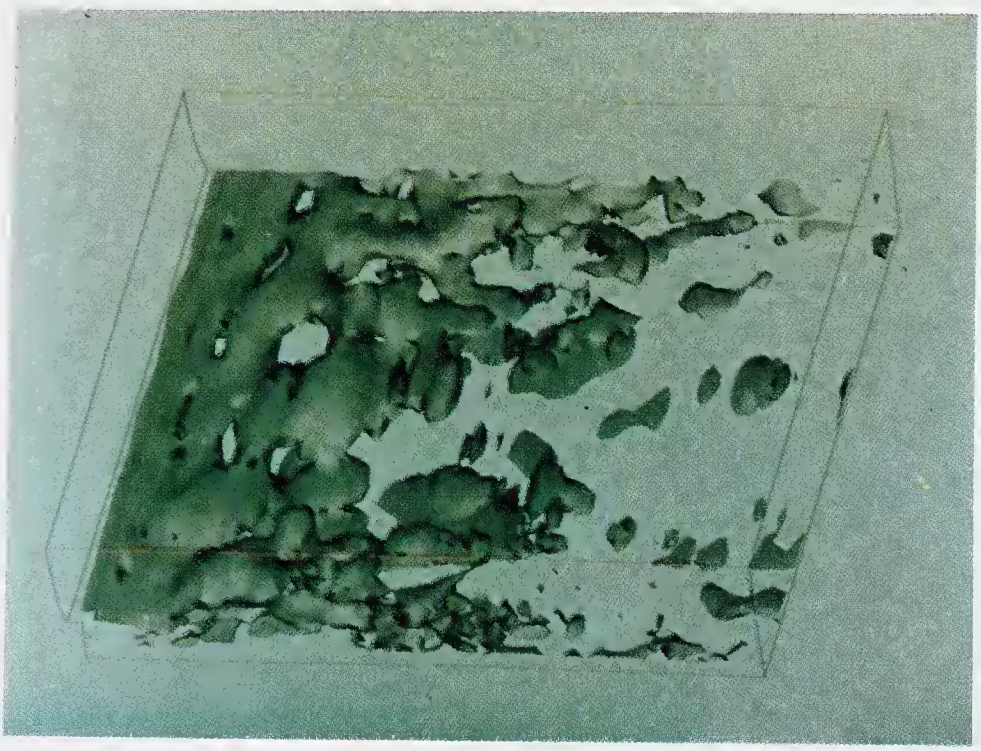

Figure 25. Instantaneous enstrophy surface of $|\zeta|^2 = 15$ near the step.

References

Amsden A A, Harlow F H 1970 A simplified MAC technique for incompressible fluid flow calculations. *J. Comput. Phys.* 6: 322–325

Anderson K A, Thomas J L, Whitfield D L 1988 Multigrid acceleration of the flux split Euler equations. *AIAA J.* 26: 649–657

Armaly B P, Durst F, Peretra J C F, Schönung D 1983 Experimental and theoretical investigation of backward-facing step flow. *J. Fluid Mech.* 127: 473–496

Baines N C, Oldfield M L G, Simons J P, Wright J M 1986 The aerodynamics development of a highly loaded nozzle guide vane. *Trans. ASME, J. Turbomach.* 108: 261–268

Beam R M, Warming R F 1978 An implicit factored scheme for the compressible Navier–Stokes equations. *AIAA J.* 16: 393–402

Chakravarthy S R, Osher S 1985 A new class of high accuracy TVD schemes for hyperbolic conservation laws. *AIAA* Paper No. 85–0363

Chang J L C, Kwak D, Rogers S E, Yang R J 1988 Numerical simulation methods of incompressible flows and application to the space shuttle main engine. *Int. J. Numer. Methods Fluids* 8: 1241–1268

Chien K Y 1981 Prediction of channel and boundary-layer flows with a low-Reynolds number turbulence model. *AIAA J.* 20: 33–38

Chorin A J 1967 A numerical method for solving incompressible viscous flow problems. *J. Comput. Phys.* 2: 12–26

Chorin A J 1968 Numerical solution of the Navier–Stokes equations. *Math. Comput.* 22: 745–762

Daiguji H, Yamamoto S 1988 An implicit time-marching method for solving the 3-D compressible Navier–Stokes equations. *Lecture notes in Physics. Vol. 323* (New York: Springer-Verlag)

Daiguji H, Yamamoto S, Motohashi Y 1987 Time-marching finite-difference schemes for three-dimensional compressible Euler equations. *Trans. Jpn. Soc. Mech. Eng.* B53: 393–399 (in Japanese)

Demirdzic I, Gosman A D, Issa R I, Peric M 1987 A calculation procedure for turbulent flow in complex geometries. *Comput. Fluids* 15: 251–273

Denton J D 1974 A time marching method for two- and three-dimensional blade to blade flows. *ARC R & M* 3775

Denton J D 1983 Am improved time-marching method for turbomachinery flow calculation. *Trans. ASME, J. Eng. Power* 105: 514–524

Dodge P R 1977 Numerical method for 2-D and 3-D viscous flows. *AIAA J.* 15: 961–965

Emery J C, Herrig L J, Erwin J R, Felix A R 1958 Systematic two-dimensional cascade tests of NACA 65-series compressor blades at low speeds. NACA Report No. 1368

Harlow F H, Welch J E 1965 Numerical calculation of time dependent viscous incompressible flow of fluid with free surface. *Phys. Fluids* 8: 2182–2189

Harten A 1983 High resolution schemes for hyperbolic conservation laws. *J. Comput. Phys.* 49: 357–393

Harten A 1989 ENO schemes with subcell resolution. *J. Comput. Phys.* 83: 148–184

Hartwich P M, Hsu C H 1988 High-resolution upwind schemes for the three-dimensional incompressible Navier–Stokes equations. *AIAA J.* 26: 1321–1328

Ikohagi T, Shin B R 1991 Finite-difference schemes for steady incompressible Navier–Stokes equations in general curvilinear coordinates. *Comput. Fluids* 19: 479–488

Ikohagi T, Shin B R, Daiguji H 1990 An implicit finite-difference scheme for the steady 3-D incompressible Navier–Stokes equations in curvilinear coordinates and its application. *Proc. 3rd Japan-China Joint Conf. Fluid Mechanics* (Osaka) 2: 227–234

Ikohagi T, Shin B R, Daiguji H 1992 Applications of an implicit time-marching scheme to 3-D incompressible flow problem in curvilinear coordinate systems. *Comput. Fluids* 21: 163–175

Karki K C, Patankar S V 1988 Calculation procedure for viscous incompressible flow in complex geometries. *Numer. Heat Transfer* 14: 295–307

Kim J, Kline S J, Johnston J P 1980 Investigation of a reattaching turbulent shear layer: flow over a backward-facing step. *Trans. ASME, J. Fluid Eng.* 102: 302–308

Kim J, Moin P 1985 Application of a fractional-step method to incompressible Navier–Stokes equations. *J. Comput. Phys.* 59: 308–323

Kondoh T, Nagano Y 1989 Numerical investigation of three-dimensional separating and reattaching flow downstream of a backward-facing step. *Proc. 3rd Int. Symp. Comput. Fluid Dynamics* (Nagoya) 1: 263–270

Launder B E, Spalding D B 1974 The numerical computation of turbulent flows. *Comput. Methods Appl. Mech. Eng.* 3: 269–289

MacCormack R W 1969 The effect of viscosity in hypervelocity impact cratering. *AIAA* paper no. 69–354

MacCormack R W 1982 A new method for solving the equations of compressible viscous flow. *AIAA J.* 20: 1275–1281

Nakamura Y, Takemoto Y 1985 Solutions of incompressible flows using a generalized QUICK method. *Proc. 1st Int. Symp. Comput. Fluid Dynamics* (Tokyo) 2: 285–296

Patankar S V 1980 *Numerical heat transfer and fluid flow* (New York: Hemisphere)

Pulliam T H, Chaussee O S 1981 A diagonal form of an implicit approximate-factorization algorithm. *J. Comput. Phys.* 39: 347–363

Rogers S E, Kwak D, Kiris C 1991 Upwinding differencing scheme for the time-accurate incompressible Navier–Stokes equations. *AIAA J.* 29: 603–610

Rosenfeld M, Kwak D, Vinokur M 1991 A fractional step solution method for the unsteady incompressible Navier–Stokes equations in generalized coordinate systems. *J. Comput. Phys.* 94: 102–139

Shin B R, Ikohagi T, Daiguji H 1991 An implicit finite-difference scheme in curvilinear coordinates for incompressible turbulent flow problems. *Proc. 4th Int. Symp. Comput. Fluid Dynamics* (Davis) 2: 1059–1064

Shin B R, Ikohagi T, Daiguji H 1992a An unsteady implicit SMAC scheme for the two-dimensional incompressible Navier–Stokes equations. *Jpn. Soc. Mech. Eng. Ser.* II, No. 92–2020, (to appear)

Shin B R, Ikohagi T, Daiguji H 1992b An implicit finite-difference scheme for solving the unsteady 3-D incompressible Navier–Stokes equations. *Computational Fluid Dynamics '92* (Amsterdam: Elsevier) 1: 457–464

Shin B R, Yamamoto S, Ikohagi T, Daiguji H 1988 Fractional step finite-difference scheme for solving the incompressible Navier–Stokes equations in curvilinear coordinates. *Proc. Soviet Union-Japan Symp. Comput. Fluid Dynamics* (Khabarousk) 2: 91–97

Shyy W, Tong S S, Correa S M 1985 Numerical recirculating flow calculation using a body-fitted coordinate system. *Numer. Heat Transfer* 8: 99–113

Steger J L, Warming R F 1981 Flux vector splitting of the inviscid gasdynamic equations with application to finite difference methods. *J. Comput. Phys.* 40: 263–293

Tamura Y, Fujii K 1991 A multi-dimensional upwind scheme for the Euler equations on structured grid. *Proc. 4th Int. Symp. CFD* (Davis) 2: 1137–1142

Tweedt D L, Schreiber H A, Starken H 1988 Experimental investigation of the performance of a supersonic compressor cascade. *Trans. ASME, J. Turbomach.* 110: 456–466

Yamamoto S, Daiguji H 1989 A numerical method for solving the unsteady compressible Navier–Stokes equations. *Proc. 3rd Int. Symp. Comput. Fluid Dynamics* (Nagoya) 2: 710–715

Yamamoto S, Daiguji H 1991a Higher-order accuracy upwind schemes for solving the compressible Euler and Navier–Stokes equations. *Proc. 4th Int. Symp. CFD* (Davis) 2: 1269–1274

Yamamoto S, Daiguji H 1991b Numerical methods for transonic cascade problems. *Comput. Fluids* 19: 461–478

Yamamoto S, Daiguji H 1991c Unsteady Navier–Stokes simulation of turbulent flows through a supersonic compressor cascade. *Proc. First Joint ASME/JSME Fluids Eng. Conf.* FED-120: 73–79

Yamamoto S, Daiguji H 1992 Numerical analyses of unsteady turbulent flows through transonic turbine and compressor cascade. *Comput. Fluid Dyn. J.* 1: 91–103

Yanenko N N 1961 On the implicit difference computing methods for solving multidimensional heat conduction equations. *Izv. Uchebn. Zaved., Mat.* 4: 148–157

Yee H C, Harten A 1985 Implicit TVD schemes for hyperbolic conservation laws in curvilinear coordinates. *AIAA* Paper No. 85–1513

Yokota J W, Caughey D A 1988 LU implicit multigrid algorithm for the three-dimensional Euler equations. *AIAA J.* 26: 1061–1069

New studies in vortex dynamics: Incompressible and compressible vortex reconnection, core dynamics, and coupling between large and small scales

FAZLE HUSSAIN, DAVINDER VIRK and MOGENS V MELANDER[†]

Department of Mechanical Engineering, University of Houston, Houston, TX 77204-4792, USA

[†] Permanent Address: Dept. of Mathematics, Southern Methodist University, Dallas, Tx 75275, USA

Abstract. Coherent structure dynamics in turbulent flows are explored by direct numerical simulations of the Navier–Stokes equations for idealized vortex configurations. For this purpose, two dynamically significant coherent structure interactions are examined: (i) incompressible and compressible vortex reconnection and (ii) core dynamics (with and without superimposed small-scale turbulence). Reconnection is studied for two antiparallel vortex tubes at a Reynolds number (Re) of 10^3. Incompressible reconnection consists of three distinct phases: inviscid advection, bridging and threading. The key mechanism, bridging, involves the 'cutting' of vortex lines by viscous cross diffusion and their subsequent reconnection in front of the advancing vortex dipole. We conjecture that reconnection occurs in successive bursts and is a physical mechanism of cascade to smaller scales.

Compressible reconnection is seen to be significantly affected by the choice of pressure and density initial conditions. We propose a polytropic initial condition which is consistent with experimental results and low-Mach number asymptotic theories. We also explain how compressibility initiates an early reconnection due to shocklet formation, but slows down the circulation transfer at late times. Thus, the reconnection timescale increases with increasing Mach number.

Motivated by the important role of helical vortex lines in the reconnected vortices (bridges), we focus our attention on the dynamics of an axisymmetric vortex column with axial variation of core size. The resulting core dynamics is first explained via coupling between swirl and meridional flows. We then show that core dynamics can be better understood by applying a powerful analytical tool – *helical wave decomposition* – which extracts vorticity wave packets, thereby providing a simple explanation of the dynamics. The increase in core size variation with increasing Re in such a vortex demonstrates the limitation of the prevalent vortex filament models which assume constant core size. By studying the columnar vortex with superimposed small-scale, homogeneous, isotropic turbulence, we address the mutual interactions between large and small scales in turbulent

flows. At its boundary the columnar vortex organizes the small scales, which, if Re is sufficiently high, induce bending waves on the vortex which further organize the small scales. Such backscatter from small scales cannot be modelled by an eddy viscosity. Based on the observation of such close coupling between large and small scales, we question the local isotropy assumption and conjecture a fractal vortex model for high Re turbulent flows.

Keywords. Vortex dynamics; vortex reconnection; compressible vortex dynamics; core dynamics; helical wave decomposition; coherent structures; large-scale/small-scale interaction; coherent structure/small-scale turbulence coupling.

1. Introduction

In the early seventies, a new avenue for turbulence research was opened with the discovery of large-scale organized motions – popularly called *coherent structures* (forerunners among the studies in this area are Kline *et al* 1967, Crow & Champagne 1971, Brown & Roshko 1974). The emphasis on local dynamics in this 'structural' approach brought fluid mechanics back into turbulence research which had essentially become a branch of statistical physics. Studies of coherent structures have yielded explanations of many heretofore unexplained events such as countergradient transport, turbulence and noise suppression by excitation, and increased entrainment in non-circular jets. The most significant advance following the recognition of coherent structures is turbulence management, i.e. suppression or enhancement of turbulence via control of coherent structures by active or passive means (Hussain 1983) – statistical approaches had failed to suggest any means of turbulence management (Narasimha 1989, p. 13). Coherent structures are central to turbulence control: *no coherent structures, no control* (Bridges *et al* 1989, p. 132). However, eduction of coherent structures and the efficacy of a structural turbulence approach to fully developed turbulent flows are still in the developmental stage.

Our approach to coherent structure studies has a distinctly different flavour. The overwhelming majority of studies in structural turbulence have been based on flow visualization; however, we have long contended that structural turbulence must be based on quantitative measurements of vorticity as flow visualization can not only be confusing but also grossly misleading (Hussain 1981). Even at unity Schmidt number, a passive scalar can faithfully mark vorticity boundaries of structures only in the case of 2D flow. If, however, the flow is 3D, and in particular turbulent, visualization may present incorrect information because the marker is depleted from regions of intense vortex stretching but accumulated in regions of minimal stretching. As a result, dynamically significant events can be easily missed or obscured by flow visualization of vortex interactions and coherent structure dynamics. Therefore, flow visualization, a highly useful tool for qualitative interpretation, must be supplemented by quantitative data.

In our continuing pursuit of structural turbulence, we build here on our long-standing assertion that coherent structures are characterized by *coherent vorticity* – the instantaneous space-correlated vorticity underlying the random vortical field that

we call turbulence (Hussain 1981). Having had a fairly rigorous methematical foundation, vortex dynamics is a (perhaps the most) tractable avenue for understanding the evolutionary dynamics of coherent structures, their role in turbulent transport phenomena, their mutual interactions (such as pairing, tearing, and reconnection) and their coupling with small-scale turbulence.

Pending the availability of experimental techniques (such as holographic particle velocimetry, being developed in our laboratory and elsewhere) to measure instantaneous 3D velocity and vorticity fields, a comprehensive study of the evolutionary dynamics of coherent structures is possible only via direct numerical simulations (DNS). Further, since DNS is restricted to relatively low Re, we have pursued a blend of experimental and numerical approaches to study turbulent shear flows. For instance, using flow visualization as well as limited quantitative hot-wire data we identified vortex reconnection as a dynamically significant interaction and then numerically simulated it in an idealized configuration (discussed below). Such studies have provided us with crucial insight into vorticity dynamics, further supplemented here by a powerful analytical tool – *helical wave decomposition.* The present paper summarizes two recent studies: (i) incompressible and compressible vortex reconnection, and (ii) core dynamics in an axisymmetric vortex with non-uniform cross section with and without superimposed small-scale turbulence.

Our interest in the reconnection process was prompted by our intuitive claim that it is a frequent event in turbulent flows (Hussain 1983), that it plays an important role in cascade, mixing, and helicity generation, that it is an important source of aeroacoustic noise (Takaki & Hussain 1985), and also that, while viscosity is crucial to reconnection, the phenomenon occurs at a convective, rather than a diffusive, timescale. Our curiosity was also piqued by the topological changes of vortex lines during reconnection. In this regard, it is an obvious extension to consider the effects of compressibility mechanisms such as generation of *new* vorticity by baroclinic production and shock-vortex interactions on reconnection.

Our attention to internal core dynamics was first drawn by the observation of an axial variation in vorticity magnitude and core shape seen in reconnection simulations (see § 2.5), which results in helical vortex lines that induce an axial flow along the vortex core. Core dynamics is also of interest for computations and modelling, because a popular vortex method is the discretization of a vorticity field into a large number of vortex filaments (Leonard 1985). Usually the self-induced axial flow inside the filaments is ignored, either by using a fixed core size (Crow 1970; Schwarz 1985), or by using an equivalent core size to conserve the volume of vortical fluid (e.g. Ashurst & Meiburg 1988). A notable exception is the filament method recently developed by Lundgren & Ashurst (1989), who employed self-consistent model equations for the evolution of a variable circular core. Here, we study core dynamics using DNS of an axisymmetric vortex with axial core size variation. Our results imply that strong core size oscillation persists in the inviscid limit and thus strongly suggest that core dynamics cannot be ignored.

By considering the above-mentioned axisymmetric vortex with superimposed small-scale 3D turbulence, we examine mutual interactions of background turbulence and the vortex. Thus, we address here the coupling between large and small scales: one of the most interesting but least understood facets of turbulence.

We use DNS for all studies discussed here. The incompressible simulations were carried out using a spectral code dealiased by a (2/3) k-space truncation and with a

fourth-order predictor-corrector algorithm for time stepping. Periodic boundary conditions are appropriate because the flows under consideration are dominated by strong local vortex interactions, which are insensitive to non-local effects such as the influence from adjacent boxes. Test runs assured that the evolution details remained unchanged when the domain size was doubled. A fully dealiased spectral code with third-order compact storage Runge–Kutta timestepping was used to solve the Navier–Stokes equations for a perfect gas in the compressible reconnection study.

1.1 *Outline*

Initial conditions and the dynamics of incompressible vortex reconnection are discussed in § 2. We have found that the initial pressure (P) and density (ρ) distributions significantly affect compressible vortex dynamics. These effects and compressible vortex reconnection are discussed in § 3. We investigate core dynamics by focussing on the coupling between swirl and meridional flows using a traditional hydrodynamic framework in § 4. Then, in § 5, we briefly introduce the helical wave decomposition and apply it to provide a much simpler explanation of core dynamics. In § 6, the interaction of a large-scale columnar vortex with surrounding homogeneous, isotropic small-scale turbulence is examined, and we end with concluding remarks in § 7.

2. Incompressible vortex reconnection

2.1 *Initial condition*

The initial condition to study reconnection consists of two antiparallel vortices with mutually inclined symmetric sinusoidal perturbations (figure 1a), which ensure that the two vortex tubes collide so as to induce and sustain reconnection; this perturbation is not central to the flow physics. This simple configuration was motivated by our experimental studies of reconnection of elliptic vortex rings in high aspect ratio elliptic jets (Hussain & Husain 1989). Initially, each vortex has a circular core with a compact support Gaussian vorticity distribution. We also studied an asymmetric initial condition as a perturbation to figure 1a. No change was noticeable in the details of the evolution of the vortex reconnection process, thus confirming that the dynamics of the symmetric geometry represent the general behaviour (see later). The symmetric initial condition is particularly useful in clearly identifying the effects of viscosity because the two symmetry planes are preserved in time and are material planes. For clarity, the xy-plane is called the 'symmetric' plane (π_s), while the yz-plane is the 'dividing' plane (π_d). In both planes, the normal velocity and the tangential vorticity vanish at all times. Furthermore, $x\omega_z \leqslant 0$ everywhere in π_s; this eliminates the problem of self-annihilation within each vortex which occurs in the simulation of Meiron *et al* (1989, p. 183). Consequently, the circulations Γ_s and Γ_d in the half planes $\pi_s^+ + (x > 0)$ and $\pi_d^- (z < 0)$ change exclusively by viscous vorticity annihilation. Also, $\mathrm{d}\Gamma_d/\mathrm{d}t = -\mathrm{d}\Gamma_s/\mathrm{d}t$, since an arbitrary vortex line must intersect either π_s or π_d.

2.2 *Three phases of reconnection*

The evolution of vortex reconnection is shown in figure 1 for $\mathrm{Re} = \Gamma/\nu = 1000$ via wire-frame plots of the vorticity norm $|\omega|$ at $t = 0$, 2·25, 3·5, 4·75 and 6 at an isosurface

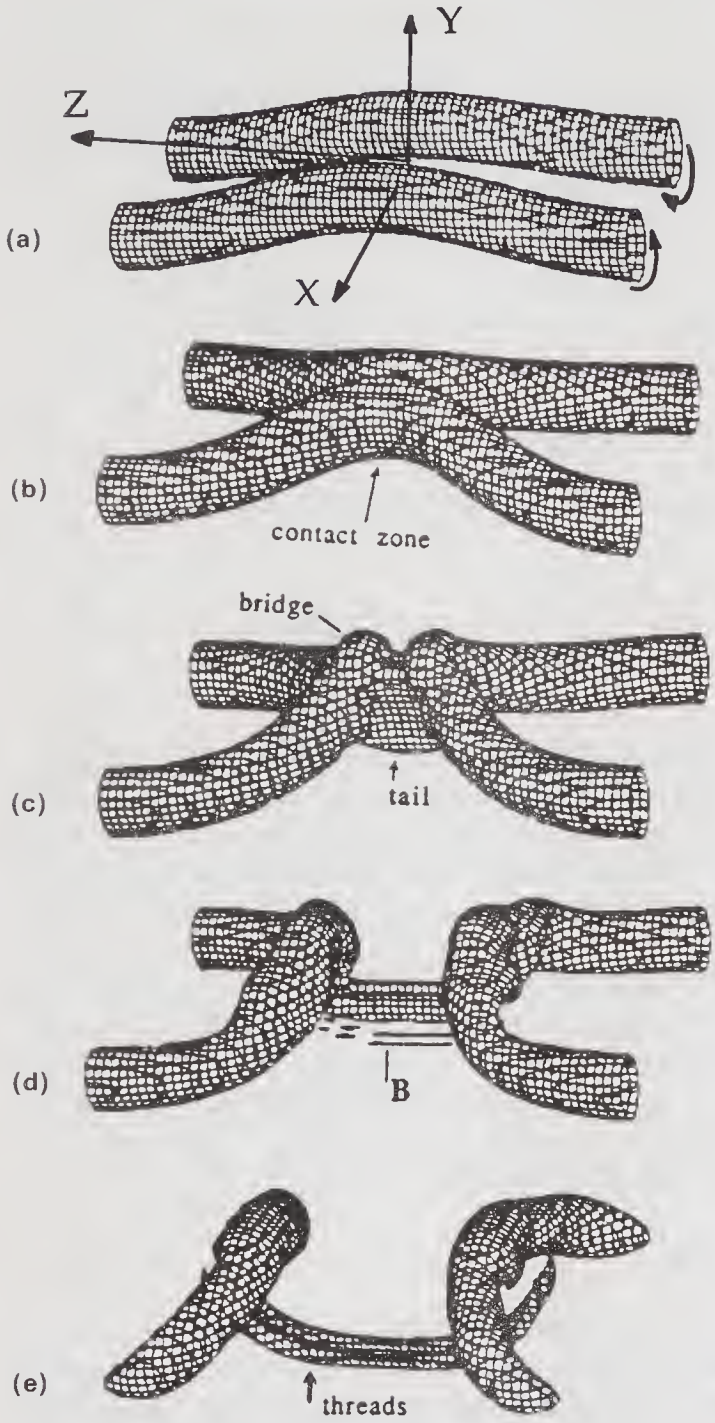

Figure 1. $|\omega|$ surfaces at 30% of initial peak vorticity in π_s. $t = 0$ **(a)**, 2·25 **(b)**, 3·5 **(c)**, 4·75 **(d)**, 6·0 **(e)**.

level of 30% of the initial peak vorticity $\omega_{\max}$ (0). A comparison of figure 1 with the evolution of circulation Γ_s (shown in figure 2) reveals *three* distinct phases.

The *first* phase is governed by inviscid vortex dynamics as almost no circulation is transferred from π_s to π_d. During this phase, while the two vortices move upward by mutual induction, self-induction presses them towards each other, flattening them and forming a contact zone with steep vorticity gradients. In the *second* phase, a dramatic change in topology takes place as a rapid transfer of circulation from π_s to π_d (figure 2) occurs due to viscous vorticity annihilation (by cross diffusion) in the contact zone. This phase, marked by 'bridging' (growing humps in figures 1c, d), is the heart of the reconnection process (discussed later). The growing bridges acquire a

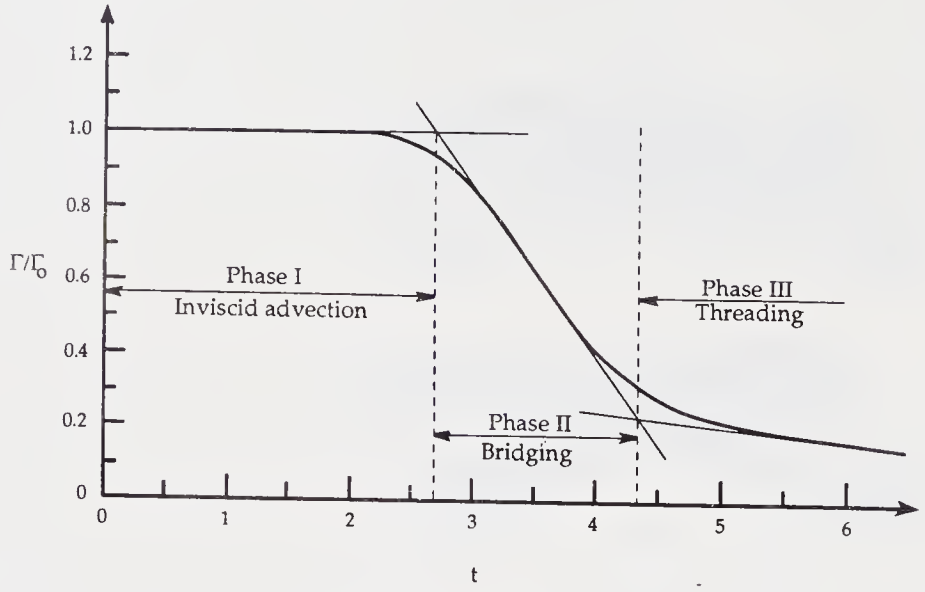

Figure 2. Circulation in $\pi_s^+ (x > 0)$. Phases of reconnection.

curved horseshoe shape, causing them to pull apart by self-induction. Simultaneously, the induced flow by the bridges stretches the dipole in π_s and sustains annihilation. The *third* phase is the evolution of the remnants of the original dipole after the rapid circulation transfer. The slender vortices, which we call 'threads', are well defined because of stretching by the bridges. These threads arise as a consequence of the incompleteness of reconnection.

With initial asymmetry, virtually the same evolution as in figures 1a–e occurs, even at $t = 6$, thus vindicating both the analysis (Takaki & Hussain 1985) and high-resolution simulations (Kerr & Hussain 1989) of the symmetric configuration. The Re dependence of the crosslinking process was tested and found to consist of the same sequence of stages and identical successive spatial patterns, except that the corresponding timescales increase with decreasing Re.

2.3 *The bridging mechanism*

The rapid circulation transfer from π_s to π_d begins when the vortices come into contact near $\pi_s \cap \pi_d$ (figures 1b, 3b) and form a contact zone C(t) with steep vorticity gradients. As the flow is highly viscous around C and nearly inviscid elsewhere, we may think of the vortex lines far away from C as material lines, merely for the sake of discussion. We use this idea schematically in figures 4a–c, where each vortex is represented by three vortex lines; one vortex line from each vortex intercepts C (figure 4a), and shortly afterwards these vortex lines annihilate each other at $x = z = 0$ by cross diffusion, producing two reconnected lines intercepting π_d at $z = \pm z_0$ (figure 4b). The π_d-intercept of z_0 quickly retreats away from $x = z = 0$, because of strong diffusion and nearly antiparallel vortex lines emerging from cusps.

The cross section AB (figure 4c) at the edge of the contact zone C reveals the two-dimensional dipole structure of the original vortices. In a co-translating frame, the streamline pattern becomes the well-known recirculation bubble of a vortex dipole (figure 4d). Although this frame is not precisely defined for an unsteady dipole, the existence of two stagnation points S_F and S_B – at the front and back of the dipole – can

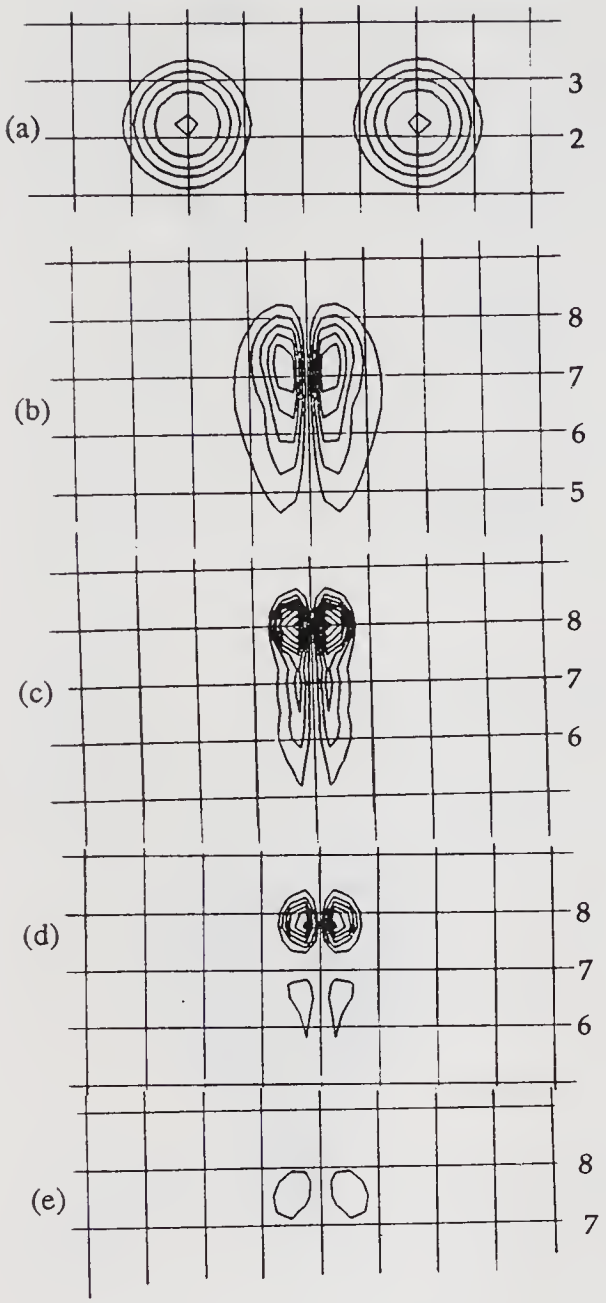

Figure 3. $|\omega|$ contours in π_s; contour increments $\Delta\omega = 4$. $t = 0$ (**a**), 3·0 (**b**), 3·75 (**c**), 4·5 (**d**), 6·0 (**e**).

be inferred. The large velocity between S_F and S_B advects z_o towards S_F, ahead of the dipole (figure 4c). The relative upward advection of z_0 stops at S_F, and a reconnected vortex line unfolds along the diverging separatrix a-a′ (figure 4d). This mechanism is schematically illustrated in a perspective view of one half of the vortex pair in figure 4e, which shows a vortex line at five different instants (1-5). Far away from C, a vortex line is simply swirled around the vortex tube. However, in C, vortex lines are reconnected as soon as they come into contact between instants 1 and 2 and are swept upward by the pumping motion of the dipole. At instant 3, the upward motion of the reconnected vortex line stops at S_F, and it gets stretched and begins to wrap around the dipolar vortex pair near S_F (vortex line at instants 4 and 5). Meanwhile, the circulatory motion in the dipole continuously pumps fresh non-reconnected lines into C near S_B (figure 4d), which in turn follow the same sequence of reconnection. Due to this mechanism, reconnected vortex lines accumulate ahead of the antiparallel vortices and align orthogonal to them.

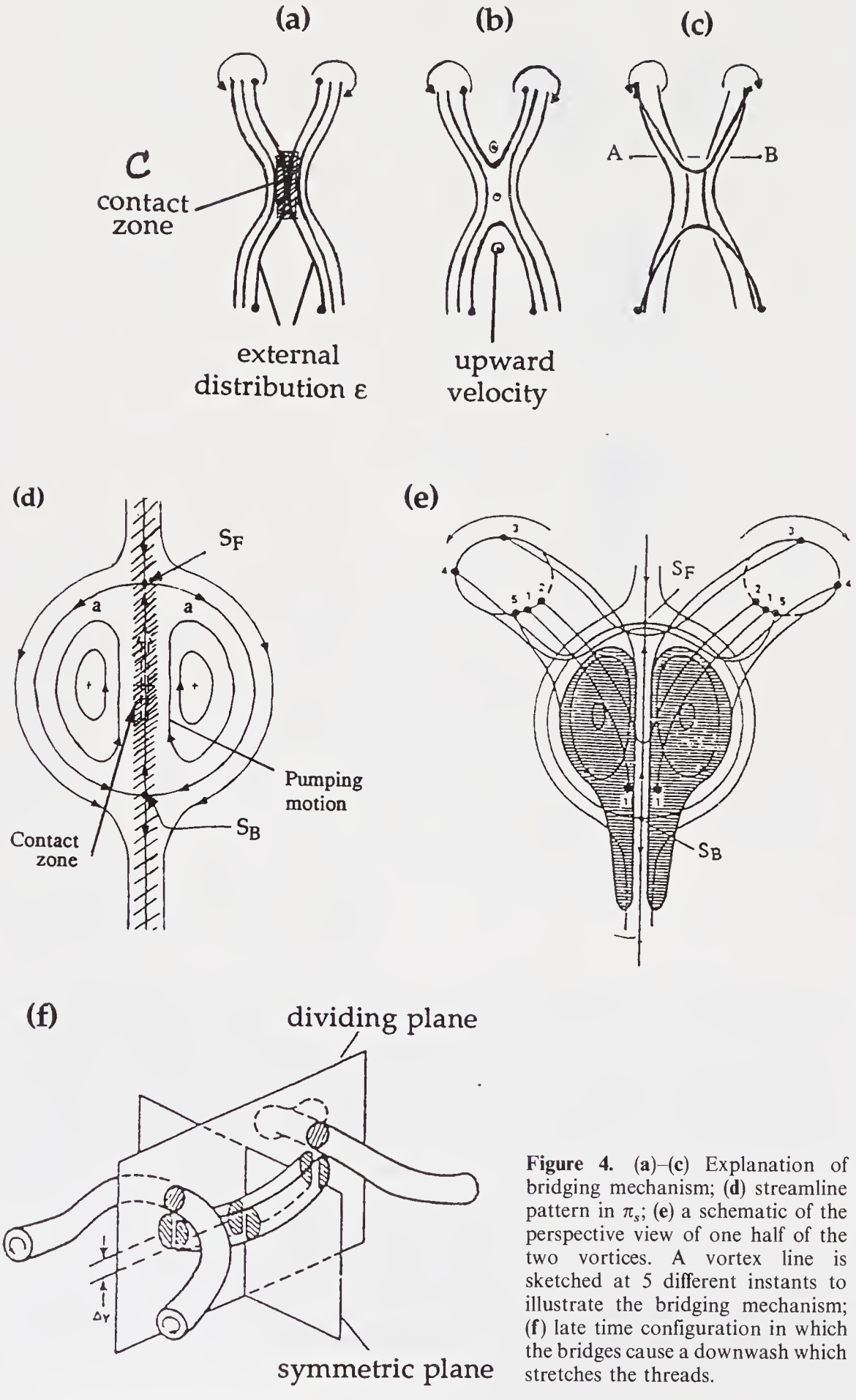

Figure 4. (**a**)–(**c**) Explanation of bridging mechanism; (**d**) streamline pattern in π_s; (**e**) a schematic of the perspective view of one half of the two vortices. A vortex line is sketched at 5 different instants to illustrate the bridging mechanism; (**f**) late time configuration in which the bridges cause a downwash which stretches the threads.

During bridging, a complex interaction of *three* effects governs the rate of vorticity annihilation by changing vorticity gradients in C. These effects are *diffusion, stretching* in the z-direction, and local *'self-induction'*. Diffusion counteracts the steepening of vorticity gradients and can only decrease the peak vorticity ω_m in the symmetry plane, while any increase in ω_m is due to stretching (normal to π_s). This 'axial' stretching is generated mainly by the vorticity distribution $\varepsilon(t)$ away from C (ε is shown in figure 4a; note that ε includes the bridges), and partly by self-induced lengthening of vortex lines near C (analogous to the axisymmetric collision of vortex rings). Depending on the relative positions of ε and the dipole in π_s, the external stretching is either positive (vortex stretching) or negative (vortex compression): positive if the dipole has fallen behind ε (figure 4f), and negative if the dipole has advanced ahead of ε. The self-induction on each side of the sheet-like region C is in π_s, and is directed towards π_d whenever the non-reconnected vortex lines in C curve upward, and away from π_d when they curve downward. The motion toward π_d increases gradients across the y-axis by compressing the vortex cores into a characteristic head–tail structure (figure 3d), while motion away from π_d decreases the gradient as the vortex cores in π_s are separated.

The above three effects – diffusion, stretching and self-induction – dominate the evolution in the following order. At first, the vortex lines in C curve upward, and the gradients across π_d increase as self-induction toward π_d presses the dipole cores into a head–tail shape. Meanwhile, the negative external stretching causes the increase in ω_m to be small. However, as the dipole in π_s falls behind ε (discussed later) such that the vortex lines in C curve downward, axial stretching increases and produces a large increase in ω_m and, consequently, large gradients. Finally, towards the end of the rapid circulation transfer from π_s to π_d (figure 2), the local self-induction away from π_d arrests cross-diffusion by producing a near balance between axial stretching, diffusion and separation of the dipole cores in π_s, causing the threads to persist.

2.4 *Curvature reversal and reconnection cascade*

Curvature reversal, which causes incomplete reconnection, is a characteristic and crucial event. It occurs because the upward motion of the dipole in π_s slows down relative to that of ε (figure 3; note that the y-position can be compared using the numbers on the right side of each panel); but why does the dipole in π_s slow down? A downward velocity field in C – downwash – opposes the dipole's own upward motion in π_s (figure 4f). Furthermore, the dipole loses circulation through vorticity annihilation; its upward motion weakens and it relaxes into a head–tail shape. The downwash is induced by the growing bridges as well as by non-reconnected vortex lines in ε, so downwash will be present even at $\mathrm{Re} = \infty$. This relaxation into a head–tail shape, an inviscid process, virtually decreases the dipole circulation, as the dipole propagation velocity is determined almost exclusively by the head. Although this inviscid effect is weak at $\mathrm{Re} = 1000$, it may well be the primary mechanism for curvature reversal at higher Re. An indication of this would be that the area A of the nearly self-similar head decreases with increasing Re, such that $\omega_m A^{1/2}$ (propagation speed of the head to leading order) is bounded as $\mathrm{Re} \to \infty$. This indicates the possibility that the amount of circulation transferred from π_s to π_d tends to zero as Re tends to infinity while the transfer is still occurring on a convective timescale.

These results have some interesting new implications. Foremost, the vortex reconnection cannot be completed in a single step. As the bridges move apart by self-

induction, the thread-dipole advects forward in the presence of the weakening 'downwash' caused by the bridge-dipole (orthogonal to the original vortex dipole). This way, the threads reverse their curvature again and then collide at the midpoint by self-induction, starting the next burst of reconnection, which occurs at a smaller scale. This is what we call reconnection cascade. Clearly, the frequency of reconnection bursts will increase and circulation transfer will decrease as the Reynolds number increases.

2.5 *Dynamical interactions between bridges and threads*

In order to provide further insight into the reconnection mechanism and the topology and dynamics of interacting vortices, we discuss the evolution of helicity, enstrophy production and vortex lines. Even though helicity density (h) is a frame-dependent quantity and hence not a suitable measure of topology (unlike the helicity integral), in the present idealized configuration it does point out some important features. Helicity is very small in the initial condition and during the first phase of reconnection, and vortex lines inside the vortex tubes are almost parallel. However, the helicity distribution after the reconnection (e.g. $t = 4{\cdot}75$ and $t = 6$) is particularly interesting, as it consists of intertwined regions of positive and negative helicity (Melander & Hussain 1988, 1990). Apart from the threads, where the helicity stands out clearly, the structure is an enigma until one examines bundles of vortex lines. Figures 5a, b show that vortex lines emerging from the threads do not wrap all the way around the bridges as one would expect from $|\omega|$ surfaces, e.g. expanded views of figure 1d, e.

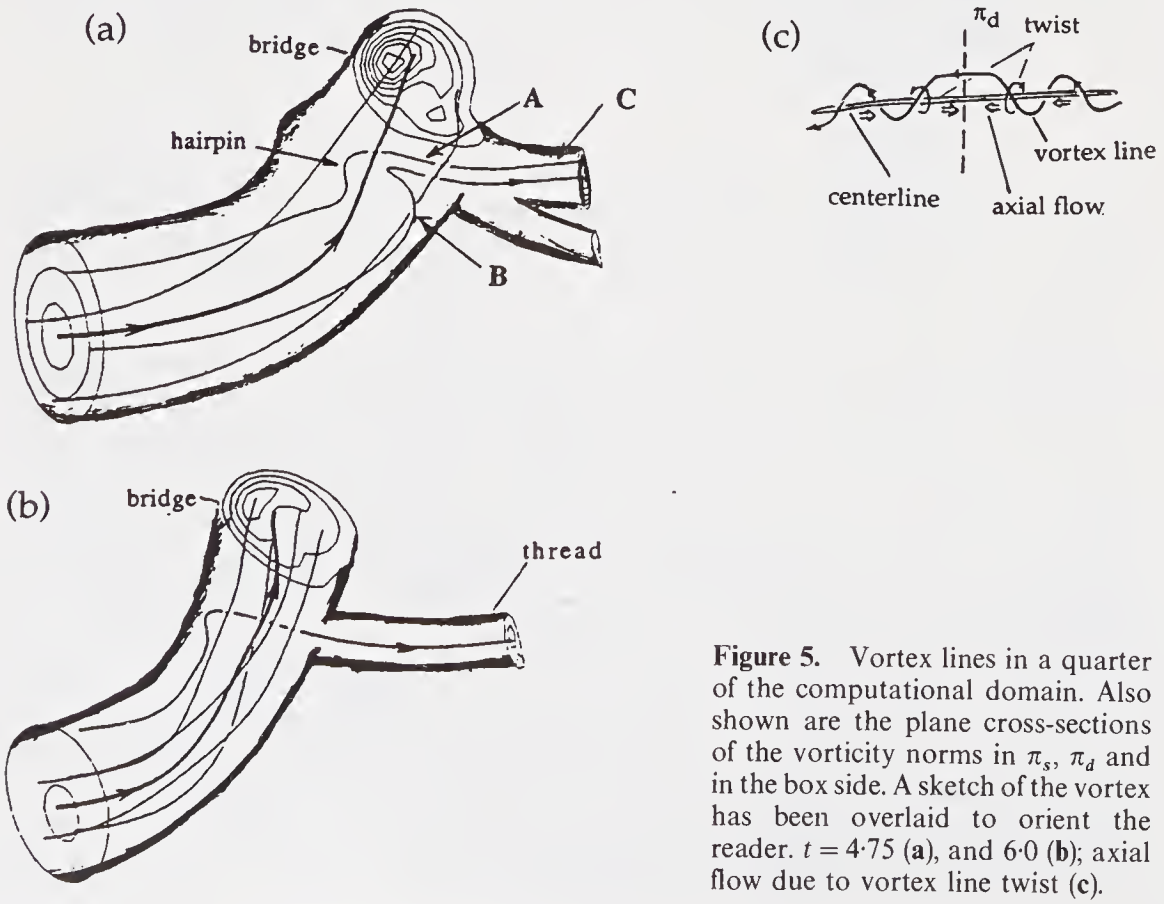

Figure 5. Vortex lines in a quarter of the computational domain. Also shown are the plane cross-sections of the vorticity norms in π_s, π_d and in the box side. A sketch of the vortex has been overlaid to orient the reader. $t = 4{\cdot}75$ (**a**), and $6{\cdot}0$ (**b**); axial flow due to vortex line twist (**c**).

Instead, they form asymmetric hairpin-like structures (see A and B, figure 5a). The vorticity is high in one hairpin leg and low in the other. Unfortunately, the vortical structures of this kind are not faithfully reflected in the surface plots of $|\omega|$. The intense leg (A) is the extension of the thread (C) and its high vorticity causes its large helicity. .The diffuse leg is difficult to identify in the helicity distribution as the $|\omega|$ there is low; also, the angle between vorticity and velocity is larger. The intense leg induces a flow away from π_d on the outside of the bridges causing vortex stretching in the outer part of the bridges (see point A in figures 6b, d).

Inside the bridge, the vortex lines have a slow helical twist near π_d (barely discernible in figure 5b). Contrary to the intense hairpin leg, the twist produces an axial flow toward π_d at the centre of the bridge. Since this axial flow is toward π_d from both sides, it results in a negative enstrophy production, as seen in a cross section of bridges parallel to π_d (dotted lines in figures 6b, d). The twisting of vortex lines results from a skewed (non-concentric) vorticity distribution in the bridges (figures 5a, b). The peak vorticity in the bridge is not at the location of the geometric centroid of the

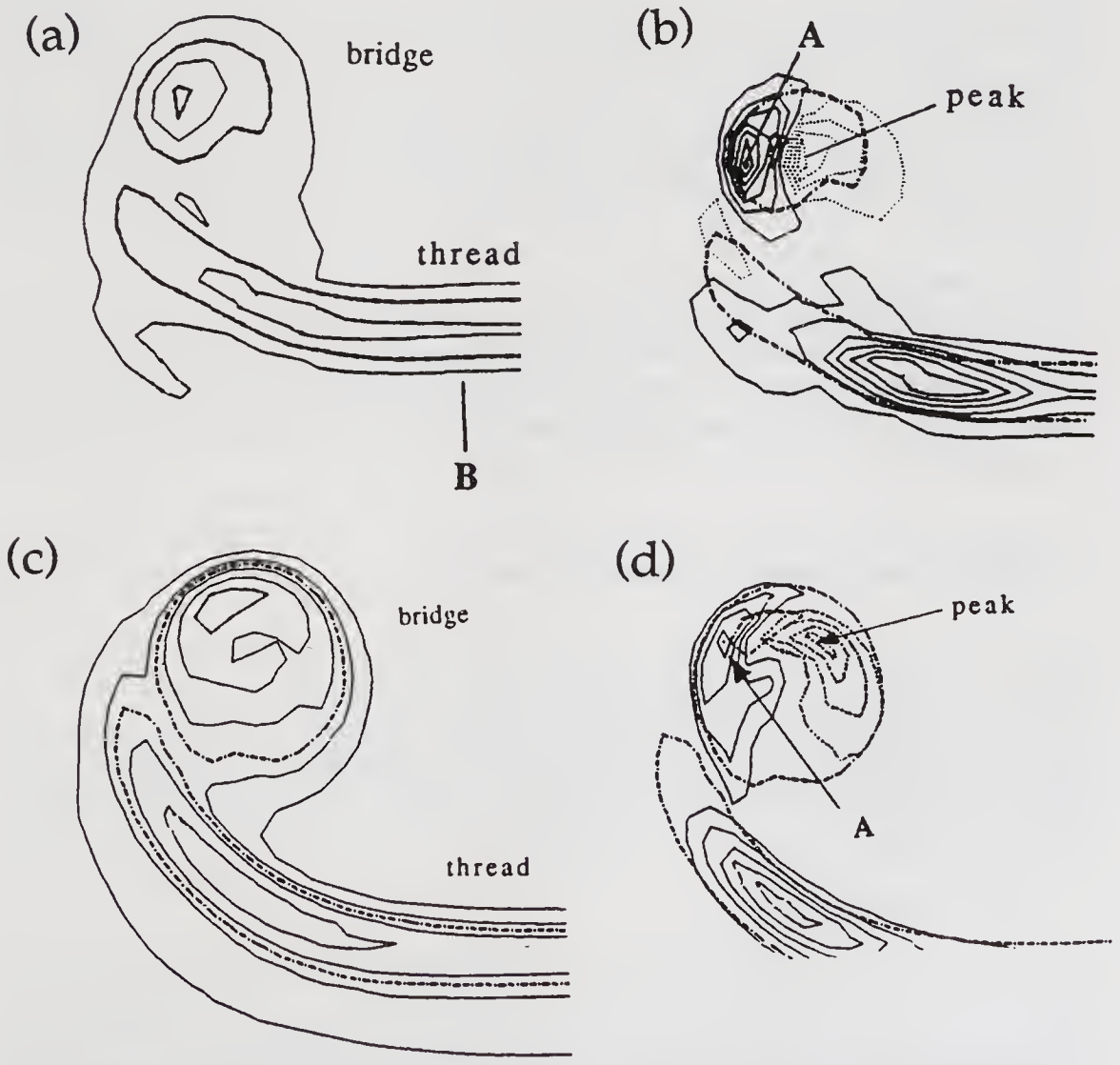

Figure 6. Plane cross section parallel to π_d but moved $\Delta x = 0{\cdot}196$. (**a**) $|\omega|$ at $t = 4{\cdot}75$; (**b**) enstrophy production P_ω at $t = 4{\cdot}75$, chain-dotted lines are $|\omega|$ contours; (**c**) $|\omega|$ at $t = 6{\cdot}0$; (**d**) P_ω at $t = 6{\cdot}0$, chain-dotted lines are $|\omega|$.

low level vorticity contours. Furthermore, the peak occurs far away from the contact zone as a consequence of earlier stretching by the dipole during bridging. Figures 5a, b show that a vortex line which follows the centreline of the vortex far away from π_d ceases to do so in the bridge. This effect clearly results in vortex line twisting and thus in an induced axial flow (figure 5c). The direction of the axial flow is determined by the orientation of the twist, which in turn is determined by the highest swirling velocity along the vortex. The bridges, having the highest peak vorticity, also have the highest swirling velocity. Hencė, the axial flow is toward π_d from both sides, resulting in vortex compression (i.e. negative enstrophy production P_ω in figures 6b, d), which decreases the peak vorticity and thereby reduces the twisting rate. This constitutes a new inviscid mechanism, clearly distinct from diffusion, which smooths the vorticity distribution of the reconnected vortices.

Interacting vortex tubes relax to a head–tail structure as shown in figure 3d. This is essentially an inviscid mechanism which was also observed in the head-on collision of inviscid vortex rings (Shariff *et al* 1988; Stanaway *et al* 1988). The principal reason for head–tail formation is the strain in π_s due to self-induced motion of the vortex tubes toward π_d. Because of higher vorticity concentration in the heads, the annihilation is higher between the heads than between the tails. The tail decays more by viscous diffusion than by annihilation. The higher circulation in the head also causes it to move faster due to mutual induction, leaving the tail behind (see separation of the head from the tail at $t = 4{\cdot}5$ in figure 3e). Such deformation of a circular vortex core into a head–tail structure increases the surface area over which vorticity diffuses into surrounding previously irrotational fluid, thereby increasing entrainment. This is in addition to the increase in surface area due to bridge formation, which also contributes to entrainment via strong downwash.

Thus, we find that vortex reconnection plays a significant role in mixing and cascade via formation of bridges and threads and their mutual interactions. Therefore, it is of interest to determine how reconnection is affected if, in addition to viscous cross diffusion, we have another mechanism, such as baroclinic vorticity production in compressible flows, to produce topological changes.

3. Effects of compressibility on vortex reconnection

To analyse compressibility effects, we simulated the same antiparallel vortex configuration, assuming the working fluid is a perfect gas. However, we found that the selection of initial pressure (P) and density (ρ) fields plays a crucial role in the evolutionary dynamics of vortices in compressible flows. Therefore, we first discuss the selection of initial conditions for compressible simulations before describing compressible reconnection.

3.1 *Initial conditions*

The initial vorticity distribution and $\mathrm{Re} = \Gamma/\nu = 1000$ for compressible simulations were the same as for the incompressible case discussed above. For compressible simulations, we need to specify initial P and ρ fields in addition to vorticity. Ideally, such simulations should be initialized with an analytical solution of a compressible vortex. Since such solutions are not currently available, we considered the initial

conditions used to date for turbulence simulations. The dependence of compressible turbulence dynamics on initial P and ρ distributions is clear from the numerical simulations by Feiereisen *et al* (1981), Passot & Pouquet (1987), Erlebacher *et al* (1990), and Lee *et al* (1991). Three different sets of initial conditions have been used for these studies. Feiereisen *et al* (1981) used constant ρ and determined P by solving the Poisson equation for an initially solenoidal velocity field. Based on later studies, others (Erlebacher *et al* 1990; Lee *et al* 1991) have suggested that this choice of initial conditions suppresses compressibility effects. Passot & Pouquet (1987) initialized their simulations with a velocity field which had both solenoidal and compressible parts, but with random P and ρ distributions. These authors were the first to observe shocklets, which increase local kinetic energy dissipation and vorticity, and can also lead to baroclinic vorticity generation, thus affecting the flow evolution. However, they did not investigate the sensitivity to initial conditions. Lee *et al* (1991) used a solenoidal velocity field and assumed both P and ρ distributions to be constant initially. They also observed shocklets in their simulations and showed the probability of shocklet occurrence to be higher for 2D flows and to increase with Mach number (M) and Re.

In the present study, we compared the evolution based on the following three P and ρ initial conditions:

(i) *Constant density initial conditions* (*CDIC*): This initialization, first used by Feiereisen *et al* (1981), assumes $V = 1/\rho =$ constant, with P obtained by imposing $\partial(\nabla.\mathbf{u})/\partial t = 0$ from

$$\nabla^2 P = (-\gamma \mathrm{M}_0^2/V)\nabla\cdot(\mathbf{u}\cdot\nabla\mathbf{u}), \tag{1}$$

where γ is the ratio of specific heats at constant pressure and constant volume, and M_0 is the reference Mach number obtained as the ratio of velocity scale and sound speed at infinity. This is equivalent to specifying the pressure gradient required to balance the centrifugal force in a 2D axisymmetric flow.

(ii) *Constant initial conditions* (*CIC*): Used by Lee *et al* (1991), this initialization assumes $V = 1/\rho =$ constant and $P =$ constant.

(iii) *Polytropic initial conditions* (*PIC*): We define a new initial condition which we found to be the most suitable among the three considered here. We simultaneously impose

$$P = aV^{-b} \quad \text{and} \quad \nabla\cdot(V\cdot\nabla P) = -\gamma \mathrm{M}_0^2 \nabla\cdot(\mathbf{u}\cdot\nabla\mathbf{u}). \tag{2}$$

The proportionality constant a was chosen to obtain the desired pointwise maximum M, and b was chosen to be γ in all the simulations reported here. This choice of b leads to homentropic initial conditions. It should be noted that the above polytropic relation is used only for initialization. The evolution for $t > 0$ follows from solutions of the Navier–Stokes equations for a perfect gas.

3.2 *Analysis of initial conditions using low-M asymptotic theories*

Using recently developed asymptotic theories of the compressible Navier–Stokes equations, it is possible to show that CIC is expected to have transients at an acoustic timescale and that both PIC and CDIC lead to incompressible solutions as $\mathrm{M} \to 0$.

3.2a *Fluctuation levels for incompressible evolution as* $M \to 0$: The theory by Zank & Matthaeus (1991) is based on Kreiss' principle for a symmetric hyperbolic system of PDEs with widely different time scales. According to this principle, solutions will vary only on a slow time scale if several time derivatives of the solution are of $O(1)$, particularly at $t = 0$ (Zank & Matthaeus 1991). Since the two time scales – acoustic and convective (viscous time scale is neglected for moderate to high Re) – are widely different at low M, Kreiss' principle can be applied to determine which initial conditions yield a solution varying only on a slow (convective) time scale. By determining the conditions for the first two derivatives of velocity and the first time derivative of pressure to be $O(1)$, Zank & Matthaeus (1991) showed that for the solutions to evolve only on a convective timescale, the initial conditions must have the lowest order variation as:

$$P = 1 + \varepsilon^2 p_1, \quad \nabla\cdot\mathbf{u} = \varepsilon^2 d, \quad \text{and} \quad \rho = 1 + \varepsilon^2 \rho_1, \tag{3a, b, c}$$

where $\varepsilon^2 = \gamma \mathrm{M}_0^2 \ll 1$, and p_1, ρ_1 and d are fluctuation pressure, density and dilatation, respectively. Since all simulations in the present study are initialized by a solenoidal velocity field, condition (3b) is always met. For CDIC and PIC, condition (3a) is also met, as the Poisson equations impose pressure fluctuations at $O(\varepsilon^2)$. For PIC, condition (3c) is met because

$$\rho = P^{(-1/b)} = (1 + \varepsilon^2 p_1)^{(-1/b)} \approx 1 - \varepsilon^2 p_1/b + \cdots.$$

For constant fields (ρ in CDIC and P and ρ in CIC), these conditions are obviously satisfied since the fluctuations vanish. Therefore, all these initial conditions satisfy (3a–c), and this analysis suggests that near $t = 0$ their solutions coincide with the incompressible solutions and evolve on a convective time scale as $\mathrm{M} \to 0$.

3.2b *Prediction of acoustic transients with* CIC: However, with CIC, strong divergence can develop. Since

$$\partial(\nabla\cdot\mathbf{u})/\partial t = -\nabla\cdot(\mathbf{u}\cdot\nabla\mathbf{u}), \tag{4}$$

initially, the dilatation field so generated violates (3b), leading to evolution on an acoustic timescale. This is seen most easily by using the analysis provided by Erlebacher *et al* (1990). They decomposed the initial velocity field into two parts via Helmholtz decomposition,

$$\mathbf{u} = \mathbf{u}^I + \mathbf{u}^C, \tag{5}$$

where superscripts I and C imply incompressible and compressible parts such that $\nabla\cdot\mathbf{u}^I = 0$, $\nabla \times \mathbf{u}^I = \nabla \times \mathbf{u}$ and $\nabla\cdot\mathbf{u}^C = \nabla\cdot\mathbf{u}$, $\nabla \times \mathbf{u}^C = 0$. This decomposition is unique for the periodic boundary conditions used here. Also, note that the harmonic (solenoidal, curl-free) part can be neglected as it is a constant which vanishes in an appropriate reference frame. $\mathbf{u}^I$ was assumed to satisfy the incompressible Euler equations, and governing equations for $\mathbf{u}^C$ were obtained by subtracting the incompressible Euler equations from the compressible equations. Further, assuming homentropic evolution, ρ was expanded as

$$\rho = 1 + \gamma^{-1} p + O(|p|^2), \quad \text{where} \quad P = 1 + p,$$

i.e. p represents pressure fluctuation, which is further decomposed as:

$$p = \gamma M_o^2 p^I + \delta p^C,$$

where δ is defined such that $|p^C(t=0)| = 1$, hence giving the relative magnitude of compressible pressure, and p^I is determined from the Poisson equation

$$\nabla^2 p^I = -\nabla\cdot(\mathbf{u}^I\cdot\nabla\mathbf{u}^I).$$

The evolutions of $\mathbf{u}^C$ and p^C over an acoustic timescale $O(1/M_0)$ have been predicted by Erlebacher *et al* (1990) as follows. There are two regimes: $\delta \leqslant \gamma M_0$ and $\delta > \gamma M_0$. For $\delta \leqslant \gamma M_0$, the initial $\mathbf{u}^C$ remains small while p^C increases significantly after an acoustic timescale, thus producing strong pressure waves. For $\delta > \gamma M_0$, initial $\mathbf{u}^C$ becomes large, and the nonlinear convective terms become important, so that shocks are likely to develop. For CIC, since $\mathbf{u}^I = O(1)$, we have $p^I = O(1)$. Also, as $p = 0$, it follows that $p^C = O(1)$ and therefore $\delta = O(\gamma M_0^2)$, i.e. $\delta/(\gamma M_0) \sim O(M_0) \ll 1$. Thus CIC belongs to the regime $\delta \leqslant \gamma M_0$, for which the analysis by Erlebacher *et al* (1990) predicts the generation of strong pressure waves.

Thus, according to low-M asymptotic theories, CIC leads to transients on an acoustic timescale and compressibility effects even as $M \to 0$ because of the compressible energy associated with p^C, which occurs because of incompatibility of the initial P distribution with the incompressible P distribution. This also suggests that the conditions derived by Zank & Matthaeus (1991), though satisfied initially, may be violated at a later time. On the other hand, CDIC and PIC are expected to suppress acoustic transients and lead to incompressible results as $M \to 0$. In other words, both CDIC and PIC appear to be appropriate for vortex interactions at low M. Since the theories used for this discussion are valid only for low M, numerical simulations are needed to study initial condition effects at higher M.

3.3 *Effects of initial conditions on iso-vorticity surfaces, timescale and extent of reconnection*

In the following, results are reported for two M: one is subsonic (denoted as M_1), and the other is supersonic (denoted as M_2). Two considerations are important in the selection of M_1. First, M_1 should be low enough to yield nearly incompressible solutions for PIC and CDIC, as expected from the theories discussed above. Second, we resolve the acoustic waves, so that at very low M (where fluid velocities are much smaller than sound speed), the number of timesteps required for dynamical evolution are larger, making the simulations more expensive. A pointwise maximum $M_1 = 0{\cdot}5$ was found to be an adequate choice, as these simulations showed nearly incompressible evolution and required only twice the number of timesteps needed for obtaining evolution over the same time as in the high M simulations. Selection of M_2 was constrained by vortex core evacuation as follows. In vortex interaction simulations, M can be increased either by increasing the strength of the vortex or reducing the ambient sound speed. We used the latter option, so that the pressure drop across the vortex core was constant, but as M increased, the mean pressure became lower. Thus, for sufficiently large M, the pressure in the vortex core becomes zero, i.e. the core becomes evacuated. For the highest M considered here, with PIC, the minimum ρ is initially 20% of the mean value. During evolution, the peak vorticity in the core

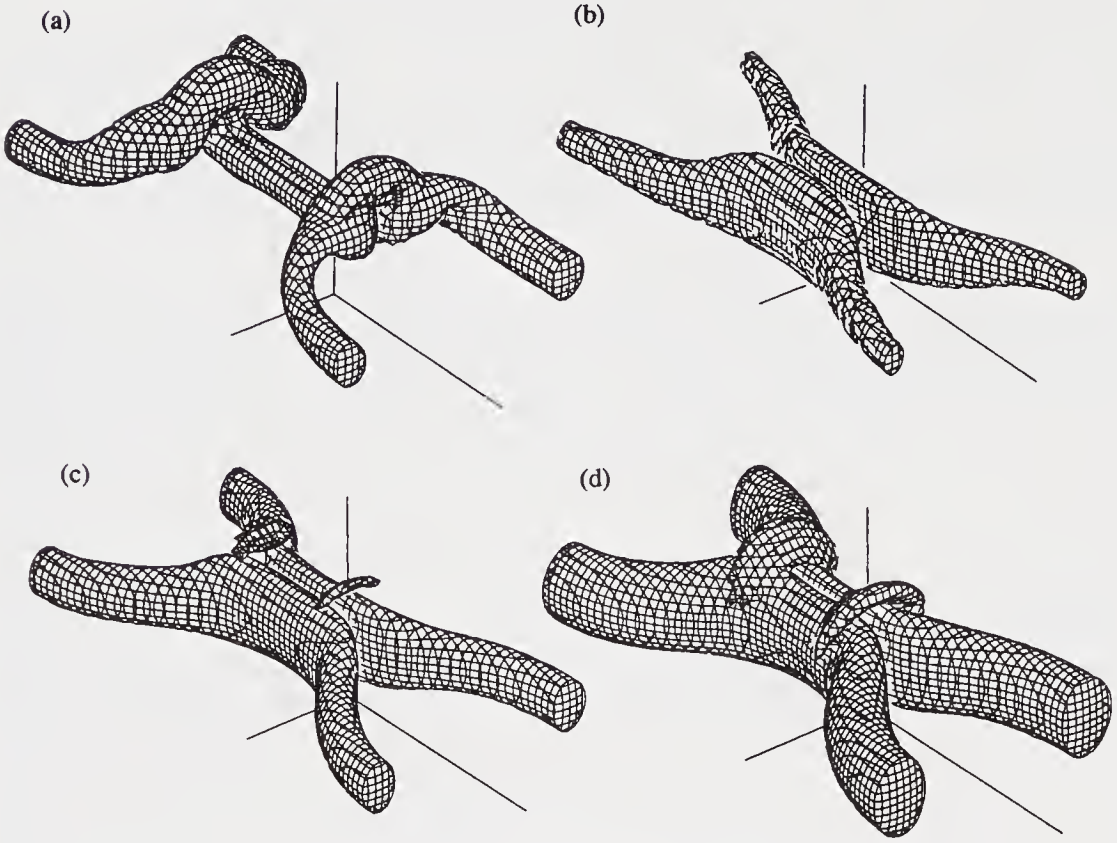

Figure 7. $|\omega|$ surfaces at 30% of the initial peak vorticity in π_s at $t = 4{\cdot}5$ for compressible reconnection simulations with three different P and ρ initial conditions. (**a**) CDIC; (**b**) CIC; (**c**) PIC; (**d**) PIC with surface level 25% of the initial peak vorticity in π_s.

increases, and the values of P and ρ are found to decrease further. At higher M_2, an evacuated core with zero P may form during the evolution, which cannot be simulated with the Navier–Stokes equations. The same restrictions also hold for CDIC and CIC.

The evolution of reconnection at $M_1 = 0{\cdot}5$ was found to be essentially the same as that in the incompressible case for all initial conditions. At sufficiently high $M_2 = 1{\cdot}45$, substantial differences were observed. In figure 7 we show the iso-vorticity surfaces at late time $t = 4{\cdot}5$ (time is nondimensionalized in the same manner as in incompressible reconnection simulations in § 2.2) for all the three initial conditions. With CDIC, very little difference from the incompressible case is seen, and even a detailed comparison of dynamical quantities at this time shows that the results are essentially the same as for the incompressible case. However, the results with CIC at M_2 are significantly different. In particular, note the absence of bridges at this surface level. Similarly, with PIC at M_2, the iso-vorticity surface plots show very little bridging.

To reveal the differences in the vorticity distribution, contours of $|\omega|$ in a plane parallel to π_s and passing through the location of peak vorticity in the bridge are shown in figure 8 for the M_2 cases. With CDIC, the results are similar to the incompressible case (not shown). For this case, the vorticity peak in the bridge is higher than that in the threads in this plane. With CIC and PIC, the bridge is much weaker than the threads. A consequence of the strong bridges in CDIC and incompressible cases is curvature reversal and hence self-induced separation of the threads at a later time. This mechanism is clearly suppressed in the simulations with PIC and CIC, where the net compressibility effects are significant.

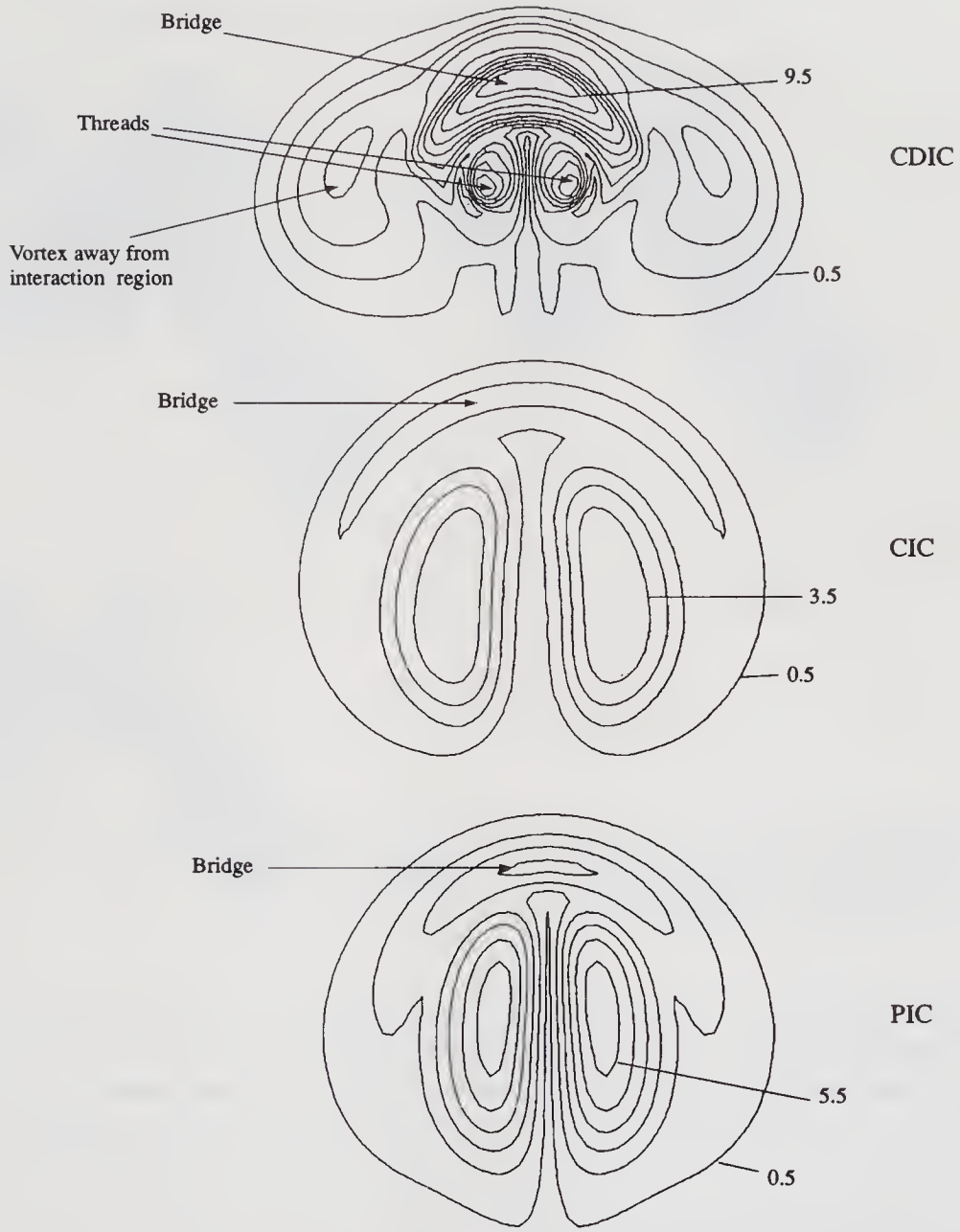

Figure 8. Vorticity contours in a plane parallel to π_s and passing through the peak vorticity in bridges for three different P and ρ initial conditions at $t = 4{\cdot}5$.

The circulation evolution in π_s is shown in figure 9 for these simulations. With CDIC, the evolution is similar to that for M_1 except for a slight increase followed by a drop in circulation at early times. This initial increase with CDIC is due to baroclinic vorticity generation. With PIC and CIC, the circulation initially remains constant and then undergoes a slight decrease around $t = 0{\cdot}5$ due to the appearance of a shocklet between the initial dipolar vortices. The PIC case then experiences a much slower rate of circulation decay until $t = 3{\cdot}0$. After $t = 3{\cdot}0$, the circulation in π_s decays at a faster rate, but the decay rate is still much lower than that for CDIC at M_2. With CIC, we see further drops in the circulation at $t = 1{\cdot}8$, $2{\cdot}5$ and a slight wiggle at $t = 3{\cdot}5$. Plots of P and ρ show that these drops correspond to the interaction of acoustic waves (from adjacent boxes) with the dipole vortices.

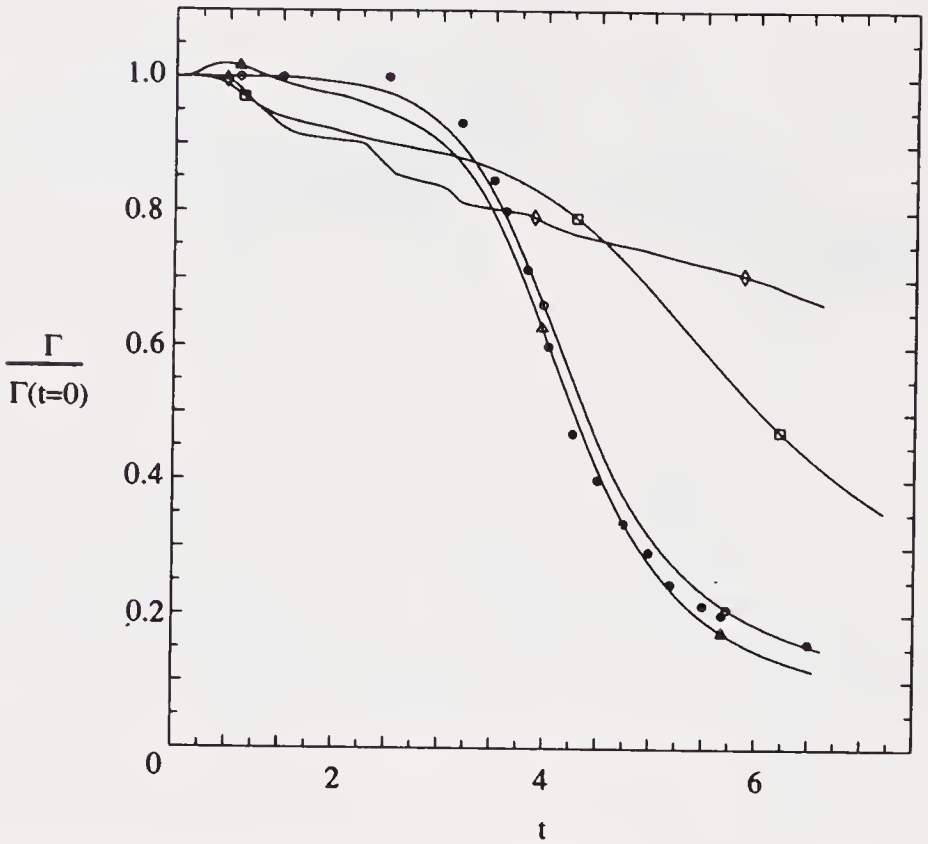

Figure 9. Evolution of circulation in π_s for PIC case at M_1 (○), and M_2 cases with PIC (□), CDIC (Δ) and CIC (◇). Solid circles denote the data from incompressible simulation.

The circulation transfer in the high M cases at early times is due to shocklet formation, which causes an increase in Γ_d and a decrease in Γ_s via both viscous cross diffusion and baroclinic vorticity production. In figure 10 we show the location of this shocklet for the three cases by an overlay plot of iso-vorticity and iso-dilatation surfaces at $t = 0{\cdot}5$ for all three initial conditions. The shocklet is characterized by a thin region of large negative velocity divergence (implying compression of fluid), across which P, ρ, $\mathbf{u}$ and M change sharply. The jumps in these quantities are consistent with the Rankine–Hugoniot relations.

Note that π_s is a material plane since the fluid velocity normal to it is zero, and the same fluid remains in the plane due to periodic boundary conditions. For such a plane, the transfer of circulation is given as

$$\frac{d\Gamma}{dt} = \underbrace{\int \frac{-1}{\gamma M_0^2} V \nabla P \cdot dc}_{R_B} + \underbrace{\int \mu \nabla^2 \mathbf{u} \cdot dc + \int \frac{\mu V}{3} \nabla(\nabla \cdot \mathbf{u}) \cdot dc}_{R_v}, \tag{6}$$

where dc is the line element along the curve demarcating the boundary of the material plane. Here, on the RHS the first term is due to baroclinic production, the third term is due to compressible viscous effects, and the second term is the usual viscous cross diffusion term. In the following, we denote the first term as R_B and the sum of the second and third terms as R_v. With PIC at M_2, both R_B and R_v are negligible at early times ($t < 0{\cdot}3$), and after shocklet formation ($t > 0{\cdot}4$), they are both negative and two orders of magnitude larger than at M_1. As a result, Γ_s decreases much earlier for PIC.

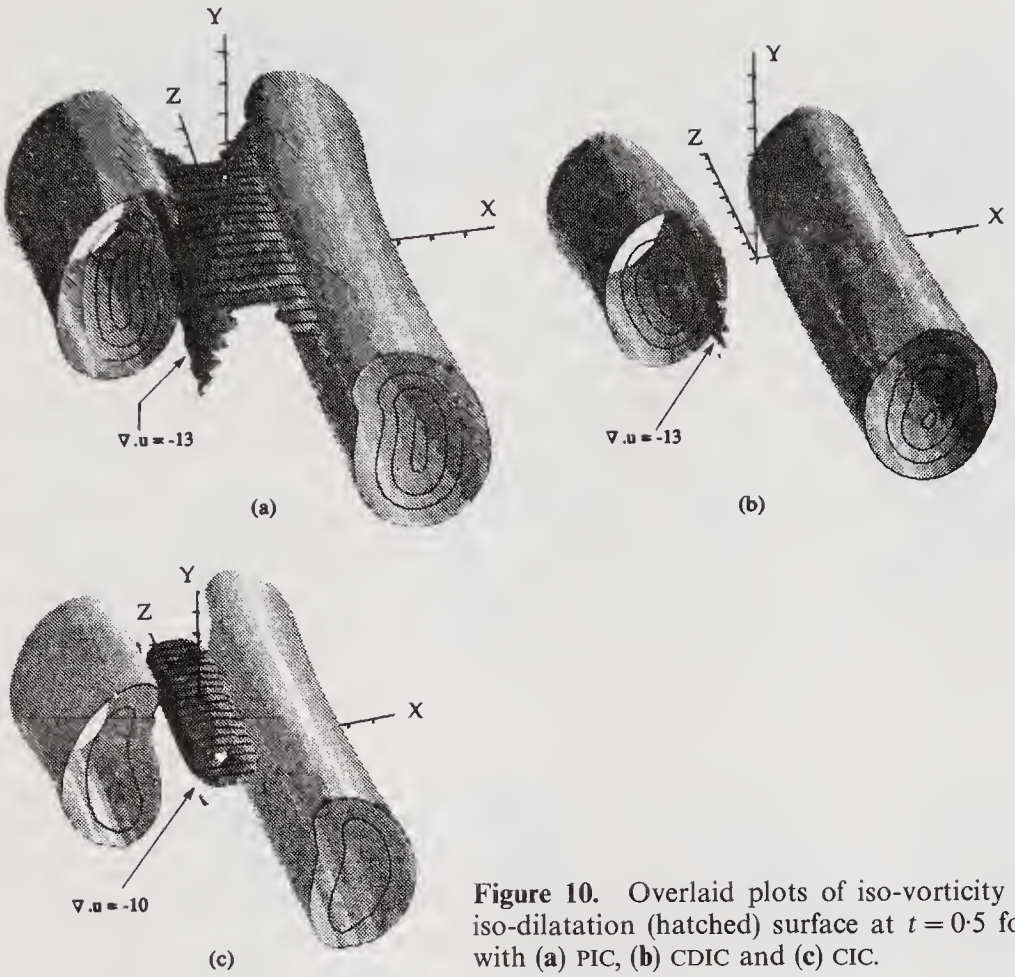

Figure 10. Overlaid plots of iso-vorticity surface and iso-dilatation (hatched) surface at $t = 0{\cdot}5$ for M_2 cases with (**a**) PIC, (**b**) CDIC and (**c**) CIC.

On the other hand, with CDIC at very early times ($t < 0{\cdot}3$), R_B is positive (as gradients of ρ caused by dipole motion are inclined to the initial P gradients) and an order of magnitude larger than negative R_v, causing Γ_s to increase during this time. After the shocklet forms ($t \sim 0{\cdot}4$), both R_B and R_v become negative, and Γ_s is reduced to nearly that at M_1. We find that after this time, R_v with CDIC and PIC are comparable, but R_B with CDIC is much smaller, perhaps due to baroclinic generation away from the shocklet region due to misaligned P and ρ. In summary, at M_2, the presence of a shocklet leads to faster transfer of Γ from π_s, but with CDIC, this effect is countered by the early Γ increase in π_s and subsequently smaller negative R_B due to baroclinic generation.

As a result, by the time the shocklet diffuses, the Γ_s with CDIC at M_2 and the M_1 cases is higher than that with PIC at M_2. This larger Γ leads to a larger growth of the initial vortex perturbation (by mutual induction of the dipole) with CDIC than for PIC. A larger perturbation corresponds to higher curvature in the interaction region and, consequently, faster self-induced motion of the interacting vortices toward π_d with CDIC, which eventually leads to faster reconnection. At late times, such as at $t = 4{\cdot}5$, the P and ρ distributions inside the core in π_s with CDIC are similar to those with PIC, as are the compressible enstrophy production terms, and the Γ transfer is predominantly due to viscous cross diffusion in both cases. However, the gradients of vorticity in the interaction region and hence Γ transfer are lower with PIC due to slower self-induced motion of the vortices towards π_d.

Thus, we find that an initial transient occurs with CDIC, in which the baroclinic production is opposite to that observed at late times (or with PIC). As a result, Γ_s is generated, which critically affects the overall evolution of vorticity. Nevertheless, the evolution with CDIC eventually tends towards that with PIC. The results with CIC are similar to those for PIC except for additional wave-vortex interactions observed with CIC.

Our observation of negligible net effect of compressibility on the rate or extent of reconnection with CDIC is consistent with the claim of Erlebacher *et al* (1990) and Lee *et al* (1991) that CDIC suppresses compressibility effects. In contrast, PIC and CIC show a much lesser extent of vortex reconnection (at M_2), thus clearly suggesting that compressibility effects are important. However, as CIC leads to strong wave–vortex interactions (hence the effects of adjacent boxes are not negligible), it is not an appropriate choice for spectral simulations. In addition to providing compressible (unlike CDIC) and clean (unlike CIC) evolutions, PIC is also preferable because experimental studies of compressible vortices (Dosanjh & Weeks 1965; Mandella 1987) also suggest a polytropic relation between P and ρ in the vortex core. Therefore, only the simulations with PIC are discussed in the following section.

3.4 *Compressibility effects in bridges*

For PIC at M_2, the above-mentioned shocklet diffuses around $t = 1{\cdot}5$, and the rate of circulation transfer to π_d is subsequently reduced (see figure 9). After this time, the compressibility effects are not significant in π_s, and the circulation transfer is predominantly due to viscous effects. However, as the threads are much stronger at M_2, we expect their influence in causing non-concentric vorticity distribution to be more significant than in the incompressible case as discussed in § 2·5. Such non-concentricity would lead to higher twisting of vortex lines and consequently an induced axial flow toward π_d. Figure 11a shows the vortex lines with PIC at M_2 at $t = 6{\cdot}0$. Contrary to expectation, the twisting of vortex lines is clearly reduced, and the vorticity distribution in the bridges is more concentric than in the low M and incompressible cases (figure 5b).

In order to determine the cause of a more concentric vorticity distribution in the bridges, in spite of stronger threads at M_2, we consider the enstrophy equation for compressible flows:

$$D(\omega\cdot\omega/2)/Dt = \underbrace{\omega\cdot(\omega\cdot\nabla)\mathbf{u}}_{\text{Term I}} \underbrace{-\omega\cdot\omega(\nabla\cdot\mathbf{u})}_{\text{Term II}} \underbrace{+(1/\gamma M_0^2)\omega\cdot(\nabla P\times\nabla V)}_{\text{Term III}} \underbrace{+\mu V\omega\cdot\nabla^2\omega}_{\text{Term IV}}$$
$$\underbrace{-\mu\omega\cdot(\nabla V\times(\nabla\times\omega))}_{\text{Term V}} \underbrace{+(4/3)\mu\omega\cdot(\nabla V\times\nabla(\nabla\cdot\mathbf{u}))}_{\text{Term VI}}. \tag{7}$$

Note that compressibility effects are represented by four new terms in this equation: II (dilatation production), III (baroclinic production), V and VI are additional viscous effects. At $t = 6{\cdot}0$, only the first four terms in (7) were found to be significant in the bridges, and these are shown in figure 11b for both M_1 and M_2. At M_1, the vortex stretching term has a distribution similar to the incompressible case (shown in figure 6); it is negative over a part of the cross section and has a large positive peak where the threads are closest to the bridges. Compared to vortex stretching, the dilatation and baroclinic production terms are negligible at M_1. At M_2, the vortex stretching is

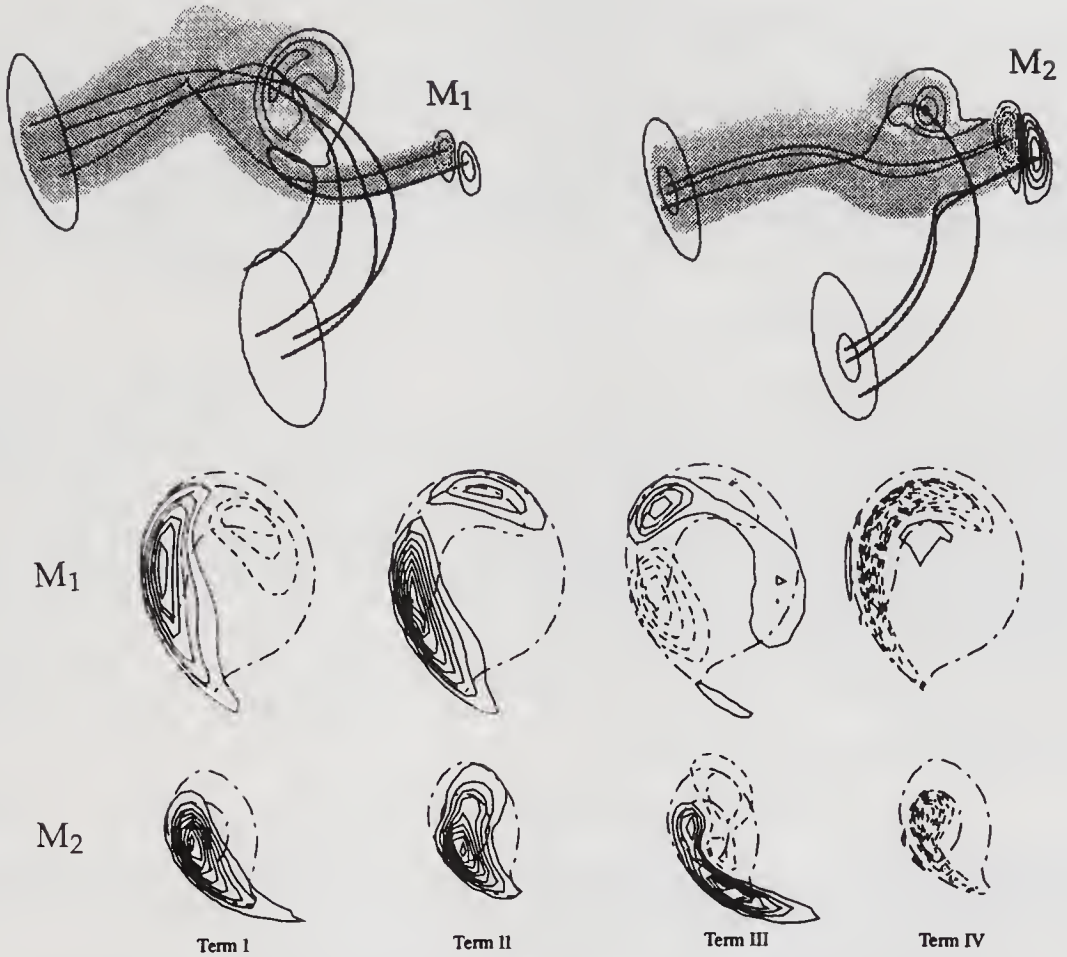

Figure 11. (**a**) Vortex lines starting at the location of peak vorticity in π_s, π_d and farthest plane parallel to π_s for cases at M_1 and M_2 with PIC. (**b**) Enstrophy production terms of (7) in π_d for M_1 and M_2 cases with PIC at $t = 6{\cdot}0$. The contour levels (min., max., increment) are: for M_1 case term I($-11{\cdot}39$, 24·98, 3·64), term II($-0{\cdot}051$, 0·469, 0·052), term III($-0{\cdot}06$, 0·056, 0·012), term IV($-18{\cdot}19$, 3·57, 2·24); for M_2 case term I($-2{\cdot}27$, 45·96, 4·82), term II($-0{\cdot}12$, 6·84, 0·7), term III($-0{\cdot}448$, 0·986, 0·14), term IV($-36{\cdot}6$, 4·9, 4·14). Chain-dotted lines are contours of ω_y.

higher than at M_1, as expected from the stronger threads. In addition, the dilatation production is significant with a similar distribution, but reduces the peak vorticity, thereby making the vorticity contours more concentric. Such subtle effects are lost if we use CDIC and are difficult to decipher for CIC due to multiple wave–vortex interactions which occur for periodic boundary conditions.

From this study, we find that bridging is initiated earlier due to the formation of a shocklet. In turn, these early bridges slow down further reconnection. Thus, in a compressible flow, the reconnection timescale is longer and its associated cascade is slower.

4. Core dynamics

In order to gain further insight into the effects of non-concentric vorticity distribution in the bridges, we consider an isolated axisymmetric column vortex with axial variation of core radius.

4.1 *The governing equations for an axisymmetric vortex*

For this study, we employ cylindrical coordinates (r, θ, z) with corresponding velocities (u, v, w). The Navier–Stokes equations are made dimensionless by introducing characteristic time and length scales, which are derived from the circulation Γ^* and average angular impulse M'^* per unit length (angular impulse is infinite because we consider an infinitely long vortex). The units $\tilde{t}$, $\tilde{L}$ for time and length are

$$\tilde{t} \equiv t^*/t = 8M'^*/\Gamma^{*2}, \quad \text{and } \tilde{L} \equiv L^*/L = (8M'^*/\Gamma^*)^{0.5}, \tag{8}$$

where $\tilde{t}$, $\tilde{L}$, are dimensionless versions of t^* and L^*. The constants in (8) are selected such that for a vortex with Gaussian vorticity distribution, $\tilde{t}$ is $1/\pi^2 \approx 0{\cdot}10$ of the turn-around time for a particle near the centre of the vortex, and L is the vortex diameter based on standard deviation. For the results presented here, $\mathrm{Re} \equiv \tilde{L}^2/\tilde{t}\nu = \Gamma^*/\nu$ ranges from 600 to virtually infinity in the cases with hyperviscosity.

The cylindrical symmetry permits the definition of a stream function ψ for the meridional flow (i.e. in the (r, z)-planes),

$$u = (1/r)(\partial\psi/\partial z), \quad w = -(1/r)(\partial\psi/\partial r) \tag{9}$$

so the azimuthal vorticity is given as

$$\omega_\theta = (1/r)(\partial^2\psi/\partial r^2) - (1/r^2)(\partial\psi/\partial r) + (1/r)(\partial^2\psi/\partial z^2). \tag{10}$$

It is well known that $\xi \equiv rv$ is convected with an inviscid axisymmetric flow (Batchelor 1967); we therefore express the evolution of v in terms of ξ, governed by

$$D\xi/Dt = (1/\mathrm{Re})[(\partial^2\xi/\partial r^2) - (1/r)(\partial\xi/\partial r) + (\partial^2\xi/\partial z^2)]. \tag{11}$$

Also, for an inviscid axisymmetric flow without swirl, $\eta \equiv \omega_\theta/r$ is convected with the flow. Therefore, we express ω_θ transport equation in terms of η as

$$D\eta/Dt = (1/r^4)(\partial\xi^2/\partial z) + (1/\mathrm{Re})[(\partial^2\eta/\partial r^2) + (3/r)(\partial\eta/\partial r) + (\partial^2\eta/\partial z^2)]. \tag{12}$$

4.2 *Initial conditions for axisymmetric vortex simulations*

In all cases, laminar as well as turbulent, the same initial vortex is used. In the laminar axisymmetric cases, only Re changes, but we concentrate on a single Re ($= 665{\cdot}2$), the laminar case L1. In the turbulent cases (discussed in § 6), the initial conditions consist of a coherent and an incoherent part. The coherent part has the same vortex and Re as in the laminar case L1. Only the properties of the incoherent part of the flow, which is initially homogeneous isotropic turbulence, are varied.

The vortex initially has a sinusoidal axial variation of the core size, and the axial vorticity profile $\omega_z(r, \theta_0, z_0)$ is self-similar, i.e. the same everywhere along the axis when scaled with the core size. The radial vorticity component is thus determined such that the vorticity field is *divergence free*. No axial flow is present initially as ω_θ is initially zero. Thus, the initial vorticity distribution is

$$\omega_r(r, \theta, z) = P\left(\frac{r}{s(z)}\right)\frac{r}{s(z)^3}\frac{\mathrm{d}s}{\mathrm{d}z}; \quad \omega_\theta(r, \theta, z) = 0; \quad \omega_z(r, \theta, z) = P\left(\frac{r}{s(z)}\right)\Big/ s(z)^2; \tag{13a, b, c}$$

here the function P determines the axial vorticity profile and $s(z)$ gives the core size variation along the vortex axis. We have

$$s(z) = r_0(1 - \mu\cos(2\pi z/\lambda)) \tag{14}$$

where r_0 is the unperturbed vortex's support radius, λ is the wavelength (equal to the computational box size), and μ is the amplitude of the sinusoidal perturbation of the vortex. The radial profile is

$$P(\zeta) = \begin{cases} \omega_0 \exp(-4\zeta^2/(1-\zeta^2))\exp(4\zeta^2 + 4\zeta^6 + 4\zeta^8), & 0 \leqslant \zeta \leqslant 1, \\ 0, & 1 \leqslant \zeta, \end{cases} \tag{15}$$

where $\zeta \equiv r/r_0$. This vorticity distribution has peak vorticity ω_0 and core support radius r_0.

The initial turbulent background is isotropic, homogeneous and consists only of scales represented by wavenumbers in a certain interval, i.e. $k \in [k_l, k_h]$. Within this interval, the phases are random with a uniform probability distribution, while the amplitudes are random with a C^∞ probability distribution $\mathscr{P}$ times a normalization factor. The normalization factor serves to give the turbulent velocity field a specified rms-value u'_{RMS}. The distribution $\mathscr{P}$ is

$$\mathscr{P}(\chi) = \begin{cases} 1 - \exp((2{\cdot}56/\chi)\exp(1/(\chi - 1))), & 0 \leqslant \chi < 1, \\ 0, & 1 \leqslant \chi, \end{cases}$$

where $\chi = 2|\mathbf{k}| - (k_h + k_l)/(2k_h - 2k_l)$. The graph of $\mathscr{P}$ is flat-top with smoothed flanks

Table 1. Initial conditions for core dynamics and vortex–turbulence interactions.

Case	N	Re	ω_0	k_1	k_h	β	$\tilde{t}$
L1	64	665·2	1·8752				0·09395
L2	64	332·6	1·8752				0·09395
L3	64	166·3	1·8752				0·09395
L4	64	83·15	1·8752				0·09395
L5	64	41·58	1·8752				0·09395
L6	64	+	1·8752				0·09395
T1	64	665·2	1·8752	18	21	0·10	0·09395
T2	64	665·2	1·8752	18	21	0·50	0·09395
T3	64	665·2	1·8752	18	21	1·25	0·09395
T4	64	665·2	1·8752	18	21	2·50	0·09395
T5	128	665·2	0·4688	30	34	1·00	0·37580
T6	128	665·2	0·4688	30	34	2·50	0·37580
T7	128	2500					0·37580
T8	128	*					0·37580
T9	128	2500					0·37580
T10	128	*					0·37580

+ In this simulation an artificial viscosity of the form $\nu_4\Delta^2$ is employed with $\nu_4 = 6{\cdot}989 \times 10^{-5}$

* In this simulation an artificial viscosity of the form $\nu_4\Delta^2$ is employed with $\nu_4 = 1{\cdot}563 \times 10^{-6}$

Non-dimensional length $\tilde{L} = 0{\cdot}6875$ for all simulations (see (8)). In (14) $\mu = 0{\cdot}5$, $r_0 = 0{\cdot}6$ and non-dimensional $\lambda = 9{\cdot}139$ for all simulations. Here $\beta = u'_{\text{RMS}}/\bar{u}_{\text{peak}}$ with $\bar{u}_{\text{peak}}$ being the peak velocity in the laminar vortex.

(Melander *et al* 1987). Note that the use of this distribution makes it easy to rerun our simulations at different resolutions. Thus the turbulent background is herewith specified by k_l, k_h, and u'_{RMS}.

The initial conditions for all simulations discussed in this paper are given in table 1. The laminar axisymmetric simulations are designated L1–L6. The turbulent cases are labelled T1–T10.

4.3 *Vortex line evolution*

For case L1, an overall impression of the vortex's evolution is provided by figure 12, which shows characteristic vortex lines at selected times, all starting from a radial

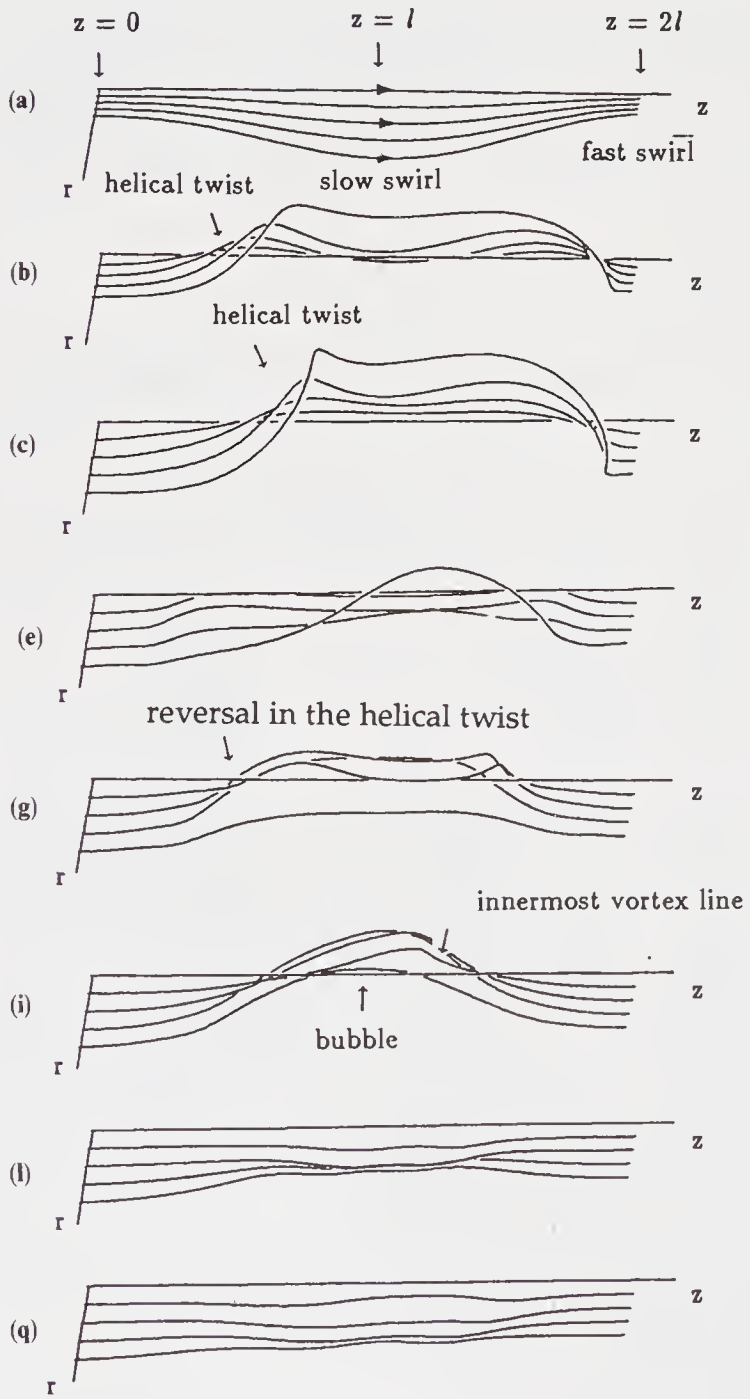

Figure 12. The evolution of case L1 (see table 1) is illustrated by four typical vortex lines at selected instants. The frames are: (**a**) $t = 0$ [$t^* = 0$]; (**b**) $t = 5{\cdot}32$ [$t^* = 0{\cdot}5$]; (**c**) $t = 10{\cdot}64$ [$t^* = 1{\cdot}0$]; (**e**) $t = 21{\cdot}29$ [$t^* = 2{\cdot}0$]; (**g**) $t = 31{\cdot}93$ [$t^* = 3{\cdot}0$]; (**i**) $t = 42{\cdot}58$ [$t^* = 4{\cdot}0$]; (**l**) $t = 58{\cdot}54$ [$t^* = 5{\cdot}5$]; (**q**) $t = 85{\cdot}15$ [$t^* = 8{\cdot}0$]; where t^* is the dimensional time and t is the non-dimensional time, the two being related by (8). The frame labelling (a, b, c, e, g,..) indicates only a few selected instants so as to retain compatibility with subsequent figures; additional instants shown below are (**d**) $t^* = 1{\cdot}5$; (**k**) $t^* = 5{\cdot}0$; (**p**) $t^* = 7{\cdot}5$; (**s**) $t^* = 8{\cdot}5$. Note that the vorticity magnitude is not constant along the vortex lines but varies significantly; see figure 14.

rake at either end of the periodic vortex. Note that one cannot show time evolution of vortex lines, as they are not material lines in these viscous simulations. At $t = 0$, all the vortex lines lie in a meridional plane (θ = constant) and therefore momentarily have no torsion (figure 12a). However, the vortex lines gain torsion immediately, because of axial variations in the swirl around the axis; $\dot{\theta} \equiv \mathrm{d}\theta/\mathrm{d}t = v/r$ is large where the core size is small, and vice versa. Near $z = l \equiv \lambda/2$ the vortex lines rotate slower around the z-axis than near $z = 0$ and $2l$. Consequently, the vortex lines start twisting between $z = 0$ and $z = l$ (figure 12b). Vortex lines close to the axis tend to twist more than those near the edge of the vortex, because $\dot{\theta}$ is in general largest on the axis. (Note that the left–right reflectional symmetry in this problem is not apparent in the oblique view, which is selected to elucidate the details of the core dynamics. Also note that because of the symmetry, this perspective provides two different views of the same coiled structure.)

The helical twists propagate towards $z = l$ (compare figures 12b, c) while the vortex core expands near $z = 0$ and $2l$ and contracts near $z = l$. A comparison of figures 12b and c also reveals the onset of a coiling reversal. Namely, the innermost vortex lines coil less around the axis in figure 12c than they do in figure 12b. This uncoiling has progressed further in figure 12e, which shows a reversal in the helieal twist of the innermost vortex line near $z = 0$ and $z = 2l$. At this instant, the reversed coiling has not yet affected the outermost vortex lines, but later (figure 12g) the helical twist of all vortex lines has reversed.

The coiling and uncoiling of the vortex lines continue (figures 12i, l, q), but dampen with time, and thus the axial flow and the core dynamics eventually die out. Initially, the ratio between the fastest and slowest swirl ($\mathrm{d}\theta/\mathrm{d}t$) around the axis is 9·0; by the end of the simulation (i.e. $t = 8$) this ratio has reduced to 1·2. Furthermore, in figure 12q a fluid element on the axis revolves about 25% slower around the axis than in the widest part of the initial vortex. Figure 12q shows essentially a rectilinear vortex, except that elose to the axis some core dynamics, though weak, still persist. Having obtained a global pictorial view of the progress, we now proceed with a systematic analysis of the evolutionary dynamics and related issues.

4.4 *The vortex core size*

Using "the kinematic vorticity number" $\mathscr{W}_k \equiv (\omega^2/2S_{ij}S_{ij})^{1/2}$, introduced by Truesdell (1954), where S_{ij} is the symmetric strain rate tensor $(\partial u_i/\partial x_j + \partial u_j/\partial x_i)/2$, we define *a vortex as any connected spatial region where* $\mathscr{W}_k > 1$. If $A(z_0, t)$ is the area of the vortex cross section in the plane $z = z_0$, we then define the instantaneous local core size as

$$\sigma(z, t) = (A(z, t)/\pi)^{1/2}, \tag{17}$$

provided that the region in the plane $z = z_0$ where $\mathscr{W}_k > 1$ is simply connected (if this is not the case we let $\sigma(z, t)$ be the radius of the outermost $\mathscr{W}_k = 1$ contour).

In order to determine whether the vortex's relaxation to a rectilinear shape is a viscous or an inviscid phenomenon, we use definition (17) to consider the evolution of the same laminar vortex for a range of different Re (i.e. cases L1–L6). Figure 13 presents the vortex core's instantaneous deviation from rectilinearity (i.e. no axial variations). The ordinate is the standard deviation of $A(z, t_0)$ normalized by the instantaneous average area $\bar{A}(t_0) \equiv \pi\bar{\sigma}^2(t_0)$, where $\bar{\sigma}(t)$ is the average (average over the vortex length) core size. Figure 13 clearly shows that the axial variations in the

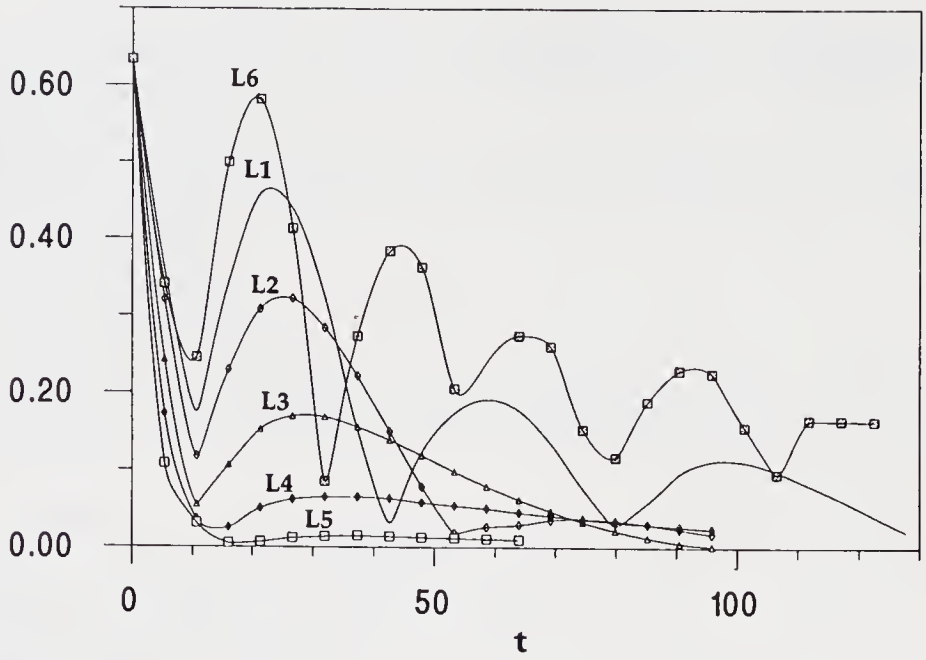

Figure 13. Evolution of the standard deviation of the core area normalized by the instantaneous average core area, i.e. $\{\overline{[A(z,t)-\bar{A}(z,t)]^2}\}^{0.5}/\bar{A}(z,t)$.

core size disappear because of viscous effects; compare the curves for L1–L6. Case L6 is a less viscous simulation due to the use of the "hyperviscosity" $\nu_4\Delta^2$, where ν_4 is chosen as small as the resolution allows. $\bar{\sigma}(t)/\bar{\sigma}(t=0)$ at the end of the simulation in case L1 was 2·0, while in case L6 it was only 1·25. Therefore, we shall think of case L6 as representative of higher Re. The decay of the axial variations has an interesting dependence on Re. Namely, the decay is not monotonic, but rather like a damped oscillation, where both amplitude and frequency depend on Re. The frequency increases significantly with Re and appears to have a finite, nonzero, high Re-limit. Case L6 is indicative of the frequency in this limit. Figure 13 leads us to conclude that the *disappearance* of the core size variations (and hence also the disappearance of the associated core dynamics) is primarily a *viscous* phenomenon.

4.5 *Vorticity evolution explained in terms of enstrophy production*

The vigour of the core dynamics is clearly reflected in figure 14, which shows the evolution of the vorticity magnitude for case L1. Here we analyse the details of this figure and explain the role of the enstrophy production ($P_\omega = \omega_i S_{ij} \omega_j$) shown in figure 15. Later, in § 4.6, we focus on the details of figure 15 and explain how P_ω is determined by the meridional flow.

Figure 14 shows cross sections of iso-vorticity surfaces. The initial enstrophy peak splits into two equal peaks of considerably smaller amplitude as seen by comparing figures 14a and b and recalling the periodic boundary conditions. The changes in the vortex's core size are linked to these changes in vorticity magnitude, because the circulation of the vortex must be conserved. The inviscid mechanism that alters the vorticity magnitude of a material particle is enstrophy production. Both positive (stretching) and negative production (compression) are seen in figure 15b. The initial vorticity peak splits because of a strong local axial compression (see the negative production contours in figure 15b).

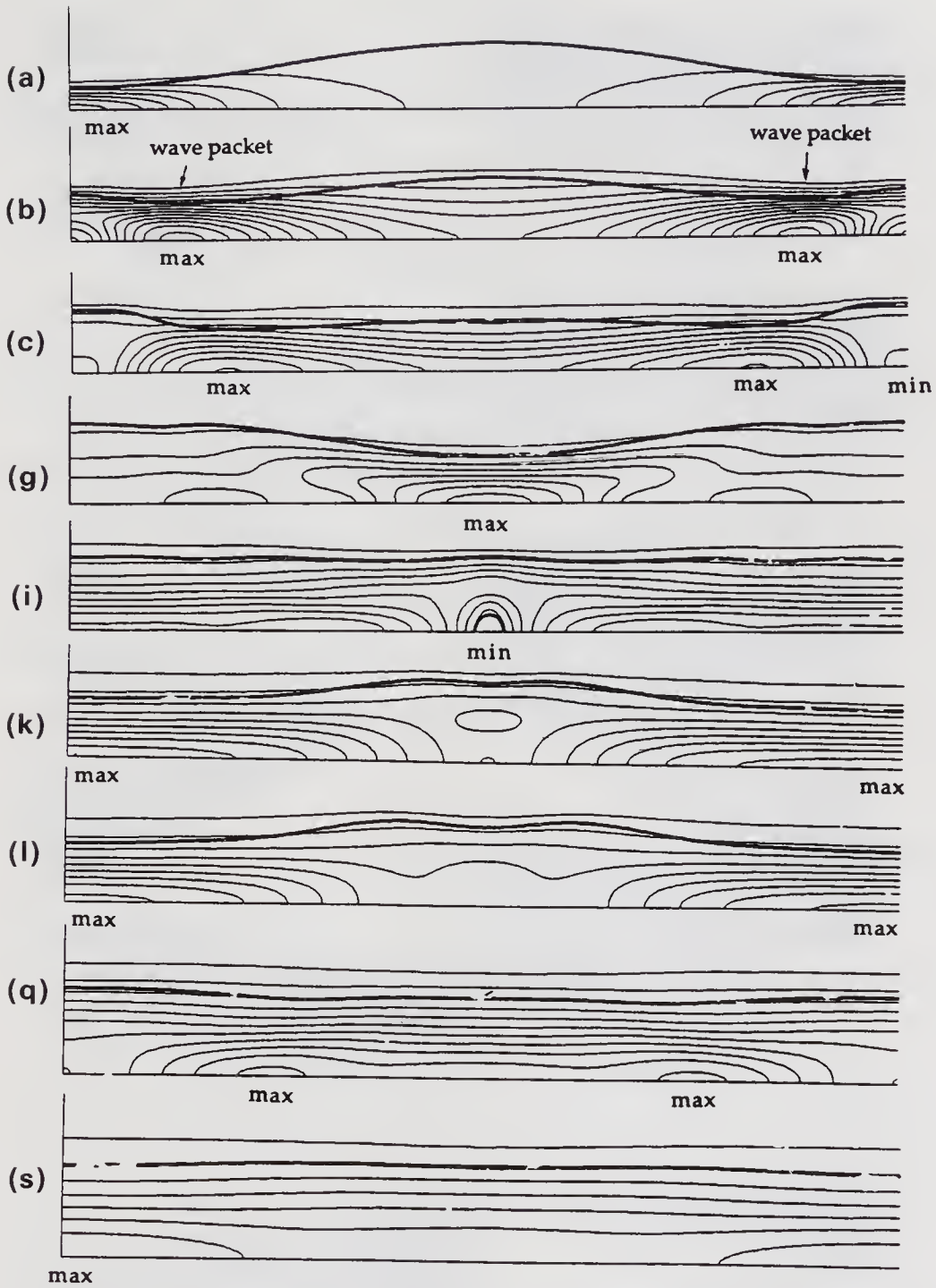

Figure 14. The instantaneous $|\omega|$ for case L1 is shown at times corresponding to those in figure 12. In each frame the iso-vorticity contours are drawn at equal increments of $\delta\omega$. In addition, the boundary of the vortex given by the contour $\mathscr{W}_k = 1$ is overlaid in each frame. Note that the contour lines have not been subjected to artificial smoothing, but are drawn on a 256^2-mesh through exact trigonometric interpolation based on the spectral coefficients of the vorticity field. Along the axis some local minima and maxima of ω are indicated so as to enable ease of dynamical interpretation. The highest contour level ω_h and the contour increment $\delta\omega$ change from frame to frame as shown in the following list, where both nondimensional and dimensional [*] values are indicated: (**a**) $\omega_h = 6{\cdot}58$[70], $\delta\omega = 0{\cdot}94$ [10]; (**b**) $\omega_h = 2{\cdot}44$ [26], $\delta\omega = 0{\cdot}188$ [2]; (**c**) $\omega_h = 1{\cdot}88$ [20], $\delta\omega = 0{\cdot}188$ [2]; (**g**) $\omega_h = 1{\cdot}50$ [16], $\delta\omega = 0{\cdot}188$ [2]; (**i**)-(**l**) $\omega_h = 0{\cdot}846$ [9], $\delta\omega = 0{\cdot}094$ [1]; (**q**) $\omega_h = 0{\cdot}517$ [5·5], $\delta\omega = 0{\cdot}047$ [0·5]; (**s**) $\omega_h = 0{\cdot}328$ [3·5], $\delta\omega = 0{\cdot}047$ [0·5].

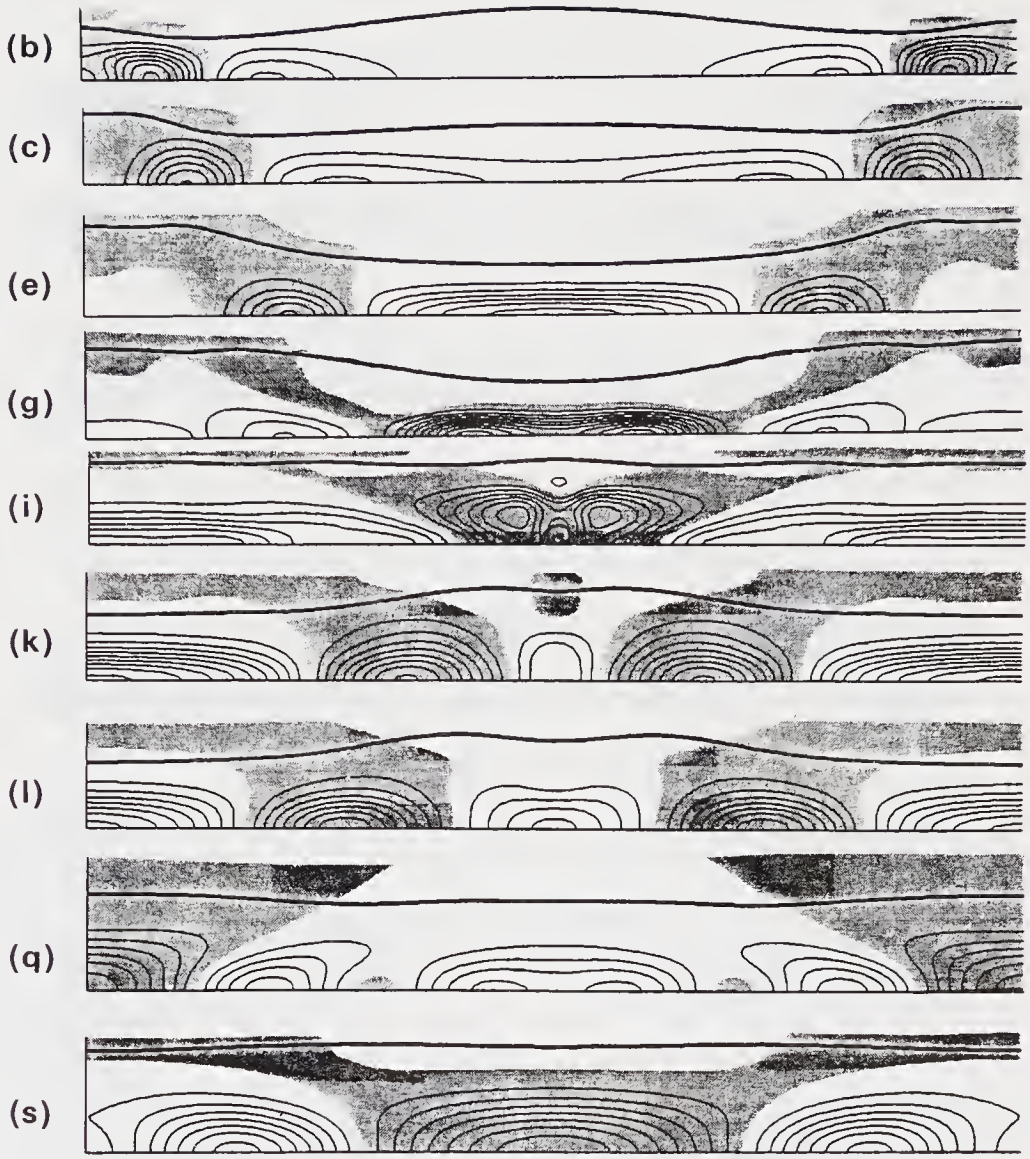

Figure 15. The enstrophy production P_ω contours for case L1 at times corresponding to those in figure 12. P_ω is negative in the gray-shaded regions and positive elsewhere. Positive values of P_ω indicate vortex stretching, while negative values represent reduction of vorticity by compression. The boundary of the vortex as given by the contour $\mathscr{W}_k = 1$ is overlaid in each frame. The contour increment δP_ω is constant in each frame, but varies between frames. The highest and lowest contour levels ($P_{\omega h}$, $P_{\omega l}$) as well as contour increment δP_ω are given in the following list as both nondimensional and dimensional [*] values: (**a**) $P_\omega \equiv 0$; (**b**) $P_{\omega h} = 0{\cdot}497$ [600], $P_{\omega l} = -1{\cdot}161$ [-1400], $\delta P_\omega = 0{\cdot}166$ [200]; (**c**) $P_{\omega h} = 0{\cdot}248$ [300], $P_{\omega l} = -0{\cdot}498$ [-600], $\delta P_\omega = 0{\cdot}0829$ [100]; (**e**) $P_{\omega h} = 0{\cdot}248$ [300], $P_{\omega l} = -0{\cdot}207$ [-250], $\delta P_\omega = 0{\cdot}0415$ [50]; (**g**) $P_{\omega h} = 0{\cdot}0497$ [60], $P_{\omega l} = -0{\cdot}149$ [-180], $\delta P_\omega = 0{\cdot}0166$ [20]; (**i**) $P_{\omega h} = 0{\cdot}0248$ [30], $P_{\omega l} = -0{\cdot}0248$ [-30], $\delta P_\omega = 0{\cdot}00415$ [5]; (**k**) $P_{\omega h} = 0{\cdot}0186$ [22·5], $P_{\omega l} = -0{\cdot}0166$ [-20], $\delta P_\omega = 0{\cdot}00207$ [2·5]; (**l**) $P_{\omega h} = 0{\cdot}0116$ [14], $P_{\omega l} = -0{\cdot}0116$ [-14], $\delta P_\omega = 0{\cdot}00166$ [2]; (**q**) $P_{\omega h} = 0{\cdot}00332$ [4], $P_{\omega l} = -0{\cdot}00498$ [-6], $\delta P_\omega = 0{\cdot}00083$ [1]; (**s**) $P_{\omega h} = 0{\cdot}00145$ [1·75], $P_{\omega t} = -0{\cdot}00145$ [$-1{\cdot}75$], $\delta P_\omega = 0{\cdot}00021$ [0·25]. The conversion formula used here is $P_\omega = P_\omega{}^* \cdot \tilde{t}^3$ (see (8)). Note the dramatic decrease in the magnitude of the enstrophy production between frames (b) and (s).

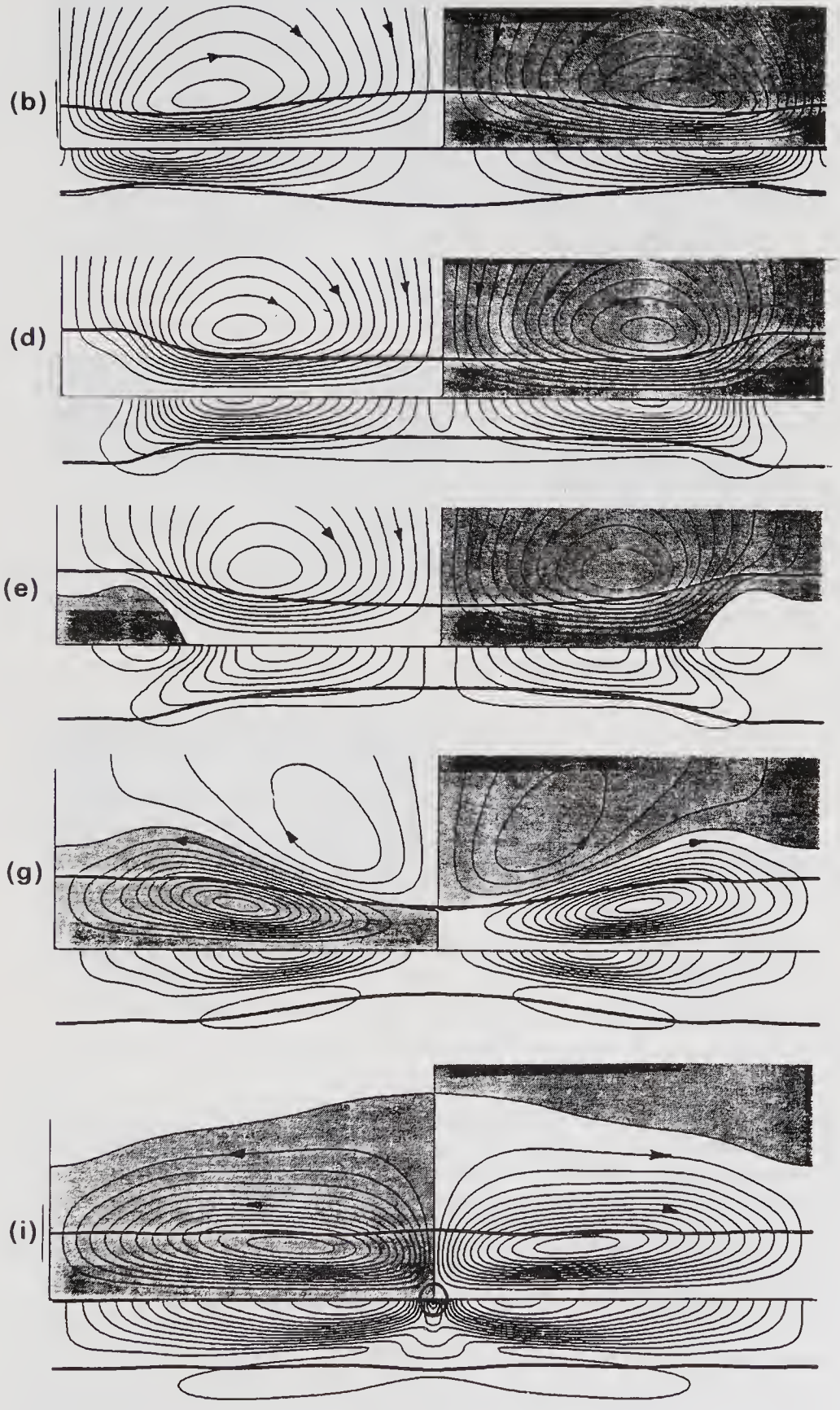

Figure 16. (Continued.)

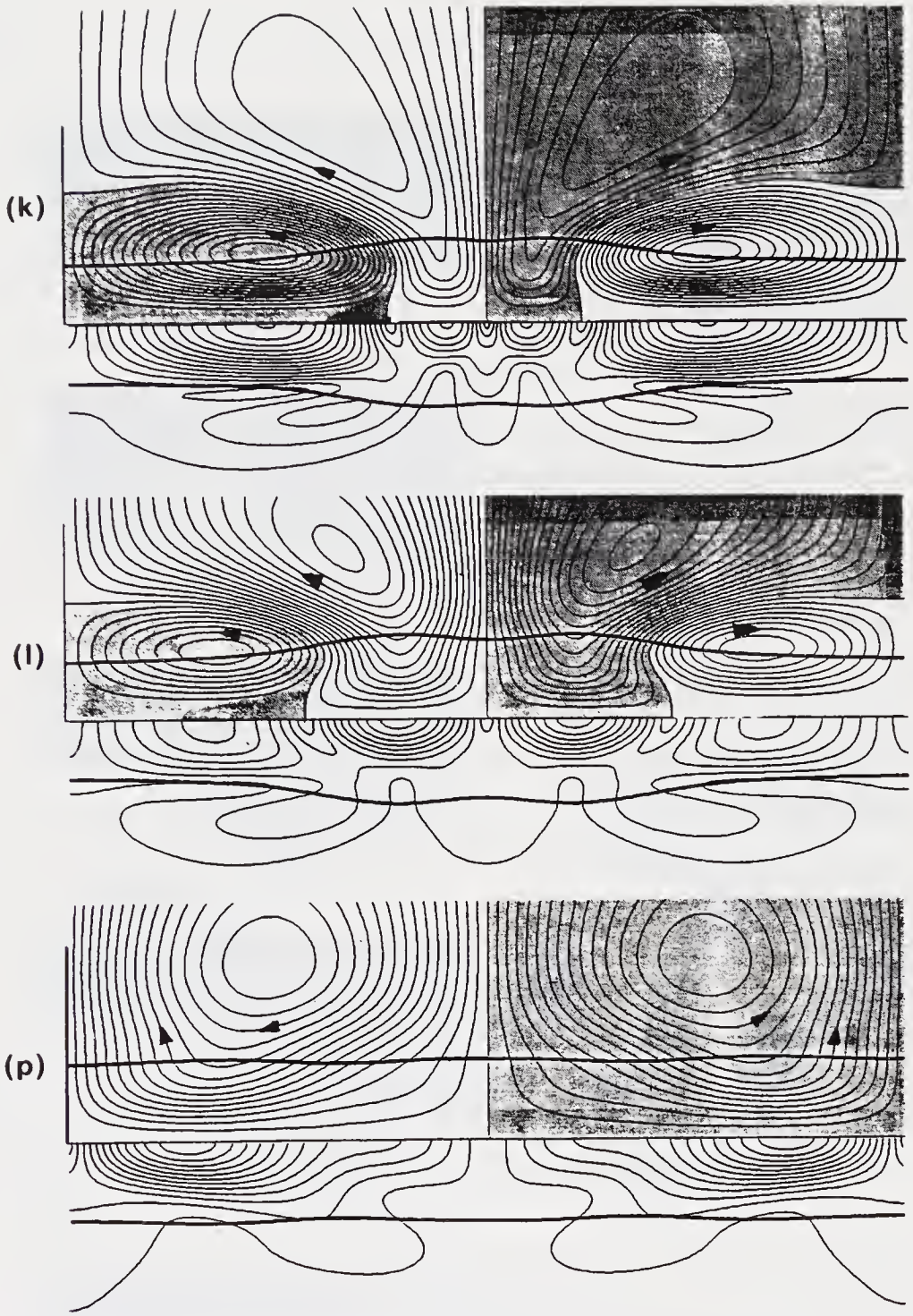

Figure 16. The evolution of the meridional flow in case L1 is shown at times corresponding to those in figure 12. Each frame includes both streamlines (above the axis) and contours of the meridional velocity magnitude (below the axis). Also shown in each frame is the boundary of the vortex given by the contour $\mathscr{W}_k = 1$. The stream function is normalized so it is zero on the axis; thus the orientation of the meridional flow's circulatory motion is determined by the sign of ψ. The motion is counter clockwise in the shaded regions ($\psi < 0$) and clockwise in the unshaded regions ($\psi > 0$). The steamfunction is calculated spectrally by solving the Poisson equation $\partial^2\psi/\partial r^2 + \partial^2\psi/\partial z^2 = r\omega_\theta - w$ in a meridional plane, the spectral solution is then evaluated on a 256^2-mesh. In each frame the meridional velocity magnitude $s \equiv (u^2 + w^2)^{0.5}$ is shown in terms of contours with a constant increment δs, which however changes between frames. The highest contour levels s_h and δs are listed for each frame below as both non-dimensional and dimensional [*] values: (**b**) $s_h = 0{\cdot}301$ [2·2], $\delta s = 0{\cdot}0273$ [0·2]; (**d**) $s_h = 0{\cdot}178$ [1·3], $\delta s = 0.0137$ [0·1]; (**e**) $s_h = 0{\cdot}0957$ [0·7], $\delta s = 0{\cdot}0137$ [0·1]; (**g**) $s_h = 0{\cdot}123$ [0·9], $\delta s = 0{\cdot}0137$ [0·1]; (**i**) $s_h = 0{\cdot}0888$ [0·65], $\delta s = 0{\cdot}0683$ [0·05]; (**k**) $s_h = 0{\cdot}0383$ [0·28], $\delta s = 0{\cdot}00273$ [0·05]; (**l**) $s_h = 0{\cdot}0246$ [0·18], $\delta s = 0{\cdot}00273$ [0·02]; (**p**) $s_h = 0{\cdot}0410$ [0·3], $\delta s = 0{\cdot}00342$ [0·025].

The vorticity transport seen in figure 14 appears to take place in the form of "wave-packets", because mass transport (given by the ψ contours in figure 16) and vorticity transport are in opposite directions (compare figures 14 and 16). Using, for example, figures 14b, c and 15b, c, we observe that P_ω changes sign near each wave-packet; enstrophy is produced in front of each packet and annihilated in the back of the packet, hence causing the packet's motion. Note that for later frames, where the packets are in close proximity or overlap, the situation is less clear. Here we face a dilemma, which is roughly similar to that occurring for the wave motions governed by the linear 1D wave equation ($\partial^2\phi/\partial t^2 = \partial^2\phi/\partial z^2$): namely, are the packets reflected off each other when they collide (figure 14g), or is there a superposition of packets moving in opposite directions? For the linear 1D-wave equation, the method of characteristics or d'Alembert formula elegantly resolves this problem. However, our present problem is nonlinear, and the mathematical extraction of wave-packets moving in opposite directions is nontrivial. In § 5, we show how these wave-packets are readily separated by the "complex helical wave decomposition".

The formation of the low enstrophy bubble in figure 14i can also be explained in terms of P_ω. There is a strong local compression at the location where the bubble forms; see figure 15g. Since the compression is only significant near the axis, it follows that the vorticity magnitude will decrease rapidly near the axis, but not near the edge of the vortex core. Hence, the vortex becomes locally hollow, as is clearly seen in figure 14i.

The bubble is not a permanent feature of the vorticity field (see figures 14i–l). Its disappearance is mainly due to a change in P_ω (figures 15i–l), and also due to "fill in" by viscous diffusion. One might therefore think that the bubble is no more than a temporary peculiarity of the evolution. However, we shall see in § 5 that when the polarized wave-packets are properly extracted from the vorticity field, a *permanent bubble* is associated with each packet.

From the last frames of figures 14 and 15, we observe that the internal core dynamics fade as variations in P_ω diminish.

4.6 *Streamlines and vortex surfaces*

We now focus on the kinematic relation between P_ω and the inviscid meridional flow. For this purpose, we consider ψ, defined in (9), as given; the dynamics governing the evolution of ψ is the subject of § 4.7.

From (10), the meridional flow vanishes in the absence of ω_θ. There is therefore no meridional flow at $t = 0$, but it develops immediately (for $t > 0$) as the vortex lines acquire torsion. Figure 16 shows the ψ contours (streamlines) as well as corresponding contours of the meridional velocity magnitude (see (9) for definition). Note that the meridional flow has significant velocities near the axis, but not elsewhere (a consequence of the continuity equation and the axisymmetric geometry). The axisymmetric vortex tubes are surfaces of constant ξ, and ξ is convected with the meridional flow (evolution (11)) in the absence of viscous effects. Hence the local cross section of a vortex tube shrinks when the meridional flow converges on the axis, and vice versa; this is clear from the evolution of $\mathscr{W}_k = 1$ contour superimposed on frames in figure 16. The axial contribution to the enstrophy changes accordingly, due to the conservation of circulation. Using figure 16b, we see that P_ω at early times has to be negative near $z = 0$ and $z = 2l$ because here the meridional flow diverges away from the axis. Further towards $z = l$ the meridional flow converges on the axis; consequently P_ω has to be

positive there due to stretching as figure 15b in fact shows. A frame by frame comparison of figures 15 and 16 reveals that P_ω can be inferred almost perfectly from ψ. The underlying justification is an *inviscid* asymptotic relation between ψ and P_ω

$$P_\omega \approx -4u\omega_z^2/r = -4\omega_z^2(1/r^2)(\partial\psi/\partial z) \tag{18}$$

which is asymptotically correct near the axis. Fortunately, P_ω is only significant when $r \ll \sigma$(figure 15).

In figure 16b we see two counter circulating cells per wavelength $\lambda = 2l$ of the vortex. We call these the *primary* cells. If they were to persist for all times the vortex would continue to expand near $z = 0$ ($z = 2l$) and contract near $z = l$. We know that this does not happen, e.g. see figure 14. The reason is that the circulatory motions in the meridional flow gradually reverse, starting with the emergence of small *secondary cells* near the axis (figure 16e). Note that the primary and secondary cells are counter circulating. Thus the secondary cells arrest the expansion of the vortex near $z = 0$ and $z = 2l$ (easily seen with the help of the kinematic arguments of the previous paragraph). The gradual progression of the flow reversal is exemplified by figures 16d–i. We observe that the reversal progresses along the axis and is almost complete in figure 16i, which shows only the secondary cells in the region of appreciable vorticity. A second flow reversal can be seen in figures 16i–p, the nature of this second reversal differs from the first in two respects. First, the new cells are not created along the axis, but outside the vortex core. Second, the growth of the new cells is different, i.e. it is radially inward rather than outward. In spite of these differences, the second flow reversal plays the same role as the first, namely to arrest expansions and contractions of the vortex tubes.

4.7 *The coupling between swirl and meridional flows*

The essence of the dynamics lies in the evolution of ψ. For as we have shown above, the knowledge of ψ allows us to deduce the evolution of other flow quantities. To complete the analysis, we focus on the evolutions of ψ and $\eta \equiv \omega_\theta/r$. Both are described by the governing equations (9)–(12). In particular, we notice that η determines ψ (10) and hence drives the meridional flow. Moreover, according to (12), the meridional flow would evolve independently of the swirling motion ($v = \xi/r$), were it not for the coupling term $r^{-4}\partial\xi^2/\partial z$, which represents the material rate of η generation.

In order to understand the physical meaning of the coupling term, we consider two material particles A and B on the same axisymmetric vortex surface $\xi = \xi_0$. Expressing the angular velocities as $\dot\theta_A = \xi_0/r_A^2$ and $\dot\theta_B = \xi_0/r_B^2$, and using a Taylor expansion for r along the vortex surface $\xi = \xi_0$, we can write

$$\left.\frac{1}{r^4}\frac{\partial\xi^2}{\partial z}\right|_A = \omega_z(z_A, r_A)\lim_{B\to A}\frac{\dot\theta_B - \dot\theta_A}{z_B - z_A}. \tag{19}$$

Note that the above limit does not equal $\partial\dot\theta/\partial z$; instead, the limit represents the change in $\dot\theta$ per unit length *along* the axisymmetric vortex tube $\xi = \xi_0$. That is, $\lim_{B\to A}[(\dot\theta_B - \dot\theta_A)/(z_B - z_A)]$ equals the *differential rotation along an axisymmetric vortex surface*. It is this differential rotation that makes the vortex lines locally helical and thus generates $\omega_\theta = r\eta$. Our result (19) states that *the material rate of η-generation (i.e. the coupling term) at a given point P equals the axial vorticity times the differential rotation along the axisymmetric vortex tube passing through P.*

From (19), we observe that when the axisymmetric vortex tubes converge in the z-direction ($\partial \xi^2/\partial z > 0$), then there is material generation of positive η. Likewise, there is material generation of negative η when the vortex tubes diverge ($\partial \xi^2/\partial z < 0$) in the z-direction. These results are true as long as the axial vorticity does not vanish; this is a condition required in the derivation of (19). Note that the *instantaneous* value of η does not influence the *instantaneous* material generation of η, a fact that will prove to be useful for understanding η-transport. Contours of η and material η-generation are shown in figures 17 and 18 and are discussed below.

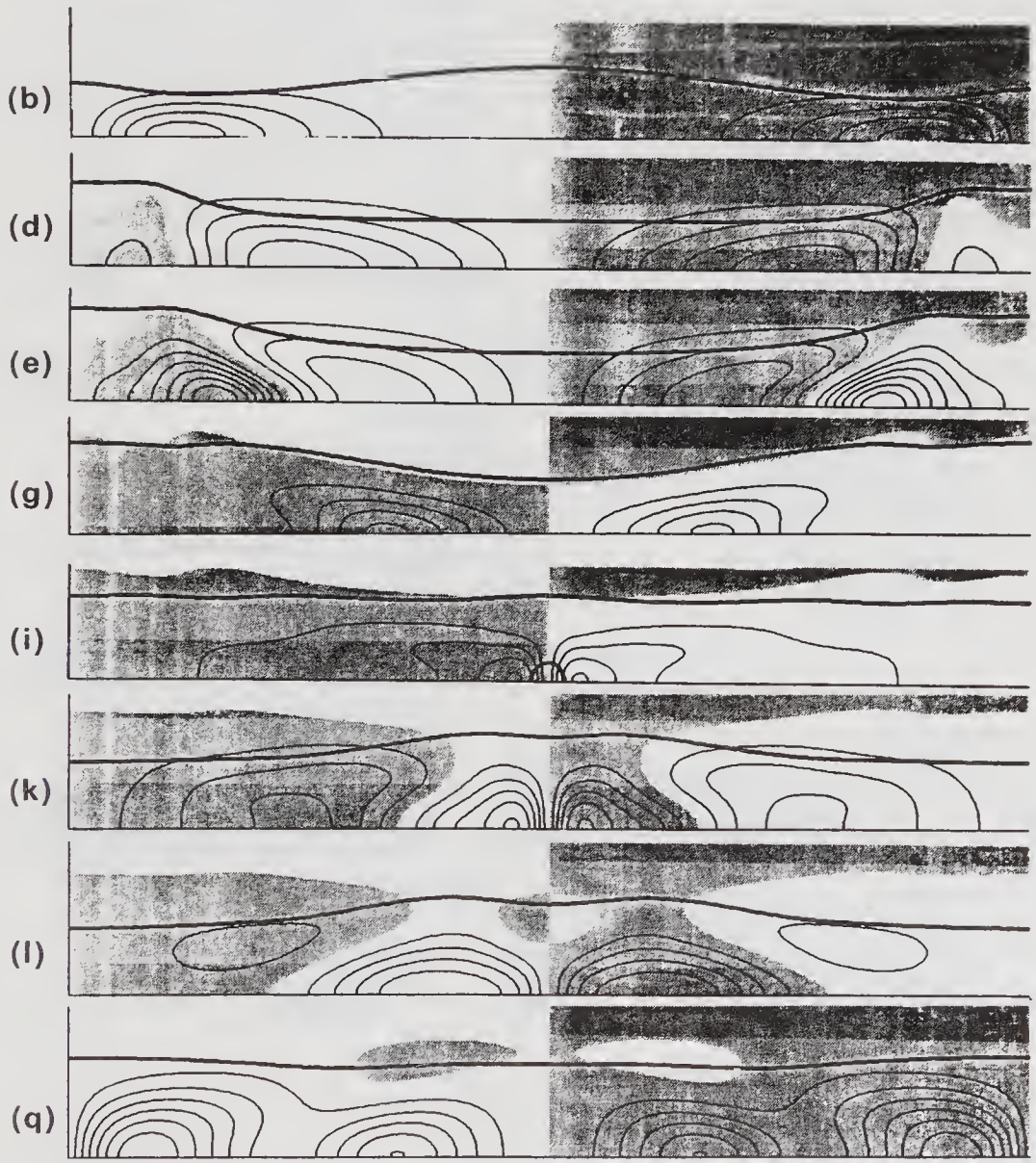

Figure 17. The evolution of the η-distribution ($\eta \equiv \omega_\theta/r$) for case L1 is shown at times corresponding to those in figure 12. η is positive inside the shaded regions and negative in the unshaded regions. The boundary of the vortex as given by the contour $\mathscr{W}_k = 1$ is also shown (heavy line). The contour levels are equally spaced in η with an increment of $\delta\eta$. The peak contour level η_h and $\delta\eta$ are listed below for each frame, dimensional values are included in brackets: (**a**) $\eta \equiv 0$; (**b**) $\eta_h = 5{\cdot}17$ [80], $\delta\eta = 1{\cdot}29$[20]; (**d**) $\eta_h = 1{\cdot}29$ [20], $\delta\eta = 0{\cdot}323$ [5]; (**e**) $\eta_h = 0{\cdot}969$ [15], $\delta\eta = (0{\cdot}161)$ [2·5]; (**g**) $\eta_h = 2{\cdot}58$ [40], $\delta\eta = 0{\cdot}646$ [10]; (**i**) $\eta_h = 1{\cdot}29$ [20], $\delta\eta = 0{\cdot}323$ [5]; (**k**) $\eta_h = 0{\cdot}322$ [5], $\delta\eta = 0{\cdot}0646$ [1]; (**l**) $\eta_h = 0{\cdot}258$ [4], $\delta\eta = 0{\cdot}0646$ [1]; (**q**) $\eta_h = 0{\cdot}194$ [3], $\delta\eta = [0{\cdot}5]$; the conversion formula used here is $\eta = (\tilde{t}\tilde{L})\eta^*$, see (8).

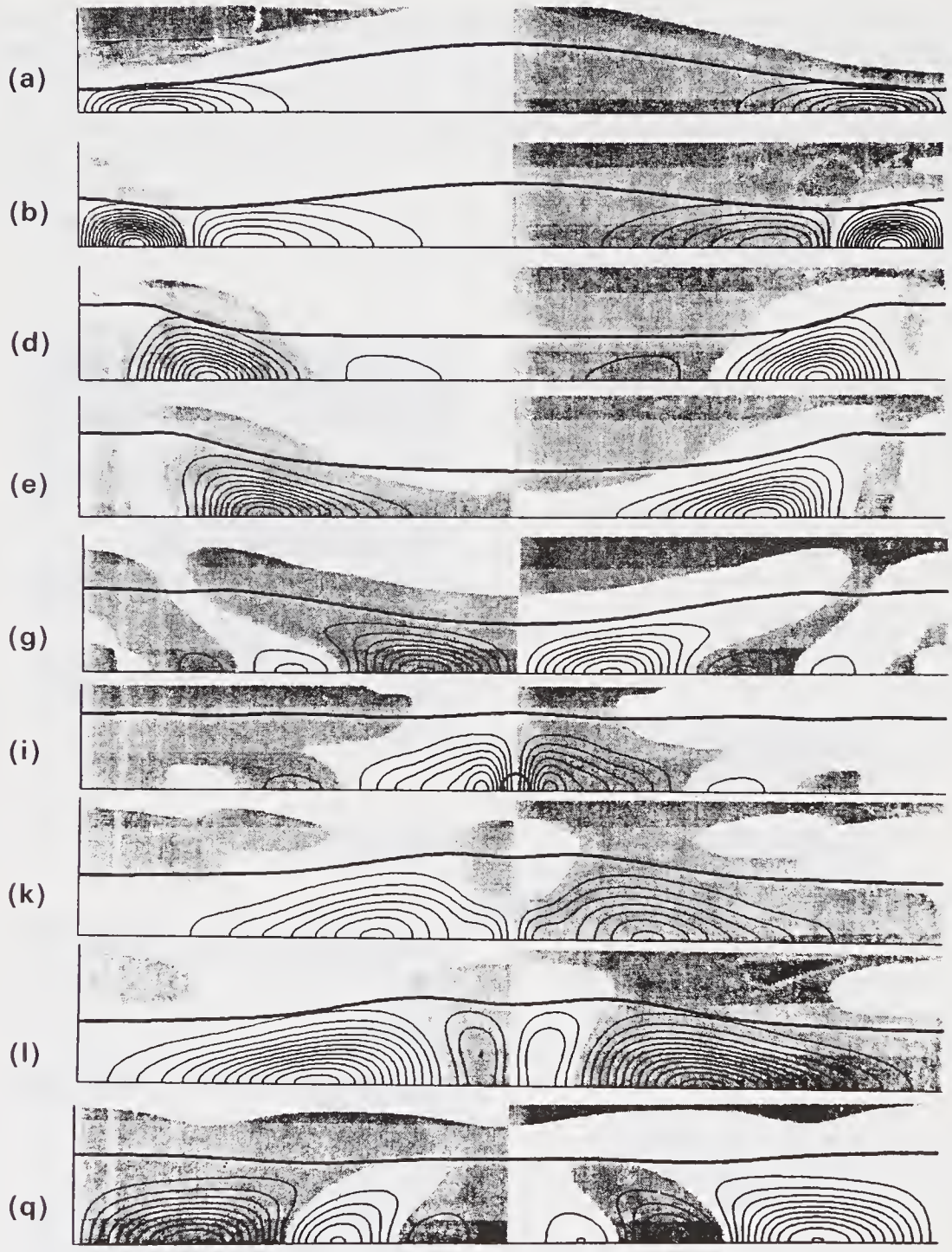

Figure 18. This figure shows the material η-generation ($\eta \equiv D\eta/Dt \equiv r^{-4}\partial\xi^2/\partial z$) for case L1 at times corresponding to those in figure 12. $\dot{\eta}$ is positive inside the shaded regions and negative in the unshaded regions. The boundary of the vortex as given by the contour $\mathscr{W}_k = 1$ is also shown (heavy line). The contour levels are equally spaced in $\dot{\eta}$ with an increment $\delta\dot{\eta}$. The peak contour level $\dot{\eta}_h$ and $\delta\dot{\eta}$ are listed below for each frame, dimensional values are included in brackets: (**a**) $\dot{\eta}_h = 7{\cdot}28$ [1200], $\delta\dot{\eta} = 1{\cdot}21$ [200]; (**b**) $\dot{\eta}_h = 1{\cdot}82$ [300], $\delta\dot{\eta} = 0{\cdot}152$ [25]; (**d**) $\dot{\eta}_h = 0{\cdot}668$ [110], $\delta\dot{\eta} = 0{\cdot}0607$ [10]; (**e**) $\dot{\eta}_h = 0{\cdot}607$ [100], $\delta\dot{\eta} = 0{\cdot}0607$ [10]; (**g**) $\dot{\eta}_h = 0{\cdot}485$ [80], $\delta\dot{\eta} = 0{\cdot}0607$ [10]; (**i**) $\dot{\eta}_h = 0{\cdot}212$ [35], $\delta\dot{\eta} = 0{\cdot}0303$ [5]; (**k**) $\dot{\eta}_h = 0{\cdot}0849$ [14], $\delta\dot{\eta} = 0{\cdot}0121$ [2]; (**l**) $\dot{\eta}_h = 0{\cdot}0728$ [12], $\delta\dot{\eta} = 0{\cdot}00607$ [1]; (**q**) $\dot{\eta}_h = 0{\cdot}0303$ [5], $\delta\dot{\eta} = 0{\cdot}00303$ [0·5]. The conversion formula $\dot{\eta} = \dot{\eta}^*(\tilde{t}^2\tilde{L})$, where $\tilde{t}$ and $\tilde{L}$ are given in (8).

From this kinematic analysis of the coupling term, it is clear how the two cells in figure 16b emerge. The initial local convergence and divergence of the axisymmetric vortex tubes immediately result in material generation of η by differential rotation. For example, the clockwise circulating cell (figure 16b), characterized by negative η (figure 17b), emerges as a result of the initial axial divergence of the vortex tubes between $z = 0$ and $z = l$ (figure 18a). Moreover, it follows from (19) that the extreme values of the material η-generation occur at the inflection points of ξ^2 (figure 18a) and not at the narrowest part of the vortex or at the point of maximum differential rotation.

At any fixed point between $z = 0$ and $z = l$, both η and $(1/r^4)(\partial\xi^2/\partial z)$ (i.e. the material η-generation) are oscillating functions of time. By comparing corresponding frames of figures 17 and 18, we observe that these oscillations are out of phase. The η-oscillation lags behind the $(1/r^4)(\partial\xi^2/\partial z)$-oscillation, and the phase shift depends both on spatial location (r, z) and time. We note that at early times, $(1/r^4)(\partial\xi^2/\partial z)$ changes sign near the z-locations where η has a maximum or a minimum (frames b–d). It may therefore be helpful to think of a roughly 90° phase difference between the two oscillations. This phase difference plays a critical role in the η-transport. To understand why, we must recall the following three kinematic results. *First*, the shape of the vortex tubes ($\xi = \xi_0$) determines the material generation/annihilation of η through the coupling term $(1/r^4)(\partial\xi^2/\partial z)$. *Second*, the meridional flow determines how the shape of the axisymmetric vortex tubes ($\xi = \xi_0$) changes with time. Here, the orientation (clockwise or counterclockwise) of the circulatory motion in the meridional flow cells (figure 16) is critical in determining where the vortex tubes expand and shrink. *Third*, the meridional flow is uniquely given in terms of η and the sign of η largely determines the circulatory motion in the cells. Specifically, the circulatory motion cannot change orientation, say from counterclockwise to clockwise, anywhere until η locally becomes sufficiently negative.

When the phase difference is viewed in the light of these three facts we see that the circulatory meridional motion cannot immediately flip from counterclockwise to clockwise anywhere when the vortex tubes change from converging to diverging in the z-direction (because locally η does not change sign at the same time as the material η-generation). On the contrary, a finite time elapses before the directional change occurs in the meridional flow. A comparison of frames from figures 16 and 15 gives many examples of this time delay; consider for example the region near $z = 0$ in frames b through e. The η-transport differs significantly from the meridional flow's material transport due to such time delays between the reversals in η-generation and subsequent reversals of the meridional flow. We proceed with a discussion of these differences.

There are two η-transport mechanisms: convection of η with the meridional flow and material η-generation/annihilation by differential rotation. At early times, these two effects compete in the primary cells. In the interval between $z = 0$ and $z = l$, the material transport of η by the meridional flow is towards $z = 0$ (figures 16b, d). However, the differential rotation annihilates η near $z = 0$, while at the same time generating η further to the right (figures 18b, d). The competition between the two effects is such that η is effectively transported away from $z = 0$ (figures 17b, d). In the secondary cell which forms later near $z = 0$ (figure 16e), the meridional flow and the differential rotation both transport η in the same direction, namely away from $z = 0$ as seen by comparing frames e, g in figures 16–18. The actual transport of η is thus faster than the material transport. We observe similar flow reversals in figures 16k, p and therefore

conclude that the η-distribution moves in the direction of the material transport in an expanding cell, only faster; in a contracting cell η moves against the meridional flow, but slower than in an expanding cell. In neither case does the η-transport behave exactly like the material transport of the meridional flow. Instead, the η-transport consists of a combination of material transport and wave motion. The latter is a consequence of the phase difference between η-generation and η.

The emergence of the secondary cells (figure 16e), marking the beginning of the reversal in the meridional flow, serves as an example illustrating the role of the phase-difference. At early times (e.g. figure 16b), the meridional flow in the primary cells expands the vortex tubes on one side of each cell (e.g. near $z = 0$) and contracts them on the other side of the cell (e.g. near $z = l$). As a result, the sign of $\partial\xi^2/\partial z$ eventually changes, resulting in oppositely signed η-generation (figure 18b). This, in turn reduces the amplitude of η until eventually the sign of the azimuthal vorticity ($\omega_\theta = r\eta$) also reverses (figures 17d, e). When sufficient oppositely signed η has been generated, the secondary cells emerge (compare frame e of figures 16 and 18).

5. Helical structure

In recent years considerable attention has been focused on the role of helicity (20) in both laminar and turbulent flows (see Moffatt & Tsinober (1990) for numerous references). The laminar vortex evolution outlined above constitutes a suitable test-bed for various ways of studying helicity and related concepts. Not only is the presence of helical structures evident and dynamically important in this case, but the dynamics are also sufficiently simple to facilitate a thorough physical understanding. Our goal therefore is to explore the extent to which helicity concepts can enhance or simplify our understanding of core dynamics.

In order to avoid confusion, we distinguish between three kinds of helicity: the helicity density h, the relative helicity h_r and the helicity integral H. The definitions of these quantities are as follows:

$$h(x, y, z) \equiv \omega \cdot \mathbf{u}, \tag{20}$$

$$h_r(x, y, z) \equiv \omega \cdot \mathbf{u}/(|\omega|\,|\mathbf{u}|), \text{ and} \tag{21}$$

$$H \equiv \int \omega \cdot \mathbf{u}\, dx\, dy\, dz, \tag{22}$$

where the integral extends over either the entire space or over a closed vortex tube. H is Galilean invariant and also a conserved quantity for inviscid flows (Moffatt 1969), provided that certain conditions are satisfied at infinity or that the flow is spatially periodic in three perpendicular directions.

5.1 *Helical wave decomposition: definition*

To study helical structures in detail, we decompose the flow field into "complex helical waves". Following Lesieur (1990), we proceed as follows. Any divergence free vector function $\mathbf{F}(x, y, z)$ has its Fourier coefficient $\hat{\mathbf{F}}(\mathbf{k})$ orthogonal to $\mathbf{k}$, i.e. $\mathbf{k}.\ \hat{\mathbf{F}}(\mathbf{k}) = 0$. Therefore, $\hat{\mathbf{F}}(\mathbf{k})$ is a linear combination of $\mathbf{a}(\mathbf{k})$ and $\mathbf{b}(\mathbf{k})$, two unit vectors normal to

each other and to $|\mathbf{k}|$. Lesieur (1990) defines the "complex helical waves" as

$$\mathbf{V}^+(\mathbf{k},x) \equiv (\mathbf{b}(\mathbf{k}) - i\mathbf{a}(\mathbf{k}))\exp(i\mathbf{k}\cdot\mathbf{x}), \tag{23}$$

$$\mathbf{V}^-(\mathbf{k},x) \equiv (\mathbf{b}(\mathbf{k}) + i\mathbf{a}(\mathbf{k}))\exp(i\mathbf{k}\cdot\mathbf{x}), \tag{24}$$

which are eigenfunctions of the curl operator corresponding to the eigenvalues $\pm|\mathbf{k}| \neq 0$. These eigenfunctions are orthogonal with respect to the inner product

$$<\mathbf{f},\mathbf{g}> = \int \mathbf{f}\cdot\mathbf{g}^* \,\mathrm{d}\mathbf{x}, \tag{25}$$

where * indicates complex conjugation and the integration extends over all space (or a periodic box). The set of all linearly independent eigenfunctions of the curl operator is eomplete, and the eigenvalues are real (Moses 1971). The complex helical waves span a subspace of vector functions. The only vector field that cannot be expanded in terms of complex helical waves is the gradient of a potential. Note that a potential vector field is an eigenfunction of the curl operator corresponding to the eigenvalue 0. Thus, the velocity field, which is divergence free, can be expressed in terms of complex helical waves and the gradient of a harmonic potential ϕ:

$$\begin{aligned}\mathbf{u}(\mathbf{x},t) &= \int_{\mathbf{k}\neq\mathbf{Q}} \mathbf{u}^+(\mathbf{k},t)\,\mathbf{V}^+(\mathbf{k},\mathbf{x})\mathrm{d}\mathbf{k} + \int_{\mathbf{k}\neq\mathbf{Q}} \mathbf{u}^-(\mathbf{k},t)\,\mathbf{V}^-(\mathbf{k},\mathbf{x})\mathrm{d}\mathbf{k} + \nabla\phi \\ &= \mathbf{u}_R + \mathbf{u}_L + \nabla\phi.\end{aligned} \tag{26}$$

The first integral ($\mathbf{u}_R$) is called the *right-handed component* of $\mathbf{u}$ and is the projection of $\mathbf{u}$ onto the vector space spanned by all eigenfunctions corresponding to positive eigenvalues ($+|\mathbf{k}|$) of the curl operator. The second integral ($\mathbf{u}_L$) is the projection of $\mathbf{u}$ onto the vector space spanned by all eigenfunctions corresponding to negative eigenvalues ($-|\mathbf{k}|$) of the curl operator. We call this *the left-handed component* of $\mathbf{u}$. $\nabla\phi$ is the projection of $\mathbf{u}$ onto the null space of the curl operator. Since $\mathbf{u}$ is divergence free, we have $\Delta\phi = 0$. If the potential part of the flow is constant at infinity, $\nabla\phi$ is a constant vector field (due to the maximum principle for harmonic functions) and can be removed by choosing an appropriate inertial frame. For the vorticity field, we have a similar decomposition

$$\omega(\mathbf{x},t) = \omega_R + \omega_L, \tag{27}$$

where it is assumed that the fluid is not rotating at infinity. Since the Fourier transforms of real vector fields have conjugate symmetry, the right- and left-handed projections are real in physical space.

The decomposition of the flow field into complex helical waves is rooted in the intrinsic physical nature of the Navier–Stokes equations and is not merely introduced for computational convenience. Namely, the eigenmodes of the curl operator are exact solutions of the Euler equations, which belong to the special class of solutions known as Beltrami flows ($\omega||\mathbf{u}$). Even in the presence of viscosity the eigenmodes of the curl operator are solutions (Beltrami flows) to the Navier–Stokes equations; the effect of viscosity makes the amplitudes of the eigenmodes decay exponentially with time.

The helicity integral extending over the entire space (or periodic box) has the

following simple expression in terms of the decomposition:

$$H = \int \omega \cdot \mathbf{u} \, d\mathbf{x} = \int \omega_R \cdot \mathbf{u}_R \, d\mathbf{x} + \int \omega_L \cdot \mathbf{u}_L \, d\mathbf{x}. \tag{28}$$

Three of the integrals (with mixed left- and right-handed integrands) in (28) vanish identically due to orthogonality of the eigenfunctions of the curl operator. The remaining two integrals are positive and negative definite, respectively. Moreover, *both integrals are Galilean invariant.* Thus H is positive if the numerical value of the first integral (the right-handed helicity) exceeds that of the second (the left-handed helicity). Similar expressions are of course valid for the energy E and enstrophy Z.

5.2 *Application of the helical decomposition to the laminar vortex evolution*

In case L1, the spatial distributions of the polarized components are not stationary, but instead move in opposite directions (figure 19). As the polarized components separate spatially, ω_R or ω_L becomes locally dominant. Note that $|\omega_R|$ is antisymmetric to $|\omega_L|$ in z with respect to $z = l$ at all times and that in frame i the local minima of ω_R and ω_L coincide (discussed below). The helical twists of the vortex lines (figure 12) result from one polarized component being locally dominant. Where ω_R dominates, the local twist is right-handed, and vice versa. As seen in figure 19, the motion of the polarized distributions is quite simple; namely, the right-handed distribution moves to the left, while the left-handed one moves to the right. Thus *the helical decomposition gives a unique separation of wave-packets moving in opposite directions on the vortex* – a striking result in light of the nonlinearity of the governing equations. In fact, this separation cannot be obtained in general by any other technique. Even in the last frame s, where the vortex has essentially relaxed to a rectilinear state, the left- and right-handed components are distinct.

A new avenue for a deeper understanding of vortex dynamics is opened by the ability of helical decomposition to extract vorticity wave-packets. For example, for core dynamics, we can view the vortex evolution in terms of the motion of polarized wave-packets and their nonlinear interaction. In order to explore this idea, we first examine the evolution of a single polarized vorticity packet and then consider the interaction between packets of opposite polarity.

The isolated motion of a single polarized wave-packet is very simple as shown in figure 20. This figure shows the result of a DNS starting from only ω_R component of the initial condition for case L1. The evolution consists mainly of a simple right-ward translation of the packet. However, the speed of this translation is significantly slower than the velocity induced by the packet. The reason for this is quite simple and follows directly from the analysis in § 4, which applies to all axisymmetric vortex flows. For the evolution shown in figure 20, the material η transport and the material η-generation compete with each other, the generation nearly outpacing the transport. As a result, the propagation speed of the polarized packet is slow. While the overall broadening of the packet is obviously the result of diffusion, there is a subtle nonlinear effect which deserves mention. A packet steepens at its front and leaves a tail behind, thereby breaking the initial front–back symmetry (figure 20a). This effect is likely to be an "overtaking phenomenon", and, at sufficiently high Re, an eventual vortex breakdown might follow. During this simulation only a small amount of left-handed vorticity is generated by nonlinearity in the Navier–Stokes equation (the peak value of $|\omega_L|$ remains less than 5% of the $|\omega_R|$ peak).

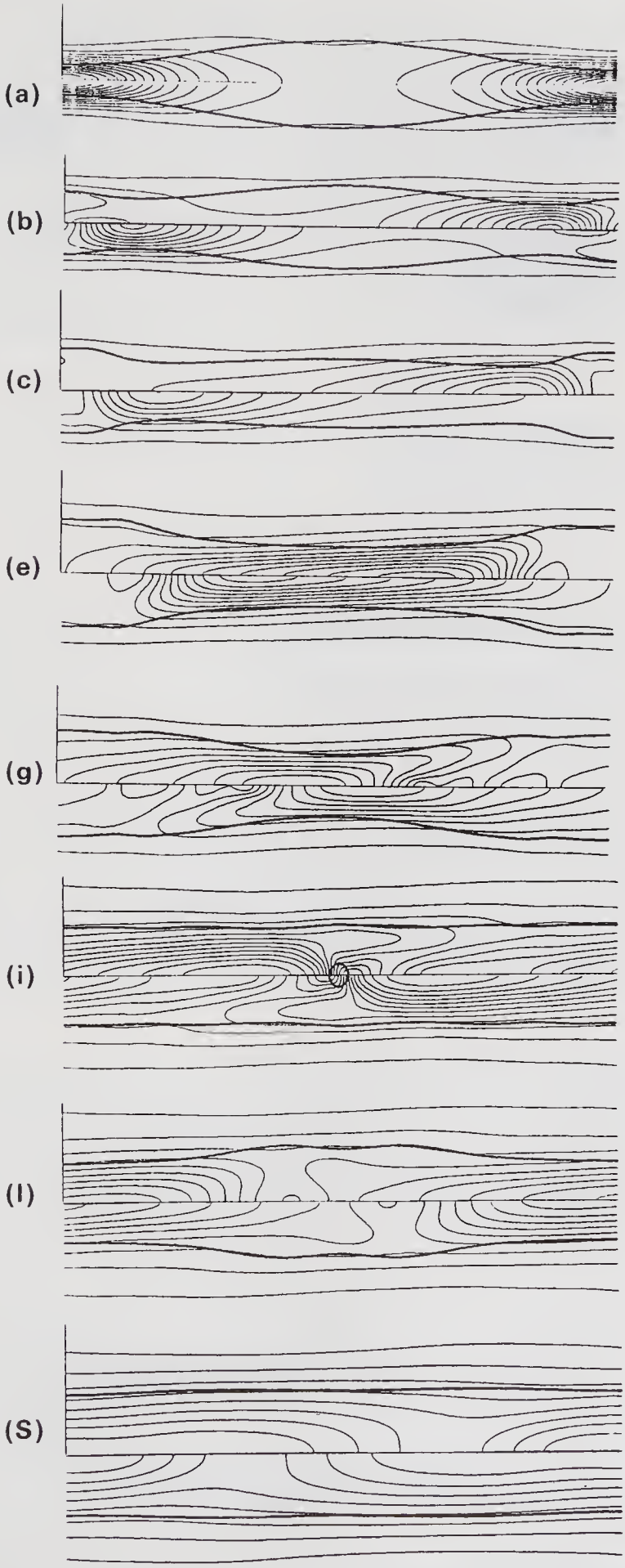

Figure 19. Evolution of $|\omega_R|$ and $|\omega_L|$. In each frame $|\omega_R|$ is shown above the axis while $|\omega_L|$ is shown below. For reference the $\mathscr{W}_k = 1$ contour is overlaid with a heavy line in each frame.

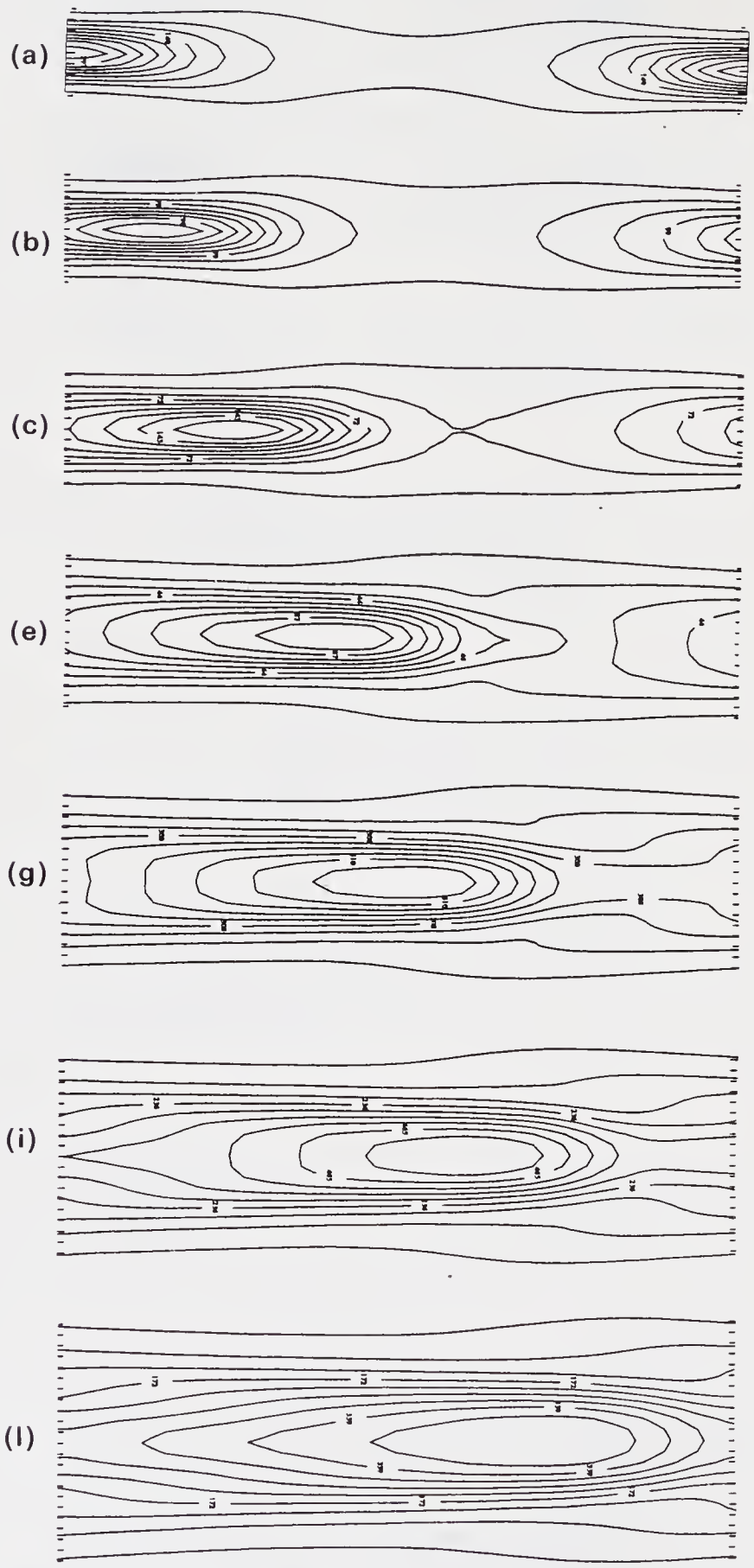

Figure 20. Evolution of $|\omega_R|$ of the initial condition for case L1 in the absence of the initial left-handed component.

The simplicity of the evolution of an isolated polarized component is the cornerstone of our new interpretation of the vortex dynamics, because the dominant effect of the nonlinearity can now be attributed to the interaction among the polarized vorticity components. In order to study the nonlinear interaction between ω_R and ω_L, we introduce two projection operators, P^+ and P^-, to extract the right- and left-handed components of a given vector field, respectively. Using these projection operators, the vorticity transport equation can be split into two coupled evolution equations, one for ω_R and the other for ω_L. In order to bring out the physical effects associated with nonlinear terms, we write the ω_R equation in the following form:

$$\begin{aligned} \partial\omega_R/\partial t = & -\nabla\times(\omega_R\times\mathbf{u}_R) && \text{(term 1)}\\ & +P^-[\nabla\times(\omega_R\times\mathbf{u}_R)] && \text{(term 2)}\\ & -P^+[(\mathbf{u}_L\cdot\nabla)\omega_R] && \text{(term 3)}\\ & +P^+[(\omega_R\cdot\nabla)\mathbf{u}_L] && \text{(term 4)}\\ & -P^+[\nabla\times(\omega_L\times\mathbf{u})] && \text{(term 5)}\\ & +(1/\mathrm{Re})\Delta\omega_R. && \text{(term 6)} \end{aligned} \tag{29}$$

Similarly, ω_L satisfies an analogous equation with R and L, and P^+ and P^- interchanged.

The terms in (29) have specific physical meanings. The first term represents the inviscid self-evolution of ω_R. The second term is the rate of generation of ω_L by the evolution of ω_R. Note that the sum of the first two terms equals $P^+[\nabla\times(\mathbf{u}_R\times\omega_R)]$. The third term is the right-handed contribution to $(\partial\omega_R/\partial t)$ from advection of ω_R by $\mathbf{u}_L$. The fourth term is the right-handed contribution from stretching of ω_R by $\mathbf{u}_L$. The fifth term represents generation of ω_R by the evolution of ω_L; this includes generation of ω_R by the self-evolution of ω_L, the right-handed contribution from the stretching and advection of ω_L by $\mathbf{u}_R$. Finally the sixth term denotes diffusion of ω_R.

In order to get a feeling for the relative importance of the different terms in (29), we have calculated the scalar product of each of the first five terms with ω_R for case L1. We observe that the terms appear in the decreasing order of importance as 3, 1, 5, 4, 2.

Interestingly, the spatial variations in the third and fifth terms have a striking qualitative resemblance. Although the physical reason for this phenomenon is not clear, it simplifies our qualitative discussion. That is, we can consider the sum of the third and fifth terms as an advection in an enhanced $\mathbf{u}_L$. Hence the evolution of ω_R can be largely understood in terms of only two effects: self-evolution and advection in an enhanced $\mathbf{u}_L$ (ignoring the fourth term). The self-evolution attempts to move the ω_R-packet to the right by adding enstrophy at the front and subtracting it at the back of the packet. On the other hand, $\mathbf{u}_L$-field advects the ω_R-packet to the left at the speed of the $\mathbf{u}_L$-field, and the fifth term enhances this left-ward motion. Since the right-ward self-induced motion of the ω_R-packet is slower than the left-ward advection by $\mathbf{u}_L$, the net result is that the packet drifts to the left – in spite of the fact that the ω_R-packet has a self-induced motion to the right. Hence advection by the velocity field of opposite polarity is the cause of the backward drift of the polarized packets in figure 19. The bubble that forms in front (with respect to the packet's self-propagation direction) of each polarized packet is also a result of the packet advection in the velocity field of opposite polarity. Because this velocity field has the

fastest axial component on the axis, it pushes the front of the packet backwards at a faster rate near the axis than away from it (e.g. figure 19g); hence the generation of a low enstrophy bubble (figure 19i). The enhanced elongation of the packet (enhanced as compared to the self evolution shown in figure 20) is a combined effect of terms three and five in (29). The interpretation of the third term is simply that the tail of the right-handed packet (figure 20) is captured by the fast velocity field inside the left-handed packet and then stretched out further. The physical nature of the fifth term is less clear.

In summary, helical wave decomposition provides us a new tool for the analysis of the core dynamics of a vortex. The interaction between packets of opposite polarity is sufficiently simple to allow a straightforward qualitative understanding of the basic features in the evolution.

6. Turbulence and small-scale organization in the neighbourhood of a coherent structure

The interactions between large and small scales are of fundamental importance for a deeper understanding of the physics of turbulent flows and their modelling, and for developing effective techniques for control of turbulence phenomena. This is particularly so for flows featuring large-scale coherent structures. In such flows, in fact in any turbulent shear flow, it is questionable if the small scales are isotropic; i.e. we have had lingering doubts about the validity of *local isotropy*, which is the centrepiece of Kolmogorov's theory and is still the breeding ground for all serious turbulence theories. Hussain (1984) speculated that in spite of wide scale-separation, large and small-scale motions are intimately coupled and that the presence of coherent structures may thus partially cripple the traditional statistical turbulence models, which assume local isotropy. In this section, we examine this issue further by using vortex dynamics.

6.1 *Initial conditions*

There can be no doubt that the rectilinear laminar vortex (case L1) discussed in § 4 qualifies as a coherent structure. Hence our idealized study of the interactions between large- and small-scales consists of this single dynamically evolving coherent structure embedded in a background flow, which initially consists of random small-scale velocity fluctuations. Thus there is no interaction with other coherent structures and no self-induced transverse displacement; moreover, the coherent structure dynamics is represented entirely by the internal core dynamics. This idealized set-up allows us to focus directly on the large-scale/small-scale coupling and may also be thought of as a model for a segment of a coherent structure in turbulent shear flows like jets, wakes and mixing layers, or of internal intermittency near a rod-like vortical structure.

The choice of the random backgrounds (described in § 4.2) is listed in table 1, each of which features a spectral gap in wavenumber between coherent and incoherent scales. Four low resolution simulations (T1–T4) with varying amplitude β of the initial random velocity fluctuations were performed so as to cover the interesting range of β. In case T1, the coherent structure emerged in an axisymmetric shape after the initial decay of the random fluctuations. In cases T2 and T3, the coherent structure emerged with bending waves excited and sustained secondary structures winding

azimuthally around the vortex. However, in case T4 the coherent structure did not survive the interaction with the small scales; that is, after the initial decay of the fluctuations the vortex had disappeared altogether. Based on these four simulations, we estimated parameter values for the high resolution simulations, T5 and T6, so as to excite bending waves on the vortex.

The initial random fluctuations, of course, cannot be characterized as "genuine" turbulence, because they have not adjusted to the presence of the coherent vortex. However, within a few rotations of the vortex, this turbulence adjusts to the presence of the coherent structure and thus becomes more realistic. During this time the small scales decay drastically. In this way, we obtain a weakly turbulent vortex which may be used as the initial condition for new simulations with increased coherent Re, because the value of the viscosity is no longer computationally restricted by the small-scale turbulence, but by the coherent vortex. Cases T9 and T10 (see table 1) are examples of such simulations.

In order to facilitate comparisons with the laminar evolution, we designed the turbulent simulations T1–T6 (table 1) such that the "coherent Reynolds number" $\mathrm{Re}_c = (\Gamma/\nu)$, based on the coherent vortex, is exactly the same as in case L1 – the reference laminar case for all turbulent simulations. Thus, the circulation of the vortex was decreased by a factor α whenever the kinematic viscosity was reduced by a factor α.

6.2 *The polarized structure resulting from small-scales' organization*

Figure 21 shows a cross section perpendicular to the axis of the vortex at a z-location. A 3D-iso-vorticity plot, figure 22, reveals that incoherent vortical structures are swirling azimuthally around the coherent structure. We recognize similarities with the growth of the boundary layer around an impulsively rotated rod (Van Dyke 1988). However, there is an important difference in that the spiral structure in our case features an obvious lack of axisymmetry (figure 21). Figures 21 and 22 provide

Figure 21. Criss section at a late time of the vortex surrounded with the small scale turbulence in case T5. The lowest contour levels are shaded gray. A smaller contour increment had been used for the low levels than for the high levels.

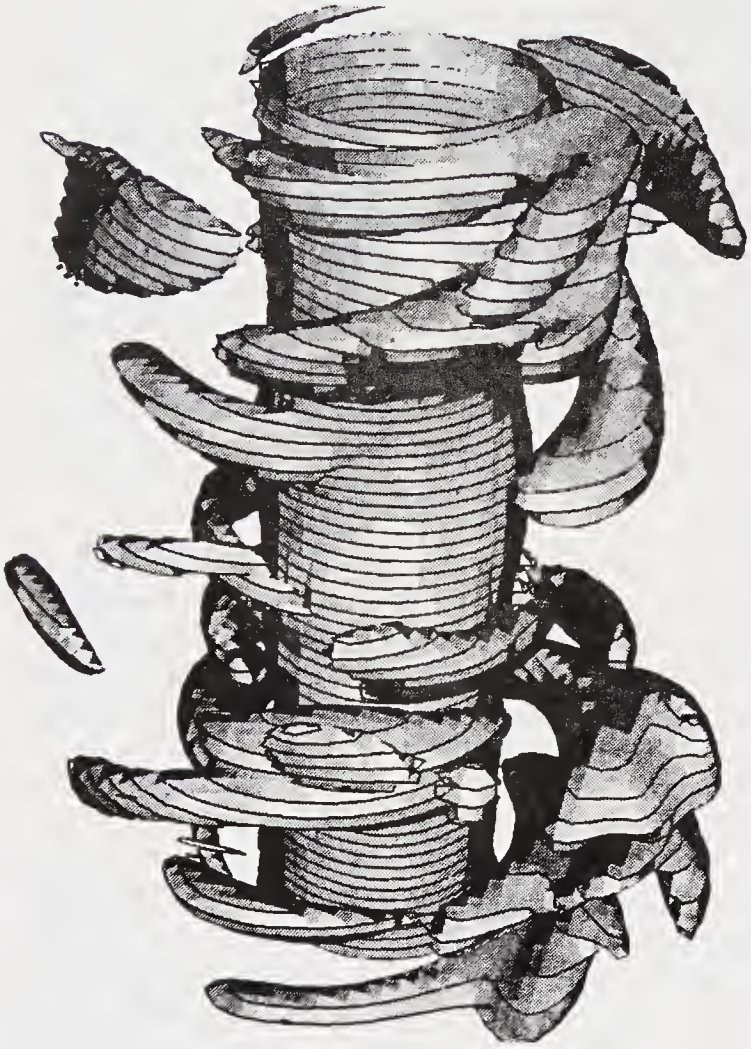

Figure 22. Iso-vorticity surface for case T5. The vorticity norm on the surface equals 10% of the peak value.

a clear perception of the organization of incoherent turbulence by a coherent structure.

At this point, it is important to realize that the spiral structure described above is very different from that suggested by Lundgren (1982). In his model, the vorticity is parallel to the vortex (i.e. the z-axis) even in the spiral structure; the structure proposed by him is similar to the spiral structure formed during the roll-up of shear layers and thus is essentially 2D. Contrary to that, our case features spiral structures with the vorticity roughly parallel or antiparallel to the azimuthal direction. Thus, the structure observed in figure 22 is fully 3D with mainly axial vorticity inside the vortex and mainly azimuthal vorticity in the smaller scales in the boundary layer surrounding it.

The complex helical wave decomposition (see § 5) can also be applied to the turbulent simulations. As for the laminar simulations, this allows us to analyse the dynamics within the coherent structure in terms of wave-packets moving in opposite directions along the axis of the coherent vortex. However, the decomposition also reveals an important new feature of the spiral vortical structures surrounding the vortex. Namely, each of these small-scale structures exhibits a strong tendency to be highly polarized, and individual structures are either predominantly right-handed or predominantly left-handed. By overlaying surfaces of $|\omega_R|$ and $|\omega_L|$, we observe that the polarized components tend to occupy separate locations in the boundary layer around the vortex. This is a clear indication of small-scale polarization and spatial

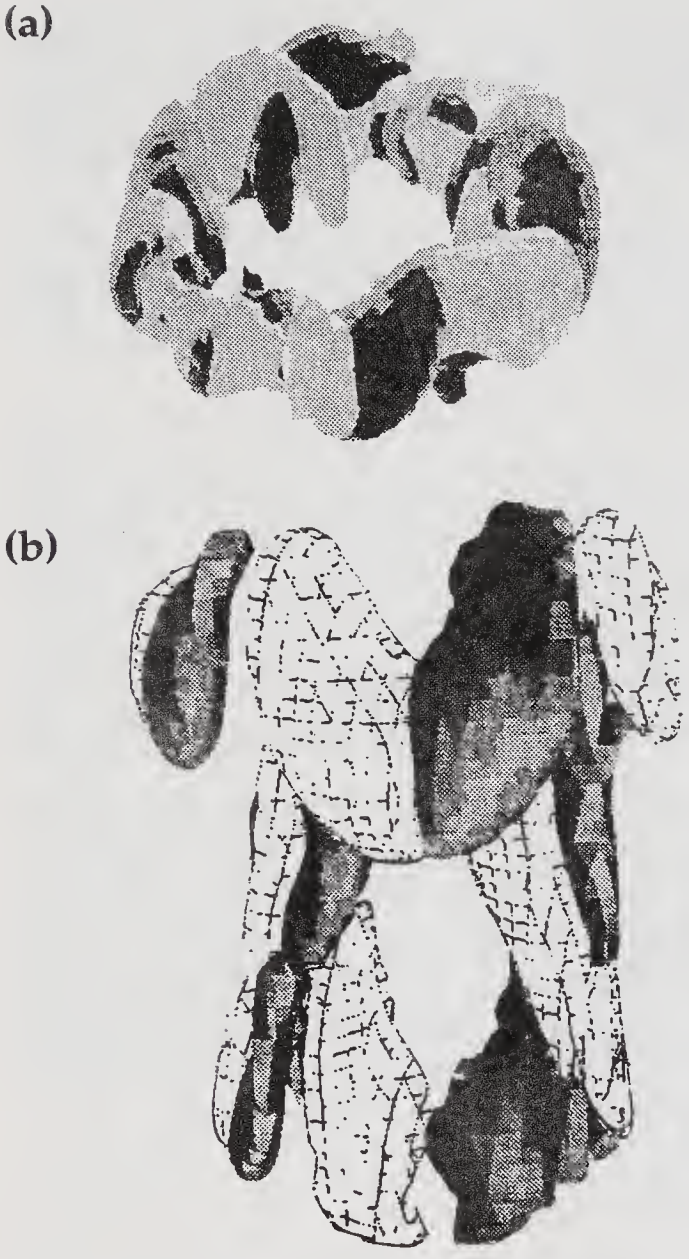

Figure 23. Iso-vorticity surfaces of ω_R (dark) and ω_L (light with wire-frame) in a circular jet at non-dimensional time (**a**) $t = 17$, (**b**) $t = 23$.

separation of right- and left-handed polarized components. Such spatial separation of polarized components was also observed during transition in a temporally evolving circular jet (Melander *et al* 1991). In these simulations of a circular jet, the ring structure formed due to roll-up is essentially unpolarized, i.e. left- and right-handed vorticity magnitudes are most equal everywhere. However, as the azimuthal perturbations grow, and the ring structure begins to breakdown, spatial segregation of polarized vorticity components is observed as shown in figure 23. Implications of such spatial segregation of polarized components for transition are being investigated.

6.3 *Viscous and inviscid aspects of the small-scale organization*

The small-scale organization starts with the azimuthal alignment of the vorticity in the boundary layer surrounding the vortex; see figure 22. This alignment is obviously an inviscid phenomenon, for it is driven by the shear induced by the coherent vortex. Once the vorticity field in the boundary layer acquires a nearly preferred direction

(parallel to the azimuthal direction), it is subject to similar geometrical constraints as 2D-vorticity dynamics. Therefore, pairing of small-scale structures must be considered as a possible inviscid mechanism for the organization. However, the simple viscous decay of the turbulent vortex also produces a growing scale and thus obscures the issue.

By following the evolution of particular small-scale structures in the boundary layer, we find events that closely resemble pairings. That is, structures of the same polarization combine into larger ones when they come in close proximity. These pairing events are of course very viscous and lack the small-scale filaments seen in 2D-simulations at much higher Re (Melander *et al* 1988).

Small-scale structures in the boundary layer pair when they come in close proximity and have the same sign of azimuthal vorticity. Moreover, we have found that such pairings occur for all Re. In this light, axial transport of small-scale structures in the boundary layer is essential, for without it, structures would not come close enough to each other to pair. Even though the axial transport is relatively slow compared to the swirl velocity, it is crucial. There are two transport mechanisms. First, mutual induction of nearby opposite-signed vortices allows transport in the form of dipoles, similar to the case in 2D-turbulence (McWilliams 1984). Second, there is also a self-induced transport due to the curvature of the azimuthally aligned vortices, not present in the 2D-case.

While the vorticity in the boundary layer organizes through the above inviscid processes and forms progressively larger scale structures from smaller ones, there are also mechanisms for generating new smaller scale vorticity. Filamentation similar to that occurring in 2D vorticity dynamics (Melander *et al* 1987, 1988) is one such mechanism. Another is that a small-scale structure can peel vorticity out of the coherent vortex if it comes in close proximity to it. In addition the coherent vortex can, through its own dynamics, shed vorticity into the boundary layer. Finally, the vortex stretching induced by the coherent shear shrinks the cores of the smaller vortical structures, thus contributing to the generation of smaller scales.

6.4 *A conjecture about local anisotropy*

In traditional turbulence theory, the assumption of local isotropy is generally invoked for scales in the inertial subrange; that is, there is no preferred direction of the vorticity associated with scales which are both much larger than the Kolmogorov scale and much smaller than the energy containing integral scale. Consequently, in the limit of infinite Re, anisotropy is only associated with the large scales of the flow. Note that the assumption of local isotropy does not imply that there are no structures in the inertial subrange, nor does it imply anything about the shape of such structures. What is does imply, however, is that the orientation of small-scale structures is statistically random. Local isotropy is indeed a strong assumption, which, however, is very convenient for calculating the transfer of energy between different scales. In essence, local isotropy implies a decoupling of large- and small-scales. As mentioned by Hussain (1984), the evolutions of large- and small-scales are intimately coupled, thus suggesting that local isotropy is suspect in turbulent shear flows. Here, we pursue that idea further by using the simulations to formulate the conjecture that a coherent structure will induce local anisotropy at all scales in its vicinity. We also present a physical space picture of how the cascade of energy from large to small scales takes place.

The presence of the coherent vortex clearly makes the large scales anisotropic. We will now examine how the large scale anisotropy cascades to the smallest scales. The first step in this cascade is the formation of secondary vortical structures in the boundary layer around the coherent vortex (e.g. figure 22) through alignment and subsequent amalgamation, as discussed above. Provided that they are sufficiently strong (e.g. $\mathscr{W}_k > 1$), these secondary structures may then dominate the strain rate in their immediate vicinity. If the Re is sufficiently large to allow the existence of even smaller scales, we can then imagine that these smaller scales align and organize azimuthally around the secondary structures. In the limit of infinite Re, this line of reasoning leads to a hierarchy of structures with decreasing scale.

6.5 *Effect on the large-scale dynamics*

The simulations T1–T6 are all of decaying flows as no energy is continually supplied to replenish dissipative losses. Consequently, these unforced flows will eventually laminarize. The time scale at which this happens depends both on the Re (based on the vortex) as well as on the initial turbulent fluctuation level (i.e. the Re based on the Taylor microscale, for the initial turbulent background flow). Depending on the initial turbulent fluctuation level, one of three things happens. For low random fluctuation levels, the coherent vortex recovers its axisymmetry completely, and although secondary structures do exist in a boundary layer around the vortex, their vorticity amplitudes continually decrease relative to the vortex. In such cases, the coherent vortex quickly ceases to be turbulent. For sufficiently high fluctuation levels, the vortex is unable to survive the turbulent environment and no sign remains of a coherent vortex after the initial decay of the turbulent background. However, the quality of the early part of the simulation is questionable for such cases, as the energy of high wavenumbers is large. For intermediate fluctuation levels the vortex survives, and the turbulence is sustained in a boundary layer around the vortex.

Bending waves can be excited if the initial fluctuation level is sufficiently high. Simulations T9 and T10 start from the last time of case T5 as the initial condition but with reduced damping. In case T9, Re is higher, and a small artificial viscosity is employed in T10. Hence, the initial condition for these simulations is a slightly turbulent vortex. The drastically reduced damping allows the small-scale vortical

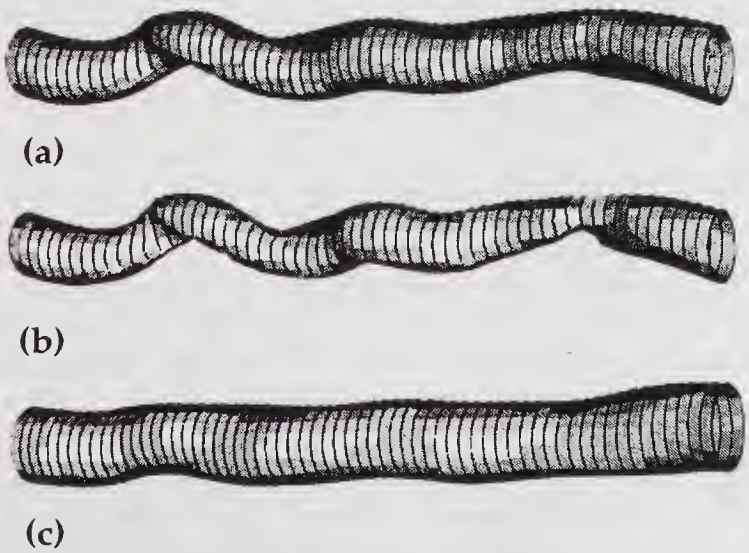

Figure 24. 65% level iso-vorticity surfaces at the end of simulations T9 (**a**) and T10 (**b**). Comparison with the end of simulation T5 (**c**), which is the initial condition of simulations T9 and T10, shows the excitation of bending waves.

structures in the boundary layer to become more energetic. This is because these structures obtain their energy from the coherent vortex through an inviscid cascade mechanism and lose energy mainly by viscous damping, which is now strongly reduced compared to case T5. By comparing iso-vorticity surfaces at the end of simulations T9, T10 (figures 24a, b) with the initial condition (figure 24c), we observe that the small scales have caused the vortex to become non-axisymmetric through the excitation of bending waves. This phenomenon is the sole result of feedback (or backscatter) from small scales to the coherent vortex, a process which clearly cannot be modelled by an enhanced diffusivity.

7. Concluding remarks

In what ways can we extend our new approaches to vortex dynamics for understanding coherent structure dynamics in turbulent shear flows? A few possibilities are discussed below.

7.1 *Vortex reconnection*

An important justification for studying reconnection was the intuitive claim that it occurs at all scales and in all turbulent flows and may be central to turbulence phenomena, including cascade, mixing and helicity and noise generation (Hussain 1986). Some support for this claim can be found in the vortex filaments simulations of Siggia (1985), who found that adjacent vortex filaments evolve into a configuration in which reconnection is inevitable in a viscous flow. We have observed evidence of vortex reconnection in some direct numerical simulations of turbulent flows. However, conclusive evidence for the preponderance of reconnection and its role can only be obtained by directly identifying vortex reconnection events in DNS data on realistic turbulent flows. A major hurdle in this regard is the absence of a rigorous definition of vortex reconnection and a general technique to identify it.

In spite of many studies of vortex reconnection, the intrinsic topological nature of the problem has not been addressed yet. To a large extent, this is because vortex lines, surfaces, and bundles of vortex lines are seldom attributed any physical meaning in viscous flows. Vortex reconnection is unquestionably a viscous phenomenon and – in analogy with magnetic line reconnection – it describes the transfer of circulation between neighbouring vortex line bundles (Greene 1990). To analyse vortex reconnection in a proper fashion, we must view instantaneous vorticity field as a dynamical system, i.e.

$$\dot{X} = \omega_1(X, Y, Z; t),\ \dot{Y} = \omega_2(X, Y, Z; t),\ \dot{Z} = \omega_3(X, Y, Z; t),$$

where time t plays the role of a bifurcation parameter. For a fixed t, the trajectories of the dynamical system are the instantaneous vortex lines. In this phase portrait, we identify *vortex islands* as maximal vortex line bundles with spatial extent such that the virtual velocity ($\hat{v}$) defined by Newcomb (1958) is non-singular along all vortex lines in the bundle; the virtual velocity $\hat{v}$ is circulation preserving and describes the frozen motion of vortex lines in a *viscous* flow. As long as the phase portrait is structurally stable, the topology of the phase portrait remains unchanged with time, and thus the island structure also remains unchanged. However, the circulation of these islands changes with time, either by annihilation or transfer. We define vortex

reconnection as *the change in the circulation of vortex islands due to transfer of circulation.* Such transfer of circulation between vortex islands occurs only where $\hat{v}$ is singular. We have successfully investigated reconnection in axisymmetric flows with swirl using this framework and are currently applying it to the fully three-dimensional reconnection in the case of two antiparallel vortex tubes described earlier in this paper.

While this approach to study reconnection is mathematically rigorous and conceptually simple, it is difficult to apply to general 3D turbulent flows. The difficulty arises due to the tremendous effort involved in determining where $\hat{v}$ is non-singular along entire vortex lines. Reconnection occurs at the singular points of $\hat{v}$, which generally include *vorticity nulls* and *closed vortex lines.* At the locations of vorticity nulls, in the simplest configuration of antiparallel vortex tubes considered here, vortex lines are locally antiparallel and the reconnection is called X-type. Near a closed vortex line (which is very hard to determine computationally), the vorticity is nonzero and vortex lines are nearly parallel; such reconnection is called O-type (see Melander & Hussain (1993a); this concept is well known in the magnetic reconnection literature). In this regard, it is relevant to note that the definition of degree of reconnection advanced by Kida & Takaoka (1990) incorrectly identifies reconnection location away from vorticity nulls and symmetry planes (π_s and π_d) in the antiparallel case studied here.

A consideration in defining reconnection in compressible flows is that topology of vortex lines can change (in addition to viscous effect) due to baroclinic generation of new vorticity. Besides reconnected and unreconnected geometries observed in the incompressible case, closed vortex lines can form due to compressibility effects. Such closed vortex lines, if they exist, would be the locations of O-type reconnection, and hence affect the vortex island structure and cascade. We did find closed lines of baroclinic vorticity generation vector in our simulations. However, closed lines were not observed for the total vorticity. At higher Re and in the presence of the shocklet, closed vortex lines are possible as early time reconnection would be predominantly due to baroclinic generation. High Re compressible simulations, with adaptive meshing to resolve shocklet, are also necessary to determine if the duration of shocklet existence and consequent circulation transfer rate reach finite limits as $\mathrm{Re} \to \infty$. We need to know these limits to construct models for compressible reconnection and to explore how the possible finite time singularity in peak vorticity (suggested by incompressible simulations) is suppressed by compressibility effects.

Further investigation is also required to test our conjecture that reconnection occurs in bursts, each burst becoming shorter with increasing Re. As $\mathrm{Re} \to \infty$, the time interval between successive bursts tends to a finite limit and the circulation transferred in each burst tends to zero, i.e. the convergence $\Gamma(t) \to \Gamma_0$ as $\mathrm{Re} \to \infty$ is non-uniform in time. In order to test this hypothesis, we need much higher resolution simulations capable of resolving smaller scales which are expected to form at higher Re. Also, to observe a second burst in the reconnection of antiparallel vortices we should have adequate resolution in the threads formed after the first reconnection.

7.2 *Core dynamics*

The internal dynamics of a vortical structure remains one of the principal obstacles to the application of vortex dynamics approaches to explain coherent structures in turbulent flows. Even though the induced velocity field far away from a vortical

structure is determined by only a few of the structure characteristics (i.e. low order spatial moments of the vorticity distribution), the details of the internal vorticity distribution (i.e. high order moments) are important for the evolution of the flow. This is because the internal vorticity dynamics do indeed influence the low order moments and hence the far field. For instance, meridional far fields of vortex rings with and without swirl are determined by meridional circulation and are indistinguishable. However, it is known that, even for the same meridional circulation, rings with swirl move slower than those without. Thus, it is necessary to include the influence of internal vorticity dynamics to determine the evolution of coherent structures in turbulent flows. The core dynamics problem is present in both two- and three-dimensional flows, and basically centres around the fact that there is no small parameter to obtain a series expansion of the local flow field. We are presently pursuing a new idea to resolve this problem for two-dimensional and axisymmetric flows. Here we outline our approach for 2D flows. For such flows,

$$\omega = \Delta\psi, \quad \text{and} \quad (\partial\omega/\partial t) + J(\psi,\omega) = \nu\Delta\omega,$$

where ψ is streamfunction, and J is Jacobian. The problem is to obtain ψ from ω without using the typical approach

$$\psi(x,y) = (1/4\pi)\int\int \omega(x_0,y_0)\ln((x-x_0)^2+(y-y_0)^2)\,\mathrm{d}x_0\,\mathrm{d}y_0$$

where Green's function $\ln((x-x_0)^2+(y-y_0)^2)$ cannot be expanded into a series for the near field flow. Thus, we consider an eigenvalue problem, with a Lamb vortex as the first eigenmode, i.e.

$$\Delta\psi = -\lambda\sigma\psi,$$

where $\sigma(r) \equiv \omega_0/\psi_0, \omega_0$ being the vorticity distribution of a Lamb vortex and $\psi_0(>0)$ the corresponding streamfunction. With appropriate boundary conditions, we thus have a Sturm–Liouville problem with a discrete spectrum. This way the streamfunction for a given concentrated vorticity distribution can easily be obtained from the expansion of ω into eigenmodes. Due to the way this eigenvalue problem is constructed, the evolution of a typical vortex can be modelled in terms of only a few eigenmodes.

7.3 *Helical wave decomposition*

Our application of helical wave decomposition to turbulent flow simulations indicates that the vortical structures in turbulent flows are polarized, i.e. the left- and right-handed vorticity fields have their main support in disjoint regions of space. A striking feature we observed in the simulation of a temporally evolving circular jet was that the transition to turbulence occurs precisely as the polarized components begin to segregate spatially. Based on this preliminary evidence, we propose a working hypothesis that 3D turbulent flows in general are characterized by high spatial fluctuation of the polarization ratio $\mathscr{R} \equiv \log_2(|\omega_R|/|\omega_L|)$. It is important to verify this hypothesis as it will have a strong impact on understanding and modelling turbulence. This is because the dynamics of polarized structures ($\mathscr{R} \neq 0$) are quite

different from that of unpolarized ($\mathscr{R} = 0$) structures, and polarization also affects cascade.

We have investigated the axisymmetric dynamics of single and interacting polarized vortex rings. We found that a single polarized ring moves slower than its unpolarized counterpart, and has a head-tail structure consisting of a columnar tail vortex with high fluctuations in $\mathscr{R}$. Pairing of rings with the same polarity is inhibited, while pairing of opposite polarity rings is found to be rapid. This result points to a new tool for turbulence management in circular jets, i.e. by adding a variable swirl to the jet, pairing can be enhanced or suppressed. In order to explore the feasibility of such turbulence control, a computational investigation of spatially/temporally evolving swirling axisymmetric jets is warranted. One can then proceed with laboratory implementation of this concept.

The polarized nature of vortical structures is also important for controlling turbulence cascade. To explain this, we consider interaction between only two isolated eigenfunctions of the curl operator as in Melander & Hussain (1993b). Then, the nonlinear term in the Navier–Stokes equations, which is responsible for cascade, can be expressed as

$$\omega \times \mathbf{u} = (\omega_1 \times \mathbf{u}_2) + (\omega_2 \times \mathbf{u}_1) = (\lambda_1 - \lambda_2)(\mathbf{u}_1 \times \mathbf{u}_2),$$

where λ_1 and λ_2 are the eigenvalues of the curl operator such that $\omega_1 = \lambda_1 \mathbf{u}_1$ and $\omega_2 = \lambda_2 \mathbf{u}_2$; note that the cross product of $\mathbf{u}$ and ω with the same subscripts is zero. Clearly, the nonlinear term, and hence cascade, is smaller if the eigenmodes are of the same polarity and larger if they are of opposite polarity. However, a vortex tube is a combination of many eigenmodes. It is, therefore, not clear if reconnection of vortex tubes with the same (opposite) polarity will also be suppressed (enhanced) and what effect the degree of polarization will have on their interaction. In view of our working hypothesis that turbulence is vortical and polarized, a study of reconnection of polarized vortex tubes is more realistic than the unpolarized ones described in this paper.

A longstanding problem in vortex core dynamics is the vortex breakdown phenomenon. We believe that many new insights into this problem can be obtained from the application of the helical wave decomposition. Our preliminary computational investigation shows that breakdown follows a continuous buildup of left- (right-) handed vorticity in a predominantly right- (left-) handed vortex column. We speculate that breakdown occurs if and only if the thus generated left-handed vorticity accumulates into a wave-packet which is strong enough to travel upstream in the right-handed velocity field. Thus, in our view, the vortex breakdown is a prime example of the coupling between left- and right-handed vorticity components.

Self-similar local organization of small scales conjectured in this paper also needs to be demonstrated by high resolution simulations which would allow much higher Re than used here and hence at least two levels of the self-similar structure. Analysis of such a simulation would provide insights necessary to develop models for subgrid scales and their backscatter.

Preparation of this manuscript was supported by National Science Foundation grant CTS-9214818 and the Air Force Office of Scientific Research grant F49620-92-J-0200.

References

Ashurst W T, Meiburg E 1988 Three-dimensional shear layers via vortex dynamics. *J. Fluid Mech.* 189: 87–116

Batchelor G K 1967 *Introduction to fluid dynamics* (Cambridge: University Press)

Bridges J, Husain H, Hussain F 1989 Whither coherent structures? In *Whither turbulence? Turbulence at the crossroads* (ed.) J Lumley (Berlin: Springer–Verlag)

Brown G L, Roshko A 1974 On density effects and large structure in turbulent mixing layers. *J. Fluid Mech.* 64: 775–816

Crow S C 1970 Stability theory of a pair of trailing vortices. *AIAA J.* 8: 2172–2179

Crow S C, Champagne F H 1971 Orderly structure in jet turbulence. *J. Fluid Mech.* 48: 547–591

Dosanjh D, Weeks T 1965 Interaction of a starting vortex as well as a vortex street with a travelling shock wave. *AIAA J.* 3: 216–223

Erlebacher G, Hussaini M, Kreiss H, Sarkar S 1990 The analysis and simulation of compressible turbulence. ICASE Rep. No. 90–15

Feiereisen W, Reynolds W, Ferziger J 1981 Numerical simulation of a compressible homogeneous, turbulent shear flow. Report No. TF-13, Stanford

Greene J M 1990 Vortex nulls and magnetic nulls. In *Topological fluid mechanics* (eds) H K Moffatt, A Tsinober (Cambridge: University Press)

Hussain F 1981 Role of coherent structures in turbulent shear flows. *Proc. Indian Acad. Sci. (Eng. Sci.)* 4: 129–175

Hussain F 1983 Coherent structure—reality and myth. *Phys. Fluids* 26: 2816–2850

Hussain F 1984 Coherent structures and incoherent turbulence. In *Turbulence and chaotic phenomena in fluids* (ed.) T Tatsumi (Amsterdam: North-Holland)

Hussain F 1986 Coherent structures and turbulence. *J. Fluid Mech.* 173: 303–356

Hussain F, Husain H 1989 Elliptic jets. Part I. Characteristics of unexcited and excited jets. *J. Fluid Mech.* 208: 257–320

Kerr R N, Hussain F 1989 Simulation of vortex reconnection. *Physica* D37: 474–484

Kida S, Takaoka M 1990 Breakdown of frozen motion of vorticity field and vortex reconnection. *J. Phys. Soc. Jpn.* 60: 2184–2196

Kline S J, Reynolds W D, Schraub F A, Runstadler P W 1967 The structure of turbulent boundary layers. *J. Fluid Mech.* 30: 741–773

Lee S, Lele S, Moin P 1991 Eddy shocklets in decaying compressible turbulence. *Phys. Fluids* A3: 657–664

Leonard A 1985 Computing three-dimensional incompressible flows with vortex elements. *Annu. Rev. Fluid Mech.* 17: 523–559

Lesieur M 1990 *Turbulence in fluids* 2nd edn (London: Kluwer)

Lundgren T S 1982 Strained spiral vortex model for turbulent fine structure. *Phys. Fluids* 25: 2193–2203

Lundgren T S, Ashurst W T 1989 Area-varying waves on curved vortex tubes with application to vortex breakdown. *J. Fluid Mech.* 200: 283–307

Mandella M 1987 *Experimental and analytical studies of compressible vortices*, Ph D thesis, Stanford University, Stanford

McWilliams J C 1984 The emergence of isolated vortices in turbulent flow. *J. Fluid Mech.* 146: 21–43

Meiron D I, Shelley M J, Ashurst W T, Orszag S A 1989 Numerical studies of vortex reconnection. In *Mathematical aspects of vortex dynamics* (ed.) R Caflisch (SIAM)

Melander M V, Hussain F 1988 Cut-and-connect of two antiparallel vortex tubes. Report-S88, 257–286, Stanford University: also, 1989 *Phys. Fluids* A1: 633–636

Melander M V, Hussain F 1990 Topological aspects of vortex reconnection. In *Topological fluid mechanics* (eds) H K Moffatt, A Tsinober (Cambridge: University Press)

Melander M V, Hussain F 1993a Topological vortex dynamics in axisymmetric viscous flows. *J. Fluid Mech.* (in press)

Melander M V, Hussain F 1993b Polarized vorticity dynamics on a vortex column. *Phys. Fluids* A5: 1992–2003

Melander M V, Hussain F, Basu A 1991 Breakdown of a circular jet into turbulence. *Turbulent Shear Flows 8*, Munich, pp. 15.5.1–15.5.6

Melander M V, McWilliams J C, Zabusky N J 1987 Axisymmetrization and vorticity gradient intensification of an isolated two-dimensional vortex through filamentation. *J. Fluid Mech.* 178: 137–159

Melander M V, Zabusky N J, McWilliams J C 1988 Symmetric vortex merger in two dimensions: causes and conditions. *J. Fluid Mech.* 195: 303–340

Moffatt H K 1969 The degree of knottedness of tangled vortex lines. *J. Fluid Mech.* 35: 117–129

Moffatt H K, Tsinober A (eds) 1990 *Topological fluid mechanics* (Cambridge: University Press)

Moses H E 1971 Eigenfunctions of the curl operator, rotationally invariant Helmholtz theorem, and applications to electromagnetic theory and fluid mechanics. *SIAM J. Appl. Math.* 21: 114–144

Narasimha R 1989 The utility and drawbacks of traditional approaches. In *Whither turbulence? Turbulence at the crossroads* (ed.) J Lumley (Berlin: Springer–Verlag)

Newcomb W A 1958 Motion of magnetic lines of force. *Ann. Phys.* 3: 347–385

Passot T, Pouquet A 1987 Numerical simulation of compressible homogeneous flows in turbulent regime. *J. Fluid Mech.* 181: 441–466

Schwarz K 1985 Three-dimensional vortex dynamics in superfluid ^{4}He: Line–line and line–boundary interactions. *Phys. Rev.* B31: 5782–5803

Shariff K, Leonard A, Zabusky N, Ferziger J 1988 Acoustics and dynamics of coaxial interacting vortex rings. *Fluid Dyn. Res.* 3: 337–343

Siggia E D 1985 Collapse and amplification of a vortex filament. *Phys. Fluids* 28: 794–805

Stanaway S, Shariff K, Hussain F 1988 Head-on collision of viscous vortex rings. NASA report CTR S-88, 287

Takaki R, Hussain F 1985 Recombination of vortex filaments and its role in aerodynamic noise. *Turbulent Shear Flows V*, Cornell University, 3.19–3.25

Truesdell C 1954 *The kinematics of vorticity*, Indiana University Publications Science Series, No. 19

Van Dyke M 1988 *An album of fluid motion* (Stanford, CA: Parabolic Press)

Zank G, Matthaeus W 1991 The equations of nearly incompressible fluids. I. Hydrodynamics, turbulence, and waves. *Phys. Fluids* A3: 69–82

Simulating three-dimensional vortex motion by a vortex blob method

M KIYA

Department of Mechanical Engineering, Hokkaido University, Sapporo, 060, Japan

Abstract. A three-dimensional vortex blob method was applied to calculate several vortex motions: the deformation of pseudo-elliptic vortex rings, the jet issuing from the pseudo-elliptic nozzle into flow of uniform velocity, the unsteady separated flow around a circular disk with an angle of attack, and the interaction of several vortex rings which approximately reproduced the Kolmogorov spectrum. In the first three cases, the viscous diffusion of vorticity was included. The pseudo-elliptic vortex rings experienced axis switching and split into a few deformed vortex rings. Rolling-up vortices in the pseudo-elliptic jet had a symmetric arrangement in the minor-axis plane and an antisymmetric arrangement in the major-axis plane in the developing region; further downstream, the vortices were arranged antisymmetrieally in both planes. The wake behind the disk normal to the main flow reproduced the spiral and columnar modes of instability. A problem in the three-dimensional vortex method is that vorticity tends to diverge at a stage of evolution of the vortex motions. An approximate method of avoiding the divergence of vorticity is proposed.

Keywords. Vortex dynamics; vortex method; turbulence; turbulent shear flows; vortex rings; non-circular jets; turbulent wakes; coherent structures; numerical simulation.

1. Introduction

Consider a high Reynolds-number flow around a bluff body. The boundary layer along the surface, which is a thin layer of vorticity, separates from the surface along a line, being shed downstream as a separated shear layer. The shear layer develops into rolling-up vortices due to the Kelvin–Helmholtz instability. The rolling-up vortices interact with each other to develop a complicated system of vortices, which is the near wake of the body. The near wake develops into the intermediate wake (Kiya & Matsumura 1985) and eventually into the far wake. Thus it is reasonable to assume that the high Reynolds-number flow around a bluff body can be simulated by tracking vorticity in the Lagrangian manner. This is the idea of a vortex method. Moreover, if turbulent flow is envisaged as a complicated motion of interacting

three-dimensional vortices, the vortex method is expected to successfully simulate a wide range of turbulent shear flows at high Reynolds numbers and homogeneous turbulent flows.

The vortex method has a number of merits: (i) It is a Lagrangian method so that there is no need to have grid systems whose construction is the heavy task in simulations by finite-difference methods; (ii) the computation can be limited only to regions of non-zero vorticity; (iii) high Reynolds-number flows can be simulated.

The purpose of this paper is to demonstrate the potentiality of a three-dimensional vortex blob method by the simulation of several vortex motions. Comprehensive reviews on the vortex methods are written by Leonard (1980, 1985) and more recently by Sethian (1990) who includes a number of flows calculated by the vortex method.

2. Vortex blob method

Let the velocity and vorticity vectors be denoted by $\mathbf{u}$ and ξ. Uniform-density viscous flow in three-dimensions is described by the equations

$$D\xi/Dt = (\xi\cdot\nabla)\mathbf{u} + (1/\mathrm{Re})\nabla^2\xi, \tag{1}$$

$$\nabla\cdot\mathbf{u} = 0, \tag{2}$$

$$\xi = \nabla\times\mathbf{u}, \tag{3}$$

with appropriate boundary conditions. Here the variables are normalized in terms of representative length and velocity scales; t is the time, and Re denotes Reynolds number. Equations (1)–(3) are the vorticity equation, the equation of continuity, and the definition of vorticity. If one introduces the vector potential ψ defined by

$$\mathbf{u} = \nabla\times\psi. \tag{4}$$

Equation (3) can be written as

$$\nabla^2\psi = -\xi. \tag{5}$$

The equation of continuity is automatically satisfied by the introduction of the vector potential. The solution of this equation is given by

$$\psi(\mathbf{x},t) = \int G(\mathbf{x}-\mathbf{z})\xi(\mathbf{z})\mathrm{d}\mathbf{z}, \tag{6}$$

with $G(\mathbf{x}) = 1/(4\pi|\mathbf{x}|)$, where $\mathbf{x}$ and $\mathbf{z}$ are the position vectors and $\mathrm{d}\mathbf{z}$ implies an infinitesimal volume whose centre is located at $\mathbf{z}$. Substituting (6) into (4), one obtains

$$\mathbf{u}(\mathbf{x},t) = \int \mathbf{K}(\mathbf{x}-\mathbf{z})\xi(\mathbf{z})\mathrm{d}\mathbf{z}, \tag{7}$$

where the kernel $\mathbf{K}$ is a tensor defined by

$$\mathbf{K}(\mathbf{x}) = \frac{1}{4\pi|\mathbf{x}|^3}\begin{pmatrix} 0 & x_3 & -x_2 \\ -x_3 & 0 & x_1 \\ x_2 & -x_1 & 0 \end{pmatrix}. \tag{8}$$

Equation (7) is the Biot–Savart law. Equations (1) and (7) determine the evolution of the velocity and vorticity fields provided that an initial distribution of vorticity $\xi(\mathbf{x}, 0)$ is given.

The Eulerian representation (1) and (7) will be transformed into the Lagrangian representation. A fluid particle initially located at a position $\mathbf{a}$ is assumed to be at the position $\mathbf{x}^a(t)$ and have the vorticity $\xi^a(t)$ at time t. In what follows, the argument t will be deleted for brevity. The kernel $\mathbf{K}(\mathbf{x})$ diverges as $|\mathbf{x}|$ goes to zero. Thus this is replaced by a smooth (regularized) kernel $\boldsymbol{K}_\sigma(\mathbf{x})$ such as $\boldsymbol{K}_\sigma(\mathbf{x}) \to \boldsymbol{K}(\mathbf{x})$ as $\sigma \to 0$, where σ is the cut-off length. The initial vorticity field is divided into a collection of sufficiently small regions (vortex blobs) of approximately the same dimensions. The vortex blob whose centre is initially at the position $\mathbf{a}$ has a volume $\Delta\mathbf{x}^a$. If inviscid flow is momentarily assumed, (7) and (1) can be written as

$$\mathrm{d}\mathbf{x}^a/\mathrm{d}t = \sum_b \mathbf{K}_\sigma(\mathbf{x}^a - \mathbf{x}^b)\boldsymbol{\gamma}^b, \tag{9}$$

$$\mathrm{d}\boldsymbol{\gamma}^a/\mathrm{d}t = (\boldsymbol{\gamma}^a \cdot \nabla)\sum_b \mathbf{K}_\sigma(\mathbf{x}^a - \mathbf{x}^b)\boldsymbol{\gamma}^b, \tag{10}$$

where $\boldsymbol{\gamma}^a = \xi^a \Delta\mathbf{x}^a$ is the 'strength' of the vortex blob $\mathbf{a}$ and the operation ∇ is made with respect to $\mathbf{x}^a$.

The kernel has the form

$$\mathbf{K}_\sigma(\mathbf{x}) = g(|\mathbf{x}|/\sigma)\mathbf{K}(\mathbf{x}), \tag{11}$$

where $g(\cdot)$ is a spherically symmetric function, an example being that proposed by Winckelmans & Leonard (1989, pp. 25–35):

$$g(y) = y^3[y^2 + (5/2)]/(y^2 + 1)^{5/2}. \tag{12}$$

This function has convergence properties equal to those of the Gaussian smoothing.

In the framework of the three-dimensional vortex blob method, the viscous diffusion of vorticity can be considered by the use of random walk of the vortex blobs (Chorin 1973), by increasing the cut-off length as a function of time (Shirayama *et al* 1985), and by the use of an integral representation for the Laplacian operator $\nabla^2\xi$ (Winckelmans & Leonard 1989, pp. 25–35). In the last method the following term is added to the right-hand side of (10):

$$(2/\mathrm{Re}\,\sigma_a^2)\sum_b (1/\sigma_b^3)\eta(|\mathbf{x}^a - \mathbf{x}^b|/\sigma_b)(\boldsymbol{\gamma}^b \mathrm{d}\mathbf{x}^a - \boldsymbol{\gamma}^a \mathrm{d}\mathbf{x}^b), \tag{13}$$

where σ_a and σ_b are the cut-off lengths of the vortex blobs initially located at $\mathbf{a}$ and $\mathbf{b}$, and the function $\eta(\cdot)$ is derived from the function $g(\cdot)$ by the relation

$$\eta(y) = -(1/y)(\mathrm{d}\zeta/\mathrm{d}y) \text{ and } g(y) = 4\pi \int_0^y \zeta(y) y^2 \mathrm{d}y. \tag{14}$$

For the smoothing function $g(\cdot)$ of (12), the functions $\eta(\cdot)$ and $\zeta(\cdot)$ are given by

$$\zeta(y) = (15/8\pi)[1/(y^2 + 1)^{7/2}], \tag{15}$$

$$\eta(y) = (105/8\pi)[1/(y^2 + 1)^{9/2}]. \tag{16}$$

The differentiation ∇ with respect to $\mathbf{x}^a$ in (10) can be made either analytically or numerically. For the core structure of (12), the analytical differentiation yields the following form of (10) with the viscous diffusion included:

$$\frac{D\boldsymbol{\gamma}^a}{Dt} = \sum_b \frac{\boldsymbol{\gamma}^b}{4\pi} \times \left\{ \boldsymbol{\gamma}^a \frac{r_{ab}^2 + \frac{5}{2}\sigma_b^2}{(r_{ab}^2 + \sigma_b^2)^{5/2}} - 3\mathbf{r}^{ab}(\boldsymbol{\gamma}^a \cdot \mathbf{r}^{ab}) \frac{r_{ab}^2 + \frac{7}{2}\sigma_b^2}{(r_{ab}^2 + \sigma_b^2)^{7/2}} \right\} + \frac{2}{\mathrm{Re}\,\sigma_a^2} \sum_b \frac{1}{\sigma_b^3} \eta\left(\frac{|\mathbf{x}^a - \mathbf{x}^b|}{\sigma_b}\right)(\boldsymbol{\gamma}^b \mathrm{d}\mathbf{x}^a - \boldsymbol{\gamma}^a \mathrm{d}\mathbf{x}^b), \tag{17}$$

where $\mathbf{r}^{ab} = \mathbf{x}^a - \mathbf{x}^b$ and $r_{ab} = |\mathbf{r}^{ab}|$.

In the above three-dimensional vortex method, the divergence-free condition of vorticity $\nabla \cdot \boldsymbol{\xi} = 0$ is only approximately satisfied because the vorticity field

$$\boldsymbol{\xi}(\mathbf{x}) = \sum_b \frac{1}{\sigma_b^3} \zeta\left(\frac{|\mathbf{x} - \mathbf{x}^b|}{\sigma_b}\right) \boldsymbol{\xi}^b \Delta\mathbf{x}^b = \sum_b \frac{1}{\sigma_b^3} \zeta\left(\frac{|\mathbf{x} - \mathbf{x}^b|}{\sigma_b}\right) \boldsymbol{\gamma}^b, \tag{18}$$

is not divergence-free. The extent to which this violation of the divergence-free condition affects the accuracy of the solutions is not established yet. This demerit is compensated by the merit that the reconnection of vortex filaments is automatically realized. Knio & Ghoniem (1990) proposed a three-dimensional vortex method in which the divergence-free condition is exactly satisfied. On the other hand, it seems difficult to incorporate the viscous effects into the Knio–Ghoniem method.

Vorticity of vortex blobs generally increases with time during the evolution of a vortex system. Thus, in order to maintain the spatial resolution, the length of a vortex blob should be subdivided into smaller vortex blobs from time to time. One way of doing this is to subdivide a vortex blob of length $|\mathbf{l}|$ into two blobs of the same vorticity and the length $|\mathbf{l}/2|$ if the length $|\mathbf{l}|$ becomes greater than twice its initial value. The cut-off length of the new vortex blobs is chosen as $2^{-1/3}$ times its initial value; this corresponds to halving the volume of the original vortex blob (Kiya & Ishii 1991). This procedure can conveniently be made if a vortex blob $\mathbf{a}$ is visualized as a circular cylinder of radius δ_a (which will be referred to as the core radius) and length $\mathbf{l}^a$. The volume $\Delta\mathbf{x}^a = |\mathbf{l}^a|\pi(\delta_a)^2$ and the circulation $\Gamma_a = |\boldsymbol{\xi}^a|\pi(\delta_a)^2 = |\boldsymbol{\gamma}^a|/|\mathbf{l}^a|$ are conserved. This condition and (17) determine the length $\mathbf{l}^a$ and the core radius δ_a at each time step of calculation.

The vortex blob is an element which is introduced to calculate the evolution of a region of distributed vorticity. The vorticity at its centre is not necessarily the vorticity of flow at that point because, as indicated by (18), vorticity at an arbitrary position $\mathbf{x}$ is the sum of the contributions of vorticity from neighbouring vortex blobs.

The accuracy of the vortex method depends on the representative dimension of the vortex blob $h = (\Delta\mathbf{x}^a)^{1/3}$, the kernel $\mathbf{K}_\sigma$, the cut-off length σ, and the time step of advancing the vortex blob Δt. Errors are estimated to be $O((\sigma/L)^n) + O[(\sigma/L)(h/\sigma)^m]$ for inviscid flows, where L is a representative (global) length scale of the problem (Winckelmans & Leonard 1989, pp. 25–35). The value of the exponent m is the number of derivatives of the smoothing function $\zeta(y)$, being large ($m = \infty$) for the function of (15). Thus one should have $h/\sigma < 1$; that is, cores of neighbouring vortex blobs should overlap. The value of the exponent n depends on the moment properties of the function $\zeta(y)$: If the integral $\int y^4 |\zeta(y)| \mathrm{d}y$ is finite, one has $n = 2$. For viscous flows errors become $O(\mathrm{Re}^{-1}(\sigma/L)^n) + O[\mathrm{Re}^{-1}(\sigma/L)^{-1}(h/\sigma)^m]$. This error is greater than that for the inviscid flow if $\mathrm{Re}^{-1} = O(1)$, while the former is of the same order

of or less than the latter if $\mathrm{Re}^{-1} = O((\sigma/L)^2)$. Thus the vortex method becomes more accurate at higher Reynolds numbers.

In discussing vortex motion associated with turbulent flows, one has to calculate such dynamical properties as the linear and angular impulses, total vorticity, helicity, enstrophy, kinetic energy, and the power spectra of the energy, enstrophy and helicity. For the core structure of (12) these dynamical properties can be obtained in terms of the strength of the vortex blobs and their positions (Winckelmans & Leonard 1993). The same expressions obtained in a different manner are summarized in the appendix. For the core structure of lower order $g(y) = y^3(y^2 + 1)^{-3/2}$, the expressions are obtained by Kiya & Ishii (1991).

In what follows, several examples of vortex motion calculated by the vortex blob method will be presented to demonstrate its potentialities.

3. Deformation of noncircular vortex rings

Turbulent jets issuing from noncircular nozzles have greater rates of growth and mixing with the surrounding fluid than those from circular nozzles of the same cross-sectional area. Immediately downstream of the nozzle a vortex ring is formed whose circumference is approximately the same as that of the nozzle. The behaviour of the single vortex ring provides useful information on the vortex structure and turbulence property in the developing region of the jet, especially when the jet is excited by a sinusoidal disturbance (Toyoda & Hussain 1989). The vortex structure in the developing region of the jet is indispensable for understanding the source of the jet noise.

A vortex dynamics simulation was made for a vortex ring whose circumference consists of two parallel line segments of the same length connected by two semicircles of the same radius R; the length of the major axis is denoted by L (Kiya *et al* 1992). The configuration of this 'pseudo-elliptic' vortex ring can be seen at the bottom of figures 1 and 2 in the yz- and xz-planes. The xyz-coordinate is defined in the same way as in figure 5 below. The initial radius of the cross-section δ_{cs} is constant along the circumference. The cross-section was represented by 25 vortex blobs, while the circumference was divided into a number of such sections. The viscous diffusion of vorticity was included by (17).

Numerical calculations were performed for the vortex rings with the aspect ratio $L/(2R) = 2{\cdot}0$–$12{\cdot}0$, the core radius $\delta_{cs}/R = 0{\cdot}20$, and Reynolds number $\mathrm{Re} = \Gamma/\nu = 1500$, where Γ is circulation of the vortex ring and ν denotes the kinematic viscosity. The modulus of vorticity of the vortex blobs was not allowed to increase beyond a prescribed value ξ_{max} to approximately simulate the balance between the intensification of vorticity due to the vortex stretching and the lateral spreading of vorticity by the viscous diffusion. The value of ξ_{max} is proportional to the initial vorticity, the local rate of strain, the square of the core radius, and the inverse of the kinematic viscosity (Batchelor 1967, p. 272). Instead of evaluating the local rate of strain, the value of ξ_{max} was rather arbitrarily chosen as 16 times the initial value of vorticity. Doubling this factor produced only insignificant changes in the global nature of deformation of the vortex rings. This procedure was introduced because the viscous diffusion term in (17) is still an approximation, and the said balance might not be correctly represented.

Figure 1 is the deformation of vortex ring with the aspect ratio $L/(2R) = 3{\cdot}0$. This

Figure 1. Axis switching of pseudo-elliptic vortex ring with $L/(2R) = 3{\cdot}0$, $\delta_{cs}/R = 0{\cdot}20$ and $\Gamma/\nu = 1500$. Visualization is made by vortex blobs. (**a**) View in yz-plane, (**b**) view in xz-plane. Numerical figures indicate non-dimensional time $\Gamma t/R^2$.

deformation includes the axis switching. The patterns in figure 1 were in general agreement with a flow visualization experiment (Kiya *et al* 1992). A wavy disturbance along the circumference in the configurations, at $\Gamma t/R^2 = 47{\cdot}43$ and $56{\cdot}91$, was also observed in the experiment, being perhaps associated with the circumferential instability discussed by Widnall (1975). The vortex ring with $L/(2R) = 6{\cdot}0$ experienced a split into two vortex rings after axis switching as shown in figure 2. This pattern was also confirmed by the experiment. Times when the axis switching and the split occurred (which are denoted by τ_{sw} and τ_{sp} respectively) were in tolerable agreement with the experiment as shown in figures 3 and 4.

The jet issuing from a nozzle is characterized by the interaction of two or more vortex rings. The number of interacting vortex rings can be controlled by a proper excitation (Toyoda & Hussain 1989). Thus it would be interesting to simulate the interaction between two or more noncircular vortex rings. This is left for study in the future.

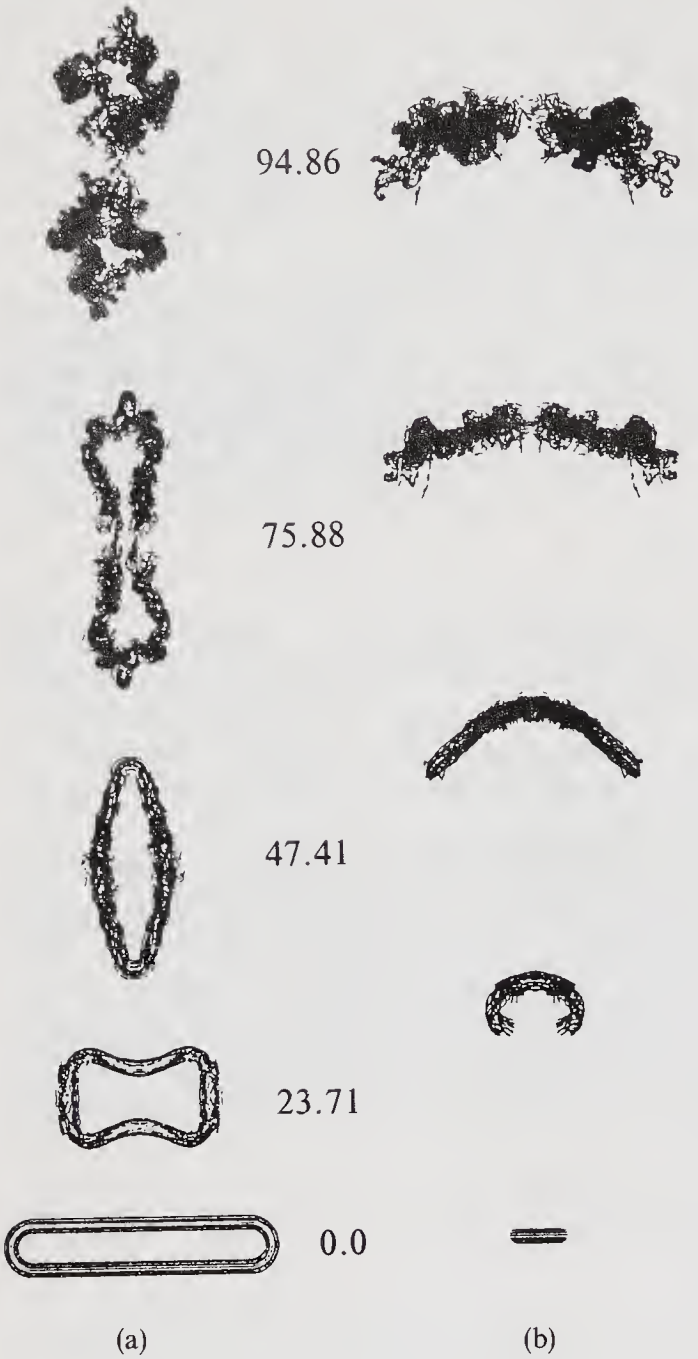

Figure 2. Axis switching and split of pseudo-elliptic vortex ring with $L/(2R) = 6{\cdot}0$, $\delta_{cs}/R = 0{\cdot}20$ and $\Gamma/\nu = 1500$. Visualization is made by vortex blobs. (**a**) View in yz-plane, (**b**) view in xz-plane. Numerical figures indicate non-dimensional time $\Gamma t/R^2$.

4. Noncircular jet

A noncircular jet issuing from a straight nozzle of pseudo-elliptic cross-section into a surrounding flow of uniform velocity was simulated by the vortex method. The aspect ratio of the cross-section was chosen as $L/(2R) = 3{\cdot}0$. The nozzle was vertically arranged on both sides of a plane of symmetry, as shown in figure 5. The flow in the nozzle was produced by arranging three sources of the same strength on the cross-section of the nozzle in the plane of symmetry. The sources were arranged at the centre of gravity of three subdivided cross-sectional regions of the same area.

The straight nozzle was constructed by arranging vortex panels on the surface. Only the part of the nozzle on one side of the symmetry plane was considered, the other being the mirror image. Preliminary calculations showed that the axial velocity

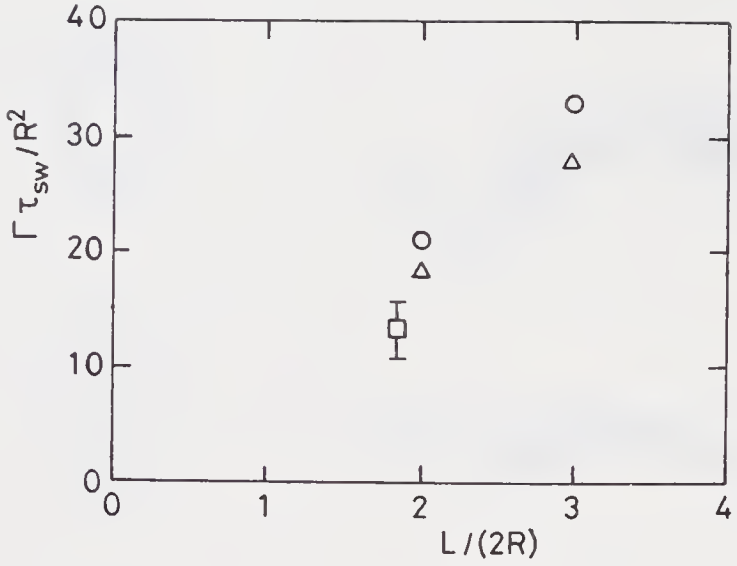

Figure 3. First period of axis switching τ_{sw} as function of aspect ratio $L/(2R)$. ○, Present simulation; Δ, Kiya & Ishii's (1991) simulation on thin vortex rings; □, experiment with $\delta_{cs}/R = 0{\cdot}22$ and $\Gamma/\nu = 3400$ (Kiya *et al* 1992).

distribution in the middle of the nozzle was uniform if its length was greater than $4R$. In this configuration the number of panels was 48 in the circumferential direction and 12 in the axial direction, being 576 in total. The cut-off length of the vortex blobs constructing the surface of the nozzle was $\sigma = 0{\cdot}1R$. This cut-off length gave rise to a boundary-layer-like velocity profile near the surface of the nozzle; the 'boundary-layer' thickness was approximately $0{\cdot}1R$.

The surrounding flow of uniform velocity U_1 was added to the flow produced by the sources and the panels. The resulting velocity of flow in the nozzle is denoted by U_2. The velocities were chosen as $U_2 = 2U_1$. Thus the velocity ratio $\lambda = (U_2 - U_1)/U_m$, where $U_m = (U_1 + U_2)/2$ is the mean velocity, was 2/3.

A vortex blob was introduced into the flow from a point near the edge of the nozzle to simulate the shedding of the boundary-layer vorticity. This nascent vortex blob was part of a vortex panel which constituted the edge of the nozzle. The

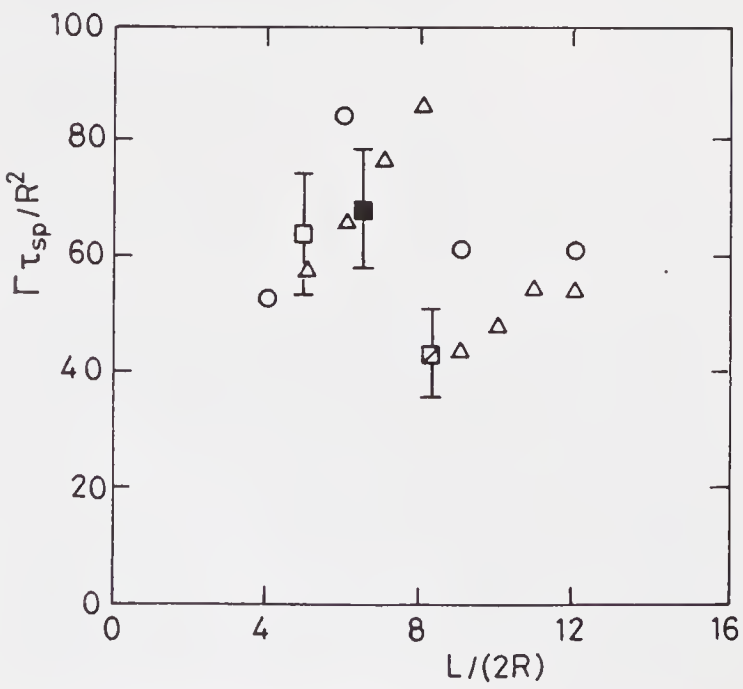

Figure 4. Time of split τ_{sp} as function of aspect ratio $L/(2R)$. ○, Present simulation; Δ, Kiya & Ishii's (1991) simulation on thin vortex rings; □, ■, ▨, experiment (Kiya *et al* 1992).

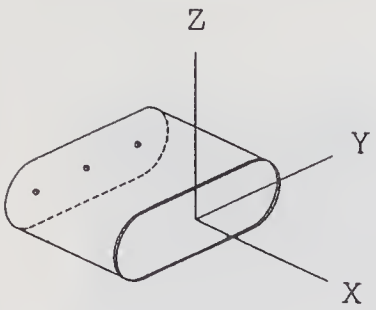

Figure 5. Configuration of pseudo-elliptic nozzle. Circles indicate positions of sources.

centre of the nascent vortex blob was located at $0{\cdot}1R$ downstream of the edge along the side of the nozzle. To satisfy Kelvin's law of conservation of circulation, the circulation of the nascent vortex blob Γ_{sj} at time t was determined from

$$\Gamma_{sj}(t) = \Gamma_j(t) - \Gamma_j(t - \Delta t_s) \tag{19}$$

with $\Gamma_{sj}(0) = \Gamma_j(0)$, where Γ_j is the circulation of the vortex blobs constructing the jth panel and Δt_s is the time step of introducing the nascent vortex. The nascent vortex was advanced by the velocity $\mathbf{v}^s$ induced at its centre which is given by

$$\mathbf{v}^s = -\frac{1}{4\pi}\sum_j\sum_i \frac{(\mathbf{x}^s - \mathbf{x}^{(j,i)}) \times \boldsymbol{\gamma}^{(j,i)}}{(|\mathbf{x}^s - \mathbf{x}^{(j,i)}|^2 + \sigma^2_{(j,i)})^{3/2}} - \frac{1}{4\pi}\sum_b \frac{(\mathbf{x}^s - \mathbf{x}^b) \times \boldsymbol{\gamma}^b}{(|\mathbf{x}^s - \mathbf{x}^b|^2 + \sigma_b^2)^{3/2}} + \mathbf{u}^0 \tag{20}$$

where $\mathbf{x}^{(j,i)}$, $\boldsymbol{\gamma}^{(j,i)}$ and $\sigma_{(j,i)}$ are the position, circulation and cut-off length of the ith vortex blob in the jth panel; the vortex blob $\mathbf{b}$ is the vortex blob which was already shed from the edge; $\mathbf{u}^0$ is the sum of the velocities of the surrounding flow and that of the source flow. If $\mathbf{x}^s$ is replaced by an arbitrary position $\mathbf{x}$, the velocity at that position can also be calculated from (20). The time step of advancing the vortex blobs Δt was $U_m \Delta t/R = 0{\cdot}06$. The nascent vortices were introduced at the time interval of $\Delta t_s (= 4\Delta t)$. The vortex blobs were removed from the flow field if they moved more than $20{\cdot}0R$ downstream of the exit of the nozzle. Reynolds number was $2RU_m/\nu = 1{\cdot}3 \times 10^5$. However, this Reynolds number is only nominal because the maximum vorticity of the vortex blobs was set four times its initial value. The global feature of vortex patterns in the jet was basically unchanged when the maximum vorticity was doubled.

Vortex patterns in the xy- and xz-planes visualized by the vortex blobs are shown in figures 6a and b, respectively. The xyz-coordinate is defined in figure 5. The xy- and yz-planes will hereinafter be referred to as the major and minor planes. The solid vertical arrows indicate a particular feature of the vortex-blob distributions. The indicated feature is not the same for the major and minor planes. In the major plane, rib-like structures are formed between two consecutive circumferential rolls indicated by the broken arrows in figure 6a in the developing flow region. The rib-like structures are not evident in more downstream regions. Another interesting feature is the different arrangements of the circumferential rolls in the major and minor planes. In the minor plane the rolls are symmetrically arranged with respect to the centreline of the jet in the developing region, while in the major plane the rolls are antisymmetrically arranged. In more downstream regions the rolls in the minor plane appear to be antisymmetrically arranged.

The jet did not experience the axis switching suggested by the deformation of the single pseudo-elliptic vortex ring with the same aspect ratio. This is because the

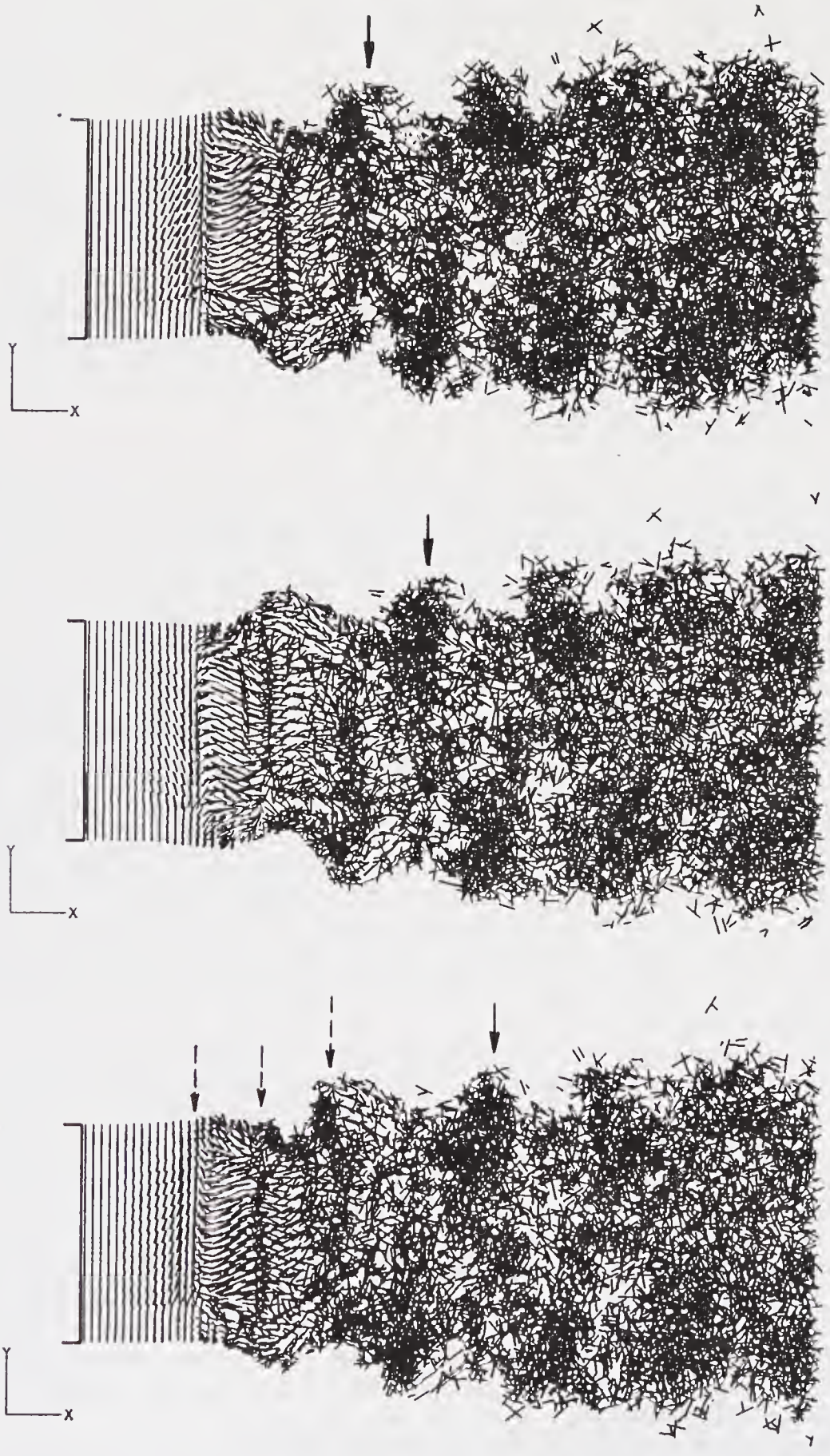

(a)

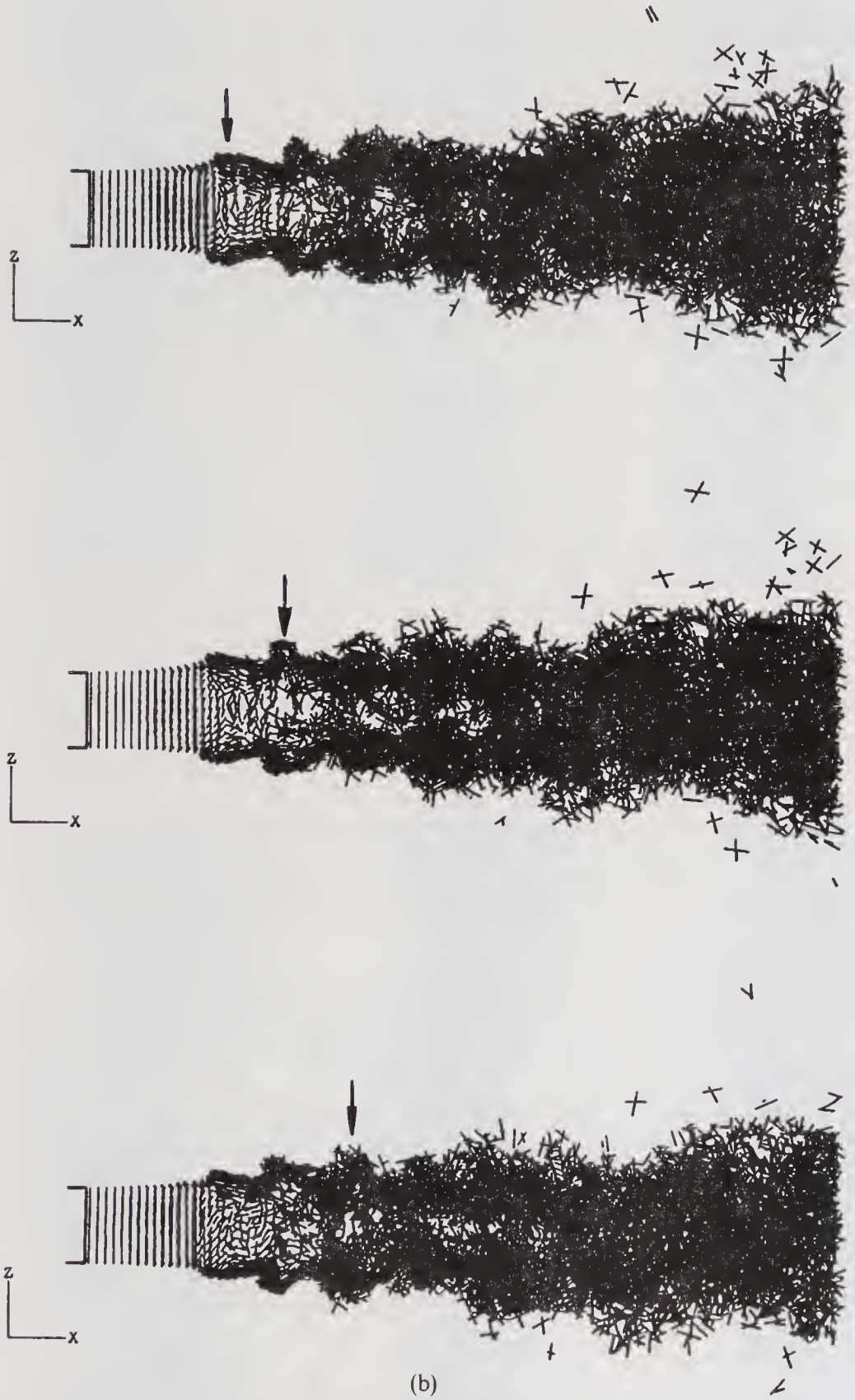

Figure 6. Jet issuing from pseudo-elliptic nozzle of aspect ratio $L/(2R) = 3{\cdot}0$. (**a**) View in xy-plane, (**b**) view in xz-plane. Visualization is made by vortex blobs. Time advances from top to bottom with interval $1{\cdot}6R/U_m$. Solid vertical arrows show motion of particular feature of jet which is different in (**a**) and (**b**), while broken vertical arrows indicate circumferential rolls.

velocity induced by the vortex rings is weaker in the jet than that of the single vortex ring, owing to the surrounding flow. Axis switching is expected for jets with larger velocity ratios λ.

5. Separated flows around a circular disk

The separated flow around a circular disk of radius R with an angle of attack α in uniform flow of velocity U_0 was calculated by a combination of the panel method and the vortex blob method (Ishii 1991). The surface of the disk was represented by 576 panels which consist of vortex blobs. The separated shear layer shed from the circumference of the disk was represented by a collection of vortex rings which were introduced near the edge at an interval of time Δt_s. Each of the vortex rings consists of 36 vortex blobs. The circulation of the blob $\Delta\Gamma$ was calculated from $\Delta\Gamma = (v_s)^2 \Delta t_s$; v_s is the modulus of the velocity vector $\mathbf{v}^s$ at the position $\mathbf{x}^s$ where the nascent vortex blob was introduced into the flow. The velocity vector $\mathbf{v}^s$ was calculated from (20) in which $\mathbf{u}^0$ is the uniform flow velocity.

The nascent vortex blob $\mathbf{x}^s$ was located in the plane of the disk at $0{\cdot}01R$ outside the edge. The cut-off radius of the nascent vortex blob is $0{\cdot}2R$. The time step of introducing the nascent vortex blobs was $U_0 \Delta t_s / R = 0{\cdot}24$; this time step was four times the time step of advancing the shed vortex blobs Δt. The vortex blobs were removed from the flow field if they were more than $10{\cdot}0R$ downstream of the centre of the disk. The maximum vorticity $\xi_{\max}$ of the vortex blobs was set at four times their initial value to avoid the divergence of vorticity. The global feature of vortex patterns in the wake was basically unchanged when the maximum vorticity was doubled. The nominal Reynolds number was $1{\cdot}3 \times 10^5$.

Figure 7 shows flow patterns visualized by distributions of vortex blobs for the disk normal to the main flow ($\alpha = 90°$). The columnar and spiral modes of instability of the wake (Berger *et al* 1990) seem to be reproduced by the present simulation. The modes appear as the shrinkage and enlargement of the near wake and the spiral-like pattern in the intermediate wake.

Figure 8 for the disk with the angle of attack $\alpha = 45°$ suggests the formation of a pair of counter-rotating longitudinal vortices in the near wake. The longitudinal vortices are demonstrated by the time-mean velocity fields in the yz-plane at $x/R = 1{\cdot}0$ and $2{\cdot}0$ (figure 9). The time-mean velocities and Reynolds normal stresses in the near wake for $\alpha = 90°$ have physically reasonable distributions, as shown in figure 10. A slight asymmetry of the distributions is due to insufficient interval of integration for averaging. Figure 11 shows distributions of the time-mean velocity components in the near wake for $\alpha = 45°$. These rather complicated distributions can be interpreted in terms of the vortex patterns in the near wake of figure 8.

Forces acting on the disk are expected to be obtained by modifying the formula of Karo & Nakaya (1990) for the present vortex blob method.

6. Interacting vortex rings

Turbulence is envisaged as a large number of interacting vortex filaments. The energy cascade at high wavenumbers is believed to be independent of viscosity, and thus, the Kolmogorov spectrum is expected to be obtained from interacting inviscid vortex

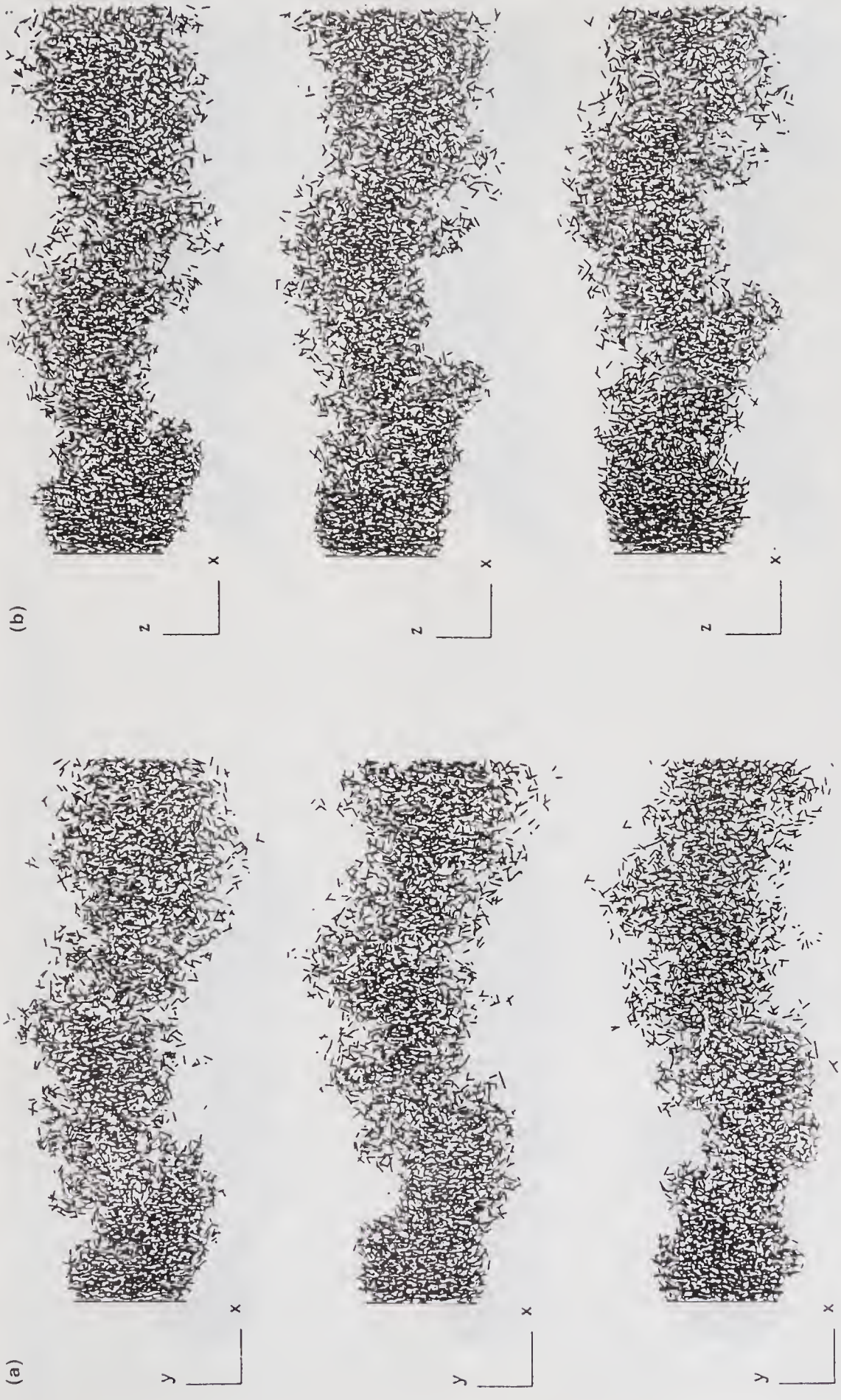

Figure 7. Wake of circular disk with attack angle $\alpha = 90°$. (**a**) View in xy-plane, (**b**) view in xz-plane. Visualization is made by vortex blobs. Time advances from top to bottom with interval $1{\cdot}2R/U_0$. Origin of xyz-coordinate is at centre of disk.

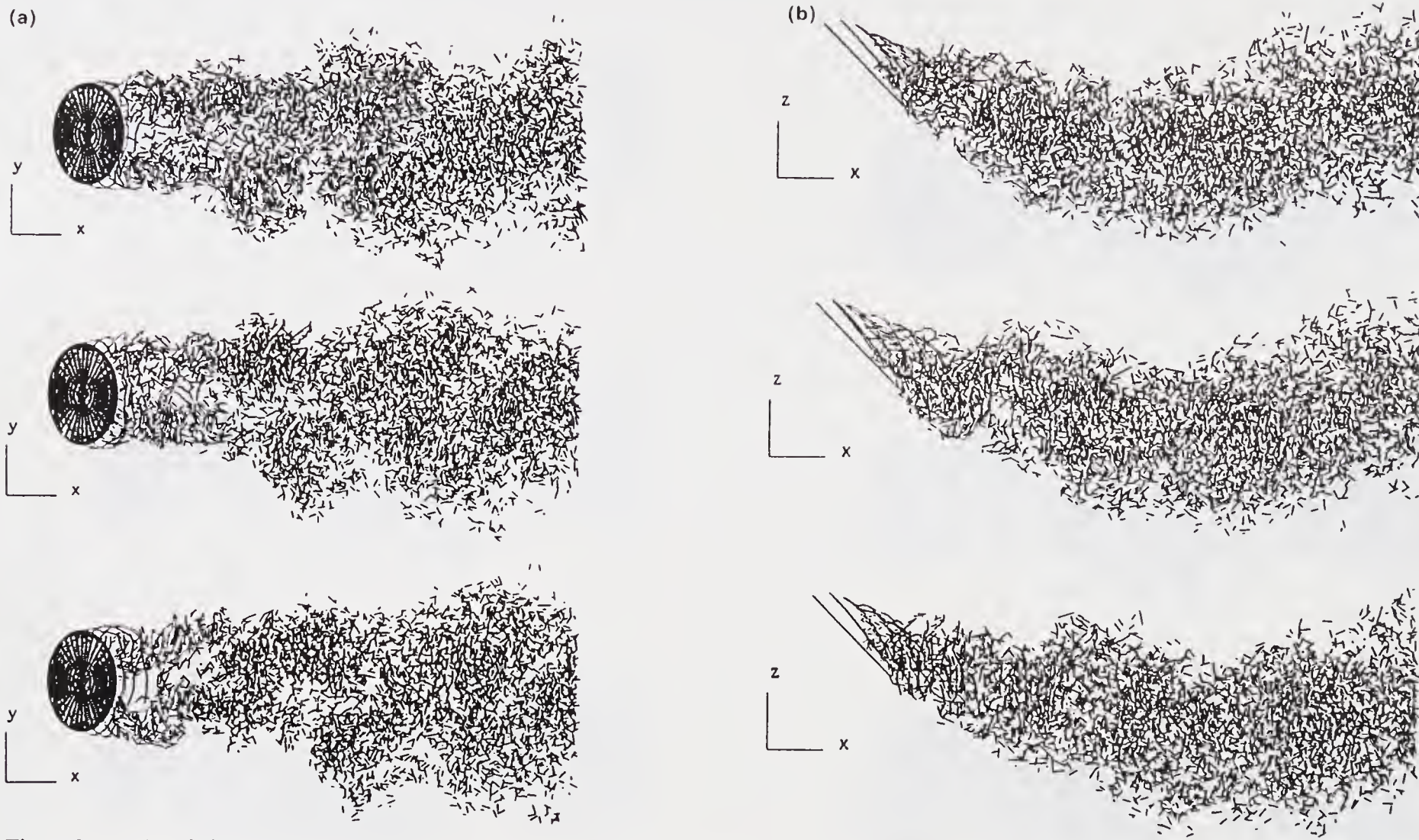

Figure 8. Wake of circular disk with attack angle $\alpha = 45°$. (**a**) View in xy-plane, (**b**) view in xz-plane. Visualization is made by vortex blobs. Time advances from top to bottom with interval $1{\cdot}2R/U_0$. Origin of xyz-coordinate is at centre of disk.

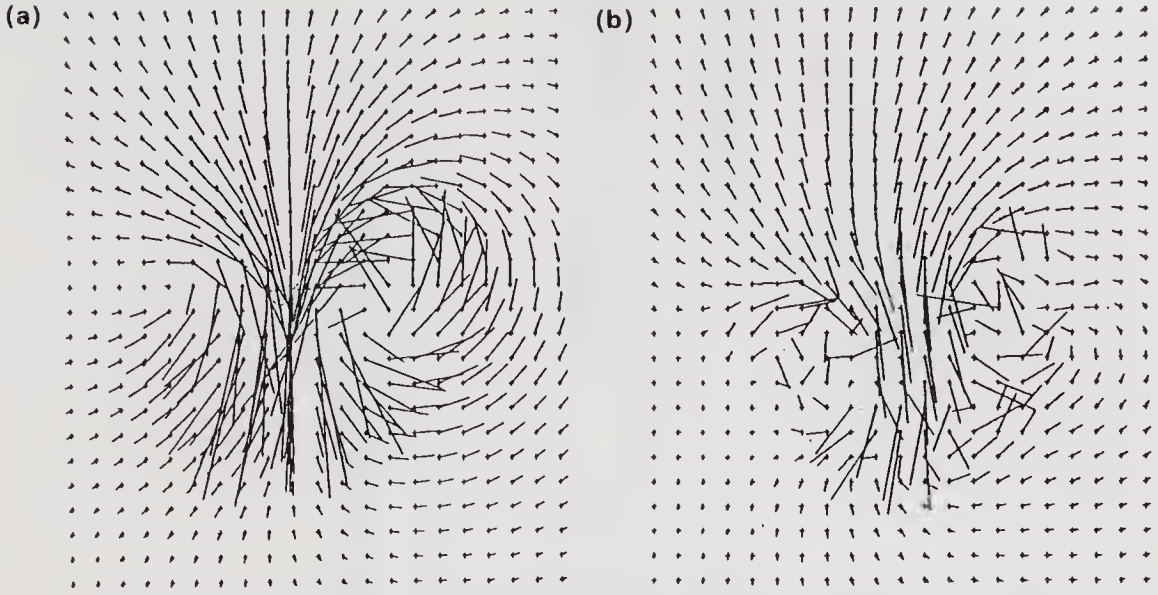

Figure 9. Time-mean velocity vector field in *yz*-plane of wake of circular disk with attack angle $\alpha = 45°$ at (**a**) $x/R = 1{\cdot}0$ and (**b**) 2·0, indicating counter-rotating longitudinal vortices.

filaments. It is worth noting that six interacting elliptic vortex rings produced an energy spectrum which is in excellent agreement with that of a homogeneous turbulence (Leonard 1985). Chorin (1982) demonstrated that a perturbed vortex filament in a periodic box produced the Hausdorff dimension of approximately 2·5, which corresponds to the $-5{\cdot}5/3$ power spectrum.

Lundgren (1982) showed that the Kolmogorov spectrum is a result of the strained spiral vortex due to the differential rotation caused by the central core. On the other hand, recent direct numerical simulations of homogeneous turbulence demonstrate that the tube-like 'worms' of high vorticity are a common feature of turbulent flows (Jimenez 1992). Hussain (1992, pp. 805–814) showed that spiral structures do exist but they are rod-like structures which are quite different from the spiral sheet-like ones proposed by Lundgren (1982). Thus the present author assumes that the worms, or swarms in the terminology of Yamamoto & Hosokawa (1988), are agents which are responsible for the Kolmogorov spectrum. There is a suggestion, however, that weaker vorticity will be drawn in around a strong stretching vortex in a spiral flow (Ashurst *et al* 1987).

The purpose of studying interacting vortex rings in this section is to find out whether the interaction really reproduces the Kolmogorov spectrum on the assumption that the common features of small-scale turbulence are worms of high vorticity. In this simulation four to eight circular vortex rings were arranged on the surface of regular polyhedrons to compute their interaction at later times (Kiya & Ishii 1991). The interaction was found to produce smaller and smaller length scales of high vorticity regions, giving rise to a wavenumber range in which the Kolmogorov spectrum is approximately realized.

Calculations were performed for circular vortex rings of the same radius R and of the same circulation Γ. A cross-section of the vortex rings consisted of one vortex blob, and the circumference was divided into a number of such sections. The initial values of the cut-off length σ were chosen as $0{\cdot}10R$ and $0{\cdot}20R$. The time step Δt for

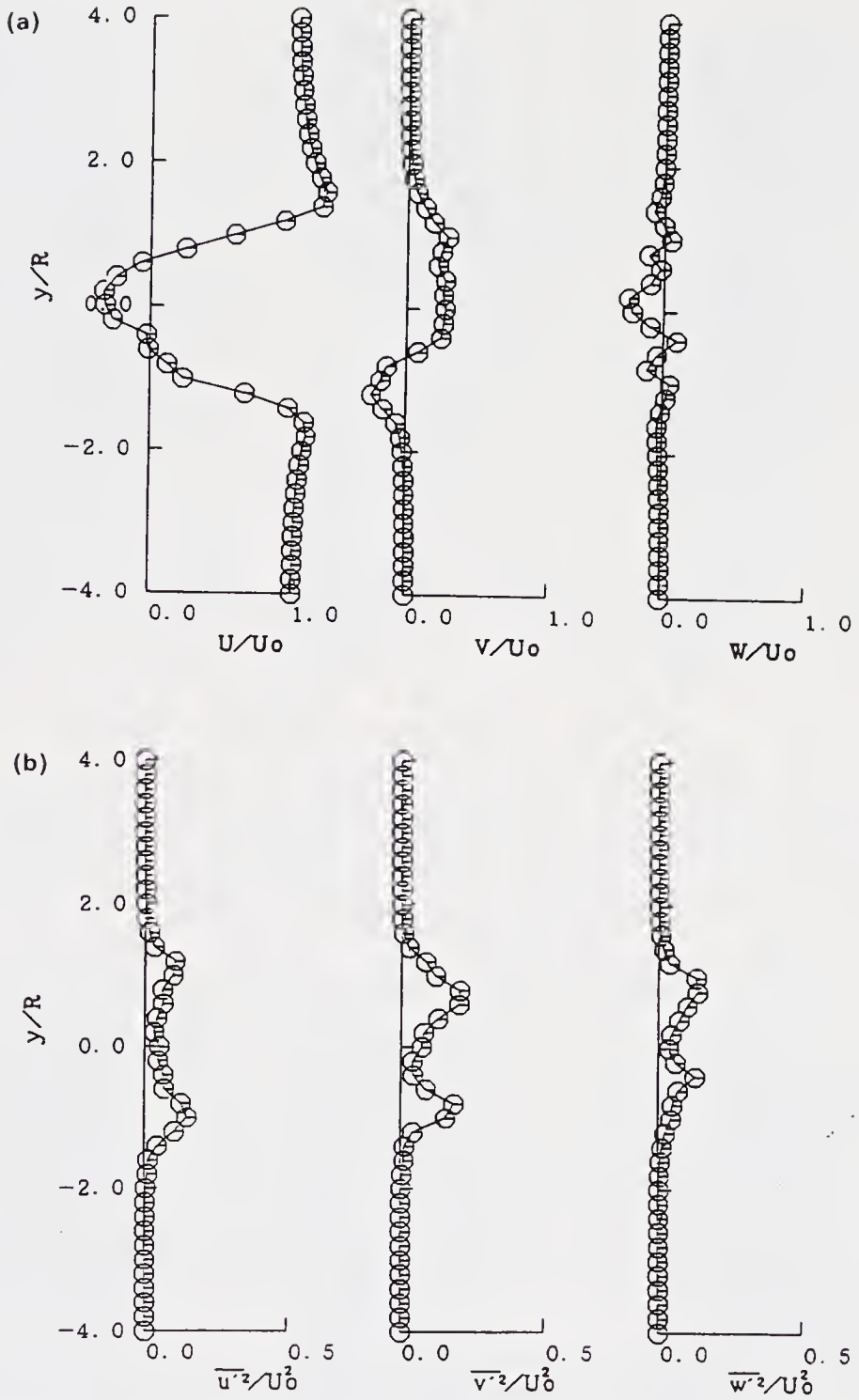

Figure 10. Distributions of (**a**) time-mean velocity components U, V, W in x-, y-, z-directions, and (**b**) corresponding normal Reynolds stresses $\bar{u}'^2$, $\bar{v}'^2$, $\bar{w}'^2$ in yz-plane at $x/R = 1{\cdot}0$ along y-axis. Attack angle $\alpha = 90°$.

advancing the vortex blobs was $\Gamma\Delta t/R^2 = 0{\cdot}00186$ and $0{\cdot}0027$ for $\sigma/R = 0{\cdot}10$ and $0{\cdot}2$, respectively. The smoothing function employed in this study was of the Rosenhead–Moore type $g(y) = y^3(y^2 + a)^{-3/2}$ with $a = 0{\cdot}4131$. The viscous term of (13) was not included. At the same time no upper limit of vorticity was set.

Figure 12 shows the deformation of four vortex rings initially arranged on the surface of a cube. The initial configuration of the vortex rings is shown in figure 12a.

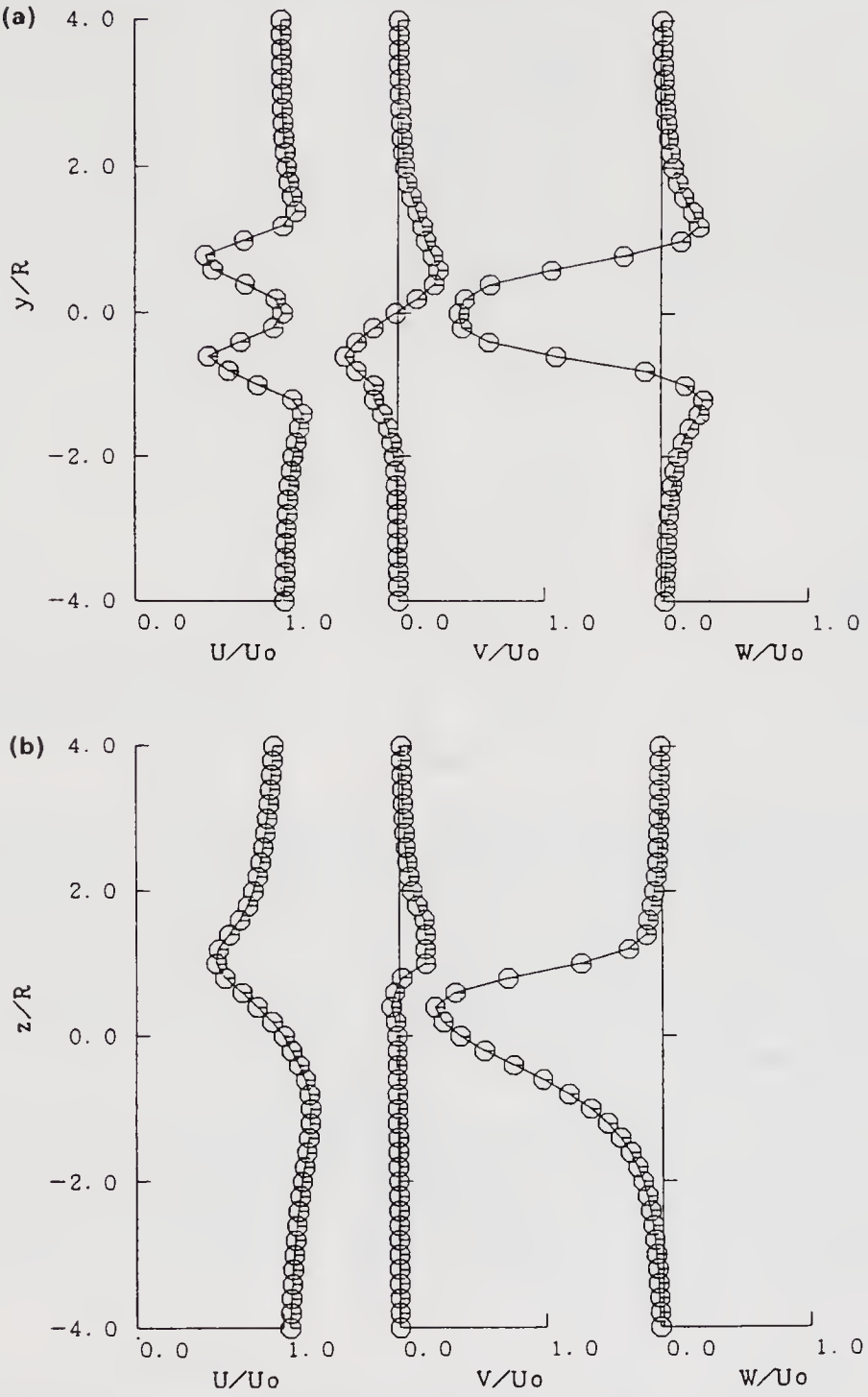

Figure 11. Distributions of time-mean velocities U, V, W in yz-plane at $x/R = 1{\cdot}0$ (**a**) along y-axis, and (**b**) along z-axis. Attack angle $\alpha = 45°$.

The interaction produces entanglement of two neighbouring vortex rings to produce regions of high vorticity. Another example of deformation is presented in figure 13 for six vortex rings initially arranged on the cube. Regions of high vorticity are indicated in figure 13c.

Figure 14 shows evolution of the energy and enstrophy spectra for four vortex rings initially arranged on the surface of the cube for $\sigma/R = 0{\cdot}10$. The energy spectrum E is seen to have an approximate $-5/3$ power law over approximately 1·5 decades at the non-dimensional time $\Gamma t/R^2 = 1{\cdot}353$. The enstrophy spectrum has the 1/3

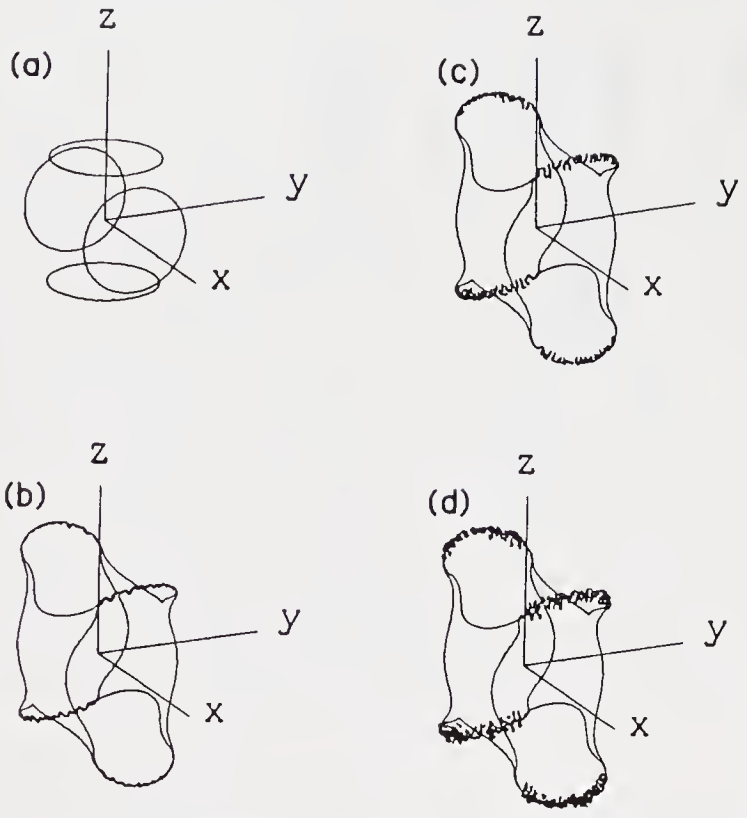

Figure 12. Interaction of four vortex rings of $\sigma/R = 0{\cdot}10$, initially arranged on surface of cube. $\Gamma t/R^2 = 0{\cdot}0$ (**a**), 1·297, (**b**) 1·334, (**c**) 1·364 (**d**).

power law in the same range. The rapid decay of the spectra at high wavenumbers is due to the cut-off structure of the vortex blobs, which is akin to filtering out high-wavenumber components. Figure 15 summarizes the energy spectra for different initial configurations of the vortex rings with $\sigma/R = 0{\cdot}10$, demonstrating that the approximate Kolmogorov spectrum is realized for all the initial configurations. The main difference between the results for $\sigma/R = 0{\cdot}10$ and $\sigma/R = 0{\cdot}20$ was that the wavenumber range of the $-5/3$ power law was narrower for the thicker cut-off length than for the thinner cut-off length.

The results of the present calculations strongly suggest that the statistical properties of velocity fields associated with interacting multiple vortices have much in common with those of homogeneous turbulence. Whether this supposition is correct or not can be settled, for example, by repeating similar calculations for a wide range of initial configurations of vortices.

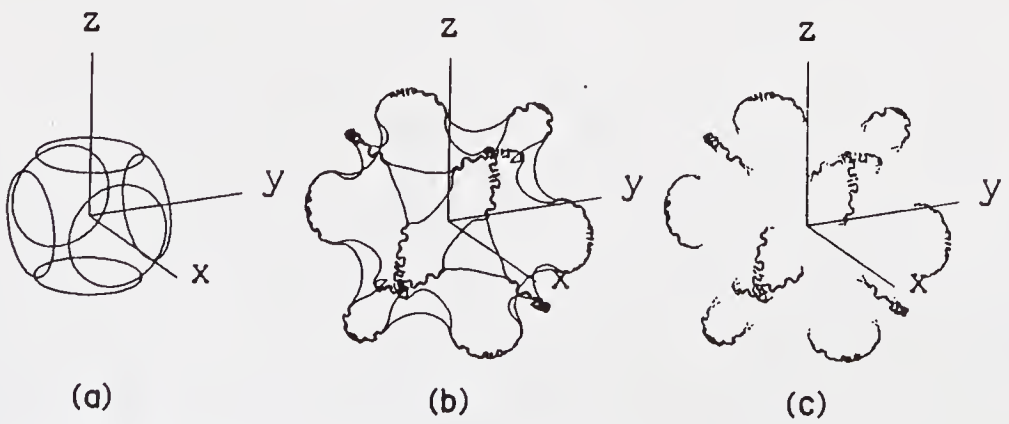

Figure 13. Interaction of six vortex rings of $\sigma/R = 0{\cdot}10$ initially arranged on surface of cube. $\Gamma t/R^2 = 0{\cdot}0$ (**a**), 1·334 (**b**); (**c**) high-vorticity region at $\Gamma t/R^2 = 1{\cdot}334$.

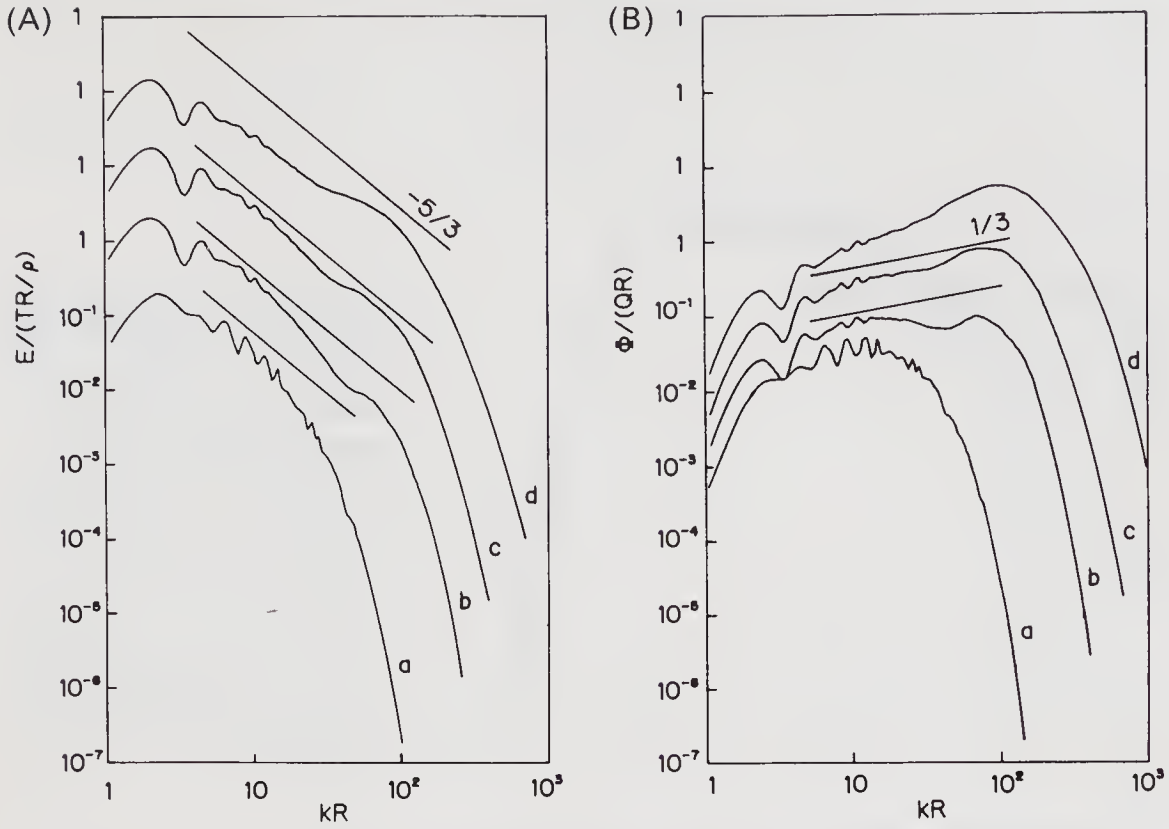

Figure 14. Evolution of energy and enstrophy spectra for interacting four vortex rings of $\sigma/R = 1{\cdot}0$ initially arranged on surface of cube. (**A**) Energy spectra and (**B**) enstrophy spectra [$\Gamma t/R^2 = 0{\cdot}0$ (a), 1·334 (b), 1·353 (c) and 1·364 (d)].

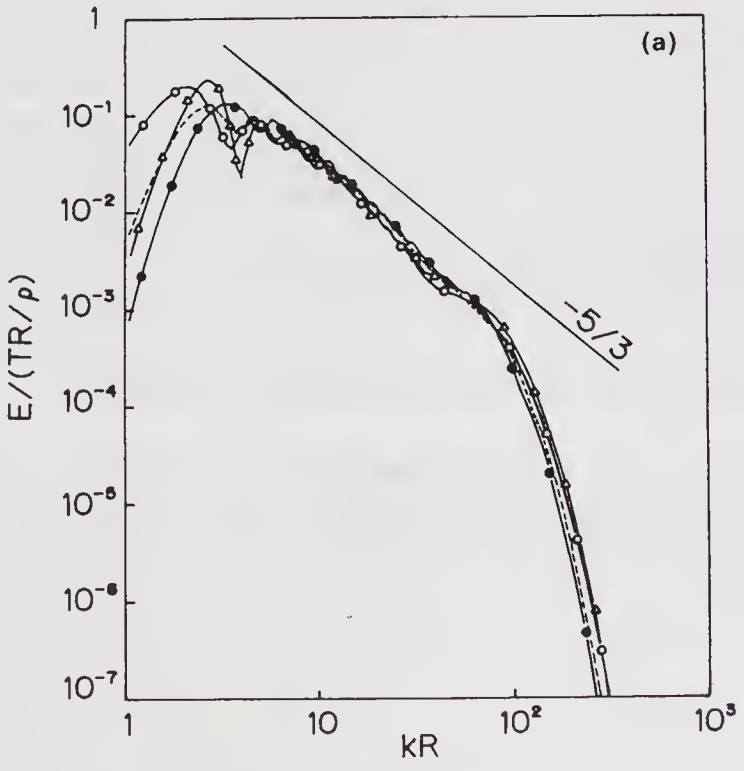

Figure 15. (a) (Caption on next page.)

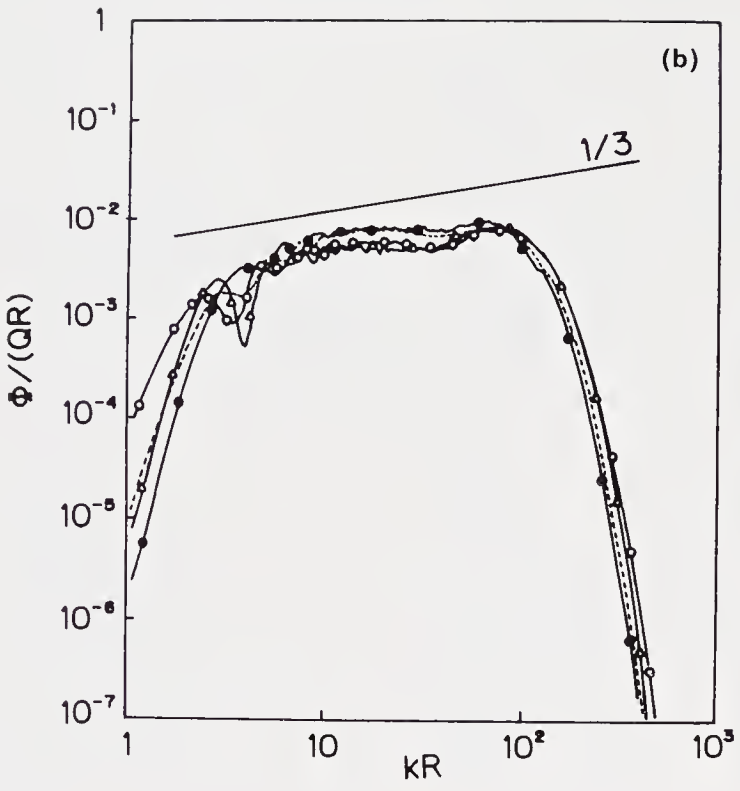

Figure 15. Energy and enstrophy spectra resulting from interaction of vortex rings of $\sigma/R = 0{\cdot}10$ with different initial configurations. (**a**) Energy spectra and (**b**) enstrophy spectra. ○, Four vortex rings on cube ($\Gamma t/R^2 = 1{\cdot}334$); – – –, four vortex rings on tetrahedron ($\Gamma t/R^2 = 1{\cdot}473$); ●, six vortex rings on cube ($\Gamma t/R^2 = 1{\cdot}336$); △, eight vortex rings on octahedron ($\Gamma t/R^2 = 1{\cdot}186$). Times were so chosen that spectra have approximately the same decay at high wavenumbers.

7. Concluding remarks

The vortex blob method has been demonstrated to be a useful means to simulate three-dimensional vortex motion. Vorticity of the vortex blobs has a tendency to diverge at a certain time after the start of interaction of inviscid vortex filaments. This perhaps corresponds to the supposition that vorticity fields governed by the Euler equations diverge within a finite time (Siggia 1985). The divergence of vorticity appeared even when the viscous diffusion of vorticity was included by the method suggested by Winckelmans & Leonard (1989, pp. 25–35). Thus we conjecture that this method might possibly fail to simulate the balance between the intensification of vorticity by vortex stretching and the viscous diffusion of vorticity. This balance can approximately be simulated by imposing a maximum value on vorticity of vortex blobs existing in the flow field. This maximum value is a function of the initial vorticity, the local rate of strain, the square of core radius, and the kinematic viscosity.

Appendix A. Expressions for the properties of vortex motion

In this appendix, the total vorticity, linear and angular impulses, Fourier transforms of the velocity and vorticity fields, the kinetic energy, the enstrophy, the helicity and their power spectra will be presented for the core structure of Winckelmans & Leonard (1989, pp. 25–35).

The total vorticity $\boldsymbol{\Omega}$, the linear impulse $\mathbf{I}$ and the angular impulse $\mathbf{A}$ are given by

$$\boldsymbol{\Omega} = \int \boldsymbol{\xi} \mathrm{d}\mathbf{x} = \sum_a \boldsymbol{\gamma}^a, \tag{A1}$$

$$\mathbf{I}/\rho = \int \mathbf{x} \times \boldsymbol{\xi} \mathrm{d}\mathbf{x} = \sum_a \mathbf{x}^a \times \boldsymbol{\gamma}^a, \tag{A2}$$

$$\mathbf{A}/\rho = (1/3)\int \mathbf{x}\times(\mathbf{x}\times\xi)\mathrm{d}\mathbf{x} = (1/3)\sum_a \mathbf{x}^a\times(\mathbf{x}^a\times\gamma^a) - (1/3)\sum_a \sigma_a^2\gamma^a. \tag{A3}$$

Fourier transform of the velocity vector $\mathbf{u}^a(\mathbf{x},t)$ is

$$\mathbf{U}^a(\mathbf{k},t) = \int \mathbf{u}^a(\mathbf{x},t)\mathrm{e}^{-i\mathbf{k}\cdot\mathbf{x}}\mathrm{d}\mathbf{x} = (1/2)i\sigma_a^2 K_2(\sigma_a k)(\mathbf{k}\times\gamma^a)\mathrm{e}^{-i\mathbf{k}\cdot\mathbf{x}a} \tag{A4}$$

where K_2 is the modified Bessel function of the second kind. Fourier transform of the vorticity vector $\xi^a(\mathbf{x},t)$ is

$$\mathbf{\Omega}^a(\mathbf{k},t) = \int \xi^a(\mathbf{x},t)\mathrm{e}^{-i\mathbf{k}\cdot\mathbf{x}}\mathrm{d}\mathbf{x} = (1/2)i\sigma_a^2 k^2 K_2(\sigma_a k)\gamma^a\mathrm{e}^{-i\mathbf{k}\cdot\mathbf{x}a} \tag{A5}$$

Total energy $T(t)$ and energy spectrum $E(k,t)$ are given by

$$T(t)/\rho = \int (1/2)\mathbf{u}\cdot\mathbf{u}\,\mathrm{d}\mathbf{x} = \int E(k,t)\mathrm{d}k. \tag{A6}$$

The spectrum $E(k,t)$ is the sum of the self energy E_{aa} and the interaction energy E_{ab}:

$$E(k,t) = \sum_a E_{aa}(k,t) + \sum_{a,b} E_{ab}(k,t), \tag{A7}$$

where

$$E_{aa}(k,t) = (1/24\pi^2)\sigma_a^2 k^4[K_2(\sigma_a k)]^2(\gamma^a\cdot\gamma^a), \tag{A8}$$

$$E_{ab}(k,t) = (1/16\pi^2)\sigma_a^2\sigma_b^2 k^4 K_2(\sigma_a k)K_2(\sigma_b k|) \times\{(\gamma^a\cdot\gamma^b)\phi_1(kr_{ab}) + (\gamma^a\cdot(\mathbf{r}^{ab}/r_{ab}))(\gamma^b\cdot(\mathbf{r}^{ab}/r_{ab})|)\phi_2(kr_{ab}|)\}. \tag{A9}$$

where

$$\phi_1(z) = z^{-3}[(z^2-1)\sin z + z\cos z],$$

$$\phi_2(z) = z^{-3}[(3-z^2)\sin z - 3z\cos z].$$

Enstrophy $Q(t)$ and enstrophy spectrum $\Phi(k,t)$ are given by

$$Q(t) = \int (1/2)\xi\cdot\xi\,\mathrm{d}\mathbf{x} = \int_0^\infty \Phi(k,t)\mathrm{d}k, \tag{A10}$$

where Φ is the sum of the self part Φ_{aa} and the interaction part Φ_{ab}:

$$\Phi(k,t) = \sum_a \Phi_{aa}(k,t) + \sum_{a,b}\Phi_{ab}(k,t), \tag{A11}$$

where

$$\Phi_{aa}(k,t) = (1/16\pi^2)\sigma_a^4 k^6[K_2(\sigma_a k)]^2(\gamma^a\cdot\gamma^a), \tag{A12}$$

$$\Phi_{ab}(k,t) = (1/16\pi^2)\sigma_a^2\sigma_b^2 K_2(\sigma_a k)K_2(\sigma_b k)[k^5\sin(kr_{ab})/r_{ab}](\gamma^a\cdot\gamma^b|). \tag{A13}$$

Helicity $H(t)$ and the helicity spectrum $F(k,t)$ are given by

$$H(t) = \int (1/2)\mathbf{u}\cdot\xi\,\mathrm{d}\mathbf{x} = \int_0^\infty F(k,t)\mathrm{d}k. \tag{A14}$$

The helicity spectrum F consists of only the interaction part F_{ab} such as

$$F(k,t) = \sum_{a,b} F_{ab}(k,t), \tag{A15}$$

where

$$F_{ab}(k,t) = -(1/8\pi^2)\sigma_a^2\sigma_b^2 k^4[\cos kr_{ab} - (\sin kr_{ab})/kr_{ab})] \times K_2(\sigma_a k)K_2(\sigma_b k)(\boldsymbol{\gamma}^a \times \boldsymbol{\gamma}^b)\cdot \mathbf{r}^{ab}. \quad \text{(A16)}$$

References

Ashurst Wm T, Kerstein A R, Kerr R M, Gibson C H 1987 Alignment of vorticity and scalar gradient with strain rate in simulated Navier–Stokes turbulence. *Phys. Fluids* 30: 2343–2353

Batchelor G K 1967 *An introduction to fluid dynamics* (Cambridge: University Press)

Berger E, Scholz D, Schumm M 1990 Coherent vortex structures in the wake of a sphere and a circular disk at rest and under forced vibrations. *J. Fluids Struc.* 4: 231–257

Chorin A J 1973 Numerical study of slightly viscous flow. *J. Fluid Mech.* 57: 785–796

Chorin A J 1982 The evolution of a turbulent vortex. *Comput. Math. Phys.* 83: 517–535

Hussain F 1992 Understanding turbulence via vortex dynamics: some new perspectives. *Proc. Fifth Asian Cong. Fluid Mech.* (eds) K-S Chang, D H Choi (Taejon, Korea: Dept. of Aerosp. Eng., KAIST)

Ishii H 1991 *Numerical analysis of three-dimensional vortex motion by vortex methods*, Ph D thesis, Hokkaido University (in Japanese)

Jimenez J 1992 Kinematic alignment effects in turbulent flows. *Phys. Fluids* A4: 652–654

Karo T, Nakaya H 1990 A formulation of unsteady forces with a three-dimensional discrete vortex method. *Trans. JSME* B56: 396–401 (in Japanese)

Kiya M, Ishii H 1991 Vortex interaction and Kolmogorov spectrum. *Fluid Dyn. Res.* 8: 73–83

Kiya M, Matsumura M 1985 Turbulence structure in intermediate wake of a circular cylinder. *Bull. JSME* 28: 2617–2624

Kiya M, Toyoda K, Ishii H, Kitamura M, Ohe T 1992 Numerical simulation and flow-visualization experiment on deformation of pseudo-elliptic vortex rings. *Fluid Dyn. Res.* 10: 117–131

Knio O M, Ghoniem A F 1990 Numerical study of a three-dimensional vortex method. *J. Comput. Phys.* 86: 75–106

Leonard A 1980 Vortex methods for flow simulation. *J. Comput. Phys.* 37: 289–335

Leonard A 1985 Computing three-dimensional incompressible flows with vortex filaments. *Annu. Rev. Fluid Mech.* 17: 523–559

Lundgren T S 1982 Strained spiral vortex model for turbulent fine structure. *Phys. Fluids* 25: 2193–2203

Sethian J A 1990 A brief overview of vortex methods. PAM-495, University of California, Berkeley

Shirayama S, Kuwahara K, Mendez R 1985 A new three-dimensional vortex method. AIAA Paper 85–1488

Siggia E D 1985 Collapse and amplification of vortex filament. *Phys. Fluids* 28: 794–805

Toyoda K, Hussain F 1989 A study of vortical structure of non-circular jets. *Trans. JSME* B55: 1452–1545 (in Japanese)

Widnall S E 1975 The structure and dynamics of vortex filaments. *Annu. Rev. Fluid Mech.* 7: 141–165

Winckelmans G, Leonard A 1989 Improved vortex methods for three-dimensional flows. *Mathematical aspects of vortex dynamics* (ed.) R E Caflish (Philadelphia: SIAM)

Winckelmans G, Leonard A 1993 Contributions to vortex particles methods for the computation of three-dimensional incompressible unsteady flows. *J. Comput. Phys.* (submitted)

Yamamoto K, Hosokawa I 1988 A decaying isotropic turbulence pursued by the spectral method. *J. Phys. Soc. Jpn.* 57: 1532–1535

Three-dimensional flow separation

V C PATEL

Department of Mechanical Engineering & Iowa Institute of Hydraulic Research, The University of Iowa, Iowa City, Iowa 52242-1585, USA

Abstract. Separation of three-dimensional flow, although much more common than its two-dimensional counterpart, has defied precise description and definition in spite of numerous attempts. Here, we briefly review the grammar that is used to describe various facets of the phenomenon, and use some recent numerical and experimental results to illustrate the outstanding difficulties of the subject.

Keywords. Three-dimensional flow separation; flow visualization; kinematic and dynamic complications.

1. Introduction

Practically all fluid flows are three-dimensional and, among these, few are free from separation. In fact, no flow can properly be described without considering the possibilities of separation and attendant unsteadiness. While the topic of three-dimensional flow separation is of interest in a vast array of fields and many aspects of the problem are common to them all, here we shall concentrate on certain basic aspects of flow structure. For this purpose, we need not distinguish between laminar and turbulent flows even though the most common ones are turbulent. Similarly, distinction between internal and external flows is also of little consequence. Separation from sharp edges and separated flows, *per se*, including the dead horse, the backward-facing step, are also excluded.

In two-dimensional flow, the criterion or definition of separation is the vanishing of skin friction or wall shear. Unfortunately, such a precise and simple definition is not possible in a three-dimensional flow, because one additional space dimension leads to flow states which are inconceivable in two dimensions. Three-dimensional flow separation has attracted a great deal of attention but the kinematic and dynamic complications of three-dimensional flows are so formidable that the phenomenon is still beyond the reach of definitive theoretical analyses or numerical calculations. The situation in experimental studies is not much better. Detailed measurements in three-dimensional separated flows are rare because of limitations of instrumentation, on the one hand, and the immense amount of information that is required for proper documentation and resolution of such flows, on the other. Laser-Doppler velocimetry (LDV), particle-image velocimetry (PIV), and holography have yet to develop the necessary resolution capabilities. Up to the present time, flow visualization in the

laboratory has been the most popular method in the study of separation in three-dimensional flows. Indeed, flow visualization, although qualitative and sometimes ambiguous, has contributed the most to our knowledge of the subject.

A number of criteria or definitions have been proposed for three-dimensional flow separation, each of which emphasizes one particular symptom or another to characterize the whole phenomenon. Often, different terms are used to describe the same flow feature, and there is as yet no unified, clear definition. However, it is generally recognized that separation is that phenomenon by which the vorticity generated in the boundary layer near the surface is ejected into the mainstream.

2. Concepts from topology

In three dimensions, flow phenomena such as flow reversal, shear layers, and vortices can often be very difficult to identify and describe, especially if the flow is unsteady. Understanding complex kinematics and devising a proper means to describe it clearly is as important as developing physical models reflecting the dynamics of flow separation. The kinematic aspects of many complex flows, observed in experiments or calculations, are best described by specifying the flow topology using the concepts of *singular* or *critical* points, usually on the basis of the velocity or the wall-shear-stress (or skin-friction) vector field.

Singular points are the salient features of continuous vector fields. A *vector field* is mathematically defined as a map which assigns to each point in the field a vector (e.g., wall shear stress, velocity, vorticity). A *continuous vector field* has the property that at any regular (nonsingular) point in the field there is one, and only one, field line (e.g., friction line, streamline, vortex line) which passes through that point. A singular point is one at which the magnitude of the vector is zero, and its direction accordingly is indeterminate. A finite number of singular points may occur within a vector field. Singular points are classified mathematically according to the behaviour of the field lines in their vicinity, and have been extensively explored in the theory of ordinary differential equations in connection with phase-plane studies.

The ideas of a continuous vector field are applicable to the limiting streamlines or skin-friction lines on a body, and also to the flow above the body surface. Singular points are classified into two main types, nodal points (N) and saddle points (S). Nodal points may be further subdivided into nodes and foci (spiral nodes). In the flow over a surface, an infinite number of friction lines are directed either into or away from a node. If the friction lines spiral into or out of a node, it is called a focus. Nodes or foci with friction lines directed into them correspond to points of flow detachment or separation (N_s), and those with friction lines directed outward are points of flow attachment (N_a). A saddle point has two common friction lines, called *separatrices*, which intersect at the point, one of which is directed toward and the other away from the singular point. All other neighbouring friction lines are asymptotic to these separatrices.

Singular points in friction lines are observed in surface-flow visualizations, and are among the most prominent features looked for in numerical solutions. The questions that follow naturally are: what types of singular points occur in a given flow, where they are located, and how they are connected to one another. The study of flow topology in terms of these singular points provides a language that enables complex three-dimensional flow patterns to be described and interpreted in a systematic

manner, whether they are obtained from experiments or computations. Furthermore, theories of topology of continuous vector fields provide the rules which apply to flows that are kinematically possible. Tobak & Peake (1982) summarize the following two rules for skin-friction lines on bodies:

$$\sum N - \sum S = 2, \tag{1}$$

for skin-friction lines on an isolated closed body; and

$$\sum N - \sum S = 0 \tag{2}$$

for skin-friction lines on a closed three-dimensinal body connected simply to a plane wall, where N and S denote nodal (node or focus) and saddle points, respectively.

It is also customary to examine three-dimensional flow fields by plotting (projections of) streamlines in certain cross-sections of the flow or in symmetry planes. Although these provide limited (and sometimes distorted) views of the total three-dimensional flow, the streamline fields bear a certain topological resemblance to the skin-friction field, and therefore, topological laws are frequently applied to them also. Thus, for flow streamlines in a crossflow plane or in a symmetry plane cutting a three-dimensional body, Tobak & Peake (1982) give the following topological law:

$$\left(\sum N + \tfrac{1}{2}\sum N'\right) - \left(\sum S + \tfrac{1}{2}\sum S'\right) = -1 \tag{3}$$

where N′ and S′ denote half-nodes and half-saddles, which arise at intersections of the planes with the body. It should be noted here that a point that appears as a singularity (N or S) in such cross-sectional views is not a singular point of the velocity-vector field because the velocity in the direction normal to the plane of view is not necessarily zero.

The topological concepts and their relation with the flow separation are summarized in a recent article by Chapman & Yates (1991). On the basis of topology, they identify three basic types of separation.

(i) Type I separation, illustrated in figure 1. Such a separation originates at a saddle point (S_s) of the skin-friction lines and the fluid surface of separation rolls up to form a vortex. The vortex centre (N) is a spiral node (focus) in the streamlines viewed in the plane of symmetry. The separation line (the friction line on the body originating from the saddle point S_s) divides the body surface into separate regions, and therefore, a node of attachment (N_a) is required to allow fluid into the separated region.
(ii) Type II separation, illustrated in figure 2. Such a separation also originates at a saddle point (S_s) of the skin-friction lines but there is no singular point in the flow. Instead, such a separation leads to vortices with origins at the spiral nodes (N_s) of the skin-friction lines. The separation line (the friction line on the body originating from the saddle point S_s) does not divide the body surface into separate regions.
(iii) Crossflow separation, illustrated in figure 3. This separation does not originate from a singular point. It is similar to the *open* separation of Wang (1974) and the *local* separation of Tobak & Peake (1982), and not even separation in the terminology of Lighthill (1963, p. 72).

Of practical interest in the study of three-dimensional flow separation is how separation patterns originate and how they succeed each other as some flow parameter, such as the Reynolds number, angle of attack, or body geometry, is varied. The structural changes taking place in the pattern of flow separation as a flow

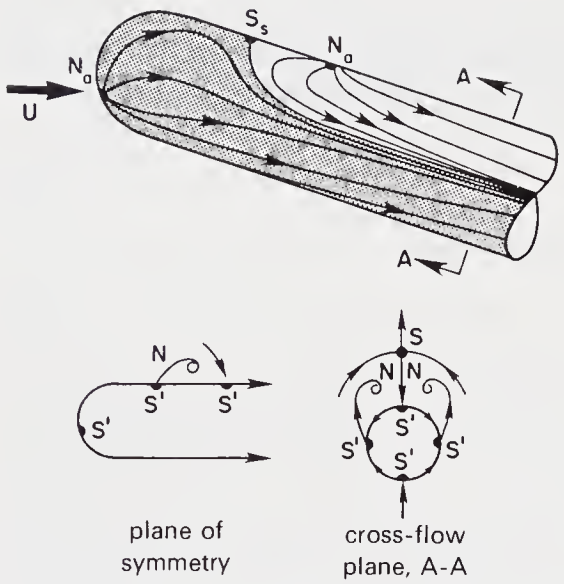

Figure 1. Type I separation (Chapman & Yates 1991).

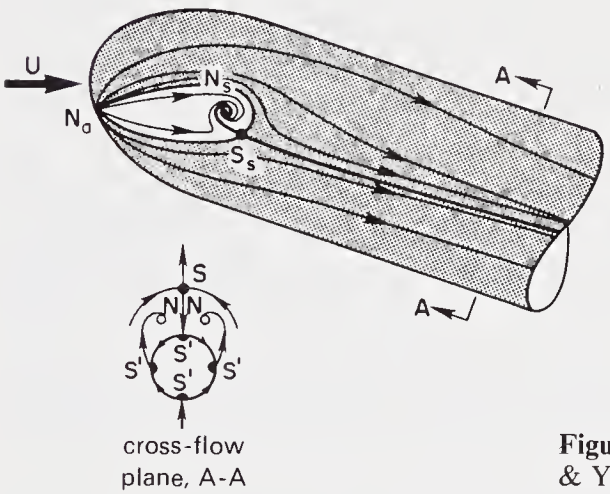

Figure 2. Type II (horn) separation (Chapman & Yates 1991).

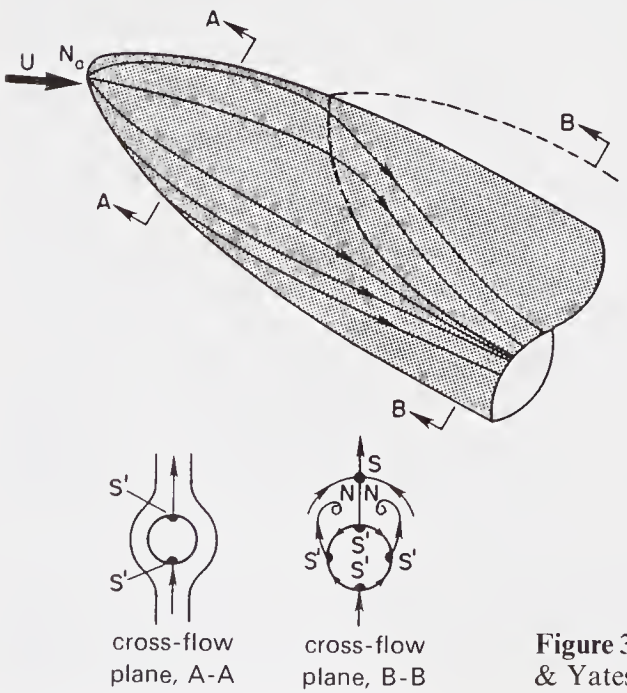

Figure 3. Cross-flow (open) separation (Chapman & Yates 1991).

parameter is varied are explained by introducing the notion of *bifurcation*, which has been one of the main themes in the study of nonlinear dynamical systems. Bifurcations signify a topological change in the flow structure as a flow parameter is varied, and they divide the whole range of the flow parameter being considered into several subranges, to each of which a distinct topological structure of the flow corresponds. Chapman & Yates (1991) discuss other manifestations of the three basic types of separation resulting from structural bifurcations which produce singular points where none existed before (*transcritical bifurcation*), disappearance of singular points (*inverse transcritical bifurcation*), splitting of a singular point into three singular points (*pitch-fork bifurcation*) or coalescence of three singular points into one (*inverse pitch-fork bifurcation*). The resulting flow patterns can be very complex, and whether they are kinematically feasible can be confirmed only by application of the topological laws listed above.

3. Vortices from flow separation

When the flow remains attached to the body surface, vorticity resides only in the thin boundary layer and wake of the body, having been transported there only by viscous diffusion and turbulent mixing. When these are the only mechanisms of vorticity transport, there is no possibility of having a concentrated vortex far from the body surface, other than in the wake. When the flow separates, however, vorticity of the boundary layer is carried away from the body in the form of a shear layer by convection as well as diffusion. In the two-dimensional case, separation leads to flow reversal and recirculation, which is often viewed as a vortex, with its axis parallel to that of the body. Under certain conditions, the vortex detaches periodically to give rise to the phenomenon of vortex shedding. In the three-dimensional case, the separated shear layer may also roll up to form a vortex but neither the point of origin of the vortex nor the location of its axis, can be readily determined, except in some degenerate cases.

It is significant that the three types of separation suggested by Chapman & Yates (1991) result in the formation of longitudinal vortices. In type I separation (figure 1), the focus of the streamlines viewed in the plane of symmetry is connected with the two foci of the streamlines observed in the transverse plane A–A and, together, they indicate the formation of a horseshoe vortex whose core lies at some distance from the body. In type II separation (figure 2), the topological features of the friction lines suggest that tornado-like vortices, attached to the surface, arise out of foci singularities (one on each side of the body) of the friction lines, and these trail into the flow as a vortex pair with cores that appear as foci of the streamlines viewed in the transverse plane. The vortices resulting from these two types of separation are relatively simple to comprehend although they are very difficult to capture precisely in either experiments or computations. The crossflow type of separation (figure 3), which does not involve a singular point in the friction lines, also leads to a vortex pair, and these vortices also appear as a pair of foci in the streamlines viewed in transverse planes. However, their origin is not clearly defined. In fact, the origin of this type of separation and the accompanying vortex is the subject of considerable speculation in the literature, and various criteria have been proposed to identify it.

Figures 1 through 3 illustrate the central difficulty of defining or classifying separation in three-dimensions. It is clear that topological analysis (and correctness) of the flow

pattern in a single cross-section (such as plane A–A in figures 1 and 2, and plane B–B in figure 3), by itself, is not sufficient to identify the type of separation. Here we have examples of what appear to be very similar vortical flow structures emanating from quite different origins. This lack of one-to-one correspondence between the topology of the skin-friction lines on the body surface and the topology of flow streamlines projected in selected planes is rarely appreciated in the application of topological rules to specific cases and is often the cause of differing interpretations of the same flow. Structural bifurcations due to changes in flow parameters introduce additional difficulties, as the following examples will reveal.

4. Separation on a prolate spheroid at incidence

The flow on a prolate spheroid has been the subject of numerous experiments, both physical and numerical. It is an excellent test case for the study of three-dimensional flow separation. However, the experimental as well as computational results are limited in one respect or another, and do not provide unequivocal evidence in support of the types of flow separations that exist under a given set of conditions. For example, even the most careful flow visualizations (see, for example, Han & Patel 1979; Werlé 1985; Wang *et al* 1990) do not reveal details of the vortices and flow features beyond separation. Rapid diffusion of tracers, such as dye and smoke, and unsteadiness of the separated flow are two principal reasons for poor visualizations. Similarly, boundary-layer methods fail at or just ahead of separation, while solutions of the Navier–Stokes equations, or some reduced form of those equations, suffer from approximations, ambiguities in specification of boundary conditions, and insufficient grid resolution. Here we examine the results of a recent numerical study (Kim 1991a; Kim & Patel 1991) of laminar flow over a spheroid of axes ratio 6 to 1 at a Reynolds number of 50,000. These solutions are unique insofar as the full Navier–Stokes equations were solved for the flow over the entire body, including the nose and the tail. Furthermore, solutions were obtained over a range of incidence angles revealing topological changes associated with structural bifurcations.

Figures 4 through 7 show the skin-friction lines constructed from the calculated wall shear–stress vectors for four typical incidence angles, namely, $\alpha = 0$, 5, 10 and 25°. In each case, the conjectured topology of the surface flow pattern is also sketched with the aid of the topological rule (1) for a closed body. The flow features will be discussed by dividing the range of incidences into four rather loosely defined categories, namely, zero, low, intermediate, and high incidences. Although significant changes occur as the incidence angle is increased from one regime to another, the boundaries of the regimes are blurred, and from a purely topological perspective, the distinctions between the regimes may not be necessary.

4.1 *Zero incidence*

Figure 4a indicates that separation occurs at $x/L = 0{\cdot}390$, where x is measured from the centre of the body and L is the body length. This is in agreement with the experimental observation of Werlé (1985). The skin-friction lines over most of the body surface appear axisymmetric, as sketched in figure 4b, but examination of other details of the solution indicate that in the separated region the flow becomes mildly three-dimensional. As indicated in figure 4c, the limiting streamlines appear to

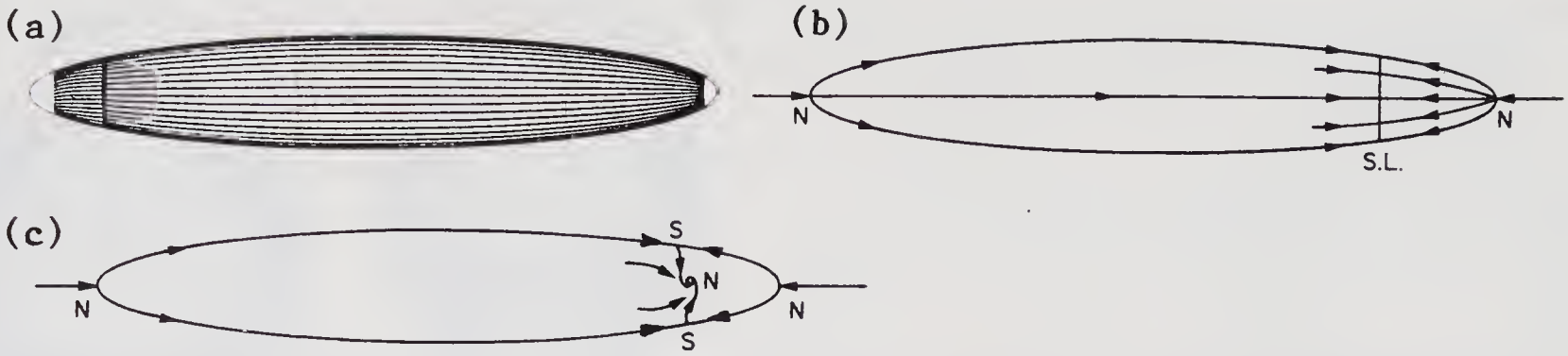

Figure 4. Skin-friction topology at $a = 0°$, (**a**) calculated friction lines; (**b**) axi-symmetric separation; (**c**) 3D separation following symmetry breaking.

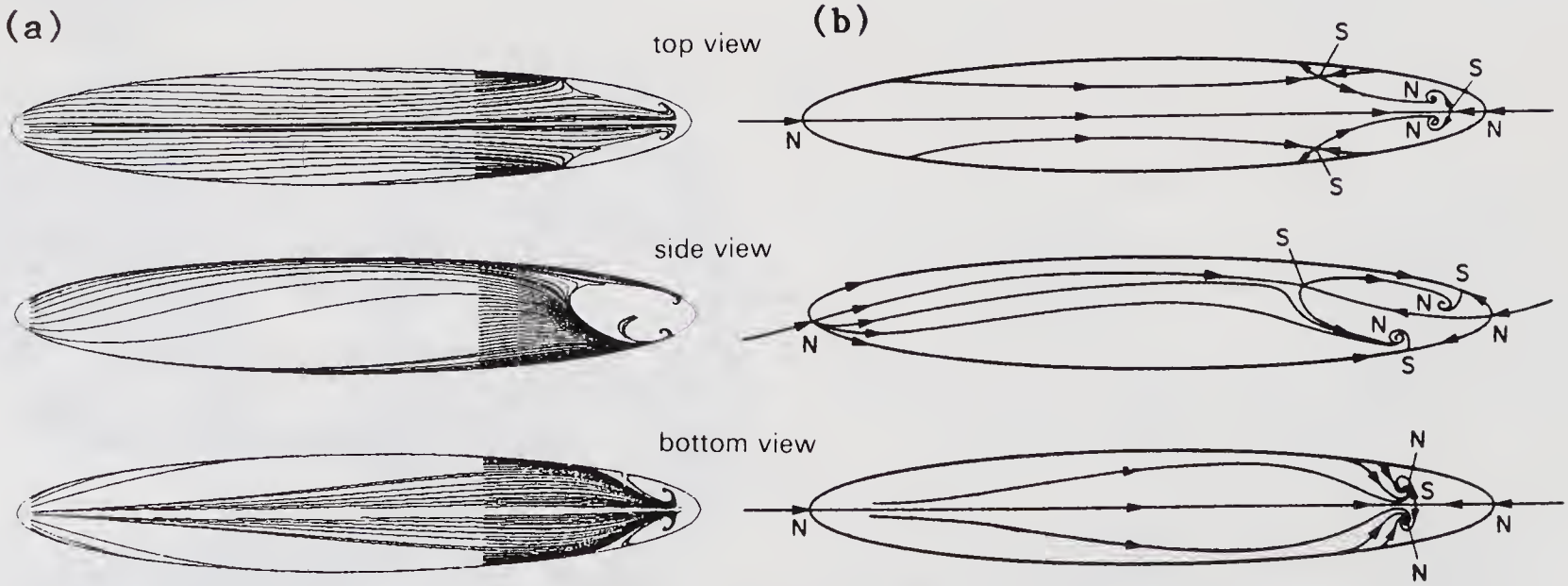

Figure 5. Skin-friction topology at low incidence, (**a**) calculated friction lines, $a = 5°$; (**b**) interpreted topology at low incidence.

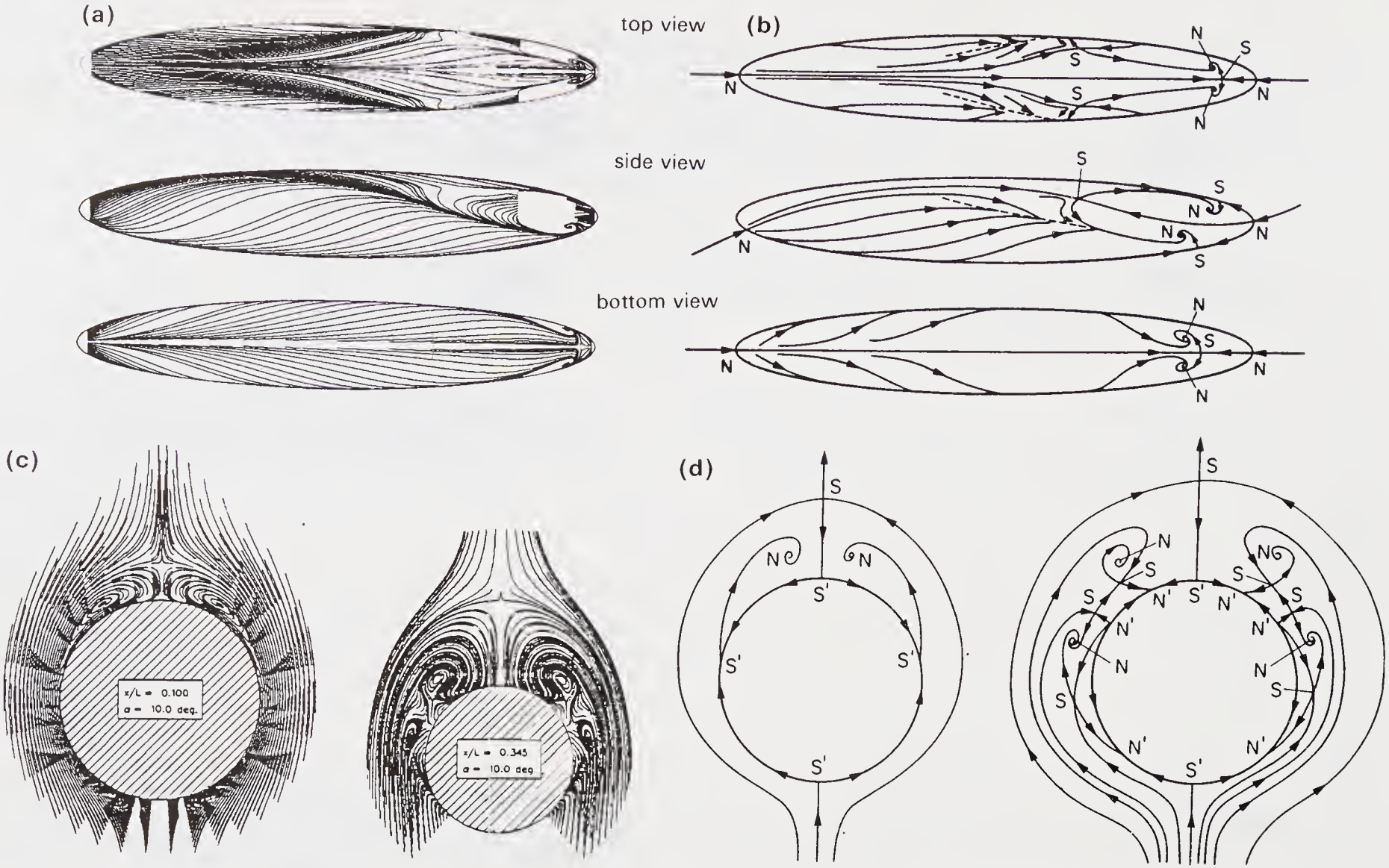

Figure 6. Details of flow topology at intermediate incidence, (**a**) calculated friction lines, $a = 10°$; (**b**) interpreted topology at intermediate incidence; (**c**) calculated crossflow "streamlines" at $a = 10°$; (**d**) interpreted crossflow topology.

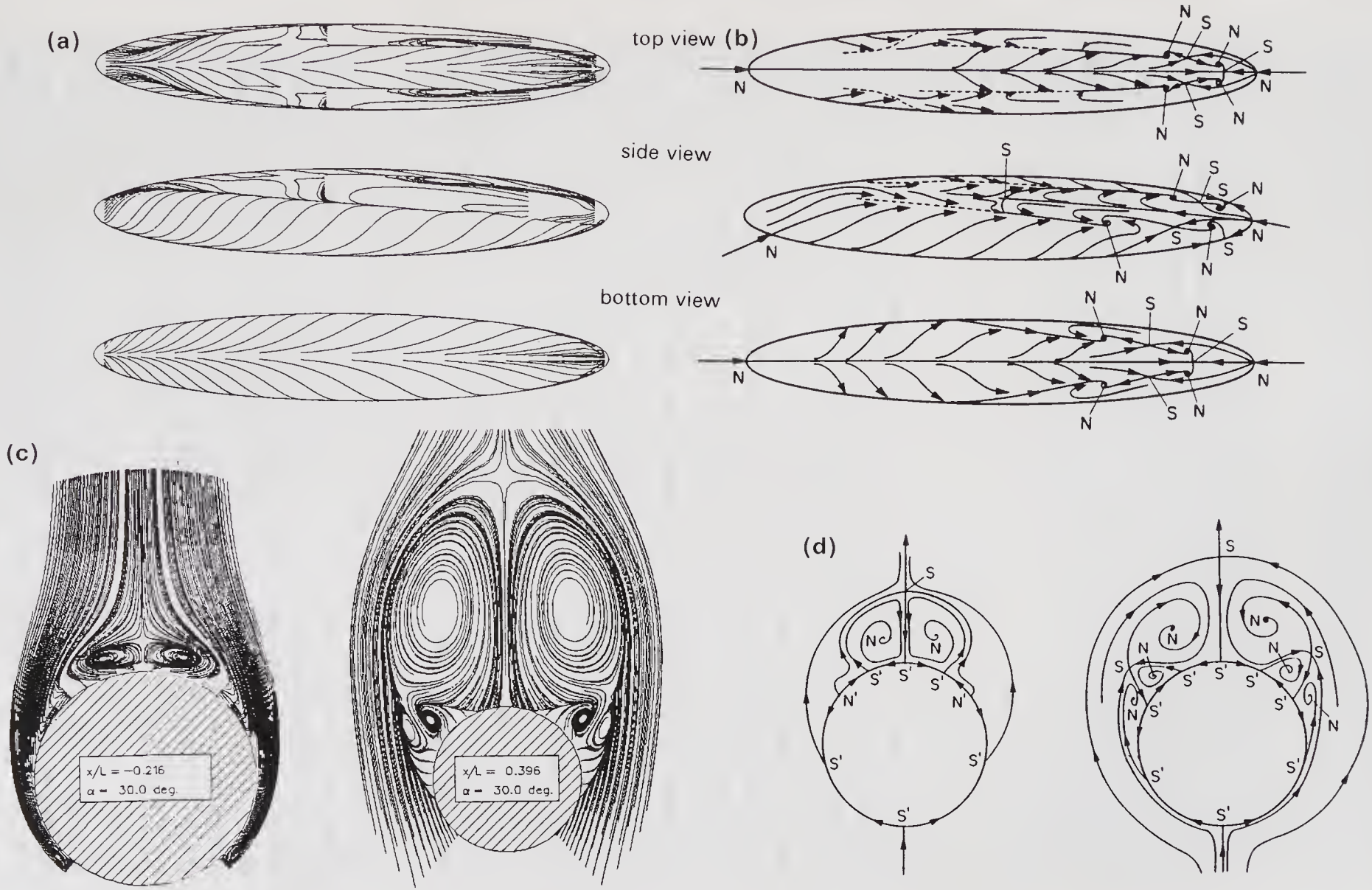

Figure 7. Details of flow topology at high incidence, (**a**) calculated friction lines, $a = 25°$; (**b**) interpreted topology at high incidence; (**c**) calculated crossflow "streamlines" at $a = 25°$; (**d**) interpreted crossflow topology.

converge into spiral nodes located on the separation line on each flank of the body. In the calculations, this destruction of axial symmetry may be triggered by the biased sweeps in the numerical procedure, but it is also the most probable form of separation in reality.

Topologically, the observed three-dimensionality is a result of a symmetry-breaking bifurcation, in which a small perturbation breaks up the singular separation line of axisymmetric flow into a closed separation line joining a number of distinct singular points. If lateral symmetry is assumed, topological law (1) requires at least two saddles, one on the leeward and the other on the windward side of the symmetry plane, and two nodes on the body flank, as shown in figure 4c. In the terminology of Chapman & Yates (1991), this is a type I separation although the appearance of a focus makes it resemble a type II separation. The calculated velocity field in the wake also suggests the presence of vortices but their strength was too weak to carry out a meaningful topological analysis.

4.2 *Low incidence*

Figure 5a shows the friction lines at $\alpha = 5^\circ$ and figure 5b shows the interpreted topology for the flow at low incidences. The points of flow reversal (zero friction) on the planes of symmetry are saddle points in the skin-friction vector field. In addition, two (four including the two on the other side of the body) spiral nodes or foci are observed, one on the leeward and another on the windward side. The limiting streamlines originating from the saddles on the symmetry plane spiral into these two nodes and lift off from the body surface, presumably in the form of a tornado-like vortex. On the leeward side of the body (top view), the limiting streamlines from upstream meet those coming from downstream and divide in two directions, with one directing leeward and eventually converging into the spiral node on the leeward side and the other directing windward and converging into the spiral node on the windward side. The configuration of the dividing streamlines strongly suggests that there is a saddle point on the flank of the body near the spiral node on the leeward side. This is supported by the topological rule (1). Including the two nodes on the nose and the tail, and the two spiral nodes on each side of the body, there are six nodal points on the body surface. Two saddle points exist on the symmetry plane. Accordingly, the two additional saddle points alluded to above are needed to satisfy the topological rule.

The sketches in figure 5b show the separation line passing through all of the singularities except, of course, the attachment points at the nose and tail. The region behind the separation line is filled by fluid coming from the rear attachment point and cannot be accessed from upstream. Thus, the separation at this incidence, and lower incidences, conforms to the criterion of a closed or singular separation. Topologically, this is also a type I separation but with an additional structural bifurcation in which each of the two nodes on the sides of the body, conjectured in figure 4c, split to produce two nodes and a saddle.

The surface flow topology suggested here compares well with flow visualizations of Wang *et al* (1990) on a spheroid of axes ratio 4, but the present interpretation differs from theirs in that a closed type separation is implied here while they interpreted their observations to indicate an open type separation. Unfortunately, differences in the axes ratio make a direct comparison difficult, but the present calculation suggests that the separation at low incidences is of the closed type and there is no evidence of an open separation occurring ahead of the closed separation. Presumably, for each

axes ratio, there is an incidence above which there is a change in this flow pattern, as discussed below.

4.3 *Intermediate incidence*

The results for $\alpha = 10°$ shown in figures 6a and b are topologically similar (with six nodes and four saddles) to those in the previous case, but the separated, axially-reversed flow region penetrates farther upstream. The separation over the rear of the body continues to be of the closed type. However, the earlier divergence of the limiting streamlines out of the leeward symmetry plane leads to squeezing or merging of the streamlines coming from the windward and leeward sides. This merging of limiting streamlines, as is well known, is the necessary condition for an open, free-vortex or crossflow type separation.

Figure 6c depicts the transverse-plane streamlines or particle paths constructed from the velocity field and figure 6d shows the interpreted crossflow topology. The singular points shown in both parts of figure 6d satisfy the topological rule (3). The topology at section $x/L = 0{\cdot}10$, which is 60% of body length from the nose, indicates two vortices emanating from half saddles of separation S′. It is clear from the topology of the friction lines that the vortices on the two sides of the body are not connected and they are not associated with any singularity of the friction lines. The locus of the half saddles S′ on the body surface is indicated by the broken lines in figure 6b. These are the lines of crossflow separation. Boundary layer fluid is thrown away from the body surface along these lines and this fluid wraps into longitudinal vortices.

Farther downstream, at section $x/L = 0{\cdot}345$, the crossflow topology is much more complicated. The calculated streamlines indicate two corotating vortices (with cores N) on each side of the body, saddle points (S) away from the body surface and several half nodes (N′) of convergent or divergent streamlines on the body. The half nodes are rare and appear here because of the contraction of the body cross-section in the downstream direction. Topologically, the half nodes on the surface and saddles in the flow arise out of bifurcation of the half saddles on the surface which are more commonly seen.

An interesting question that arises immediately is how the crossflow topology evolves in the streamwise direction, from the simple one observed upstream to the complicated pattern downstream. The answer to this is not entirely clear. To attempt an answer, however, we first consider the origin of the line of crossflow separation. We speculate that this is the result of a bifurcation of a single half node on the body into a half saddle on the body (S′ shown in the first of figure 6d), and a node (N) forming the vortex core. Then, as the shear layer generated from the crossflow separation intersects the reversed flow of the closed separation, further bifurcations take place along and above the line of closed separation. Here, we have taken snap shots at only two sections. A complete picture of the evolution would require analysis of the crossflow topology at several sections. With regard to the coexistence of crossflow and closed separations, the topology of the friction lines is in accordance with the experiments of Han & Patel (1979).

4.4 *High incidence*

The results for $\alpha = 25°$, presented in figure 7, are typical of those at 20° and 30°. Compared to the previous case, additional nodes and saddles appear in the friction lines, and the region of closed separation (the flow coming from the rear attachment

point) penetrates farther upstream. The limiting streamlines on the windward side diverge rapidly toward the leeward side and converge onto the primary crossflow separation line which starts on the leeward side as far ahead as $x/L = -0{\cdot}40$. This line is slanted slightly toward the windward side. The limiting streamlines near the leeward plane of symmetry also diverge out of that plane and converge onto a secondary crossflow separation line which also starts near the nose and runs nearly parallel to the plane of symmetry. Near the front, the limiting streamlines between the two crossflow separation lines diverge, run downstream for a short fetch, and merge into the separation lines. In the rear part of the region the limiting streamlines also diverge, run upstream, and merge into the separation lines. This indicates that the flow attaches to the body along a line in that region. The flow topology in the juncture between the streamlines coming from upstream and from downstream is not clear, however. It is postulated that there exists a saddle point in that juncture, as in the case of the lower incidences. It is also suggested that there is a region of closed separation downstream of the two separatrices (running leeward and windward) originating from the saddle point. The topology that is consistent with the crossflow streamlines and vortex pattern of figure 7c is shown in figure 7d. The separation lines observed in the friction lines now appear as half saddles.

5. Separation on a wing intersecting a plane

Flow separation on a low aspect ratio "wing" intersecting a plane is the second example considered. In this case, the results of an extensive flow-visualization study by Johnson (1991) are reviewed. The geometry is depicted in figure 8. The wing is one-half of a 12:6:1 tri-axial ellipsoid, and is mounted on the flat wall of a wind tunnel or water channel. Dye was used in water and surface oil-flow and smoke-wire methods were used in the wind tunnel.

For the case reported here, the wing chord Reynolds number was approximately 250,000 and the wing centre was placed three chord-lengths from the end of the

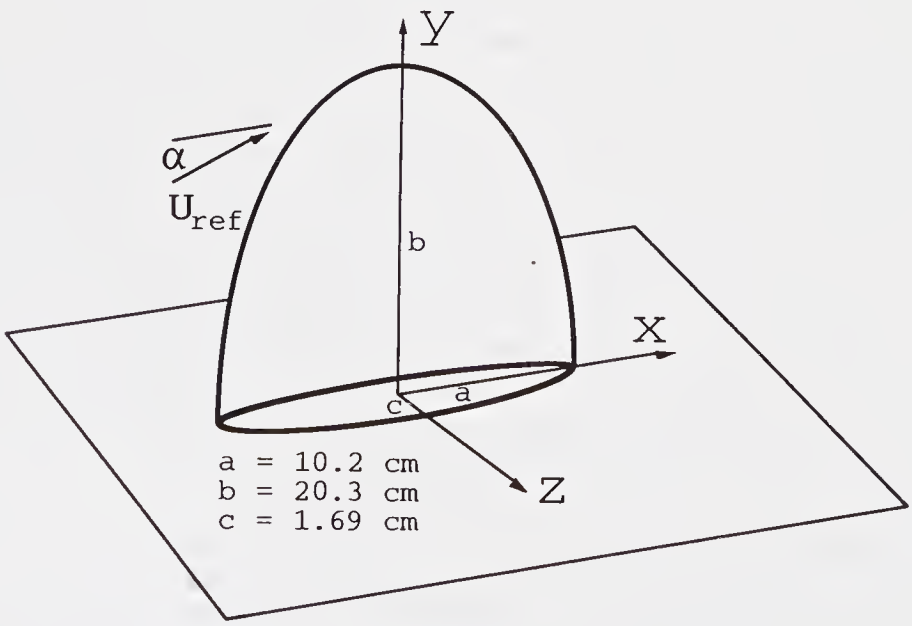

Figure 8. Semi-ellipsoid wing on a plane.

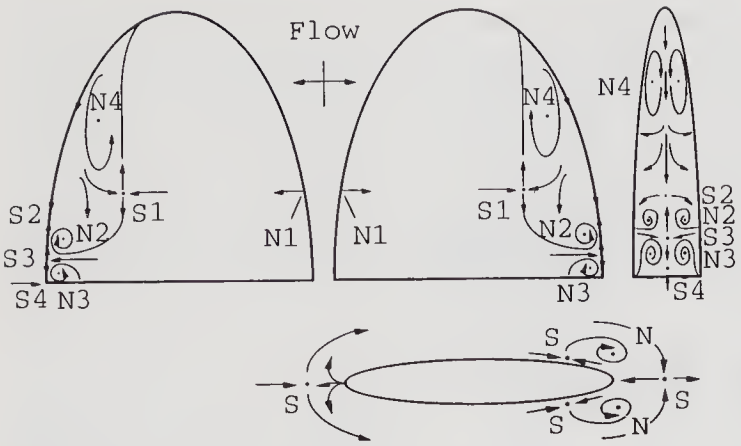

Figure 9. Observed skin-friction topology at zero incidence.

wind-tunnel contraction. The wing incidence was varied from 0 to 25°, in increments of 5°. The flow over the wing was essentially laminar although, as will be pointed out, transition influenced the flow pattern in some cases. Results of the different flow-visualization methods were interpreted together to deduce the overall flow topology. This required numerous photographs from different perspectives. As the surface oil-flow method yielded the most detailed results, the following discussion is restricted to the topology of the skin-friction field. Based on the occurrence of two major bifurcations around 10 and 20°, the incidence range is divided into four categories, namely, zero (symmetry), low, intermediate and high incidences. The results are shown in figures 9 through 12. Four views are shown in each case, the pressure side of the wing on the left, the suction side in the middle, the trailing edge on the right, and the wall flow at the bottom.

5.1 *Zero incidence*

The friction line topology deduced from the flow visualizations with the wing at zero incidence is shown in figure 9. On the wall there are two nodes and four saddles, while on the wing there are seven nodes and five saddles, and therefore, the entire pattern satisfies the topological law (2). The flow attaches to the wing along an attachment line, but for the purpose of topological description, only one point on the line is designated as the node of attachment (N1). The flow remains attached over 75% of the wing surface and separates along a line that is roughly normal to the freestream. Before the separation line reaches the wall it turns abruptly

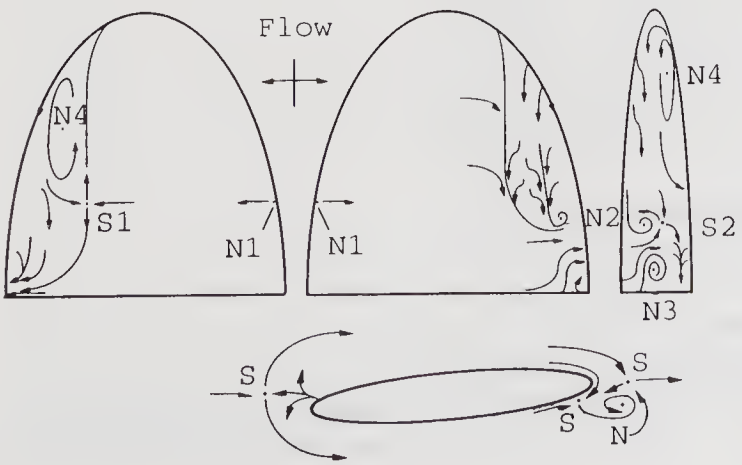

Figure 10. Observed skin-friction topology at $a = 5°$.

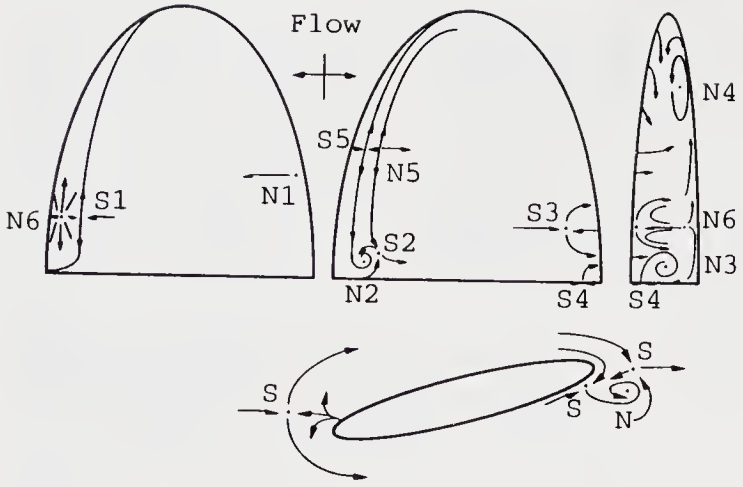

Figure 11. Observed skin-friction topology at $a = 15°$.

downstream toward the trailing edge. Located on this primary separation line and about 1/3 span from the wall is a saddle point (S1). At the downstream end of the separation, near the wall, accumulation of oil indicated the presence of a focus of separation (N2). In this regard, the separation line is similar to that observed on the spheroid, and it may be classified as a type II separation. The focus is understood to be the region where the separated stream-surface rolls up into a free vortex. Between the junction and N2 was another spot of oil accumulation. Although the visualizations were not able to provide complete confirmation, this spot is also believed to be a focus of separation (N3). This second focus is associated with the trailing edge foci visible in the wall pattern. The extended region of attachment leading to this focus and which causes the primary separation to turn downstream is either a wall boundary layer or horseshoe vortex effect. Since the wall Reynolds number is three times larger than that of the wing it is likely that the boundary layer is turbulent and separation may be delayed due to the turbulent mixing near the wall.

Up to the primary separation the flow pattern is fairly straightforward. Downstream the situation becomes more complicated because flow visualizations were not conclusive. However, the flow pattern can be derived by extending the friction vectors from around the known singular points into the unknown downstream region. The resulting pattern is shown in figure 9. From observations of oil patterns and dye injection, the direction of flow on the outer end of the trailing edge was found to be toward the

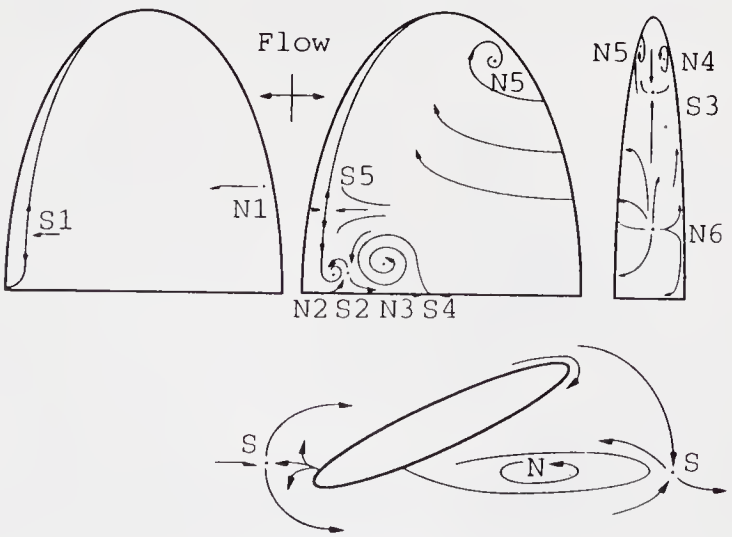

Figure 12. Observed skin-friction topology at $a = 25°$.

wall. On the other hand, node N2 necessarily induces flow up the wing in the areas immediately downstream of it. Extension of these two flow directions along the trailing edge results in the need for the saddle point S2. The exact location of S2 is not provided from this extrapolation procedure, however. Following the method of deriving S2, and now looking at the region influenced by N3, a second saddle, S3, is implied. Continuing down the trailing edge, the flow must be analysed in conjunction with the wall flow. The point of intersection between the reverse flow generated by the two wall vortices and the downward flow of N3 becomes a fourth saddle, S4. The final area of interest is the distal region bounded by the separation line, the trailing edge and the separatrix feeding the downstream side of S1. The consistent clockwise direction of the friction vectors on these boundaries indicates the presence of a node, N4, somewhere between them. Note, however, that the nature of this node, i.e., separation or attachment, could not be determined from the oil flow. Since all of the remaining vectors are consistent with one another, the singular point description of the flow on the wing, with the exception of the nature of N4, can be considered complete.

The flow topology at zero incidence was not completely symmetric due to a slight twist inadvertently built into the model during manufacture. Experiments with a larger wing, with much better geometric symmetry, showed the same flow topology near the base, but S1 and N4 in figure 9 were replaced by a line of crossflow separation along the S1 separatrix. With or without the twist, there was no evidence to indicate that the separation lines on the pressure and suction sides are connected at the tip. This was also the case at the low and intermediate incidences considered next. This, and the lack of any significant topological structures in the vicinity of the tip, suggests that the tip vortex is not well formed and is at most the result of a crossflow type of separation.

5.2 *Low incidence*

The low incidence category is bounded from below by symmetry and from above by the occurrence of the first major bifurcation at an angle of attack around 10°, although the exact angle is not known. The results obtained at 5° incidence are presented in figure 10 and discussed below.

The flow is now asymmetric. On the wall, the effect of the angle of attack is to push the saddle off centre, toward the pressure side and farther away from the wing as the effective diameter of the obstruction is increased. In place of the two symmetrically positioned trailing edge vortices at zero incidence, there is only one and the entire structure is pushed around to the suction side. The disappearance of the second node necessarily involves the disappearance of its associated saddle, in accordance with topological laws. Also, from the assumed association of the wing and wall vortices near the trailing edge, it is expected that only one focus will be present on the wing adjacent to the wall.

On the suction side of the wing, the separation line makes a sharp turn downstream and ends in a focus of separation (N2) with no saddle point on the line. The trail of oil accumulation leading to N2 was observed to be a line of convergence, indicating separation. Whether or not this is a second separation line distinct from the primary separation is not known. If it is indeed a crossflow separation in its own right, it is likely that it is a result of the shear layer between the primary separated streamsurface and the reverse flow adjacent to the wing surface.

On the pressure side of the wing, the separation line passes through the saddle point S1 but it cannot be classified as closed because the region behind it is still accessible to the flow originating at the forward attachment point from the suction side. It appears to be a type II separation according to the classification of Chapman & Yates (1991). Near the junction the separation extends almost entirely to the wall. Because of this, there is no room for a corner focus. The trailing edge region on the pressure side is better developed than that on the suction side. The node N4 arises because of the saddle point which leads to opposing directions in the friction vectors of the distal region.

The topological structure is completed by linking the pressure and suction side patterns across the trailing edge. This requires a node N3, and a saddle S2. Adding up the singular points on the wall and the wing shows that the topological law (2) is satisfied.

5.3 *Intermediate incidence*

The intermediate incidences begin around 10° and extend to somewhere below 20°. The results presented in figure 11 were obtained at 15° and are representative of the intermediate angles. As the incidence is increased and the separations grow in size and influence, the visualization methods begin to perform less and less well. Because of this, fewer structures can actually be seen and more conjecturing is necessary. It is here that the topological rules gain their importance by ensuring kinematically correct shear stress fields.

The wall flow pattern is essentially the same as the one for low incidences, the only difference being the downstream movement of the trailing edge node. The movement of the upstream saddle point away from the wing occurs as expected.

The presence of a major bifurcation is obvious from the flow on the suction side. Oil flow as well as dye visualizations revealed a separation bubble with recirculating fluid within. Downstream of the separation, smoke-wire tests revealed turbulent flow. In fact it is this turbulent mixing which causes the flow to reattach and form the bubble. In the topological representation, a single node is used to represent the entire line, so that the reattachment line is reduced to the node N5 and the primary separation line to the single saddle S5. The junction end of the bubble clearly does not extend all the way to the wall. A spot of oil collected at the end indicated a vortex denoted N2. Transition to turbulent flow downstream of the bubble collapses the separation to a crescent-shaped region around the saddle point S3. On the pressure side, the primary separation spans the entire wing and contains a saddle point S1. Downstream of this separation there is a node of attachment N6. As in the previous case, the topology is completed by linking the pressure and suction side patterns across the trailling edge. This requires a node N4, similar to that observed in the previous cases but now pushed to the trailing edge, and node N3 and saddle S4. Once again, the topological rule (2) is satisfied.

5.4 *High incidence*

The high incidence regime is characterized by the second major bifurcation. The onset of this occurs around 20°. The results presented in figure 12 correspond to 25°. The flow separating from the leading edge is now unable to reattach and the flow on the entire suction side is reversed.

The extent of the bifurcation can be seen in the flow pattern on the wall. While the pattern is topologically identical to the previous case, the physical geometry is dramatically different. The trailing edge saddle has shifted far downstream, from a point immediately off the wing base to almost a chord length downstream. The node just off the trailing edge is now located farther upstream. The back flow around the node extends more than half way up the base. The leading edge saddle has moved farther upstream.

On the pressure side of the wing, not much could be determined except that the flow was laminar up to separation. The pattern looks much the same as that for 15° with the separation displaced downstream. Nothing can be discerned over the trailing edge due to the narrow width of the area. Along the leading edge is the typical line of attachment. Most of the topological structure thus arises from analysis of the suction side. Over the suction surface, there are two nodes of separation, N3 and N5. Dye visualization failed to detect the structure of node N5 due to unsteadiness and turbulence in the separated flow. Node N3, however, was seen to be the footprint of a tornado vortex. It should be pointed out that this vortex is present only in the mean, an average of a structure that comes and goes with the unsteady fluctuations. Patching together the results from the pressure and suction sides produces the trailing edge pattern shown. Node N4, which has remained throughout the changes in incidence, is a necessity because of the outward flow on the pressure side and the inward flow induced by N5. The size of N4 must be greatly diminished, based solely on the restricted space that is now available. The saddle S3 is the collision point of downward flow between the two nodes and the reattached flow from node N6. The entire suction side is reverse flow and since the separation on the pressure side is closed, N6 serves as the source for all the suction side friction lines. A spanwise view from the tip showed that, at this high incidence, the separation lines on the pressure and suction sides are continuous so that the entire suction side is covered by a truely closed separation. A quick check of the singularities shows that the topological rule is again satisfied.

The velocity field at an incidence of 25° has been recently measured by Parthasarathy *et al* (1993) using a three-component LDV to construct the topology of the flow associated with the observed friction lines. The measurements reveal that the flow on the entire suction side of the body is separated, with the reversed-flow region extending to one-chord length behind the body and with mean reversed velocities as high as 25% of the freestream velocity. The primary separation line on the suction side of the body gives rise to a large vortex whose footprint is observed as the line of separation on the wall. Part of the reversed flow resulting from the primary separation moves towards the tip and interacts with another vortex attached to the suction side in the spiral node of friction lines observed in the flow visualizations. The two vortices, together with the flow on the pressure side, proceed downstream forming one large vortical structure. This final vortex was found to be more diffused and less tightly wound than the tip vortex usually found in the wakes of lifting wings. Further analysis of these data is in progress.

6. Evolution of a vortex from a crossflow separation

To illustrate an open or crossflow separation and evolution of a longitudinal vortex, we consider developing turbulent boundary-layer flow in a curved duct of rectangular

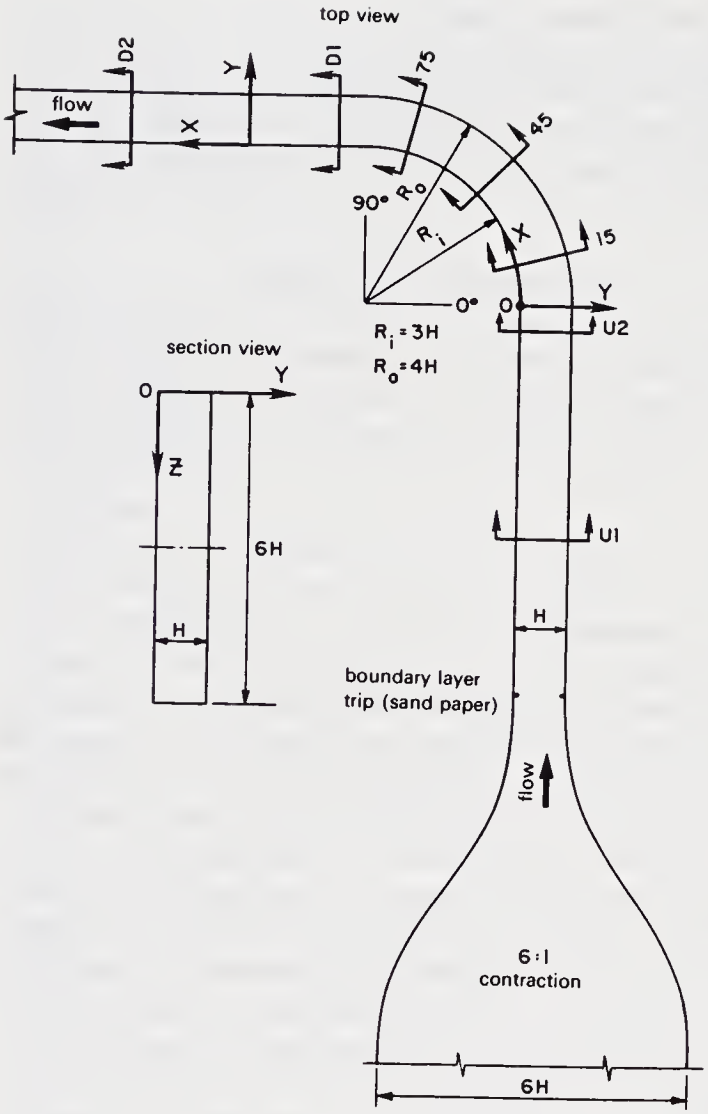

Figure 13. Curved-duct wind tunnel.

cross-section. Kim (1991b) has made extensive measurements and obtained numerical solutions of the Reynolds-averaged Navier–Stokes equations to document the pressure-driven secondary motion imposed by curvature. Figure 13 shows an outline of the wind tunnel, the coordinates, and the location of the measurement stations. For the purpose of the present review, it suffices to examine some selected results. The measured contours of the longitudinal velocity component, and those of the longitudinal component of vorticity, obtained by numerical differentiation of the measured secondary velocity components, are shown in figure 14.

The symmetric vortices on the top wall at station U2 ahead of the bend arise in the wind-tunnel contraction by essentially the same mechanism as that which produces the vortex on the convex wall further downstream. Near the top wall, the boundary layer on the convex wall thickens as it is fed by fluid coming down from the top-wall boundary layer driven by the radial pressure gradient. By station 75 there appears a longitudinal vortex with its core approximately at $Y/H = 0{\cdot}08$ and $Z/H = 0{\cdot}7$. Vortical flow now begins to fill the top of the channel. The vortex on the convex wall grows in size and is pushed away from the top. The vortex persists even after the end of curvature. At station D2, the core of the vortex, identified by low axial velocity and high longitudinal vorticity, is located around $Y/H = 0{\cdot}17$ and $Z/H = 1{\cdot}0$. The evolution of this longitudinal vortex on the convex wall is the result of what is

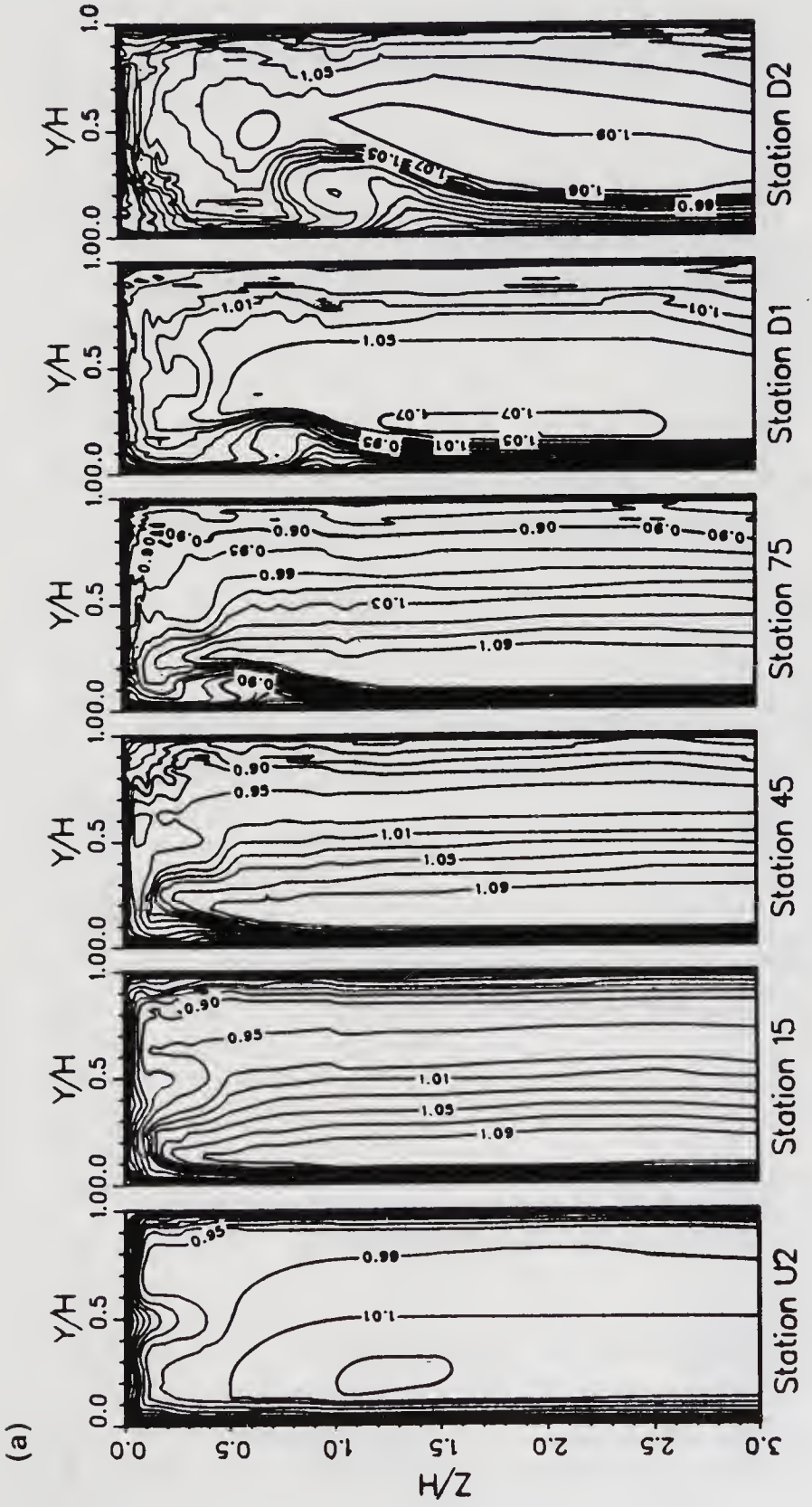

Figure 14. **(a)** (Caption on next page.)

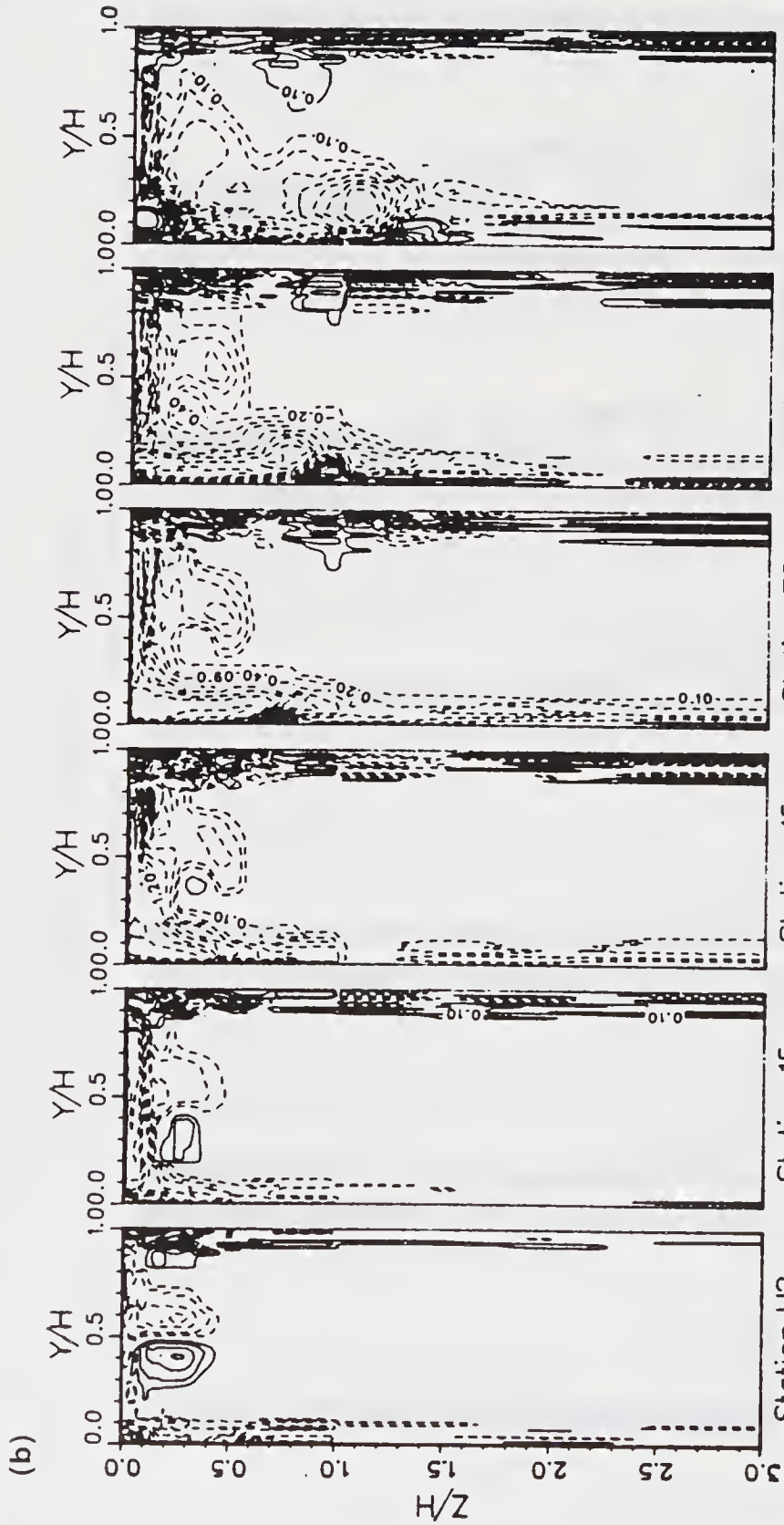

Figure 14. Measurements at six sections along the duct. (**a**) Contours of longitudinal velocity; (**b**) Contours of longitudinal component of vorticity.

commonly called an open type of separation. Note that there is no singular point in the friction lines associated with this phenomenon, and the only symptom on the wall is a convergence of friction lines from both sides. In general, in the numerical simulations, the evolution of the vortex was delayed but its decay or diffusion was accelerated. This example illustrates the additional uncertainty that arises in the case of turbulent flow in which the turbulence model plays an important role in defining the flow structure, if not the topology.

7. Concluding remarks

This paper has presented highlights of some recent investigations conducted to understand the phenomenon of separation in three-dimensional flows. Examples are drawn from numerical solutions in laminar flow, flow visualizations in laminar and transitional flow, and measurements in turbulent flow. Concepts from topology were applied to provide a description of the different types of separation, and those of structural bifurcations were invoked to illustrate how one flow pattern evolves into another. The classification of separation types proposed by Chapman & Yates (1991) has been applied to the extent possible. However, it became clear that when one considers practical configurations that involve many interconnected singular points the distinction between type I and type II singular or closed separations becomes blurred. While the concept of a crossflow or open type of separation is found to be useful, when it arises in combination with singular or closed separations, the resulting flow pattern is extremely complex and, once again, the distinctions become blurred.

The results reviewed here clearly raise more questions than are answered. This is, in part, due to our limited ability to perceive and quantitatively describe fluid motions in three dimensions. Limitations of experimental techniques and, to a lesser extent, those of numerical methods, are frequently cited as factors hindering progress in the understanding of three-dimensional flow topology. More details of the motion are obviously needed to investigate the connection between the singular points of the friction lines, the rules for which are relatively well established and readily interpreted, and those of streamlines viewed in special planes, in order to construct the total three-dimensional structure of the flow field. This is particularly important because flow patterns which appear quite similar when viewed in some planes may be connected with very different skin-friction topologies, and conversely, as pointed out by Dallmann (1983), quite different flow fields can produce the same skin-friction topology.

There are other issues in need of further work. One is obviously that of the structural bifurcations which accompany changes in incidence and transition from laminar to turbulent flow. While more detailed solutions of the Navier–Stokes equations will be forthcoming, it is not at all clear how numerical methods *per se* will determine the occurrence of bifurcations even when transition to turbulence is not a factor. Second, experiments and computations with laminar flow indicate that the flow beyond separation is rarely steady, and often becomes turbulent. This suggests that much greater effort should be devoted to unsteady flows. Finally, it is frequently assumed or implied that studies of laminar flow separation and topology have some bearing on turbulent flow. Yet, turbulent flows, in the average sense, do not show the richness of topology that is observed in laminar flow. The question that arises then is the relevance of studies in flow topology to turbulent flow, especially in the time-average sense.

This research was supported by the Office of Naval Research, under Contract N00014-88-K-0001 and Grant N00014-89-J-1342, monitored by Dr E P Rood, and Grant N1132-90-A0159, monitored by Dr L P Purtell. I am especially grateful to my students, Tim Johnson, Sung-Eun Kim, Wu-Joan Kim, and Joel Walter for their contributions on which this review is based.

References

Chapman G T, Yates L A 1991 Topology of flow separation on three-dimensional bodies. *Appl. Mech. Rev.* 44: 329–345

Dallmann U 1983 Topological structures of three-dimensional vortex flow separation. AIAA-83-1735

Han T-Y, Patel V C 1979 Flow separation on a spheroid at incidence. *J. Fluid Mech.* 92: 643–657

Johnson T A 1991 *Visualization of topology of separated flow over a semi-elliptic wing at incidence intersecting a plane wall*, M S thesis, Mechanical Engineering, University of Iowa, Iowa City, Iowa

Kim S E 1991a Numerical studies of three-dimensional flow separation, Ph D dissertation, Mechanical Engineering, University of Iowa, Iowa City, Iowa

Kim S E, Patel V C 1991 Flow separation on a spheroid at incidence: laminar flow. AIAA-91-1803

Kim W J 1991b An experimental and computational study of longitudinal vortices in turbulent boundary layers, Ph D dissertation, Mechanical Engineering, University of Iowa, Iowa City, Iowa

Lighthill M J 1963 Attachment and separation in three-dimensional flow. *Laminar boundary layers* (ed.) L Rosenhead (Oxford: University Press)

Parthasarathy R N, Sirviente A I, Patel V C 1993 LDV measurements in separated flow on an elliptic wing mounted at an angle of attack on a wall. *Symposium on Separated Flows*, ASME Fluids Engineering Division Summer Meeting, Washington DC

Tobak M, Peake D J 1982 Topology of three dimensional separated flows. *Annu. Rev. Fluid Mech.* **14** 61–85

Wang K C 1974 Boundary layer over a blunt body at high incidence with an open-type of separation. *Proc. R. Soc.* **A340** 33–55

Wang K C, Zhou H C, Hu C H, Harrington S 1990 Three-dimensional separated flow structure over prolate spheroids. *Proc. R. Soc.* **A421** 73–90

Werlé H 1985 Principaux types de decollement libre observes sur maquettes ellipsoidales, ONERA, France, Report FR ISSN 0078–3781

Analysis and control of dynamic stall phenomenon using Navier–Stokes formulation involving vorticity, stream function and circulation

K N GHIA, J YANG, U GHIA[+] and G A OSSWALD

Department of Aerospace Engineering and Engineering Mechanics, [+]Department of Mechanical, Industrial and Nuclear Engineering, Computational Fluid Dynamics Research Laboratory, University of Cincinnati, Cincinnati, Ohio 45221, USA

Abstract. An unsteady Navier–Stokes (NS) analysis is developed for studying flow past a maneuvering body. The present inclusion of *circulation* in the earlier NS analysis of the authors makes it feasible, *for the first time*, to accurately simulate the asymptotic far-field boundary condition. In the overall analysis, a clustered conformal mesh with *C*-grid topology is used, with the governing differential equations being solved using the implicit ADI-BGE technique. The effects of grid size and clustering on the flow solution, and the effect of grid stretching on the far-field solution, are studied using the flow configuration with $Re = 45{,}000$ and constant-rate pitch-up motion, with $\dot{\alpha}^+ = 0{\cdot}2$. The results obtained for this case compare very satisfactorily with available experimental data. Other numerical results are also used for carefully validating the analysis developed here. An *active control strategy*, consisting of modulated suction/injection at the airfoil surface, is studied, and provides satisfactory control of the unsteady separation process and, hence, of the dynamic stall vortex.

Keywords. Unsteady incompressible flow; Navier–Stokes analysis; vorticity, stream function and circulation formulation; dynamic stall phenomenon; active control.

1. Introduction

The realization of supermaneuverable flight necessitates the use of unsteady non-equilibrium flow analyses and examination of a more comprehensive parameter envelope to capture significant time-dependent effects. The numerous complex flow phenomena and interactions which might occur during a supermaneuver in the high-alpha (generally between 30° and 90°) flight regime are highly nonlinear primarily due to flow separation, presence of vortex-dominated flows and unsteadiness. As a consequence, a strong coupling between the prevailing aerodynamics and flight dynamics, sometimes leads to chaotic flow and loss of control of the aircraft due to tail spin. To improve the maneuverability of high-performance military aircraft at

very high angles of attack, researchers are currently developing analytical and experimental design tools that can take full advantage of unsteady aerodynamics. By operating in the post-stall flight regime, supermaneuverability permits improved combat capability.

The initiation of a high-alpha maneuver may involve large-amplitude deflections of control surfaces or rapid pitch-up motions of the lifting surface itself. During this post-stall maneuver, instead of experiencing massive flow separation and the resulting loss of lift, the lifting surface develops an energetic dynamic-stall vortex, which temporarily leads to a significant increase in lift and drag forces. Thus, during the time that the dynamic-stall vortex is created on the suction surface and convects over it, the flow field is characterized by a number of dominant flow features which include growth of boundary layer, separation, unsteadiness, primary and secondary shear layer instability, unsteady separation, shock/boundary-layer and inviscid-viscid interactions, and vortex–vortex and vortex–surface interactions. Thus, the dynamic stall event is richly endowed with many basic fluid mechanics phenomena. The understanding and control of this event are important not only for supermaneuverable aircraft, but also for helicopter rotor blades, compressor blades, wind turbines etc.

Toward the development of a supermaneuverable flight capability, Lang & Francis (1985) had articulated many of the research problems that are currently being pursued by researchers. Many of the concepts discussed by them are now being tested in the first international X-plane, namely, the X-31, known officially as the Enhanced Flight Maneuverability Demonstrator; see Lerner (1991). This is the first aircraft which has successfully maneuvered in the post-stall regime, thereby making this liability an asset. Thus, any insight gained in understanding the dynamics of the post-stall regime could be very valuable in improving the performance and flight envelope of this type of aircraft.

Since April 1990, there have been three major workshops/conferences, where the research issues as well as the results of the studies in the area of post-stall maneuvers have been discussed. Carr (1990, pp. 17–19), Gustafson & Wyss (1990) and Fant & Rockwell (1992) provide sources where current work is published, and the reader would benefit immensely from them. In light of these references, together with recent excellent review articles by Carr (1985), Helin (1989) and Visbal (1990, pp. 127–47), it is decided to not include a review of the literature in the present paper.

The present authors have been studying forced unsteady separated flows, using the NACA 0015 airfoil for some time. Specifically, K Ghia *et al* (1990) provided, for very low Re, results that very vividly showed four stages, as classified by Walker (1992), that describe the dynamic-stall event. These are:

(i) *triggering phase*, in which flow separation occurs near the leading edge (LE) on the suction surface due to adverse pressure gradient;
(ii) *separation*, in which vorticity accumulates in the surface layer and the onset of interaction with the outer fluid is about to occur;
(iii) *strong interaction*, in which a vorticity plane erupts; and finally,
(iv) *inviscid interaction phase*, in which the dynamic-stall vortex is formed due to roll-up of the free shear layer, which entrains fluid from the boundary layer.

The details of the analysis were given by Osswald *et al* (1990). Subsequently, K Ghia *et al* (1991) provided the results for higher-Re flows by treating the nonlinear convection terms using a third-order accurate biased upwind differencing scheme, while still retaining the central differencing scheme for all other spatial derivatives.

Thereafter, K Ghia *et al* (1992b) demonstrated the suppression of the dynamic-stall vortex using an active control strategy of suction/injection. In addition, K Ghia *et al* (1992a) successfully studied the dynamic-stall phenomenon using a modified NACA 0012 airfoil undergoing sinusoidal oscillations. The primary objective in that investigation was to simulate and analyse the Grand Challenge Problem posed by Carr (1990, pp. 17–19). The experimental data for this problem were those of McAllister & Carr (1979). Further, Osswald *et al* (1992) extended the analysis to provide a more accurate far-field boundary condition, which required the coupling of viscous circulation $\Gamma(t)$ with the original analysis of the authors (K Ghia *et al* 1992a), which used $(\bar{\omega}_I, \psi_I^D)$, thereby arriving at a $(\bar{\omega}_I, \psi_I^D, \Gamma(t))$ formulation. In addition, some results were provided for $\mathrm{Re} = 45{,}000$ with constant pitch-rate $\dot{\alpha}^+ = 0{\cdot}2$, and $\mathrm{Re} = 52{,}000$ with $\dot{\alpha}^+ = 0{\cdot}072$.

The primary objective of the present study is to extend the analysis of K Ghia *et al* (1992b) to provide an accurate far-field boundary condition by correctly implementing the prevailing viscous circulation there. Although this analysis parallels that of Osswald *et al* (1992), it has some significant differences in the way the mathematical formulation is set up and particularly in the details of the numerical procedure. In addition, it is also the goal of this study to analyse the simulation results more fully in the light of the available experimental data or numerical results, so as to assess the overall 2-D $(\bar{\omega}_I, \psi_I^D. \Gamma(t))$ formulation, where $\Gamma(t)$ is the viscous circulation at infinity.

2. Mathematical formulation

The time-dependent flow around a maneuvering airfoil is governed by the unsteady Navier–Stokes (NS) equations. The selection of the specific forms of these nonlinear coupled, partial differential equations used in the present work is based primarily on two factors, namely, (i) dependent variables, and (ii) reference frame.

2.1 *On the choice of dependent variables*

K Ghia *et al* (1977) used a regular non-staggered grid and solved the primitive variable form of the NS equations in which the continuity equation was satisfied using the Poisson equation for pressure. Osswald (1981) examined various 2-D formulations of the NS equations and concluded that the 2-D primitive-variable formulation, with the Poisson equation for pressure, should be discretized using a staggered grid, rather than a regular grid, if the discrete equations are to be exactly consistent with the continuous equations. U Ghia & K Ghia (1987) had reviewed various NS analyses for 3-D flows; their study included:

(i) velocity–pressure $(\bar{V}, p)$,
(ii) velocity–vorticity $(\bar{V}, \bar{\omega})$, and
(iii) vector-potential–vorticity $(\bar{A}, \bar{\omega})$ formulations.

Osswald *et al* (1987) further clarified that, although primitive-variable formulations are widely used due to their popularity in compressible-flow analyses, the velocity–vorticity formulation is equally competitive and perhaps more advantageous because it directly provides the vorticity, which is the most relevant quantity in the flow. In addition, it was pointed out that the $(\bar{V}, \bar{\omega})$ formulation leads to a natural decoupling

of the governing equations, since the spin dynamics of a fluid particle governed by the vorticity–transport problem can be decoupled from the translational kinematics of the fluid particle represented by the elliptic velocity problem. This is not the case for the primitive-variable formulation. It was also pointed out that a careful analysis of the $(\bar{V}, \bar{\omega})$ formulation could reduce its computational requirements to match those of the $(\bar{V}, p)$ formulation. Finally, it was pointed out that the vector-potential–vorticity formulation required specification of a non-physical boundary condition to correctly set up the problem and that this poses numerical difficulties. Huang *et al* (1992) have revisited this issue and have provided some additional details. Gatski (1991) as well as Gresho (1991) have also reviewed the various NS formulations and have provided some insight into the selection process for the dependent variables.

2.2 *On the selection of reference frame*

Even for maneuvering bodies, it is possible to work with an inertial reference frame, with boundary-aligned coordinates being computed at every instant of time to provide for the body motion. Chyu *et al* (1981) as well as Salari & Roache (1990) have provided analyses using an inertial reference frame. The major advantage with this approach is that the far-field boundary conditions remain undisturbed. On the other hand, Mehta (1977), Sankar & Tassa (1980), Visbal & Shang (1989) and the present authors have elected to work with the body-fixed non-inertial reference frame. In this approach, although the grid remains undistorted, the far-field boundary conditions require special attention. In the present study of 2-D forced unsteady separated flow, the $(\bar{V}, \bar{\omega})$ formulation is used in generalized coordinates in the body-fixed non-inertial reference frame. Osswald *et al* (1990) have shown that, for the $(\bar{V}, \bar{\omega})$ formulation with divergence and curl operators expressed in the generalized coordinate non-inertial reference frame, the inertial vorticity diffuses as for the case of a fixed body, but advects with apparent velocity rather than with inertial velocity. Thus, except for the appearance of the apparent velocity, the velocity–vorticity formulation of the unsteady NS equations is "nearly" form-invariant under a generalized non-inertial coordinate transformation. This offers a significant advantage, in that it leads to a unified algorithm for both non-maneuvering and maneuvering body flows. Thus, in the present study for 2-D flow past a maneuvering body, the $(\psi, \bar{\omega})$ formulation is used in a body-fixed non-inertial reference frame. This form has been shown by Osswald *et al* (1988) to be equivalent to the $(\bar{V}, \bar{\omega})$ formulation, but is computationally more efficient. Speziale (1987) had also shown that, for the special case of rotation, the $(\bar{V}, \bar{\omega})$ formulation is form-invariant and that, under this condition, non-inertial effects will enter the solution only through the initial and boundary conditions.

2.3 *Governing differential equations*

An arbitrary maneuver can be completely defined by specifying the trajectory $\bar{r}_{B/I}(t)$ of some point B fixed on the body (see figure 1), with respect to an inertial observer, together with the specification of the instantaneous angular velocity $\bar{\Omega}_B(t)$ of the body. Kinematically, the translational velocity of the origin B of the body-fixed frame is then $\bar{V}_{B/I}(t) = \mathrm{d}(\bar{r}_{B/I})/\mathrm{d}t$, and the translational acceleration is $\bar{a}_{B/I}(t) = \mathrm{d}^2(\bar{r}_{B/I})/\mathrm{d}t^2$, while the angular acceleration is $\bar{\alpha}_B(t) = \mathrm{d}(\bar{\Omega}_B)/\mathrm{d}t$. In the present analysis, these functions, which define a specific maneuver, are assumed to be explicitly prescribed functions of time, and will be given in a later section.

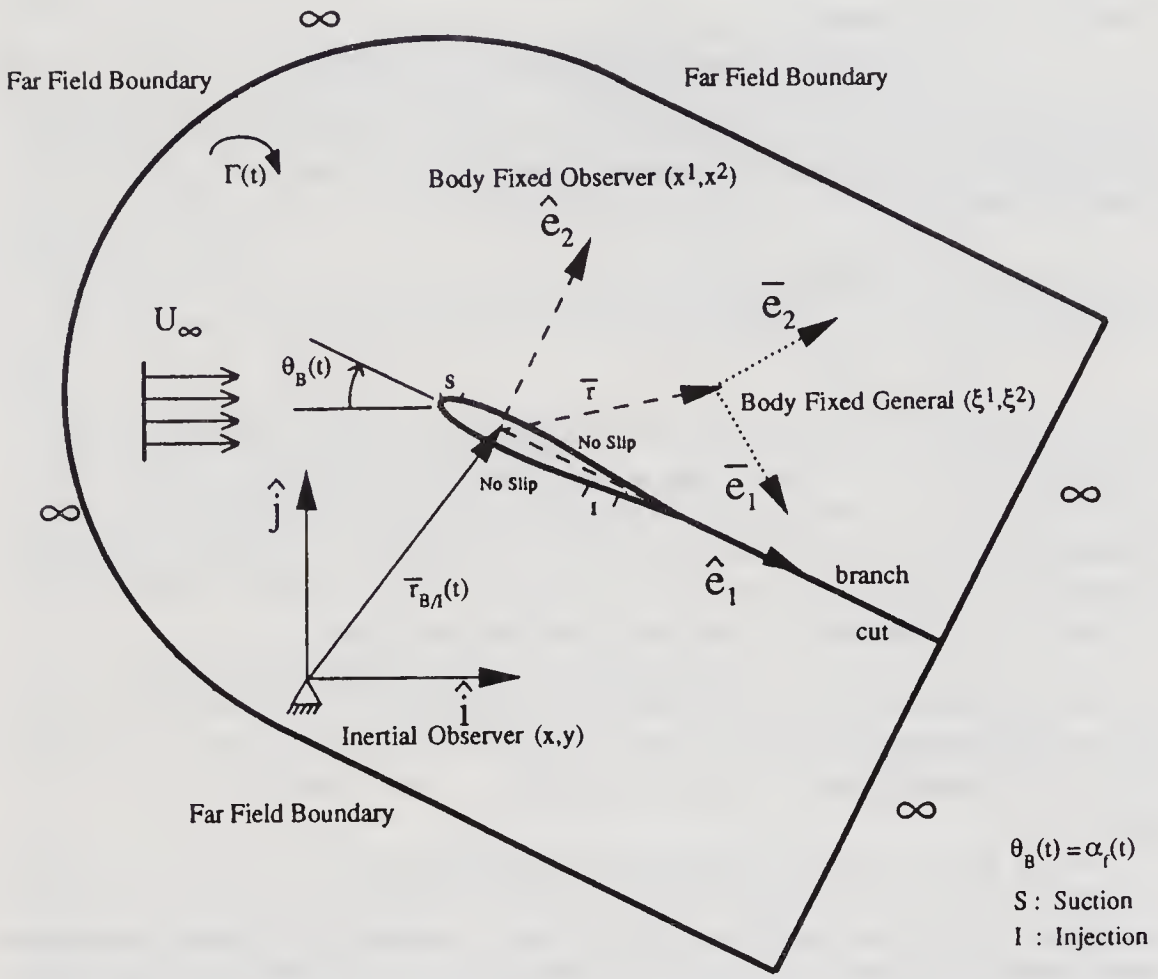

Figure 1. Inertial/body-fixed coordinate systems and boundary conditions for flow past an arbitrary maneuvering body.

For an inertial reference frame, the unsteady incompressible Navier–Stokes equations are given in terms of the derived variables $(\bar{V}_I, \bar{\omega}_I)$ as follows.

Continuity equation and kinematic definition of vorticity:

$$\nabla_I \cdot \bar{V}_I = 0, \tag{1}$$

$$\nabla_I \times \bar{V}_I = \bar{\omega}_I. \tag{2}$$

Vorticity–transport equation:

$$(\partial \bar{\omega}_I / \partial t) + \nabla_I \times (\bar{\omega}_I \times \bar{V}_I) + (1/\mathrm{Re})(\nabla_I \times \nabla_I \times \bar{\omega}_I) = 0, \tag{3}$$

where $\mathrm{Re} = cU_\infty / \nu$ such that U_∞ is the reference free-stream velocity and c is the airfoil chord length. Also, the subscript I on ∇_I denotes that the implied spatial differentiation is with respect to inertial coordinates. The transformation of (1)–(3) to a generalized coordinate non-inertial body-fixed reference frame, as carried out by Osswald *et al* (1990), leads to the following form.

Continuity equation and kinematic definition of vorticity:

$$\nabla \cdot \bar{V}_I = 0, \tag{4}$$

$$\nabla \times \bar{V}_I = \bar{\omega}_I. \tag{5}$$

Vorticity–transport equation:

$$(\partial\bar{\omega}_I/\partial t) + \nabla \times (\bar{\omega}_I \times \bar{V}) + (1/\mathrm{Re})(\nabla \times \nabla \times \bar{\omega}_I) = 0, \tag{6}$$

where all divergence and curl operators are with respect to the generalized-coordinate non-inertial reference frame, the apparent velocity $\bar{V}$ is kinematically related to the inertial velocity as

$$\bar{V} = \bar{V}_I - \bar{V}_{B/I}(t) - \bar{\Omega}_B(t) \times \bar{r}, \tag{7}$$

and the position vector $\bar{r}$ is given as

$$\bar{r} = \bar{r}_I - \bar{r}_{B/I}(t), \tag{8}$$

with $\bar{V}_{B/I}(t), \bar{\Omega}_B(t), \bar{r}_{B/I}(t)$ being the known functions which define a specific maneuver.

Hence, except for the appearance of the apparent velocity, the velocity–vorticity formulation of the unsteady Navier–Stokes equations is form-invariant under a generalized non-inertial coordinate formulation. Therefore, the algorithm developed to solve (1)–(3) remains valid for the solution of (4)–(6). The analysis described so far is valid for 3-D flows with six-degree-of-freedom maneuvers.

For the 2-D simulations of interest here, it is computationally more efficient to use the $(\psi, \bar{\omega})$ variables rather than the $(\bar{V}, \bar{\omega})$ variables. Furthermore, due to the unbounded nature of the stream function in the far field at true infinity, it is essential that a deviational stream function be employed as the dependent variable; this is given as

$$\psi_I = y - y_{B/I}(t) + \psi_I^D(\xi^1, \xi^2, t) + [\Gamma(t)/2\pi] \ln(r/a), \tag{9}$$

where $y - y_{B/I}(t)$ is the vertical inertial coordinate passing through the instantaneous location of the pitching axis. The viscous circulation $\Gamma(t)$ is positive in the clockwise direction and 'a' is the radius of the circle to which the airfoil is transformed. The inertial velocity then becomes

$$\bar{V}_I = \hat{i} + \left[\frac{\mathrm{Real}(V^*\bar{e}_1)}{g_{11}} + \frac{1}{g^{\frac{1}{2}}}\frac{\partial\psi_I^D}{\partial\xi^2}\right]\bar{e}_1 + \left[\frac{\mathrm{Real}(V^*\bar{e}_2)}{g_{22}} - \frac{1}{g^{\frac{1}{2}}}\frac{\partial\psi_I^D}{\partial\xi^1}\right]\bar{e}_2. \tag{10}$$

Here, V^* is the complex velocity defined as $i[\Gamma(t)/2\pi r]$ due to the generation of circulation, and $\hat{i}$ is the unit base vector of the inertial Cartesian reference frame shown in figure 1. Further, $\bar{e}_1$ and $\bar{e}_2$ are the covariant base vectors of the generalized-coordinate (ξ^1, ξ^2) non-inertial body-fixed reference frame. The determinant of the metric tensor g appearing in (10) is given as

$$g = (g_{11}g_{22} - g_{12}g_{21}),$$

where

$$g_{ij} = \sum_{k=1}^{2} (\partial x^k/\partial\xi^i)(\partial x^k/\partial\xi^j). \tag{11}$$

The independent variables (x^1, x^2) represent the body-fixed Cartesian coordinates whose unit base vectors are $\hat{e}_1$ and $\hat{e}_2$ as shown in figure 1.

In the light of (7) and (10), the contravariant components of the apparent velocity are

$$g^{\frac{1}{2}}V^1 = [1/(g_{11}/g^{\frac{1}{2}})][\{\cos\theta_B(t) - V^1_{B/I}(t) + x^2\Omega_B(t)\}\hat{e}_1\cdot\bar{e}_1 + \{\sin\theta_B(t) - V^2_{B/I}(t) - x^1\Omega_B(t)\}\hat{e}_2\cdot\bar{e}_1 + \mathrm{Real}(V^*\bar{e}_1)] + (\partial\psi_I^D/\partial\xi^2), \tag{12}$$

and

$$g^{\frac{1}{2}}V^2 = [1/(g_{22}/g^{\frac{1}{2}})][\{\cos\theta_B(t) - V^1_{B/I}(t) + x^2\Omega_B(t)\}\hat{e}_1\cdot\bar{e}_2 + \{\sin\theta_B(t) - V^2_{B/I}(t) - x^1\Omega_B(t)\}\hat{e}_2\cdot\bar{e}_2 + \text{Real}(V^*\bar{e}_2)] - (\partial\psi^D_I/\partial\xi^1), \tag{13}$$

where $[-\theta_B(t)] = \alpha_f(t)$ is the instantaneous pitch angle of the airfoil and $\bar{V}_{B/I}(t) = V_{B/I}(t)\hat{e}_1 + V^2_{B/I}(t)\hat{e}_2$.

Hence, the unsteady Navier–Stokes equations in generalized orthogonal non-inertial body-fixed coordinates take the following form.

Stream function equation:

$$\frac{\partial}{\partial\xi^1}\left(\frac{g_{22}}{g^{\frac{1}{2}}}\frac{\partial\psi^D_I}{\partial\xi^1}\right) + \frac{\partial}{\partial\xi^2}\left(\frac{g_{11}}{g^{\frac{1}{2}}}\frac{\partial\psi^D_I}{\partial\xi^2}\right) = -g^{\frac{1}{2}}\omega_I, \tag{14}$$

Vorticity-transport equation:

$$g^{\frac{1}{2}}\frac{\partial\omega_I}{\partial t} + \frac{\partial}{\partial\xi^1}(\omega_I[g^{\frac{1}{2}}V^1]) + \frac{\partial}{\partial\xi^2}(\omega_I[g^{\frac{1}{2}}V^2]) = \frac{1}{\text{Re}}\left\{\frac{\partial}{\partial\xi^1}\left(\frac{g_{22}}{g^{\frac{1}{2}}}\frac{\partial\omega_I}{\partial\xi^1}\right) + \frac{\partial}{\partial\xi^2}\left(\frac{g_{11}}{g^{\frac{1}{2}}}\frac{\partial\omega_I}{\partial\xi^2}\right)\right\}. \tag{15}$$

In (14) and (15), the elliptic problem for the deviational stream function is coupled with the temporally parabolic vorticity–transport equation. The mathematical formulation can be completed by providing the boundary and initial conditions. However, before discussing these, the control strategy developed for this study will be examined. The boundary and initial conditions can then be presented in their final form.

2.4 *Active control using suction and injection*

From a theoretical consideration, Osswald (1992) has pointed out that the vorticity created at the surface drives some of the unsteady flow phenomena. Thus, flow phenomena such as incipient separation and subsequent development of vortical structure near the surface can perhaps be controlled by managing the creation of surface vorticity, which is governed by the vorticity boundary condition at the surface and, hence, is external to the governing equation. Thus, modulated suction/injection (MSI) control is developed. The active control model developed is based on the principal objective of delaying the unsteady separation to suppress the formation of the dynamic-stall vortex. A secondary goal is to increase the lift and reduce drag. In addition to these objectives, the constraints used in developing the active control model are that:

(i) the maximum non-dimensionalized mass flow rate be at the most 1%,
(ii) the net mass addition be zero and, finally,
(iii) the control model for MSI be as simple as possible.

Constraint (ii) is not critical; however, if employed, it allows the downstream boundary condition for the basic flow without MSI to remain valid for the flow even with the implementation of active control.

The active control model depends on a large number of variables, some of which are location, magnitude, suction/injection rate, duration, etc. A careful numerical optimization led to a trapezoidal profile for the MSI velocity, with the key parameters being depicted in figure 22 (see § 5.5). In the present study, the suction velocity is taken to be between 3·5 and 4·5% of the free-stream velocity, and is applied on the upper surface of the airfoil over approximately 9% of the chord starting from the leading edge (LE). The physical injection velocity is slightly smaller in magnitude as compared to the physical suction velocity. It should also be pointed out that the segment of the airfoil surface in the computational plane over which suction is applied is the same as that over which injection is applied. Then, to satisfy the constraint of zero net mass addition, injection is applied over 14% of the chord on the lower surface near the trailing edge (TE) of the airfoil. In fact, the constraint can be expressed as follows. In the physical plane, for suction applied over the upper surface near the LE segment (a–b), and injection over the lower surface near the TE segment (c–d), zero net mass addition requires

$$\int_a^b [1/(g_{22})^{\frac{1}{2}}](\bar{V}\cdot\bar{e}_2)\mathrm{d}l|_{\text{suc.}} + \int_c^d [1/(g_{22})^{\frac{1}{2}}](\bar{V}\cdot\bar{e}_2)\mathrm{d}l|_{\text{inj.}} = 0, \tag{16}$$

where the apparent velocity $\bar{V}$ on the surface can be written as

$$\begin{aligned}\bar{V} &= T(\xi^1, \xi^2_w, t)\hat{t} + N(\xi^1, \xi^2_w, t)\hat{n} \\ &= T(\xi^1, \xi^2_w, t)[\bar{e}_1/(g_{11})^{\frac{1}{2}}] + N(\xi^1, \xi^2_w, t)[\bar{e}_2/(g_{22})^{\frac{1}{2}}].\end{aligned} \tag{17}$$

In the non-inertial reference frame of the generalized-coordinates (ξ^1, ξ^2), (16) is given as

$$\int_{\xi^1_{np}} (g_{11})^{\frac{1}{2}} N(\xi^1, \xi^2_w, t)\mathrm{d}\xi^1 = 0. \tag{18}$$

where ξ^1_{np} represents the non-porous segments of the airfoil surface in the computational plane.

2.5 *Boundary conditions*

Using (12) and (13), the apparent velocity $\bar{V}$ can be expressed as

$$\begin{aligned}\bar{V} = {} & [\cos\theta_B(t) - V^1_{B/I}(t) - x^2\Omega_B(t)]\hat{e}_1 + [\sin\theta_B(t) - V^2_{B/I}(t) + x^1\Omega_B(t)]\hat{e}_2 \\ & + [(\mathrm{Real}(V^*\bar{e}_1)/g_{11}) + (1/g^{\frac{1}{2}})(\partial\psi^D_I/\partial\xi^2)]\bar{e}_1 \\ & + [(\mathrm{Real}(V^*\bar{e}_2)/g_{22}) - (1/g^{\frac{1}{2}})(\partial\psi^D_I/\partial\xi^1)]\bar{e}_2.\end{aligned} \tag{19}$$

From (17) and (19),

$$\begin{aligned}(g_{22}/g^{\frac{1}{2}})(\partial\psi^D_I/\partial\xi^1)|_{\text{body}} = {} & [\{\cos\theta_B(t) - V^1_{B/I}(t) + x^2\Omega_B(t)\}\hat{e}_1 \\ & + \{\sin\theta_B(t) - V^2_{B/I}(t) - x^1\Omega_B(t)\}\hat{e}_2]\cdot\bar{e}_2 \\ & + \mathrm{Real}(V^*\bar{e}_2) - (g_{22})^{\frac{1}{2}} N(\xi^1, \xi^2_w, t).\end{aligned} \tag{20}$$

Equation (20) leads to the boundary condition for the stream function at the surface as

$$\psi_I^D(\xi^1, \xi_w^2, t) = \{x^2[V_{B/I}^1(t) - \cos\theta_B(t)] - x^1[V_{B/I}^2(t) - \sin\theta_B(t)] - (\Omega_B(t)/2)[(x^1)^2 + (x^2)^2]\} - (\Gamma(t)/2\pi)\ln(r/a) - \int_{\xi_{np}^1} (g_{11})^{\frac{1}{2}} N(\xi^1, \xi_w^2, t)\mathrm{d}\xi^1, \tag{21}$$

where ξ_{np}^1 represents the non-porous segments of the body surface. Now, the surface vorticity can be evaluated from the following equation:

$$\omega_I|_{\text{body}} = -\frac{1}{g^{\frac{1}{2}}}\left[\frac{\partial}{\partial\xi^1}\left(\frac{g_{22}}{g^{\frac{1}{2}}}\frac{\partial\psi_I^D}{\partial\xi^1}\right) + \frac{\partial}{\partial\xi^2}\left(\frac{g_{11}}{g^{\frac{1}{2}}}\frac{\partial\psi_I^D}{\partial\xi^2}\right)\right]_{\text{body}}, \tag{22}$$

subject to the constraint of zero slip, which leads to

$$(g_{11}/g^{\frac{1}{2}})(\partial\psi_I^D/\partial\xi^2)|_{\text{body}} = -[\{\cos\theta_B(t) - V_{B/I}^1(t) + x^2\Omega_B(t)\}\hat{e}_1 + \{\sin\theta_B(t) - V_{B/I}^2(t) - x^1\Omega_B(t)\}\hat{e}_2]\cdot\bar{e}_1 - \text{Real}(V^*\bar{e}_1) + (g_{11})^{\frac{1}{2}}T(\xi^1, \xi_w^2, t). \tag{23}$$

Equation (20) is also used in the evaluation of (22). The corresponding condition in the far field can be written as

$$\psi_I^D = 0, \tag{24}$$

$$\omega_I = 0. \tag{25}$$

The examination of this boundary condition reveals that the viscous circulation $\Gamma(t)$ is still not determined; its determination is described in the next section.

2.6 *Viscous circulation and necessary condition for its determination*

The inviscid circulation $\Gamma_{in}(t)$ is given as

$$\Gamma_{in}(t) = 4\pi a \sin\alpha_f(t) \tag{26}$$

where a is the radius of the circle to which the airfoil is transformed (see figures 3d & e, § 3.1) and α_f is the flow angle at the given instant of time. The circulation $\Gamma(t)$ for the overall viscous flow is related to the inertial velocity $\bar{V}_I$ as

$$\Gamma(t) = \oint_{C_\infty} \bar{V}_I\cdot\mathrm{d}\bar{l} = -\oint_{C_\infty} \bar{V}_I\cdot\mathrm{d}\bar{l}, \tag{27}$$

taken around a circle C_∞ with its radius equal to infinity. The use of the Stokes' theorem leads to

$$\Gamma(t) = -\int_{S_0} (\nabla\times\bar{V}_I)\cdot\bar{n}\mathrm{d}s = -\int_{S_0} \bar{\omega}_I\cdot\bar{n}\mathrm{d}s, \tag{28}$$

where S_0 is the corresponding area of the entire flow domain whose boundary curve is C_∞. Even with this condition, the stream-function and vorticity equations, (14) and (15), respectively, still constitute a singular system of equations due to the linear dependence amongst them. This led to imposing the condition that the pressure in the multiply-connected flow domain be single valued and continuous along the body surface, i.e.,

$$\oint_{\text{body}} (\nabla p)\cdot \mathrm{d}\bar{l} = 0. \tag{29}$$

For flow past a square cylinder in a channel, again a multiply-connected domain, Matida *et al* (1975) had used (29) to close the equation set for their internal flow problem. This has provided the impetus to use this equation in the present analysis also. Indeed, (29) is used in the present analysis and serves to close the equation set. This condition is an alternative statement of the Kutta condition for viscous unsteady flow, namely, that the pressure at the TE has to be continuous and single valued. Osswald *et al* (1992) have pointed out that the only influence that pressure has on an incompressible flow is that it controls the creation and distribution of surface vorticity. Furthermore , this condition helps to close the problem, thereby implying that advanced wall vorticity can now be accurately determined. The initial conditions used are discussed next.

2.7 *Initial conditions*

To determine the flow field past a maneuvering body, initially the simulation of the flow past a stationary airfoil at fixed angle of attack is carried out. For this latter stationary configuration, the motion is started impulsively from rest at $t = 0$ and the corresponding inviscid solution is used as the initial condition. The viscous flow past a stationary body at a given angle of attack is determined. Next, up to an asymptotic time, $\tilde{t} = T$, the maneuvering motion is initiated at $\tilde{t} = T$ and the viscous circulation at the start is taken as

$$\Gamma(t)|_{t=0} = \Gamma_0(T), \tag{30}$$

where $\lim_{\tilde{t}\to T}\Gamma(\tilde{t}) = \Gamma_0(T)$ is the asymptotic value of the circulation computed by accounting for the angular acceleration $\tilde{\alpha}_{B/I}(t)$ due to maneuvering motion in the value of the circulation around a stationary airfoil.

2.8 *Pressure and force coefficients*

The analysis to be discussed here follows the development provided by Yang (1992). In the present $(\omega_I, \psi_I^p, \Gamma(t))$ formulation, pressure does not appear and, as such, to determine pressure, it is necessary to revert back to the linear-momentum equation given as

$$(\partial \bar{V}_I/\partial t) + (\nabla \times \bar{V}_I) \times \bar{V}_I + (1/\mathrm{Re})(\nabla \times \nabla \times \bar{V}_I) = -\nabla[p + (|\bar{V}_I|^2/2)]. \tag{31}$$

The pressure field in the incompressible flow can be evaluated accurately using the pressure Poisson equation obtained by taking the divergence of the linear-momentum equation, (31). If, on the other hand, only surface pressure is desired, it can be

determined more readily by carefully evaluating (31), along the surface; this leads to

$$\frac{\partial(p+q)}{\partial\xi^1}\Big|_{\text{body}} = \underbrace{-(g_{11})^{\frac{1}{2}}\frac{\partial T(\xi^1,\xi^2_w,t)}{\partial t}}_{\substack{\text{tangential acceleration}\\ \text{due to circulation control}\\ \text{along the body surface}}} - (\alpha_{B/I}(t)\times\bar{r})\cdot\bar{e}_1$$

$$\underbrace{+(g_{11})^{\frac{1}{2}}N(\xi^1,\xi^2_w,t)\omega_I}_{\substack{\text{pressure gradient due to}\\ \text{mass transfer along the}\\ \text{body surface as a result}\\ \text{of MSI}}} - \frac{1}{\text{Re}}\frac{g_{11}}{g^{\frac{1}{2}}}\frac{\partial\omega_I}{\partial\xi^2}, \tag{32}$$

where

$$q = \underbrace{\tfrac{1}{2}\{T^2(\xi^1,\xi^2_w,t)+N^2(\xi^1,\xi^2_w,t)\}}_{\text{addition of kinetic energy due to MSI}} + a^1_{B/I}(t)x^1 + a^2_{B/I}(t)x^2 - \tfrac{1}{2}\{(x^1)^2+(x^2)^2\}\Omega^2_B(t). \tag{33}$$

For evaluation of the terms involving apparent velocity on the surface, not all terms are zero and, for some additional details, see Yang (1992). Careful examination of (32) reveals that the temporal increase of the tangential control velocity can accelerate the flow, since $\partial p/\partial\xi^1 < 0$ and, for suction with $N(\xi^1,\xi^2_w,t) < 0$, as implemented in the unsteady separation region where $\omega_I > 0$, $(g_{11})^{\frac{1}{2}}N(\xi^1,\xi^2_w,t)\omega_I$ will also produce a favorable pressure gradient and lead to reduction in the boundary layer thickness. Thus, integrating (32) leads to

$$p|^{f_{\text{TE}}}_{i_{\text{TE}}} = -q|^{f_{\text{TE}}}_{i_{\text{TE}}} + \int_{\xi^1_0}^{\xi^1_1}\left\{(g_{11})^{\frac{1}{2}}N(\xi^1,\xi^2_w,t)\omega_I - (g_{11})^{\frac{1}{2}}\frac{\partial T(\xi^1,\xi^2_w,t)}{\partial t}\right\}\mathrm{d}\xi^1 - \int_{\xi^1_0}^{\xi^1_1}\left\{(\bar{\alpha}_{B/I}(t)\times\bar{r})\cdot\bar{e}_1 + \frac{1}{\text{Re}}\frac{g_{11}}{g^{\frac{1}{2}}}\frac{\partial\omega_I}{\partial\xi^2}\right\}\mathrm{d}\xi^1. \tag{34}$$

This then permits the determination of the surface pressure.

The force and moment coefficients as well as the surface force due to viscosity are now calculated using the surface pressure from (34), and the definition of the coefficient of pressure as

$$C_p = p^*/(\tfrac{1}{2}\rho U^2_\infty) = 2p, \tag{35}$$

where p^* is the dimensional pressure. Further, the force coefficient $\bar{C}_{F_p}$ is defined as

$$\bar{C}_{F_p} \triangleq \bar{F}_p/(\tfrac{1}{2}\rho U^2_\infty cb), \tag{36}$$

where the spanwise length b is taken as unity. Substituting (34) into (35), (36) is then written as

$$\bar{C}_{F_p} = -\oint_{\text{body}}\{[(g_{11})^{\frac{1}{2}}/(g_{22})^{\frac{1}{2}}]C_p\bar{e}_2\}\mathrm{d}\xi^1. \tag{37}$$

Similarly, the net dimensional force $\bar{F}_v$ due to viscosity is given as

$$\bar{F}_v = \oint_{\text{body}} 2\mu^* \{\tfrac{1}{2}[(\nabla^* \bar{V}_I^*) + \bar{V}_I^* \nabla^*)] - \tfrac{1}{3}(\nabla^* \bar{V}_I^*)\bar{\bar{I}}\} \cdot \hat{n} ds^*, \tag{38}$$

where μ^* is the dynamic viscosity and $\bar{\bar{I}}$ is the identity tensor. The coefficient of the viscous shear force is defined as

$$\bar{C}_{F_v} \triangleq \bar{F}_v / (\tfrac{1}{2}\rho U_\infty^2 cd). \tag{39}$$

Use of the expression for apparent velocity, (7), permits (39) to be expressed as

$$\bar{C}_{F_v} = (2/\text{Re}) \oint_{\text{body}} [(\nabla \bar{V}) + (\bar{V}\nabla)] \cdot \hat{n} ds. \tag{40}$$

For flows with MSI, an expression for (40) can be obtained in non-inertial body-fixed generalized coordinates (ξ^1, ξ^2) as

$$\bar{C}_{F_v} = \frac{2}{\text{Re}} \oint_{\text{body}} \left\{ \bar{e}^1 \frac{\partial \bar{V}}{\partial \xi^1} + \bar{e}^2 \frac{\partial \bar{V}}{\partial \xi^2} + \frac{\partial \bar{V}}{\partial \xi^2} e^{-2} \right\} \cdot \bar{e}_2 \frac{(g_{11})^{\frac{1}{2}}}{(g_{22})^{\frac{1}{2}}} d\xi^1, \tag{41}$$

where $\bar{e}^1$ and $\bar{e}^2$ are the contravariant base vectors of the generalized coordinates (ξ^1, ξ^2). In addition, by defining

$$(\partial \bar{V}/\partial \xi^1) \equiv A^1 \bar{e}_1 + A^2 \bar{e}_2 \quad \text{and} \quad (\partial \bar{V}/\partial \xi^2) \equiv B^1 \bar{e}_1 + B^2 \bar{e}_2, \tag{42}$$

(41) can be rewritten as

$$\bar{C}_{F_v} = \frac{2}{\text{Re}} \oint_{\text{body}} \left\{ \left[\frac{(g_{22})^{\frac{1}{2}}}{(g_{11})^{\frac{1}{2}}} A^2 + \frac{(g_{11})^{\frac{1}{2}}}{(g_{22})^{\frac{1}{2}}} B^1 \right] \bar{e}_1 + 2 \frac{(g_{11})^{\frac{1}{2}}}{(g_{22})^{\frac{1}{2}}} B^2 \bar{e}_2 \right\} d\xi^1. \tag{43}$$

Along the nonporous body surface, (41) is simplified to give

$$\bar{C}_{F_v} = \frac{2}{\text{Re}} \oint_{\text{body}} \left\{ \frac{(g_{11})^{\frac{1}{2}}}{(g_{22})^{\frac{1}{2}}} \frac{\partial}{\partial \xi^2} (V^1) \bar{e}_1 \right\} d\xi^1. \tag{44}$$

A similar analysis leads to the moment coefficient $\bar{C}_{M_p}$ and $\bar{C}_{M_v}$ as

$$\bar{C}_{M_p} = \oint_{\text{body}} \left[\frac{(g_{11})^{\frac{1}{2}}}{(g_{22})^{\frac{1}{2}}} C_p(\xi^1) \{x^1(\hat{e}_1 \times \bar{e}_2) + x^2(\hat{e}_2 \times \bar{e}_2)\} \right] d\xi^1, \tag{45}$$

and

$$\bar{C}_{M_v} = -\frac{2}{\text{Re}} \oint_{\text{body}} \left[\left\{ \frac{(g_{22})^{\frac{1}{2}}}{(g_{11})^{\frac{1}{2}}} A^2 + \frac{(g_{11})^{\frac{1}{2}}}{(g_{22})^{\frac{1}{2}}} B^1 \right\} \{x^1(\hat{e}_1 \times \bar{e}_1) + x^2(\hat{e}_2 \times \bar{e}_1)\} \right] d\xi^1$$
$$- \frac{4}{\text{Re}} \oint_{\text{body}} \left[\frac{(g_{11})^{\frac{1}{2}}}{(g_{22})^{\frac{1}{2}}} B^2 \{x^1(\hat{e}_1 \times \bar{e}_2) + x^2(\hat{e}_2 \times \bar{e}_2)\} \right] d\xi^1. \tag{46}$$

For nonporous body surface,

$$\bar{C}_{M_v} = -\frac{2}{\text{Re}} \oint_{\text{body}} \left[\frac{(g_{11})^{\frac{1}{2}}}{(g_{22})^{\frac{1}{2}}} \frac{\partial V^1}{\partial \xi^2} \{x^1(\hat{e}_1 \times \bar{e}_1) + x^2(\hat{e}_2 \times \bar{e}_1)\} \right] d\xi^1. \tag{47}$$

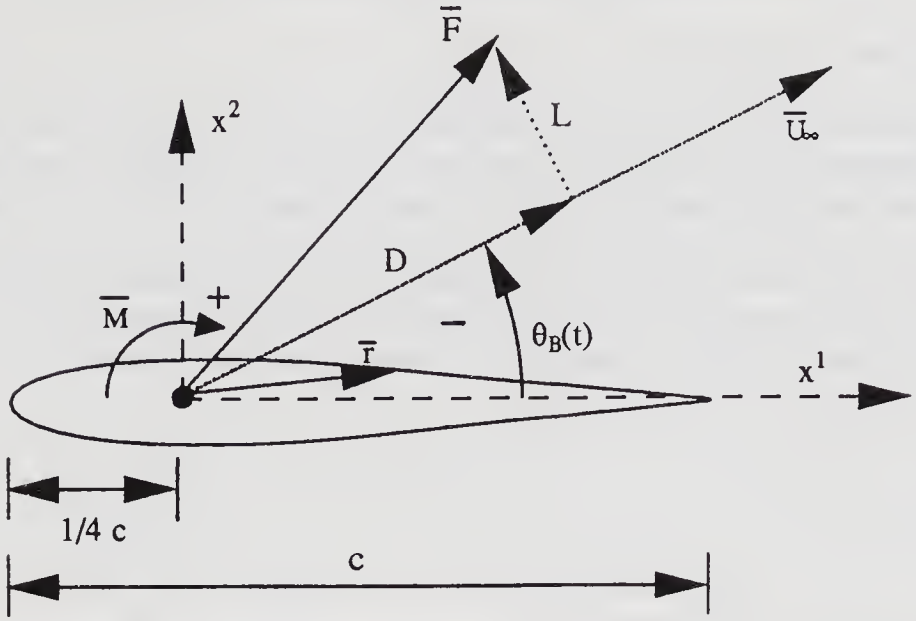

Figure 2. Depiction of forces and moments on the maneuvering airfoil.

To calculate the lift and drag coefficients from $\bar{C}_{F_p}$ and $\bar{C}_{F_v}$, it is convenient to define the force vector $\bar{F}$ as a complex variable such that

$$\bar{F} = \text{Real}(\bar{F})\hat{e}_1 + \text{Imag}(\bar{F})\hat{e}_2, \tag{48}$$

With this definition in (44), as shown in figure 2, the lift and drag coefficients become

$$\begin{aligned}
C_{L_p} &= \text{Imag}(\bar{C}_{F_p}) \times \cos\theta_B(t) - \text{Real}(\bar{C}_{F_p}) \times \sin\theta_B(t),\\
C_{D_p} &= \text{Real}(\bar{C}_{F_p}) \times \cos\theta_B(t) + \text{Imag}(\bar{C}_{F_p}) \times \sin\theta_B(t),\\
C_{L_v} &= \text{Imag}(\bar{C}_{F_v}) \times \cos\theta_B(t) - \text{Real}(\bar{C}_{F_v}) \times \sin\theta_B(t),\\
C_{D_v} &= \text{Real}(\bar{C}_{F_v}) \times \cos\theta_B(t) + \text{Imag}(\bar{C}_{F_v}) \times \sin\theta_B(t).
\end{aligned} \tag{49}$$

Further,

$$C_L = C_{L_p} + C_{L_v}, \tag{50}$$

$$C_D = C_{D_p} + C_{D_v}, \tag{51}$$

$$C_M = C_{M_p} + C_{M_v}. \tag{52}$$

3. Analytical grid generation technique

The mathematical problem formulated in § 2 is governed by a set of partial differential equations which can be solved efficiently using an advanced numerical technique. The overall solution technique requires a carefully generated grid that satisfies numerous criteria as far as quality of the grid is concerned. The grid should also provide the resolution of dominant length scales in the various critical regions that evolve in the flow field. The use of appropriate grid topology with a given mathematical formulation is also critical, since certain Navier–Stokes operators may turn out to be singular on a specific grid topology. The generalized Schwarz–Christoffel grid generation technique originally described by Davis (1979) and further developed by Osswald *et al* (1989) for flow past an arbitrary airfoil is used in this study.

3.1 *Conformal transformation*

The generalized mapping technique used here is conformal and provides analytic metric information, guarantees orthogonality, and has the capability of handling arbitrary bodies with sharp corners that occur for example at TE etc. As shown in figure 3a, a conformal mapping from the physical z-plane permits the airfoil to be transformed into a line segment in the upper half ζ-plane, as shown in figure 3b. A second conformal transformation permits this line segment in the upper half ζ-plane to be transformed to the complex potential plane P, as shown in figure 3c. This is

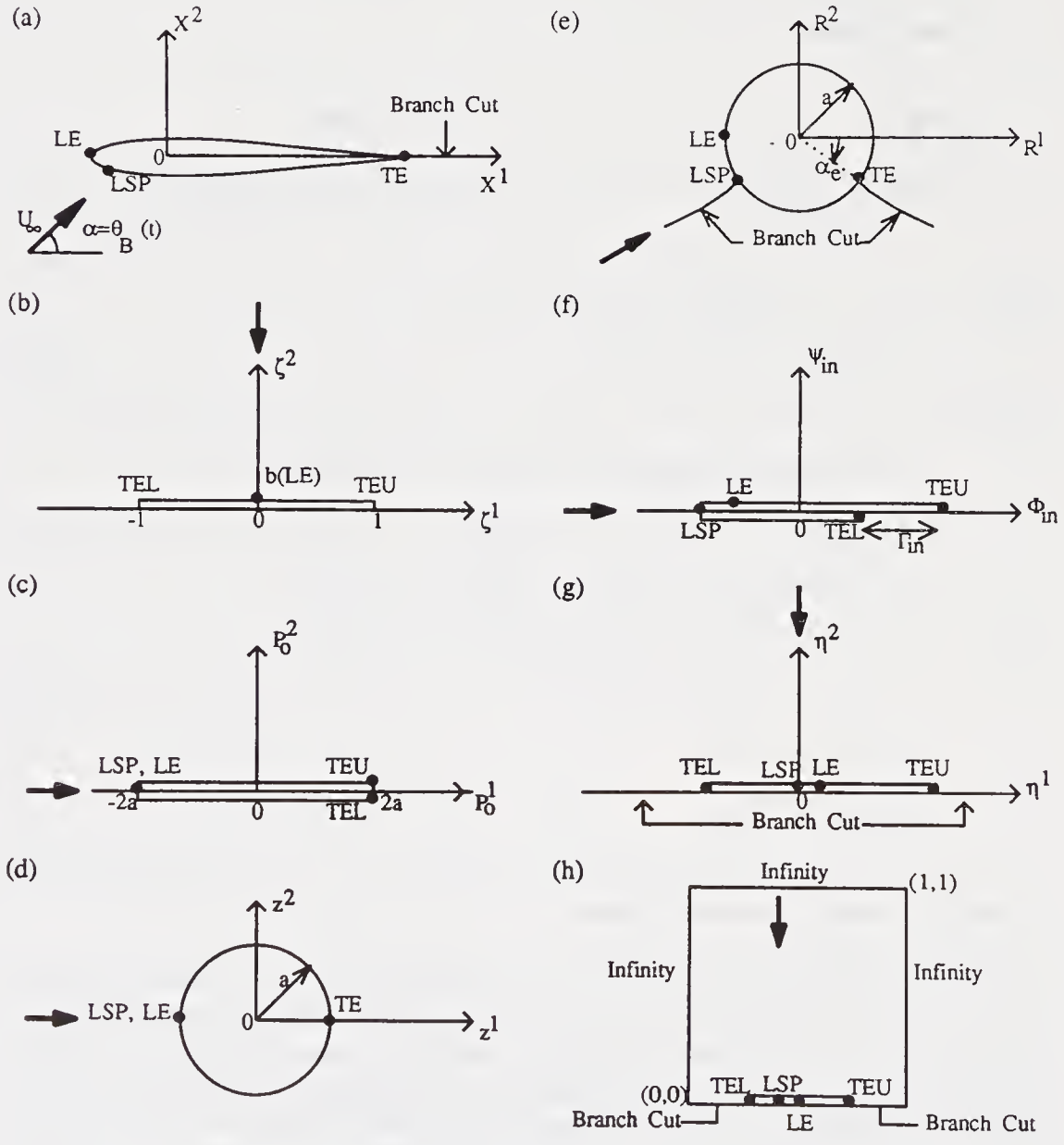

Figure 3. Representation of inviscid flow past a symmetric NACA 0015 airfoil at angle of attack (with circulation), in physical and various transformed planes. (**a**) Physical plane (z-plane); (**b**) stagnation-point flow plane (zero lift, ζ-plane); (**c**) complex potential plane (zero lift, P_0-plane); (**d**) circular cylinder plane (zero lift, Z-plane); (**e**) circular cylinder plane (lift, R-plane); (**f**) complex potential plane (lift, P-plane); (**g**) stagnation-point flow plane (lift, η-plane); (**h**) computational plane (ξ-plane).

subsequently transformed using the Joukowski transformation to a circle in the Z-plane, as shown in figure 3d. For lifting cases at non-zero incidence α_f, the Z-plane can be rotated by the effective angle of attack, $\alpha_e = \alpha_f + \beta$ to the circle-R plane, as shown in figure 3e, where a is the flow incidence angle and $-\beta$ is the angle of zero lift. The complex potential P for a uniform stream at incidence α_f past an arbitrary airfoil is obtained from the knowledge of the complex potential for flow past a circular cylinder. The complex potential P-plane is depicted in figure 3f and, if used as a final plane, it leads to a mesh with H-grid topology in the physical plane. This H-type grid does not provide sufficient resolution in the rounded-LE region. Therefore, yet one more parabolic conformal transformation is used to transform the airfoil to the complex η-plane, as shown in figure 3g. This now leads to a C-grid topology in the physical plane. Even though the C-grid will provide some clustering in the LE region, the far-field boundary condition to be placed at infinity will lead to numerical difficulties if the η-plane is used. Hence, the final transformation contracts this η-plane to the computational plane and is described in the next section.

3.2 *Clustering transformations*

One-dimensional clustering transformations are used to transform the upper-half stagnation point η-plane to a unit square in the computational ξ-plane. Osswald *et al* (1989) as well as Rohling (1991) have provided the details of the general cubic-spline functions used. In the streamwise direction, independent cubic-spline functions are used to achieve streamwise grid clustering along the suction and pressure surfaces and in the mid-wake and near-wake regions, both above and below the streamline which emanates from the trailing edge. The far-wake regions above and below the

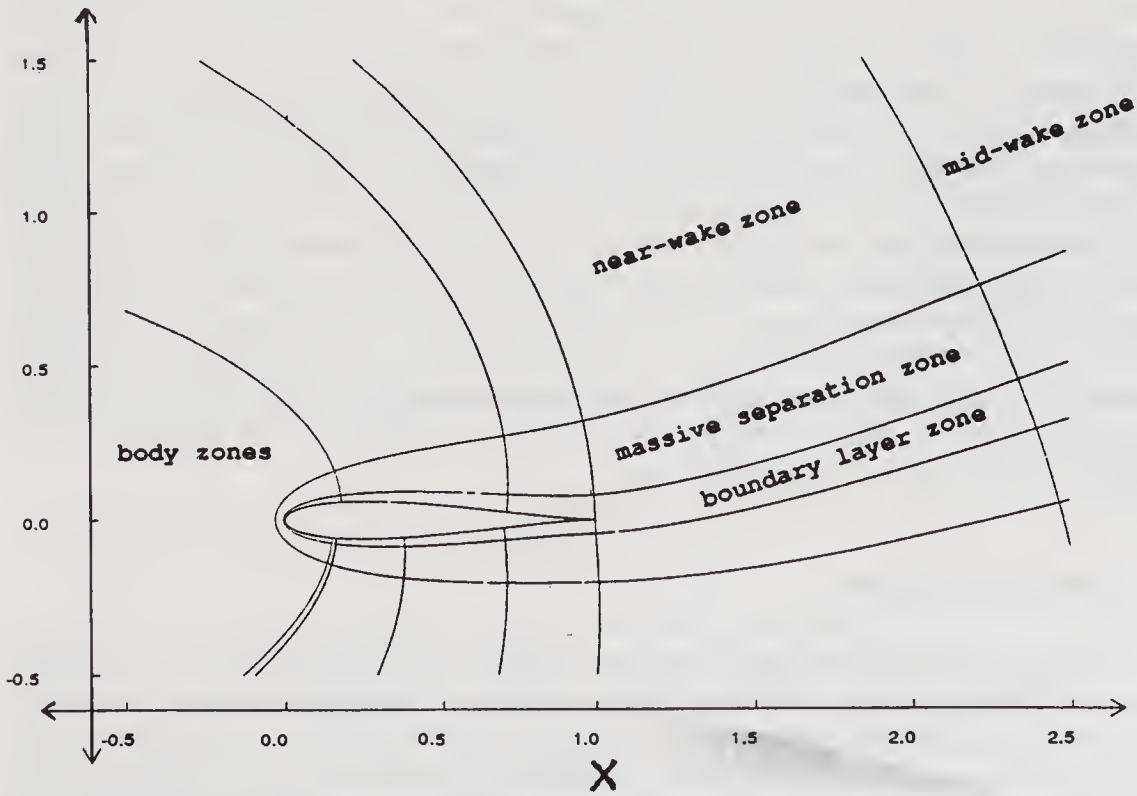

Figure 4. Depiction of various zones for streamwise and normal 1-D analytical cubic spline clustering transformations.

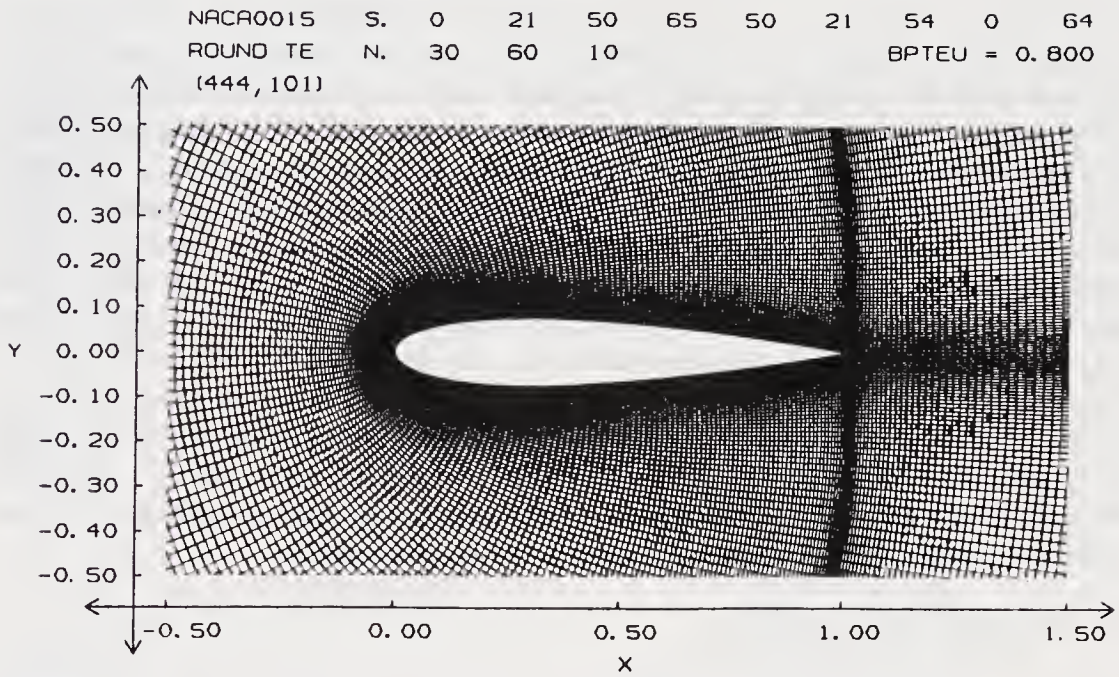

Figure 5. Grid distribution for an NACA 0015 airfoil with (444 × 101) mesh points.

TE streamline are contracted using 1-D inverse tangent transformations. Similarly, 1-D cubic-spline tranformations are also used in the normal directions in two zones, namely, (i) boundary layer and (ii) massively separated region which also includes the LE shear layer. Finally, a 1-D inverse tangent transformation is again required to map the far-field infinity boundary to a unit distance in the computational ξ-plane. The various regions discussed here are depicted in figure 4. A typical grid distribution for a NACA 0015 airfoil with (444 × 101) mesh points is shown in figure 5. An attempt has been made to resolve as many of the dominant scales as possible; these include the boundary layer scale of $O(\mathrm{Re}^{-1/2})$ for attached flow, the streamwise and normal scales of $O(\mathrm{Re}^{-3/8})$ and $O(\mathrm{Re}^{-5/8})$, respectively, near the separation point, the separated free shear layer with the scale of the order of its thickness, the massively separated zone of $O(1)$ and the scale of $O(\mathrm{Re}^{-5/11})$ for the boundary layer eruption in the separated region. This is important in order to ensure that the simulation results truly preserve the physics of the problem. The way in which this is partially achieved is by generating a grid with zonal attributes with continuous metrics across all of the zones both in streamwise and normal directions. Not only is the clustered conformal grid generated here by an analytical-numerical procedure, but the evaluation of the metric tensor and base vector is also carried out analytically once the transformations have been defined.

4. Numerical method

The basic numerical technique for maneuvering motion was developed by Osswald *et al* (1990). Variations of this approach have been used by the present researchers in some of their earlier papers. It is a fully implicit finite-difference method involving direct matrix inversion methodology. All of the spatial derivatives are approximated using second-order accurate central difference approximations, except for the convective terms. These latter nonlinear terms are approximated using a biased,

third-order accurate, upwind differencing-scheme to be able to simulate higher Reynolds number flows. The vorticity transport equation, (15), is solved using a variation of the alternating-direction implicit (ADI) technique of Douglas & Gunn (1964). When this technique is cast in delta form, it is computationally efficient. The elliptic stream function equation, (14), is solved by a direct block Gaussian elimination (BGE) technique. No explicit artificial dissipation is added in the implementation of the overall ADI-BGE method.

The algorithm consists of a forward elimination sweep for the vorticity and stream function equations. This is followed by the determination of advanced wall vorticity, together with the computation of the viscous circulation. This is achieved with the help of (29) which requires continuity of the pressure at the trailing edge. Both the wall vorticity and $\Gamma(t)$ are determined using an iterative technique and by maintaining a strict convergence criterion, such that the relative percentage error is less than 10^{-6}, and the residue in the instantaneous wall vorticity is negligible. Subsequently, the back substitution sweep for the vorticity and stream function equations is carried out to achieve the final solution. It should be noted that, due to the use of the third-order biased upwind differencing, the discretized problem leads to a pentadiagonal matrix which can be solved using a generalized Thomas algorithm.

One final comment corresponds to the determination of the pressure field. The analysis provided so far is adequate if only surface pressure is of interest. On the other hand, if the entire pressure field is desired, the solution of a Neumann–Poisson problem for pressure can be carried out as given by K Ghia *et al* (1992a). The results obtained in the present study are discussed next.

5. Results and discussion

The continuous and discrete analyses developed in the earlier sections are used to study the motion past maneuvering NACA airfoils. In this section, first the constant-rate pitch-up motion studied will be outlined, followed by validation and verification studies. Finally, some detailed results will be provided for constant-rate pitch-up motion; these results are computed without and with modulated suction/injection. Simulation results are also obtained in the form of a colour video animation and, while discussing the results, the present authors have taken the liberty to use these animations to clarify various research issues and provide further insight into the prevailing flow phenomena.

A total of three flow configurations have been studied; these are as listed below.

Configuration	Re	$\dot{\alpha}^+/k$	Remarks
I	5,000	1·0	for verification study
II	45,000	0·2	without flow control
III	45,000	0·2	with modulated suction/injection

In addition, results have been obtained for a flow configuration with Re = 52,000 and $\dot{\alpha}^+ = 0{\cdot}072$. These results have been discussed by Yang (1992).

5.1 *Constant-rate pitch-up maneuver*

In all the earlier studies by the authors, the constant-rate pitch-up motion used is the one defined by Visbal & Shang (1989) as:

$$\bar{r}_{B/I}(t) = 0,$$
$$\theta_B(t) = \Omega_0[t - (t_0/(4{\cdot}6))(1 - e^{-(4{\cdot}6/t_0)t})] \tag{53}$$

where $\Omega_0 = \dot{\alpha}^+ = \Omega c/U_\infty$ is the non-dimensional pitch rate and $\theta_B(t)$ is the instantaneous pitch angle of the airfoil. In the present study, $t_0 = 0{\cdot}5$, $\Omega_0 = 0{\cdot}2$ and the airfoil is pitched about the axis through the quarter-chord point (QCP).

5.2 *Verification study*

We have established earlier (K Ghia *et al* 1990–1992; Osswald *et al* 1990) that the mathematical model is accurate and that the modification in the far-field boundary condition which necessitates the use of viscous circulation $\Gamma(t)$ has indeed given better results, as shown by Osswald *et al* (1992). Thus, the main emphasis here is on the verification study, rather than on validation of the mathematical model. In this verification study, the accuracy of the numerical solutions obtained is examined critically, and the influence of the discretized parameters of the problem on the solution is assessed.

Flow configuration II described above is used for the verification study. The parameters for this basic flow configuration II are $\mathrm{Re} = 45{,}000$, $\dot{\alpha}^+ = 0{\cdot}2$. Three different grid sizes, namely (i) coarse grid with (330×75) points, (ii) medium (standard) grid with (444×101) points, and (iii) fine grid (544×121) points are used. The minimum grid spacings for the standard grid in the streamwise and normal directions near the leading edge are $0{\cdot}54 \times 10^{-3}$ and $0{\cdot}26 \times 10^{-4}$, respectively. To resolve the temporal scale of this unsteady separated flow problem and to achieve time consistency of the solution, a value of $\Delta t = 0{\cdot}001$ was chosen. The code has been fully vectorized and requires 7·5 micro-seconds per time step, per mesh point, using a single processor of the CRAY Y-MP 8/864 of The Ohio Supercomputer Center.

5.2a *Effect of grid stretching on the solution*: Unique to the present analysis is the fact that the far-field boundary condition is implemented at true infinity. As discussed earlier in § 3.2, 1-D clustering transformations are used to treat the infinite domain numerically. It is the arc-tangent transformation that permits the mapping of the boundary at infinity to a finite location in the computational plane. This implies that the grids are stretched exponentially, and it is important to examine the variation of the dependent variables in the far field and, specifically, their approach to the imposed far-field boundary conditions, if the solutions are to be accurate. Due to the clustering transformation, cells of semi-infinite extent occur in the physical plane. The effect of large grid stretching on the solution can be seen best in the computational plane, and is now discussed.

Vorticity attenuates exponentially away from the surface where it is created. Figures 6a &b show the vorticity contours for flow past a NACA 0015 airfoil undergoing constant-rate pitch-up motion with $\dot{\alpha}^+ = 0{\cdot}2$, for two different instantaneous positions, $\alpha = 20{\cdot}54°$ and $36{\cdot}58°$, respectively. The global views for both instants are shown in this figure, as are the enlarged views in the far-field, which clearly show that the

vorticity smoothly approaches the far-field boundary condition, $\bar{\omega}_I = 0$. The effect of grid stretching on the corresponding stream function is shown in figure 7. A close look at figures 7a & b clearly shows that the far-field boundary is reached as the value of the deviational (i.e., the disturbance) stream function approaches zero, i.e., as $\psi_I^D = 0$.

A round-off error study was also performed, and the procedure is as follows. In the Dirichlet–Poisson equation for ψ_I^D, (14), ψ_I^D is assumed to be known analytically as any one of the two functions prescribed in figure 8. With this function, the source term involving ω_I is computed numerically using a finite-difference stencil, with extended precision. The computed values of ω_I are used to solve the stream function equation, (14), and the numerically computed values of ψ_I^D are compared with the corresponding known analytical values. The difference in the two solutions represents the round-off error on the present (444 × 101) grid. Figure 8 clearly shows that the maximum error never exceeds 10^{-7} for a solution field which lies between 0 and 1. The error also does not exceed the maximum truncation error of $O(10^{-4})$. In addition, the metric coefficients used in the calculations are shown in figure 9; these are well behaved as expected.

5.2b *Grid-refinement study*: The grid distribution for all of the three grids mentioned earlier, in the proximity of the NACA 0015 airfoil are depicted in figure 10. For the airfoil at zero angle of attack in flow configuration II, the instantaneous vorticity contours near the TE and, subsequently, in the near wake, are presented here. They show that the flow structure consisting of nearly symmetric vortices at the TE prevails for all of the grids at $t = 3{\cdot}5$. As t increases to 4·5, the results of the finer grid show that the vortex symmetry is broken, that is the Hopf bifurcation has just occurred forming the asymmetric needle-type vortex structures of opposite sign in the flow field. At still larger time $t = 5{\cdot}5$, the flow field results of medium grid show the vortex shedding process is not only lagging behind the fine grid results but is also out of phase with the latter results. The coarser results still continue to show further growth of symmetric vortical structure near the TE. For truly unsteady flow, it is difficult to carry out this grid refinement study, but, in light of the present results the degree to which the differences are observed is clarified.

Once the asymptotic state is achieved for the flow field with the airfoil at zero angle of attack, the constant-rate pitch-up motion with $\dot{\alpha}^+ = 0{\cdot}2$ is initiated. The results in terms of the instantaneous vorticity contours for $15{\cdot}96° \leqslant \alpha \leqslant 35{\cdot}44°$ are delineated in figure 11. The coarse-grid results are quantitatively different. It should also be stated that, compared to the results in figure 10, results for the medium grid do show a departure from the fine-grid results, although qualitatively the two structures are very similar. Thus, the results in figure 11 suggest that the grid be further refined and then see if the changes are smaller than the previous refinement in which grid size was changed from (444 × 101) to (544 × 121). Unfortunately, the results with the (544 × 121) are computationally very costly, with the total CPU time for the fine grid case nearly 5 times higher than for the medium grid using a single processor on the CRAY Y-MP 8/864 at the Ohio Supercomputer Center. Next, the C_p- distribution at the surface as well as the wall vorticity are plotted in figures 12a, b for $\alpha = 14{\cdot}81°$ and 29·71°, respectively. For $\alpha = 14{\cdot}81°$, where the flow is mostly attached, the surface C_p-distribution for all three grids is in conformity and it even agrees well with the experimental data of Walker *et al* (1985). The corresponding wall vorticity shows similar behaviour, as shown in figure 12a; however, there are no experimental data

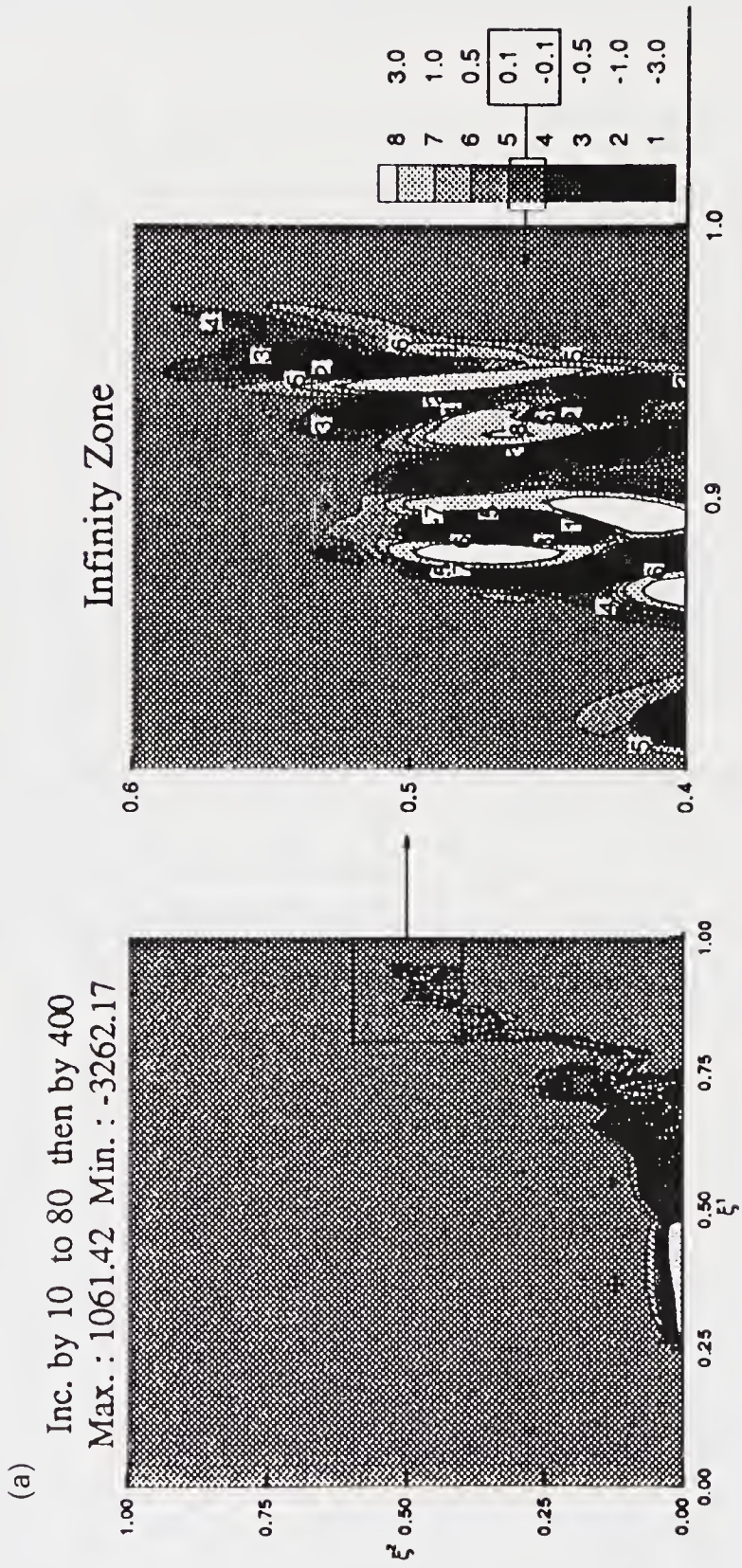
(a)
Inc. by 10 to 80 then by 400
Max. : 1061.42 Min. : -3262.17
Infinity Zone
8 7 6 5 4 3 2 1
3.0 1.0 0.5 0.1 -0.1 -0.5 -1.0 -3.0
1.00 0.75 0.50 0.25 0.00
0.00 0.25 0.50 0.75 1.00
0.6 0.5 0.4
0.9 1.0

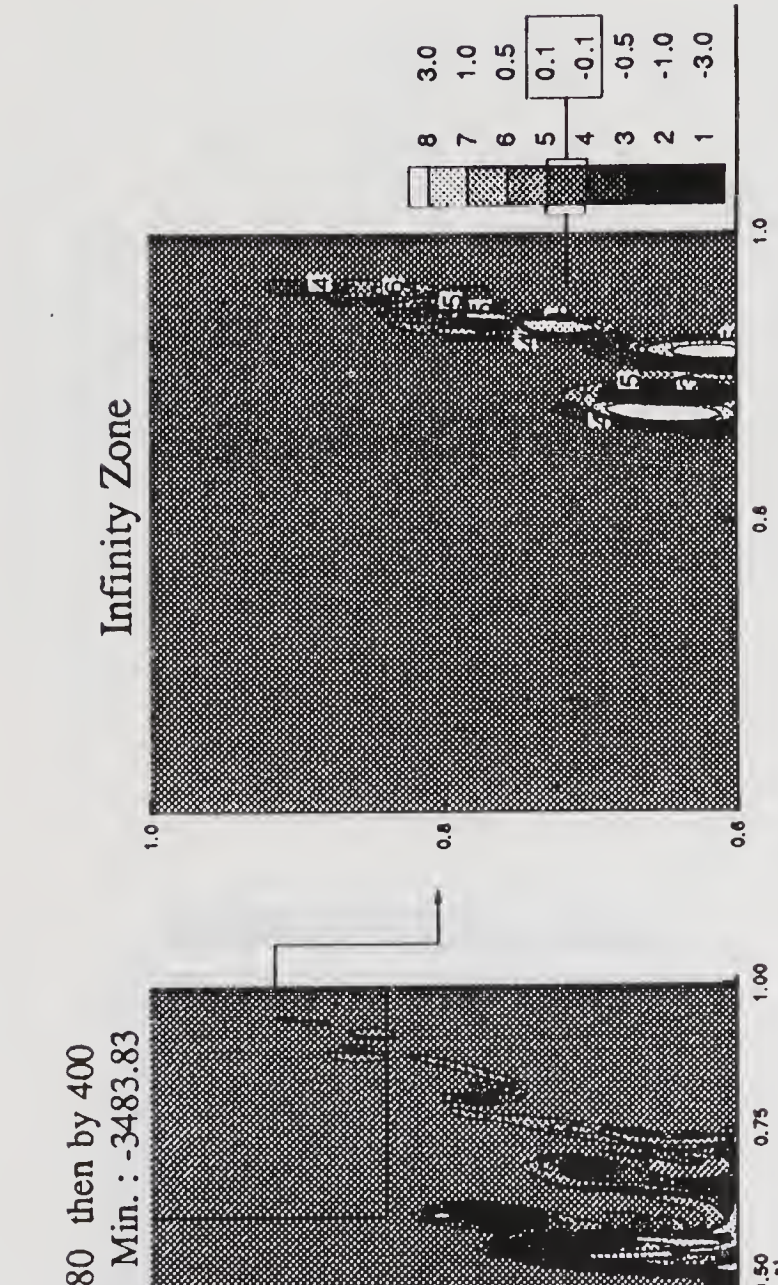

Figure 6. Effect of grid stretching on far-field solution – vorticity contours in computational plane. (Constant pitch-up motion; NACA 0015 airfoil, Re = 45,000; *C*-grid (444, 101); vorticity distribution (ADI solution).) (**a**) Time = 1·50, $\alpha = 20{\cdot}54°$; (**b**) time = 3·30, $\alpha = 36{\cdot}58°$.

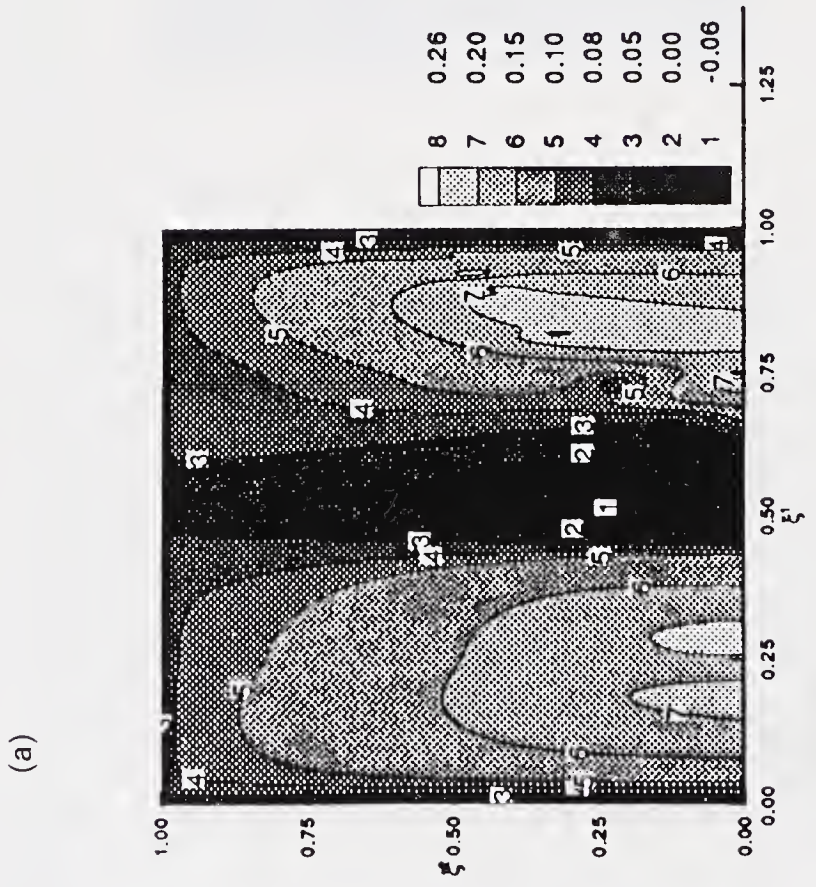
(a)
1.00
0.75
0.50
0.25
0.00
ξ
0.00
0.25
0.50
0.75
1.00
1.25
η'
8 0.26
7 0.20
6 0.15
5 0.10
4 0.08
3 0.05
2 0.00
1 -0.06
● Dirichlet (body surface, infinity)
with symmetric condition (branch-cut)
– Poisson problem for BGE solution
● $\alpha = 20.50°$
Max.$|\Psi_\ell^D|$:0.266 at (0.817, 0.32)
● $\alpha = 36.58°$
Max.$|\Psi_\ell^D|$:0.355 at (0.601, 0.41)
● $0.0° \leqslant \alpha \leqslant 36.58°$
$0.083 \leqslant$ Max.$|\Psi_\ell^D| \leqslant 0.355$

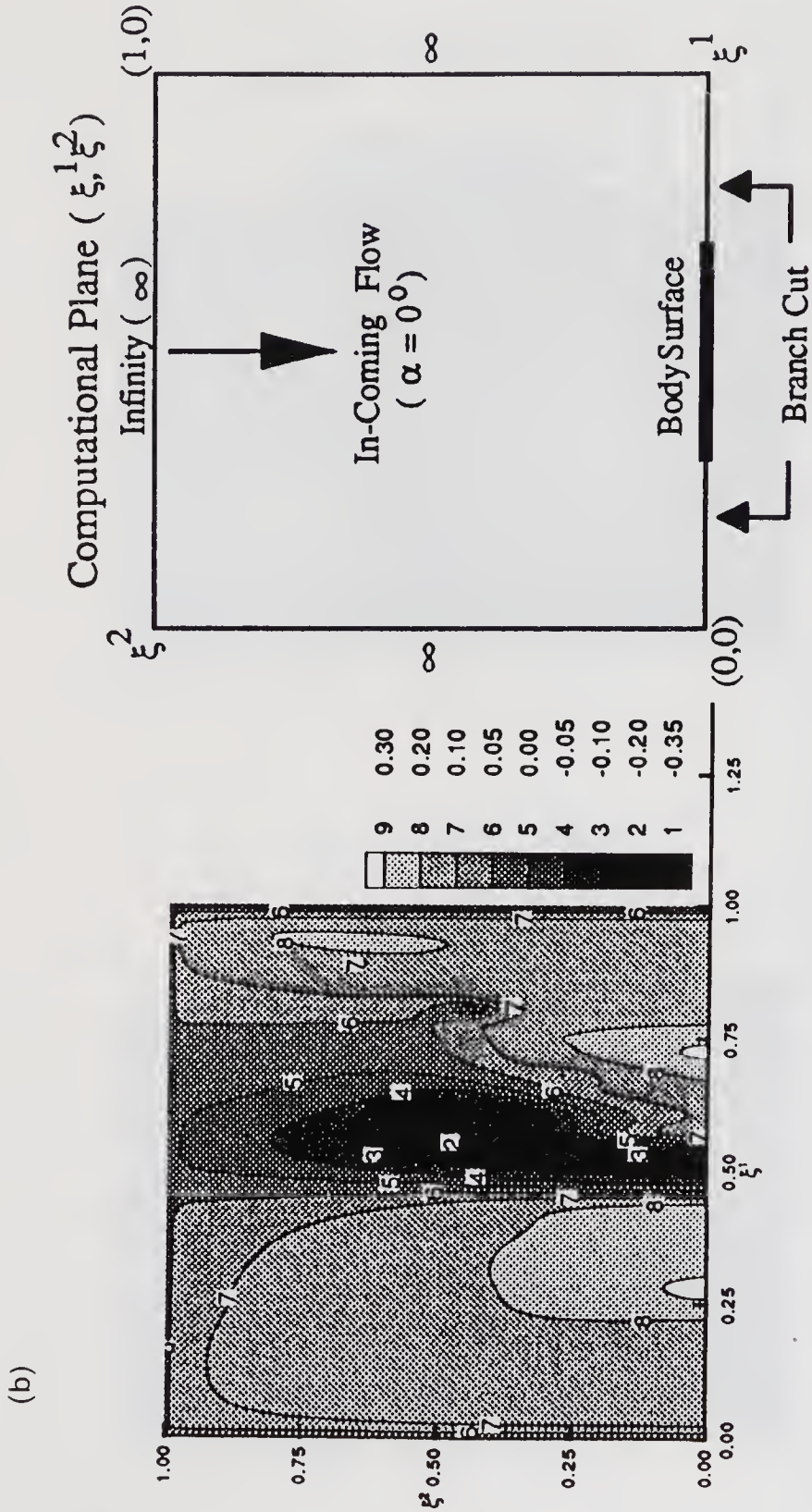

Figure 7. Effect of grid stretching on far-field solution – disturbance stream function distribution (BGE solution) in computational plane. Other conditions including time and α values for (**a**) and (**b**) as in figure 6.

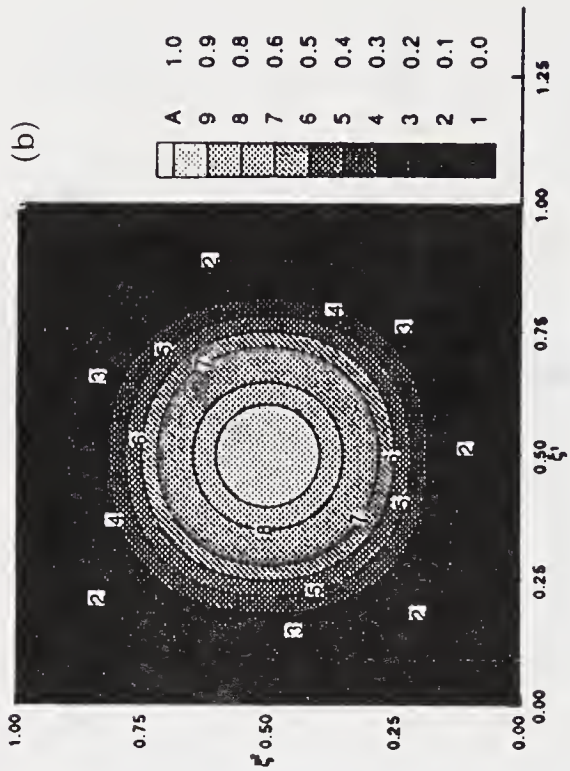

$$F(\xi^1,\xi^2) = \frac{1}{4}\,[1-\cos(2\pi\xi^1)]\,[1-\cos(2\pi\xi^2)]$$

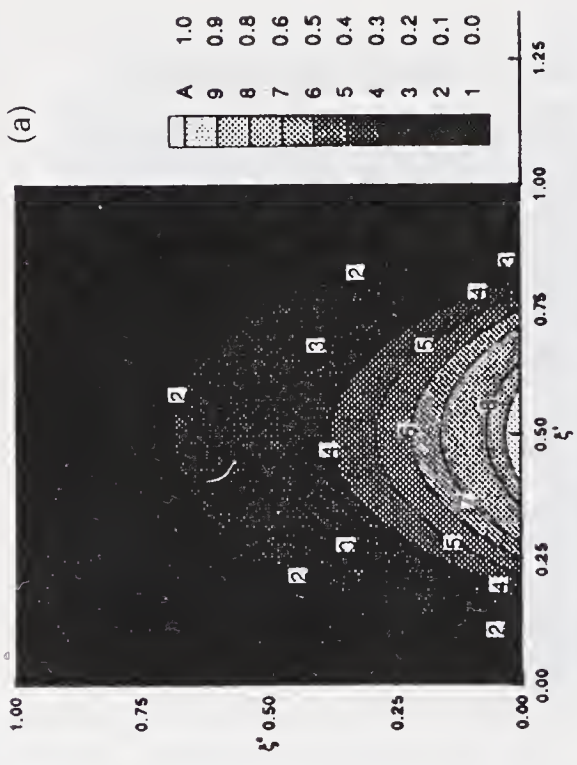

$$F(\xi^1,\xi^2) = -\frac{1}{2\sinh(\pi)}\,[1-\cos(2\pi\xi^1)]\,[\sinh(\pi(\xi^2-1))]$$

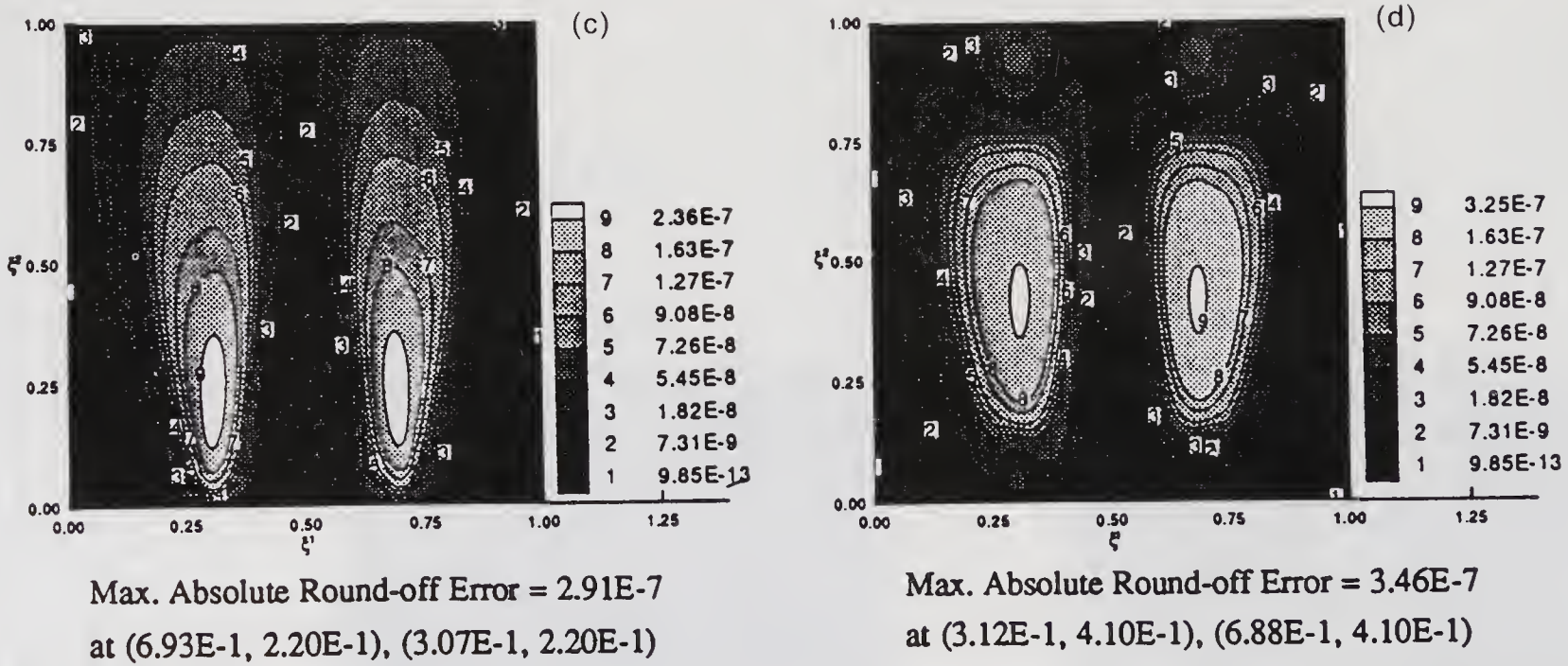

Figure 8. Estimation of accumulated round-off error distribution due to grid stretching in block-Gaussian elimination solution (Dirichlet-Poisson problem; computational plane (ξ^1, ξ^2); truncation error in space: $O((\Delta\xi^1)^2, (\Delta\xi^2)^2)$, $(\Delta\xi^1)^2 = 5{\cdot}1\text{E}-6$, $(\Delta\xi^2)^2 = 1{\cdot}0\text{E}-4$; grid size: (444, 101)). (**a**) & (**b**) Normalized $F(\xi^1, \xi^2)$ distributions; (**c**) & (**d**) absolute round-off error distributions.

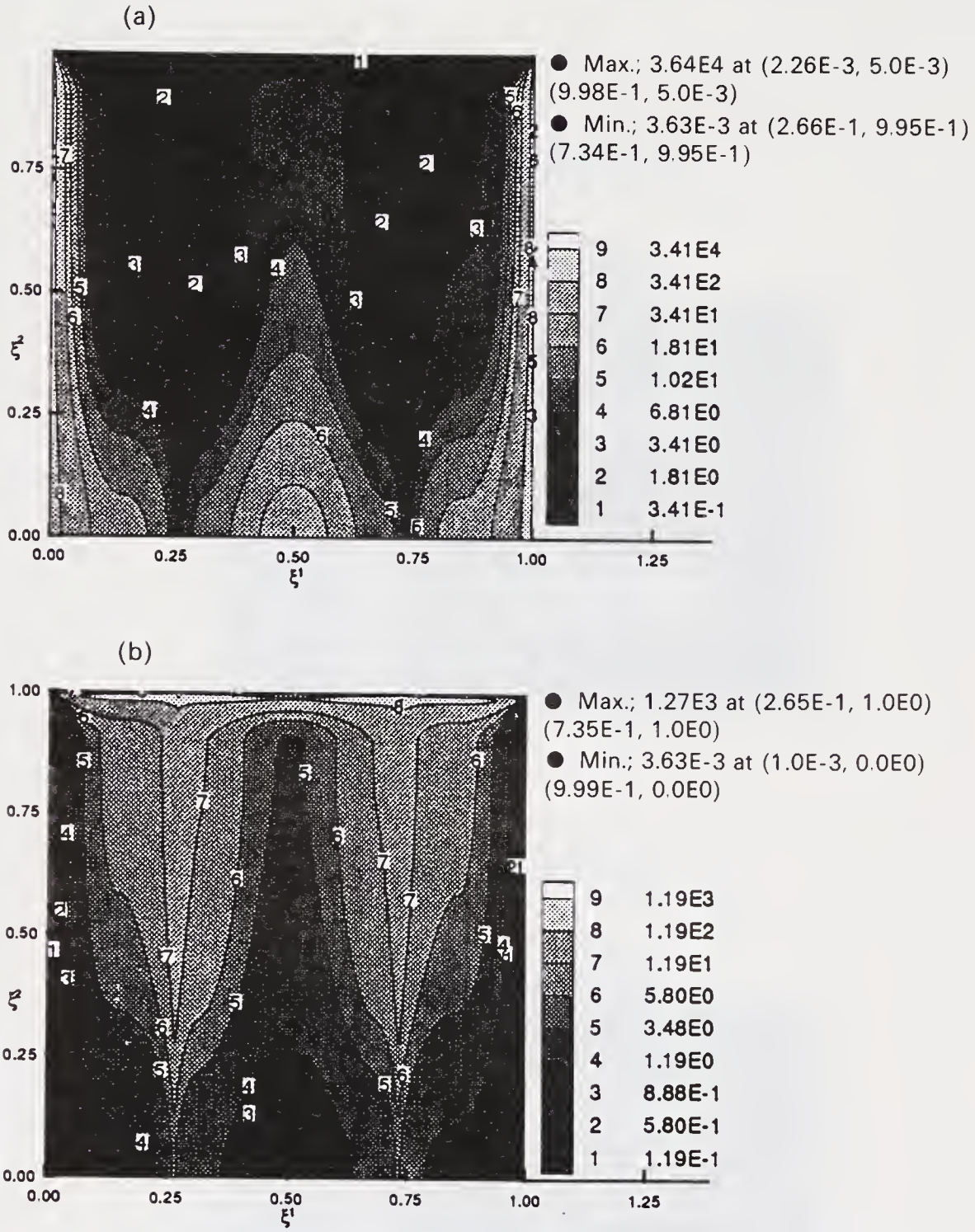

Figure 9. Distribution of metric coefficients, for round-off error study (computational plane (ξ^1, ξ^2); grid size: (444, 101)). (**a**) G11, (**b**) G22β.

available for wall vorticity. On the other hand, at $\alpha = 29{\cdot}71°$, with massively separated flow regions, the surface C_p-distributions show significant changes, although qualitatively they do conform to the experimental results given by Walker *et al* (1985). In figure 12b, the wall vorticity on the suction surface does show significant departures, again questioning the grid independence of the results between the medium and fine grid at this level of the grid size. The only satisfactory comparison is that for C_L, as shown in this figure. It depicts that the coarse-grid results compare well with the

experimental data of Walker *et al* (1985). However, the medium- and fine-grid results predict higher C_L-distribution in the massively separated flow regime. A careful examination of the experimental set-up reveals that Walker *et al* (1985) had only 36 surface static pressure taps, as compared to about 207 grid points in the present simulation with (444 × 101) grid points. Thus, better resolution in the computational simulation permits determination of each of the individual vortices that evolve and carries with it somewhat higher values for C_L-distribution as compared to the corresponding experimental values. Hence, for the finest grid presently used, still larger values of C_L are seen in this figure.

5.2c *Comparison with available Navier–Stokes results*: Simulation results are also obtained for a sinusoidally pitching NACA 0012 airfoil with $\mathrm{Re} = 5{,}000$, $\alpha = 10°(1 - \cos kt)$, and reduced frequency based on chord length, $k = 1.0$. Some experimental data are available for this configuration from Werlé (1976). Also, Mehta (1977) has provided carefully simulated Navier–Stokes results using the NS equations in terms of $(\bar{\omega}, \psi)$. He has used an O-grid topology and provided detailed results. As seen in figure 13, the streaklines for the present results compare favorably with the experimental data of Werlé (1976) and show a flow structure representative of unsteady flows. The flow is separated over the entire suction surface. Also shown in this figure are the contours of instantaneous vorticity and the velocity vectors. The better resolution of the present results is clear and these results conform well with those of Mehta (1977). For this sinusoidally pitching airfoil, the instantaneous stream-function contours are compared in figure 14. The results first show one instant for $\alpha = 18.59°$ in the upward stroke, which goes up to $\alpha = 20°$, and then four values of α for the return stroke. For the stream function, which is not very sensitive, the agreement is good. For the same values of α, comparison is also provided for the instantaneous vorticity contours in figure 15. The qualitative agreement between the two sets of results is very good, although the better resolution of the present results due to the use of a finer grid, made possible by a better and larger computer, is very evident. The complete evolution of the dynamic stall event is vivid, and some of the interactions that take place can be inferred from this figure. Finally, the C_L-distribution, as well as the surface pressure coefficients for two values of α, namely, $\alpha = 18.57°$ during pitch-up and $\alpha = 11.11°$ during pitch-down, are shown in figure 16. Also shown in this figure are the results of Sankar & Tassa (1980). In general, C_L compares qualitatively with the existing results, but there are significant deviations. For the time being, this completes the verification study; additional verification with experimental data is provided in the next section.

5.3 *Influence of initial state on the flow field*

For flow configuration II, results are initially obtained to determine the asymptotic state at fixed angle of attack. Since this asymptotic state is not unique, the effect of the initial state of flow will prevail in the final solution. To determine this effect, three different asymptotic states are selected, and correspond to states (b), (c) and (d) on the C_L-history curve in figure 17 corresponding to $\alpha = 0°$. With these states as the starting solutions, three different calculations are made for constant-rate pitch-up motion and the results are compared in figure 17. The lift coefficient distribution, as well as the viscous circulation, for all three cases do conform with one another and do not show strong influence of the initial state. The instantaneous vorticity contours

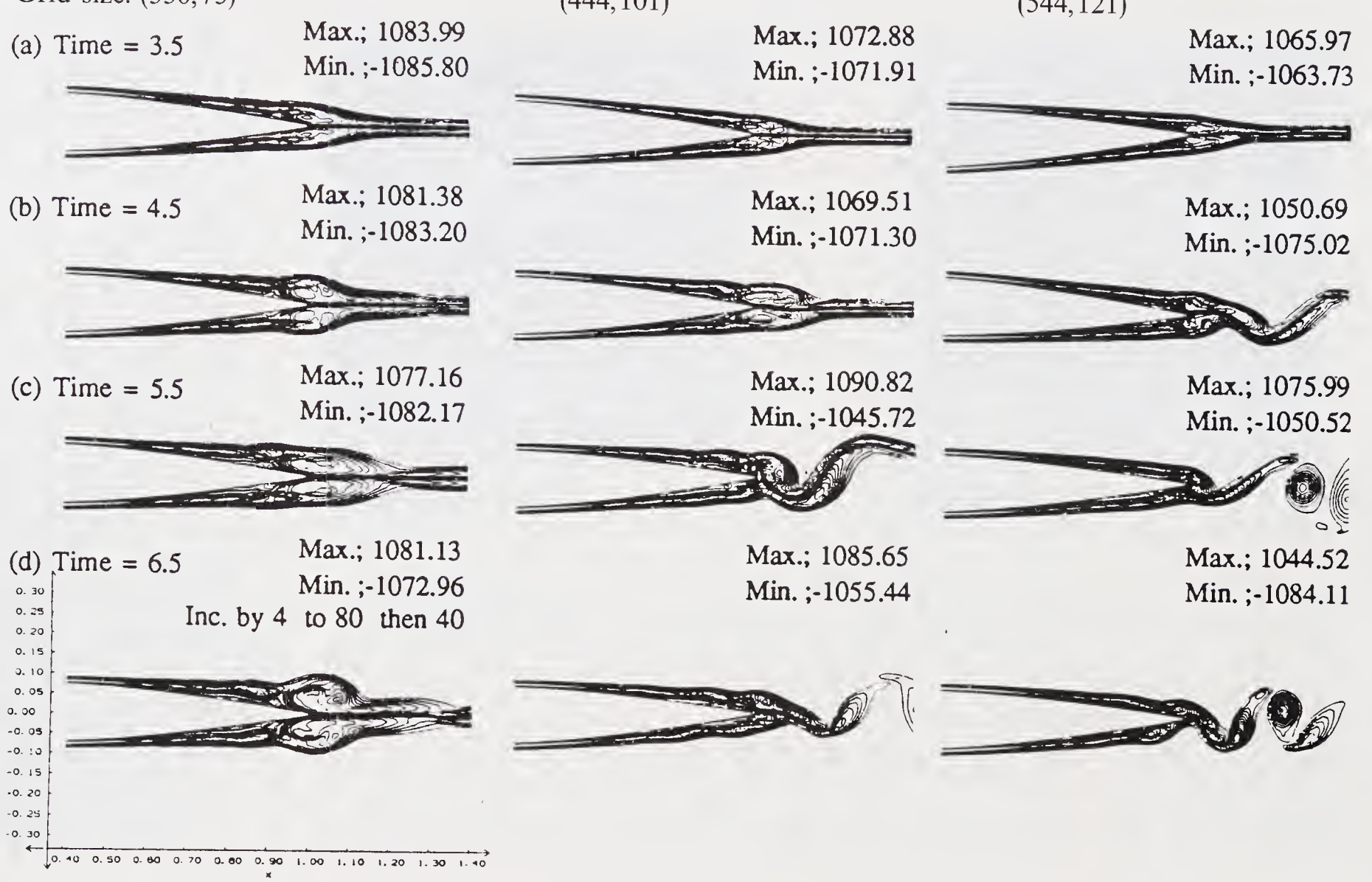
Grid size: (330,75)
(444,101)
(544,121)
(a) Time = 3.5
Max.; 1083.99
Min. ;-1085.80
Max.; 1072.88
Min. ;-1071.91
Max.; 1065.97
Min. ;-1063.73
(b) Time = 4.5
Max.; 1081.38
Min. ;-1083.20
Max.; 1069.51
Min. ;-1071.30
Max.; 1050.69
Min. ;-1075.02
(c) Time = 5.5
Max.; 1077.16
Min. ;-1082.17
Max.; 1090.82
Min. ;-1045.72
Max.; 1075.99
Min. ;-1050.52
(d) Time = 6.5
Max.; 1081.13
Min. ;-1072.96
Inc. by 4 to 80 then 40
Max.; 1085.65
Min. ;-1055.44
Max.; 1044.52
Min. ;-1084.11
0.30
0.25
0.20
0.15
0.10
0.05
0.00
-0.05
-0.10
-0.15
-0.20
-0.25
-0.30
0.40 0.50 0.60 0.70 0.80 0.90 1.00 1.10 1.20 1.30 1.40
x

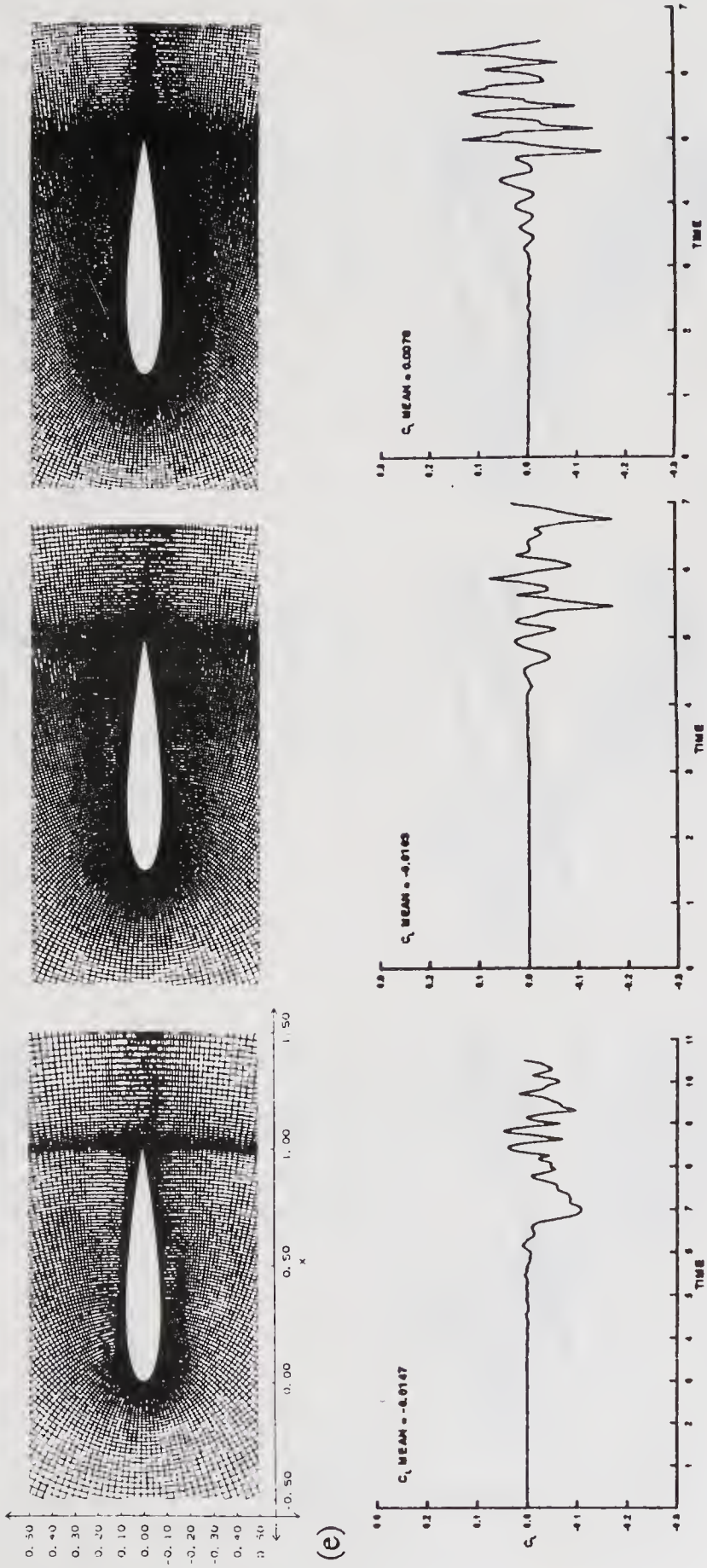

Figure 10. Effect of three different grid distributions on asymptotic flow solution at $\alpha = 0°$, for $Re = 45{,}000$, $\dot{\alpha}^+ = 0{\cdot}2$. (**a**)–(**d**) Vorticity contours near TE, (**e**) time history of lift coefficient at $\alpha = 0°$.

Grid Size ; (330,75) (444,101) (544,121)

(a)

Max.; 703.42
Min. ;-3089.45

Max.; 1061.42
Min. ;-3262.17

Max.; 827.00
Min. ;-3339.18

(b)

Max.; 2044.22
Min. ;-4137.37

Max.; 2905.62
Min. ;-4230.13

Max.; 3397.65
Min. ;-4482.60

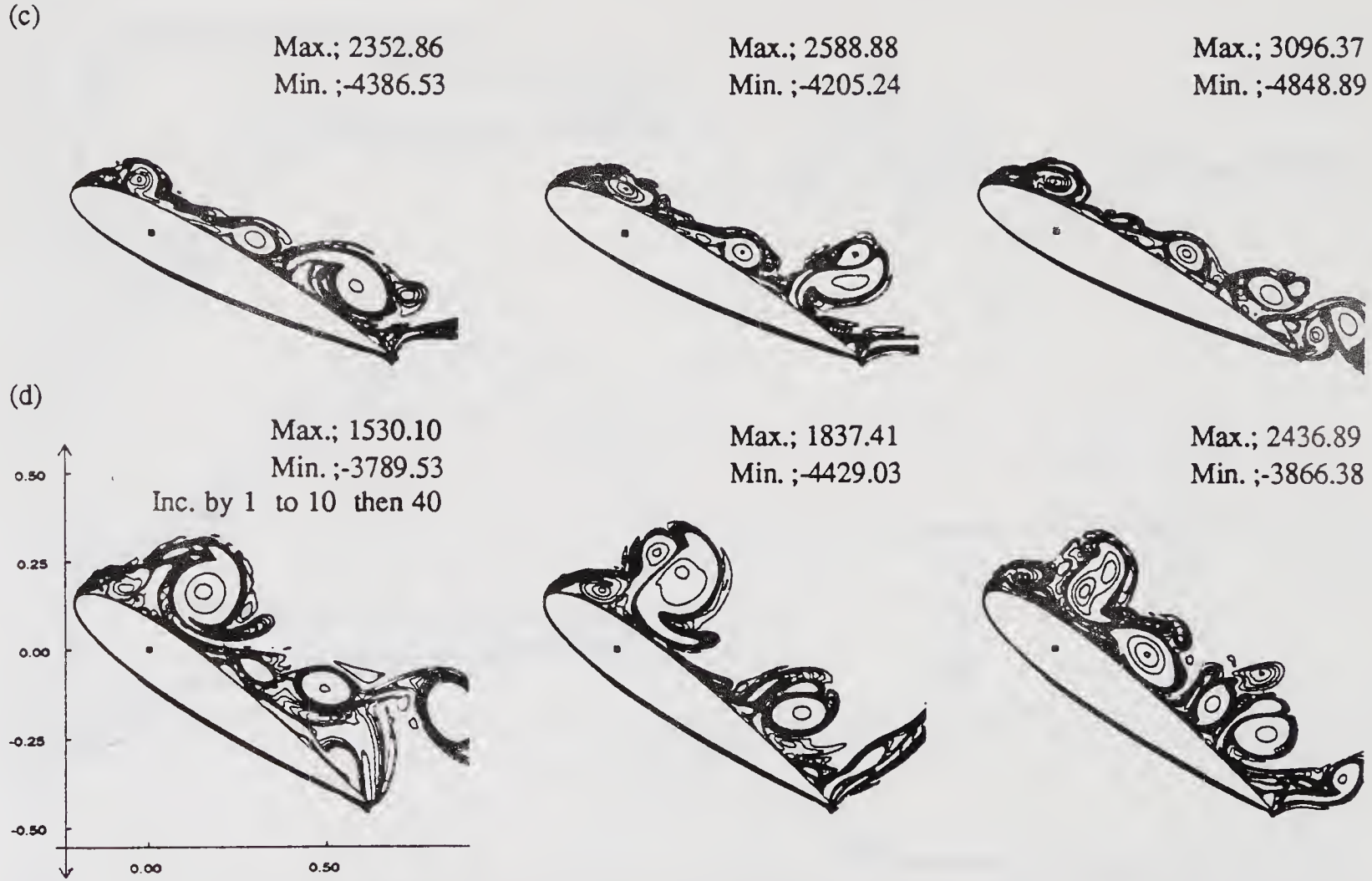

Figure 11. Effect of three different grid distributions on flow past an NACA 0015 airfoil for Re = 45,000, $\dot{\alpha}^+ = 0{\cdot}2$ – contours of instantaneous vorticity. Time = 1·501, 2·101, 2·501 & 3·201, and $\alpha = 15{\cdot}96°$, 22·83°, 27·41°, & 35·44°, respectively, for (**a**)–(**d**).

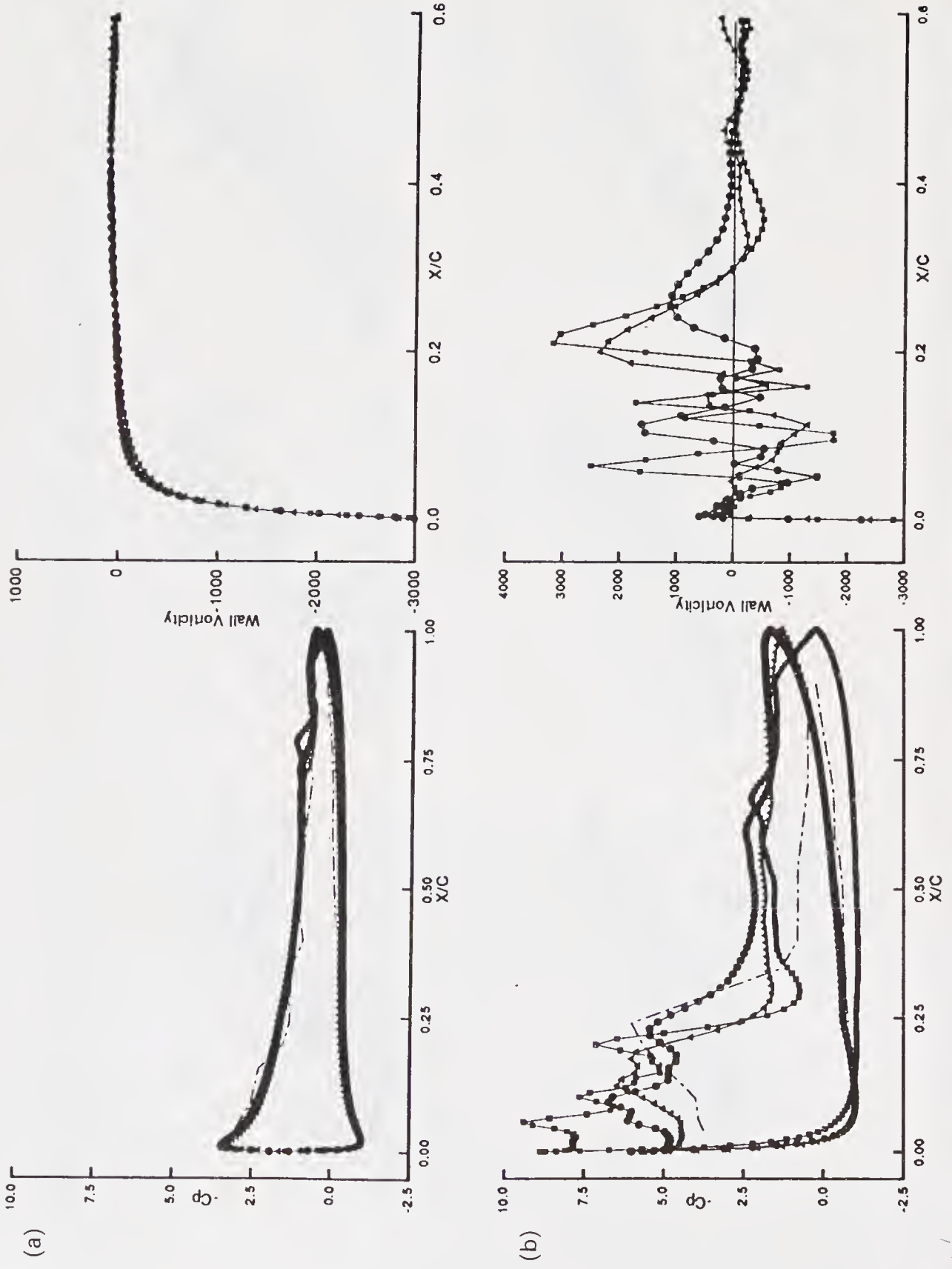
(a)
(b)
-Cp
X/C
Wall Vorticity
0.00
0.25
0.50
0.75
1.00
0.0
0.2
0.4
0.6
10.0
7.5
5.0
2.5
0.0
-2.5
4000
3000
2000
1000
0
-1000
-2000
-3000

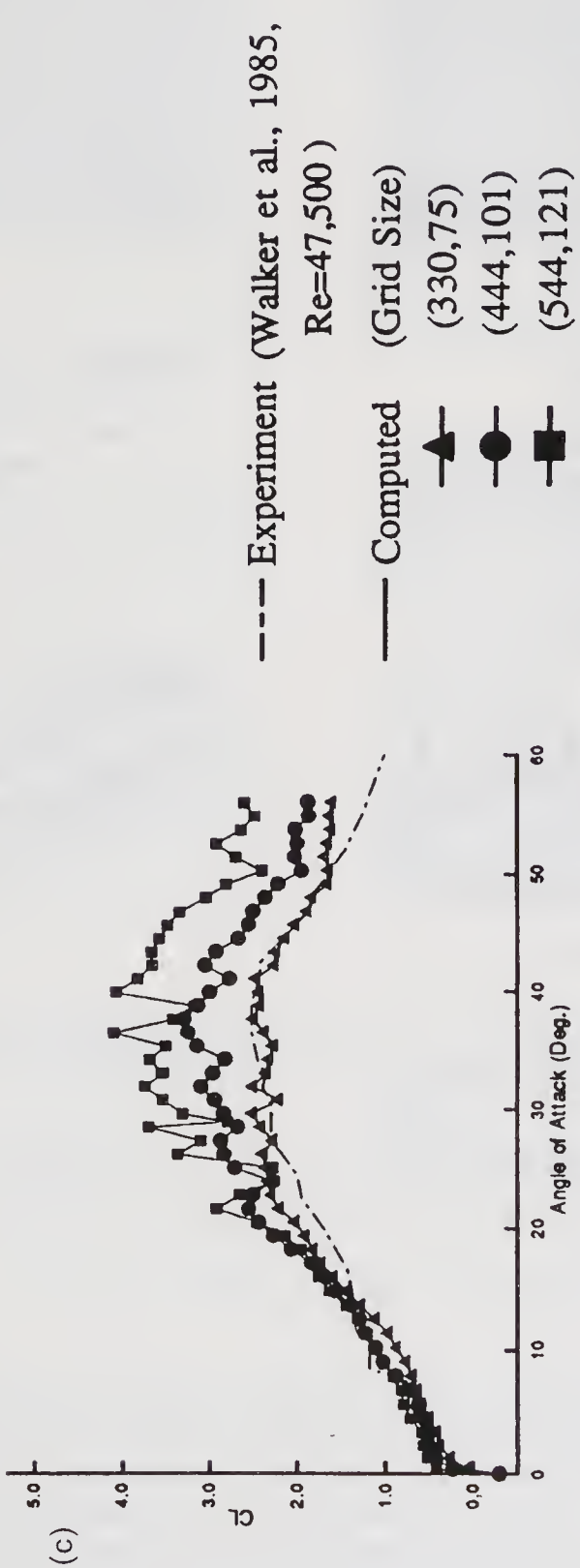

Figure 12. Effect of three different grid distributions on flow past an NACA 0015 airfoil for Re = 45,000, $\dot{\alpha}^+ = 0{\cdot}2$. Cp – distribution and wall vorticity on suction surface at time = 1·401, $\alpha = 14{\cdot}81°$ (**a**), and time = 2·701, $\alpha = 29{\cdot}71°$ (**b**). C_L – distribution (**c**).

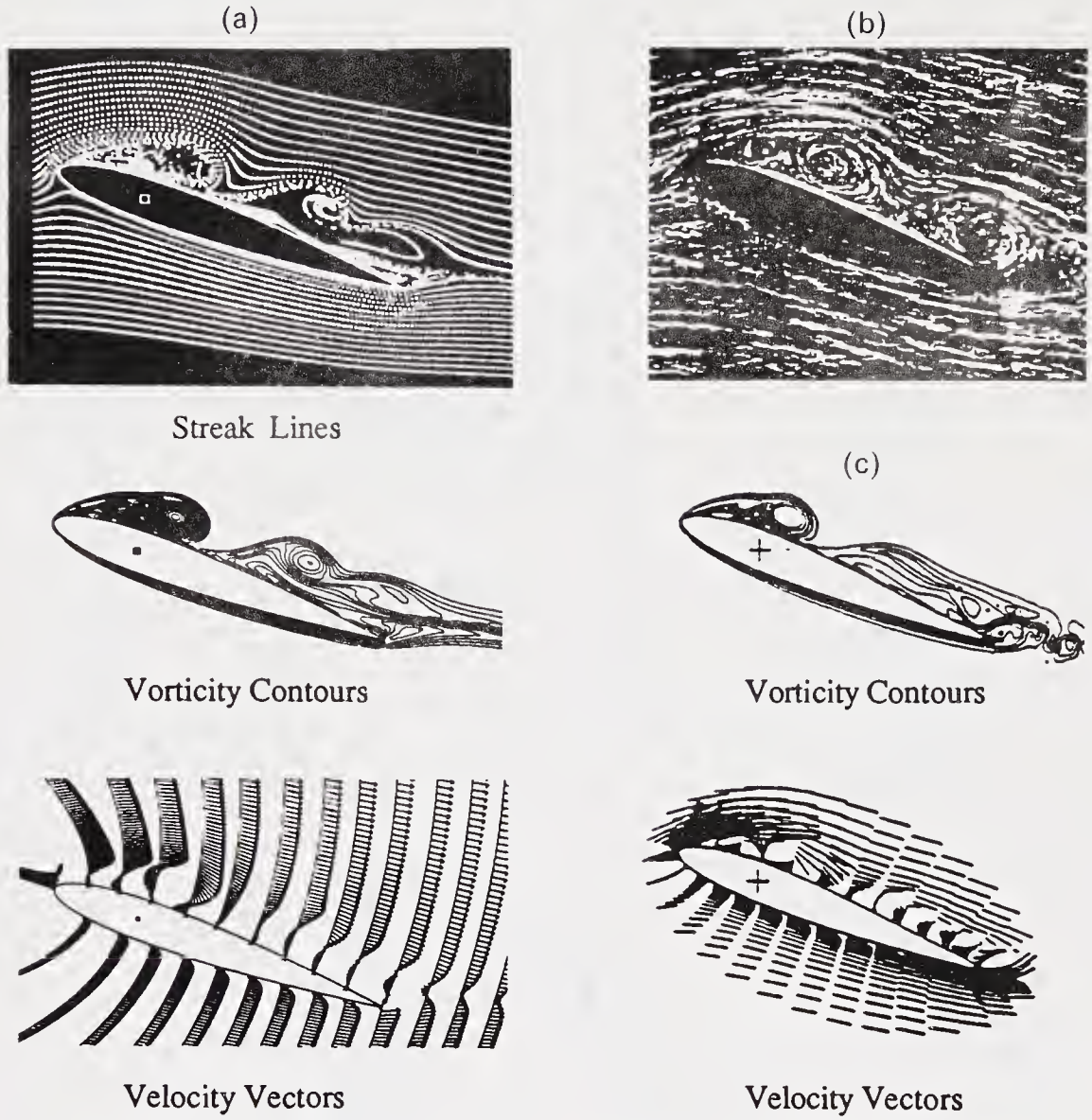

Figure 13. Comparison of present work (**a**), with experimental data of Werlé (1976, ONERA experiment) (**b**), and numerical results of Mehta (1977) (**c**), for NACA 0012 airfoil, Re = 5,000, $k = 1{\cdot}0$.

are also shown in this figure and, although there is a phase difference in the development of the wake, the overall influence is minimal.

5.4 *Flow structure for configuration II: Re = 45,000, no suction*

For this configuration, Walker *et al* (1985) have provided flow visualization photographs for six selected values for angle of attack. These photographs very vividly show initially the region of separated flow near LE and TE and, subsequently, the formation of a highly energetic dynamic stall vortex. Streaklines are plotted in figure 18 at $\alpha = 24°$, 27°, 30°, 40° and 47° and they compare well with the flow visualization data. Further, the C_L-history, as well as the surface distribution of C_p, are compared with the experimental data in figures 19a & b. As seen in figure 19a the C_L-distribution agrees qualitatively, but shows higher values of C_L. It was also pointed out that

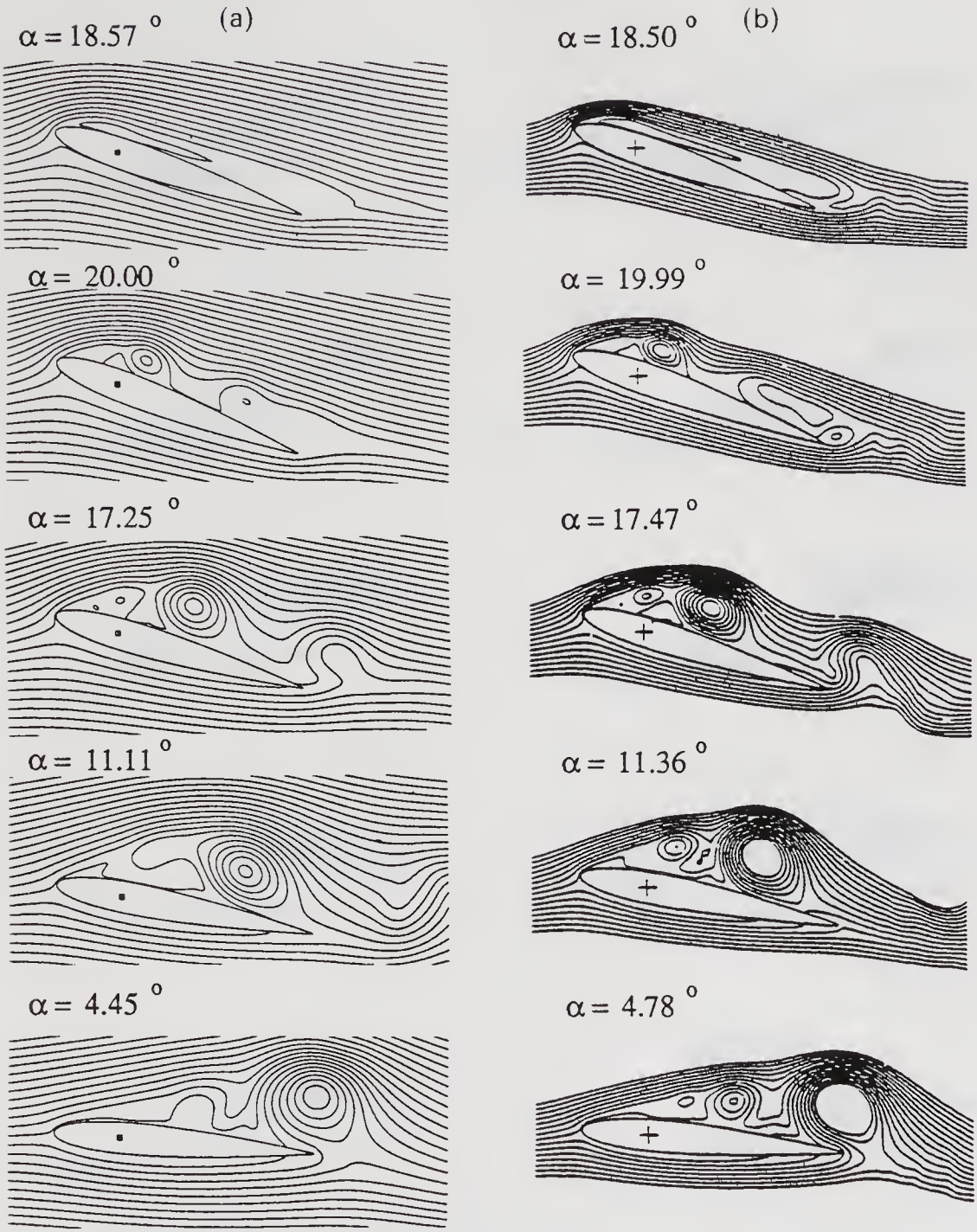

Figure 14. Comparison of numerical results – (**a**) present, and (**b**) those of Mehta (1977) – for NACA 0012 airfoil, Re = 5,000, $k = 1{\cdot}0$ – instantaneous stream function.

better agreement with experimental data is obtained for the coarse grid simulation using (330 × 75) points. Also shown here is C_L-distribution predicted by Visbal & Shang (1989); this, too, agrees better with the experimental data. In the opinion of the present authors, this is again due to their relatively somewhat coarser grid of (203 × 101) points, coupled with their treatment of the far-field boundary condition. Next, the coefficient of surface pressure distribution is compared for two values, $\alpha = 14.81°$ and $29.71°$, in figure 19b. As seen here, the comparison with the experimental data of Walker *et al* (1985) is good for $\alpha = 14.81°$, whereas, for $\alpha = 29.71°$, the two-

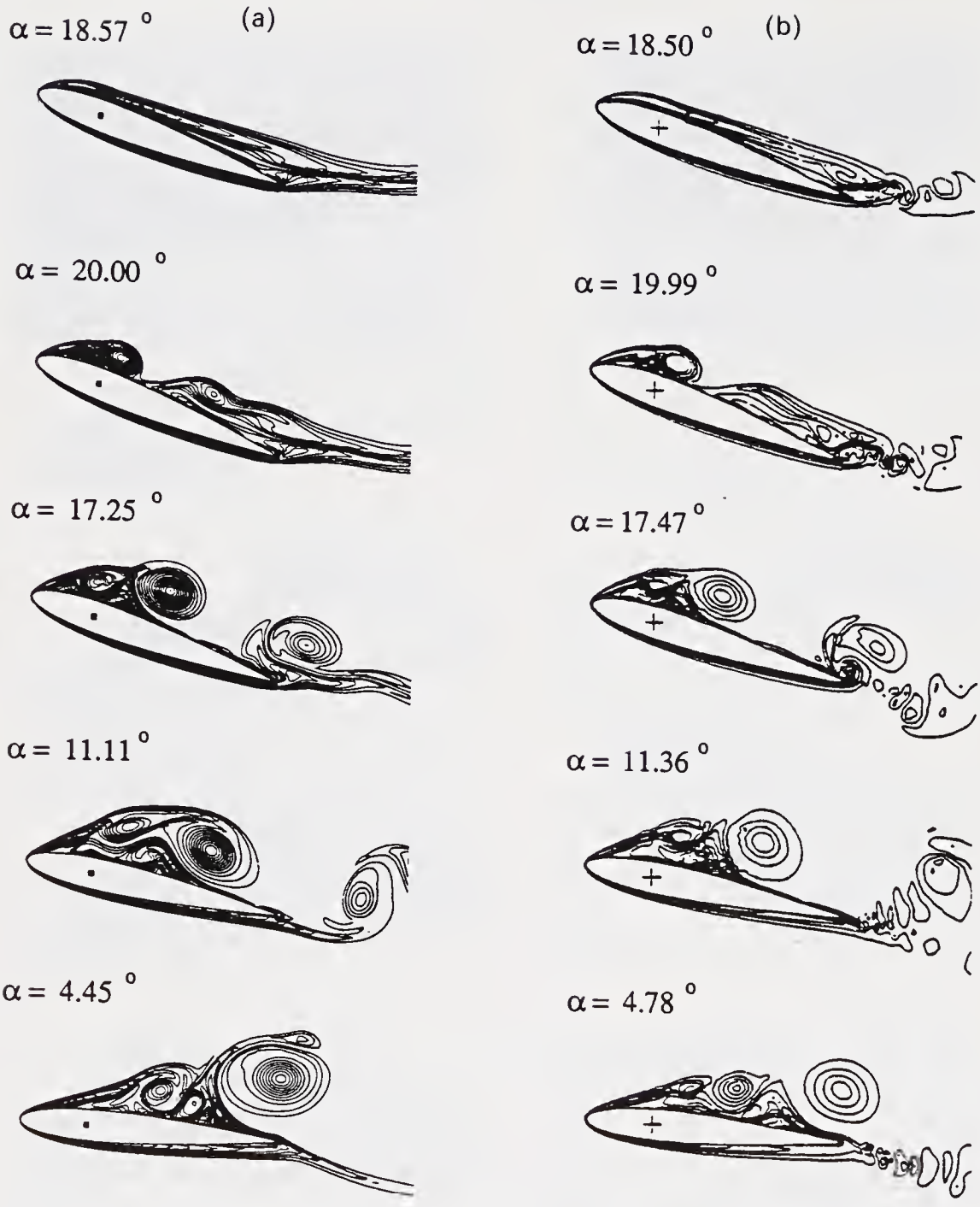

Figure 15. Comparison of numerical results, (**a**) present with (**b**) those of Mehta (1977), for NACA 0012 airfoil, Re = 5,000, $k = 1{\cdot}0$ – instantaneous vorticity contours.

distributions depart significantly at the suction surface. It is again the opinion of the authors that this is due to three-dimensionality in the flow field. The results presented so far provide additional verification of the present analysis.

Next, the detailed flow structure is depicted in figures 20 & 21 using the instantaneous vorticity contours with α varying from 11.37° to 29.71°. Here, global flow structure information is made available, along with an enlarged view showing the LE flow structure. As the airfoil is pitched-up, flow reversal takes place near the LE as shown in this figure. Subsequently, the flow reversal evolves into secondary, tertiary and

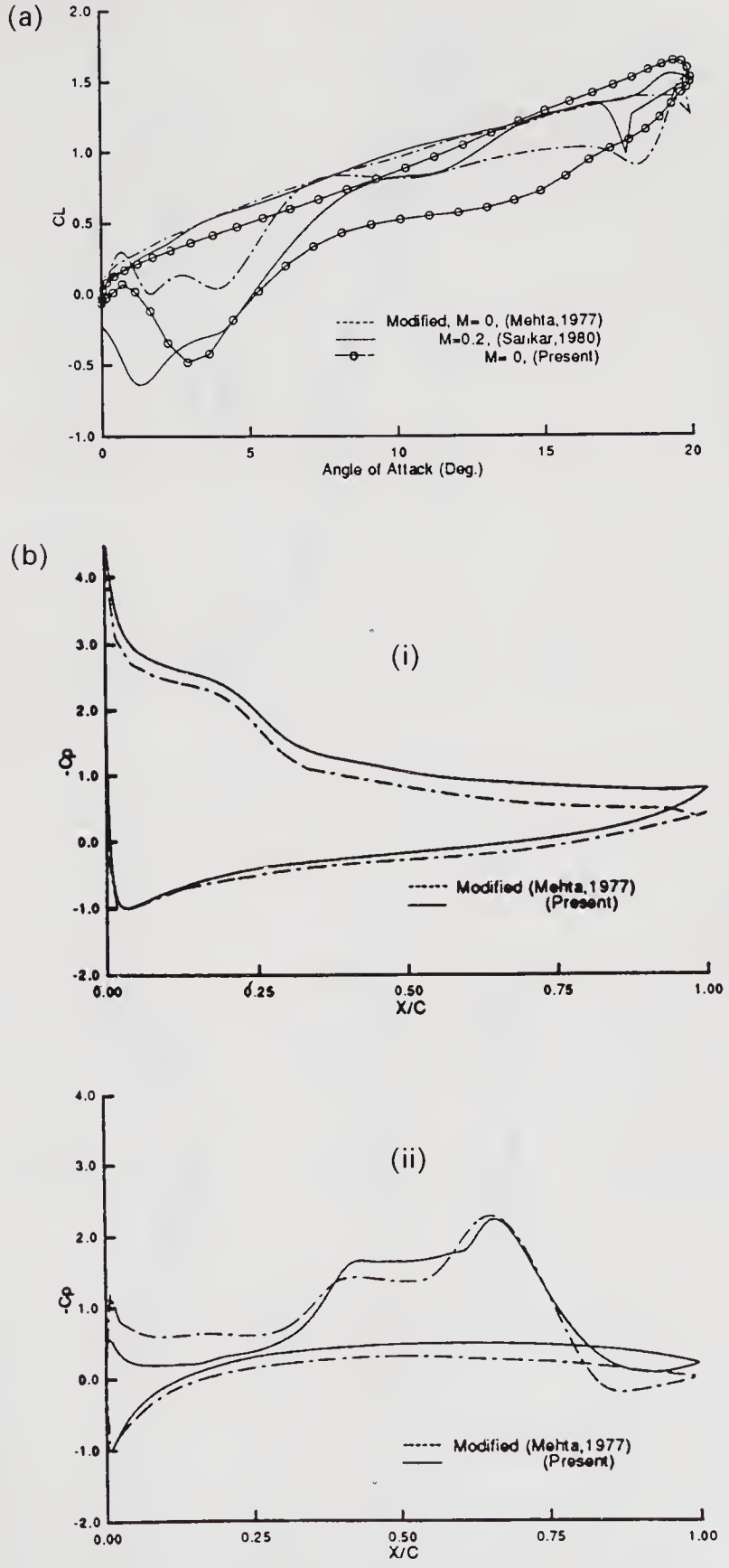

Figure 16. Comparison with numerical results of Mehta (1977) and Sankar & Tassa (1980) for NACA 0012 airfoil; Re = 5,000, $k = 1{\cdot}0$. (**a**) C_L vs. α. (**b**) C_p – distribution for (i) time = 2·601, $\alpha = 18{\cdot}57°$ (pitch-up) and (ii) time = 4·601, $\alpha = 11{\cdot}11°$ (pitch-down).

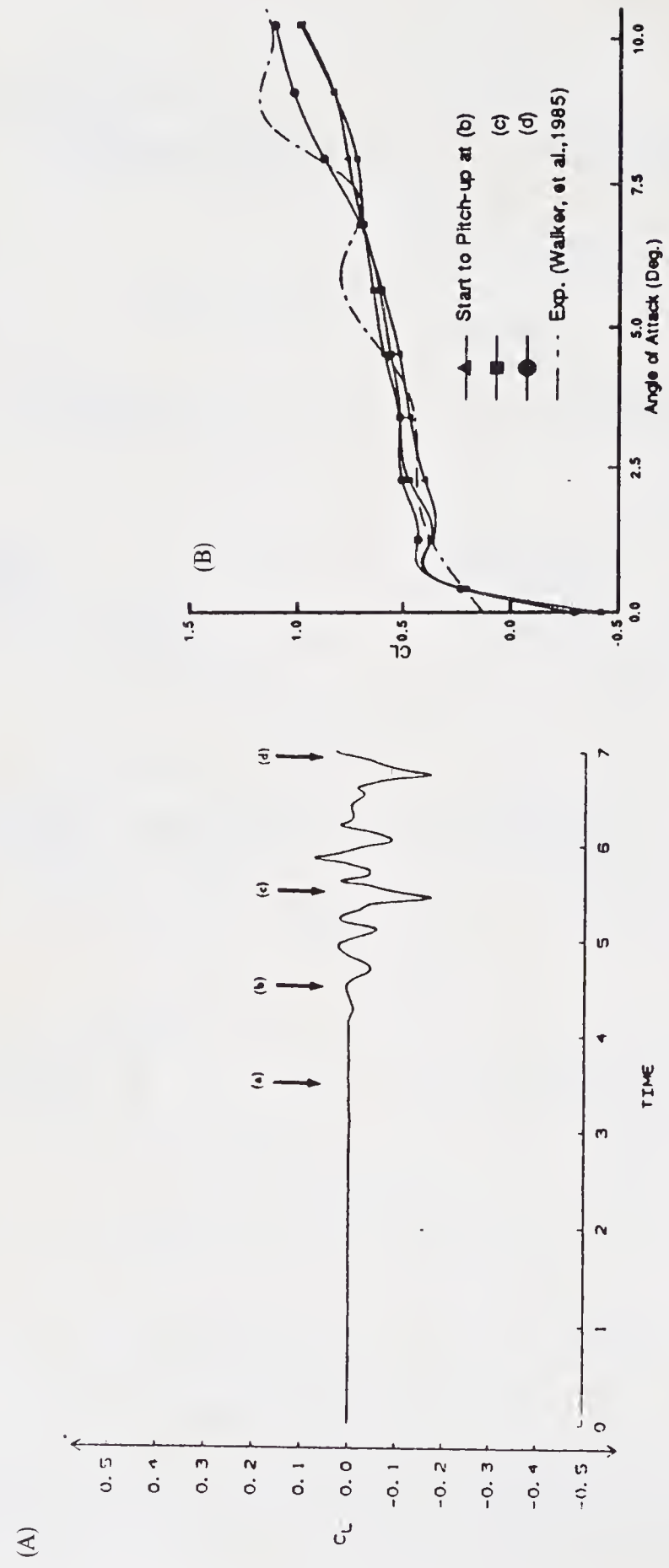
(A)
C_L
0.5
0.4
0.3
0.2
0.1
0.0
-0.1
-0.2
-0.3
-0.4
-0.5
0
1
2
3
4
5
6
7
TIME
(a)
(b)
(c)
(d)
(B)
C_D
1.5
1.0
0.5
0.0
-0.5
0.0
2.5
5.0
7.5
10.0
Angle of Attack (Deg.)
Start to Pitch-up at (b)
(c)
(d)
Exp. (Walker, et al.,1985)

(C)

Start to pitch-up at (b)

Max. : 637.55
Min. : -2097.82
CL : 0.980

Start to pitch-up at (c)

Max. : 548.50
Min. : -2083.26
CL : 0.990

Start to pitch-up at (d)

Max. : 498.01
Min. : -2166.54
CL : 1.106

(D)

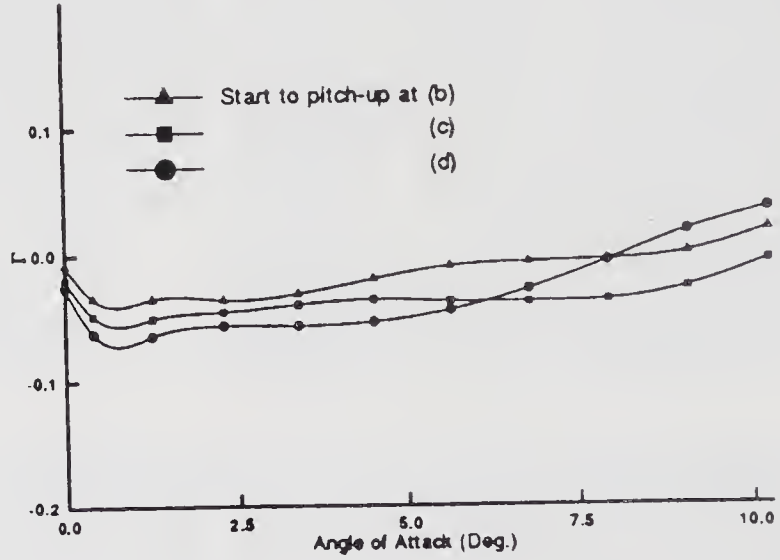

Figure 17. Effect of three different initial states on flow past an NACA 0015 airfoil; Re = 45,000, $\dot{\alpha}^+ = 0{\cdot}2$. (**A**) Time history of lift coefficient at $\alpha = 0°$; (**B**) comparison of lift coefficients, (**C**) instantaneous vorticity contours at $\alpha = 10{\cdot}23°$; and (**D**) calculated unsteady circulation.

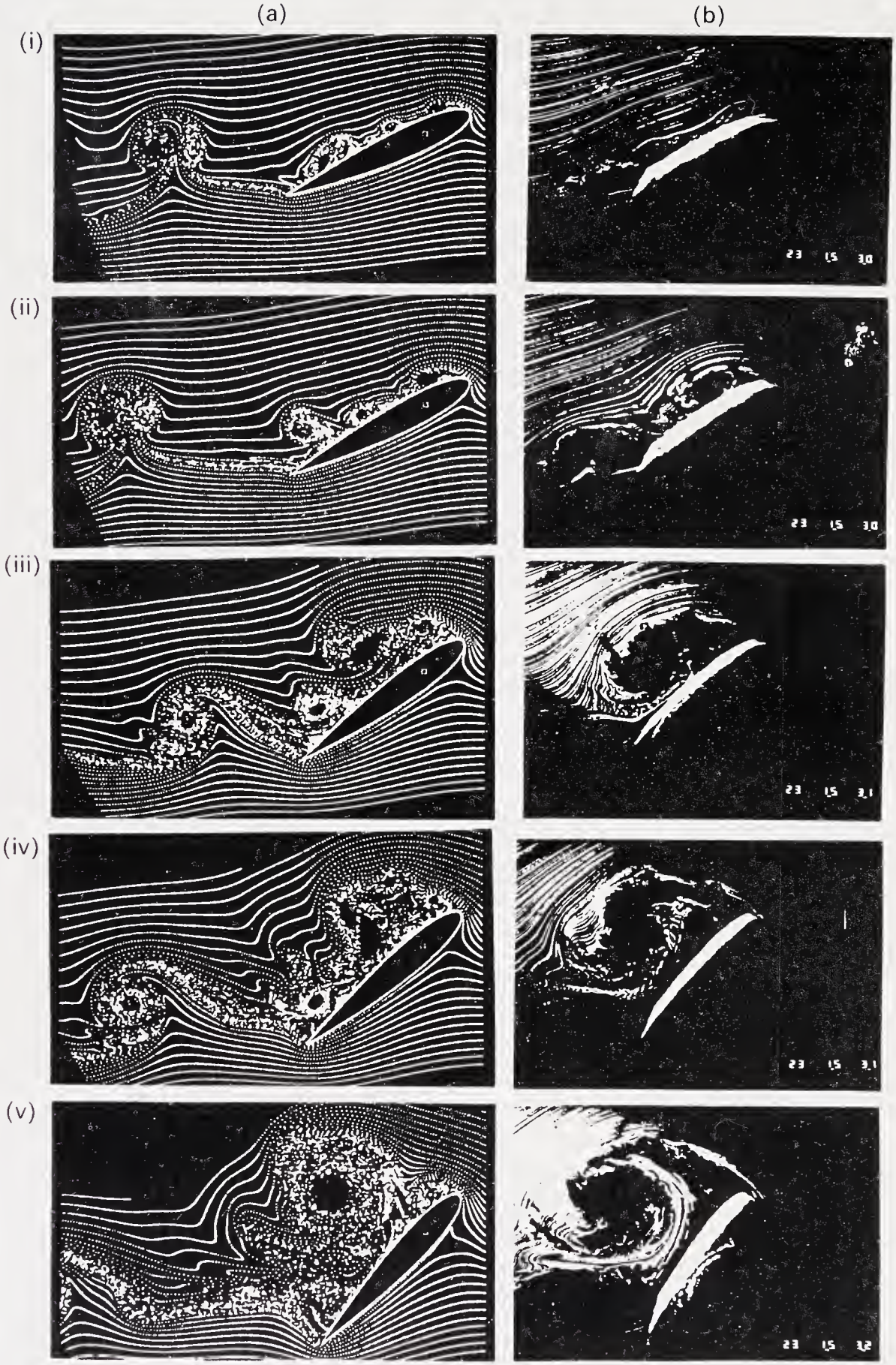

Figure 18. Comparison of present work (**a**), with experimental data of Walker *et al* (1985) (**b**), for flow past an NACA 0015 airfoil; Re = 45,000, $\dot{\alpha}^+ = 0{\cdot}2$ – streaklines. $\alpha = 24°$, 27°, 36°, 40° and 47°, respectively, for (i)–(v).

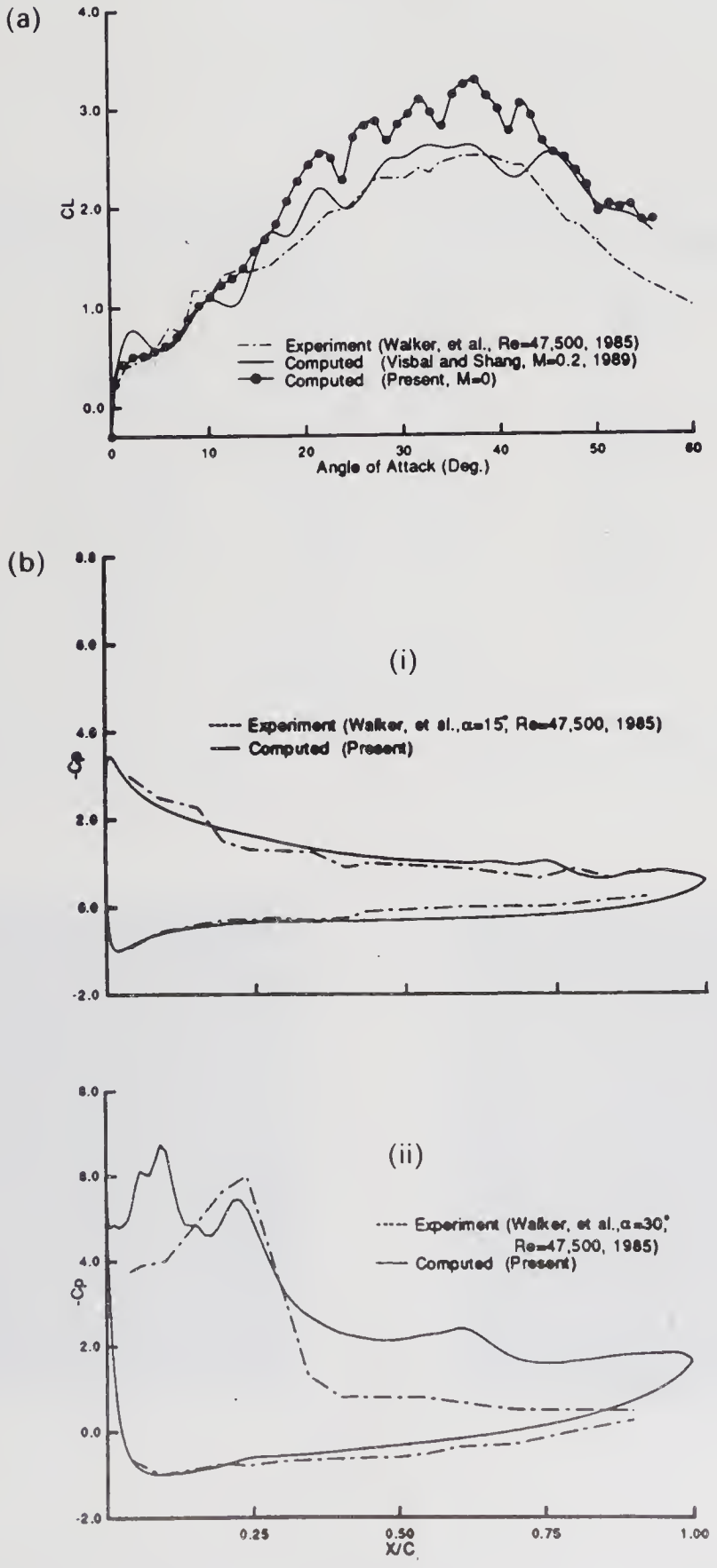

Figure 19. Comparison with experimental data of Walker *et al* (1985) for flow past an NACA 0015 airfoil; Re = 45,000, $\dot{\alpha}^+ = 0{\cdot}2$. (**a**) C_L vs. α; (**b**) C_p – distribution for (i) time = 1·401, $\alpha = 14{\cdot}81^\circ$ and (ii) time = 2·701, $\alpha = 29{\cdot}71^\circ$.

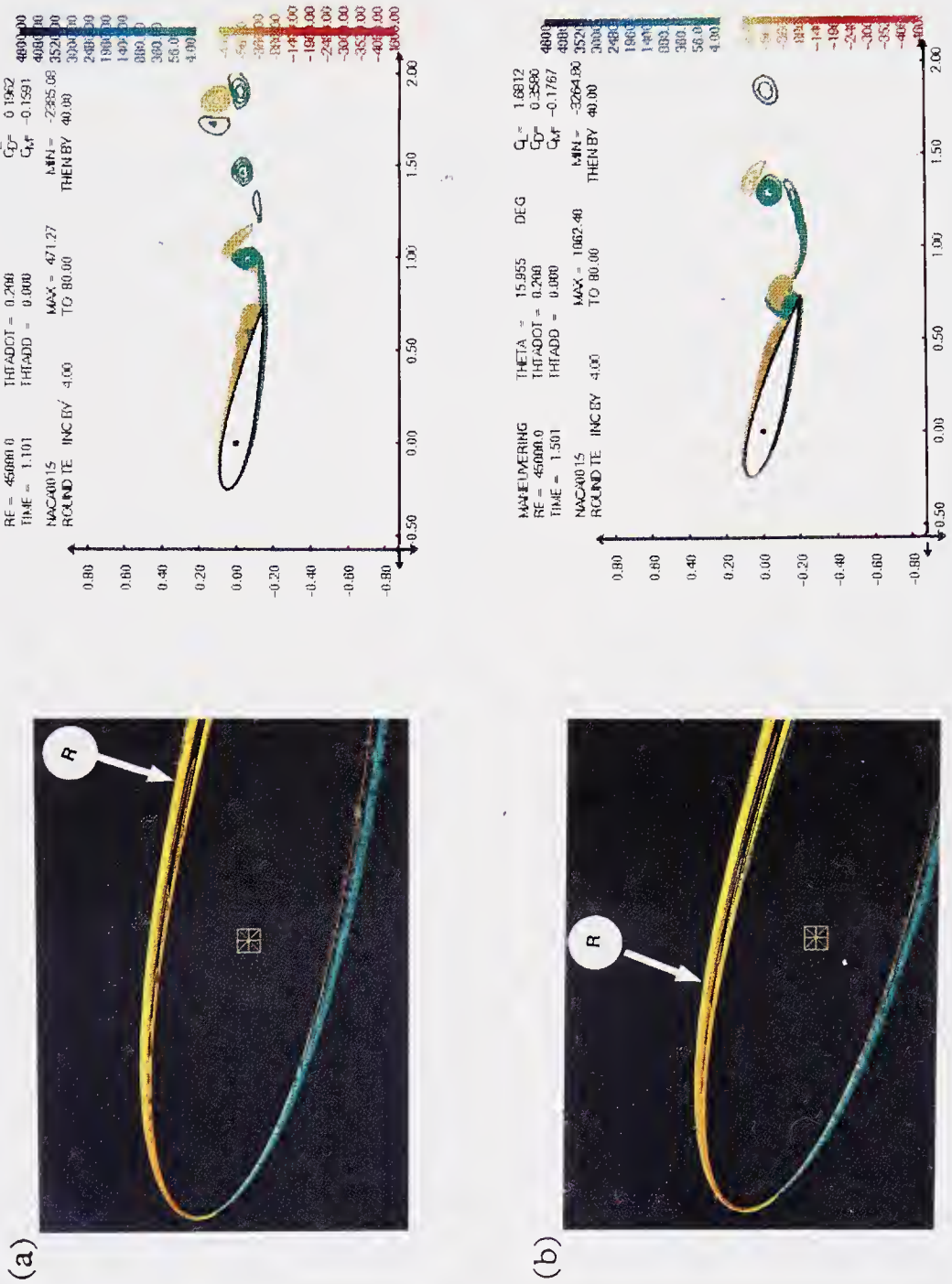
(a)
R
MAPELMERING
RE = 45000.0
TIME = 1.101
NACA0015
ROUND TE INC BY 4.00
THETA = 11.371 DEG
THTADOT = 0.298
THTADD = 0.000
MAX = 471.27
TO 80.00
CL = 1.2245
CD = 0.1962
CM = -0.1591
MIN = -2385.08
THEN BY 40.00
480.00
400.00
320.00
240.00
160.00
80.0
56.0
4.00
-72.00
-152.00
-232.00
-312.00
-392.00
-472.00
-552.00
-632.00
-712.00
-792.00
-872.00
-952.00
-1032.00
0.80
0.60
0.40
0.20
0.00
-0.20
-0.40
-0.60
-0.80
0.50
0.00
0.50
1.00
1.50
2.00
(b)
R
MAPELMERING
RE = 45000.0
TIME = 1.501
NACA0015
ROUND TE INC BY 4.00
THETA = 15.955 DEG
THTADOT = 0.298
THTADD = 0.000
MAX = 1062.48
TO 80.00
CL = 1.6812
CD = 0.3586
CM = -0.1767
MIN = -3264.80
THEN BY 40.00
480
400
320
240
160
80.0
56.0
4.00
0.80
0.60
0.40
0.20
0.00
-0.20
-0.40
-0.60
-0.80
0.50
0.00
0.50
1.00
1.50
2.00

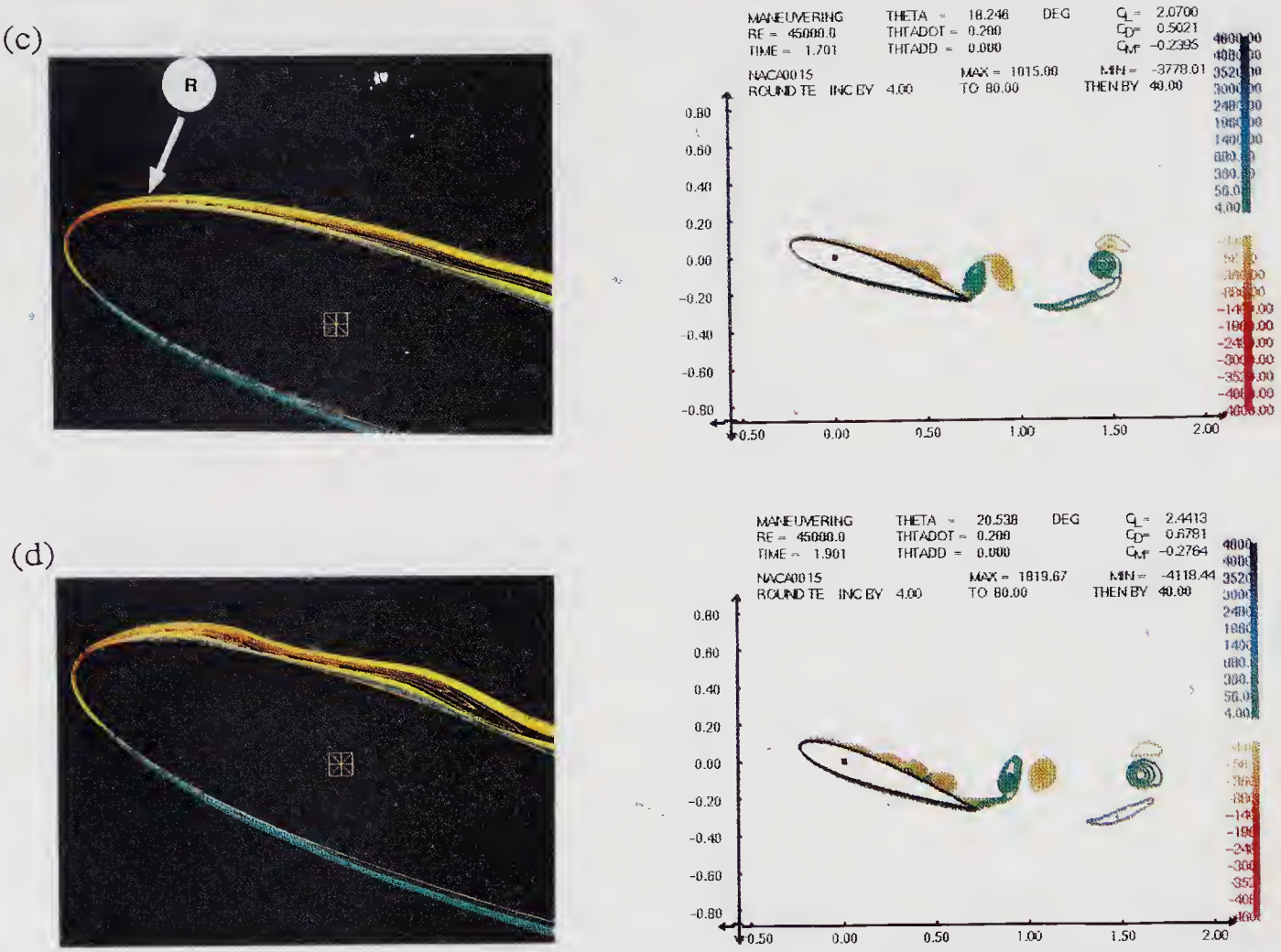
(c)
R
MANEUVERING THETA = 18.246 DEG
RE = 45000.0 THTADOT = 0.200
TIME = 1.701 THTADD = 0.000
NACA0015 MAX = 1015.00 MIN = -3778.01
ROUND TE INC BY 4.00 TO 80.00 THEN BY 40.00
(d)
MANEUVERING THETA = 20.538 DEG
RE = 45000.0 THTADOT = 0.200
TIME = 1.901 THTADD = 0.000
NACA0015 MAX = 1819.67 MIN = -4118.44
ROUND TE INC BY 4.00 TO 80.00 THEN BY 40.00

Figure 20. Details of flow structure for NACA 0015 airfoil; Re = 45,000, $\dot{\alpha}^+ = 0{\cdot}2$ – instantaneous vorticity contours for time = 1·101, 1·501, 1·701 & 1·901, and $\alpha = 11{\cdot}37°$, 15·96°, 18·25° & 20·54°, respectively, for (**a**)–(**d**).

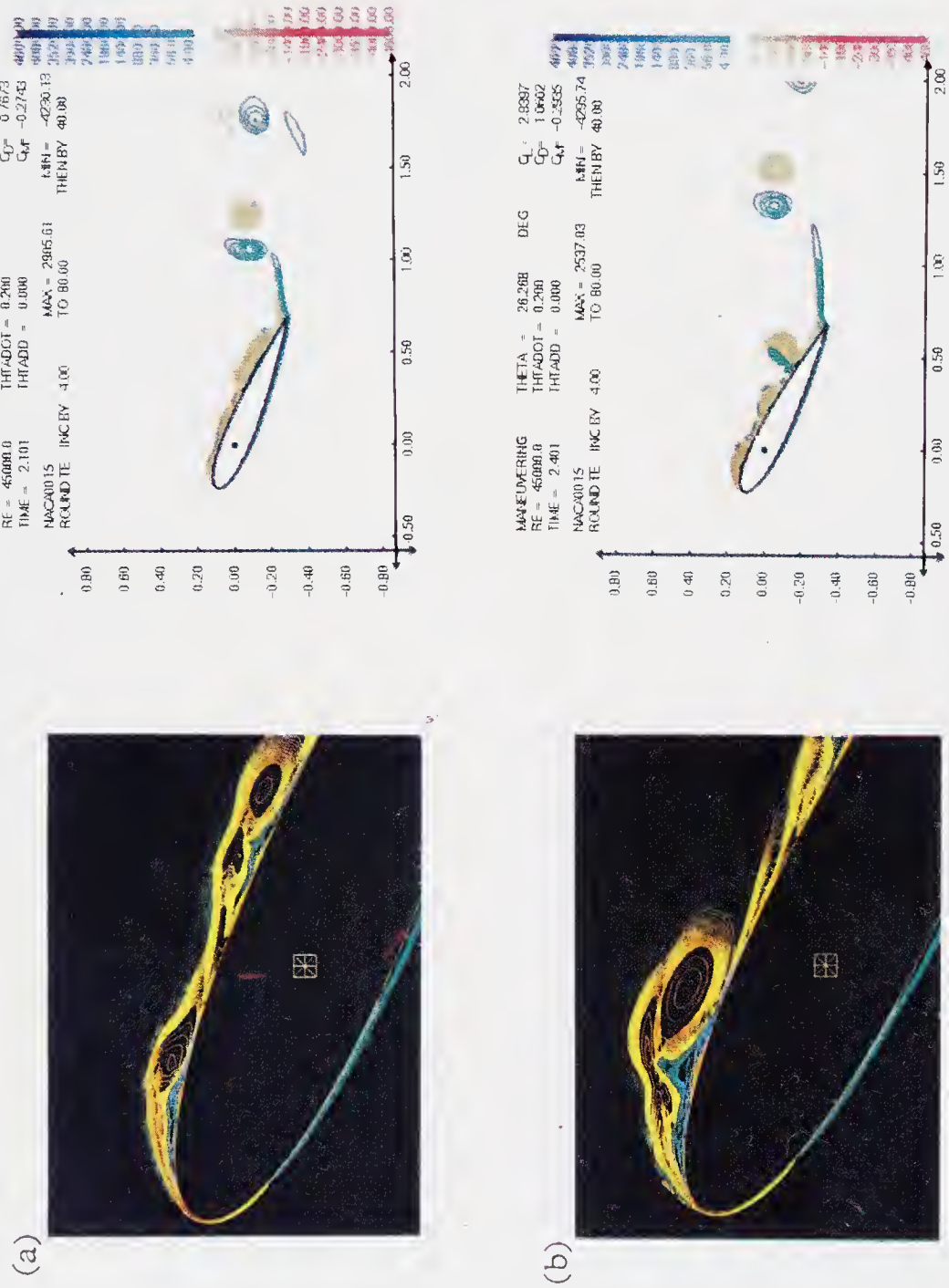
(a)
MANEUVERING
RE = 45000.0
TIME = 2.101
NACA0015
ROUND TE
THETA = 22.830 DEG
THTADOT = 0.290
THTADD = 0.000
MAX = 2985.61
INC BY 4.00
TO 80.00
CL = 2.5650
CD = 0.7673
CM = -0.2745
MIN = -4290.13
THEN BY 40.00
(b)
MANEUVERING
RE = 45000.0
TIME = 2.401
NACA0015
ROUND TE
THETA = 26.268 DEG
THTADOT = 0.290
THTADD = 0.000
MAX = 2537.03
INC BY 4.00
TO 80.00
CL = 2.8397
CD = 1.0602
CM = -0.3535
MIN = -4295.74
THEN BY 40.00

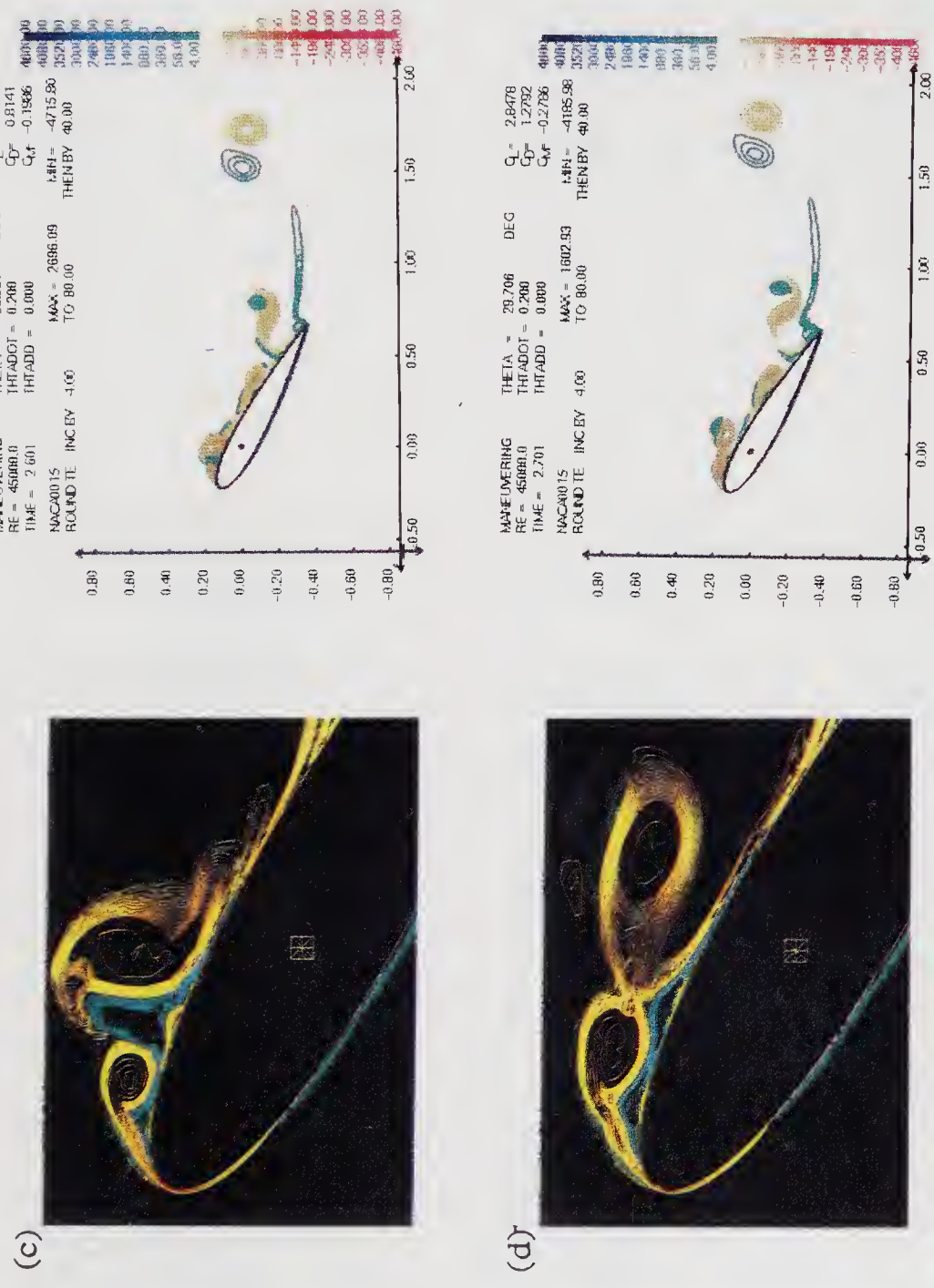

Figure 21. Details of flow structure for NACA 0015 airfoil; $\alpha = 22{\cdot}83°$, $26{\cdot}27°$, $28{\cdot}56°$ & $29{\cdot}71°$, respectively, for (**a**)–(**d**) (other details as in figure 20).

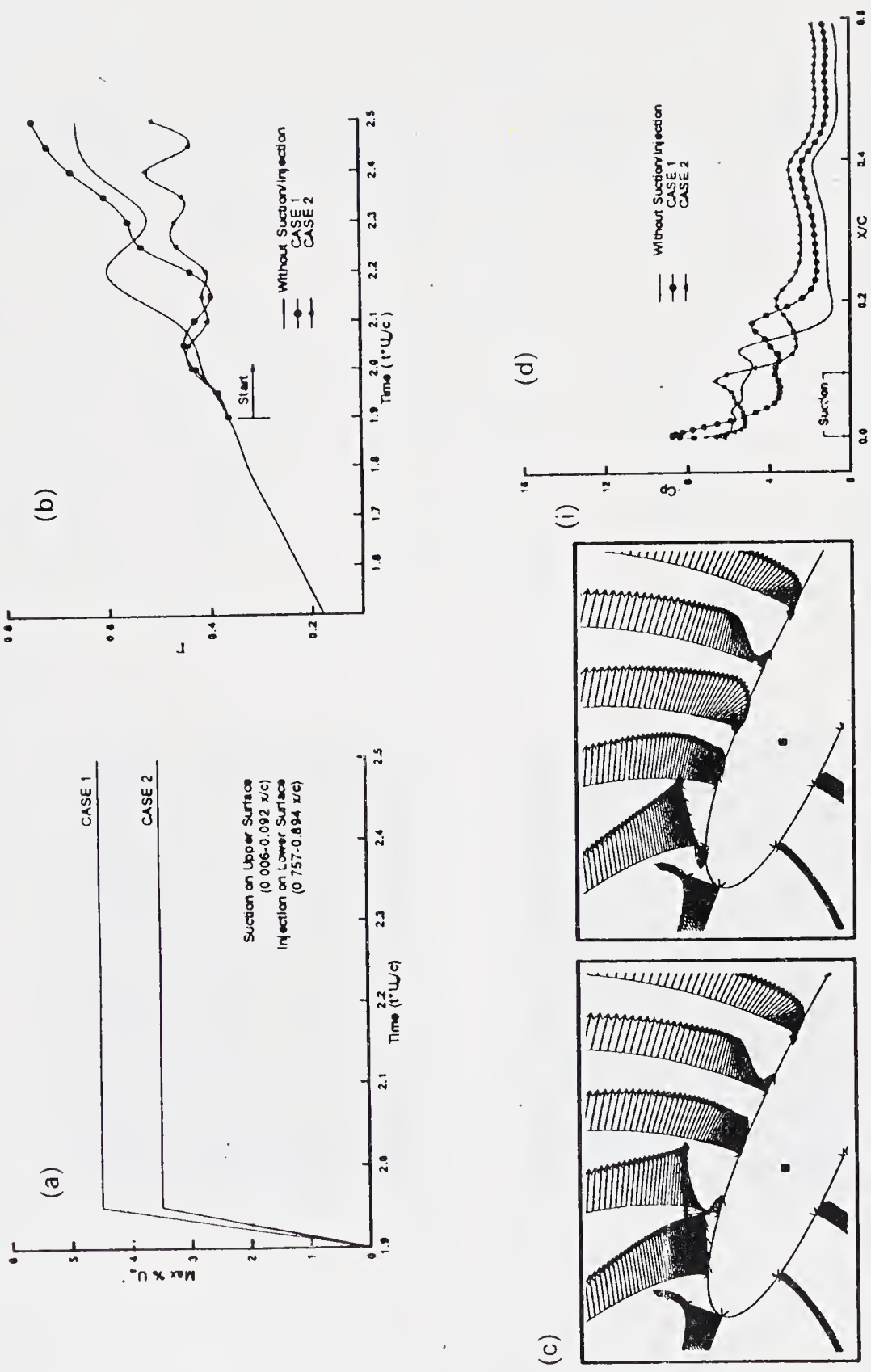
(a)
CASE 1
CASE 2
Suction on Upper Surface
(0.006-0.092 x/c)
Injection on Lower Surface
(0.757-0.894 x/c)
Time (t*U∞/c)
(b)
Start
Without Suction/Injection
CASE 1
CASE 2
Time (t*U∞/c)
(c)
(d)
Without Suction/Injection
CASE 1
CASE 2
Suction
X/C

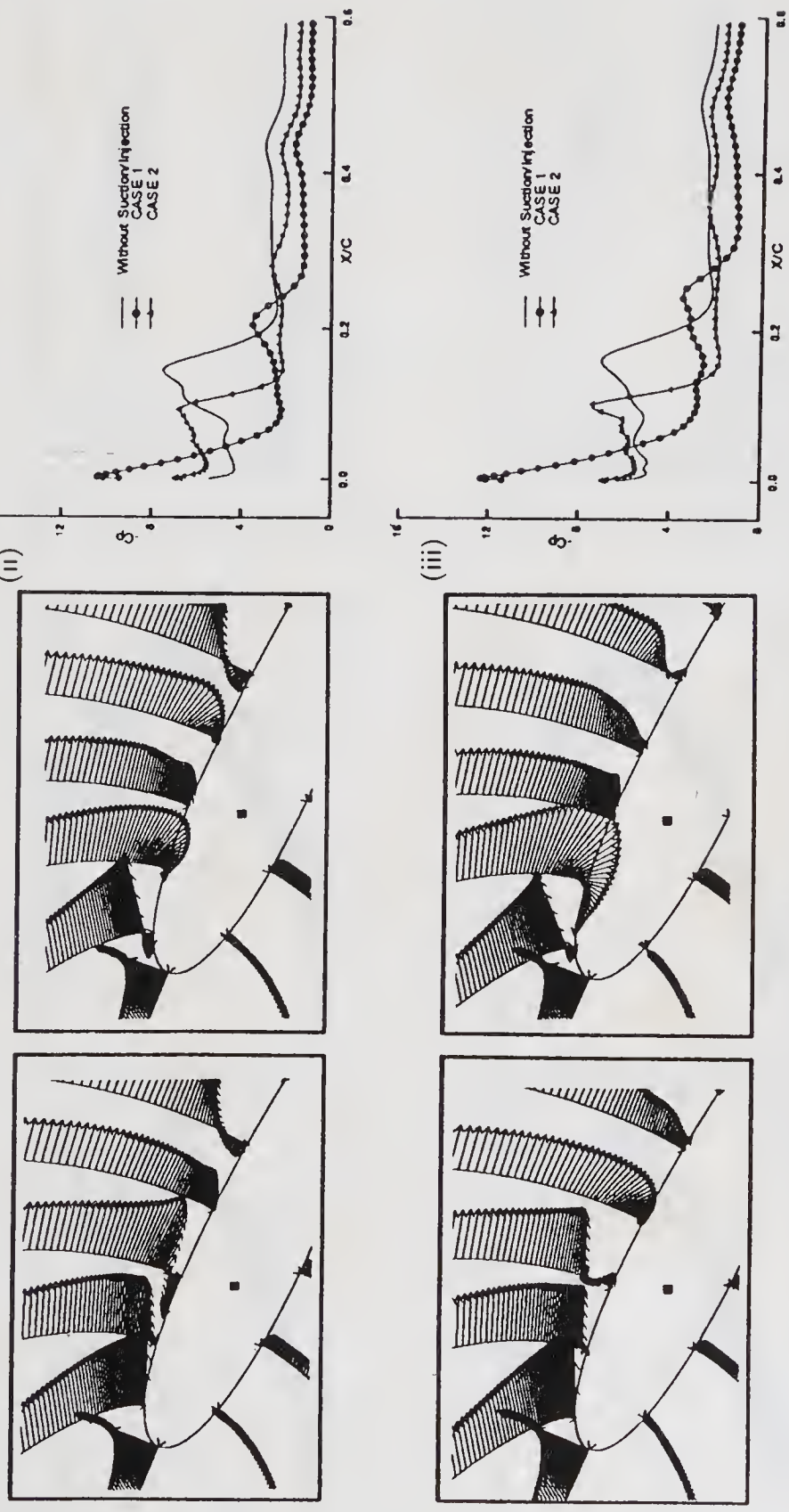

Figure 22. Effect of suction/injection for NACA 0015 airfoil; $\mathrm{Re} = 45{,}000$, $\dot{\alpha}^+ = 0{\cdot}2$, $v_s/U_\infty = 0{\cdot}045$ (case 1) and $0{\cdot}035$ (case 2). (**a**) Time history of control model for suction/injection; (**b**) calculated unsteady circulation; (**c**) velocity vectors; (**d**) C_p distribution. Time = 2·201, 2·301 & 2·401, and $\alpha = 23{\cdot}98°$, 25·12° & 26·27°, for (i)–(iii), respectively.

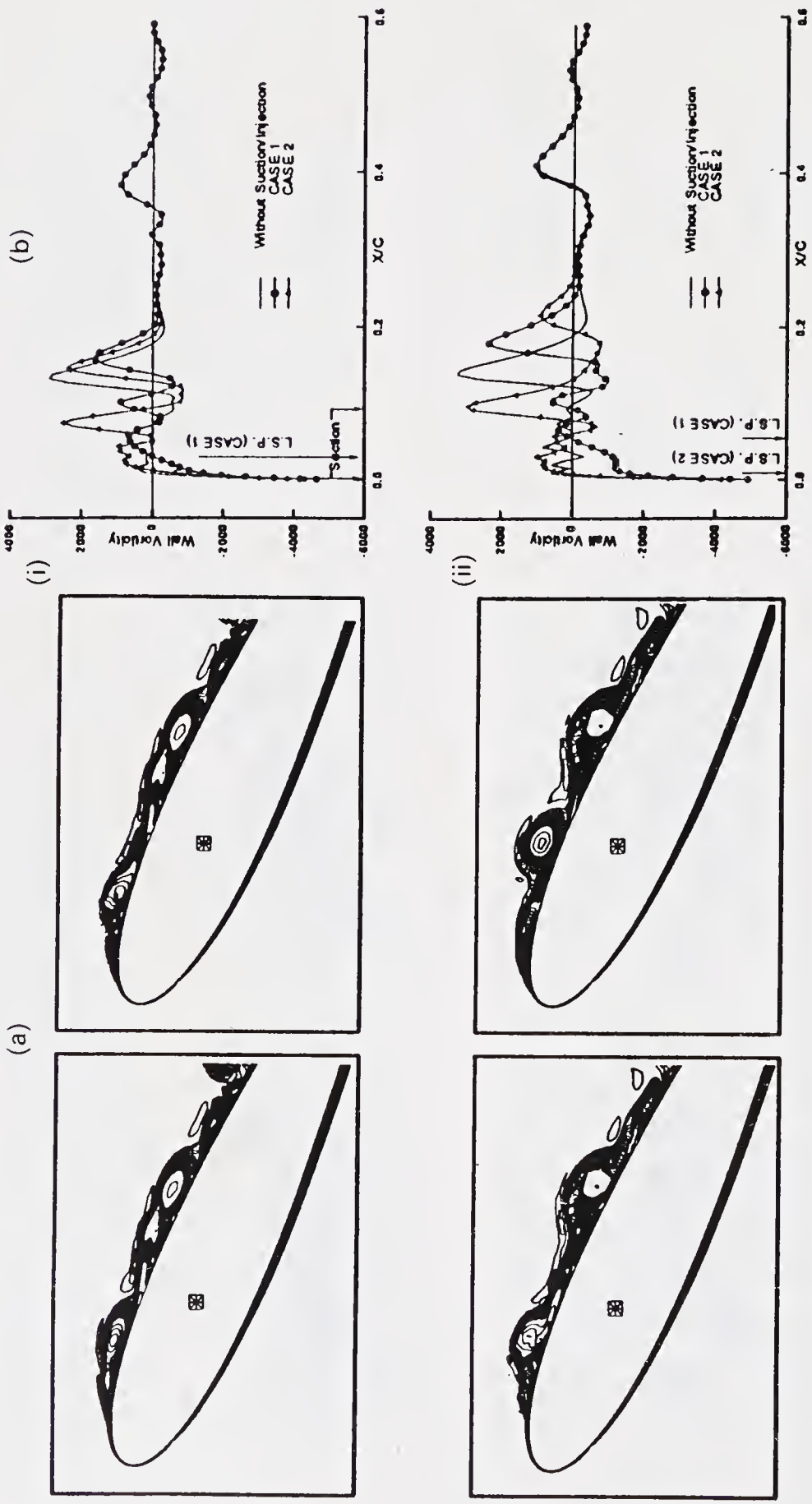
(a)
(b)
(i)
(ii)
Wall Vorticity
X/C
Without Suction/Injection
CASE 1
CASE 2
L.S.P. (CASE 1)
L.S.P. (CASE 2)
Section

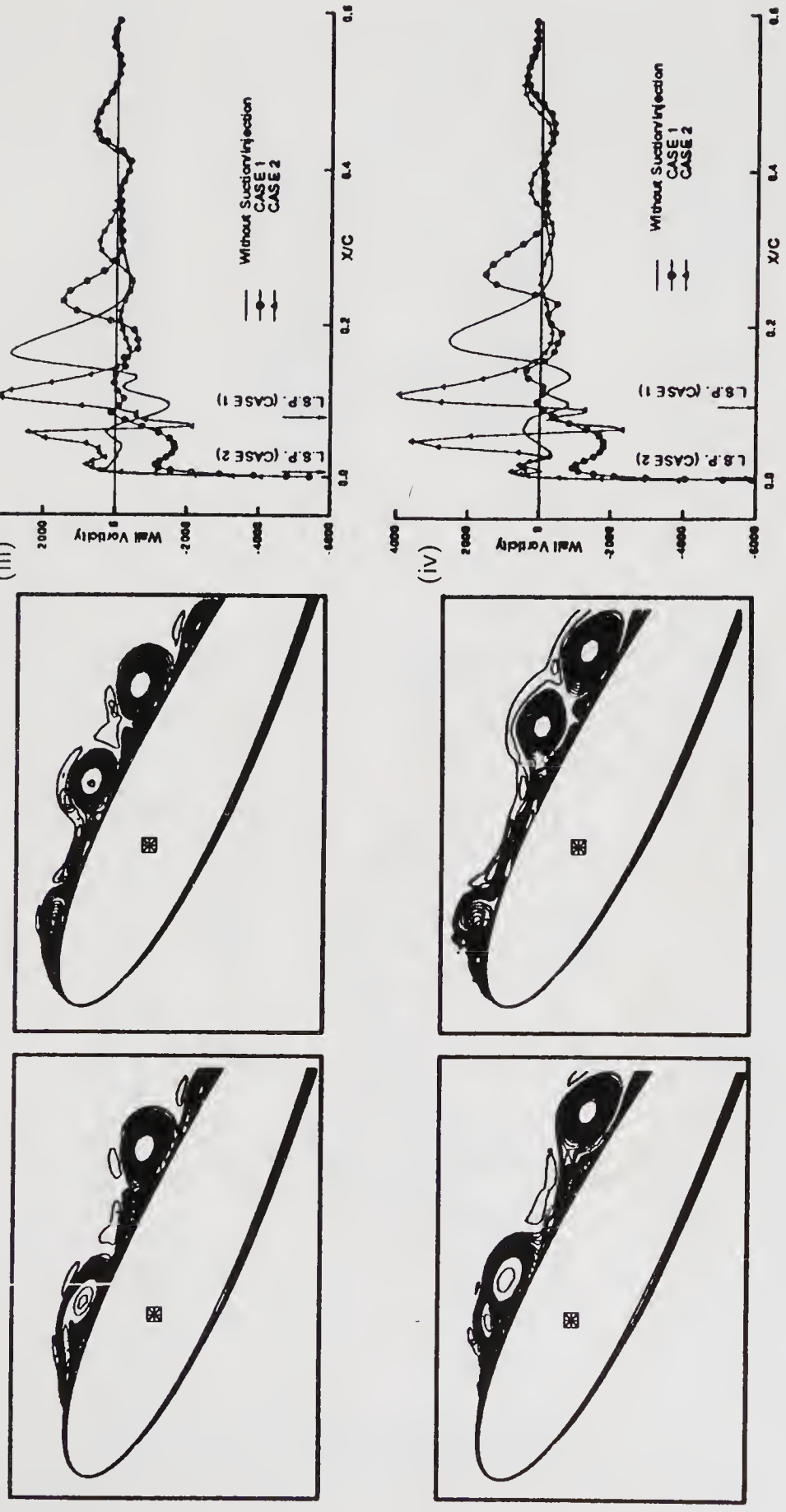

Figure 23. Effect of suction/injection for NACA 0015 airfoil; (**a**) instantaneous vorticity contours, and (**b**) wall vorticity distributions. Time = 2·101, 2·201, 2·301 & 2·401, and $\alpha = 22{\cdot}83°$, 23·98°, 25·12° & 26·27°, respectively, for (i)–(iv). (Other conditions as in figure 22.)

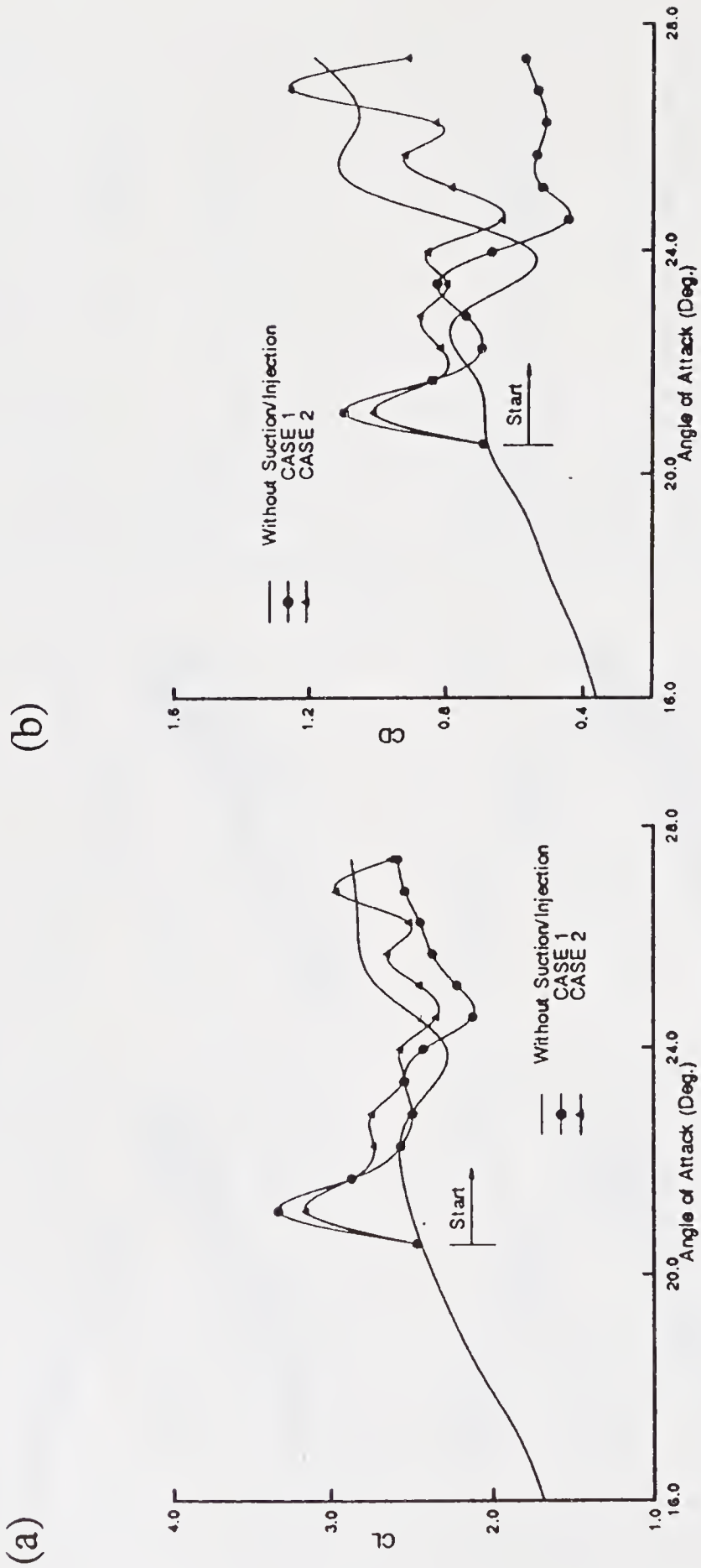
(a)
(b)
Without Suction/Injection
CASE 1
CASE 2
Start
Angle of Attack (Deg.)
16.0
20.0
24.0
28.0
1.0
2.0
3.0
4.0
0.4
0.8
1.2
1.6

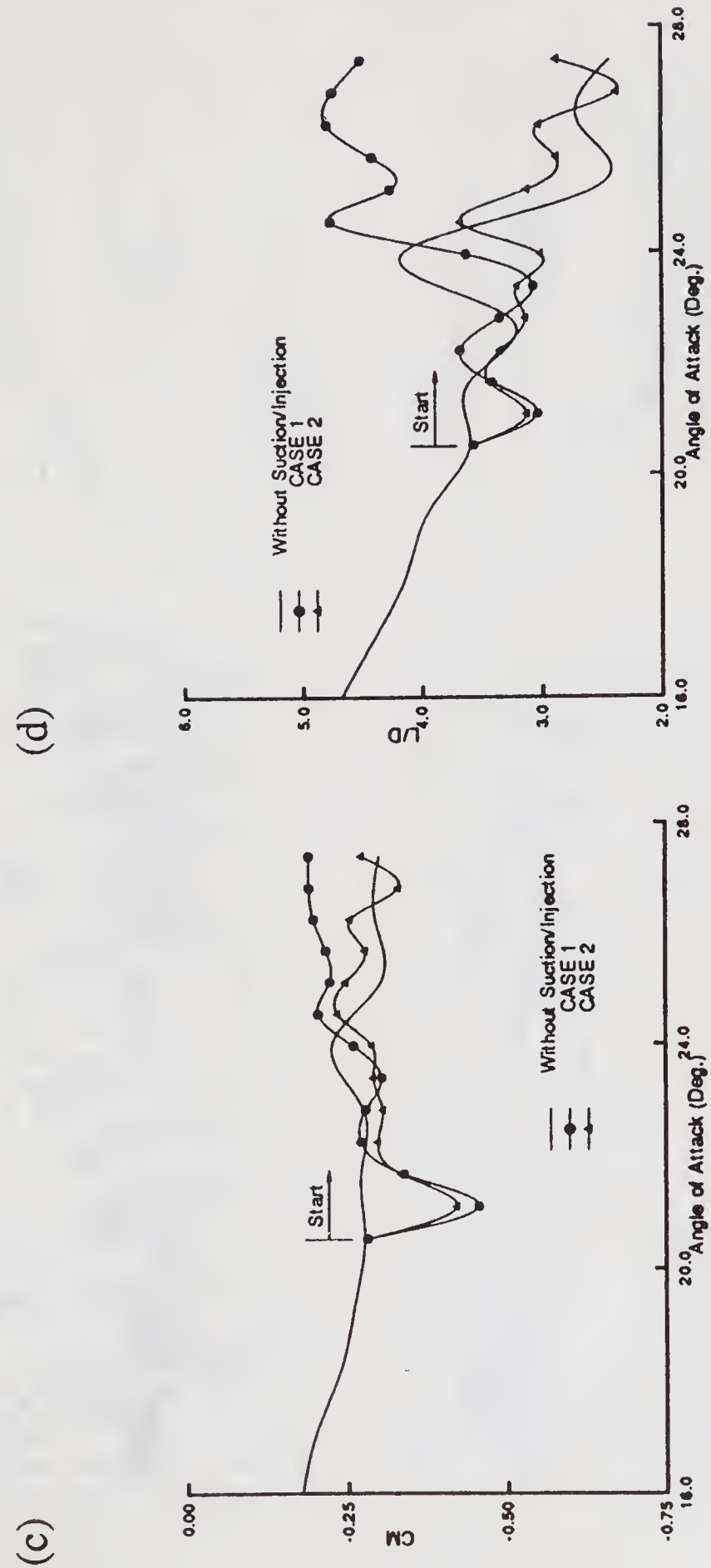

Figure 24. Effect of suction/injection for NACA 0015 airfoil. Comparison of computed lift coefficients (**a**), drag coefficients (**b**), moment coefficients (**c**) and lift/drag ratios (**d**). (Other conditions as in figure 22.)

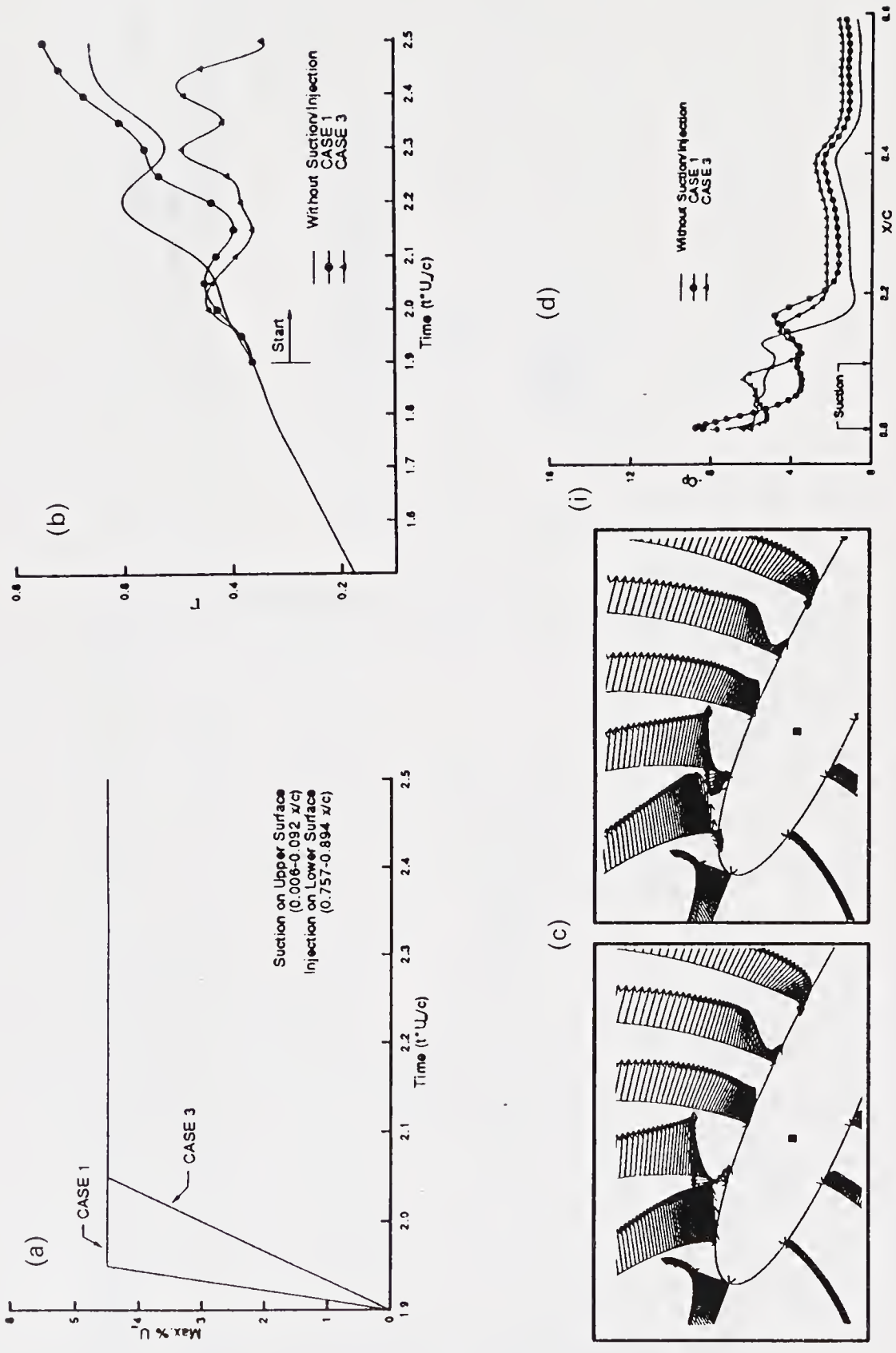
(a)
CASE 1
CASE 3
Suction on Upper Surface
(0.008-0.092 x/c)
Injection on Lower Surface
(0.757-0.894 x/c)
Time (t*U∞/c)
(b)
Start
Without Suction/Injection
CASE 1
CASE 3
Time (t*U∞/c)
(c)
(d)
(i)
Without Suction/Injection
CASE 1
CASE 3
Suction
X/C

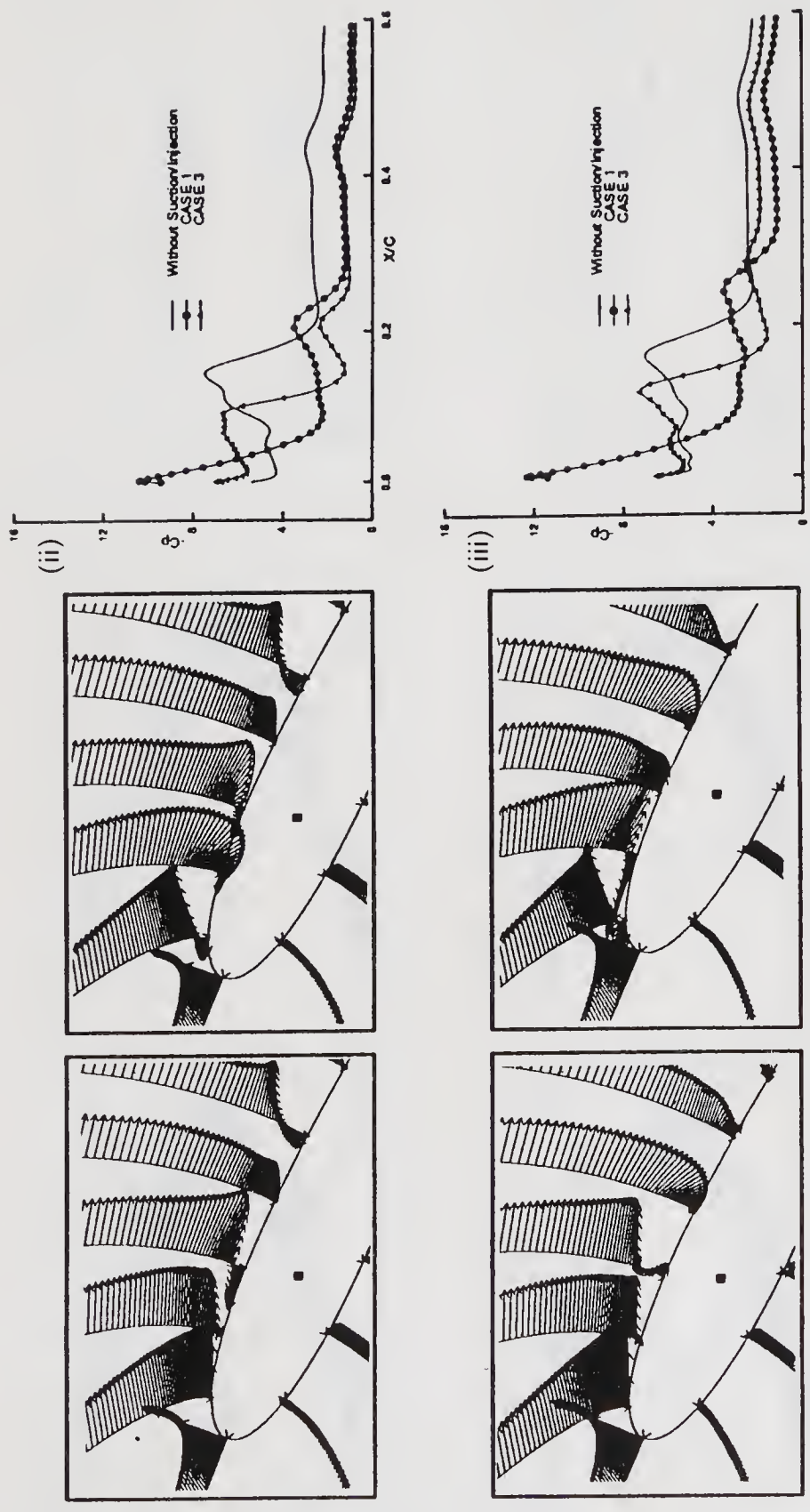

Figure 25. Effect of suction/injection for NACA 0015 airfoil; Re = 45,000, $\dot{\alpha}^+ = 0{\cdot}2$, $v_s/U_\infty = 0{\cdot}045$, $t_0 = 0{\cdot}05$ (case 1) and $0{\cdot}15$ (case 3). (**a**) Time history of control model; (**b**) calculated unsteady circulation; (**c**) velocity vectors; and (**d**) coefficients of pressure distribution. Time = 2·201, 2·301 & 2·401 and $\alpha = 23{\cdot}98°$, 25·12° & 26·27° for (i)–(iii), respectively.

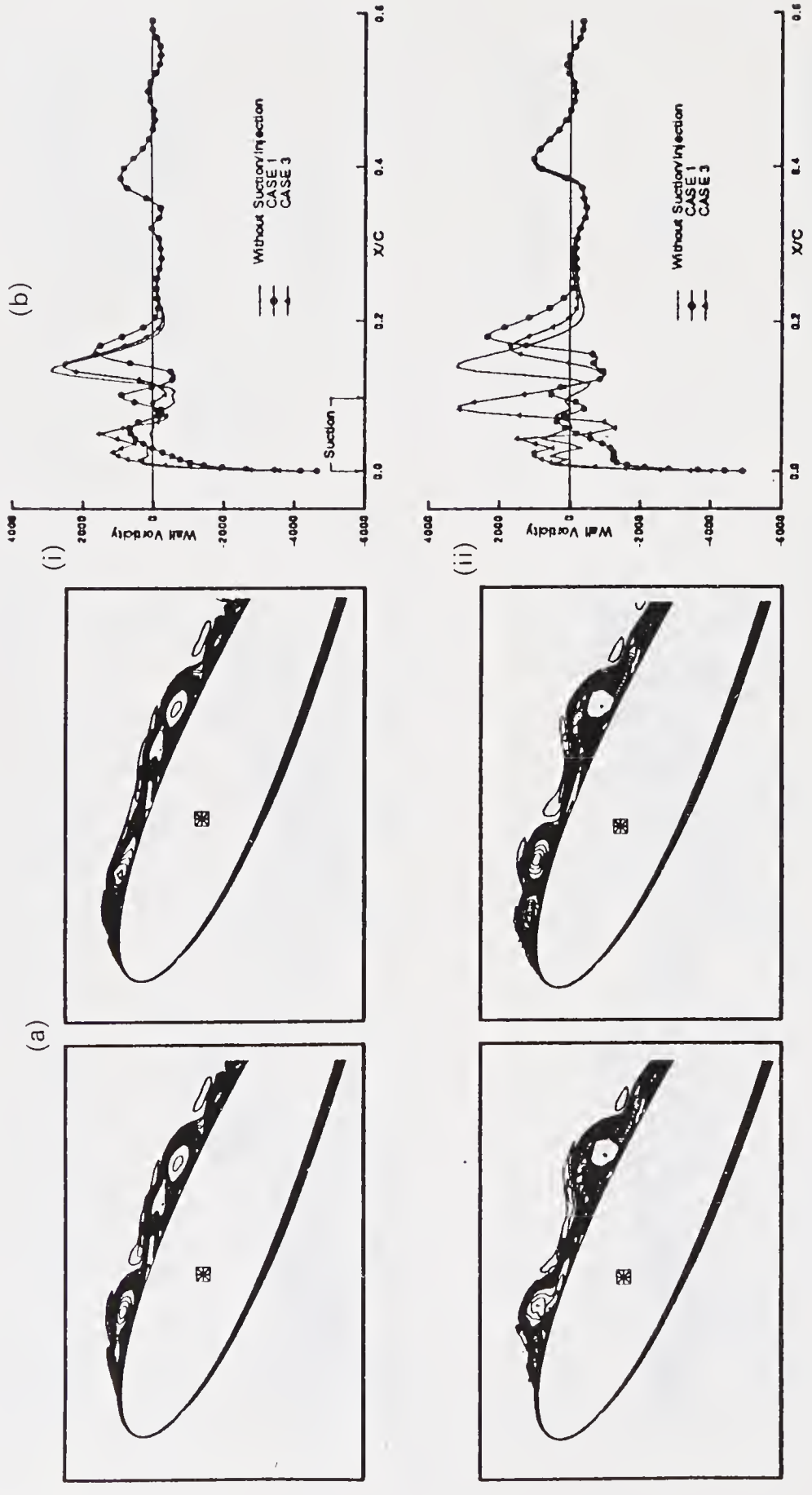
(a)
(b)
(i)
(ii)
Without Suction/Injection
CASE 1
CASE 3
Suction
Wall Vorticity
X/C
4000
2000
0
-2000
-4000
0.0
0.2
0.4
0.6

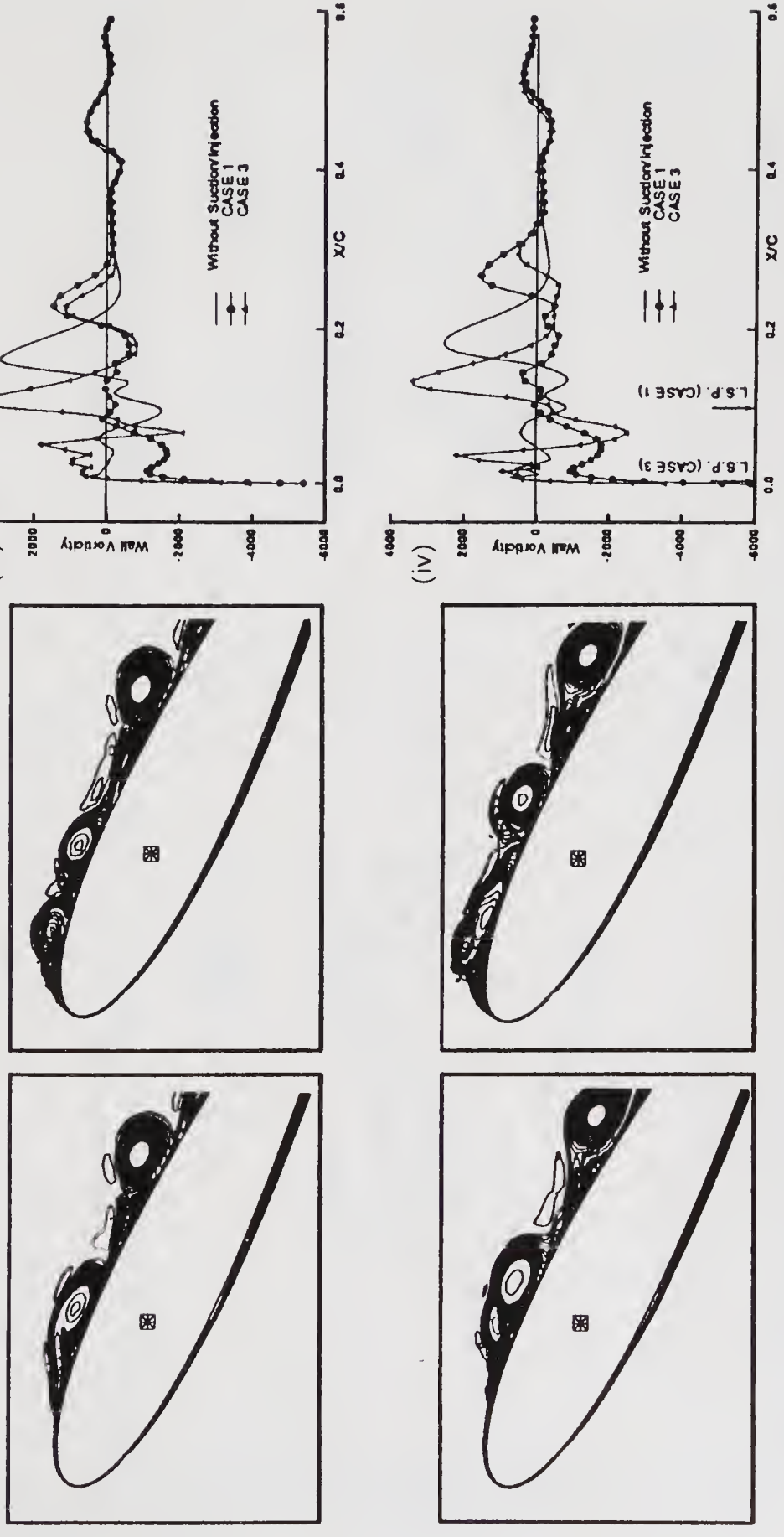

Figure 26. Effect of suction/injection for NACA 0015 airfoil; (**a**) instantaneous vorticity contours; (**b**) wall vorticity distributions. Time = 2·101, 2·201, 2·301 & 2·401 and $\alpha = 22{\cdot}83°$, $23{\cdot}98°$, $25{\cdot}12°$ & $26{\cdot}27°$ respectively for (i)–(iv). (Other conditions as in figure 25.)

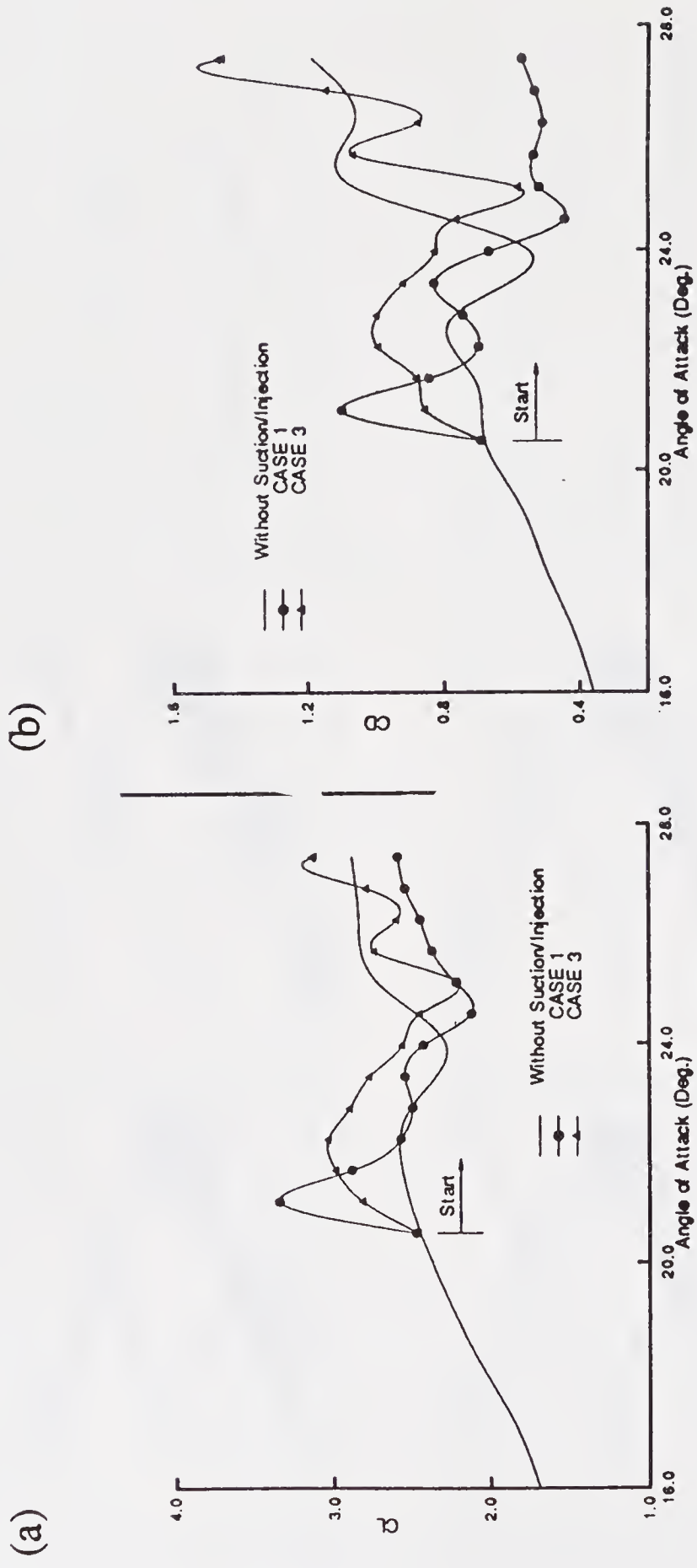
(a)
(b)
Without Suction/Injection
CASE 1
CASE 3
Start
Angle of Attack (Deg.)
16.0
20.0
24.0
28.0
1.0
2.0
3.0
4.0
0.4
0.8
1.2
1.6

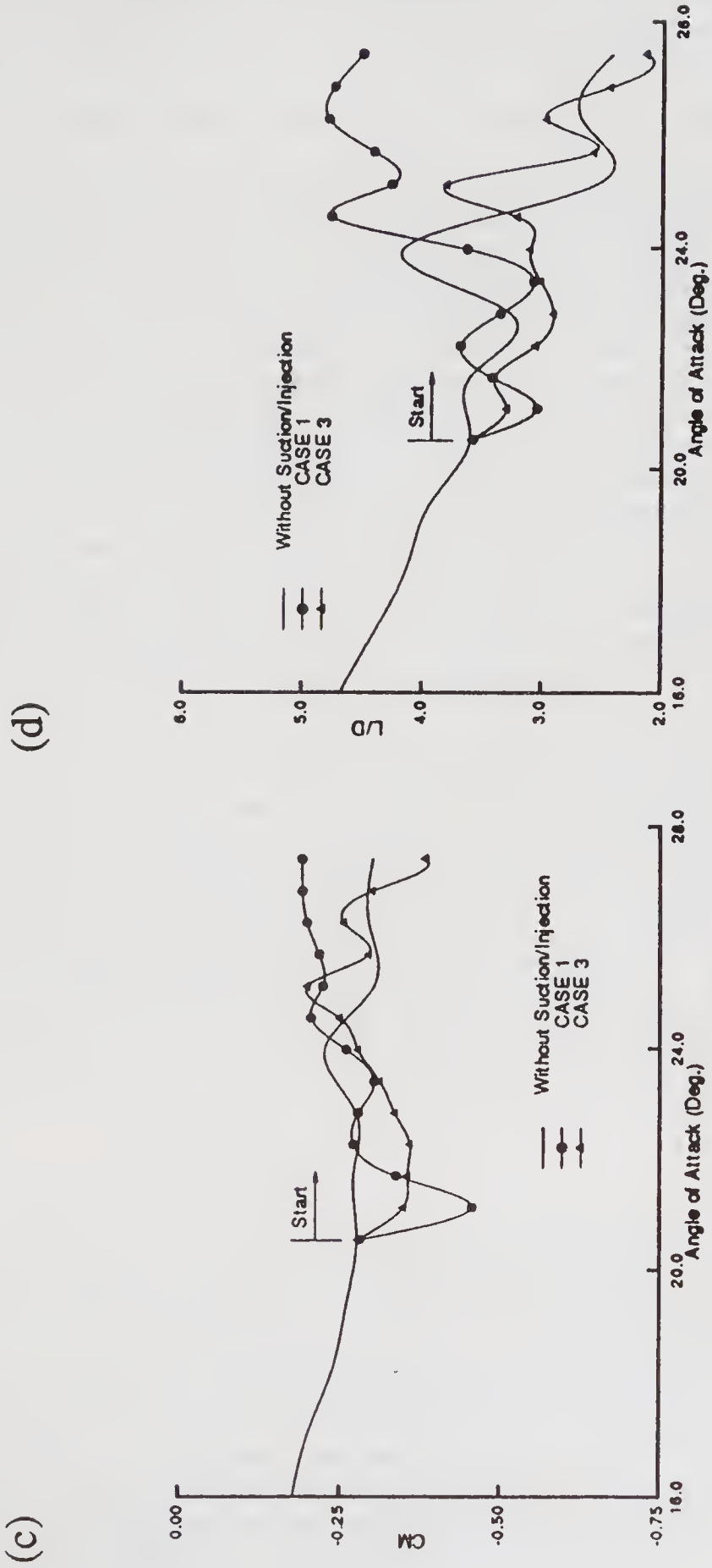

Figure 27. Effect of suction/injection for NACA 0015 airfoil. Comparison of computed lift coefficients (**a**), drag coefficients (**b**), moment coefficients (**c**) and lift/drag ratios (**d**). (Other conditions as in figure 25.)

quaternary vortices. The eruption of this secondary vortex structure initiates the formation of the energetic dynamic-stall vortex. K Ghia *et al* (1992b) have provided further details of this behaviour.

5.5 *Flow structure for configuration III: Re = 45,000 with modulated suction injection*

In an attempt to control the formation of the dynamic stall vortex, two specific MSI controls were used. These are case 1 with $v_s/U_\infty = 0.045$ and case 2 with $v_s/U_\infty = 0.035$, as presented in figure 22. The ramp functions used for these two configurations to bring the magnitude of suction velocity to its final magnitude are shown in this figure; these magnitudes are held constant thereafter. Also shown in this figure is the viscous circulation for configuration II as well as for both cases of configuration III. The start of the MSI is also indicated. In addition, the velocity vectors are shown for both cases for three different values, $\alpha = 23.98°$, $25.12°$ and $26.27°$. Also shown here are the velocity vectors as well as C_p-distribution on the suction surface for flow without and with MSI. In figure 23, the instantaneous vorticity contours as well as the wall vorticity are shown for configurations II and III. In this figure, results are also plotted for one additional value of $\alpha = 22.83°$. The instantaneous vorticity contours for various values of α show that the dynamic stall vortex does not develop with MSI activated. Further, the controlled wall vorticity does not show sharp spikes leading to suppression of the formulation of the stall vortex. The results showing the effect of MSI on C_L, C_D, C_M and L/D are most significant, since they show directly whether or not the desired control is achieved. Figure 24a shows that there is not much significant change in C_L, but, as seen in figure 24b, C_D is considerably reduced by MSI for case 1 at higher α. Although C_M distribution does not show a clear trend in figure 24c, L/D in figure 24d increases rapidly as compared to that for the flow without MSI. Finally, controlled modulated suction/injection is also attempted using configuration III, with a more gradual application of MSI control as shown in figure 25. Compared to case 1, the viscous circulation is sufficiently reduced for this new case 3. As before, the velocity vectors as well as C_p-distribution on the suction surface are also plotted. The corresponding instantaneous vorticity contours and wall vorticity are shown in figure 26. The results for case 3 with its gradually implemented MSI are very similar to those for case 2, as seen from figures 24 and 27. Finally, the effect of gradually applying MSI also shows significant changes as compared to the standard case 1.

6. Conclusion

An unsteady NS analysis is developed using the $(\bar{\omega}_I, \psi_I^D, \Gamma(t))$ formulation. Inclusion of viscous circulation permits accurate treatment of the far-field boundary condition. The implicit ADI-BGE numerical technique provides a uniformly second-order accurate solution, with higher accuracy for the nonlinear convective terms. The grid-refinement study shows that, for this constant-rate pitch-up motion in the regimes where the flow is massively separated, the finest-grid solutions still show more than desired deviation from those of the medium grid used here to obtain all the solutions. Also, since the experimental pressure distribution is measured using a limited number of pressure taps, the coarse-grid C_L-distribution agrees well with these results. We discussed the role of unsteady separation in detail earlier (K Ghia *et al* 1992) which is therefore not described here. Based on the earlier description, a modulated suction/

injection control strategy was developed and used in this study. The suppression of LE-flow separation provides a very effective means of controlling the formation of the dynamic stall vortex, even with small volumetric suction rate $S = -0.00237$.

Recently, the present authors have been able to systematically arrive at a control law using a modulated suction/injection strategy; this work has been presented at the AIAA 3rd Shear Flow Control Conference in July 1993 in Orlando, Florida. In this study, although the authors have attempted to analyse the flow using the critical-point theory of Perry & Chong (1987), it is our belief that the usefulness of this theory in identifying organized vortex structures is perhaps more pertinent in conjunction with the $(\bar{V}, p)$ formulation of the Navier–Stokes equations. In the current $(\omega_1, \psi_1^D, \Gamma(t))$ formulation, the vorticity is computed directly, and the vortex structures and locations are directly available.

Some of the fundamental research issues have been listed by K Ghia (1992, pp. 157–73) and addressed in a paper by K Ghia *et al* (1993). These outstanding issues are summarized here for emphasis. The 2-D analysis developed here is accurate and any further discrepancies observed are due to the three-dimensionality effect. An effort should be made to accurately simulate the three-dimensional flow past this 2-D geometry. Effort is also necessary to incorporate an adaptive-grid refinement in this analysis, in order to obtain higher-Re solutions and also resolve the time scale of the eruption of the secondary structure of $O(\mathrm{Re}^{-2/11})$. The three-dimensional analysis should also be coupled with a large-eddy simulation technique in order to obtain higher-Re solutions of greater practical interest.

The authors are sincerely indebted to many of the personnel of the Computational Fluid Dynamics Research Laboratory, University of Cincinnati; in particular, Chad Yoshikawa, Rahul Rathod, Chris Noll, K S Muralirajan, Keith Blodgett, Tom Rohling, and Tae-Seung Yoo have helped in preparing the video animation and in preparation of the manuscript using LATEX.

This research is supported, in part, by AFOSR Grant Nos. 90-0249 and F49620-92-J-0292, and Ohio Supercomputer Center Grant No. PES080.

List of symbols

a	radius of airfoil in circle plane;
$\bar{a}_{B/I}$	translational acceleration;
c	airfoil chord length;
C_D, C_L, C_M	drag, lift, and moment coefficients, respectively;
$\bar{C}_{F_p}$, $\bar{C}_{F_v}$	coefficients of pressure and viscous forces, respectively;
C_p	pressure coefficient;
d	wing span;
ds^*	increment of surface area;
$\hat{e}_1, \hat{e}_2$	Cartesian unit vectors in the physical plane;
$\bar{e}_1, \bar{e}_2$	local covariant base vectors;
$\bar{F}$	complex force vector;
$\bar{F}_p$, $\bar{F}_v$	net forces due to pressure and viscosity, respectively;
g	determinant of the metric tensor;
g_{ij}	element of covariant metric tensor;

$G, G11, G22\beta$	metric coefficients of Dirichlet problem;
$\hat{i}, \hat{j}$	unit base vector of the inertial Cartesian frame;
$\underline{\mathrm{I}}$	inertial coordinate subscript;
$\bar{\bar{I}}$	identity tensor;
J	Jacobian determinant;
k	reduced frequency based on chord;
LE	leading edge;
LSP	leading-edge stagnation point;
$\bar{M}$	net moment due to pressure and viscosity;
MSI	modulated suction/injection;
$\hat{n}$	unit normal vector to the surface;
$N(\xi^1, \xi^2_w, t)$	normal velocity component for MSI;
p	pressure; also, pole location of cusped trailing edge;
P	complex-potential plane coordinate;
P_0	complex-potential plane coordinate for zero-lift;
$\bar{r}$	apparent position vector;
R	complex circle plane coordinate;
Re	Reynolds number;
t	nondimensional time;
$\hat{t}$	unit tangential vector to the surface;
t^*	dimensional time;
$T(\xi^1, \xi^2_w, t)$	tangential velocity component for MSI;
TE	trailing edge;
U_∞	freestream velocity;
v_s	constant MSI rate;
$\bar{V}, \bar{V}_{B/I}, \bar{V}_I, \bar{V}^D, V^*$	apparent, translational, inertial, disturbance, and complex velocity vectors, respectively;
x^1, x^2	body-fixed Cartesian coordinates;
z	complex physical plane coordinate;
Z	circular cylinder plane coordinate;
α_f	flow angle of attack;
$\bar{\alpha}_B$	angular acceleration of pitch-up maneuver;
$\dot{\alpha}^+$	non-dimensional pitch rate;
Γ	viscous circulation at infinity;
Γ_{in}	inviscid circulation;
η	complex η-plane coordinate;
η^1, η^2	η-plane coordinates;
θ_B	angle of pitch-up maneuver;
ν	kinematic viscosity of the fluid;
ξ	complex computational plane coordinate;
ξ^1, ξ^2	generalized-coordinates of the non-inertial body-fixed frame;
ρ	free stream density;
Σ	summation symbol;
Φ_{in}	inviscid potential function;
ψ	stream function;
ψ^D_I	disturbance stream function;
Ψ_I, Ψ_{in}	inertial and inviscid stream functions, respectively;
$\bar{\omega}_I$	inertial vorticity;
$\bar{\Omega}_B$	angular velocity vector of pitch-up maneuver.

References

Carr L W 1985 Dynamic stall: Progress in analysis and prediction. AIAA paper No. 85–1769

Carr L W (ed.) 1990 *Proc. of NASA/AFOSR/ARO Workshop on Physics of Forced Unsteady Separation* (Moffett Field, CA: NASA Ames Res. Center)

Chyu W J, Davis S S, Chang K S 1981 Calculation of unsteady transonic flow over an airfoil. *AIAA J.* 19: 684–690

Davis R T 1979 Methods for coordinate generation and potential flow solution based on Schwarz–Christoffel transformations. AIAA CP 799, pp. 180–194

Douglas J, Gunn J E 1964 A general formulation of alternating direction methods, Part I. Parabolic and hyperbolic problems. *Numer. Math.* 6: 428–453

Fant D B, Rockwell D (eds) 1992 *Proceeding of Workshop on Supermaneuverability: Physics of unsteady separated flow at high angle-of-attack* (Bethlehem, PA: Lehigh University)

Gatski T B 1991 Review of incompressible fluid flow computations using the vorticity-velocity formulation. *Appl. Numer. Math.* 7: 227–239

Ghia K N 1992 Analysis of two-dimensional flow structures of forced unsteady separated flows. *Proceeding of Workshop on Supermaneuverability: Physics of unsteady separated flow at high angle-of-attack* (eds) D B Fant, D Rockwell (Bethlehem, PA: Lehigh University)

Ghia K N, Ghia U, Osswald G A 1990 Characterization of dynamic stall phenomenon using two-dimensional unsteady Navier–Stokes equations. *Proc. NASA/AFOSR/ARO Workshop on Physics of Forced Unsteady Separation* (ed.) L W Carr (Moffett Field, CA: NASA Ames Res. Center); also 1992 NASA CP 3144, pp. 129–147

Ghia K N, Hankey W L, Hodge J K 1977 Study of incompressible Navier–Stokes equations in primitive variables using implicit numerical techniques. AIAA paper No. 77–0648; also *AIAA J.* 17: 298–301

Ghia K N, Yang J, Ghia U, Osswald G A 1992a Analysis of dynamic stall phenomenon through simulation of forced oscillatory flows. *Proc. 5th Symp. on Numerical and Physical Aspects of Aerodynamics*, Long Beach, CA

Ghia K N, Yang J, Osswald G A, Ghia U 1991 Study of the dynamic stall mechanism using simulation of two-dimensional Navier–Stokes equations. AIAA paper No. 91–0546; also see – Physics of forced unsteady flow for a NACA 0015 airfoil undergoing constant pitch-up motion. *J. Fluid Dyn. Res.* (1992) 10: 351–369

Ghia K N, Yang J, Osswald G A, Ghia U 1992b Study of the role of unsteady separation in the formation of dynamic stall vortex. AIAA paper No. 92–0196

Ghia K N, Yang J, Osswald G A, Ghia U 1993 Analysis of experimental and computational results for incipient separation and dynamic stall. Invited paper to be presented at *3rd World Conference on Experimental Heat Transfer, Fluid Mechanics and Thermodynamics*, November 1–5, 1993, Honolulu, Hawaii

Ghia U, Ghia K N 1987 Navier–Stokes equations for incompressible flow. In *Handbook of fluids and fluid machinery* (ed.) A Fuchs (New York: McGraw Hill) chap. 3

Gresho P M 1991 Incompressible fluid dynamics: Some fundamental formulation issues. *Annu. Rev. Fluid Mech.* 23: 412–453

Gustafson K, Wyss W (eds) 1990 *Proceedings of IMACS 1st International Conference on Computational Physics*, University of Colorado at Boulder, Boulder, CO, pp. 11–15

Helin H E 1989 The relevance of unsteady aerodynamics for highly maneuverable and agile aircraft. *Proc. of 4th Symposium on Numerical and Physical Aspects*, Long Beach, CA

Huang Y, Ghia U, Ghia K N 1992 Development of a 3-D unsteady Navier–Stokes analysis for submarine afterbody flows. Aerospace Engineering Report, AFL 92-8-77; University of Cincinnati, Cincinnati, OH

Lang J D, Francis M S 1985 Unsteady aerodynamics and dynamic aircraft maneuverability. *Proc. AGARD Symposium on Unsteady Aerodynamics – Fundamentals and applications to aircraft dynamics* (Göttingen: AGARD) no. 386, pp. 29.1–29.19

Lerner P 1991 Stall tactics. The X-31 is teaching old dogfighters new tricks. *Air Space* 6: 29–37

Matida Y, Kuwahara K, Takami H 1975 Numerical study of steady two-dimensional flow past a square cylinder in a channel. *J. Phys. Soc. Jpn.* 38: 1522–1529

McAllister K W, Carr L W 1979 Water tunnel visualizations of dynamic stall. *J. Fluids Eng.* 101: 376–380

Mehta U B 1977 Dynamic stall of an oscillating airfoil. AGARD CP 227, paper No. 23, pp. 1–32

Osswald G A 1981 *Analysis and numerical solutions of unsteady two dimensional Navier–Stokes equations in primitive and derived variables*, Master's thesis, University of Cincinnati, Cincinnati, OH

Osswald G A 1992 Some critical issues associated with the physics of unsteady flows during maneuvers to high angles of attack. *Proc. 5th Symp. on Numerical and Physical Aspects of Aerodynamics*, Long Beach, CA, pp. 223–224

Osswald G A, Ghia K N, Ghia U 1987 A direct algorithm for solution of incompressible three-dimensional unsteady Navier–Stokes equations. AIAA CP 874, pp. 408–421

Osswald G A, Ghia K N, Ghia U 1988 Direct solution methodologies for the unsteady dynamics of an incompressible fluid. *Computational mechanics 88* (eds) S N Atluri, G Yagawa (Berlin: Springer-Verlag) vol. 2, pp. 5351–5354

Osswald G A, Ghia K N, Ghia U 1989 Analysis of potential and viscous flows past arbitrary two-dimensional bodies with sharp trailing edges. AIAA CP 895, pp. 668–677

Osswald, G A, Ghia K N, Ghia U 1990 Simulation of dynamic stall phenomenon using unsteady Navier–Stokes equations. *Proc. of IMACS 1st Int. Conf.*, Boulder, CO, pp. 252–261; also, *Comput. Phys. Commun.* 65: 209–218

Osswald G A, Ghia K N, Ghia U 1992 A direct implicit methodology for the solution of the rapid pitch-up of an airfoil with and without leading edge flow control. *Lecture notes in physics* (New York: Springer-Verlag) 414: 463–467

Perry A E, Chong M S 1987 A description of eddying motions and flow patterns using critical-point concepts. *Annu. Rev. Fluid Mech.* 19: 125–155

Rohling T C 1991 *Simulation of chaotic flow past airfoils at high incidence using the unsteady Navier–Stokes equations*, Master's thesis, University of Cincinnati, Cincinnati, OH

Salari K, Roache P J 1990 The influence of sweep on dynamic stall produced by a rapidly pitching wing. AIAA paper 90–0581

Sankar N L, Tassa Y 1980 Reynolds number and compressibility effects on dynamic stall of a NACA 0012 airfoil. AIAA paper No. 80–0010

Speziale C G 1987 On the advantages of vorticity-velocity formulation of the equations of fluid dynamics. *J. Comput. Phys.* 73: 476–480

Visbal M R 1990 On some physical aspects of airfoil dynamic stall. *Proc. of Int. Symp. on Nonsteady Fluid Dynamics* (ed.) J A Miller, D P Telionis (New York: ASME) FED-vol. 92

Visbal M R, Shang J S 1989 Investigation of the flow structure around a rapidly pitching airfoil. *AIAA J.* 27: 1044–1055; also *Proc. of AFOSR/FJSRL/DRAM/UC Workshop II on Unsteady Separated Flows*, FJSRL-TR-88-084, pp 91–108

Walker J D A 1992 Unsteady boundary-layer separation in two-dimensional flows. *Proc. 5th Symp. on Numerical and Physical Aspects of Aerodynamics*, Long Beach, CA, pp. 131–156

Walker J M, Helin H E, Strickland J H 1985 An experimental investigation of an airfoil undergoing large amplitude pitching motions. *AIAA J.* 23: 1141–1142, also, AIAA paper no. 85–0039

Werlé H 1976 Visualization hydrodynamique de L'écoulement Autour d'une Pale Oscillante. ONERA Rapport Technique No. 56/1369 AN

Yang J 1992 *Study of dynamic stall phenomenon and its control using vorticity, stream function and circulation form of the unsteady Navier–Stokes equations*, doctoral dissertation, University of Cincinnati, Cincinnati, OH

Turbulence/shock wave interactions in chemically reacting flows

T J CHUNG

[1]Department of Mechanical and Aerospace Engineering, The University of Alabama in Huntsville, Huntsville, AL 35899, USA

Abstract. Physical interactions between turbulence and shock waves are very complex phenomena. If these interactions take place in chemically reacting flows, the degree of complexity increases dramatically. Examples of applications may be cited in the area of supersonic combustion, in which the controlled generation of turbulence and/or large scale vortices in the mixing and flame-holding zones is crucial for efficient combustion. Equally important, shock waves interacting with turbulence and chemical reactions affect the combustor flowfield resulting in enhanced relaxation and chemical reaction rates. Chemical reactions in turn contribute to dispersion of shock waves and reduction of turbulent kinetic energies. Computational schemes to address these physical phenomena must be capable of resolving various length and time scales. These scales are widely disparate and the most optimum approach is found in explicit/implicit adjustable schemes for the Navier–Stokes solver. This is accomplished by means of the generalized Taylor–Galerkin (GTG) finite element formulations. Adaptive meshes are used in order to assure efficiency and accuracy of solutions. Various benchmark problems are presented for illustration of the theory and applications. Geometries of ducted rockets, supersonic diffusers, flame holders, and hypersonic inlets are included. Merits of proposed schemes are demonstrated through these example problems.

Keywords. Turbulence/shock wave interactions; chemically reacting flows; supersonic combustion; finite element formulations.

1. Introduction

The last decade has seen unprecedented technological innovations in computational fluid dynamics, prompted particularly by the increase in technical requirements of aerospace industries. Namely, the flowfields due to high velocities, compressibility, shock waves, turbulence, high temperature, and chemical reactions have been the focus of intensive research (Gnoffo & McCandless 1986; Dwyer & Kumar 1987; Gnoffo *et al* 1987; Kunik *et al* 1987; Drummond *et al* 1989; Kim & Chung 1989; Northam 1989; Stalker 1989; Bakos *et al* 1990; Harradine *et al* 1990; Chung & Yoon 1991, 1992).

There are two basically different flowfields: the internal flows of propulsion systems and the external flows in aerodynamics associated with various aerospace vehicles. When turbulence is involved in shock waves and chemical reactions in both internal and external flows, special considerations are required due to widely disparate length and time scales, corresponding to different physical phenomena: turbulence microscales, shock wave surface discontinuities, and reaction rates of chemical species. Here we are faced with the smallest length and time scales which may severely affect the computational requirements.

To cope with such requirements various numerical strategies have been developed using finite difference methods (FDM) and finite element methods (FEM). Incorporated or implemented into either FDM or FEM are the finite volume methods (FVM) and spectral methods (SPM). Modelling of turbulence has been the controversial subject. Closure models (algebraic, one-equation or two-equation models), probability density functions (PDF), large eddy simulation (LES), direct numerical simulation (DNS), and other methods have been reported. Whatever the numerical simulation techniques chosen, they should be capable of capturing the complex physics depicting the interactions between shock waves, turbulence, and chemical reactions.

Toward this end, one of the most effective numerical simulation strategies appear to be the adaptive finite element methods with unstructured meshes, facilitated by DNS for turbulent flows with parallel processing. This attempt is currently under progress (Chung & Yoon 1991, 1992). However, the present paper is confined to the chemically reacting turbulent flows based on the K–ε model with shock wave interactions characterized by explicit/implicit adjustable Taylor–Galerkin finite elements. Exhaustive numerical examples are presented for the finite rate chemistry of hydrogen and hydrocarbon fuels.

2. Mixed explicit/implicit Navier–Stokes solver

To cope with widely disparate length and time scales, it is important to provide adjustable explicit/implicit schemes as required by the degree of stiffness of the equations, particularly when chemically reacting processes so dictate. In this vein, it is convenient to write all governing equations in conservation form as follows:

$$(\partial \mathbf{U}/\partial t) + (\partial \mathbf{F}_j/\partial x_j) + (\partial \mathbf{G}_j/\partial x_j) = \mathbf{B}, \tag{1}$$

$$\mathbf{U} = \begin{bmatrix} \rho \\ \rho v_i \\ \rho E \\ \rho Y_k \\ \rho K \\ \rho \varepsilon \end{bmatrix}, \quad \mathbf{F}_j = \begin{bmatrix} \rho v_j \\ \rho v_i v_j + p\delta_{ij} \\ (\rho E + p) v_j \\ \rho Y_k v_j \\ \rho K v_j \\ \rho \varepsilon v_j \end{bmatrix}, \quad \mathbf{G}_j = \begin{bmatrix} 0 \\ -\tau_{ij} \\ -\tau_{ij} v_i + q_j \\ \rho D Y_{k,j} \\ \mu_k K_{,j} \\ \mu_\varepsilon \varepsilon_{,j} \end{bmatrix}, \quad \mathbf{B} = \begin{bmatrix} 0 \\ \rho F_i \\ S_e + \rho F_i v_i \\ \omega_k \\ S_k \\ S_\varepsilon \end{bmatrix},$$

where τ_{ij} denotes the sum of both physical and turbulence shear stresses, Y_k is the mass fraction of the species k, K and ε are the turbulent kinetic energy and its rate, respectively, and **B** contains all source terms. Note also that all variables are in terms of time averages for turbulence.

In general, explicit schemes are inexpensive but less accurate in comparison with implicit schemes for regions of high pressure or velocity gradients. In case of rapid

variations of gradients throughout the domain it is often desirable to devise a scheme in which implicitness can be adjustable in accordance with gradients, more implicit for the region of high gradients and less implicit or fully explicit for the region of low gradients (Zienkiewicz *et al* 1990; Chung & Yoon 1992).

In expanding $\mathbf{U}^{n+1}$ in a Taylor series about $\mathbf{U}^n$, we introduce the implicitness parameters s_1 and s_2 for the first and second derivatives of $\mathbf{U}$ with respect to time, respectively,

$$\mathbf{U}^{n+1} = \mathbf{U}^n + \Delta t(\partial \mathbf{U}^{n+s_1}/\partial t) + (\Delta t^2/2)(\partial^2 \mathbf{U}^{n+s_2}/\partial t^2) + O(\Delta t^3), \tag{2}$$

with

$$(\partial \mathbf{U}^{n+s_1}/\partial t) = (\partial \mathbf{U}^n/\partial t) + s_1(\partial \Delta \mathbf{U}^{n+1}/\partial t), \tag{3a}$$

$$(\partial^2 \mathbf{U}^{n+s_2}/\partial t^2) = (\partial^2 \mathbf{U}^n/\partial t^2) + s_2(\partial^2 \Delta \mathbf{U}^{n+1}/\partial t^2). \tag{3b}$$

Substituting (3) into (2) yields

$$\Delta \mathbf{U}^{n+1} = \Delta t\left(\frac{\partial \mathbf{U}^n}{\partial t} + s_1 \frac{\partial \Delta \mathbf{U}^{n+1}}{\partial t}\right) + \frac{\Delta t^2}{2}\left(\frac{\partial^2 \mathbf{U}^n}{\partial t^2} + s_2 \frac{\partial^2 \Delta \mathbf{U}^{n+1}}{\partial t^2}\right) + O(\Delta t^3). \tag{4}$$

It follows from (1) that

$$(\partial \mathbf{U}/\partial t) = -(\partial \mathbf{F}_j/\partial x_j) - (\partial \mathbf{G}_j/\partial x_j) + B. \tag{5}$$

Here $\mathbf{F}_j$ is a function of $\mathbf{U}$ and $\mathbf{G}_j$ is a function of $\mathbf{U}$ and its gradient $\mathbf{U}_k$, so that we denote the convective Jacobian $\mathbf{a}_j$, dissipative Jacobian $\mathbf{b}_j$, and dissipative gradient Jacobian $\mathbf{c}_{jk}$ as

$$\mathbf{a}_j = (\partial \mathbf{F}_j/\partial \mathbf{U}), \quad \mathbf{b}_j = (\partial \mathbf{G}_j/\partial \mathbf{U}), \quad \mathbf{c}_{jk} = (\partial \mathbf{G}_j/\partial \mathbf{V}_k) = (\partial \mathbf{G}_j/\partial \mathbf{U}_{,k}).$$

The second derivative of $\mathbf{U}$ with respect to time may now be written in terms of these Jacobians.

$$\frac{\partial^2 \mathbf{U}}{\partial t^2} = \mathbf{a}_j \frac{\partial}{\partial x_j}\left(\frac{\partial \mathbf{F}_i}{\partial x_i} + \frac{\partial \mathbf{G}_i}{\partial x_i} - \mathbf{B}\right) + \mathbf{b}_j \frac{\partial}{\partial x_j}\left(\frac{\partial \mathbf{F}_i}{\partial x_i} + \frac{\partial \mathbf{G}_i}{\partial x_i} - \mathbf{B}\right) + \mathbf{c}_{jk} \frac{\partial^2}{\partial x_j \partial x_k}\left(\frac{\partial \mathbf{F}_i}{\partial x_i} + \frac{\partial \mathbf{G}_i}{\partial x_i} - \mathbf{B}\right). \tag{6}$$

Substituting (5) and (6) into (4) yields

$$\begin{aligned}\Delta \mathbf{U}^{n+1} = \Delta t\left[-\frac{\partial \mathbf{F}_j^n}{\partial x_j} - \frac{\partial \mathbf{G}_j^n}{\partial x_j} + \mathbf{B}^n + s_1\left(-\frac{\partial \Delta \mathbf{F}_j^{n+1}}{\partial x_j} - \frac{\partial \Delta \mathbf{G}_j^{n+1}}{\partial x_j} + \Delta \mathbf{B}^{n+1}\right)\right] \\ + \frac{\Delta t^2}{2}\left\{\left[(\mathbf{a}_j + \mathbf{b}_j)\frac{\partial}{\partial x_j}\left(\frac{\partial \mathbf{F}_i^n}{\partial x_i} + \frac{\partial \mathbf{G}_i^n}{\partial x_i} - \mathbf{B}^n\right) + \frac{\partial \mathbf{B}^n}{\partial t}\right]\right. \\ \left. + s_2\left[(\mathbf{a}_j + \mathbf{b}_j)\frac{\partial}{\partial x_j}\left(\frac{\partial \Delta \mathbf{F}_i^{n+1}}{\partial x_i} + \frac{\partial \Delta \mathbf{G}_i^{n+1}}{\partial x_i} - \Delta \mathbf{B}^{n+1}\right)\right]\right\} + O(\Delta t^3).\end{aligned} \tag{7}$$

In order to provide different implicitness (different amounts of damping or

dissipation) to different physical quantities, we reassign s_1 and s_2 associated with $\mathbf{G}_j$, respectively,

$$s_1 \Delta \mathbf{G}_j = s_3 \Delta \mathbf{G}_j, \tag{8a}$$

$$s_2 \Delta \mathbf{G}_j = s_4 \Delta \mathbf{G}_j, \tag{8b}$$

with the various implicitness parameters defined as

s_1 = first order convective implicitness parameter,
s_2 = second order convective implicitness parameter,
s_3 = first order dissipative implicitness parameter,
s_4 = second order dissipative implicitness parameter.

Neglecting the third order spatial derivatives of conservation variables associated with $\mathbf{c}_{ij}$ in (7) and substituting (8a,b) into (7) leads to the residual,

$$\begin{aligned}\mathbf{R} = \Delta \mathbf{U}^{n+1} &+ s_1 \Delta t \left(\mathbf{a}_j \frac{\partial \Delta \mathbf{U}^{n+1}}{\partial x_j} - \Delta \mathbf{B}^{n+1} \right) + \\ & s_3 \Delta t \left(\mathbf{b}_j \frac{\partial \Delta \mathbf{U}^{n+1}}{\partial x_j} + \mathbf{c}_{ji} \frac{\partial^2 \Delta \mathbf{U}^{n+1}}{\partial x_j \partial x_i} \right) - s_2 \frac{\Delta t^2}{2} (\mathbf{a}_j \mathbf{a}_i + \mathbf{b}_j \mathbf{a}_i) \frac{\partial^2 \Delta \mathbf{U}^{n+1}}{\partial x_j \partial x_i} \\ & - s_4 \frac{\Delta t^2}{2} \left[(\mathbf{a}_j \mathbf{b}_i + \mathbf{b}_j \mathbf{b}_i) \frac{\partial^2 \Delta \mathbf{U}^{n+1}}{\partial x_j \partial x_i} \right] + \Delta t \left(\frac{\partial \mathbf{F}_j^n}{\partial x_j} + \frac{\partial \mathbf{G}_j^n}{\partial x_j} - \mathbf{B}^n \right) \\ & - \frac{\Delta t^2}{2} \left\{ (\mathbf{a}_j + \mathbf{b}_j) \left[\frac{\partial}{\partial x_j} \left(\frac{\partial \mathbf{F}_i^n}{\partial x_i} + \frac{\partial \mathbf{G}_i^n}{\partial x_i} - \mathbf{B}^n \right) \right] + \frac{\partial \mathbf{B}^n}{\partial t} \right\} + O(\Delta t^3) = 0.\end{aligned} \tag{9}$$

where all Jacobians $\mathbf{a}_i$, $\mathbf{b}_j$ and $\mathbf{c}_{ji}$ are assumed to remain constant spatially within each time step and to be updated at subsequent time steps.

The Galerkin finite element analysis of (9) may now be carried out as follows:

$$\int_\Omega W_\alpha \mathbf{R}(\mathbf{U}, \mathbf{F}_j, \mathbf{G}_j) \mathrm{d}\Omega = 0, \tag{10}$$

where W_α refers to the test functions and the conservation variables are interpolated by the trial functions Φ_α as

$$\mathbf{U}(x,t) = \Phi_\alpha(x) \mathbf{U}_\alpha(t), \quad \mathbf{F}_j(x,t) = \Phi_\alpha(x) \mathbf{F}_{\alpha j}(t), \quad \mathbf{G}_j(x,t) = \Phi_\alpha(x) \mathbf{G}_{\alpha j}(t). \tag{11}$$

Substituting (11) into (9) and (10) yields

$$(A_{\alpha\beta} \delta_{rs} + B_{\alpha\beta rs}) \Delta U_{\beta s}^{n+1} = H_{\alpha r}^n + N_{\alpha r}^{n+1} + N_{\alpha r}^n, \tag{12}$$

where

$$\begin{aligned} B_{\alpha\beta rs} = \int_\Omega \Big\{ & \Delta t [- s_1 a_{jrs} \Phi_{\alpha,j} \Phi_\beta - s_3 (b_{jrs} \Phi_{\alpha,j} \Phi_\beta + c_{jirs} \Phi_{\alpha,j} \Phi_{\beta,i})] \\ & + (\Delta t^2/2) [s_2 (a_{jrq} a_{isq} + b_{jrq} a_{isq}) \Phi_{\alpha,j} \Phi_{\beta,i}] \Big\} \mathrm{d}\Omega, \end{aligned}$$

$$\begin{aligned} H_{\alpha r}^n = \int_\Omega \Big\{ & \Delta t [\Phi_{\alpha,j} \Phi_\beta (F_{\beta jr}^n + G_{\beta jr}^n) + \Phi_\alpha \Phi_\beta B_{\beta r}^n] \\ & - (\Delta t^2/2)(a_{jrs} + b_{jrs}) [\Phi_{\alpha,j} \Phi_{\beta,i} (F_{\beta is}^n + G_{\beta is}^n) - \Phi_\alpha \Phi_{\beta,j} B_{\beta s}^n] \end{aligned}$$

$$-(\Delta t/2)\Phi_\alpha \Phi_\beta \Delta B^n_{\beta s}\Big\}\mathrm{d}\Omega,$$

$$N^{n+1}_{\alpha r} = \int_\Gamma \Big\{\Delta t[s_1 a_{jrs}\overset{*}{\Phi}_\alpha \Delta U^{n+1}_s n_j - s_3(b_{jrs}\overset{*}{\Phi}_\alpha \Delta U^{n+1}_s n_j + c_{jirs}\overset{*}{\Phi}_\alpha \Delta U^{n+1}_{s,i} n_j)]$$
$$+(\Delta t^2/2)[s_2(a_{jrq}a_{isq} + b_{jrq}a_{isq})\overset{*}{\Phi}_\alpha \Delta U^{n+1}_{s,i} n_j$$
$$+ s_4(a_{jrq}b_{isq} + b_{jrq}b_{isq})\overset{*}{\Phi}_\alpha \Delta U_{s,i} n_j]\Big\}\mathrm{d}\Gamma,$$

$$N^n_{\alpha r} = -\int_\Gamma [\Delta t \overset{*}{\Phi}_\alpha (F^n_{jr} + G^n_{jr})n_j - (\Delta t^2/2)(a_{jrs} + b_{jrs})\overset{*}{\Phi}_\alpha (F^n_{is,i} + G^n_{is,i})n_j]\mathrm{d}\Gamma.$$

Notice that indices $i, j, k = 1, 2$ associated with the Jacobians imply directional identification of each Jacobian matrix ($\mathbf{a}_1$, $\mathbf{a}_2$, $\mathbf{b}_1$, $\mathbf{b}_2$, $\mathbf{c}_{11}$, $\mathbf{c}_{12}$, $\mathbf{c}_{21}$, $\mathbf{c}_{22}$) with $r,s = 1$, 2, 3, 4, denoting entries of each of the 4×4 Jacobian matrices. It should be warned, however, that these Jacobian matrices must be multiplied precisely as dictated by summing through repeated indices, not through matrix multiplications as a whole.

The solution of (13) may be carried out using the two-step scheme as follows:

Step 1

$$A_{\alpha\beta}\delta_{rs}X^{(1)}_{\beta s} = H^n_{\alpha r} + N^{n+1}_{\alpha r} + N^n_{\alpha r}. \tag{13a}$$

Step 2

$$A_{\alpha\beta}\delta_{rs}X^{(2)}_{\beta s} = -B_{\alpha\beta rs}X^{(1)}_{\beta s}, \tag{13b}$$

where

$$X^{(1)}_{\beta s} = \Delta U^{(1)}_{\beta s}, \tag{14a}$$

$$X^{(2)}_{\beta s} = \Delta U^{(2)}_{\beta s} - \Delta U^{(1)}_{\beta s}, \tag{14b}$$

with

$$\Delta U^{(1)}_{\beta s} \to \Delta U^{(2)}_{\beta s} = U^{n+1}_{\beta s} - U^n_{\beta s}. \tag{15}$$

A glance at (14a,b) suggests that the solution of (14a) for $X^{(1)}_{\beta s}$ (step 1) can be substituted into the RHS of (14b) to determine $X^{(2)}_{\beta s}$ (step 2). It follows from (14) through (16) that

$$U^{n+1}_{\beta s} = U^n_{\beta s} + X^{(1)}_{\beta s} + X^{(2)}_{\beta s}. \tag{16}$$

Although the Taylor–Galerkin finite element solution characterized by (14a,b) is efficient in dealing with steep gradients, additional measures may be implemented in order to control solution stability and convergence. To this end, we may either utilize the generalized Petrov–Galerkin test function for W_α in (10) (Zienkiewicz *et al* 1990) or the tensorial artificial numerical viscosity added to (1) in the form,

$$(\partial \mathbf{U}/\partial t) + (\partial \mathbf{F}_j/\partial x_j) + (\partial/\partial x_j)(\mathbf{G}_j + \hat{\mathbf{G}}_j) = \mathbf{B}, \tag{17}$$

where

$$(\partial \hat{\mathbf{G}}_j/\partial x_j) = (\partial \hat{\mathbf{G}}_j/\partial \mathbf{U}_{,k})(\partial \mathbf{U}_k/\partial x_j) = \hat{c}_{jk}(\partial^2 \mathbf{U}/\partial x_j x_k) = \hat{\mu} Q_{jk}(\partial^2 \mathbf{U}/\partial x_j \partial x_k) \tag{18}$$

with

$$\hat{\mu} = c_\mu A v_{m,i} Q_{mi}, \quad Q_{mi} = S_m S_i, \quad S_m = q_{,i}/|q_{,i}|, \quad q = (v_i v_i)^{1/2}.$$

A most rigorously formulated solution scheme may fail in extremely physically complicated flows such as occur in interactions of shock waves, turbulence, and chemical

reactions, particularly for widely disparate length scales. Unstructured adaptive methods have been proven to be effective for these problems. There are many options: h-methods in which the refinement of mesh is performed proportional to errors, r-methods where mesh points are moved closer together in the vicinity of larger errors, p-methods in which polynomial spectral orders are increased for elements with large errors. A preferable approach is to refine the mesh (h-methods) until further refinement is unproductive, at which time the spectral degrees of freedom (p-methods) are increased in order to reduce errors as desired, such as in the region of a turbulent viscous sublayer. However, another desirable approach is to optimize between the mesh refinement and spectral orders. Thus, the most crucial aspect of the combined h-p method is to determine the best possible change in the mesh structure to reduce the local error to a minimum.

Since the exact solution is not known *a priori*, we must depend on *a posteriori* error estimates once the finite element solution for a given mesh configuration is obtained, with iterative steps as follows.

(1) Provide the initial coarse mesh.
(2) Compute an initial solution. Check the error of each element (compared to the previous cycle) to see if adaptation is needed.
(3) The h-p optimization methods – choose an optimal approximation structure for most effectively reducing the error, the mesh (h) or spectral order (p).
(4) The h-p sequential methods – instead of step (3) above, repeat the h-refinements with the initial spectral order until error reduction reaches its predetermined limit at which time the spectral orders (p) are increased until desired accuracy is achieved.

Computational strategies include the gather–scattering process for vectorization and tridiagonalization of matrices via line relaxation through four-noded elements.

3. Chemical kinetics and thermodynamic models

The reaction rate ω_k appearing as a source term **B** in (1) is of the form

$$\omega_k = W_k \sum_{j=1}^{N} (\nu''_{i,j} - \nu'_{i,j}) \left(K_{f,j} \prod_{i=1}^{M} c_i^{\nu'_{i,j}} - K_{b,j} \prod_{i=1}^{M} c_i^{\nu''_{i,j}} \right), \tag{19}$$

where W_k is the molecular weight, ν'_i and ν''_i denote the reactant and product stoichiometric coefficients, respectively. K_f and K_b are the forward and backward reaction rate constants, respectively, and c_i refers to the molar concentration.

The specific heat at constant pressure, C_p, is given by

$$C_{pk} = A_k + B_k T + C_k T^2 + D_k T^3 + E_k T^4,$$

with the temperature related to the static enthalpy,

$$h = \sum_{k=1}^{M} Y_k h_k(T) = \sum_{k=1}^{M} Y_k \left(h_{fk} + \int_{T_0}^{T} C_{pk} \, \mathrm{d}T \right). \tag{20}$$

The most commonly used fuels are hydrogen and hydrocarbons. Although the chemical kinetics of fuels are extremely complex, we shall limit our consideration to

some of the well-known reactions in the next section on applications. Further details of chemical kinetics are given in appendices A and B.

4. Applications

In order to demonstrate the validity of theoretical formulations and numerical schemes, we shall examine (1) propane–air combustion for a subsonic ducted rocket (see appendix A for its chemical kinetics), (2) hydrogen–air reactions for supersonic combustors (scramjet) with the two-step global model and the eighteen-step combustion mechanism (appendix B), and (3) the scramjet flame holder hydrogen–air combustion without and with viscous effects. Here we set the implicitness parameters, $s_1 = s_3 = s_4 = 0$, $s_2 = 1$, and $b_{jrq}a_{isq} = s_{jirs}/\Delta t$.

Consider the ducted rocket geometry in two dimensions for propane-fuel combustion as shown in figure 1. The following data and boundary conditions are used.

	Fuel-rich gas	Ram-air
Location	$x = 0{\cdot}0$, $y = 0{\cdot}032$	$x = 0{\cdot}055$, $y = 0{\cdot}06$
Inlet width	0·0022 m	0·0145 m
Density	2·3 kg/m^3	3·8 kg/m^3
Pressure	715 kPa	592 kPa
Temperature	1021 K	535 K
X-velocity	78·9 m/s	193 cos(θ) m/s
Y-velocity	0·0	193 sin(θ) m/s
Mass fraction	$Y(C_3H_8)$	$Y(O_2) = 0{\cdot}233$
	$Y(N_2) = 0{\cdot}706$	$Y(N_2) = 0{\cdot}767$

The currently available code designed for high Mach number reacting flows with interactions of shock waves and turbulence has been modified to handle the flow mixed with low Mach numbers. In the regions of mixing and recirculation, there are

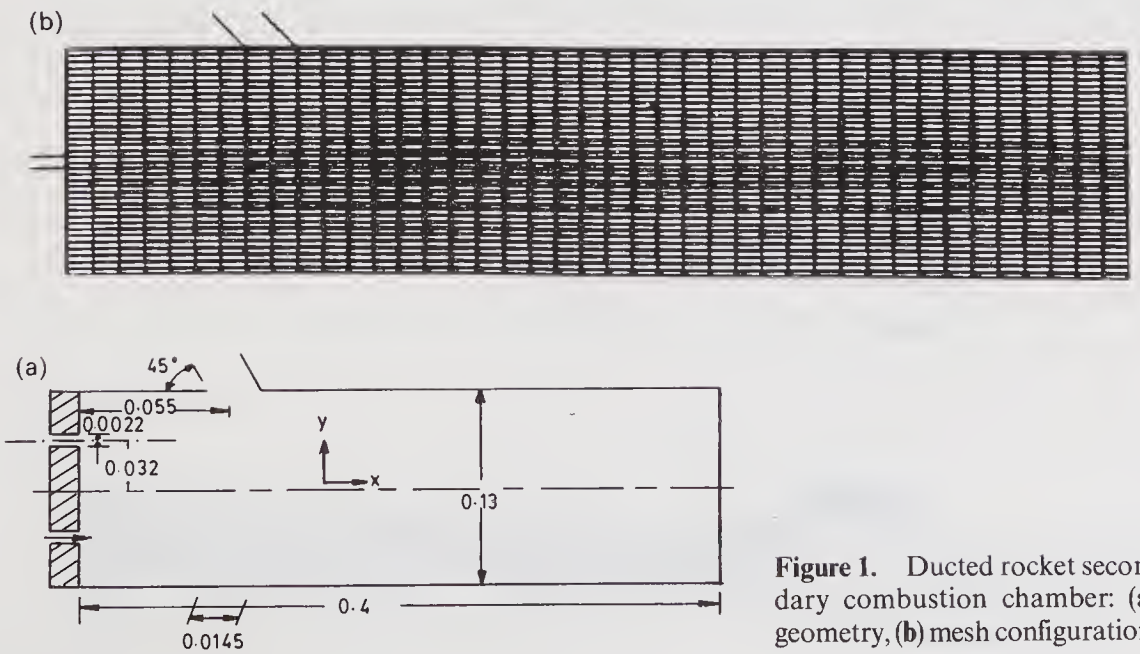

Figure 1. Ducted rocket secondary combustion chamber: (**a**) geometry, (**b**) mesh configuration.

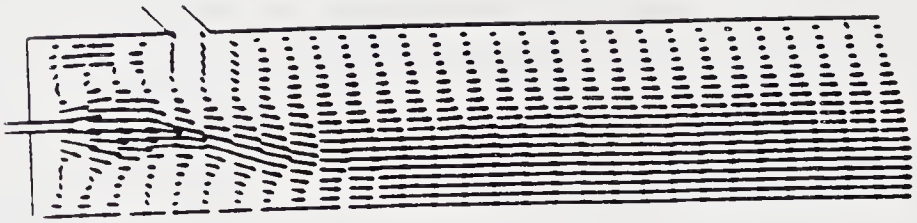

Figure 2. Velocity distribution.

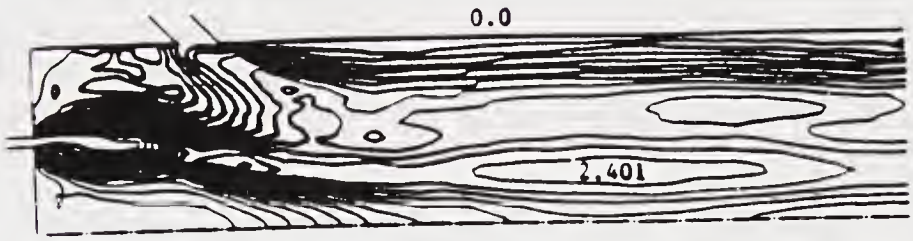

Figure 3. Mach numbers contours: max = 2·401, min = 0, Δ = 0·12.

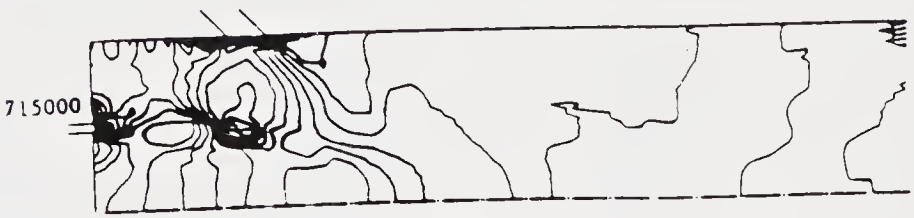

Figure 4. Pressure contours: max = $7{\cdot}15 \times 10^5$, min = $1{\cdot}503 \times 10^4$, Δ = $3{\cdot}5 \times 10^4$.

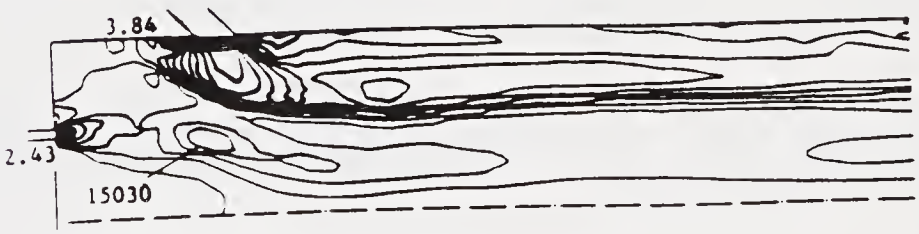

Figure 5. Density contours: max = 3·84, min = 2·43, Δ = 0·07.

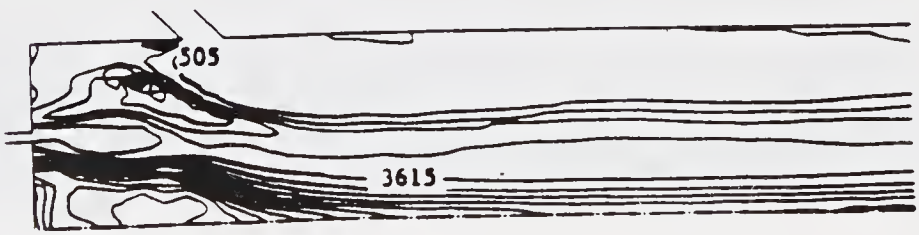

Figure 6. Temperature contours: max = 3615, min = 535, Δ = 154.

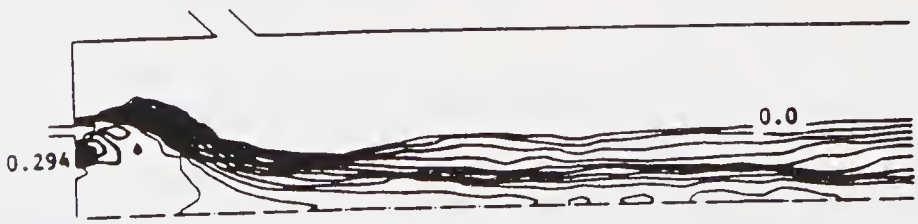

Figure 7. C_3H_8 mass fraction contours: max = 0·233, min = 0, Δ = 0·0165.

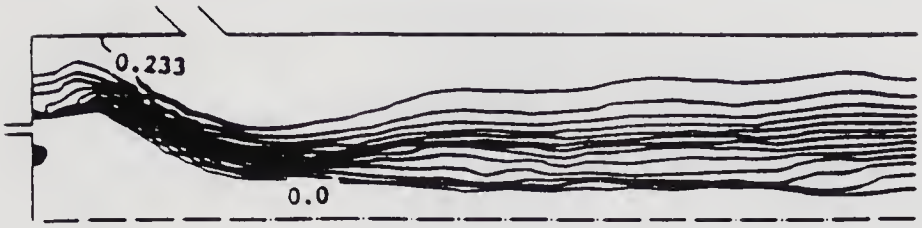

Figure 8. O_2 mass contours: max = 0·233, min = 0, Δ = 0·0165.

pockets of incompressible flow, causing the governing equations to be of mixed elliptic, parabolic and hyperbolic form. The conservation of mass in this situation must be satisfactorily resolved. The basic strategy introduced in § 3 by means of a mixed explicit/implicit scheme is considered the most versatile approach known to date. Thus, the purpose of the present study is aimed at testing this scheme.

Note that mixing is evident in the vicinity of fuel and air intake as seen in velocity distributions (figure 2), Mach number contours (figure 3), pressure contours (figure 4), density contours (figure 5) temperature contours (figure 6), C_3H_8 contours (figure 7), and O_2 contours (figure 8). At $x = 0{\cdot}35$ m, temperature rises to a maximum (figure 9) where the mass fractions of C_3H_8 and O_2 intersect, an interesting consequence as expected. Effects of turbulence upon chemical reactions prevail not only in activation and promotion of reacting process but also for mixing in the flowfield.

To demonstrate the effects of finite rate chemistry, in comparison with equilibrium and frozen chemistry, a supersonic diffuser as shown in figure 10 is analysed using the two-step global model for hydrogen–air combustion (Yoon 1992). As seen in figure 11 the temperature calculated from the finite rate chemistry is somewhere between the equilibrium and frozen chemistry models. In the case of pressure, however, the difference between equilibrium and finite rate chemistry models is very small. Effects of finite rate chemistry for reactants (figure 12) are less prominent than those for products (figure 13), with the finite rate model producing larger hydroxyl mass fractions than the equilibrium model. The trend is opposite for water.

Effects of chemical reaction mechanism due to 2-step global models and 18-step reaction models are examined for the ramjet geometry (figure 14) (Yoon 1992). Notice that the 2-step global model tends to overestimate temperature and pressure towards

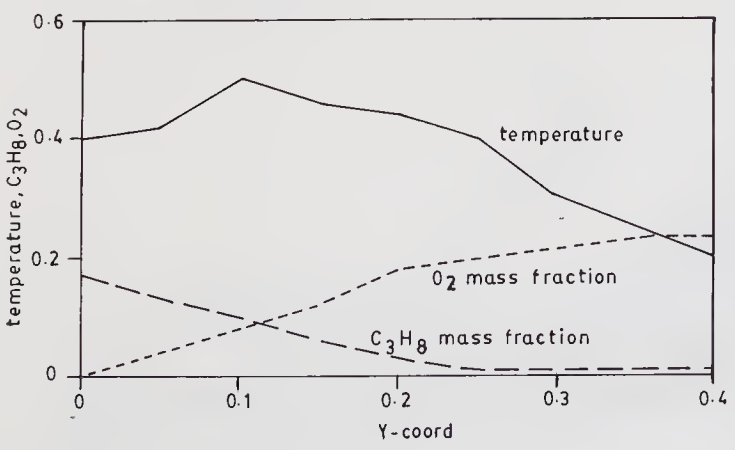

Figure 9. Vertical distribution of temperature, C_3H_5, and O_2 at $x = 0{\cdot}35$.

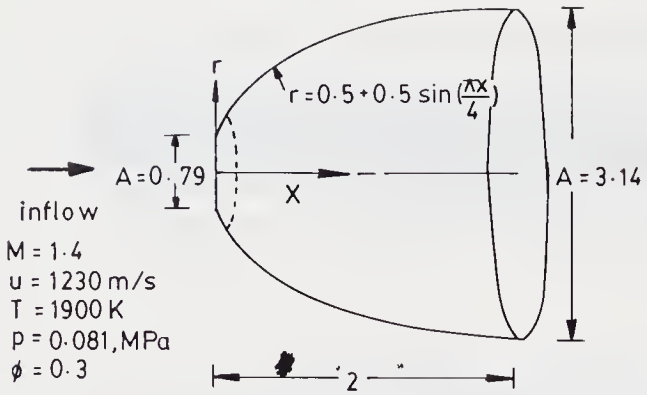

Figure 10. Supersonic diffuser.

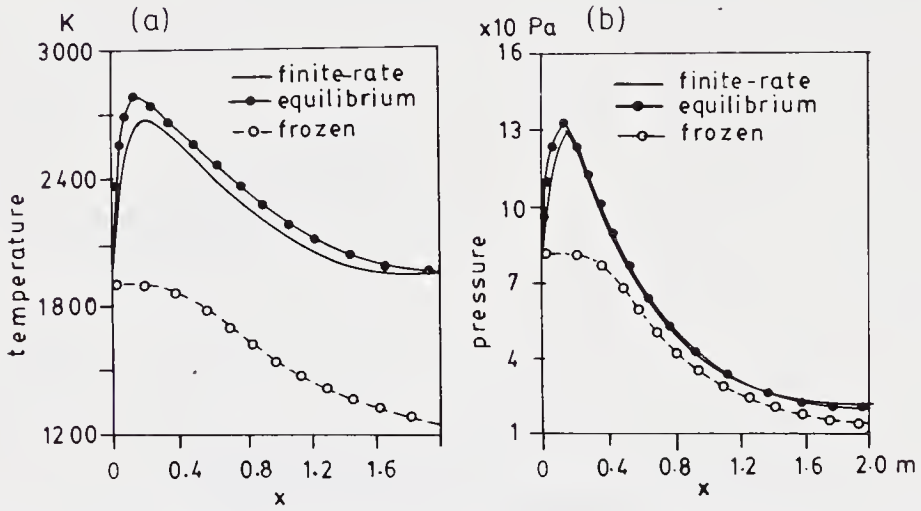

Figure 11. Comparisons among finite rate, equilibrium, and frozen chemistry, (**a**) temperature, (**b**) pressure.

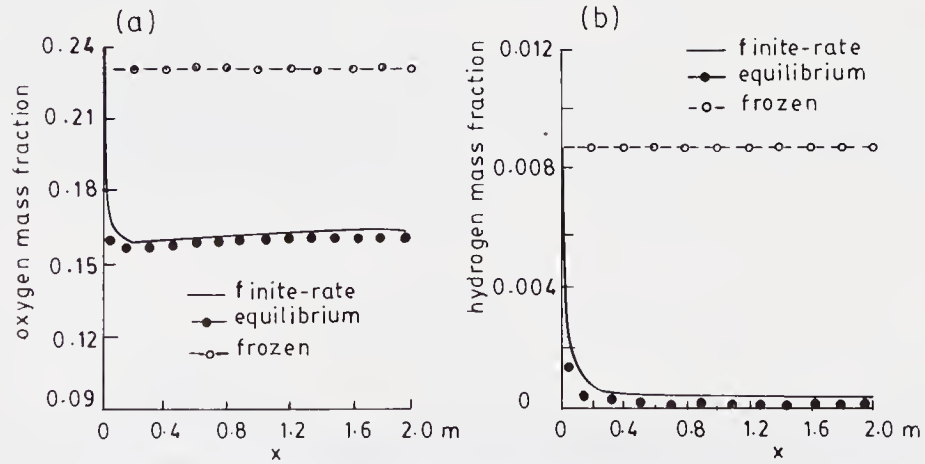

Figure 12. Comparisons among finite rate, equilibrium, and frozen chemistry, (**a**) oxygen, (**b**) hydrogen.

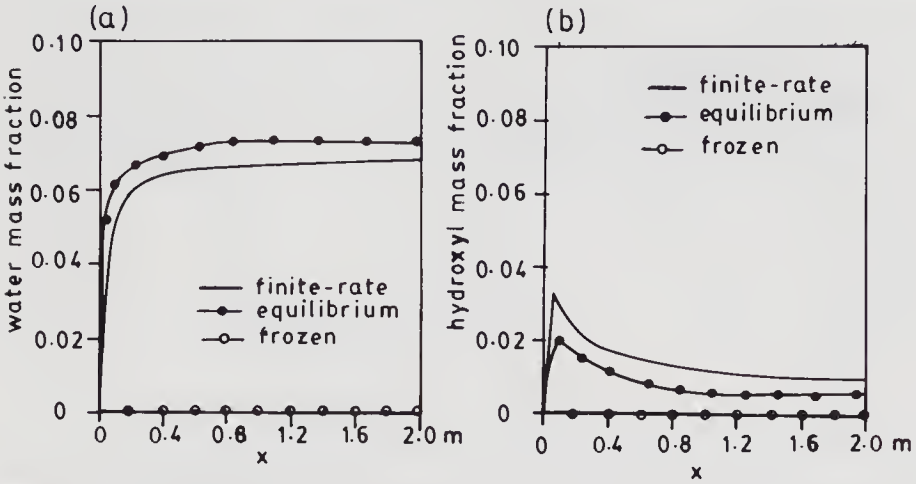

Figure 13. Comparisons among finite rate, equilibrium, and frozen chemistry, (**a**) water, (**b**) hydroxyl.

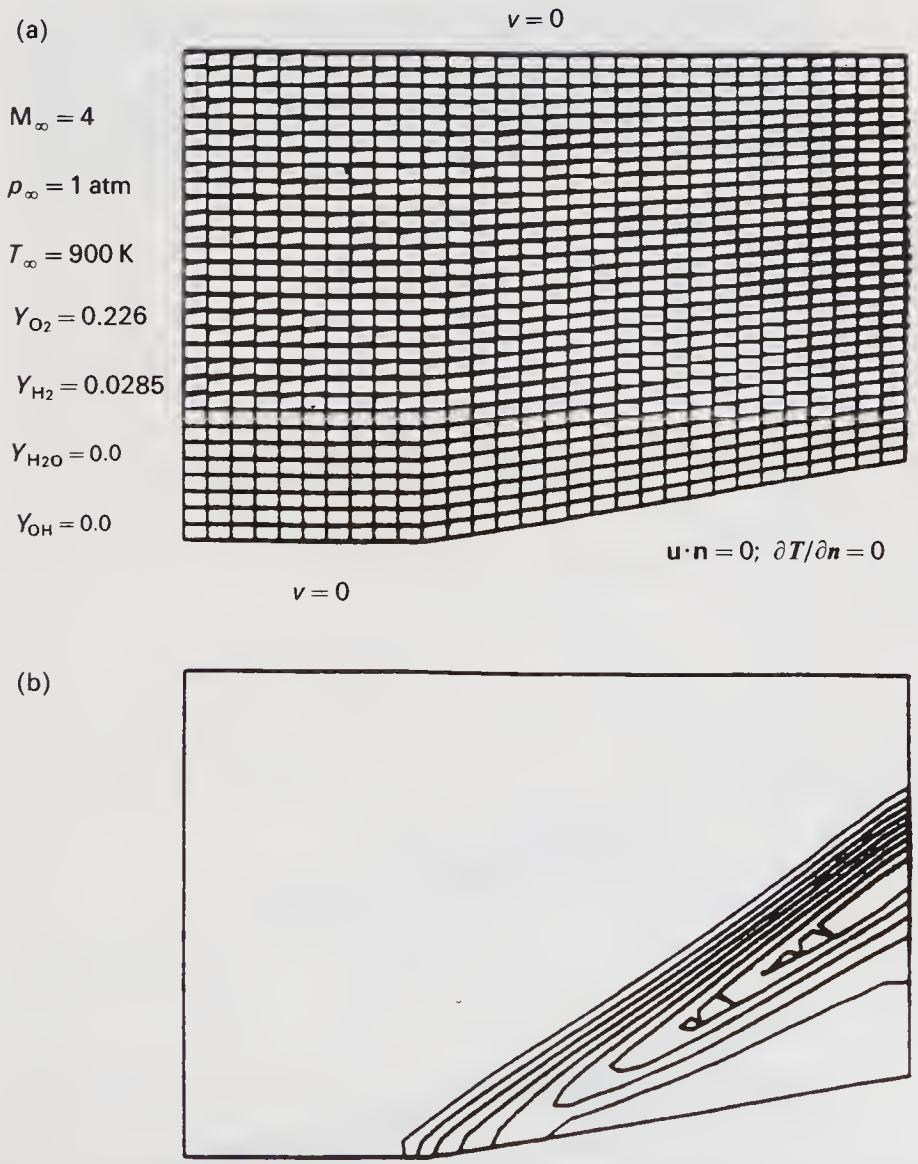

Figure 14. Ramjet (hydrogen/oxygen combustion): (**a**) geometry, (**b**) density contours. max = 0·532 kg/m^3, min = 0·275 kg/m^3, Δ = 0·0257 kg/m^3.

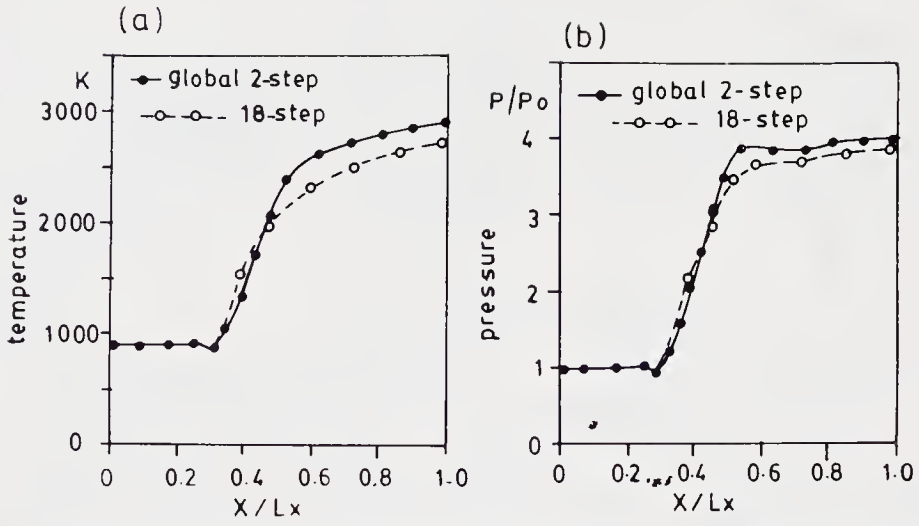

Figure 15. Comparisons between 2-step and 18-step models, (**a**) temperature, (**b**) pressure.

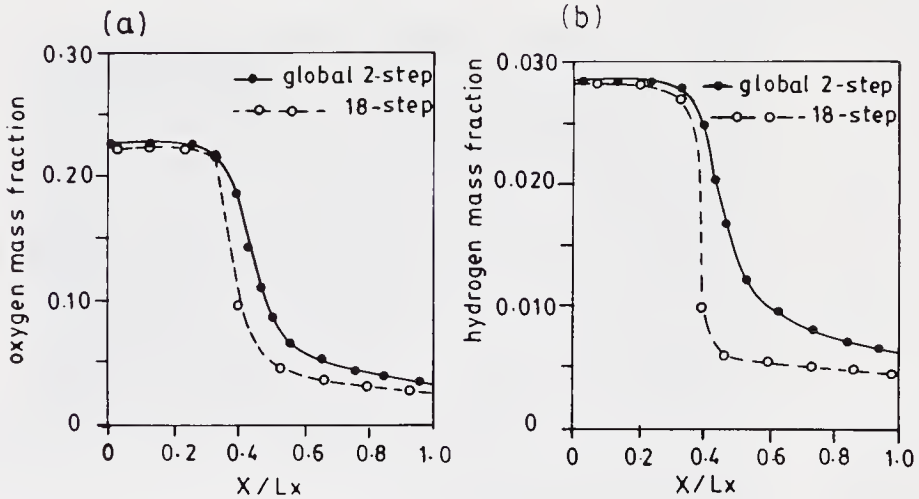

Figure 16. Comparisons between 2-step and 18-step models, (**a**) oxygen, (**b**) hydrogen.

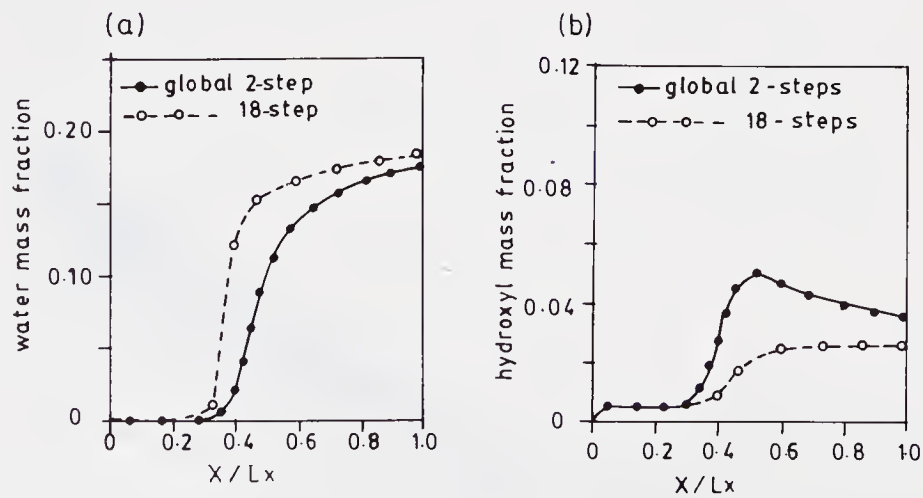

Figure 17. Comparisons between 2-step and 18-step models, (**a**) water, (**b**) hydroxyl.

the downstream region (figure 15). Similar trends exist for both reactants and products (figures 16 and 17).

Consider now a typical hydrogen–air scramjet flame holder and discretization for the analysis of flow fields without and with viscosity as shown in figures 18 and 19, respectively. As expected the oblique shock and expansion wave are evident in figures 18b and c. The corresponding pressure, density and temperature are shown in figures 18d, e, and f, respectively. Chemical reactions of both reactants and products (2-step global model) are triggered by the shock waves. However, shock waves do not appear to be influenced (dispersed) as was the case for lower Mach number (M = 2.5) (Chung & Yoon 1991).

For viscous flow (figure 19a), the development of boundary layers is clearly seen (figures 19b and c). Also, the effect of viscosity causes the inlet shock to appear and the oblique ramp shock waves to be considerably dispersed (figures 19d, e, and f). Chemical reactions are triggered by both oblique and inlet shock waves and combustion appears to be completed in the vicinity of the ramp corner.

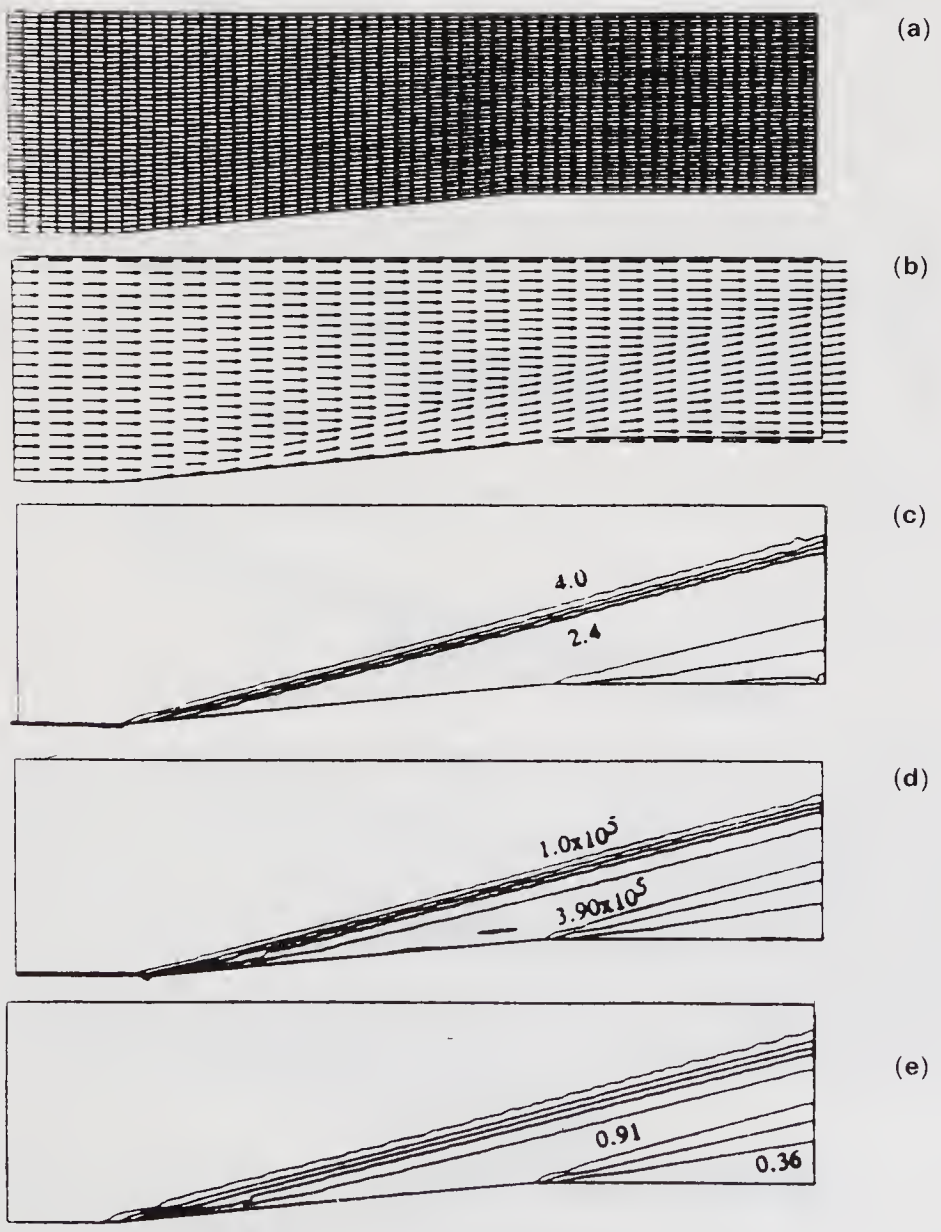

Figure 18. (a–e) (Caption on next page.)

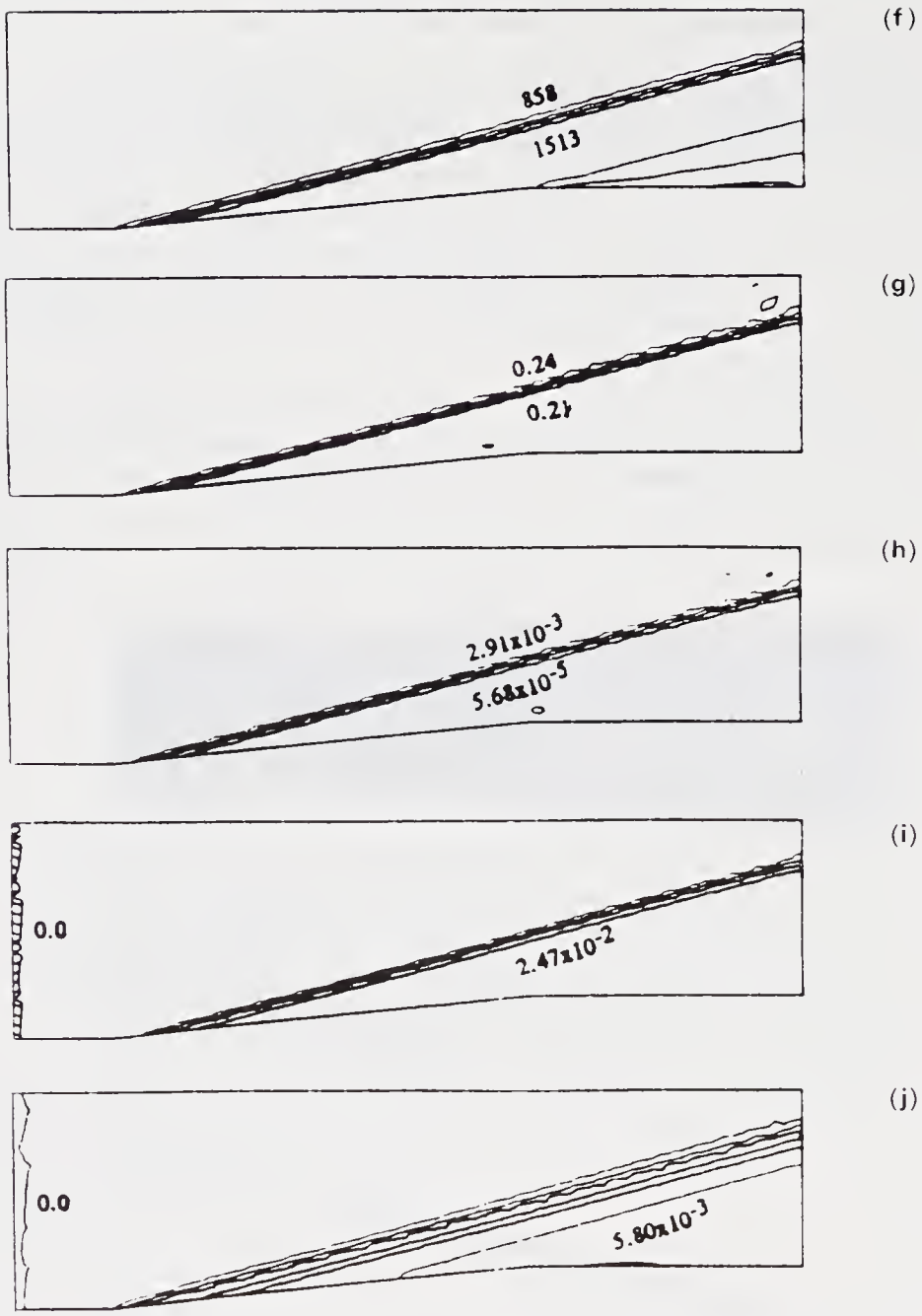

Figure 18. Scramjet flame holder for inviscid flow. Inlet boundary conditions: $\rho = 0{\cdot}443\,\text{kg/m}^3$, $p = 0{\cdot}119\,\text{mPa}$, $T = 900\,\text{K}$, $\gamma = 1{\cdot}38$, $\text{M} = 4{\cdot}0$, $Y_{O_2} = 0{\cdot}2356$, $Y_{H_2} = 0{\cdot}00291$, $Y_{N_2} = 0{\cdot}76149$, $\phi = 0{\cdot}1$. (**a**) Geometry; (**b**) velocity distribution; (**c**) Mach number contours (max = 4·0, min = 2·4, $\Delta = 0{\cdot}31$); (**d**) pressure contours (max = $3{\cdot}9 \times 10^5$, min = $1{\cdot}0 \times 10^5$; $\Delta = 5{\cdot}8 \times 10^4$; (**e**) density contours (max = 0·91, min = 0·36, $\Delta = 0{\cdot}11$); (**f**) temperature contours (max = 1513, min = 858, $\Delta = 131$); (**g**) O_2 mass fraction contours (max = 0·24, min = 0·21, $\Delta = 0{\cdot}005$); (**h**) H_2 mass fraction contours (max = $2{\cdot}91 \times 10^{-3}$, min = $5{\cdot}68 \times 10^{-5}$, $\Delta = 5{\cdot}71 \times 10^{-4}$); (**i**) H_2O mass fraction contours (max = $2{\cdot}47 \times 10^{-2}$, min = 0·0, $\Delta = 4{\cdot}93 \times 10^{-4}$); (**j**) OH mass fraction contours (max = $5{\cdot}80 \times 10^{-3}$, min = 0·0, $\Delta = 1{\cdot}16 \times 10^{-3}$).

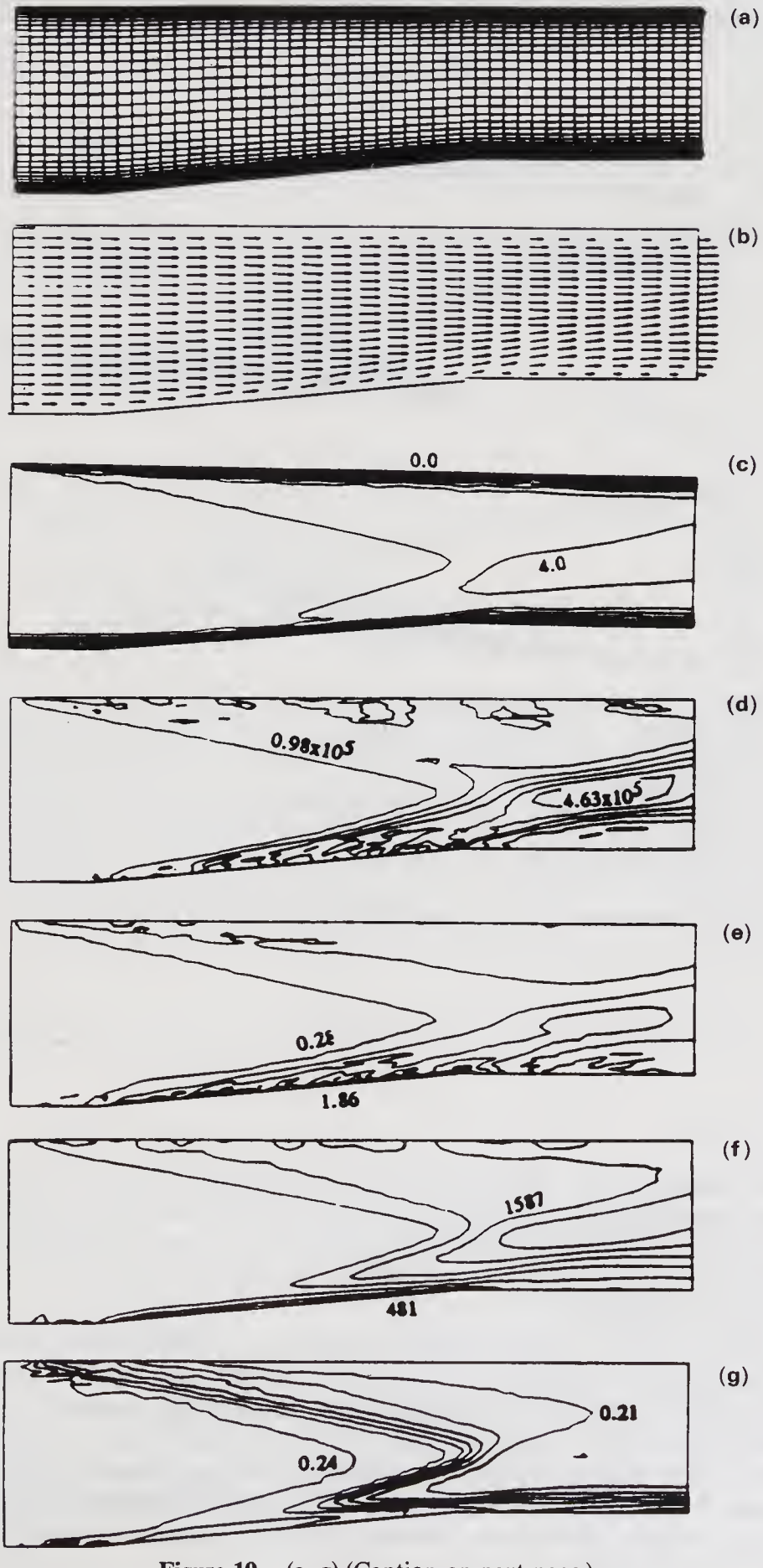

Figure 19. (a–g) (Caption on next page.)

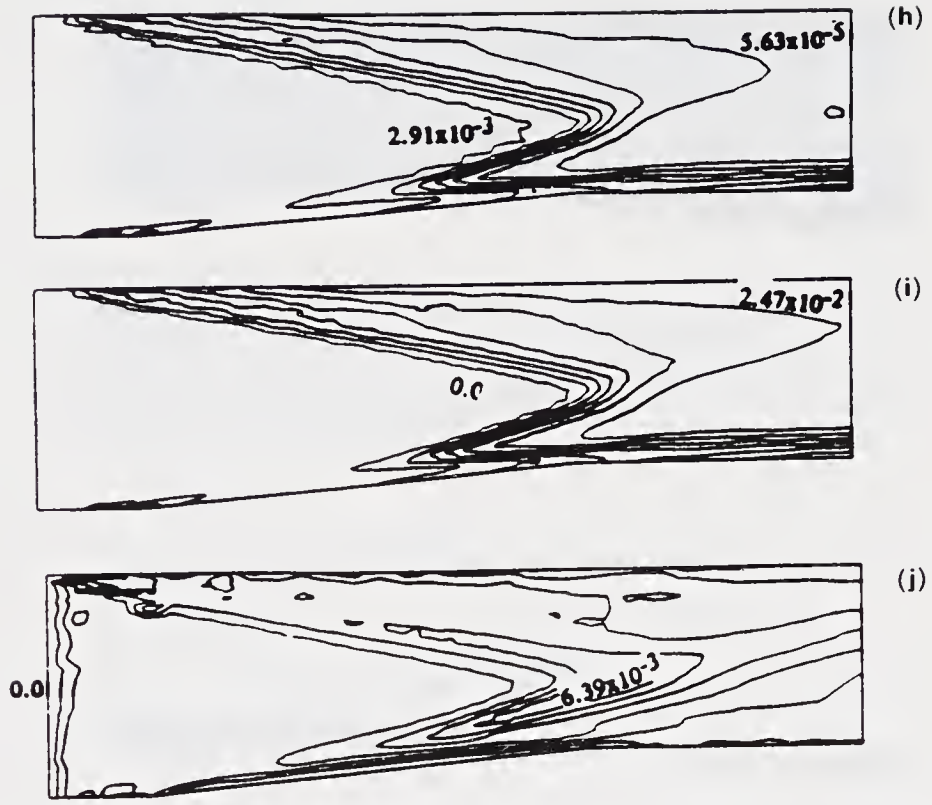

Figure 19. Scramjet flame holder for viscous flow inlet boundary conditions $\rho = 0{\cdot}443\,\text{kg/m}^3$, $p = 0{\cdot}119\,\text{mPa}$, $T = 900\,\text{K}$, $\gamma = 1{\cdot}38$, $\text{M} = 4{\cdot}0$, $Y_{O_2} = 0{\cdot}2356$, $Y_{H_2} = 0{\cdot}00291$, $Y_{N_2} = 0{\cdot}76149$, $\phi = 0{\cdot}1$, $\text{Re} = 50{,}000$. (**a**) Geometry; (**b**) velocity distribution; (**c**) Mach number contours (max = 4·0, min = 0·0, $\Delta = 0{\cdot}32$); (**d**) pressure contours (max = $4{\cdot}63 \times 10^5$, min = $0{\cdot}93 \times 10^5$; $\Delta = 4{\cdot}56 \times 10^4$; (**e**) density contours (max = 1·86, min = 0·28, $\Delta = 0{\cdot}2$); (**f**) temperature contours (max = 1587, min = 481, $\Delta = 138$); (**g**) O_2 mass fraction contours (max = 0·24, min = 0·21, $\Delta = 0{\cdot}003$); (**h**) H_2 mass fraction contours (max = $2{\cdot}91 \times 10^{-3}$, min = $5{\cdot}68 \times 0^{-5}$, $\Delta = 3{\cdot}57 \times 10^{-4}$); (**i**) H_2O mass fraction contours (max = $2{\cdot}47 \times 10^{-2}$, min = 0·0, $\Delta = 3{\cdot}09 \times 10^{-4}$); (**j**) OH mass fraction contours (max = $6{\cdot}39 \times 10^{-3}$, min = 0·0, $\Delta = 0{\cdot}80 \times 10^{-3}$).

5. Conclusions

Solutions of mixed partial differential equations of elliptic, parabolic, and hyperbolic types in chemically reacting flows have been examined using the mixed explicit/implicit scheme of Taylor–Galerkin finite elements. The proposed approach has demonstrated its effectiveness and potential applications for the analysis of turbulence/shock wave interactions in reacting flows.

It is shown that the ducted rocket combustion is significantly influenced by turbulence through triggering and enhancement of reaction mechanism. Furthermore, the roles of finite rate chemistry and various reaction-step models in supersonic combustors have been closely examined. Effects of viscosity are also shown to be important in reacting processes of chemical species for the hydrogen–air flame holder combustion. Examples of unstructured adaptive *h-p* methods in dealing with reacting hypersonic turbulence-shock wave interactions are not included here and will be the subject of a future paper.

This research was supported by the US Army Missile Command (DAAH01-91-D-R002) and National Science Foundation (ASC-8918081) and contributions were made by a number of graduate students, notably by W S Yoon.

Appendix A. Chemical kinetics for propane–air

$$C_3H_8 + 3{\cdot}5(O_2 + nH_2) \rightarrow 3CO + 4H_2O + 3{\cdot}5nN_2$$
$$3CO + 1{\cdot}5(O_2 + nN_2) \rightarrow 3CO_2 + 1{\cdot}5nN_2$$

The conservation of mixture fraction f is defined as

$$f = (\xi_n - \xi_{n,a})/(\xi_{n,f} - \xi_{n,a}), \quad n = 1, 2, 3,$$

where

$$\xi_1 = \bar{Y}_{O_2} - (b_1 + b_2 b_4)\bar{Y}_{fu} - b_4 \bar{Y}_{CO},$$
$$\xi_2 = \bar{Y}_{CO_2} + b_5 \bar{Y}_{CO} + b_2 b_5 \bar{Y}_{fu},$$
$$\xi_3 = \bar{Y}_{H_2O} + b_3 \bar{Y}_{fu},$$
$$b_1 = 3{\cdot}5 W_{O_2}/W_{fu}, \quad b_2 = 3 W_{CO}/W_{fu}, \quad b_3 = 4 W_{H_2O}/W_{fu},$$
$$b_4 = 0{\cdot}5 W_{O_2}/W_{CO}, \quad b_5 = W_{CO_2}/W_{CO}.$$

Here the mass fractions $\bar{Y}$ of O_2, CO_2, H_2O and N_2 can be written in terms of mass fractions of C_3H_8, CO and the mixture fraction f.

$$\bar{Y}_{O_2} = (1-f)\bar{Y}_{O_2,a} + b_4 \bar{Y}_{CO} + (b_1 + b_2 b_4)(\bar{Y}_{fu} - f\bar{Y}_{fu'f}),$$
$$\bar{Y}_{CO_2} = b_2 b_5 (f\bar{Y}_{fu'f} - \bar{Y}_{fu}) - b_5 \bar{Y}_{CO} + \bar{Y}_{CO_2,f},$$
$$\bar{Y}_{H_2O} = b_3 (f\bar{Y}_{fu'f} - \bar{Y}_{fu}) + f\bar{Y}_{H_2O,f},$$
$$Y_{N_2} = 1 - \bar{Y}_{fu} - \bar{Y}_{CO} - \bar{Y}_{O_2} - \bar{Y}_{CO_2} - \bar{Y}_{H_2O}.$$

The closure of turbulent flow equations can be established by means of the Arrhenius and eddy-break-up methods and by choosing appropriate reaction rates.

$$\bar{\omega}_{fu} = -\min \begin{cases} = F_1 \bar{\rho}^{1{\cdot}5} \bar{Y}_{fu}^{0{\cdot}5} \bar{Y}_{O_2} \exp(-E_1/R_0 \bar{T}), \\ = 3\bar{\rho} \min(\bar{Y}_{fu}, \bar{Y}_{O_2})\varepsilon/K, \end{cases}$$

$$\bar{\omega}_{CO} = -b_2 \bar{\omega}_{fu} - \min \begin{cases} = F_2 \bar{\rho}^2 \bar{Y}_{CO} \bar{Y}_{O_2} \exp(-E_2/R_0 \bar{T}), \\ = -4\bar{\rho} \min(\bar{Y}_{CO}, \bar{Y}_{CO}, \bar{Y}_{O_2})\varepsilon/K, \end{cases}$$

where

$$F_1 = 3{\cdot}3 \times 10^{14}, \quad F_2 = 6 \times 10^8,$$
$$E_1/R_0 = 27{,}000, \qquad E_2/R_0 = 27{,}000.$$

Appendix B. Chemical kinetics for hydrogen–air

B1. Two-step global model

$$H_2 + O_2 \overset{k_{f1}}{\rightleftharpoons} 2OH,$$

$$2OH + H_2 \overset{k_{f2}}{\rightleftharpoons} 2H_2O,$$

$k_{f1} = A_1(\phi)\, T^{Ni} \exp(-E_1/RT)$,

$A_1(\phi) = (8{\cdot}917\phi + 31{\cdot}433/\phi - 28{\cdot}95) \times 10^{47}\,(\mathrm{cm^3/mol\,s})$

$E_1 = 4865\,\mathrm{cal/mol}, \quad N_1 = -10$

$A_2(\phi) = (2 + 1{\cdot}333/\phi - 0{\cdot}833\phi) \times 10^{64}\,(\mathrm{cm^6/mol^2\,s})$

$E_2 = 42{,}500\,\mathrm{cal/mol}, \quad N_5 = -13$

$T_0 = 1000\text{–}2000\,\mathrm{K}, \quad 0{\cdot}2 \leqslant \phi \leqslant 2$

B2. Eighteen-step hydrogen–air combustion mechanism

Reaction	A(mol)	N(cm^3)	E(cal/gm-mol)
(1) $O_2 + H_2 \leftrightarrow OH + OH$	$1{\cdot}70 \times 10^{13}$	0	48150
(2) $O_2 + H \leftrightarrow OH + O$	$1{\cdot}42 \times 10^{14}$	0	16400
(3) $H_2 + OH \leftrightarrow H_2O + H$	$3{\cdot}16 \times 10^{7}$	1·8	13750
(4) $H_2 + O \leftrightarrow OH + H$	$2{\cdot}07 \times 10^{14}$	0	13750
(5) $OH + OH \leftrightarrow H_2O + O$	$5{\cdot}50 \times 10^{13}$	0	7000
(6) $H + OH + M \leftrightarrow H_2O + M$	$2{\cdot}21 \times 10^{22}$	−2·0	0
(7) $H + H + M \leftrightarrow H_2 + M$	$6{\cdot}53 \times 10^{17}$	−1·0	0
(8) $H + O_2 + M \leftrightarrow HO_2 + M$	$3{\cdot}20 \times 10^{18}$	−1·0	0
(9) $OH + HO_2 \leftrightarrow O_2 + H_2O$	$5{\cdot}0 \times 10^{13}$	0	1000
(10) $H + HO_2 \leftrightarrow H_2 + O_2$	$2{\cdot}53 \times 10^{13}$	0	700
(11) $H + HO_2 \leftrightarrow OH + OH$	$1{\cdot}99 \times 10^{14}$	0	1800
(12) $O + HO_2 \leftrightarrow O_2 + OH$	$5{\cdot}0 \times 10^{13}$	0	1000
(13) $HO_2 + HO_2 \leftrightarrow O_2 + H_2O_2$	$1{\cdot}99 \times 10^{12}$	0	0
(14) $H_2 + HO_2 \leftrightarrow H + H_2O_2$	$3{\cdot}01 \times 10^{11}$	0	18700
(15) $OH + H_2O_2 \leftrightarrow H_2O + HO_2$	$1{\cdot}02 \times 10^{13}$	0	1900
(16) $H + H_2O_2 \leftrightarrow H_2 + O_2$	$5{\cdot}0 \times 10^{14}$	0	10000
(17) $O + H_2O_2 \leftrightarrow OH + HO_2$	$1{\cdot}99 \times 10^{13}$	0	5900
(18) $H_2O_2 + M \leftrightarrow OH + OH + M$	$1{\cdot}21 \times 10^{17}$	0	45500

References

Bakos R J, Tamangno J, Rizkalla O, Pulsonetti M V, Chinitz W, Erdos J I 1990 Hypersonic mixing and combustion studies in the GASL hypulse facility. AIAA/SME/ASEE 26th Joint Propulsion Conference. AIAA paper no. 90–2095

Chung T J, Yoon W S 1991 Effects of reacting flows with turbulence and shock waves on efficiency of scramjet combustors. 28th JANNAF Combustion Meeting, CPIA, Johns Hopkins University

Chung T J, Yoon W S 1992 Numerical studies on supersonic/hypersonic combustion. AIAA 36th Aerospace Sciences Meeting & Exhibit. AIAA paper no. 92–0094

Drummond J P, Carpenter M H, Riggins D W, Adams M S 1989 Mixing enhancement in a supersonic combustor. AIAA paper no. 89–2794

Dwyer D S, Kumar A 1987 Computational analysis of hypersonic air breathing aircraft flow fields. AIAA 25th Aerospace Sciences Meeting. AIAA paper no. 87–0279

Gnoffo P A, McCandless R S 1986 Three-dimensional AOTV flowfields in chemical non-equilibrium. AIAA 24th Aerospace Sciences meeting. AIAA paper no. 86–0230

Gnoffo P A, McCandless R S, Yee H C 1987 Enhancements to Program Laura, for computation of three-dimensional hypersonic flow. AIAA 25th Aerospace Sciences Meeting. AIAA paper no. 87–0280

Harradine D M, Lyman J L, Oldenborg R C, Schott G L, Watanabe H H 1990 Hydrogen/air combustion calculations: The chemical basis of efficiency in hypersonic flows. *AIAA J.* 28: 1740–1744

Kim Y M, Chung T J 1989 Finite-element analysis of turbulent diffusion flames. *AIAA J.* 27: 330–339

Kunik W G, Bensen T J, Ng W F, Taylor A 1987 Two- and three-dimensional viscous computations of a hypersonic inlet flow. AIAA 25th Aerospace Sciences Meeting. AIAA paper no. 87–0283

Northam G B 1989 Evaluation of parallel injector configurations for supersonic combustion. AIAA/ASME/SAE/ASEE 25th Joint Propulsion Conference. AIAA paper no. 89–2525

Stalker R J 1989 Hypervelocity aerodynamics with chemical nonequilibrium. *Annu. Rev. Fluid Mech.* 21: 37–60

Yoon C S 1992 Finite element analysis for supersonic combustion with finite rate chemistry, Ph D dissertation, University of Alabama in Huntsville

Zienkiewicz O C, Szmelter J, Peraire J 1990 Compressible and incompressible flow: An algorithm for all seasons. *Comput. Methods Appl. Mech. Eng.* 78: 105–121

Gas particle industrial flow simulation using RANSTAD

CLIVE A J FLETCHER

Centre for Advanced (Numerical) Computation in Engineering & Science, University of New South Wales, PO Box 1, Kensington, NSW 2033, Australia

Abstract. A turbulent gas particle finite-volume flow simulation of a representative coal classifier is presented. Typical values of the loading ratio permit a one-way coupling analysis. As a case study, the computational fluid dynamics code, RANSTAD, and the modelling aspects are discussed in some detail. The simulation indicates that small ($\approx 30\,\mu$m) coal particles pass through the classifier to the furnace but that large ($\approx 300\,\mu$m) particles are captured and remilled. The computational simulation indicates that the classifier performance can be improved by internal geometric modification.

Keywords. Gas particle flows; computational fluid dynamics; Eulerian particulate model; turbulence model; coal classification.

1. Introduction

The development of computational fluid dynamics (CFD) codes for complex industrial flows requires emphasis on the use of the CFD code as a design tool (Cross *et al* 1988; Fletcher 1991), where the key factors are cost effectiveness and time efficiency. The code must provide accurate and reliable answers in a small execution time. This implies that the underlying algorithm is robust and that the code is user-friendly in operation and in the way that the results are presented to avoid excessive designer time in analysing the results.

Industrially significant flows usually involve complex geometric domains and turbulent flow, sometimes unsteady flow either locally or globally, and typically include supplementary processes (e.g. multiphase). The application of CFD codes to such flows is often motivated by the excessive cost (economic and/or temporal) or the technical difficulties of undertaking physical simulation or direct full-scale measurements. Multiphase gas/particle flows in power station boilers and coal classifiers are appropriate examples.

In this paper a CFD code, RANSTAD, is described which has been developed for complex industrial flows. RANSTAD uses a simple domain decomposition procedure combined with a multisurface technique (Fletcher 1991, vol. 2, p. 108 ff.) to generate a grid that gives a smooth distribution of internal points even when internal obstructions and walls are present. RANSTAD combines an algebraic Reynolds

stress–turbulence model (ASM) with a two-layer wall function (Armfield *et al* 1990) to provide the mean flow and Reynolds stress predictions. A higher-order finite volume discretisation (Cho *et al* 1991) with inbuilt limiters combines enhanced robustness with higher-order accuracy on relatively coarse grids. Where appropriate a multigrid augmented velocity potential correction scheme (Fletcher & Bain 1991) is used to accelerate solution convergence.

Here RANSTAD is applied to a three-dimensional, gas particle flow within a coal classifier. For this very complex flow RANSTAD is able to obtain accurate and economical solutions for both the gas and particulate phases so that geometric modifications to optimise the classifier performance are quickly made and tested.

A coal classifier is a device for separating large and small coal particles by relying on centrifugal forces to cause different size particles to follow different trajectories. A typical classifier layout is shown in figure 1. Hot air and raw coal are carried to the base of the classifier and move up and over the baffle plate. Small particles are able to follow the air flow inside the baffle plate and are eventually delivered to the furnace. Large particles ($> 300\,\mu$m) are rejected via the conveyor for remilling to a smaller size and recycling through the classifier.

In §2, gas particle flows are discussed – first, from the perspective of the particle

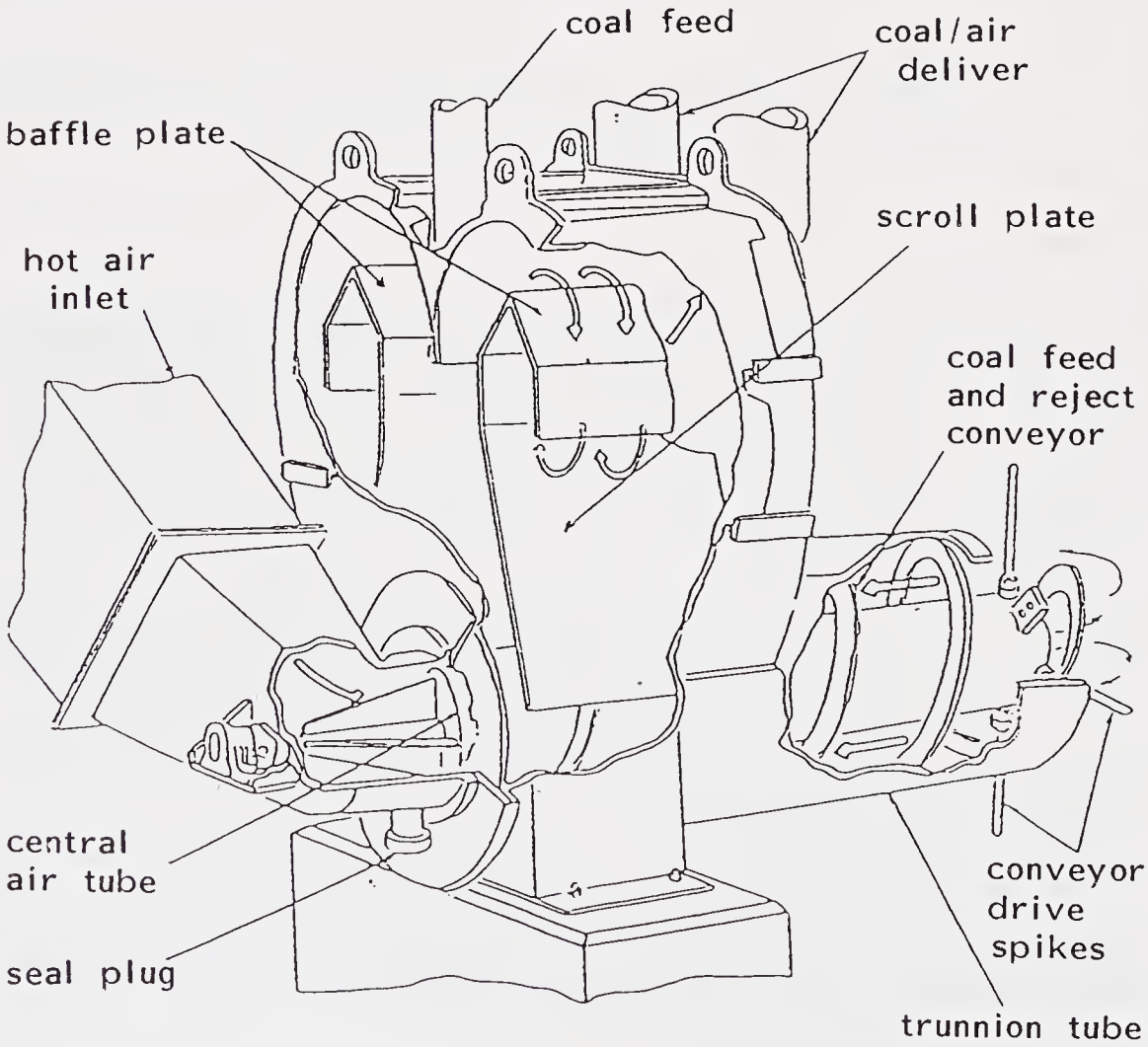

Figure 1. Ball-mill classifier: internal arrangement.

loading ratio. For typical classifier operation, it is established that the assumption of one-way coupling is capable of producing an accurate representation of the physical interaction. Second, the Stokes number is considered to assess the likely different response of small and large particles to the underlying flow behaviour. The supplementary influence of gravity is also examined. Third, the governing equations, boundary conditions and appropriate turbulence models for both phases are indicated.

In § 3, the discretisation and solution algorithms used by RANSTAD are described, starting from the role of area vectors to show the equivalence between the use of generalised coordinates in computational space and the finite volume formulation in physical space. It is shown that the same finite volume formulation in conjunction with higher-order discretisation and a sequential solution procedure can be extended to the particulate phase. In § 4, RANSTAD is used to simulate the flow and particulate behaviour in a typical ball-mill coal classifier in order to analyse the classifier performance.

2. Gas particle flows

A computational simulation of the coal classifier provides a very cost effective means of exploring geometric and process-dependent parameter sensitivity. In order to carry out the simulation it is necessary to set up the equations that govern the motion, temperature and density of the carrier gas and the coal particles as a two-phase mixture. The setting-up requires an assessment of the degree of coupling between the carrier gas and particulate phases and the responsiveness depends on the inertia of the individual particles in relation to the unsteadiness, i.e. turbulence, of the carrier gas. In turn this implies that some form of turbulence modelling will be required.

2.1 *Particle loading and Stokes number*

The two key parameters (Crowe 1982) determining the degree of interaction between the carrier gas and the particles are the particle loading ratio, β, and the Stokes number, St. The loading ratio determines if the particles will influence the behaviour of the carrier gas and the Stokes number determines how closely an individual particle will respond to the local carrier gas velocity field.

The loading ratio, β, is defined by

$$\beta = \rho_p/\rho_g, \tag{1}$$

where ρ_p is the particulate bulk density (i.e. particulate mass per unit volume of the mixture) and ρ_g is the gas bulk density. For dilute gas particle flows this is approximately equal to the material density of the gas, ρ'_g.

For typical coal classifiers the average loading is about 10%. This implies that

$$\beta \approx \alpha_p \gamma \tag{2}$$

where α_p is the particulate volume fraction and γ is the material density ratio (particulate to gas). Typical values assumed here are (R A Platfoot 1990, private communication)

$$\rho'_\rho = 1440\,\text{kg/m}^3, \text{ and } \rho'_g = 1{\cdot}20\,\text{kg/m}^3, \text{ i.e. } \gamma \approx 1200.$$

From (2) this implies $\alpha_p \approx 0{\cdot}10/1200 \approx 0{\cdot}8 \times 10^{-4}$. The above average loading of

$\beta = 0{\cdot}10$ might correspond to a maximum local loading of $\beta \approx 0{\cdot}30$. For such small values of β the presence of the particles has a small effect on the carrier gas (Crowe 1982). That is, to a reasonable approximation, the carrier gas has the same velocity and temperature distribution whether the particles are present or not. This is a very important simplification because it implies that the carrier gas behaviour can be determined independently of the velocity and bulk density distributions of the coal particles.

How the particulate bulk density and velocity distributions depend on the local gas velocity is controlled by the value of the Stokes number. Intuitively, smaller particles (implying a smaller Stokes number) follow the carrier gas motion more closely than larger particles.

The Stokes number is defined as $\mathrm{St} = t_A/t_s$, where t_A is the response time due to aerodynamic drag on the particle and t_s is a characteristic time of the system. If the Stokes number is less than 0·01 the individual particle is assumed to respond almost immediately to changes in the carrier gas motion (di Giacinto *et al* 1982). If $\mathrm{St} \gg 0{\cdot}01$, significant slip will occur between the particles and the carrier gas, i.e. the particle trajectories will differ substantially from the flow streamlines.

The response times are defined as follows,

$$t_A = \gamma d_p^2/(18 v_g f), \text{ and } t_s = L_s/V_s. \tag{3}$$

In (3a) v_g is the kinematic viscosity of the carrier gas and f is an empirical particle Reynolds number correction (Kitchen 1990) to Stokes Law associated with large slip velocities. In (3b) L_s and V_s are a characteristic length and velocity of the system. Consequently the Stokes number is given by

$$\mathrm{St} = (\gamma d_p^2 V_s)/(18 v_g f L_s). \tag{4}$$

For a typical coal classifier (and setting $f = 1{\cdot}0$),

$$L_s = 1{\cdot}0\,\mathrm{m}, \text{ and } V_s = 10\,\mathrm{m/s}, \quad t_s = 0{\cdot}1\,\mathrm{s}.$$

$$\text{For } d_p = 30\,\mu\mathrm{m}, \quad t_A = 0{\cdot}004\mathrm{s} \text{ and } \mathrm{St} = 0{\cdot}04.$$

$$\text{For } d_p = 300\,\mu\mathrm{m}, \quad t_A = 0{\cdot}4\mathrm{s} \text{ and } \mathrm{St} = 4{\cdot}0.$$

Thus it may be expected that a coal particle of $d_p = 30\,\mu$m deviates from the local flow direction but is still significantly affected by it. However, large particles, $d_p = 300\,\mu$m, are relatively insensitive to the carrier gas and move (almost) independently of it.

However, the Stokes number, as defined above, essentially provides a comparison of the aerodynamic drag on the particle with the inertia of the particle. The motion of the coal particles in a coal classifier is also influenced significantly by the gravitational force. In "upflow" regions, e.g. at the back of the baffle plate (figure 1), both aerodynamic drag and the gravitational force oppose the motion of the particle leading to a rapid deceleration. But in "downflow" regions, e.g. on the downward side near the lip of the baffle plate (figure 1), the gravitational force opposes the aerodynamic drag. In this region, the gravitational force causes the particle to accelerate downwards whereas the aerodynamic force causes the particle to decelerate.

The nondimensional Lagrangian equation of motion for a single particle are

$$\mathrm{d}u_p/\mathrm{d}t = (u_g - u_p)/\mathrm{St}, \tag{5}$$

$$\mathrm{d}v_p/\mathrm{d}t = (v_g - v_p)/\mathrm{St} - 1/Fr^2, \tag{6}$$

Table 1. Particle response for typical classifier.

Particle size, d_p (μm)	t_A (s)	St	"upflow" v_{p_∞}/V_s	downflow v_{p_∞}/V_s	time to $0{\cdot}90\,\Delta v_{p_\infty}$ (s)
30	0·004	0·04	1·96	−2·04	0·01
300	0·40	40	−2·0	−6·0	0·9

where $Fr^2 = V_s^2/gL_s$, and L_s and V_s are the nondimensionalising length and velocity scales. Here it is assumed that gravity acts in the negative y-direction.

For a typical classifier the air and particle vertical velocity components are positive at entry (figure 1), and become negative in passing over the top of the baffle. The air vertical velocity component eventually becomes positive again, before exiting the classifier.

If v_g remained constant then (6) has the analytic solution

$$\{(v_g - S_g) - v_p\} = \{(v_g - S_g) - v_{p_0}\}\exp(-t/\mathrm{St}), \tag{7}$$

where $S_g = \mathrm{St}/Fr^2$ and can be interpreted as a gravity Stokes number. For a typical classifier, $Fr = 1$, so $S_g \approx \mathrm{St}$. Thus (7) determines how quickly the particle's (vertical) velocity changes from its initial value, v_{p_0}, to its final value,

$$v_{p_\infty} = (v_g - S_g). \tag{8}$$

Equation (7) can be used to examine the importance of gravity forces compared with aerodynamic forces, in determining the responses of particles of different sizes to the presence of the carrier gas. Some results for a typical classifier are shown in table 1. In a typical upflow region, e.g. the back of the classifier, $v_g \approx 2V_s$. In a typical downflow region, $v_g = -2V_s$. The last column shows the time for the difference between the initial particle speed and the final particle speed to reduce by 90%. The major effect of gravity is on the terminal velocity. For small particles ($d_p = 30\,\mu$m) the terminal velocity of the particle is very close to that of the carrier gas and a short time is required to reach this state. For large particles ($d_p = 300\,\mu$m) the terminal velocities are very different from the local carrier gas velocity and a significant time is required to reach this state. Thus for large particles a significant slip velocity is to be expected.

Depending on the particle size the residence time within the classifier is about 0·5 to 1·0 s. Thus large particles never adjust to the local carrier gas, which, contrary to the assumption underlying (7), is itself rapidly varying. However, small particles respond sufficiently quickly that they follow approximately the motion of the carrier gas.

2.2 *Governing equations*

The behaviour of the carrier gas is accurately described by the isothermal Reynolds-averaged steady Navier–Stokes equations (a superscript p or g is used to distinguish between particle and gas velocity components),

$$\frac{\partial}{\partial x_i}(\rho u_i^g) = 0 \tag{9}$$

$$\frac{\partial}{\partial x_i}(\rho u_i^g u_j^g + \delta_{ij} p_j - \tau_{ij} + \rho u_i^{g'} u_j^{g'}) = \frac{1}{Fr^2} - \frac{\beta}{\mathrm{St}}(u_j^g - u_j^p). \tag{10}$$

The value of β for a typical classifier is such that the aerodynamic drag interaction terms on the right-hand side of (10) have a negligible influence on the carrier gas solution. This is the characteristic one-way coupling situation (di Giacinto *et al* 1982) in which the presence of the particulate has no influence on the carrier gas solution. Consequently (9) and (10) with appropriate boundary conditions can be solved, once and for all, for the carrier gas behaviour. Subsequently, particulate behaviour is obtained with the influence of the carrier gas being experienced primarily through the aerodynamic drag term.

Equations (10) contain Reynolds stresses that are represented either by a k–ε or an ASM turbulence model. With either model a two-layer wall function is used (Armfield *et al* 1990) to provide both solution and boundary conditions close to those of solid surfaces without requiring a very fine grid. The results presented in §4 are based on placing the first grid point (centre of control volume) at a $y^+ \approx 50$–100 from the wall.

For the present simulation of the flow inside the classifier, all the velocity components are set at the inflow boundary with the exception of the pressure which is set at the exit. Also at the exit streamwise gradients of the velocity components are set to zero. At solid surfaces the no-slip condition is imposed on the velocity components. In addition the two-layer wall function effectively imposes a logarithmic velocity profile between the wall and the first grid point.

Two approaches are possible (Crowe 1982) to determine the behaviour of the particulate phase. In the Lagrangian method, representative individual particles are tracked. This technique is effective when the Stokes number is not too large and the carrier gas velocity gradients are small. However, if large carrier gas velocity gradients occur, a large number of particles must be tracked to obtain useful *quantitative* data. This implies large computer execution times. If turbulence or gross unsteadiness is significant the Lagrangian approach often includes a supplementary Monte Carlo procedure (Mostafa & Mongia 1988) to allow for fluctuating particle velocities. In addition, any coupling or influence of the particles on the carrier gas requires the counting of all the contributions to the momentum source for each control volume used to obtain the carrier gas solution. We prefer to use the Lagrangian approach to provide preliminary qualitative information.

In the Eulerian approach the particulate phase is treated as a continuum. Conservation of mass and momentum equations are established to determine the particulate bulk density, ρ_p, and the particulate velocity components, u_i^p, as functions of space and time. Following di Giacinto *et al* (1982), these equations are written

$$\frac{\partial \rho_p}{\partial t} + \frac{\partial}{\partial x_i}(\rho_p u_i^p) = 0, \tag{11}$$

$$\frac{\partial}{\partial t}(\rho_p u_i^p) + \frac{\partial}{\partial x_i}(\rho_p u_i^p u_j^p) = -g\rho_p/Fr^2 + \rho_p(u_j^g - u_j^p)/\mathrm{St}, \tag{12}$$

where $g^T = \{0, 1, 0\}$, i.e. gravity acts in the negative y-direction. Since $\rho_p = \alpha_p \rho_p'$, equivalent equations could be written in terms of the particulate volume fraction, α_p. The influence of the carrier gas on the particulate motion enters through the aerodynamic drag term on the right-hand side of (12).

As with the carrier gas, it is the mean behaviour that is of primary practical importance. After Reynolds averaging, the steady forms of (11) and (12) become

$$\frac{\partial}{\partial x_i}(\rho_p u_i^p) = -\frac{\partial}{\partial x_i}(\overline{\rho_p' u_i^{p'}}), \tag{13}$$

$$\frac{\partial}{\partial x_i}(\rho_p u_i^p u_j^p) = -g\rho_p/Fr^2 + \rho_p(u_j^g - u_j^p)/\mathrm{St} - \frac{\partial}{\partial x_i}(\rho_p \overline{u_i^{p'} u_j^{p'}} + u_j^p \overline{\rho_p' u_i^{p'}} + u_i^p \overline{\rho_p' u_j^{p'}}). \tag{14}$$

The second-order correlation terms in the drag force expression have been neglected (Pourahmadi & Humphrey 1983). The modelling of the second-order correlation terms in (13) and (14) is considered in §2.3. In deriving (13) and (14) third-order correlation terms are neglected (Adeniji-Fashola & Chen 1990).

Boundary conditions for the particulate phase are similar to those for the carrier gas at inflow and outflow. That is at inflow ρ_p and u_i^p are specified. At outflow, the streamwise gradient of these quantities is set to zero.

Appropriate boundary conditions at solid surface are more difficult. First, the boundary conditions in an Eulerian formulation should be consistent with an equivalent Lagrangian formulation. This is particularly important where the Eulerian solution is to be used to construct an equivalent Lagrangian solution which will then be used as input to the prediction of erosion. For example where abrasive flyash is of concern in boiler economisers (Kitchen & Fletcher 1990).

Some progress has been made by Bar-Yoseph & Fletcher (1991) in using the analogy with rarefied gas flow problems to define a particle Knudsen number,

$$\mathrm{Kn} = l_{gp}/L_s, \tag{15}$$

where the gas particle interaction length, $l_{gp} = t_A \mathbf{u}_R' = L_h$. To characterise the turbulent gas particle interactions,

$$\mathbf{u}_R' = \overline{[\mathbf{u}^{g'} - \mathbf{u}^{p'}]^2}^{\frac{1}{2}}. \tag{16}$$

However, to extract suitable boundary conditions, L_h is the distance of the nearest grid point from the wall. So that

$$u_{t,1}^p = u_{t,w}^p + \mathrm{Kn}[\partial u_t^p/\partial \eta]_w, \tag{17}$$

where η is the nondimensional coordinate normal to the wall. By linking this with the Lagrangian velocity components at the wall (ε_T, ε_N are the restitution coefficients linking the Lagrangian incident and reflected components),

$$u_{t,w}^p = 0{\cdot}5u_t^{p,i}(1+\varepsilon_T), \quad u_{n,w}^p = 0{\cdot}5u_n^{p,i}(1-\varepsilon_N), \tag{18}$$

a generalised boundary condition is obtained

$$\varphi_w + \beta^\phi [\partial\varphi/\partial n]_w = 0, \tag{19}$$

where $\varphi^T = \{\rho_p, u_i^p\}$.

For very small particles and a perfect collision ($\varepsilon_T, \varepsilon_N = 1{\cdot}0$) the particulate will follow the carrier gas and have the same boundary conditions, $u_i^p = 0$. However, for

large particles that are insensitive to the local carrier gas behaviour, the boundary condition $[\partial\varphi/\partial n]_w = 0$ is more appropriate. Thus β^ϕ is a function of particle diameter. The precise choice of β^ϕ is best determined empirically.

2.3 *Turbulence models*

For the carrier gas either a $k-\varepsilon$ or ASM turbulence model is used. For the ASM turbulence model, the following transport equations govern the behaviour of k and ε,

$$\frac{\partial}{\partial x_i}(u_i^g k) = \frac{\partial}{\partial x_j}\left\{(\nu + C_s(k/\varepsilon)\overline{u_i^{g'} u_j^{g'}})\frac{\partial k}{\partial x_i}\right\} + P_k - \varepsilon, \tag{20}$$

and

$$\frac{\partial}{\partial x_i}(u_i^g \varepsilon) = \frac{\partial}{\partial x_j}\left\{\nu + C_\varepsilon(k/\varepsilon)\overline{u_i^{g'} u_j^{g'}}\frac{\partial \varepsilon}{\partial x_i}\right\} + \left[\frac{\varepsilon}{k}\right]\{C_{\varepsilon 1} P_k - C_{\varepsilon 2}\varepsilon\},$$

with

$$P_k = -\{\overline{u_i^{g'} u_k^{g'}}\,\partial u_j/\partial x_k + \overline{u_i^{g'} u_k^{g'}}\,\partial u_k/\partial x_j\}. \tag{21}$$

For the equivalent $k-\varepsilon$ model, the turbulent diffusion coefficients are replaced by ν_T/σ_k and ν_T/σ_ε, respectively, where $\nu_T = C_\mu k^2/\varepsilon$. The production term,

$$P_k = \nu_T(\partial u^i/\partial x_k + \partial u^j/\partial x_k)(\partial u_i/\partial x_j).$$

In the ASM model, Rodi's (1976) approximation is introduced which leads to

$$\{\overline{u_i^{g'} u_j^{g'}}/k\}(P_k - \varepsilon) = p^{ij} + \Phi^{ij} - (2/3)\varepsilon, \tag{22}$$

where p^{ij} and Φ^{ij} are the production and pressure–strain terms. Further details may be found in Armfield *et al* (1990) and Cho & Fletcher (1991).

For gas particle two-phase flows, it is generally accepted (Modaress *et al* 1984) that the presence of the particulate absorbs some of the turbulent energy present in the carrier gas flow. This effect is typically modelled with extra dissipation terms in the k and ε transport equations (e.g. Adeniji-Fashola & Chen 1990). However, in the present application, this is expected to be a second-order effect and, consequently, has not been included.

The second-order correlation terms in (13) and (14) are modelled using a gradient hypothesis (Choi & Chung 1983; Melville & Bray 1979)

$$-\overline{\rho_p' u_i^{p'}} = D_p \partial\rho_p/\partial x_i, \tag{23}$$

$$-\overline{u_i^{p'} u_j^{p'}} = \nu_p(\partial u_i^p/\partial x_j + \partial u_j^p/\partial x_i). \tag{24}$$

Following a similar strategy to that of Adeniji-Fashola & Chen (1990), the particulate turbulent diffusivities are related to the carrier-gas diffusivity, ν_T, by

$$D_p = \nu_T/\mathrm{Sc} \text{ and } \nu_p = K_p \nu_T, \tag{25}$$

where the turbulent Schmidt number, $\mathrm{Sc} = 0{\cdot}7$. The weight factor, K_p, accounts for the particle inertia and is given by

$$K_p = \max\{\mathrm{Kn}, 1/(1+\mathrm{St}^t)\}, \tag{26}$$

where Kn is a numerical dissipation ($\approx 0{\cdot}1$) and the turbulent Stokes number, $\mathrm{St}^t = t_A/t_e$. The eddy characteristic time

$$t_e = 0{\cdot}125k/\varepsilon. \tag{27}$$

For large particle diameters, t_A is large (3) and K_p is small reflecting the small transfer of turbulence energy to the particulate phase due to the (relatively) high particle inertia.

3. Discretisation and solution algorithm

3.1 *Discretisation*

The governing equations, (9) and (10), can be written symbolically as

$$\partial F^{il}/\partial x_i = S^l. \tag{28}$$

This type of representation lends itself to a general finite-volume discretisation (Fletcher 1991, vol. 1, p. 105 ff.) either directly in physical space or in computational space. The linking factor is the role of the area vectors (Fletcher 1991, vol. 2, p. 51 ff.). For each face of the control volume, the surface area defines the magnitude and the normal defines the direction of the area vector. Figure 2 illustrates the concept in two dimensions.

The Cartesian components of the area vectors can be formed into an area vector matrix, which is 2×2 in two-dimensions and 3×3 in three-dimensions. If the grid intervals $(\Delta\xi, \Delta\eta)$ in computational space are unity then the area vector matrix can be related to the Jacobian of the transformation between computational and physical space,

$$\mathbf{A} = |\mathbf{J}^{-1}|\mathbf{J}. \tag{29}$$

Here $|\mathbf{J}^{-1}|$ is the effective volume of the control volume and can be evaluated from

$$|\mathbf{J}^{-1}| = (1/3)\mathbf{A}\cdot x^{cf}, \tag{30}$$

where x^{cf} is the vector of the centroids of the faces of the control volume. This becomes an effective scale factor so that the Jacobian, $\mathbf{J}$, is a normalised area vector matrix. This is a useful interpretation if the discretisation is formally carried out in

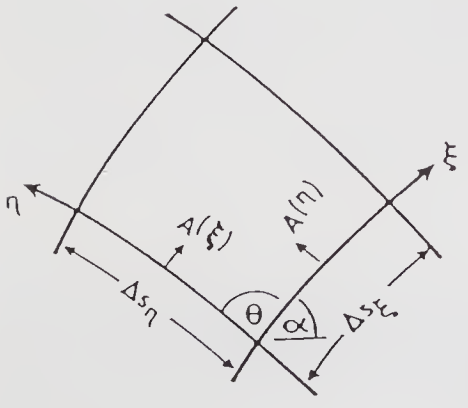

Figure 2. Area vectors and the computational grid.

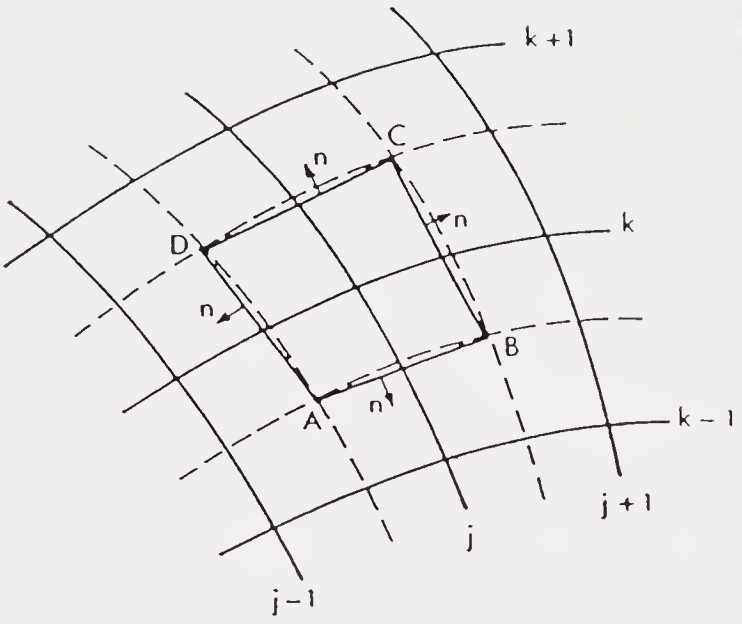

Figure 3. Finite volume arrangement in a two-dimensional grid.

computational space. This occurs if the equations of motion are first transformed into generalised coordinates (e.g. Steger 1978) leading to the explicit appearance of transformation matrices, ξ_x, embedded in the governing equation.

In two dimensions, the ξ_x component of **J**, evaluated at the centre of the control volume (figure 3), is related to the A_{11} component of **A** by

$$\xi_x = A_{11}/|\mathbf{J}^{-1}|. \tag{31}$$

But $A_{11} = 0{\cdot}5\,(y_D - y_A + y_C - y_B)$, so that ξ_x can be evaluated directly once the physical grid is known. However the evaluation of (31) and the explicit appearance of ξ_x etc. in the generalised coordinate governing equations can be avoided by discretising the governing equations directly in physical space. In this case (28) becomes, for a six-sided control-volume,

$$\sum_{n=1}^{6} F_n^{il} \cdot A_n = |\mathbf{J}^{-1}| \langle S^l \rangle \tag{32}$$

where $F_n^{il} \cdot A_n$ indicates the scalar product of the flux F^{il} and the area vector of the nth face. The "volume" of the control volume is evaluated using (30) and $\langle S^l \rangle$ denotes that the source term is evaluated at the centre of the control volume. Thus the components of the area vectors play the same role as the transformation metrics, like ξ_x, but are evaluated directly at the control surfaces rather than at the centre of the control volume. This implies a more accurate discretisation on a highly distorted grid.

Given the transport nature of the governing equations it is possible, and illuminating, to write F^i as

$$F^i = \rho u^i \psi - \mu(\partial\psi/\partial x^i), \tag{33}$$

where ψ is a general scalar, e.g. u in the x-momentum equation and T or h in the energy equation. Thus one component of the left-hand side of (32) becomes

$$F_n^i \cdot A_n = \{\rho \mathbf{u} \cdot A^{(i)} \psi - \mu A^{(i)} \cdot \nabla\psi\}_n, \tag{34}$$

and $\mathbf{u}\cdot A^{(i)}$ represents the normal flux or volume flow rate through the nth surface. Thus the first term on the right-hand side gives the flux of ψ through the nth surface. The second-term can either be evaluated in terms of physical coordinates,

$$A^{(i)}\cdot\nabla\psi = A^{(i)}_j(\partial\psi/\partial x_j), \tag{35}$$

or in terms of generalised coordinates, ξ^j

$$A^{(i)}\cdot\nabla\psi = [A^{(i)}A^{(j)}]/[|\mathbf{J}^{-1}|](\partial\psi/\partial\xi^j). \tag{36}$$

It is convenient to evaluate generalised convection and diffusion coefficients,

$$C^i_n = \{\rho\mathbf{u}\cdot A^{(i)}\}_n, \tag{37a}$$

$$D^{ij}_n = \mu A^{(i)}_n\cdot A^{(j)}_n/|\mathbf{J}^{-1}|, \tag{37b}$$

so that (34) becomes

$$F^i_n\cdot\mathbf{A}_n = C^i_n\psi_n - D^{ij}_n(\partial\psi/\partial\xi_j)_n. \tag{38}$$

The area vectors for each face of the control volume are evaluated once and for all. Consequently, it is efficient to use (36) and (37). However, the coefficients C^i_n, D^{ij}_n are evaluated at the centre of each face, whereas the dependent variables, e.g. ρ, $\mathbf{u}$ etc. are evaluated at the centre of the control volume. The evaluation of $\partial\psi/\partial\xi^j$ for derivatives normal to the face is then very compact. Thus if (ξ,η,ζ) are associated with increasing (i,j,k) grid values,

$$(\partial\psi/\partial\xi)|_{i+1/2} = 0{\cdot}5(\psi_{i+1,j,k} - \psi_{i,j,k}). \tag{39}$$

The grid is laid out in computational space and it is assumed that $\Delta\xi = \Delta\eta = 1{\cdot}0$. If the grid is also uniform in physical space, (39), and the equivalent evaluation of $\partial\psi/\partial\xi|_{i-\frac{1}{2}}$ leads to a conventional second-order three-point evaluation of $\partial^2\psi/\partial x^2$ if the x and ξ coordinate directions coincide. However, (38) also includes derivatives parallel to the control volume face. For example,

$$\begin{aligned}\left.\frac{\partial\psi}{\partial\eta}\right|_{k+\frac{1}{2}} &= 0{\cdot}5\left\{\left.\frac{\partial\psi}{\partial\eta}\right|_k + \left.\frac{\partial\psi}{\partial\eta}\right|_{k+1}\right\}\\ &= 0{\cdot}25\{\psi_{i,j+1,k} - \psi_{i,j-1,k} + \psi_{i,j+1,k+1} - \psi_{i,j-1,k+1}\}.\end{aligned} \tag{40}$$

The evaluation of $C^i_n\psi_n$ requires interpolation from nearby grid values. A local linear interpolation from values at grid points $(i-1,i)$, for example, leads to a three-point central difference scheme for $\partial F/\partial x$ if the x and ξ coordinate directions coincide. However, this does not lead to a robust algorithm to solve the discrete equations. It is better to interpolate asymmetrically, biased in the upstream direction. On a uniform physical grid, with $F^c = C^i\psi$

$$F^c_{i-\frac{1}{2}} = F^c_i + \varphi_{i-\frac{1}{2}}\{0{\cdot}5\Delta F_i - (q/3)(\Delta F_i - \Delta F_{i-1})\}. \tag{41}$$

Here $\varphi_{i-\frac{1}{2}}$ is a Roe-type limiter (Roe 1986) which is activated if very strong gradients, e.g. shocks, are expected. In the present study, $\varphi_{i-\frac{1}{2}} = 1{\cdot}0$. The parameter q allows additional control over the dispersion (Fletcher 1991, vol. 1, p. 296 ff.) properties. If $q = 0$ the three-point centred-difference scheme is recovered for $\partial F/\partial x$. If $q = 1{\cdot}5$ a

three-point fully upwind scheme is obtained. This is a robust scheme and effective for high-speed flows. The choice $q = 0{\cdot}5$ leads to a third-order accurate determination of $\partial F/\partial x$ on a uniform grid and has excellent dispersion-suppression properties (Fletcher 1988).

In the solution algorithm each momentum equation in discrete form evaluated at every internal grid point produces a linear (C_n^i frozen) system of equations in ψ; $\psi \equiv u, v, w$ for the x, y, z momentum equation. A typical contributing equation would be

$$\sum_{n=1}^{7} a_n \psi_n = S' + [\mathbf{J}^{-1}] S_{ijk}. \tag{42}$$

Here the dependent variable values on the seven-point stencil are handled implicitly. All other terms arising from the evaluation of F_n^i. $\mathbf{A}_n$ in (38) are contained in S' and evaluated as a deferred correction to the iterative solution. Also the discrete evaluation of the continuity equation, ΣC_n, is added to the coefficient of $\psi_{i,j,k}$ if this will increase diagonal dominance.

For the momentum equation,

$$S_{ijk} = -pA_k^{(i)}/|\mathbf{J}^{-1}| + \sum_n \left\{ \mu_T \mathbf{A} \cdot \frac{\partial \mathbf{u}}{\partial x^k} \right\}_n. \tag{43}$$

If the $(k - \varepsilon)$ turbulence model is used, μ_T is the total viscosity, including both laminar and turbulent parts.

3.2 *Solution algorithm*

The governing equations for the fluid phase are solved sequentially at each iteration to obtain the dependent variables,

x-momentum equation	$\Rightarrow u$,
y-momentum equation	$\Rightarrow v$,
z-momentum equation	$\Rightarrow w$,
velocity potential equation	$\Rightarrow p$,
k transport equation	$\Rightarrow k$,
ε transport equation	$\Rightarrow \varepsilon$.

The derivation of the velocity potential equation is indicated below. At each global iteration each equation is iterated, typically 3 to 5 times, using the strongly implicit procedure (SIP) (Fletcher 1991, vol. 1, p. 198 ff.). The SIP procedure (due originally to Stone 1968) can be illustrated in relation to the system

$$(\mathbf{N} - \mathbf{P})\psi = B, \tag{44}$$

where $\mathbf{N}$ is close to $\mathbf{A}$ but is easier to factorise into $\mathbf{L}\cdot\mathbf{U}$. Stone (1968) was able to show that $\mathbf{N}$ can be chosen so that $\mathbf{L}$ has only three non-zero diagonals and $\mathbf{U}$ has only two non-zero diagonals with unity on the main diagonal. $\mathbf{P}$ is found to have two non-zero diagonals multiplying $\psi_{i+1,j-1}$ and $\psi_{i-1,j+1}$. Schneider & Zedan (1981) develop a more robust version with four non-zero diagonals in $\mathbf{L}$ and $\mathbf{U}$ and unity on the main diagonal of $\mathbf{U}$. The non-zero coefficients in $\mathbf{L}$, $\mathbf{U}$ and $\mathbf{P}$ are evaluated once and for all.

The SIP algorithm is implemented in two stages. First, a forward sweep solves

$$\mathbf{L}\pi^{(n+1)} = B + \mathbf{P}\psi^{(n)}. \tag{45}$$

This is followed by a back-substitution

$$\mathbf{U}\psi^{(n+1)} = \pi^{(n+1)}. \tag{46}$$

Further details are provided by Fletcher (1991, vol. 1, p. 198 ff.).

The solution for the velocity obtained by SIP is denoted by $\mathbf{q}^*$, where $\mathbf{q}^T \equiv \{u, v, w\}$. To satisfy continuity it is necessary that

$$\nabla\cdot(\rho\mathbf{q})^{n+1} = 0. \tag{47}$$

Therefore, a correction is introduced (Cho *et al* 1991)

$$(\rho\mathbf{q})^{n+1} = (\rho\mathbf{q})^* + (\rho\mathbf{q})^c, \tag{48}$$

and the correction velocity field is obtained from a velocity potential

$$\mathbf{q}^c = \alpha\nabla\varphi. \tag{49}$$

The auxiliary potential method (Fletcher & Bain 1991) shows that the correction to the pressure and density can also be obtained from φ. Thus

$$\rho^c = -\delta\varphi/(a^*)^2, \quad p^c = -\beta\varphi. \tag{50}$$

In (49) and (50), α, β and δ are under-relaxation factors and a^* is the speed of sound,

Substitution into (47) gives the following transport equation for φ,

$$\delta\frac{\partial}{\partial x_i}\left\{\frac{u_i^*\varphi}{(a^*)^2}\right\} - \alpha\frac{\partial}{\partial x_i}\left\{\rho^*\frac{\partial\varphi}{\partial x_i}\right\} \equiv \nabla\cdot(\rho\mathbf{q}^*) - \gamma\frac{\partial^4\varphi}{\partial\xi^{i4}}. \tag{51}$$

The last term on the right-hand side of (51) is introduced in computational space to assist in the damping of any pressure oscillations that may occur due to the fact that the velocity components and pressure are specified at the same points. However (41) is also applied to the pressure field and this also contributes to the suppression of any pressure oscillations.

Equation (51) is solved iteratively using the SIP scheme. Once the current velocity and pressure solutions have been obtained, the SIP scheme is applied successively to the k and ε transport equations (20), (21) to obtain k^{n+1} and ε^{n+1}. Subsequently, at each grid point, the Reynolds stresses are evaluated from the algebraic equations, (22).

3.3 *Particulate phase*

To exploit the finite volume formulation described above, the governing equations for the particulate phase, (13), (14), (23)–(27), are written in the generic transport form,

$$\frac{\partial}{\partial x_i}(\rho_p u_i^p\psi) - \frac{\partial}{\partial x_i}\left[\alpha_p\frac{\partial\psi}{\partial x_i}\right] = S, \tag{52}$$

where

$$\psi^T \equiv \{\rho_p, u^p, v^p, w^p\}. \tag{53}$$

Equation (52) is "natural" for the particulate momentum equations, (14), if new convection coefficients are established in place of (37a) based on ρ_p and u_i^p. However, the particulate continuity equation, (13), written in the format of (52) leads to $\alpha_p = \rho_p D_p$ and

$$S = \frac{\partial \rho_p}{\partial x_i} \cdot \left[\rho_p u_i^p - D_p \frac{\partial \rho_p}{\partial x_i} \right]. \tag{54}$$

For the particulate momentum equation, $\alpha_p = \rho_p \nu_p$, and

$$S = \frac{\partial}{\partial x_i}\left[\rho_p \nu_p \frac{\partial u_i^p}{\partial x_k} \right] + \frac{\partial}{\partial x_i}\left\{ D_p \left[u_i^p \frac{\partial \rho_p}{\partial x_k} + u_k^p \frac{\partial \rho_p}{\partial x_i} \right] \right\} + \rho_p (u_k^g - u_k^p)/\mathrm{St}, \tag{55}$$

where $\mathrm{St} = \gamma d_p^2 f/(18\nu_g)$.

After finite volume discretisation as in §(3.2), (52) are solved sequentially at each iteration, after the fluid phase has been iterated, using the SIP scheme. It is assumed that the particulate behaviour has no influence on the fluid flow solution. A separate system of equations, like (52), is required for each particulate size distribution. However, it is assumed that there is no coupling between particulates of different sizes.

4. Results and discussion

4.1 *Simulation details*

The airflow inside a "Coal Classifier" has been simulated by solving the governing flow equations, (9), (10), (13), (14) with a finite volume computer code, RANSTAD, to accurately represent the geometric details, e.g. the simulated inflow, baffle and scroll plate locations, coal feed, external geometry and exit area.

A representative classifier is shown in figure 1. In discussing the results, the "hot air inlet" side will be referred to as the *front* of the classifier. Thus the conveyor drive (outer annulus) causes air and coal to enter the classifier through the back wall. The pulverised fuel is also delivered to the furnace via an exit duct in the back wall. This exit duct appears to be 'inside' the baffle plate when viewed from the front.

The transverse grid used to generate the simulation is shown in figure 4 for the downsweep side. The upsweep side also includes the coal feed which is modelled as a solid blockage down to the air inflow location (AD in figure 4). A nonuniform grid is used in the direction along the baffle. The behaviour within the classifier is primarily two-dimensional, i.e. the flow is similar in each plane parallel to that shown in figure 4. Consequently, most of the results will be shown in planes cutting through the baffle and scroll plates as in figure 4. Based on the known mass flow rate, an average inlet vertical flow velocity of 8·4 m/s is set at the boundary AD. However the vertical velocity is assumed to vary linearly from the back to the front of the classifier (figure 1).

The surface ADC (figure 4) lines up with the top of the trunnion tube and simulates the surface of the coal. Along AD a longitudinal velocity component in the direction of the conveyor drive is assumed to be 10% of the average vertical velocity at A (figure 4) which lines up with the trunnion tube. This longitudinal velocity component is assumed to fall linearly to zero at D, where the scroll plate intercepts the surface of the incoming coal fragments. On the return side, DC in figure 4, the longitudinal velocity is assumed to be zero.

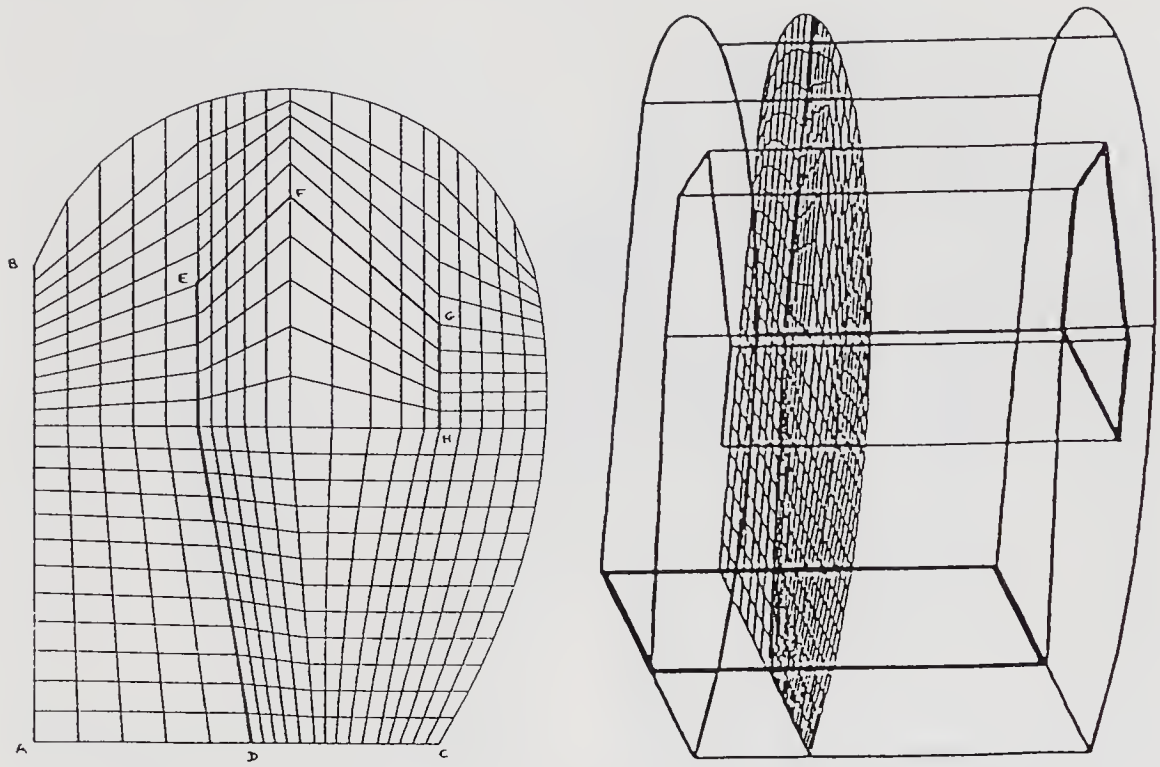

Figure 4. (**a**) Computational grid – transverse section; (**b**) Computational domain and transverse grid.

The motion of the conveyor creates a lateral velocity component of magnitude 1·33 m/s at A. This component is assumed to fall to zero at D and to remain at zero on the coal return side, DC in figure 4. The direction of the lateral velocity component depends on whether the upsweep or downsweep side is being considered.

The baffle plates are set to correspond to normal operating conditions. To obtain better resolution and hence more accurate results, the flow simulation considers half of the classifier. However, by adjusting the inflow velocity components and by including (or not) the coal feed blockage, both upsweep and downsweep sides of the classifier can be investigated. Backflow on the return side of the scroll plate has been simulated by assuming a seepage flow through the coal surface DC in figure 4.

The equations are solved repeatedly for 500 iterations. At the end of this process the equations are satisfied to better than 0·001% with mass conserved to about 0·0003%. These levels imply that the predicted velocities will not change (in relation to the inherent accuracy of the simulation) if the equation residuals are reduced to a lower level.

4.2 *Flow behaviour*

The discussion of the flow behaviour is based, primarily, on the flow solution produced by RANSTAD. However, key features of the predicted behaviour are confirmed by measurements and flow visualisation in a 1:4 scale model of the classifier (Bagust & Fletcher 1992). The broad flow character of the classifier is two-dimensional. The main features can be established from the transverse velocity vectors at $K = 9$ (roughly half way along the classifier) shown in figure 6.

The flow accelerates to the top of the classifier under the constricting effect of the scroll plate and baffle, DEF (figure 4). Beyond F these is evidence of locally reversed

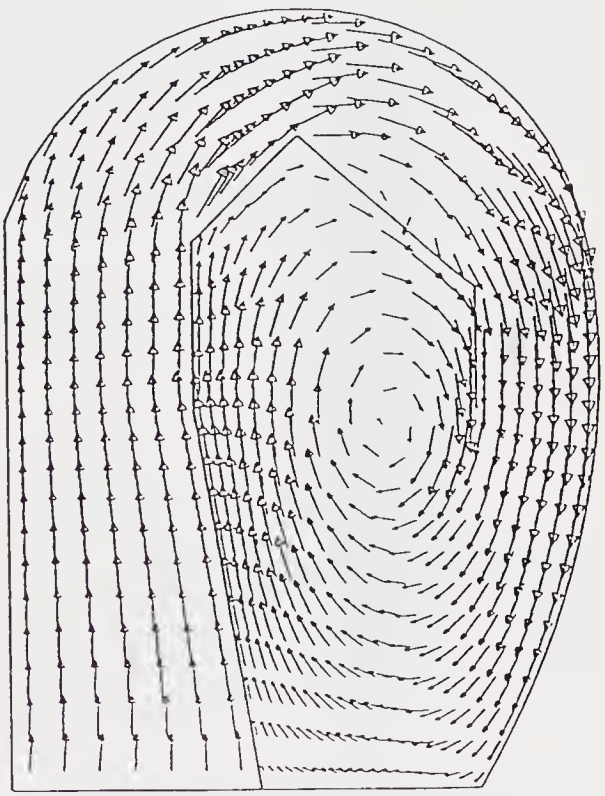

Figure 5. Transverse velocity behaviour– K-plane = 3; near front of classifier.

flow adjacent to the baffle plate (figure 6). Towards the back of the classifier, at $K = 15$ (figure 7), the flow has also reversed locally. Similar behaviour is present at the front ($K = 3$) of the classifier (figure 5). This reversed flow contributes to a higher pressure drop through the classifier. However, by reshaping EFG it is possible to avoid this flow reversal (figures 11 to 14).

Figure 6. Transverse velocity behaviour – K-plane = 9; midsection of classifier.

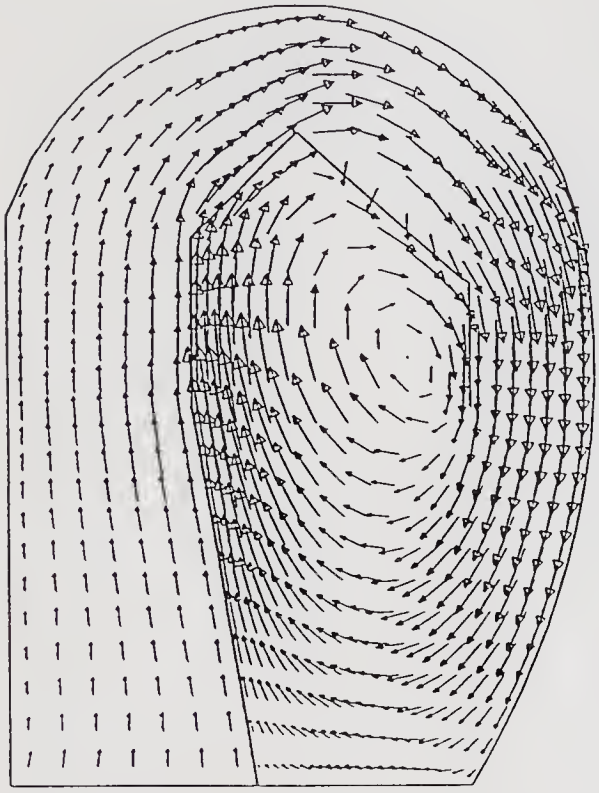

Figure 7. Transverse velocity behaviour – K-plane = 15; near rear of the classifier.

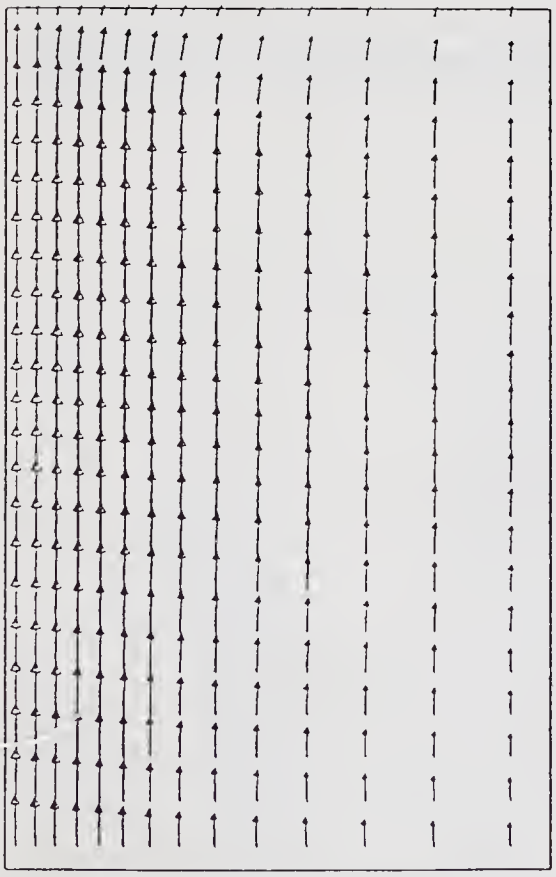

Figure 8. Longitudinal velocity behaviour – I-plane = 3; back of scroll plate.

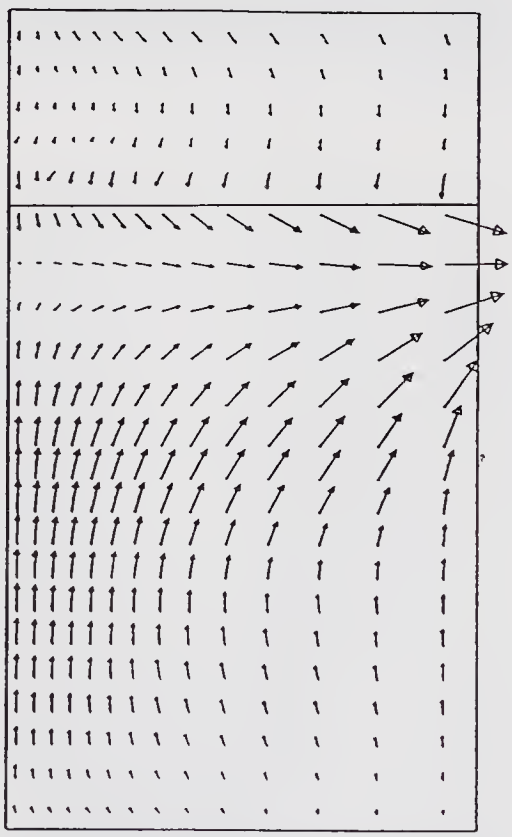

Figure 9. Longitudinal velocity behaviour – I-plane = 10; cutting through baffle.

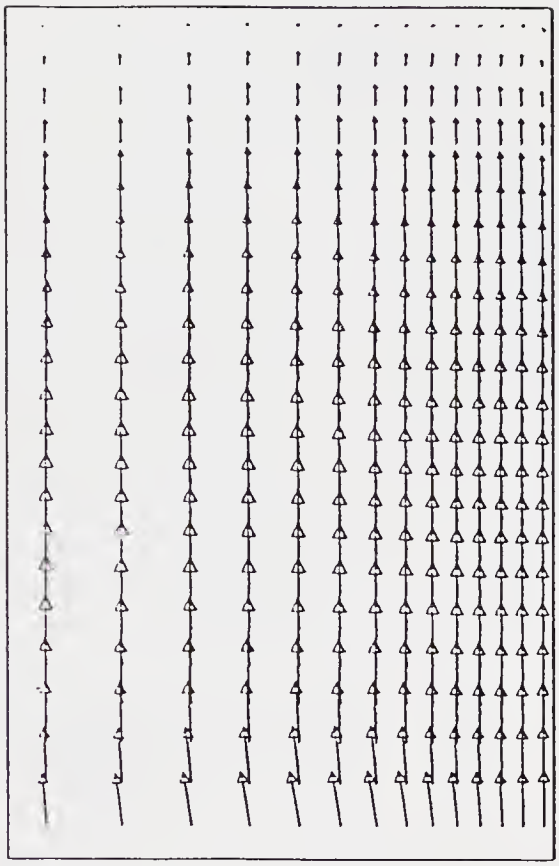

Figure 10. Longitudinal velocity behaviour – I-plane = 16; between baffle and outer wall.

The flow undergoes a further acceleration adjacent to GH producing a local velocity of about 20 m/s directed downwards. Under the influence of this momentum, the flow tends to fill the whole of the cavity, down to DC (figure 4), but with some

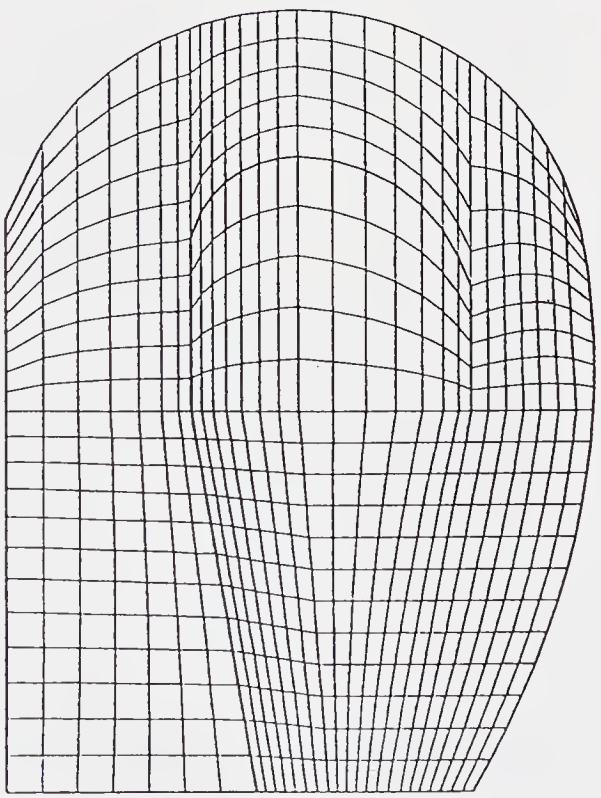

Figure 11. Computational grid – improved baffle.

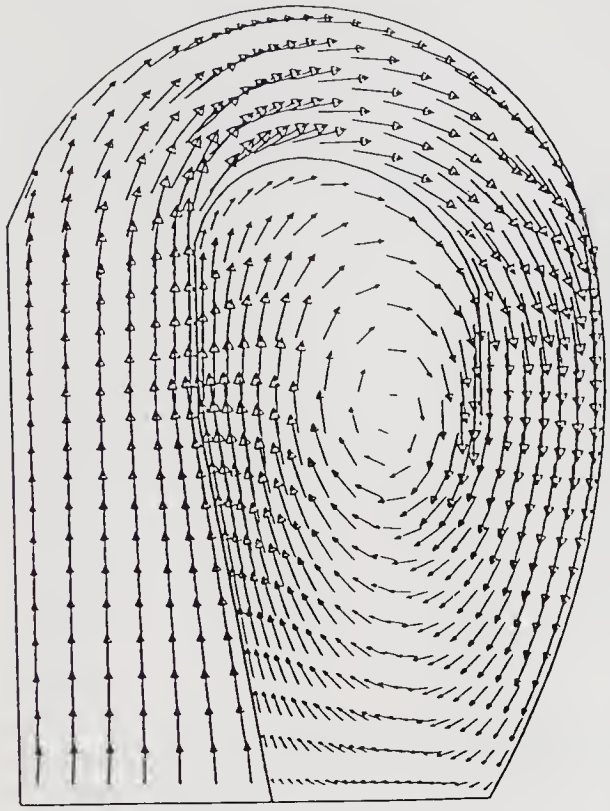

Figure 12. Transverse velocity behaviour – improved baffle near front of classifier.

reduction in velocity magnitude. In addition, the maximum velocities tend to occur adjacent to the outer wall.

However, the disposition of the baffle plate does induce a swirling or vortex-like motion but the vortex centre is located close to the lip of the baffle plate, H in figure 4, and well inside the baffle. This behaviour occurs at all stations along the classifier

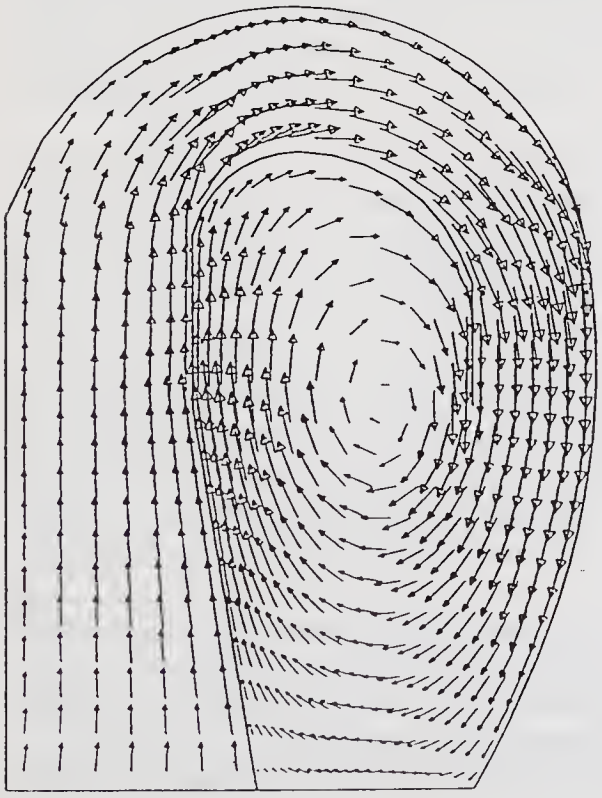

Figure 13. Transverse velocity behaviour – improved baffle midsection of classifier.

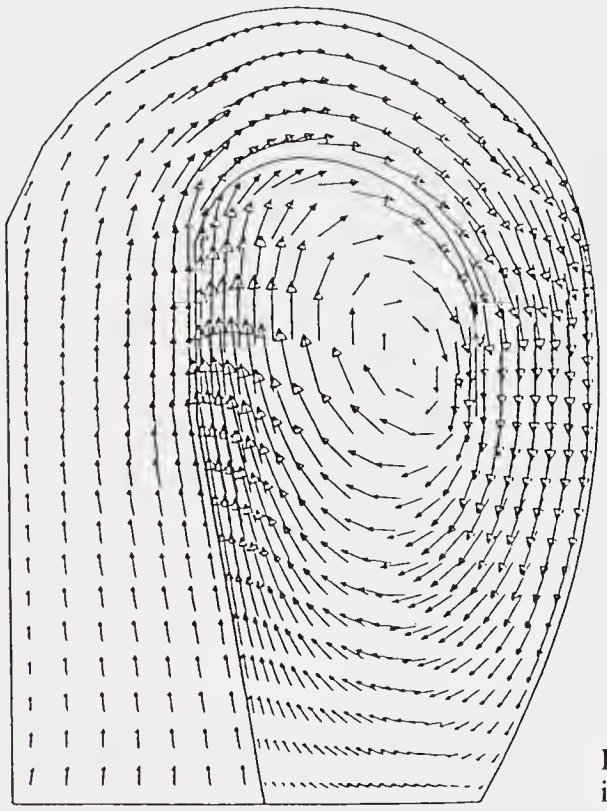

Figure 14. Transverse velocity behaviour – improved baffle near rear of the classifier.

(figures 5 to 7). Once inside the baffle plate, the flow gradually accelerates to the exit. That is the W velocity component gradually increases with increasing values of K. The longitudinal velocity vectors at $K = 3, 9$ and 15 are shown in figures 8 to 10. It is apparent that the W component outside of the baffle is generally small, except at the top, but there is some return flow inside the scroll plate at the bottom. This can be traced to the presence of the longitudinal variation in the vertical velocity component at AD in figure 4. The maximum W values occur close to the inside of the baffle, GH in figure 4, and increase in magnitude as the exit duct is approached (increasing K).

The simulation indicates that the original classifier generates a vortex-like motion that should form the basis of the separation process. However, the velocity magnitudes are small and the vortex is relatively weak. In addition, the baffle induces some reversed flow adjacent to the surface FG, which distorts the velocity distribution and increases the pressure losses.

A major improvement can be made to the top section of the baffle plate (EFG in figure 4). This is replaced with a continuous curve (figure 11). The location of F is lowered so that the flow is continually and smoothly accelerated from BE to the opposite side adjacent to G. That is, the cross-sectional area is smoothly reduced. The result is a velocity field that has no reversed flow regions (figures 12 to 14) over the top of the baffle plate and a better velocity distribution between the baffle plate and the outer wall of the classifier.

The lack of flow reversal close to FG (comparing figures 6 and 13, for example) leads directly to a smaller overall pressure drop across the classifier. The vortex strength is increased slightly and the location of the vortex core is lower. This makes the flow velocity field more effective in capturing the particles.

The transverse velocity behaviour is similar at all longitudinal stations (figures 12

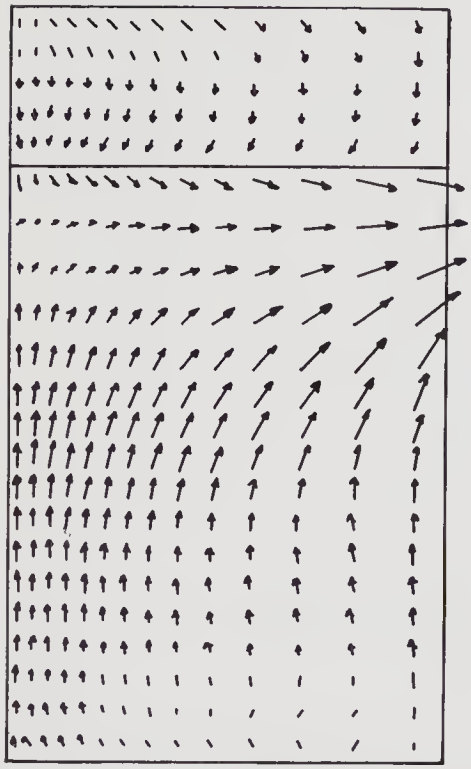

Figure 15. Longitudinal velocity behaviour – improved baffle cutting through baffle.

to 14). The longitudinal velocity vector distribution for $K = 9$ (approximate midplane of the classifier) is shown in figure 15. The general character is similar to that described earlier (figure 9). This is also true for other longitudinal locations.

4.3 *Particulate behaviour*

To assess the basic classifying ability of the present configuration, particle trajectories of the following sizes:

a) 30 μm,
b) 75 μm,
c) 150 μm,
d) 300 μm,

are examined. The particles have been considered to start from a carpet covering the inlet area (figure 4). The inlet velocity of the particulate is set equal to the inlet flow velocity. Typical trajectories projected into the transverse plane are shown in figure 16.

It is clear that the smaller particles are more influenced by the flow (due to their lower inertia). However, the large velocities and circular path throw all particles to the outer wall. In addition, as the smaller particles leave the wall, they are immediately swept by the locally large flow velocity keeping their trajectories close to the outer wall. The larger particles tend to bounce more. They typically have a larger wall approach velocity and in leaving the wall surface can penetrate the flow velocity field better due to their larger inertia.

Beyond the top of the classifier the particles are accelerated downwards (adjacent to GH in figure 4) due to gravity (§ 2.1). This, combined with their inertia, makes them less responsive to the vortex-like motion of the fluid that is trying to turn the path of the particles inside the baffle. As a result, a large proportion of all particles sizes, except the smallest (30 μm diameter), are expected to be rejected and remilled.

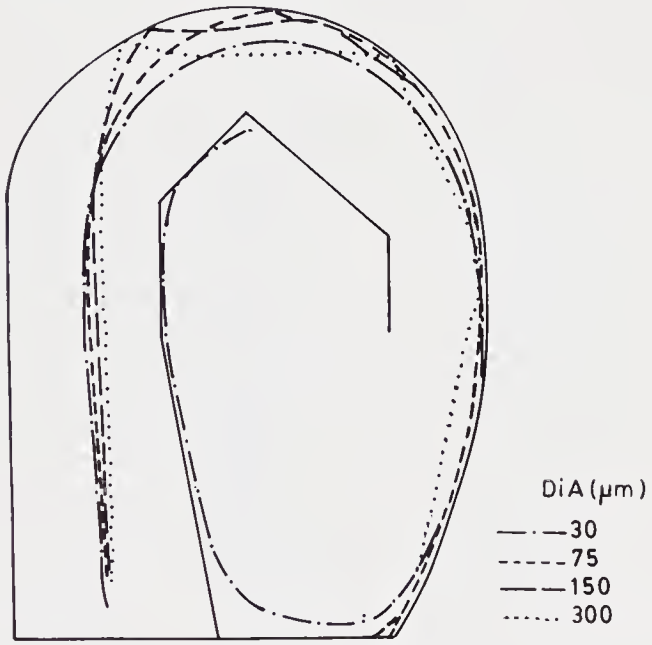

Figure 16. Particle trajectories, front view, standard baffle.

The changed baffle plate shape shown in figure 11 has been used to generate the flowfield that the particle trajectories shown in figure 17 are associated with. It is clear, from comparison with figure 16, that the resulting change in the trajectories is not sufficient to improve the classifier performance markedly.

Typical trajectories for 30 μm diameter particles released from $z = 0{\cdot}20$ m are shown in figure 18, which shows a three-quarter view to indicate the path between inlet and outlet. For particles of diameter $= 30\,\mu$m and smaller, the particles follow the streamlines approximately, no wall collisions occur and the particles eventually exit to the furnace.

Typical trajectories for 75 μm diameter particles released from $z = 0{\cdot}20$ m are shown in figure 19. Due to the greater inertia, the particles strike either the top or side walls and are thrown further into the centre of the classifier where they come under the

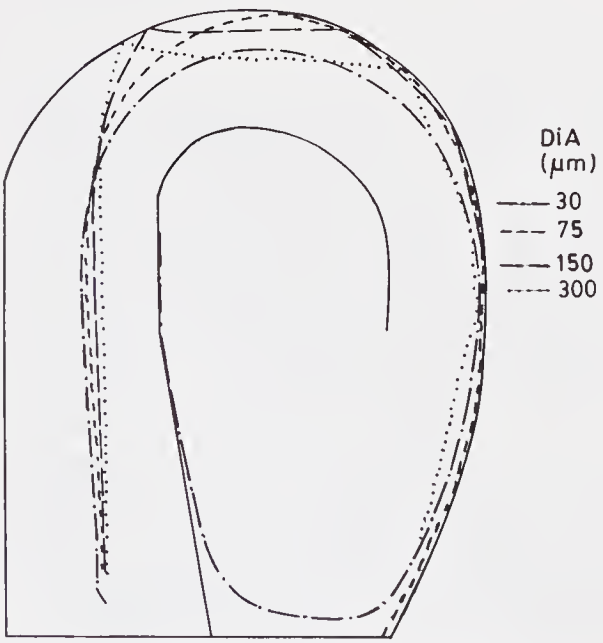

Figure 17. Particle trajectories, front view, improved baffle.

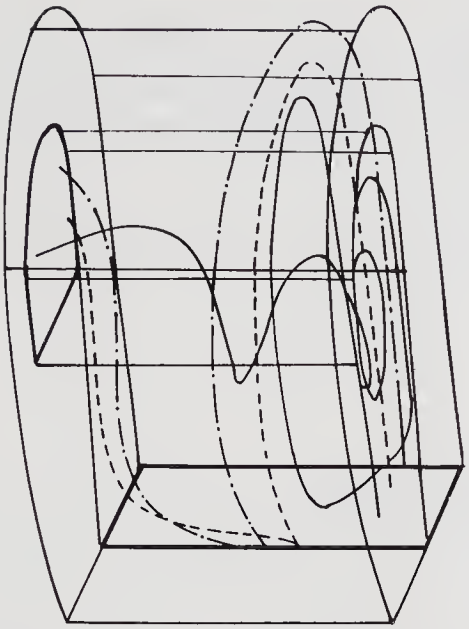

Figure 18. Particle trajectories, three-quarter view, $d_p = 30\,\mu$m.

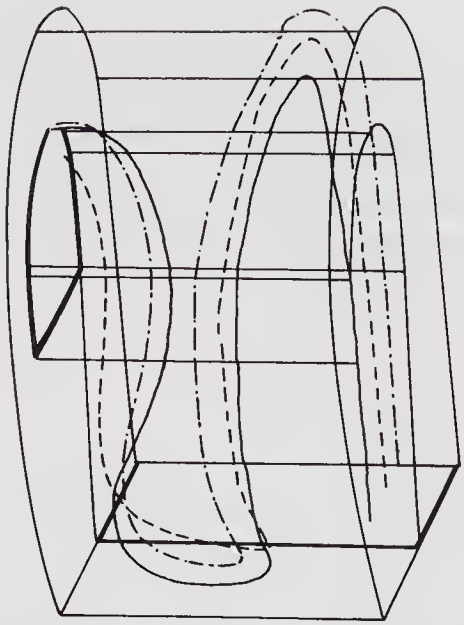

Figure 19. Particle trajectories, three-quarter view, $d_p = 75\,\mu$m.

influence of the trapped vortex. Similar collision patterns arise for particles released at $z = 0{\cdot}50$ m and $0{\cdot}90$ m. For this size, the back flow has a slight influence associated with turning the down flow and decelerating the downward motion of the particles. It is expected that some of the 75 μm particles will exit conventionally to the furnace without being remilled to a smaller size.

For 300 μm diameter particles, released at $z = 0{\cdot}50$ m, representative trajectories are shown in figure 20. It may be noted that the trajectories indicate rejection and remilling but the collisions with the top and side walls are more pronounced than for the smaller particles and the subsequent trajectories are less responsive to the local flow behaviour. Occasionally, due to the higher inertia of the larger particles, it is possible for the particles to be thrown into the region inside the baffle and from

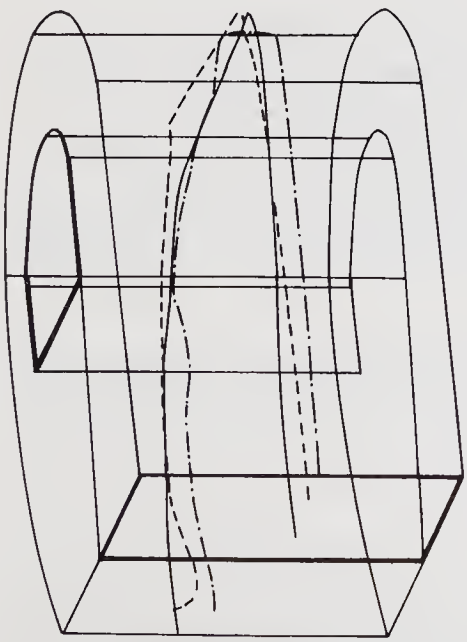

Figure 20. Particle trajectories, three-quarter view, $d_p = 300\,\mu$m.

there to be swept out of the exit of the classifier. However, the situation shown in figure 20 is more common. That is the particles are carried over the baffle plate, and due to the larger downward velocity, are rejected for remilling. Due to the higher inertia, there is not much axial movement along the classifier while the larger particles are inside the classifier.

Thus, there is a clear trend that, as the particle diameter increases, the collisions with the bounding surfaces determine the particle motion rather than the influence of the carrier gas.

5. Concluding remarks

The results in § 4 have been presented as a partial case study to indicate what modern CFD codes, such as RANSTAD, are capable of. The present results formed part of a preliminary investigation carried out in conjunction with the Electricity Commission of New South Wales (Australia) to improve the performance of ball-mill classifiers.

Subsequently, an operational classifier was modified to alter the collision characteristics of the outer surface in such a way as to achieve a sharper particle diameter cut-off between small particles that pass directly through the classifier and larger particles that are rejected by the classifier for remilling. Sampling of the pulverised fuel exiting the classifier indicated that the geometric modifications to the classifier had, indeed, improved the particle size distribution being delivered to the furnace.

Used intelligently, CFD provides detailed information that is too expensive and too time-consuming to measure directly for alternative classifier modifications under consideration. In this sense, CFD is an example of Computational Engineering. A finite element simulation of a car crash to design the safe distortion of structural components would be another example.

The essence of Computational Engineering is to combine the computer's power with the engineer's understanding of the physical processes distilled into a design computer code. There is now widespread acceptance of the following advantages of the expert use of computer simulation codes.

(1) The lead time in design and development is reduced significantly.
(2) Computational simulation provides more detailed and comprehensive information than can be obtained by direct measurement or physical simulation.
(3) Conditions can be simulated that are not reproducible in experimental tests.
(4) The design process is substantially more cost-effective and time-efficient.

The ultimate benefit for industry is greater productivity and hence greater profitability.

The commitment of the Electricity Commission of New South Wales (Pacific Power) to the exploitation of Computational Engineering for the improvement of all aspects of electricity generation is acknowledged.

References

Adeniji-Fashola A, Chen C P 1990 Modelling of confined fluid-particle flows using Eulerian and Lagrangian schemes. *Int. J. Heat Mass Transfer* 33: 691–701

Armfield S W, Cho N-H, Fletcher C A J 1990 Prediction of turbulence quantities for swirling flow in conical diffusers. *AIAA J.* 28: 453–460

Bagust K, Fletcher C A J 1992 Flow behaviour in coal classifiers. *Fifth Asian Congress of Fluid Mechanics*, Taejon, Korea

Bar-Yoseph P, Fletcher C A J 1991 On continuum modelling of gas–solid flows with application to erosion prediction. Dept. of Mechanical Engineering Report, University of Sydney, November

Cho N-H, Fletcher C A J 1991 Computation of turbulent conical diffuser flows using a non-orthogonal grid system. *Comput. Fluids* 19: 347–361

Cho N-H, Fletcher C A J, Srinivas K 1991 Efficient computation of wing body flows. *Lecture notes in physics* (Heidelberg: Springer) 371: 167–191

Choi Y D, Chung M K 1983 Analysis of turbulent gas–solid suspension flow in a pipe. *J. Fluids Eng.* 105: 329–384

Cross M, Richards C W, Knight B, Markatos N C 1988 In *Computational fluid dynamics* (eds) G de Vahl Davis, C A J Fletcher (Amsterdam: North-Holland)

Crowe C T 1982 Review – Numerical models for dilute gas–particle flows. *J. Fluids Eng.* 104: 297–303

di Giacinto M, Sabetta F, Piva R 1982 Two-way coupling effects in dilute gas–particle flows. *J. Fluids Eng.* 104: 304–312

Fletcher C A J 1988 Computational modelling of severe gradients with mass operator constructions. *Comput. Math. Appl.* 16: 31–39

Fletcher C A J 1991 *Computational techniques for fluid dynamics* 2nd edn (Heidelberg: Springer) vols. 1 and 2

Fletcher C A J, Bain J G 1991 An approximate factorisation explicit method for CFD. *Comput. Fluids* 19: 61–74

Kitchen A K 1990 *Flyash erosion prediction in economisers*, M E (Res.) thesis, University of Sydney

Kitchen A K, Fletcher C A J 1990 Computational approach to the prediction of erosion in economiser tubebanks. *Proc. Computational Techniques & Applications Conference-89* (eds) B J Noye, W Hogarth (New York: Hemisphere)

Melville W K, Bray K N C 1979 A model of the two-phase turbulent jet. *Int. J. Heat Mass Transfer* 22: 647–656

Modaress D, Tan H, Elghobashi S 1984 Two-component LDA measurement in a two-phase turbulent jet. *AIAA J.* 22: 624–630

Mostafa A A, Mongia H C 1988 On the interaction of particles and turbulent fluid flow. *Int. J. Heat Mass Transfer* 31: 2063–2075

Pourahmadi F, Humphrey J A C 1983 Modeling solid-fluid turbulent flows with application to predicting erosive wear. *Int. J. Phys. Chem. Hydro* 4: 191–219

Rodi W 1976 A new algebraic relation for calculating the Reynolds stresses. *Z. Angew. Math. Mech.* 56: 219–222

Roe P L 1986 Characteristic-based schemes for the Euler equations. *Annu. Rev. Fluid Mech.* 18: 337–365

Schneider G E, Zedan M 1981 A modified strongly implicit procedure. *Numer. Heat Transfer* 4: 1–19

Steger J L 1978 Implicit finite-difference simulation of flow about arbitrary two-dimensional geometries. *AIAA J.* 16: 679–686

Stone H 1968 A strongly implicit procedure for parabolic equations. *SIAM J. Numer. Anal.* 5: 530–558

Numerical study of bluff body flow structures

GUOCAN LING

Laboratory for Nonlinear Mechanics, Institute of Mechanics, Chinese Academy of Sciences, Beijing, 100080, China

Abstract. Our recent progress in numerical studies of bluff body flow structures and a new method for the numerical analysis of near wake flow field for high Reynolds number flow are introduced. The paper consists of three parts. In part one, the evolution of wake vortex structure and variation of forces on a flat plate in harmonic oscillatory flows and in in-line steady-harmonic combined flows are presented by an improved discrete vortex method, as the Keulegan–Carpenter number (KC) varies from 2 to 40 and ratios of U_m to U_0 are of $O(10^{-1})$, $O(1)$ and $O(10)$, respectively. In part 2, a domain decomposition hybrid method, combining the finite-difference and vortex methods for numerical simulation of unsteady viscous separated flow around a bluff body, is introduced. By the new method, some high resolution numerical visualization on near wake evolution behind a circular cylinder at $\mathrm{Re} = 10^2$, 10^3 and 3×10^3 are shown. In part 3, the mechanism and the dynamic process for the three-dimensional evolution of the Kármán vortex and vortex filaments in braid regions as well as the early features of turbulent structure in the wake behind a circular cylinder are presented numerically by the vortex dynamics method.

Keywords. Near wake evolution; hybrid method; three-dimensional evolution; turbulent structure; bluff body.

1. Introduction

Bluff body flow has received a great deal of attention especially for the prediction of loads on engineering structures such as offshore platform supports, ocean pipelines, risers, high buildings, bridge piers etc. and for analysis of wake control in aeronautical engineering as well. Of special interest, from a more fundamental point of view, are recent investigations of flow structures from bluff cylinders in incompressible flows, which may be classified into three aspects. (1) The complex flow structure from an oscillating cylinder, which contains different modes of vortex formation around the cylinder as the Keulegan–Carpenter (KC) number varies; mode competition when the cylinder is subjected to forced oscillations in a steady stream with varying frequency and amplitude or in a different direction with respect to the steady flow; vortex lock-in etc. In these cases, the flow development and the force variation on the cylinder will exhibit complicated nonlinear behaviour. (2) The high Reynolds number separated

flow about the bluff body, such as the long time behaviour of vortex structures containing different scales near and behind the cylinder, the interaction among secondary vortices and the primary vortex, the mechanism of vortex shedding, flow instability and transition. (3) The three dimensionality and coherent structures in the wake of two-dimensional bluff bodies, which cover the mechanism of 3-D development of wake flow, the different types of large structures in near-wake, intermediate-wake and far-wake, respectively, the topological structure and the 3-D spatial organizations of vorticity, and the driving mechanism responsible for the growth of these large structures. In the last ten years, numerous research efforts have led to a better insight into some of the relevant mechanisms referred to above [e.g. for the first aspect, see Sarpkaya (1986), Obasaju *et al* (1988) and Ongoren & Rockwell (1988); for the second, see Bouard & Coutanceau (1980) and Braza *et al* (1986); and for the third, see Okubo *et al* (1988) and Williamson (1986, 1992); owing to paucity of space a complete review is not given here]; however, there are a number of interesting features of bluff body flow that have largely remained unexplored. Moreover, most of the previous studies are concerned with experiments. It is believed that further study is needed, especially by numerical simulation. Concerning this point, there are crucial difficulties in the numerical analysis of high Reynolds number flow, containing detailed simulation of vortex structure evolution with different scales and flow transition in near wake of cylinders, and for flow field analysis of oscillating flow over cylinders, where flow transition occurs and Reynolds numbers may range from subcritical to supercritical, as well as for the three-dimensional transition of plane wake flow and computation of coherent structures. Hence it is desirable to develop a more effective numerical method which will reduce the difficulty in finite-difference solutions of Navier–Stokes (N–S) equations at high Reynolds numbers and overcome the theoretical weakness of the vortex method which fails in predicting accurately the flow field near a vorticity layer and body surface. The new method should not only be capable of precisely predicting the small structures near the body but also yield satisfactorily the global feature of vortex shedding flow. Besides, further effort should be made using some improved vortex (vortex filaments) method based on inviscid vortex dynamics, to study the global features of bluff body flow and the character of early three-dimensional transition of the wake flow.

In this paper, our recent progress in numerical studies of bluff body flow structure and a new method for numerical analysis of the near-wake flow field for high Reynolds number separated flow are introduced. New results and findings on the evolution of vortex patterns, variation of force, detailed behaviours of flow structure behind a flat plate and a circular cylinder in steady and steady-harmonic flow, as well as some new insights into the mechanism of three-dimensional evolution of wake vorticity structure are reported. The paper is in three sections.

2. Evolution of wake structures and variation of forces of a flat plate

In this section, results on the evolution of wake structure and variation of the forces on a flat plate in harmonic oscillatory flows and in in-line steady-harmonic combined flows are presented numerically by an improved discrete vortex method (Ling & Luo 1991; Ling & Liu 1992). For the oscillatory oncoming flow case, our calculations present a new mode of vortex motion in the wake of the plate for low KC number ($KC < 5$) describing vortex shedding, pairing and moving in a period of the oscillatory flow starting from rest, as shown in figure 1. That is, during the wake reversal, the

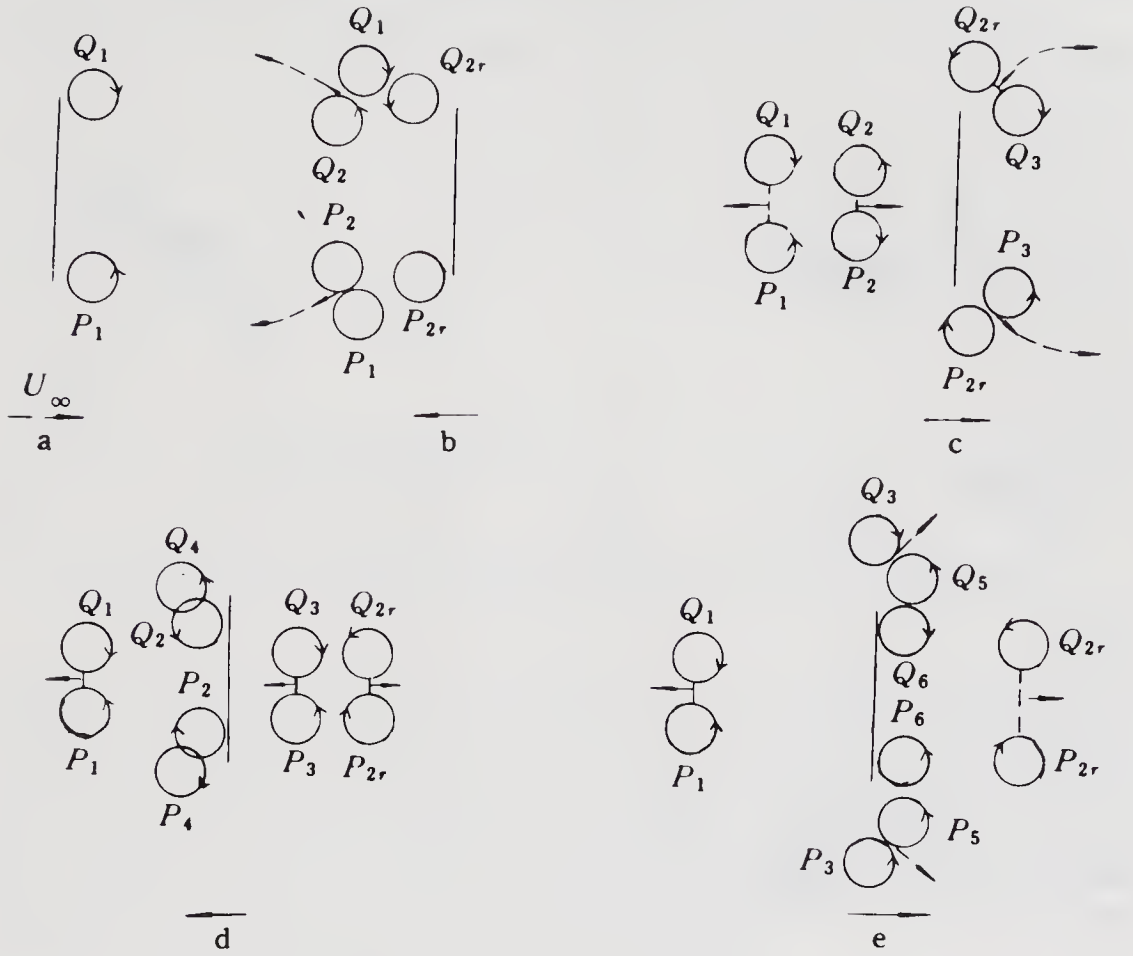

Figure 1. Scheme of vortex motion.

vortices are periodically paired and re-paired; the movements of paired vortices are regular; a pair of vortices moves away from the plate while another comes close to the plate, the phenomenon occurring on both sides of the plate with a phase difference. For long time behaviour of the vortex structure, when the KC number varies from 2 to 40, the vortex pattern changes from horizontal distributed vortex cluster in the range of small KC numbers to a slightly inclined "harmonic wave" shaped vortex-cloud in the range of moderate KC numbers, then becomes a vortex cluster inclined at an angle of nearly 50° to the oncoming flow at KC = 20, and finally, as KC number increases still further, it is like a normal Kármán vortex street. The evolution of vortex pattern with KC number is shown in figure 2. The predicted drag and inertia force coefficients are closer to the experimental results of Keulegan & Carpenter (1958) as compared with previous vortex simulation by other authors (see figures 3 and 4). The existence of a minimum inertial force coefficient near KC = 20 is also well predicted and the reason for this phenomenon has been given through an analysis of the vortex structure. For a steady oncoming flow case, the calculated global features of the separated flow, the variations of time-averaged longitudinal velocity component, the turbulence intensity $(\bar{u}'^2)^{1/2}/U_\infty$, and the Reynolds stress $-\overline{u'v'}/U_\infty^2$ in the wake, are in fair agreement with or close to previous vortex simulation or experimental measurements, respectively. Some examples are shown in figure 5(a–c). For the steady-harmonic combined oncoming flow case, there are three vortex modes, namely a vortex street, a "longitudinal wave" shaped vortex-cloud, and a vortex cluster structure corresponding to three typical in-line combinations of oncoming flow components, i.e. the ratios U_m to U_0, which are $O(10^{-1})$, $O(1)$ and $O(10^1)$,

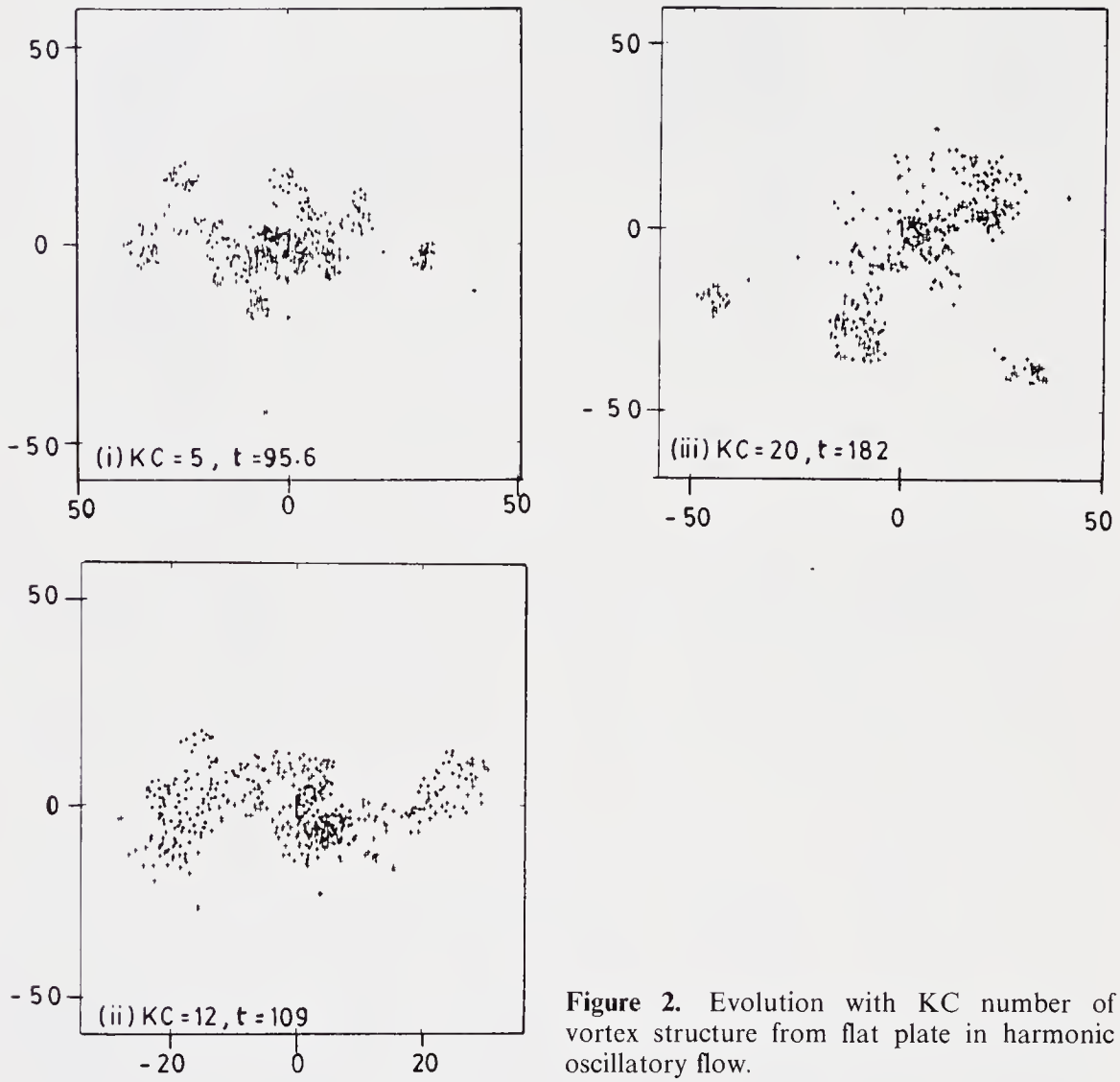

Figure 2. Evolution with KC number of vortex structure from flat plate in harmonic oscillatory flow.

respectively. Some examples are shown in figure 6. The variation of forces on and vorticity shedding rate from the plate in the combination flow are obtained. The effect on the prediction of forces on the plate and vorticity shedding rate from the disturbance component in combined flow is demonstrated quantitatively and

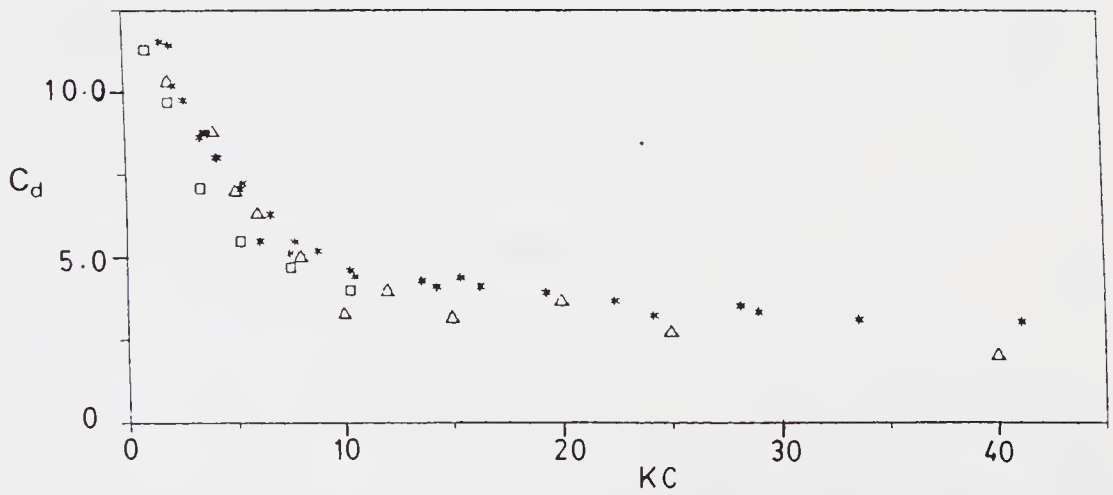

Figure 3. Variation with KC number of drag coefficient for flat plate. [Δ – Present results; ∗ – Keulegan & Carpenter (1958); □ – Lian (1980).]

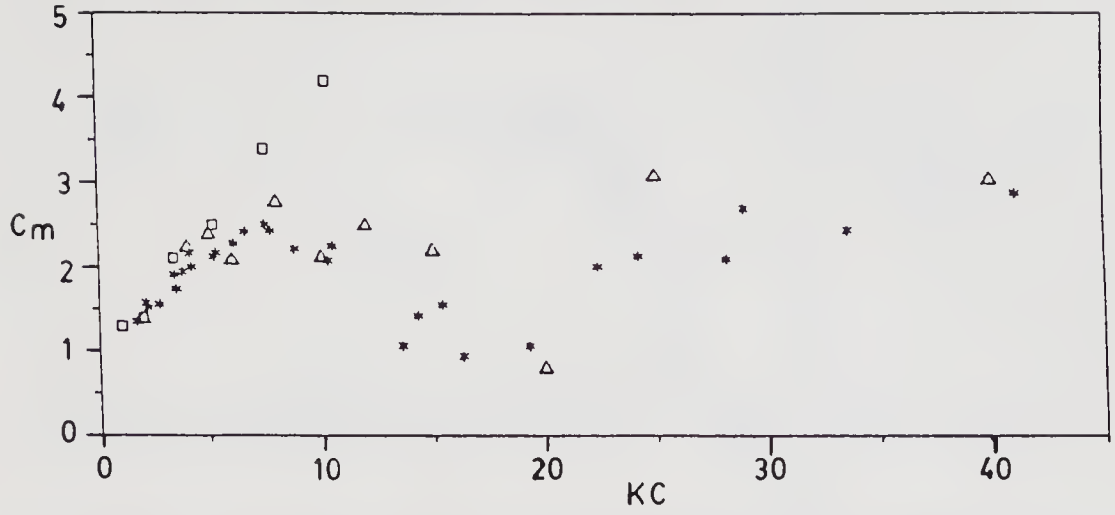

Figure 4. Variation with KC number of inertia force coefficient for flat plate. [Δ – Present results; * – Keulegan & Carpenter (1958), □ – Lian (1980).]

analysed. In general, superposing a steady flow as a disturbance component on oscillatory oncoming flow makes the mean value of drag coefficient decrease, and vice versa, imposing an oscillatory flow on steady oncoming flow increases the drag and vorticity shedding rate; especially in the small KC number case the disturbance has considerable influence, but there is no big influence on the inertia force coefficient. The vortex lock-in phenomenon has been simulated. From our calculations for parameters KC = 2–8, $U_m/U_0 = 0{\cdot}8$–10, a correlation of drag coefficient with KC and U_m/U_0 has been found, namely

$$C_d^2 = 17{\cdot}7[(1/\mathrm{KC})\cdot(U_m/U_0)] + 0{\cdot}105$$

or

$$C_d^2 = 17{\cdot}7\,V_r^{-1} + 0{\cdot}105$$

where V_r is reduced velocity. The corresponding curve is shown in figure 7.

3. Domain decomposition hybrid method and numerical visualization of near-wake flow structure behind a circular cylinder

In order to reduce the difficulties in the finite-difference solutions for N–S equations for high Reynolds number bluff body flows and to overcome the theoretical weakness of the vortex method, which is unable to predict precisely the small scale structure near the body, while taking advantage of both methods, a domain decomposition hybrid method combining the finite-difference and vortex methods has now developed (Ling *et al* 1992b). The full flow field is decomposed into an interior domain Ω1 near the body surface and an exterior domain Ω2, and an interface. The extent of the interior domain is $O(R)$ (R is a characteristic length of the body). In the domain Ω1, the flow is viscous and computed by a finite-difference scheme based on the N–S equations and the Poisson stream function equation. In Ω2, the flow is regarded approximately as an inviscid potential flow. The convection of vortices is calculated by a discrete vortex model using the vortex-in-cell method. The flows in the two domains are coupled and solved simultaneously. The boundary values of the vorticity on the interface required for solving the vorticity transport equation in Ω1 are given

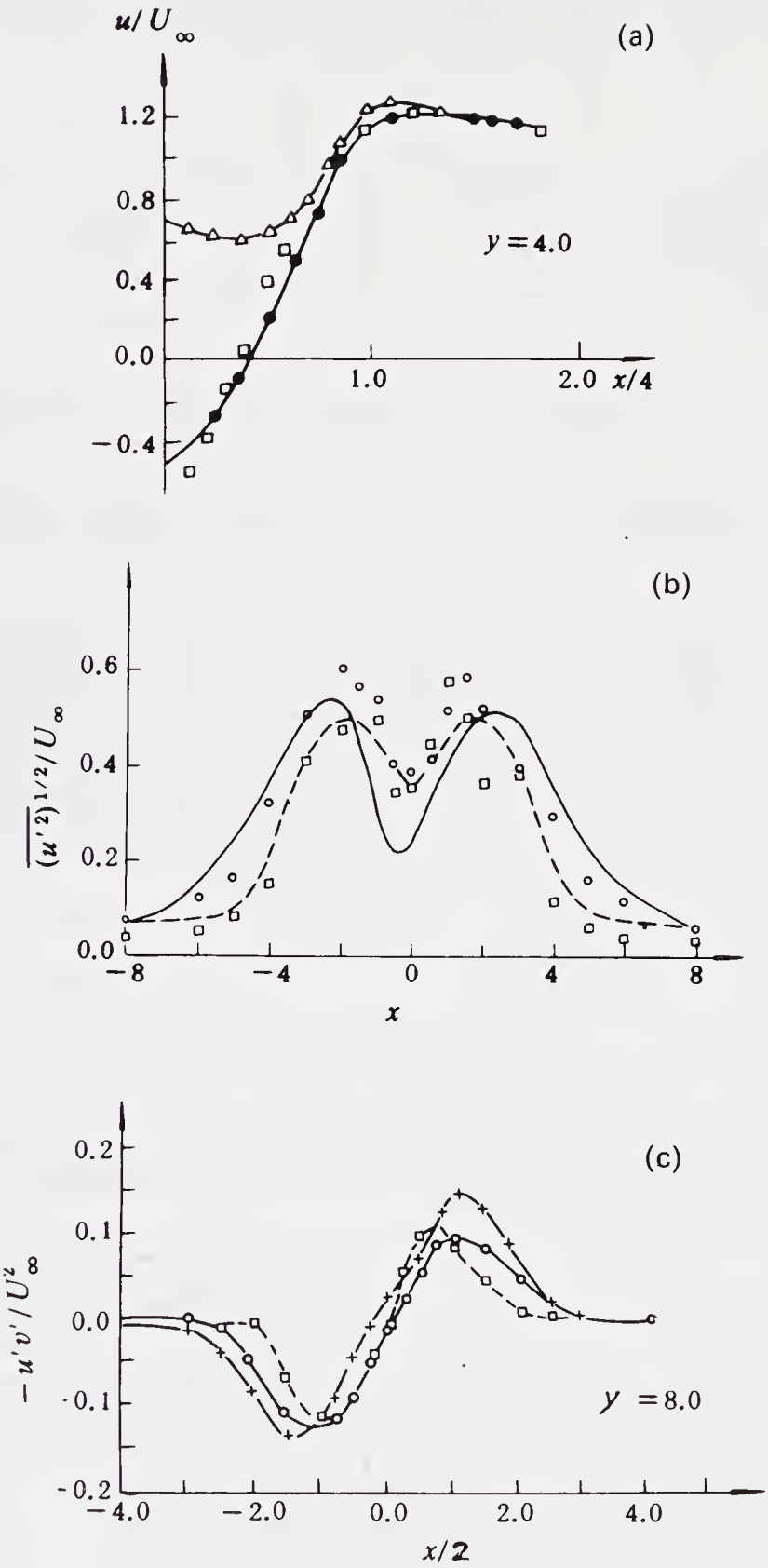

Figure 5. (**a**) Time-averaged longitudinal velocity component in the wake ($\alpha = 90°$); ∘– present results, –△, –□ Bradbury (1976). (**b**) Time-averaged longitudinal turbulent intensity (at $y = 4{\cdot}0$), —present results, ---Bradbury (1976), □ Kiya & Arie (1980), ∘ Chein & Chung (1988). (**c**) Time-averaged Reynolds stress in the wake ($\alpha = 20°$), –+–present results, –∘–Chein & Chung (1988), –□ Kiya & Arie (1980).

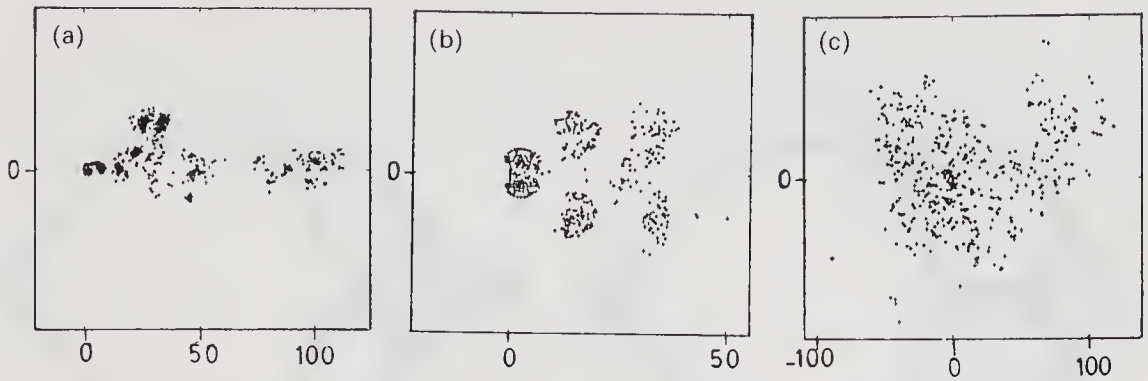

Figure 6. Vortex patterns over long times in the wake of flat plate in steady-harmonic flows. (**a**) $U_m/U_0 = 0{\cdot}5$, $t = 159{\cdot}3$, KC = 10; (**b**) $U_m/U_0 = 1{\cdot}0$, $t = 42{\cdot}0$, KC = 4; (**c**) $U_m/U_0 = 10$, $t = 79{\cdot}2$, KC = 40.

carefully. Matching conditions for the flow in the two domains are established and numerical schemes for the hybrid method are described in detail (Ling *et al* 1992b).

As an application of the present method, numerical solutions for flows around a circular cylinder at $\mathrm{Re}_\infty = 100, 1000$ and 3000 are given in detail. For $\mathrm{Re} = 3 \times 10^3$, the calculated flow structures are in excellent agreement with the experimental results given by Bouard & Coutanceau (1980). In addition some new features of the complex flow structure at long times have been discovered for the first time, using a small interior domain, a second-order accurate scheme and very small mesh size. The calculated results show that in the near wake there are three kinds of vortex structures

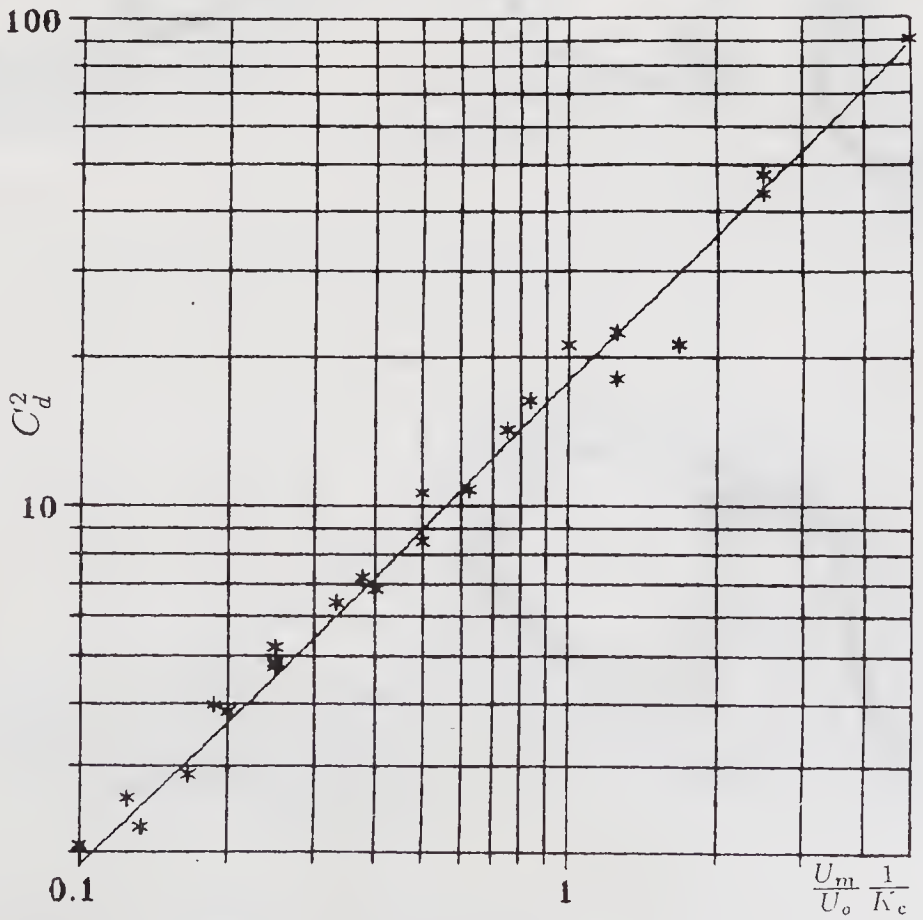

Figure 7. C_d^2 vs(U_m/U_0)/KC for a flat plate in steady-harmonic flow.

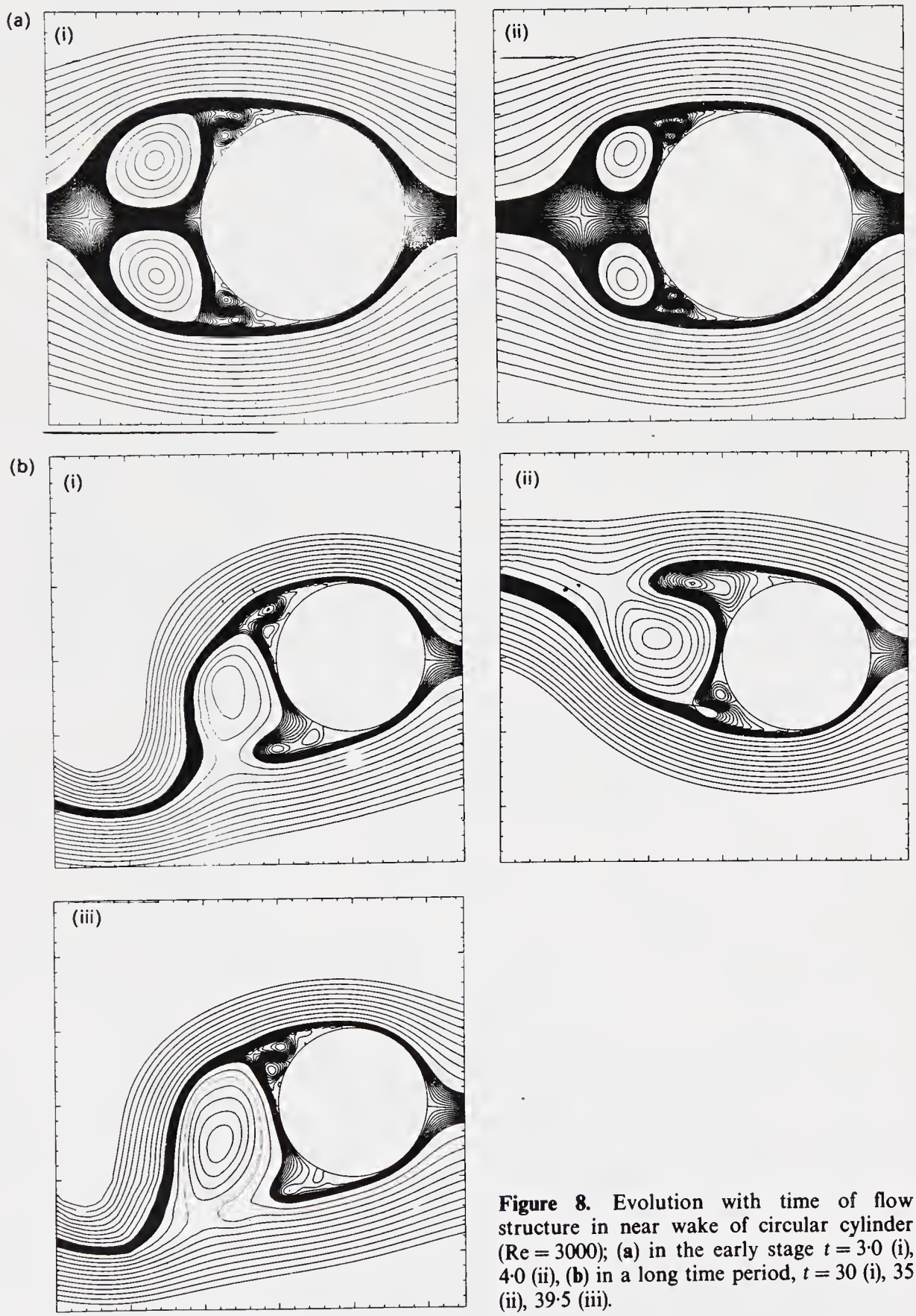

Figure 8. Evolution with time of flow structure in near wake of circular cylinder (Re = 3000); (**a**) in the early stage $t = 3{\cdot}0$ (i), 4·0 (ii), (**b**) in a long time period, $t = 30$ (i), 35 (ii), 39·5 (iii).

with different scales, i.e. the primary vortex with a scale of $O(R)$, the secondary vortices generated in the vicinity of the cylinder surface with a small scale of $O(\sqrt{v})$, and further secondary vortices near the separated shear layer, with a variable scale, which are similar to the results given by Braza *et al* (1986). Our results exhibit detailed interaction processes among these vortices, such as the growth and merging of secondary vortices forming finally a new primary vortex. Results also show the periodic generation and disappearance of secondary vortices near the body surface. Figures 8a and b show some examples of the evolution of vortex structure in the near wake in the early stages and over long time periods of the flow respectively. The calculated flow features, such as the separation angles, the radial velocity component behind the cylinder, the drag and the Strouhal numbers, are compared with many previous measurements and pure numerical solutions of the N–S equations (e.g. Ta Phuoc Loc & Bouard 1985), respectively, and satisfactory agreement is obtained. The numerical simulation of separated flow about the cylinder in steady flow at high Reynolds number and with harmonically oscillatory oncoming flow at different KC and β parameters has also been carried out. The instability phenomenon of flow structure containing multiple small-scale vortices in the vicinity of the cylinder surface is simulated, the vorticity distribution near the cylinder and the force on the cylinder are obtained and compared with some previous results from Bouard & Coutanceau (1980) and Obasaju *et al* (1988) respectively. Our results also show that the present method has the advantage of the finite-difference method for the solution of N–S equations in accurately predicting the fine structure of the flow field, as well as the advantage of the vortex method in efficiently computing the global characteristics of the separated flow. Moreover, it saves computer time.

4. Three-dimensional evolution of vortex structure and the early features of the coherent structure behind a 2-D circular cylinder

In this section, the mechanism and dynamic process for the three-dimensional evolution of Kármán vortices and vortex filaments in the braid regions, and the early features of turbulent structure in the wake behind a circular cylinder at moderate and high Reynolds numbers, are studied numerically (Ling *et al* 1992a; Ling & Wu 1992). The vortex filaments in the wake flow field are tracked by the inviscid vortex dynamics and the localized-induction approximation (LIA) method. The time-averaged velocity field of the wake, which can be obtained from experimental measurements or simulated numerically by disposing concentrated vortices, and the Kármán vortex street flow field, are considered as two kinds of the background flow. The interaction among the Kármán vortices is considered in the calculation.

The results show that the Kármán vortex and the vortex filament in the braid region have spanwise instability. Through the interaction between the self-induced motion and the background flow, the initial Kármán vortex in the time-averaged velocity field evolves into a special configuration akin to a "horseshoe-like" vortex (in the inclined plane) in the topological structure of the vorticity field. The upper and lower "horseshoe" vortices lie respectively on planes at approximately 45° and 135° to the x-z plane (x is the streamwise direction and z is the spanwise direction). Figure 9a shows examples of evolution with time of the Kármán vortices. An initial spanwise vortex filament at the saddle point of the braid region is turned gradually to the plane of the principal strain and is stretched. Eventually this vortex filament

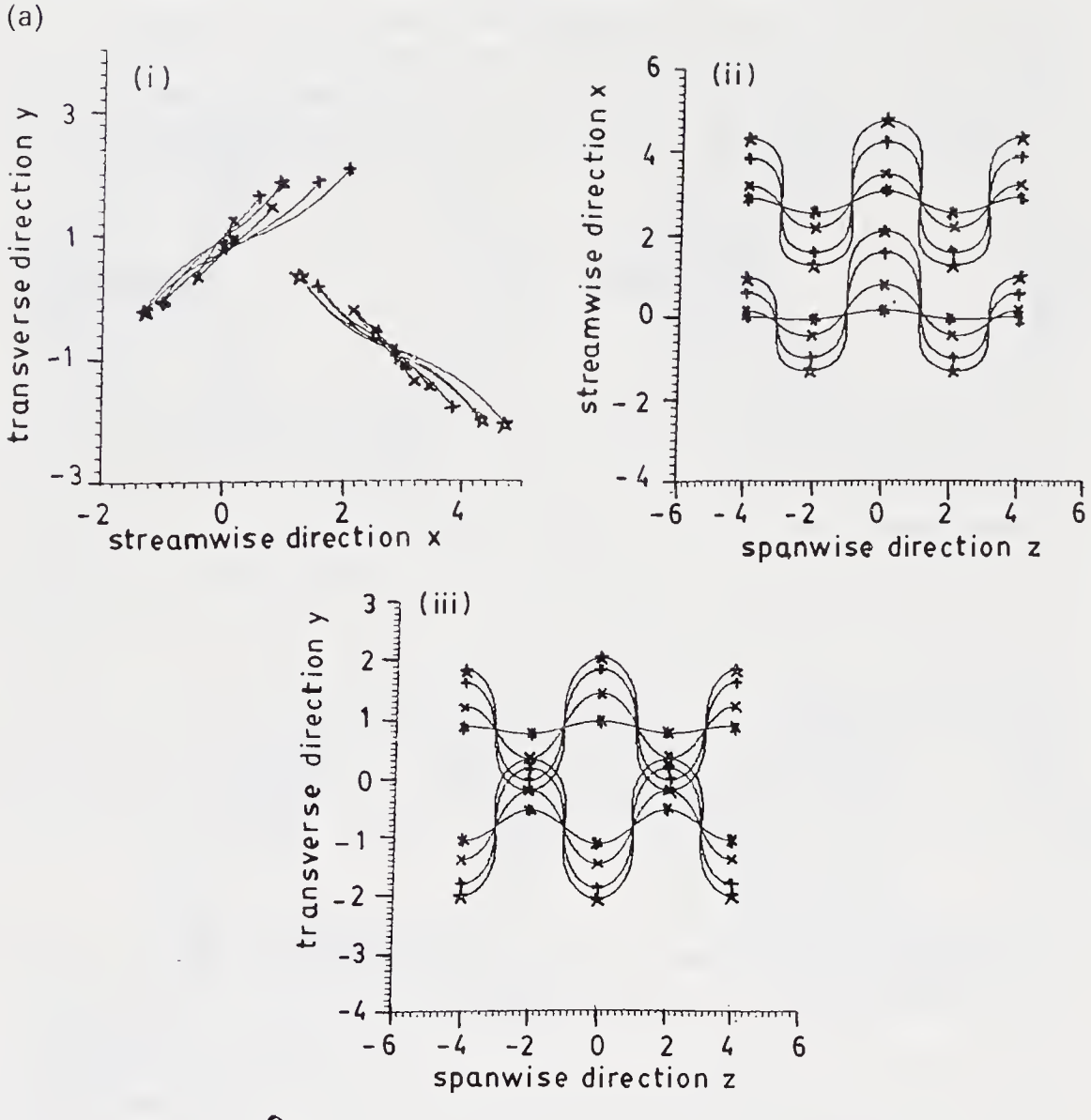

Figure 9. (**a**) Three-dimensional evolution with time of Kármán vortex filaments. Initial disturbance angle $\theta = 0°$; $t = 10$ (∗), 12(×), 14(+), and 15(☆). (i) Side, (ii) top, and (iii) end views. (**b**) Spatial configuration of the evolved vortex filaments in two consecutive braid regions.

connects with two consecutive Kármán vortices and forms a closed vortex loop. The alternating sign vortex loops in two consecutive braid regions are all aligned in the streamwise direction. Depending on the orientation of the initial disturbance, the closed vortex loops along the spanwise direction show either a symmetric or an asymmetric configuration. Figure 9b shows the spatial configuration of the evolved vortex filaments in two consecutive braid regions and the closed vortex loops for the asymmetric configuration. Our calculations present the temporal and spatial processes for the reorientation and the redistribution of the initial spanwise vorticity field, and the streamwise vorticity arises from natural instability. It demonstrates that the deformation and stretching of Kármán vortices and the vortex filaments in the braid region lead to three-dimensional vortex systems which consist of spatial large scale "horseshoe" vortices and three-dimensional small scale vortex loops. They exhibit the early features of the coherent structure of turbulent flow in wake development. The mechanism of the formation of 3-D structure based on present results is different than that in the numerical model of Okubo *et al* (1988), where a 3-D structure is formed only by deformation of Kármán vortices, but is akin to the suggestion of Williamson (1988) where the braid region effect is stressed. However, the present results are, in some aspects, in agreement with the previous experimental flow visualization. The calculated global features of the structures are not related to the orientation of the initial small disturbance.

This study was supported by the National Natural Science Foundation of China and the Laboratory for Nonlinear Mechanics, Institute of Mechanics, Chinese Academy of Sciences, as well as by the National Basic Research project "Nonlinear Science".

References

Bouard R, Coutanceau M 1980 The early stage of development of the wake behind an impulsively started cylinder for $40 < Re < 10^4$. *J. Fluid Mech.* 101: 583–608

Bradbury L J S 1976 Measurements with a pulsed-wire and a hot-wire anemometer in highly turbulent wake of a normal flat plate. *J. Fluid Mech.* 77: 493–497

Braza M, Chassaing P, Minh H H 1986 Numerical study and physical analysis of the pressure and velocity fields in the near wake of a circular cylinder. *J. Fluid Mech.* 165: 79–130

Chein R, Chung J N 1988 Discrete-vortex simulation of flow over inclined and normal plates. *Comput. Fluids* 16: 405–427

Keulegan C H, Carpenter L H 1958 Forces on cylinders and plates in an oscillating fluid. *J. Res. Natl. Bur. Stand.* 60: 323–339

Kiya M, Arie M 1980 Discrete-vortex simulation of unsteady separated flow behind a nearly normal plate. *Bull. JSME* 23: 1451–1458

Lian W 1980 A numerical study of two dimensional separated flow past bluff bodies at moderate KC numbers. *Appl. Ocean Res.* 10: 114–119

Ling G C, Guo L, Wu Z B, Ma H Y 1992a Preliminary study of the three-dimensional deformation of the vortex in Karman vortex street. *Acta Aerodyn. Sin.* 10: 90–97 (in Chinese)

Ling G C, Ling G P, Wang Y P 1992b Domain decomposition hybrid method for numerical simulation of bluff body flows. *Sci. China (Sci. Sin)* A35: 977–990 (No. 1, pp. 70–79, in Chinese)

Ling G C, Liu G H 1992 Flow structures and force characteristics for flat plate in oscillatory flows with KC number from 2 to 40 and in combined flows. *Acta Mech. Sin.* 8: 35–43

Ling G, Luo C M 1991 Investigations of wake flows of a flat plate in steady, oscillatory and combined flows. *Acta Mech. Sin.* 7: 21–30

Ling G C, Wu Z B 1992 Numerical study on the three-dimensional evolution of the vortex and the early features of coherent structure in the wake behind a circular cylinder. *Proc. Int. Conf. on Fluid Mechanics and Theoretical Physics*, June, Beijing, China, pp. 85–86

Obasaju E D, Bearman P W, Graham J M R 1988 A study of forces, circulation and vortex patterns around a circular cylinder in oscillating flow. *J. Fluid. Mech.* 196: 467–494

Okubo M, Yamane R, Oshima S 1988 Coherent structure in the turbulent wake behind a circular cylinder. 2. Numerical simulation using the vortex filament model. *Fluid Dyn. Res.* 4: 39–46

Ongoren A, Rockwell D 1988 Flow structure from an oscillating cylinder. *J. Fluid Mech.* 191: 197–223, 225–245

Sarpkaya T 1986 Force on a circular cylinder in viscous oscillatory flow at low Keulegan–Carpenter numbers. *J. Fluid Mech.* 165: 61–71

Ta Phuoc Loc, Bouard R 1985 Numerical solution of the early stage of the unsteady viscous flow around a circular cylinder: a comparison with experimental visualization and measurements. *J. Fluid Mech.* 160: 93–117

Williamson C H K 1988 The existence of two stages in the transition to three dimensionality of a cylinder wake. *Phys. Fluids* 31: 3165–3168

Williamson C H K 1992 The natural and forced formation of spot-like 'vortex dislocations' in the transition of a wake. *J. Fluid Mech.* 243: 393–442

State-of-the-art in research on Mach reflection of shock waves

KAZUYOSHI TAKAYAMA[1] and GABI BEN-DOR[2]

[1]Institute of Fluid Science, Tohoku University, 2-1-1 Katahira, Aoba Sendai, Japan 982-02
[2]Department of Mechanical Engineering, Ben-Gurion University of the Negev, Beer Sheva, Israel

Abstract. Reflected shock transition from Mach to regular reflection over wedges and state-of-the-art of Mach reflection research are presented. Examples of shock wave reflection from multiple wedges and curved wedges are given in conjunction with the Mach reflection research.

Keywords. Mach reflection; regular reflection; von Neumann–Mach reflection.

1. Introduction

Ernst Mach was the first to visualize not only a shock wave generated around a flying bullet but also observe shock-wave interactions over a sooted glass plate, which later proved, although indirectly, the existence of what we now call a Mach reflection. In this sense, scientists who are working in flow visualization of shock wave phenomena and try to study Mach reflection may be called students of Ernst Mach.

Figure 1 shows a reproduction of Mach's experiment (Reichenbach 1985) in which two electrodes were simultaneously discharged on a sooted glass plate. Regions exposed to high pressures and high particle velocities behind the spark-generated shock waves appear white, since soot on the glass plate is removed. Clear V-shapes, later called Mach-V, are the first evidence of irregular shock reflection and are now called Mach reflection (Courant & Friedrichs 1948), that is, when two shock waves generated by the electrical discharges interact, the mutual reflection is at first regular, and later turns into Mach reflection. In the region where Mach reflection appears, vortices emanating from the triple point of the Mach reflection scratch the sooted glass surface and remove the soot.

Mach and regular reflections are typical nonlinear gas-dynamic phenomena. Although recent comprehensive overviews concerning transition between Mach and regular shock reflections explain the physics of shock wave reflection (Ben-Dor 1991; Dewey 1992, pp. 113–120), there are still important problems left unsolved (Ben-Dor & Takayama 1992). This paper describes the state-of-the-art of Mach reflection mainly from the point of view of optical flow visualization studies of reflection of shock waves in shock tubes. Experiments were conducted in a 60 mm × 150 mm cross

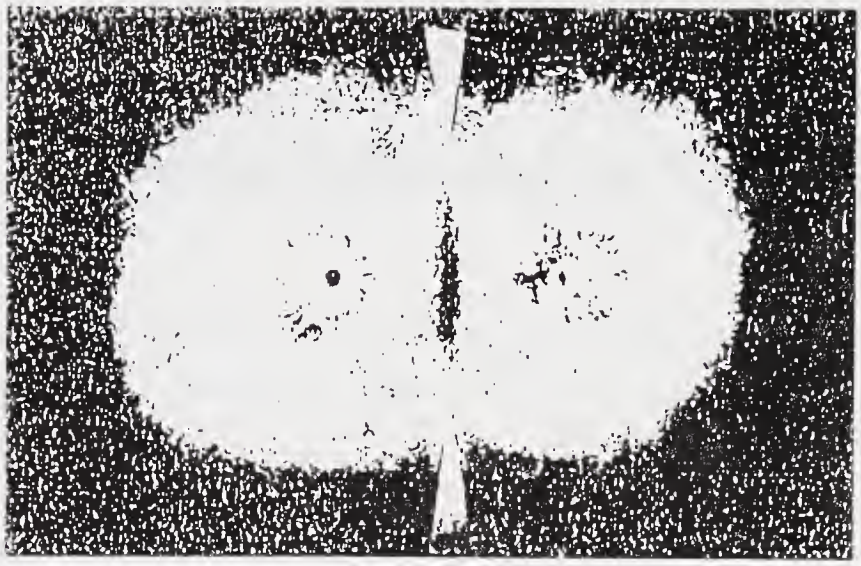

Figure 1. Mach-V (courtesy of Dr H Reichenbach).

sectional shock tube for shock Mach numbers ranging from 1·1 to 2·3 in air and for strong shock waves in polytropic gases.

2. Experiments

2.1 *Shock tube*

Figure 2 presents a schematic diagram of a shock tube and a holographic interferometric optical arrangement. A pressure-driven 60 mm × 150 mm cross-sectional shock tube was used. The test section had a field of view of 150 mm × 250 mm, in which a movable wedge model was installed. The shock tube had a 150 mm dia high pressure chamber 2 m in length and a transitional area change section which connected a 150 mm dia circular diaphragm section to a 60 mm × 150 mm cross-sectional low pressure channel. This transitional section caused negligible effects on shock formation and propagation along the low pressure channel. Diaphragms were Mylar films of 0·025 to 0·18 mm thickness. Driver gases were nitrogen or helium. Shock Mach numbers ranged from 1·1 to 2·3 in air, from 2·0 to 5·0 in CO_2 and 7·8 in SF_6. Shock Mach numbers were measured by using two pressure transducers, Kistler Model 603B, which were installed just ahead of the test section with a 250 mm separation. Good repeatability of a series of shock tube experiments was obtained. Although the test section of the shock tube was located 4·5 m from the diaphragm section, attenuation and deceleration of the shock waves at the test section were negligible.

2.2 *Holographic interferometry (Takayama 1983)*

A holographic ruby laser, Apollo Laser Inc. 22HD, with 2 J/ pulse and pulse duration of 25 ns was the light source. The ruby laser (RL) was always operated in the TEM_{00} mode. Often, without using double pulse operations, the RL was repeatedly operated twice at approximately 40 second intervals. A first exposure was carried out before the passage of the shock wave and a second exposure was triggered by the output

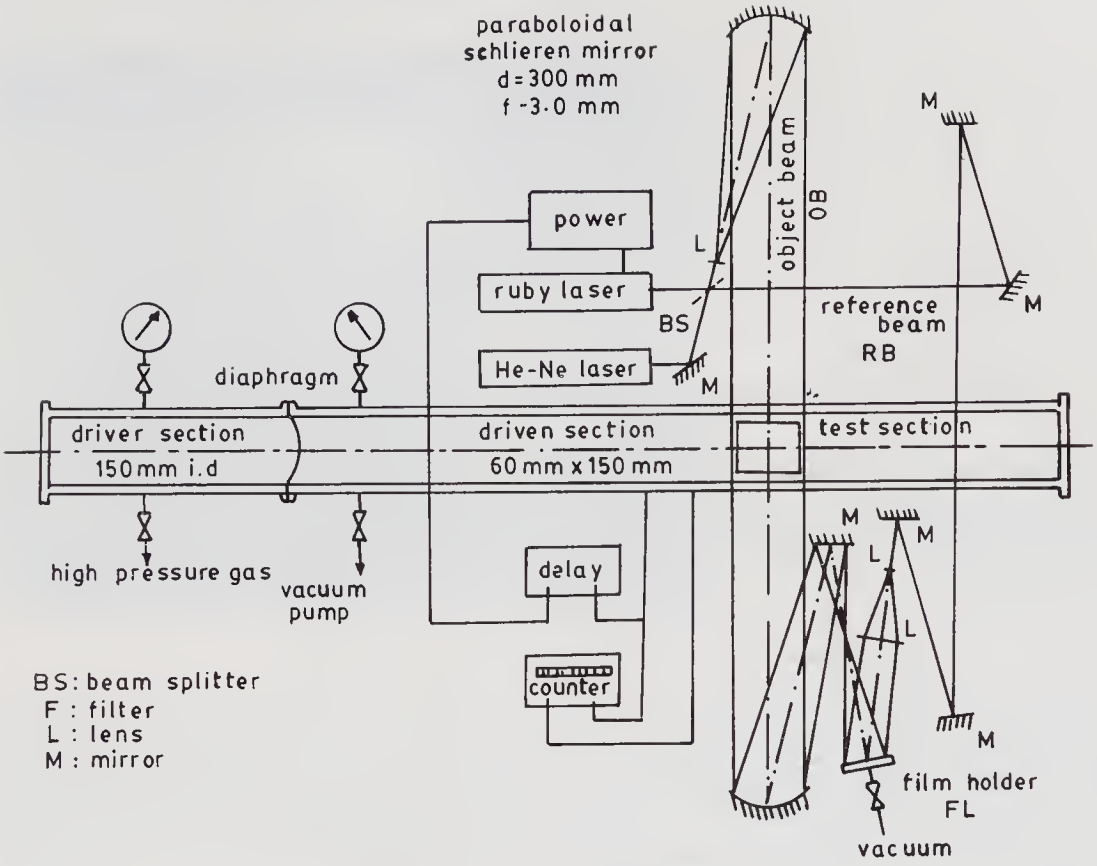

Figure 2. Experiment setup.

signal of one of the pressure transducers via a delay controller when the shock wave arrived at a particular location of the test section.

The optical arrangement in figure 2 is self-explanatory. The ruby laser beam was split into an object beam (OB) and a reference beam (RB) using a 6:4 beam splitter (BS) and 60% of the ruby laser light was directed to the object beam. A pair of paraboloidal schlieren mirrors, of 300 mm dia and 3,000 mm focal length, was used. The reference beam, which was transmitted to a film holder (FL) by plane mirrors and collimated by a plano-convex lens on the holder was superimposed with the object beam on the holder. The difference in pathlengths between the object and reference beams was adjusted, by using plane mirrors (M), within not more than a few centimetres. Images of the shock waves, caused by change of refractive index associated with local density variation across the shock waves, were focused on holo-films by using a relay lens. Agfa 10E75 100 mm × 125 mm sheet films were used, which were placed on the film holder. An argon ion laser of 543·5 nm wavelength was used for reconstruction.

3. Mach reflection

When a plane shock propagates over a wedge, either Mach or regular reflection occurs depending on the shock strength and wedge angle. Figure 3a illustrates a Mach reflection (MR) and figure 3b, a regular reflection (RR). An incident shock wave propagating over a wedge is defined by *i*, a reflected shock from the wedge by *r*, and a third shock wave which is perpendicular to the wedge is a Mach shock or Mach

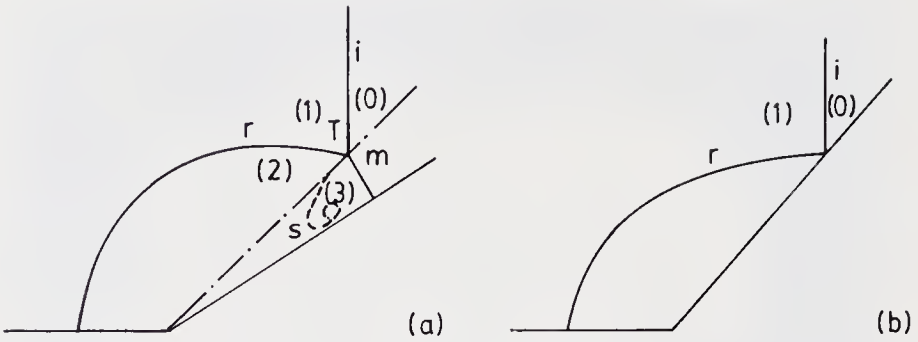

Figure 3. Reflection of shock wave. (**a**) Mach reflection, (**b**) regular reflection.

stem *m*. A slip line divides a region behind *r* from that behind *m*. The slip line is a contact discontinuity along which the direction of the particle velocity vectors is identical and across which the pressure is constant but the density and temperature are different.

3.1 *von Neumann–Mach reflection* (NMR) (*Sasoh et al 1992*)

When a plane and relatively weak shock is disturbed in such a way that shock waves pass over a wedge with a small wedge angle or over any slender obstacles or are caught up by a weak flow non-uniformity from behind, the resulting shock configuration would be either continuously curved or discontinuously bent depending on the intensity of flow non-uniformities.

Shock waves can bend continuously against weak flow non-uniformities which are commonly seen in supersonic flows. When a shock wave propagates over wedges with a relatively small wedge angle, then the particle flow vector over the wedge surface would be slightly deflected from the uniform flow direction. Accordingly the disturbance caused by this flow non-uniformity is weak so that the incident shock wave *i* is slightly deformed by being caught up with this disturbance and a resulting Mach reflection pattern appears to be continuous and never shows a discontinuous triple point.

Figure 4 presents a double exposure holographic interferogram for shock Mach number $M_s = 1{\cdot}15$ in air and wedge angle $\theta_w = 15°$. It is noted that the *i*, *r*, and *m* do not meet at a triple point in a way similar to that seen in figure 3a and appear to intersect continuously. The oblique shock relations (Courant & Friedrichs 1948; Ben-Dor 1991; Dewey 1992, pp. 113–120) which are valid only for distinct triple point structures, have no valid solutions to predict such a three-shock confluence of a gradually curved *m* and a very weak *r* as shown in figure 5. Birkhoff (1959) named this discrepancy between the oblique shock solutions and experimental observations the von Neumann paradox.

The von Neumann paradox is not, however, really paradoxical but is simply due to a lack of physical recognition that relatively weak shock waves, if exposed to weak disturbances from behind, could bend continuously. From this point of view, a wedge was recognized as a source of flow disturbance which could generate a controlled flow disturbance by changing the wedge angle. A local change of radius of curvature of *m* in figure 4 was measured using a spline function. The local radius of curvature *R* for $M_s = 1{\cdot}15$ and $\theta_w = 15°$ is shown in the ordinate in figure 5 against a distance *y* perpendicular to the wedge surface. *R* and *y* are normalized by the length of shock passage along the wedge surface *L*.

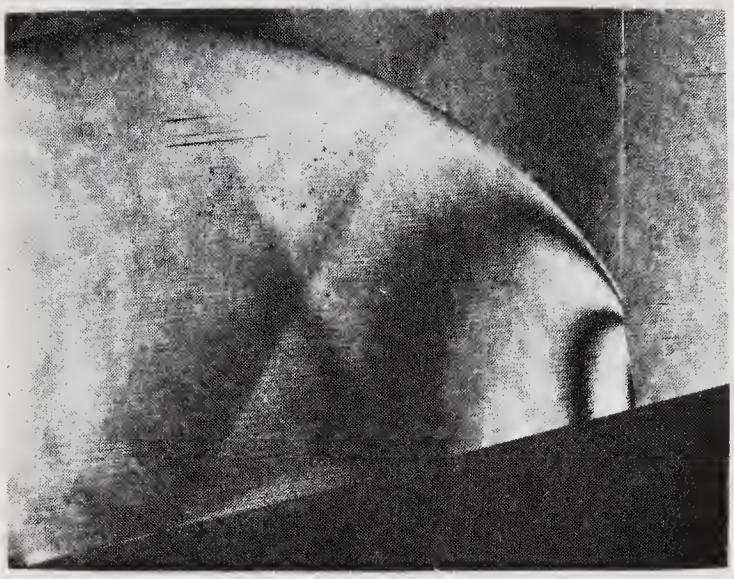

Figure 4. von Neumann–Mach reflection for $M_s = 1{\cdot}15$, $\theta_w = 15{\cdot}0°$.

The result of a numerical simulation (shown by a dashed line) is also compared with the experimental result. The numerical simulation was carried out using a total variation diminishing (TVD) finite difference scheme (Sasoh *et al* 1992) with 400 × 800 grid points in order to obtain finer spatial resolution of the shock configuration. The numerical and experimental results agreed qualitatively. It is found that the R/L curve is discontinuous at $y = P/L$ where the i and r first meet and is a maximum at $y = S/L$.

Since a shock configuration over straight wedges is self-similar, the trajectory angles of the P and S shown by χ are invariable. The χ of the P and S trajectories for various wedge angles are plotted in figure 6. The ordinate is the χ and the abscissa is the wedge angle. Filled circles and squares are for P and S trajectories, respectively, while open symbols present the results of the numerical simulation. P trajectory angles lie approximately on a line which crosses the ordinate at a glancing incidence angle (Ames Report 1953). S trajectory angles also lie on a line, which incidentally agrees with Whitham's (1980) shock-shock angle. At a certain wedge angle these empirical lines of P and S trajectory angles intersect. When this wedge angle is exceeded, the S

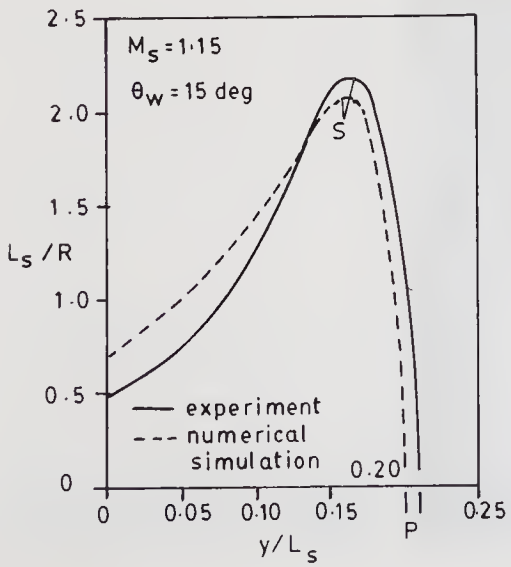

Figure 5. Local change of radius of curvature.

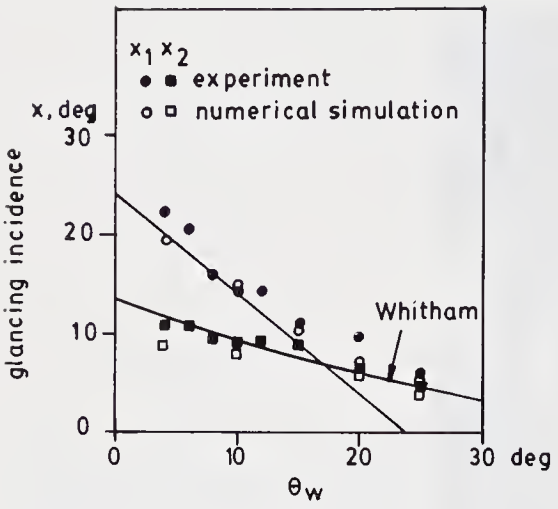

Figure 6. Trajectory angles vs wedge angles.

and P trajectory angles appear to merge with each other. Subsequently at this wedge angle an NMR is terminated to have a discontinuous three-shock confluence.

3.2 *Simple Mach reflection (SMR)*

Figure 7 shows a Mach reflection for $M_s = 1{\cdot}5$ in air and $\theta_w = 35{\cdot}0°$ in which i, r, and m discontinuously meet at a triple point. This Mach reflection pattern is known as a typical Mach reflection and can, in comparison with the complicated triple point structure of NMR, be better defined as a simple Mach reflection (SMR). In the SMR, a slip line (SL) originating from a triple point is visible, whereas in the case of the NMR the density change across an SL is so minute that it is not visible on an interferogram. The flow region (2) behind r in figure 3a is always subsonic so that r is always curved.

3.3 *Transitional Mach reflection (TMR)*

With increase of wedge angles, the particle velocity in region (2) increases with respect to the first triple point. Although in the case of SMR the flow in region (2) remains

Figure 7. Simple Mach reflection, $M_s = 1{\cdot}5$, $\theta_w = 35{\cdot}0°$.

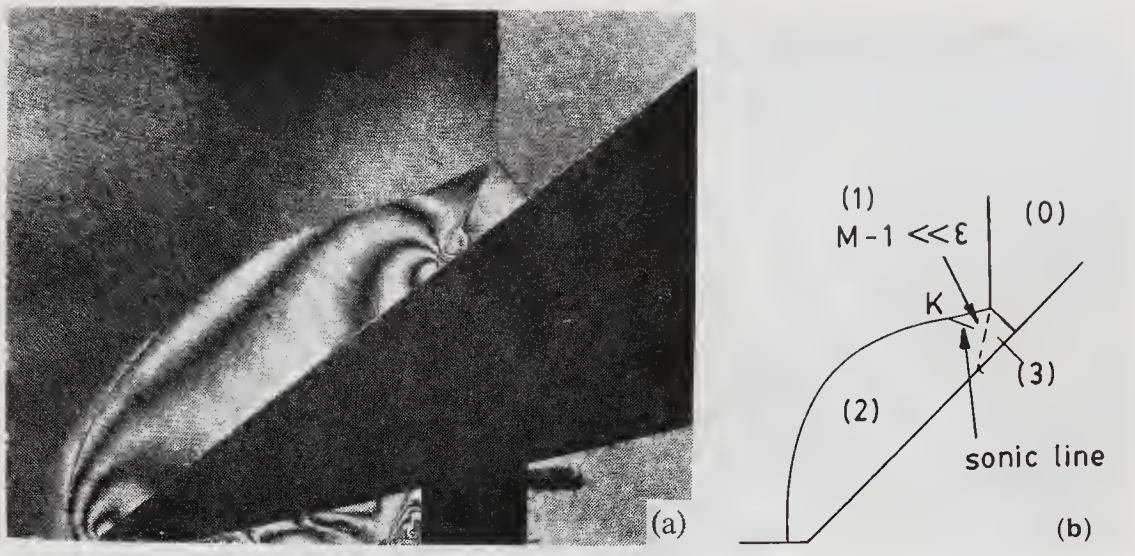

Figure 8. (**a**) Transitional Mach reflection, TMR, $M_s = 1{\cdot}98$, $\theta_w = 40{\cdot}0°$, (**b**) sketch of the kink.

subsonic, it now becomes sonic or transonic. The *r* appears to be straight in the vicinity of the triple point and is connected to a curved *r* behind which the flow is subsonic. The curved *r* is connected continuously to a straight part of the *r*. This reflected shock pattern, appearing only in a narrow range of wedge angles bridging SMR and DMR, is somehow transitional.

Figure 8 shows a transitional Mach reflection TMR: $M_s = 1{\cdot}98$ in air and $\theta_w = 40{\cdot}0°$. The local curvature of the intersection point of a straight and a curved *r* changes its sign and, subsequently, the intersection point appears to be a kink (Ben-Dor 1991). At the kink a bundle of compression waves or a sonic line is generated, which is weak and consequently invisible. Replacing the straight *r* with *i*, the curved *r* with *m*, and the bundle of compression waves with a reflected wave or reflected shock, a triple point can be replaced with a three-shock confluence of a very weak shock such as an NMR. Therefore, the TMR has a character analogous to an NMR (figure 8b).

3.4 *Double Mach reflection (DMR)*

With further increase of wedge angles, the flow in region (2) becomes supersonic with respect to the first triple point in the frame of reference of the trajectory angle of the first triple point. A bundle of compression waves or a sonic line in figure 8b becomes a second shock wave, which clearly divides a subsonic region (3) and a supersonic region (2). Figure 9 shows a typical DMR for $M_s = 2{\cdot}0$ in air and $\theta_w = 45{\cdot}0°$. A three-shock confluence of this shock wave and the existing curved and straight reflected shock waves create a discontinuous second triple point as illustrated in figure 9b.

The process of formation of the second triple point is analogous to that of shock transition from NMR to SMR. The second triple point appears when the reflected shock, which is replaced with *i* in figure 8b, is exposed to a relatively strong local flow non-uniformity, whereas, against a weak local flow non-uniformity, a kink appears on the *r*. Shock polar analysis (Ben-Dor 1991) and also numerical simulation (Glaz & Glass 1985) can correctly predict the formation of DMR for a wide range of test gases and shock Mach numbers.

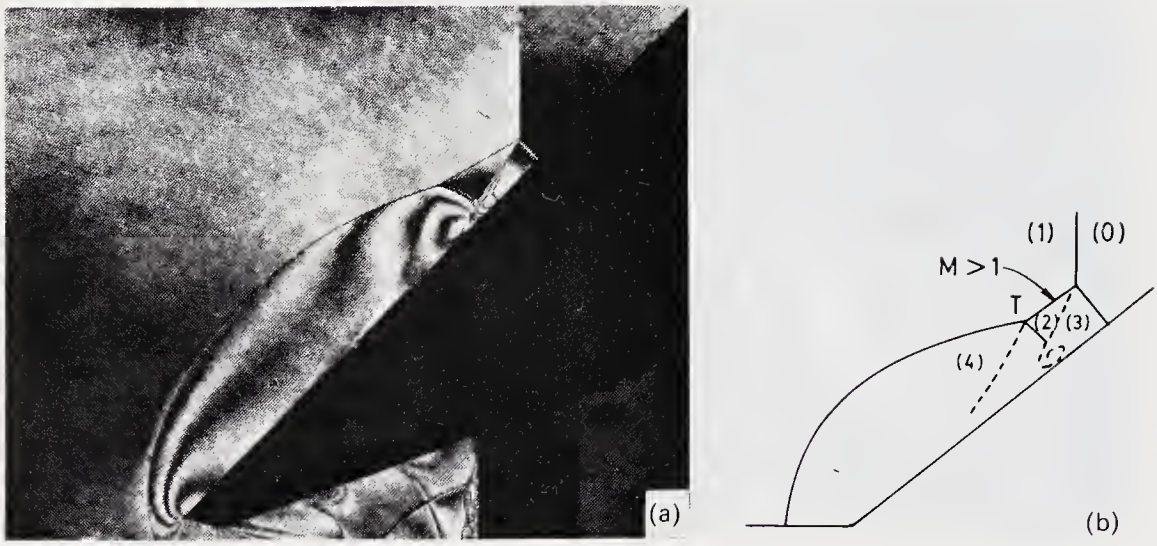

Figure 9. (**a**) Double Mach reflection, DMR, $M_s = 2{\cdot}0$, $\theta_w = 45{\cdot}0°$, (**b**) sketch of the second triple point.

3.4a *Terminal double Mach reflection*: In Mach reflections, as seen in figures 8 and 9, trajectory angles of the kink or the second triple point χ_2 are, for monoatomic and diatomic gases, larger than that of the first triple point χ_1. However, in polyatomic gases such as CO_2, depending upon a combination of shock Mach number and wedge angles, the second triple point trajectory angle χ_2 is not necessarily larger than χ_1 (Matsuo *et al* 1986).

Figure 10 shows an interferogram of this case: $M_s = 2{\cdot}0$ in CO_2 and $\theta_w = 30{\cdot}0°$. In polyatomic gases having specific heat ratios close to unity, χ_2 becomes even smaller than χ_1 for a wide range of wedge angles. At a wedge angle very close to the reflected shock transition angle from DMR to RR, the χ_2 appears to be nearly identical to the wedge angle. That is, the second triple point nearly touches the wedge surface. This peculiar reflected shock pattern is called a terminal double Mach reflection (TDMR) (Glass 1991). TDMR occur mostly for polyatomic gases having specific heat ratios close to unity. Across shock waves in polyatomic gases have larger than that of

Figure 10. Terminal double Mach reflection, $M_s = 2{\cdot}0$ in CO_2 and $\theta_w = 30{\cdot}0°$.

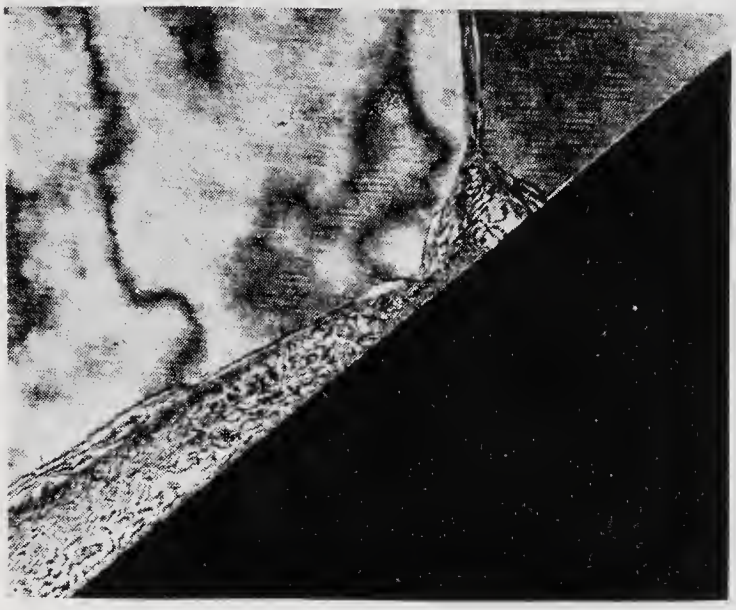

Figure 11. Terminal double Mach reflection, $M_s = 7{\cdot}8$ in SF_6 and $\theta_w = 45{\cdot}0°$.

monatomic or diatomic gases since the density ratios across strong shock waves is roughly proportional to the inverse of $\gamma - 1$. Accordingly, flow deflection angles across oblique shocks are even larger in polyatomic gases so that the angle of intersection of i and r finally becomes even larger than 90°.

Figure 11 shows a typical TDMR for $M_s = 7{\cdot}8$ in SF_6 of $\gamma = 1{\cdot}038$ and $\theta_w = 45{\cdot}0°$. Although, in this interferogram, the second triple point appears to be nearly on the wedge surface, it can never physically lie on the wedge surface.

4. Regular reflection (RR)

For a wedge angle larger than the critical transition angle θ_{crit}, the triple point of a Mach reflection MR merges on a wedge surface and a Mach reflection terminates to form a regular reflection RR. The configuration of RR is determined by analytically solving the Rankine–Hugoniot relations for oblique shock waves (Ben-Dor 1991).

4.1 *Sonic regular reflection (SoRR)*

The flow just behind a reflected shock of RR is sonic or supersonic with respect to a reflection point as shown in figure 3. If the flow behind the reflected shock is sonic or transonic, the reflected shock configuration in the vicinity of the reflection point is curved so that a corner signal can catch up very close to the reflection point. This is a sonic regular reflection SoRR. Figure 12 exhibits an interferogram of SoRR for $M_s = 1{\cdot}5$ in air and $\theta_w = 45{\cdot}0°$.

4.2 *Supersonic regular reflection (SuRR)*

When the wedge angle further increases, the flow in the vicinity of the reflection point becomes supersonic with respect to the reflection point. This is a supersonic regular reflection SuRR and the r close to the reflection point appears to be straight, which connects smoothly to the curved r. A sonic line is visible from the intersection point

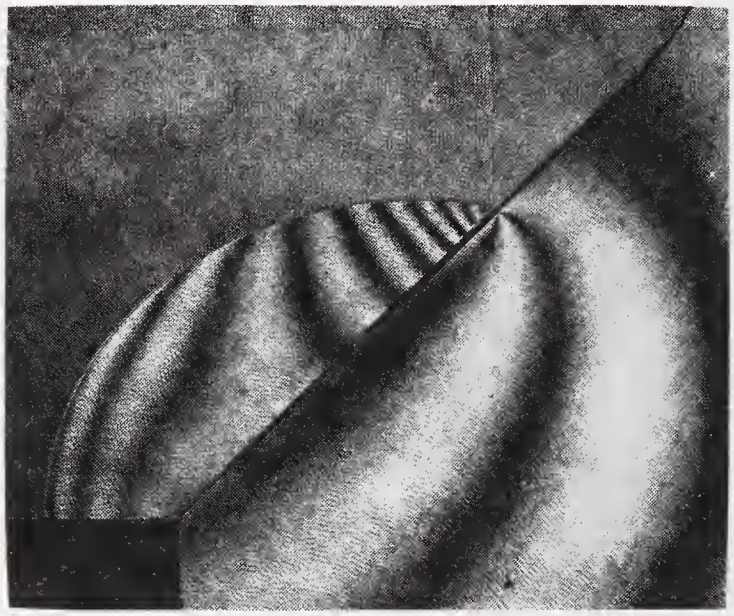

Figure 12. Sonic regular reflection, $M_s = 1{\cdot}5$, $\theta_w = 45{\cdot}0°$.

of the straight and curved *r*. Figure 13 shows a typical SuRR: $M_s = 2{\cdot}18$ in air and $\theta_w = 60{\cdot}0°$.

It is observed that when a plane shock propagates over a steep straight wedge with surface roughness, an SuRR appears. In this case, the curved reflected shock is attenuated due to the surface roughness. A reflected shock in the vicinity of the reflection point experiences only the local change of a wedge surface. The envelope of local reflected shocks appears to be straight showing an SuRR. However, at the point at which the curved and straight *r*'s intersect each other, a kink appears. Figure 14 shows a shadowgraph of a shock reflection over a wedge with a surface roughness for $M_s = 1{\cdot}5$ in air and $\theta_w = 45{\cdot}0°$. The shape of the surface roughness is saw-tooth.

5. Multiple wedges

The following three shock reflection patterns appear over double wedges in which two straight wedges are superimposed. A second wedge is placed on a first straight wedge to form a multiple wedge along which a wall changes discontinuously from

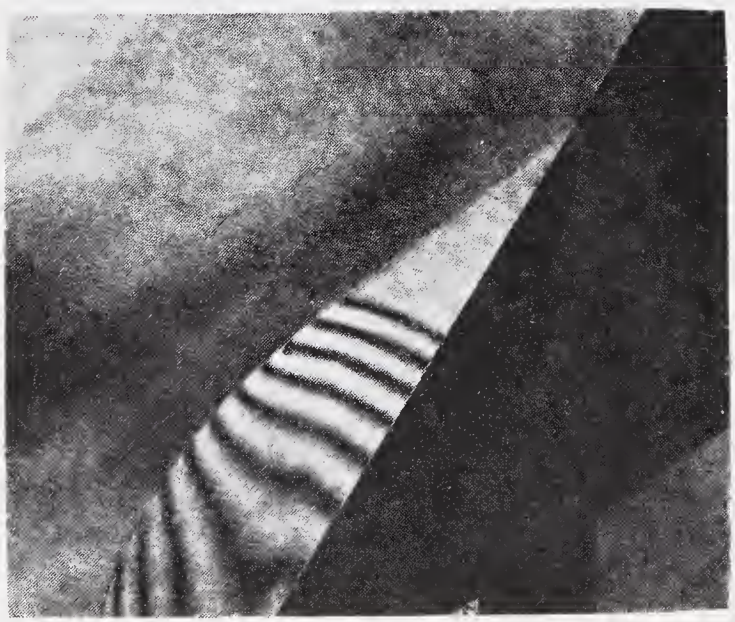

Figure 13. Supersonic regular reflection, $M_s = 2{\cdot}18$, $\theta_w = 60{\cdot}0°$.

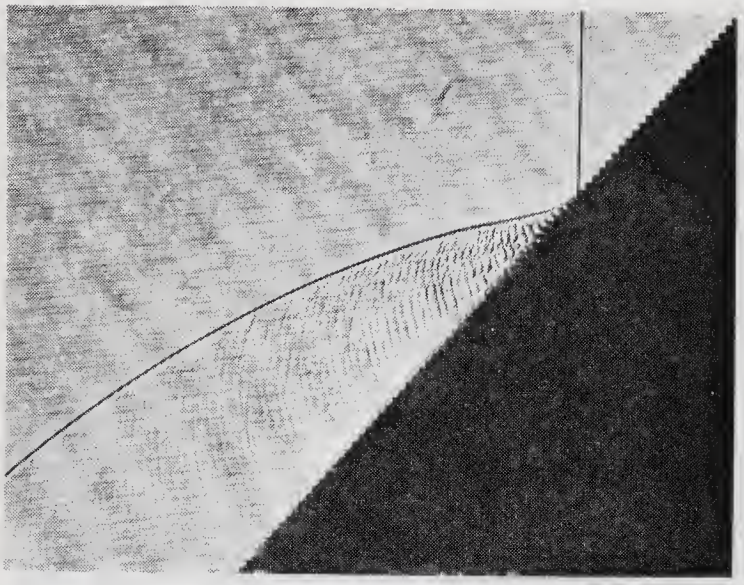

Figure 14. Shock reflection over a wedge with surface roughness for $M_s = 1{\cdot}5$ and $\theta_w = 45{\cdot}0°$.

the first to the second wedge surface. The behaviour of shock waves over these multiple wedges is similar to that over a concave circular wall.

Over the first straight wedge, the shock reflection is a Mach reflection. This Mach stem is successively reflected from the second wedge and a second Mach reflection appears locally. The triple point of the first Mach reflection is not disturbed until it encounters that of the second Mach reflection. Then these two triple points collide with each other and finally form the third triple point of a resulting third Mach reflection. The third Mach reflection patterns are, according to Courant & Friedrichs (1948) who noticed triple point trajectory angles of general shock reflections, divided into three types as shown in figure 15.

5.1 *Direct Mach reflection (DiMR)*

This is the case in which the third triple point is moving away from the wedge surface, and consequently, χ is positive, in figure 15a. This shock configuration is self-similar and is called a direct Mach reflection (DiMR). Figures 16a and b show sequential interferograms of $M_s = 2{\cdot}2$ in air and first and second wedge angles of $\theta_{1,2} = 16{\cdot}0°$ and $35{\cdot}0°$.

5.2 *Stationary Mach reflection (StMR)*

For a particular combination of M_s and the two wedge angles, the third triple point moves exactly parallel to the second wedge surface, i.e., $\chi = 0$ in figure 15b. The

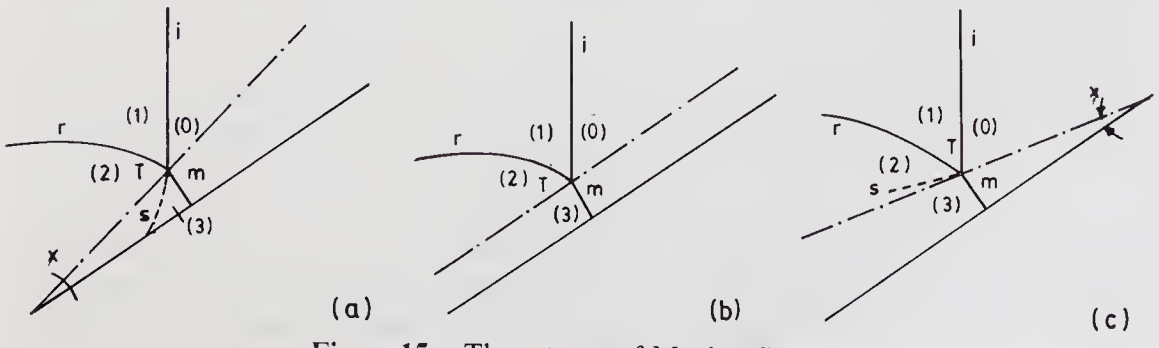

Figure 15. Three types of Mach reflection.

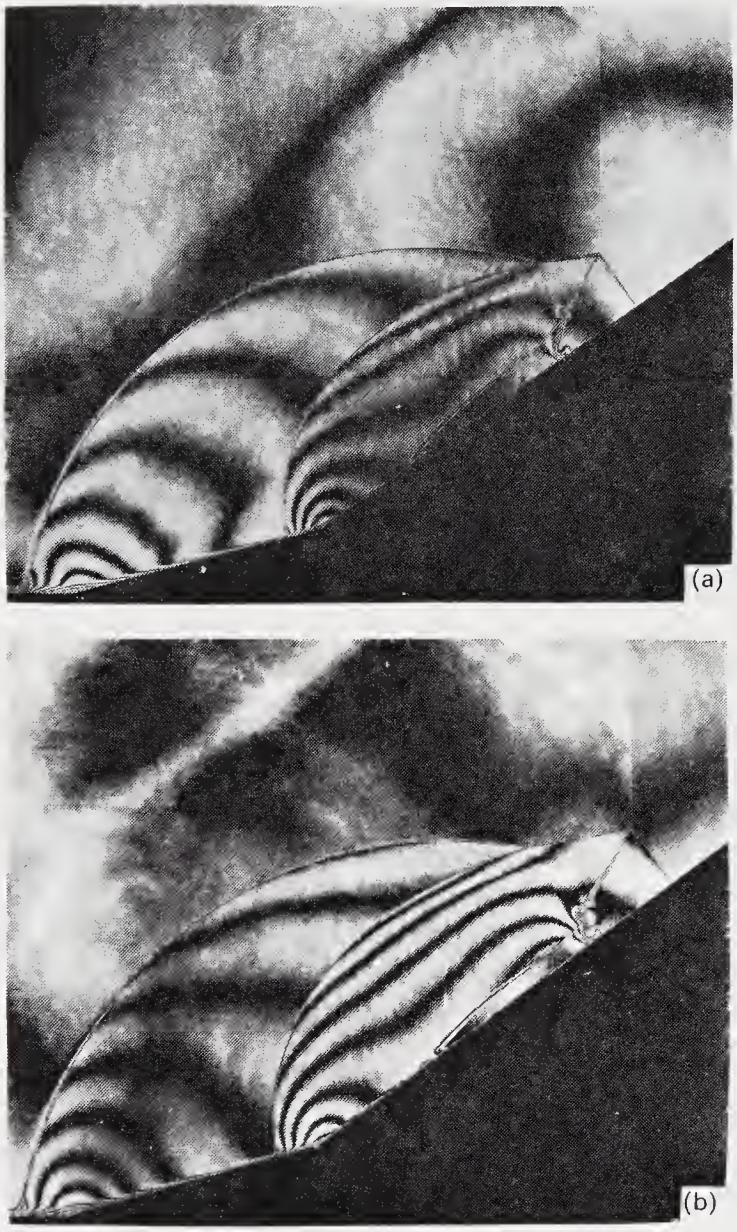

Figure 16. DiMR for $M_s = 2{\cdot}2$ and first and second wedge angles of $\theta_{1,2} = 16{\cdot}0°$ (**a**) and $35{\cdot}0°$ (**b**).

configuration of the third Mach reflection is invariable with lapse of time and is stationary. Consequently, it was named a stationary Mach reflection (StMR). Shock tube flows are in general quasi-stationary so that it is interesting to find that stationary Mach reflections exist in shock tube flows.

Figure 17 presents an StMR for $M_s = 1{\cdot}9$ in air and first and second wedge angles of $\theta_{1,2} = 15{\cdot}0°$ and $40{\cdot}0°$, respectively. The slip line of the third triple point is parallel to the second wedge. The behaviour of the slip line appears to be a mixing of two-layered gas flows having different temperatures and densities across the slip line. Figure 17 appears to be similar to a shadowgram of laminar mixing of a layered jet but a fine resolution of the density profile across the slip line is clearly observable. This is the advantage of using holographic interferometry for observing shock wave phenomena. Onset of instability along the slip line is quantitatively observed. Rolling-up of isopycnics is gradually strengthened along the slip line. However, in previous schlieren photographs or shadowgraphs, the rolling-up of isopycnics appeared to be a twisting rope which gradually increased in diameter.

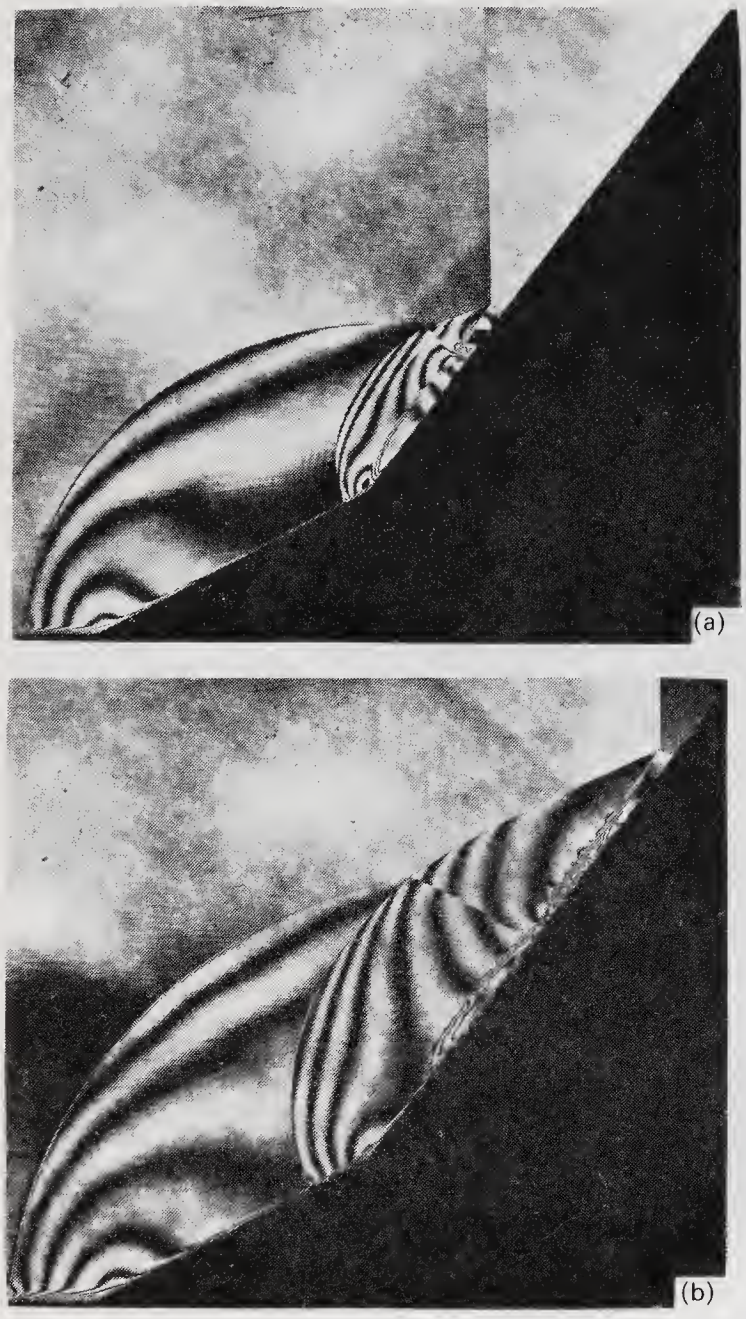

Figure 17. StMR for $M_s = 1{\cdot}9$ and first and second wedge angles of $\theta_{1,2} = 15{\cdot}0°$ (**a**) and $40{\cdot}0°$ (**b**).

5.3 *Inverse Mach reflection (InMR)*

For a larger second wedge angle, the third triple point finally collides with the second wedge and the third Mach reflection terminates. Consequently, the χ becomes negative. Disappearance of the third Mach reflection results in a regular reflection (figure 16c). The slip line initiated from the third triple point is maintained by a fourth triple point which successively follows the regular reflection. These wave interactions are truly non-stationary processes. This kind of reflection is called inverse Mach reflection (InMR) (Courant & Friedrichs 1948).

Figure 18 shows sequential interferograms for $M_s = 1{\cdot}8$ in air, and first and second wedge angles of $\theta_{1,2} = 15{\cdot}0°$ and $40{\cdot}0°$, respectively. The third triple point, after impinging on the second wedge surface, disappears and a regular reflection is created. The slip line of the third triple point, however, is succeeded by the fourth triple point

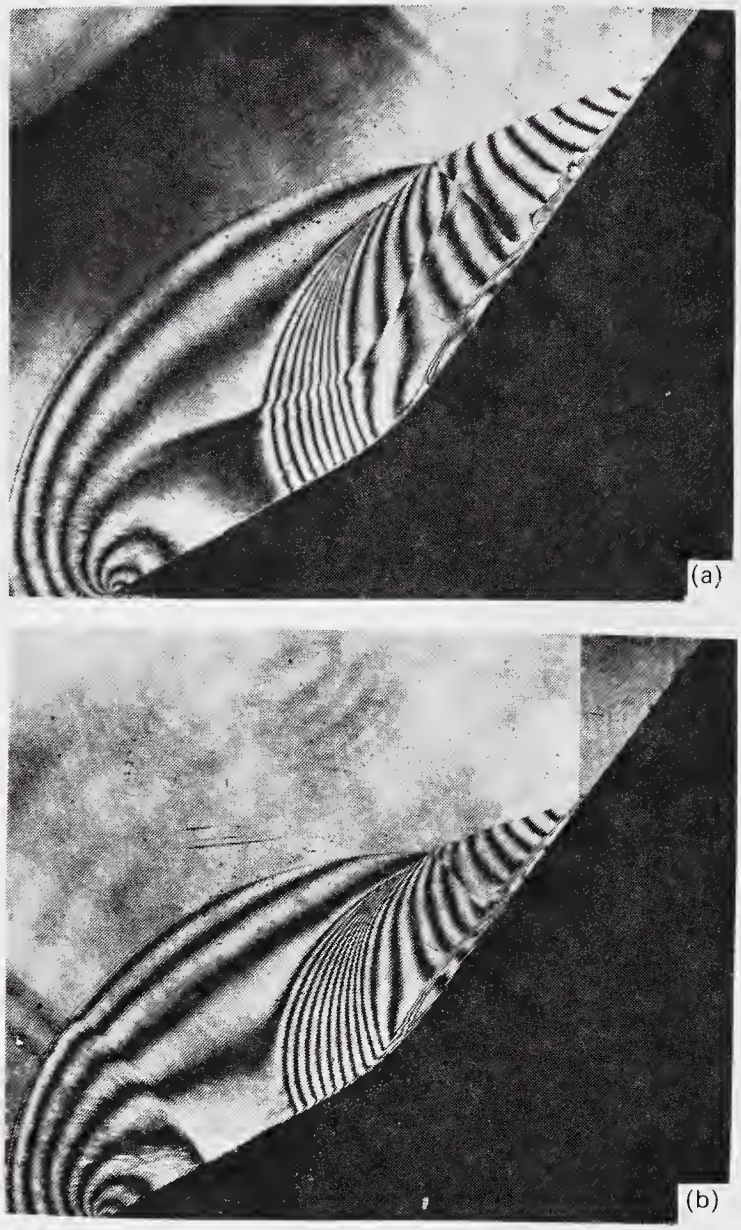

Figure 18. InMR for $M_s = 1{\cdot}8$ and first and second wedge angles of $\theta_{1,2} = 15{\cdot}0°$ **(a)** and $40{\cdot}0°$ **(b)**.

just behind the regular reflection. The entire process of InMR is analogous to that of shock reflection over a concave circular wall.

6. Shock transition over curved wedge (Takayama & Ben-Dor 1992)

All the above mentioned shock reflection patterns appear successively when a plane shock wave propagates along a concave wall whose local inclination angle increases continuously from 0° to 90°. Over a concave wedge with a glancing incidence angle, the shock reflection pattern is at first an NMR and becomes an SMR with increment of the wedge angle. Depending on the shock strength, the shock reflection pattern changes from SMR to TMR and DMR. Figure 19 presents sequential interferograms of shock propagation along a concave circular wedge: $M_s = 1{\cdot}25$ in air. An NMR appears for a small wall angle in figure 19a. The discontinuous triple point of the SMR appears for relatively large wall angle and a slip line becomes visible in figure 19b. These Mach reflections belong to a DiMR. With shock propagation, StMR and InMR

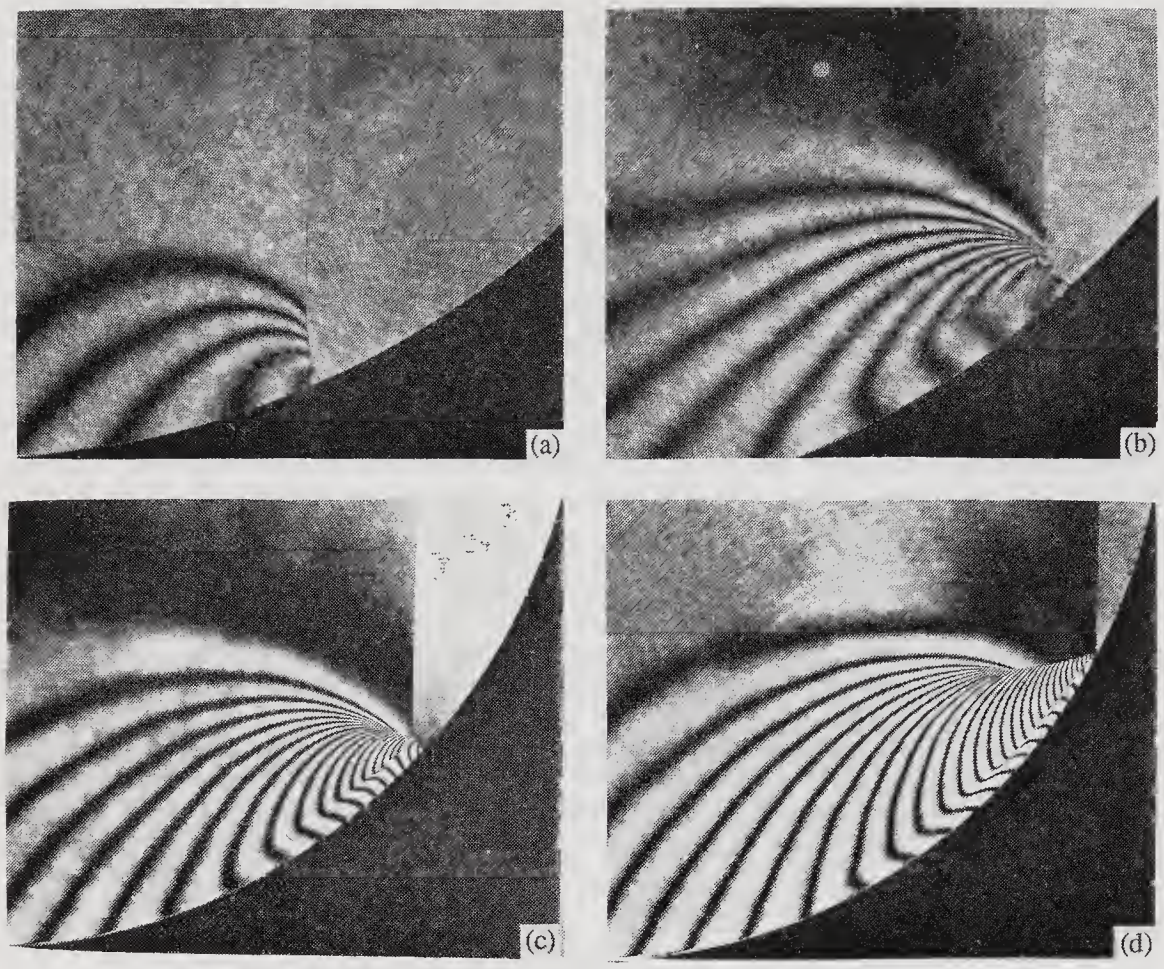

Figure 19. Sequential interferograms of shock propagation along a concave circular wedge: $M_s = 12{\cdot}5$. NMR appears for a small wall angle (**a**). Discontinuous triple point of the SMR appears for relatively large wall angle and a slip line becomes visible. These Mach reflections belong to a DiMR (**b**). With shock propagation StMR and InMR appear in (**c**) and (**d**), respectively.

successively appear in figures 19c and d. The reflected shock transition angle θ_{crit} over a concave wall is larger than that over a straight wedge.

7. Conclusions

The reflection of shock waves over wedges has been reviewed based on the experimental data obtained mainly by holographic interferometric optical flow visualization techniques. Patterns of the shock reflection over straight wedges were categorized, as already described in various publications, into types of Mach reflections such as von Neumann–Mach reflection (NMR), simple Mach reflection (SMR), transitional Mach reflection (TMR), double Mach reflection (DMR), and, in special cases – terminal Mach reflection TDMR, and regular reflections such as sonic regular reflection (SoRR) and supersonic regular reflection (SuRR). It is, however, emphasized that the von Neumann–Mach reflection appears when weak disturbances, which arc created by the wedges, catch up with a shock wave which is not necessarily very weak. When the disturbances are relatively strong, a discontinuous three-shock confluence, an SMR, appears. Evolution of shock wave reflections over a concave

circular-curved wall and multiple wedges successively follows these shock reflection patterns.

We wish to express our thanks to Professor Kuen-Shik Chang of the Korean Advanced Institute of Science and Technology for giving us the opportunity to present our recent research on reflection of shock waves. We also thank Professor A Sasoh and Mr O Onodera of the Institute of Fluid Science, Tohoku University, for their assistance in this research. We thank Mr. Nagoya for help with the paper. The present shock wave research has been supported by a Grant-in-Aid for Priority Area Shock Waves No. 03238104 offered by the Ministry of Education, Science, and Culture, Japan.

References

Ames Report 1953 Equations, tables and charts for compressible flow. Ames Aeronautical Laboratory, Rep. 1135

Ben Dor G 1991 *Shock wave reflection phenomena* (New York: Springer Verlag)

Ben-Dor G, Takayama K 1992 The phenomena of shock wave reflection -- Review of unsolved problems and future research needs. *Shock Waves* (to be published)

Birkhoff G 1959 *Hydrodynamics, a study in logic, fact and similitude* (Princeton, NJ: University Press)

Courant R, Friedrichs K O 1948 *Supersonic flow and shock waves* (New York: Wiley-Interscience)

Dewey J M 1992 Mach reflection research - Paradox and progress. *Shock Waves, Proc. 18th Int. Symp. on Shock Waves* (Heidelberg: Springer Verlag)

Glass I I 1991 Over forty years of continuous research at UTIAS on stationary flows and shock waves. *Shock Waves* 1: 75–86

Glaz H, Glass I I 1985 Numerical study of oblique shock wave reflections with experimental comparisons. *Proc. R. Soc. London* A398: 698–705

Matsuo K, Ikui T, Aoki T 1986 Investigations of Mach reflection of a shock wave. Pt. 4. *Bull. Jap. Soc. Mech. Eng.* 29: 434–438

Reichenbach H 1985 Contribution of E Mach to fluid mechanics. *Annu. Rev. Fluid Mech.* 15: 1–28

Sasoh A, Takayama K, Saito T 1992 A weak shock wave reflection over wedges. *Shock Waves* 2: 277–281

Takayama K 1983 Application of holographic interferometry to shock wave research. *Proc. SPIE* 389: 174–179

Takayama K, Ben-Dor G 1992 The phenomenon of shock wave reflection. *Shock Waves* 2: 211–224

Whitham G B 1980 *Linear and nonlinear waves* (New York: Wiley)

The fluid mechanics of phase change

P N SHANKAR

Computational & Theoretical Fluid Dynamics Division, National Aerospace Laboratories, Airport Road, Bangalore 560017, India

Abstract. The phenomena of evaporation and condensation are subject to the laws of fluid mechanics. While the usual continuum equations hold in the bulk of the vapour, the exchange processes near the interfaces have to be modelled more accurately by the laws of molecular dynamics. When an inert gas is present, the mass fluxes are diffusion-controlled and tend to be small; the fluxes are much greater in the kinetic-controlled pure vapour case. Strange phenomena, namely, jumps in the temperature and possible inversion in the temperature field, are predicted by the theory for the pure vapour case. While the jumps have been found experimentally, the whole phenomenon has yet to be fully understood and remains an interesting field for fluid mechanical investigations.

Keywords. Fluid mechanics; phase change; molecular gas dynamics; temperature jumps; temperature inversion.

1. The phase change problem

It is a remarkable fact that to this day the phenomena of evaporation and condensation are poorly understood from a fundamental point of view. This is because of the fact that, even though continuum fluid mechanics governs fluid transport over most of the field, the exchange processes near the liquid boundaries are molecular processes that are still poorly understood. The actual rates of evaporation can then be considered to be determined by the nature of the coupling between these fields. It is found that there still exist controversial, and apparently paradoxical, features in the phase change process that have yet to be resolved.

First let us look at the phenomenon qualitatively by considering a liquid in a closed beaker (figure 1) in equilibrium with its vapour. In this condition, the liquid and vapour temperatures have to be equal and the vapour pressure has to equal the saturation vapour pressure at that temperature. Although the two phases are in 'equilibrium', the phase boundary is really, in a sense, in a state of flux. Molecules are being ejected from the liquid surface into the vapour and vapour molecules are bombarding the liquid surface, which must under sufficient magnification appear to be ill-defined; the net flux of vapour will, however, be zero. This we call 'equilibrium'. Note that when an inert gas is present, the vapour molecules have to 'diffuse' past the inert gas molecules. Also, by continuity, the flux of inert gas molecules hitting

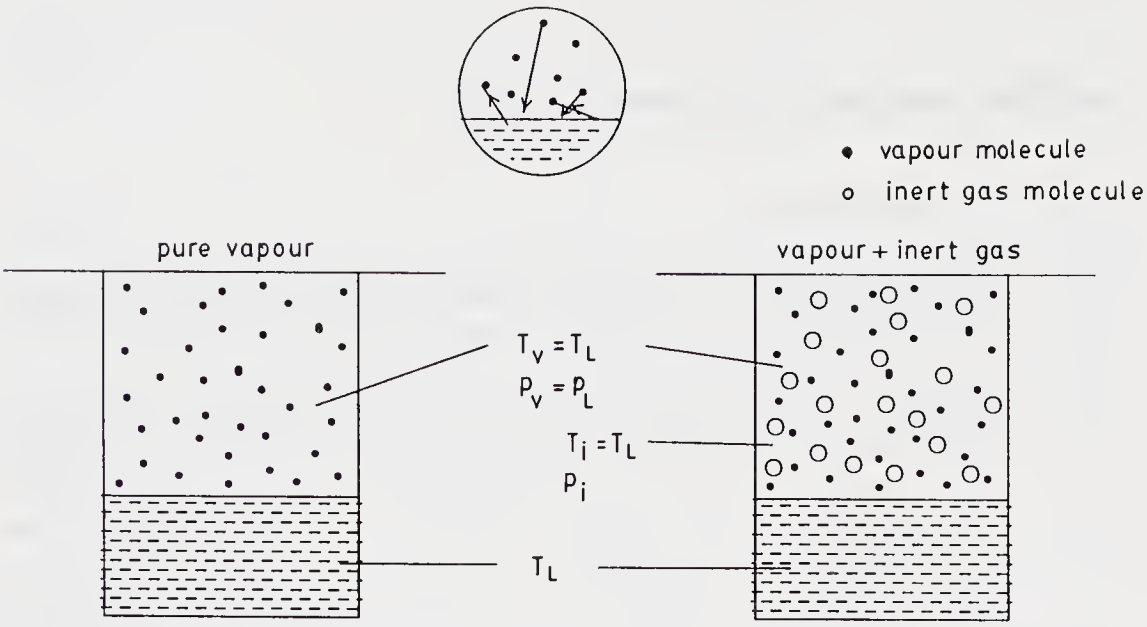

Figure 1. The equilibrium situation.

the liquid surface must be equal to the flux ejected by the liquid. Again, the nature of the boundary is, in reality, very complex. The 'non-equilibrium' situation occurs when $T_v \neq T_L$ or $p_v \neq p_L$ and a net flux of vapour either leaves the liquid (evaporation) or flows into it (condensation). The situations where the vapour is pure and where it is contaminated by an inert gas are quite different.

2. The gas mixture case

In some ways the gas mixture case (figure 2) is simpler to understand. This is because, generally, even a small quantity of the inert gas is sufficient to permit diffusion to dominate the phenomenon; and, diffusion being a relatively slow process, the fluxes are small. The earliest investigation of this situation is due to Maxwell (1890). If Γ_v is the total mass of vapour crossing the spherical surface of radius r, Maxwell wrote

$$\Gamma_v = 4\pi r^2 \dot{m}_v = -4\pi r^2 D_{vi}(\mathrm{d}\rho_i/\mathrm{d}r), \tag{1}$$

where D_{vi} is the diffusion coefficient, and integrated this, assuming $\rho_v(r = r_0) = \rho_L$, to obtain for the total mass flow

$$\Gamma_v = \Gamma_{v0} = 4\pi r_0 D_{vi}(\rho_L - \rho_{v\infty}). \tag{2}$$

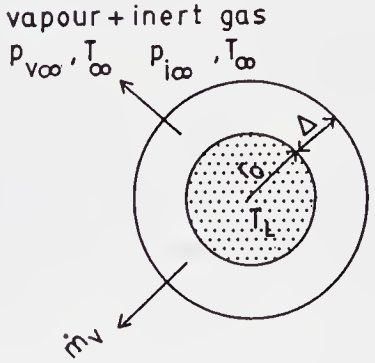

Figure 2. The gas-mixture case for a droplet.

This analysis is very crude because (i) it ignores the mean motion of the vapour–gas mixture, and (ii) the assumption that the vapour pressure at the droplet surface $p_v(r_0)$ is equal to saturation vapour pressure p_L is seriously in error. This is corrected (i) by taking into account the mean motion of the gas and vapour to conclude that

$$\Gamma_v = \Gamma_{v0}\{1 + (p_L + p_{v\infty})/[2(p_{v\infty} + p_{i\infty})]\}. \tag{3}$$

Objection (ii) is removed in an *ad hoc* manner. It is assumed that the continuum equations hold upto a distance Δ (of the order of the mean free path λ) from the drop; within this region transport is assumed to take place in a collisionless manner. With a few additional assumptions

$$\Gamma_v \simeq \Gamma_{v0}\{1 - [\Delta/(r_0 + \Delta)] + (D_{vi}/r_0\alpha_m)(2\pi/R_v T_L)^{1/2}\}^{-1} \tag{4}$$

where α_m is the mass accomodation coefficient. For a more satisfactory treatment, one has to deal with the Boltzmann equation over the whole field. This was done in Shankar (1970) using a moment method; the resulting formula reduced to a version of (4) in the continuum limit and to the correct free molecule limit in that case. See also Onishi (1986) for a more recent computation of the gas mixture case.

3. The pure vapour case

When there is no inert gas present to slow down the vapour molecules, the phenomenon is controlled by the kinetic processes close to the liquid–vapour interface. The boundary conditions in this, the more subtle case, are shown in figure 3 for the general unsteady, half-space problem. The complete vapour conditions ($p_{v\infty}$, $T_{v\infty}$ etc) are known far from the interface; but at the liquid surface only the temperature and pressure (T_L, p_L) of the molecules leaving the liquid are known. *That is the full distribution function (df) is known far from the liquid but only half the df is available at the liquid surface.*

The first person to correctly solve this problem was Marble (1969) who used a clever continuum analysis. He assumed that the continuum gas dynamic equations held in the main; near the liquid surface he patched on a Knudsen layer, where the

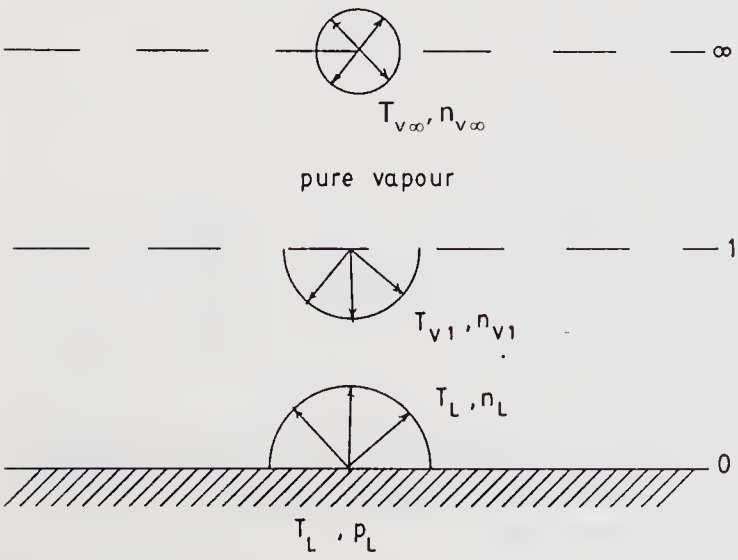

Figure 3. The boundary conditions for the pure vapour, plane, half-space problem – Maxwellians and half Maxwellians.

transport was kinetic. In this manner, for small deviations from equilibrium, he obtained for the mass flux

$$\dot{m}_v = 0{\cdot}145\rho_L(2\pi R_v T_L)^{1/2}\Delta p/p_0, \tag{5}$$

where $\Delta p = p_L - p_{v\infty}$. Note that this holds in the continuum limit; in the free molecule limit the mass flux is given by the Hertz–Knudsen formula (Hertz 1882; Knudsen 1915)

$$\dot{m}_v \simeq (1/2\pi)\rho_L(2\pi R_v T_L)(\Delta p/p_0 - \Delta T/2T_0). \tag{6}$$

A more rational approach to this problem was given in Shankar (1968) and Shankar & Marble (1971) where the Boltzmann equation was solved approximately for the whole field with the proper boundary conditions. In the free molecule limit the mass flux was shown to reduce to the Hertz–Knudsen formula. In the continuum limit one obtained

$$\begin{aligned}\dot{m}_v &= \rho_L(2\pi R_v T_L)^{1/2}\{(5/6\pi)^{1/2}/[(5/3) + (9\pi/8)(5/6\pi)^{1/2}]\}(\Delta p/p_0)\\ &\simeq 0{\cdot}148\rho_L(2\pi R_v T_L)^{1/2}(\Delta p/p_0),\end{aligned} \tag{7}$$

which shows that Marble's (1969) calculation was very good indeed. It should be emphasised that the fluxes given by (7) represent transport at speeds that are orders of magnitude larger than those obtaining under diffusion control.

4. The anomalous temperature distribution

It was Pao (1971) who first showed that there was something very strange about the gas dynamic field in the evaporating or condensing vapour. Consider the two-dimensional case of two plane liquid surfaces separated by a distance H. Pao (1971) pointed out that the vapour temperature would suffer large jumps at the interface; large enough, in fact, for the temperature gradient in the bulk of the fluid to oppose the applied temperature gradient. It may be mentioned that this curious result was implicit in Shankar (1968, 1970) and Shankar & Marble (1971) but the earlier investigators had failed to examine the temperature field.

In the linearized case, the temperature distribution is given approximately by

$$T(y) = T_{v0} + [(T_{v1} - T_{v0})/(\exp(H/\delta) - 1)](\exp(y/\delta) - 1), \tag{8a}$$

$$T_{L0} - T_{v0} = T_{v1} - T_{L1} = (\beta + 1)\Delta T_L/9 = (\beta + 1)(T_{L0} - T_{L1})/9 = K\Delta T_L, \tag{8b}$$

$$\delta = k_v/\dot{m}_v c_{pv}, \quad (\beta + 1) \simeq L/R_v T_{L0}, \tag{8c}$$

where 0 and 1 refer to the hot and cold liquid planes, say, and L is the latent heat of vaporization. Note that (8b) implies that the vapour is colder than the liquid at the hot interface and hotter than the liquid at the cold interface. In fact, if K in (8b) is large enough, the temperature gradient in the bulk of fluid (see (8a)) will actually oppose the applied temperature difference.

For a pure monoatomic vapour, the above theory predicts that the jumps can be as much as twice the applied temperature difference. Internal degrees of freedom (Aoki & Cercignani 1983) and contamination (Shankar & Deshpande 1990) can drastically reduce the jumps but not remove them.

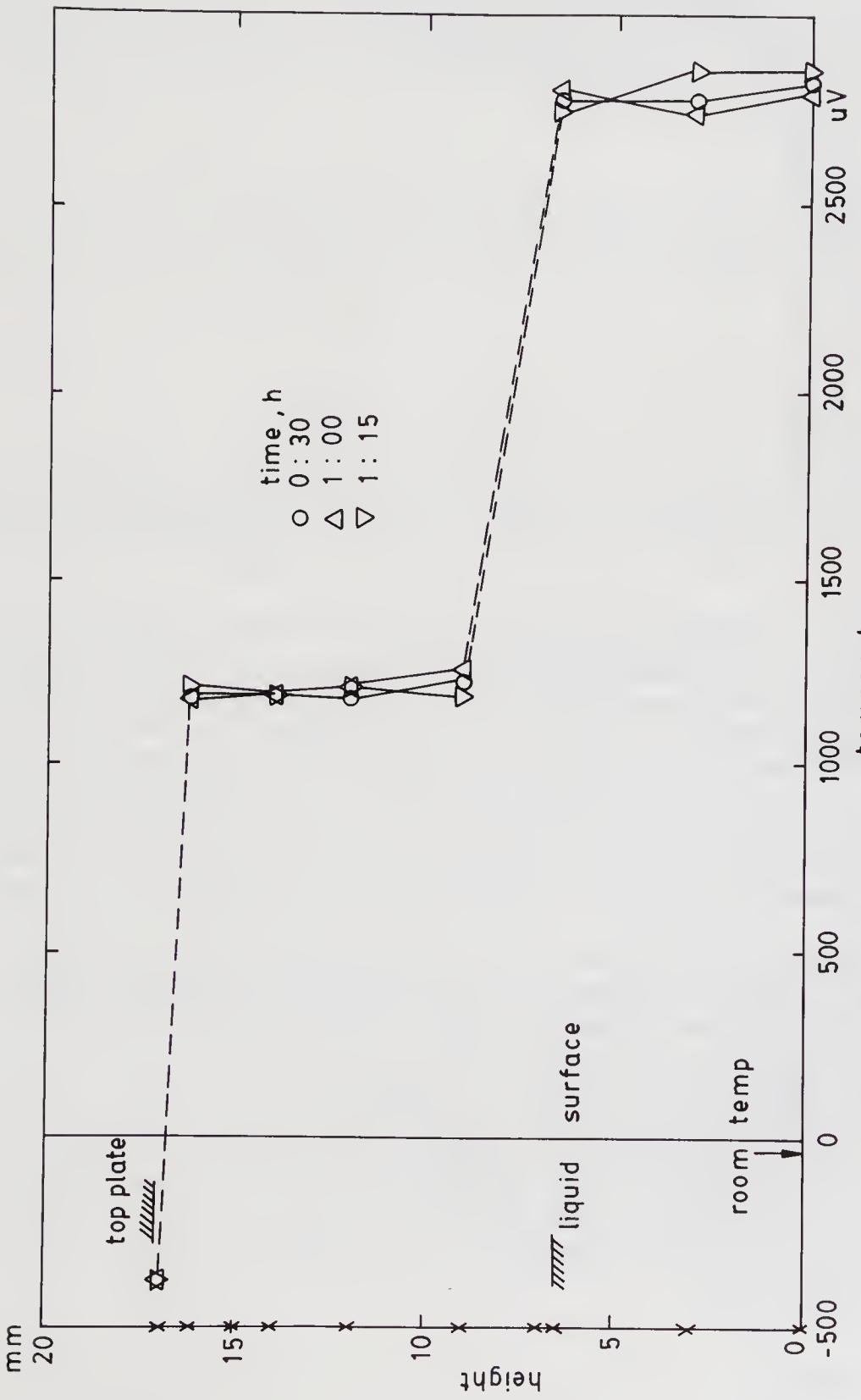

Figure 4. Temperature profiles in mercury vapour: $\hat{p}_0 \approx 36\,\mathrm{N/m^2}$, $\hat{l}_0 \approx 0{\cdot}17\,\mathrm{mm}$.

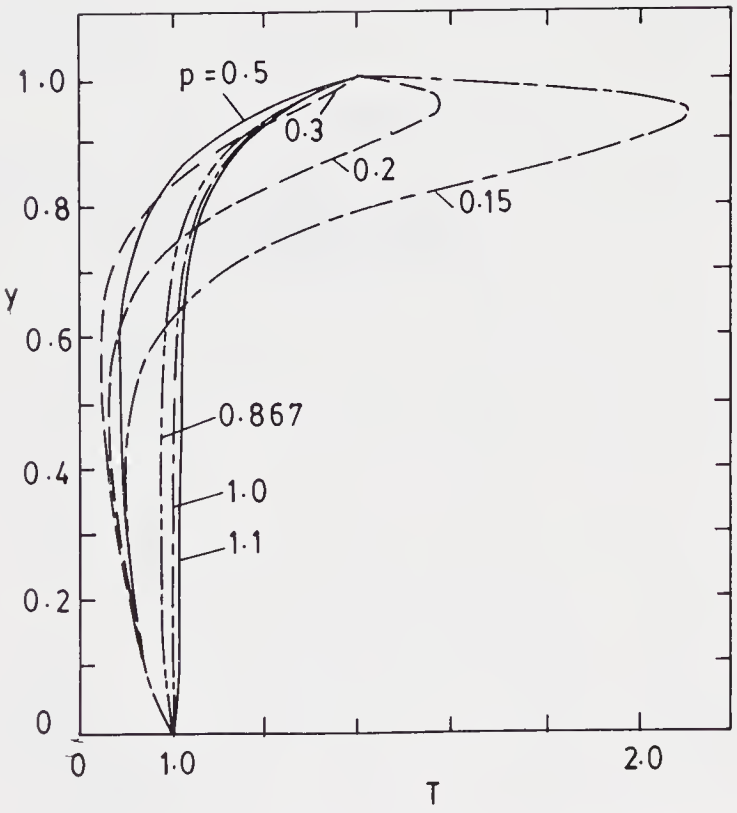

Figure 5. Nonlinear, viscous continuum calculations showing temperature over- and undershoots.

It was only in 1988 that an experiment (Shankar & Deshpande 1990) was carried out to try to confirm the above controversial theoretical results. Mercury, in spite of its dangerous and toxic nature, was chosen as the working fluid because of (i) its monoatomic nature in the vapour state, (ii) its low latent heat, and (iii) its good thermal conductivity in the liquid state. Figure 4 shows one sample of the results obtained. Large temperature jumps were, indeed, found for the first time near the vapour–liquid interfaces, but the anomalous temperature distribution could neither be confirmed nor rejected. It is still not certain how much surface contamination, vapour contamination or some other more subtle effects, contributed to this negative result.

It is interesting to note that, in the experiments, the temperature profiles often appeared to depart in character from that predicted by the linearized theories. A doubt that arose was whether nonlinearity could be playing a larger role than previously assumed. Since these discrepancies occurred in the bulk of the fluid it was felt that it might be worthwhile to study the behaviour of the nonlinear, viscous gas dynamic equations under rather general boundary conditions. Not only were temperature profiles qualitatively similar to the experimental results obtained (Shankar & Deshpande 1991) but other new features were seen. For example (figure 5), one can get large temperature undershoots and overshoots, which are quite unexpected. These results show that the complex roles of nonlinearity and viscosity have so far been underestimated.

6. Conclusion

It should be clear from the above that the ubiquitous phenomenon of liquid–vapour phase change is principally a fluid mechanical one. What is surprising is that even

in its simplest manifestation, i.e. in one-dimension with a single species, the resulting field is complex in structure and elusive in real understanding. This is due at least in part to our current poor understanding of the exchange processes taking place at the interfaces. For a better appreciation, more work will have to be done, both theoretical and experimental, to determine more clearly the actual nature of the complex molecular interactions taking place at the interfaces.

I would like to acknowledge my indebtedness to my colleague, Dr M D Deshpande, with whom I have collaborated on some of the work reported here. I also thank Prof R Narasimha, who has consistently supported our endeavours.

References

Aoki K, Cercignani C 1983 Evaporation and condensation on two parallel plates at finite Reynolds number. *Phys. Fluids* 26: 1163–1164

Hertz 1882 (a) Ueber die Verdungstung der Flussigkeiten, Insbesondere des Quecksilbers, im luftleern Raume. (b) Ueber den Druck des gesaltigten Quecksilberdamfes. *Ann. Phys.* 17: (a) 177–192, (b) 193–200

Knudsen M 1915 Die maximale Verdamp fungsgeschwindig keit des Quecksilbers. *Ann. Phys.* 47: 697–709

Marble F E 1969 Some gasdynamic problems in the flow of condensing vapors. *Astronaut. Acta* 14: 585–614

Maxwell J C 1890 *Collected works* (Cambridge: University Press) vol. 2

Onishi Y 1986 The spherical-droplet problem of evaporation and condensation in a vapour–gas mixture. *J. Fluid Mech.* 163: 171–194

Pao Y P 1971 Application of kinetic theory to the problem of evaporation and condensation. *Phys. Fluids* 14: 306–312

Shankar P N 1968 *A kinetic theory of condensation and evaporation*, Ph D thesis, California Inst. of Technology

Shankar P N 1970 A kinetic theory of steady condensation. *J. Fluid Mech.* 40: 385–400

Shankar P N, Deshpande M D 1990 On the temperature distribution in liquid-vapour phase change between plane liquid surfaces. *Phys. Fluids* A2: 1030–1038

Shankar P N, Deshpande M D 1991 The gas dynamics of massive evaporation and condensation. *Philos. Trans. R. Soc. London* A335: 487–511

Shankar P N, Marble F E 1971 Kinetic theory of transient condensation and evaporation at a plane surface. *Phys. Fluids* 14: 510–516

The hydrodynamic analysis of fish propulsion performance and its morphological adaptation

BING-GANG TONG[1], LI-XIAN ZHUANG and JIAN-YU CHENG[2]

Department of Modern Mechanics, University of Science and Technology of China, Hefei, Anhui 230026, People's Republic of China
[1] Present address: Graduate School of USTC, P.O. Box 3908, Beijing 100039, China
[2] Present address: FB 13.4-Zoologie, Bau. 6, Universität des Saarlandes, D-6600 Saarbrücken, Germany

Abstract. The hydrodynamic performance of fish undulatory swimming has been studied by means of the linear three-dimensional and the non-linear two-dimensional waving-plate theories developed recently by the present authors. The morphological adaptation of the anguilliform mode, carangiform mode, and lunate-tail swimming propulsion in the biological evolution process of fishes has been understood tentatively from the point of view of hydrodynamic analysis.

Keywords. Hydrodynamics; unsteady flow; swimming; energetics; morphology; fish propulsion.

1. Introduction

The undulatory motion of aquatic living beings in the form of a transverse wave propagating along their bodies from head to tail is one of the most effective and major methods of propulsion for almost the entire range of swimming Reynolds numbers from 10^{-6} for bacteria, to 10^3–10^5 for a great variety of fishes, 10^6 for migrating fishes, and even 10^8 for the most rapid marine cetaceans (porpoise, whale etc.). In this paper, the large Reynolds number undulatory swimming property of fishes and cetaceans is investigated, including the anguilliform mode, carangiform mode, and lunate-tail propulsion.

Fishes using the anguilliform mode (AM) are flexible over the whole body, and the propulsive wave amplitude is significant all along its length, though slowly increasing posteriorly. Their body shape is mostly characterised by nearly unchanging span-width. In the carangiform mode (CM), as a development of AM, the amplitude of undulation becomes significant and increases quickly only in the posterior half or even one-third of the fish body, while the anterior portion is almost inflexible. Its body shape is characterised by a narrowing at the rear part connected to a wide-span caudal fin, and also by a deep dorsal–ventral cross-section near the mass-centre. In particular, the fastest marine fishes and cetaceans have adopted essentially the

carangiform mode, their tails having converged to a crescent-moon shape functioning like an effective propeller, which is termed lunate-tail propulsion (LTP).

For 'elongated' fishes which are geometrically characterized by slender cylindrical forms, Lighthill (1975) developed the classical potential elongated-body theory (EBT). Wu (1961) treated the fish as a flexible plate and developed the classical linear potential two-dimensional waving plate theory (2-DWPT), using which he first discussed the optimum shape problem (Wu 1971). To analyse lunate-tail swimming propulsion, Lighthill (1975), Chopra & Kambe (1977), Lan (1979), Cheng & Murillo (1984), Ahmadi & Widnall (1986) and Karpouzian *et al* (1990) have used 2-D and 3-D unsteady wing theory to treat problems like the flow past pitching and heaving rigid plates.

Our recent work in this field consists of: 1) the development of a linear potential 3-D waving plate theory for both the direct problem and optimum problem in the fish cruising regime, 2) the tentative understanding of the morphological adaptation of these fish propulsion modes in the biological evolution process, 3) the accelerated propulsion performance study on the basis of the 3-D waving plate model, 4) the development of the nonlinear potential 2-D waving plate theory and the nonlinear potential 2-D pitching and heaving rigid plate theory.

In this paper, we will give a physical overview of the hydrodynamic performance of fish undulation propulsion and try to elucidate the morphological adaptation of different propulsion modes from the point of view of hydrodynamic analysis.

2. 3-D waving plate simulation and its energetics

In view of the fact that a great majority of fishes have flat bodies with finite span-width, the study of a swimming 3-D waving plate model seems more realistic than that of the elongated body and 2-D waving plate for swimming fish. In the large Re condition, the problem is treated as an incompressible unsteady potential flow past a deformable thin plate (in the x, y-plane) of finite aspect ratio with a rounded leading edge and a sharp trailing edge, performing an undulatory motion of small amplitude in a stream of accelerated velocity $U(t)$ (in the x-direction) in general and constant U in particular. The lateral displacement of the plate in the z-direction is taken as a set of progressive planar waves of variable amplitudes:

$$z = h(x, y, t) = \sum_{m=0}^{M} A_m x^m \cos(\omega t - kx + \psi_m), \tag{1}$$

where $A_m \ll 1, \omega, k, \psi_m$ are the amplitude, reduced frequency, wave number and initial phase angle respectively. All quantities are taken as nondimensional.

In this way, the problem is formulated in a coordinate system moving with the plate, governed by the Laplace equation, with initial flow condition and linear boundary conditions imposed on the plate surface, on the vortex wake surface and at infinity as well as the unsteady Kutta condition at the trailing edge (Tong & Wang to the leading edge suction; (2) power input coefficient C_E which means the time rate of work done by the plate to maintain its lateral motion; (3) propulsive efficiency $\eta = C_T/C_E$, which means the availability of power input; (4) thrust ratio contributed by the leading edge suction $\gamma_s = C_{T_s}/C_T$, where a very high suction may lead to flow dimensional energetic coefficients, showing the hydrodynamic swimming performance of the waving plate, are obtained. The main energetics, normalized by instantaneous

dynamic pressure, consist of the following quantities: (1) thrust coefficient C_T, which involves one part C_{Tp} due to the pressure difference ΔC_p and another part C_{Ts} due to the leading edge suction; (2) power input coefficient C_E which means the time rate of work done by the plate to maintain its lateral motion; (3) propulsive efficiency $\eta = C_T/C_E$, which means the availability of power input; (4) thrust ratio contributed by the leading edge suction $\gamma_s = C_{Ts}/C_T$, where a very high suction may lead to flow separation and a considerable thrust reduction; (5) side-force coefficient C_L and side-moment coefficient C_M, which, fluctuating laterally, may cause undesirable large recoil movements.

In the case of constant speed propulsion, the mean energetic coefficients are usually defined by cyclic averaging of the corresponding instantaneous energetics, such as $\bar{C}_T, \bar{C}_E, \bar{\eta}, \bar{\gamma}_s$.

3. Swimming performance of the anguilliform mode propulsion

Fishes adopting AM propulsion can reasonably be modelled by a rectangular waving plate with constant amplitude (Cheng *et al* 1989). Practical observations indicate that the reduced frequency $\omega = \omega^* L/U$, based on the whole fish length L, takes a value around 10, and the wavelength is about equal to the body length, i.e. $k \approx 2\pi$, so that the non-dimensional phase velocity $c = \omega/k \approx 1.6$, which means that the dimensional phase velocity $c^* = cU$ is about 1.6 times greater than swimming velocity U. A set of representative results is shown in figure 1, which gives the mean energetics versus k for a rectangular waving plate of aspect ratio $AR = 8, 1, 0{\cdot}5$ with reduced frequency $\omega = 8, 10$ and constant wave amplitude. From figure 1 and other results which are not shown here, we can find the following.

(1) Thrust $\bar{C}_T$ and power input $\bar{C}_E$ are positive only when $|c| > 1$. Further, $\bar{C}_T$ will increase and η decrease with increasing c. This agrees with the theories EBT and 2-DWPT.

(2) When the wave propagates in an inverse direction marked by $-k$, i.e. from tail to head, which has been found to be physical in nature (e.g. some polychaete worms in general like *Nereis* and *Nephthys*), the variation with $-k$ of $\bar{C}_T$ and $\bar{C}_E$, which may still remain positive, is similar to that with k, but η is much lower.

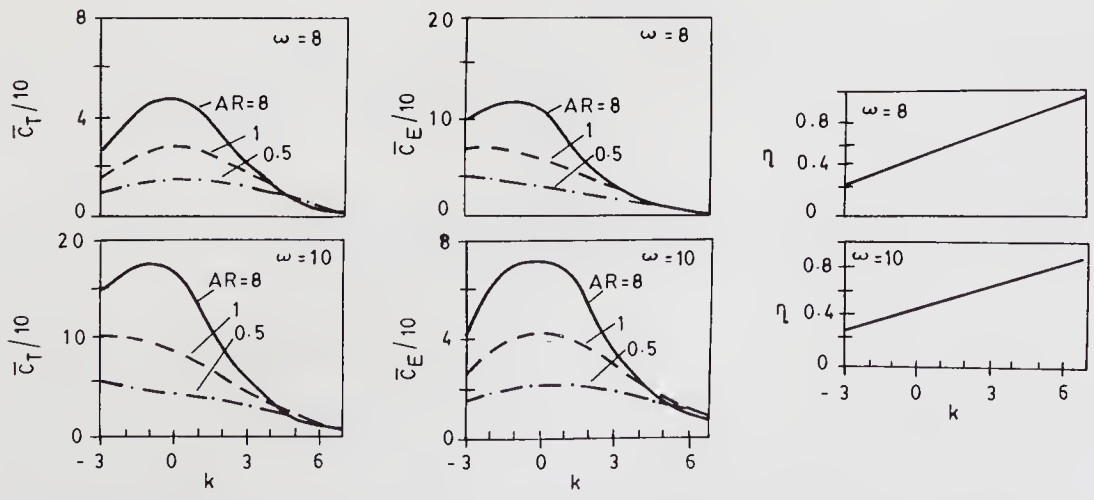

Figure 1. $\bar{C}_T$, $\bar{C}_E$ and η versus k for rectangular constant-amplitude waving plates of different aspect ratios.

(3) It is very striking to know that a waving plate can reduce the effect of aspect ratio. Especially when the wavelength is close to the body length, 3-D effects almost disappear; in other words, the swimming performance of a 3-D waving plate with even a very small aspect ratio is almost the same as that of a 2-D waving plate. The mechanism of this phenomenon may be that the down-wash or up-wash on the side edges of the rectangular waving plate is distributed sinusoidally in the chordwise direction, and the strength of chordwise wake vortices is then cancelled out by one another, so that the wake energy consumption is minimum.
(4) If the wavelength is close to the body length, $\bar{\gamma}_s$, C_L and C_M approach their minimum values, independent of plate aspect ratios. This means no risk of flow detachment from the leading edge of the plate and the smallest lateral recoil.
(5) After numerical investigations on various types of amplitude increasing along the plate chord by putting $m = 0, 1, 2, 3$ respectively in (1), comparison between them shows that the constant amplitude case ($m = 0$) gives a little higher thrust and propulsion efficiency in case of $\omega \approx 10$, $k \approx 2\pi$. It is noted that for an increasing-amplitude wave, the critical phase velocity to obtain positive thrust is a little larger than 1, which is also confirmed by observations.

All the above arguments may lead to the conclusion that the existing AM propulsion can give the most desirable swimming performance in the particular locomotion speed range, and so the biological evolution of adapting AM may be reasonably explained by the hydrodynamic analysis.

4. Swimming performance of the carangiform mode propulsion

The CM propulsion covers a wide Re range, bordering on that of AM, and may be regarded as the common propulsion pattern adopted by most fish species in the class Pisces and sea animals from the subcarangiform mode to the lunate-tail propulsion. It is characterized by narrowing of the body anterior to the caudal fin, a very wide span near its centre of mass to reduce recoil and a steep increase of wave amplitude towards the tail in the last one-third of the body length, which is much less than a whole wavelength. Observations show that the reduced frequency ω based on the undulating part of the body length is about 4, and the wave number is in the range 0 to π, owing to no complete wavelength being apparent.

A triangular waving plate might be appropriate for modelling CM (Cheng *et al* 1991b). In order to seek the secret of the shape adaptation of CM, the propulsive characteristics are calculated for a triangular and a rectangular plate, both with semispan $b = 0{\cdot}25$, and with four types of increasing-amplitude, i.e. $m = 0, 1, 2, 3$ respectively in (1).

We find that in the constant wave amplitude case ($m = 0$), the η curve of the triangular plate is obviously lower than that of the rectangular plate, and the $\bar{C}_T$ curve of the triangular plate is lower than that of the rectangular plate in the range of lower k values. This indicates that, for an undulation of nearly constant amplitude, the swimming performance of a slender rectangular plate is better than that of a slender triangular plate. But for the increasing-amplitude case ($m = 1, 2, 3$), the $\bar{C}_T$ curves of the triangular plate are higher than those of the rectangular plate at lower values of k and the curves of η of the triangular plate are a little lower than those of the rectangular plate. This means that for an increasing-amplitude wave the swimming performance of a rectangular plate is no longer better, and is perhaps even

worse than that of a triangular plate. This may be one of the reasons for the morphological adapation of fish for CM propulsion.

In order to examine our 3-D waving plate theory, the observation data on a rainbow trout by Webb (1971), which have been used to get its swimming performance by Yates (1983, pp. 177–213), provided a base for checking the calculated results of the present theory. The trout has its swimming mode between AM and CM, but is closer to CM with a tail having an almost straight trailing edge. The amplitude variation of first power ($m = 1$) is chosen. At $b = 0{\cdot}38$, $\omega = 4$, $k = 2{\cdot}36$, the predicted drag coefficient C_D, which is calculated from the thrust in the steady locomotion, is given by EBT and the present theory as follows:

$C_D =$	EBT	*Present theory*
	$3{\cdot}51 \times 10^{-2}$	$1{\cdot}43 \times 10^{-2}$

The laminar and turbulent drag coefficients of a smooth flat plate are approximately equal to 4×10^{-3} and 8×10^{-3}, respectively, at $\mathrm{Re} = 1{\cdot}29 \times 10^5$. The values of C_D from deceleration measurements during glide runs, although showing considerable scatter, are close to the value predicted by the boundary layer theory (Yates 1983, pp. 177–213). Now the C_D value estimated by the present theory is closer to the measured values than that by EBT. Considering some obvious errors coming from the absence of leading edge suction over part of the tail due to the peduncle in front and also from the small amplitude assumption, these may cause a reduction of 20% in thrust as well as the drag.

5. Optimum motion analysis and caudal fin-shape adaptation

An optimum motion theory for 3-D waving plates is developed to discuss the optimum shapes and motions of the undulating carangiform caudal fin and lunate tail. The analysis intends to elucidate tentatively the influence of water on swimming body configurations and so to determine the hydrodynamic mechanism of their evolution.

The general problem of determining the optimum motion for waving plates of various prescribed planforms can be stated as follows: from a class of waving functions (1), with $A_m \exp[i\psi_m]$, unknown, find the optimum one that may minimize the power input for a fixed average thrust (Cheng *et al* 1991a).

Four types of tail motions are discussed in the analysis of caudal fin propulsion: (a) $m = 0$; (b) $m = 1$; (c) $m = 0$ in combination with $m = 1$, denoted by $(0, 1)_{\mathrm{op}}$; (d) $m = 1$ in combination with $m = 2$, denoted by $(1, 2)_{\mathrm{op}}$.

Figure 2 shows, on the left, typical tail shapes in the sub-CM, CM and LTP, the order of which indicates the speed increasing sequence; and on their right an assumed series of various geometrical planforms are tested, based on optimum motion analysis to select the one which might give the best swimming performance.

5.1 *Caudal fin with almost straight trailing edge*

Fishes with this kind of tail shape, belonging to sub-CM, e.g. in Gadidae, Serranidae and Scianidae, have lower cruising speeds and more or less the property of AM locomotion. Let the tail length $L = 0{\cdot}2$, $\omega = 4$. Three kinds of triangular waving plates are considered as follows (figure 2):

(a) convex rearward trailing edge: $l_T = b/4, b/2, b$;

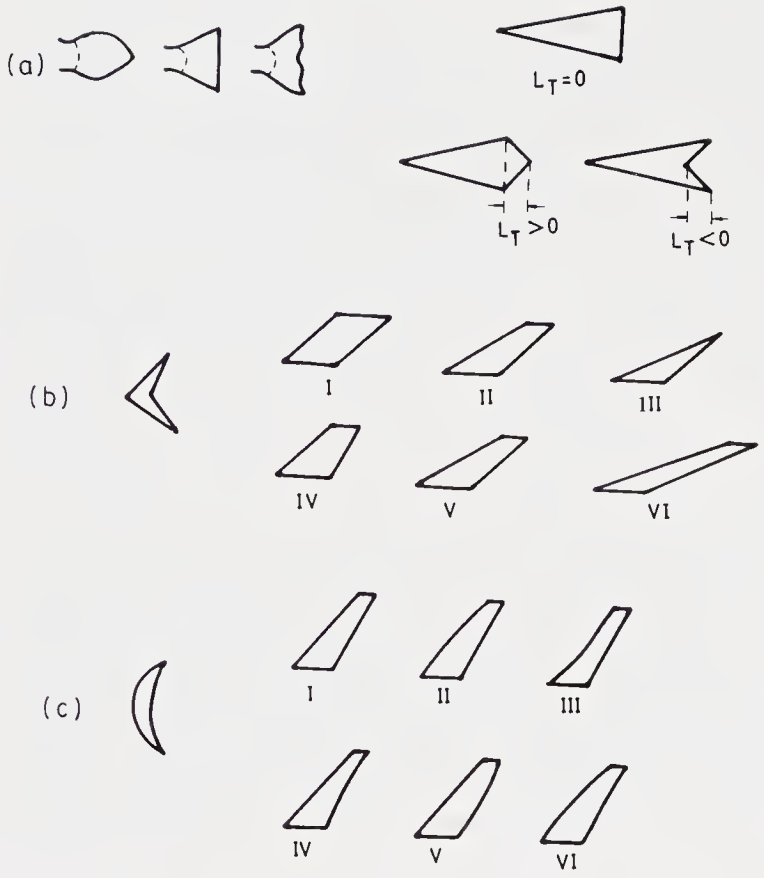

Figure 2. The typical tail shapes (left hand side) and assumed configurations (right hand side) for optimum studies. (**a**) Sub-carangiform mode; (**b**) Carangiform mode; (**c**) Lunate tail propulsion.

(b) flat trailing edge: $l_T = 0$;
(c) concave forward trailing edge: $l_T = -b/2, -b, -3b/2$;

where l_T is the chordwise distance of slanted trailing edge, and b the half-span (normalized by L).

Based on the calculated results for the above cases, we can draw some conclusions.

(1) Tail shape has an explicit influence on propulsive performance, particularly, for undulating amplitude changing markedly along the body axis.
(2) In general, the efficiency increases with l_T, and thrust coefficient reaches its maximum at l_T around $b/4$. The forward slanted trailing edge, i.e. $l_T < 0$, gives the worst propulsive performance. It is also observed that fishes with the swimming mode close to sub-CM often have tails with such convex rearward or almost straight trailing edges.
(3) For this sub-CM swimming, fish should undulate in a weaker wavy pattern with the waving speed around half of the swimming speed.

5.2 *Arrow-like caudal fin*

Fishes of typical CM with arrow-like caudal fins such as those in Scombroidae, Carangidae, Exocetidae etc., have narrower peduncle regions and caudal fins scooped out internally in a V-shape. The undulation is basically confined to the rear one-third part of the fish-body. The caudal fin extending to about one half of the undulation part has its length $L \approx 1/6$, so that $\omega = 2$ is taken in calculations. Considering that these fishes are highly streamlined in their forebodies without large thrust needed, further evolution of their caudal fin propulsion should be direct to gain higher effi-

ciency, and two patterns of variable wave amplitude $(0, 1)_{op}$ and $(1, 2)_{op}$ are assumed. As shown in figure 2, six planforms with different tapering and sweepback angles of leading and trailing edges on the right side of the arrow-like caudal fin are tested by the optimum motion analysis, and this leads to the following conclusions.

(1) The η values for the $(0, 1)_{op}$ pattern are about 10% to 20% higher than those of the $(1, 2)_{op}$ pattern. This means that the wave amplitude should increase steeply in the neck part and then maintain a large and slightly increasing value along the tail. This is confirmed by observations.
(2) A decrease of taper ratio results in an increase of thrust parameter, a decrease of γ_s and a slight decrease of optimum η. Hence, performance is maintained, or even improved by the pointed tip of the arrow-like caudal fin.
(3) Increasing the sweepback angle results in decrease of η and γ_s and increases the thrust parameter to its maximum value at moderate sweepback angle after which it decreases. Hence, high sweepback leads to bad performance, particularly to a marked reduction of η, which has been also pointed out for the pitching-heaving rigid plate case by Chopra & Kambe (1977). Therefore, a moderate sweepback angle may give better overall performance.

5.3 *Lunate tail*

Almost all the fast marine animals, namely certain scombroid fishes, sharks and all the cetacean mammals, have essentially adopted CM, their tails having converged to a cresent-moon shape of high aspect ratio through different pathways of evolution in the pursuit of high propulsive efficiency.

All available studies of LTP are restricted to the rigid plate model. In fact, the rear-body movements of marine swimmers, including their tails, still have a somewhat wavy behaviour, though only a part of the whole wavelength is apparent. Hence, we discuss tail-shapes by applying a 3-D waving plate model and optimum motion analysis to these six different configurations on the right side of the crescent-moon tail in figure 2. We find the following.

(1) As a special case of waving plates, the pitching and heaving rigid plate ($k = 0$) has the lowest η and the highest C_T. Once the wavy motion is performed, η increases and C_T decreases. So, the best way to maintain sufficient total thrust with high η is to increase tail span. This is the reason why marine fast swimmers always hold their tails at high aspect ratios.
(2) A curved leading edge (planform P2) or curved trailing edge (planform P4) has considerable effect on improving propulsion performance. In fact, the planform P2 gives the lower C_T but the highest optimum η, and P4 gives relatively higher η and highest C_T. It is expected that the combination of P2 and P4, which becomes P6, similar to the crescent-moon shape, will give both high η and high C_T.
(3) In most cases, tapering or adequate increase in sweepback may result in significant improvment in propulsive performance of the crescent-moon shape (P6), i.e., thrust parameter and η both increase, or one increases and another at least maintains its value. Therefore, the lunate tail is superior to the arrow-like caudal fin with a straight edges in this respect.

It turns out that the crescent-moon shape can give the most desirable overall performance.

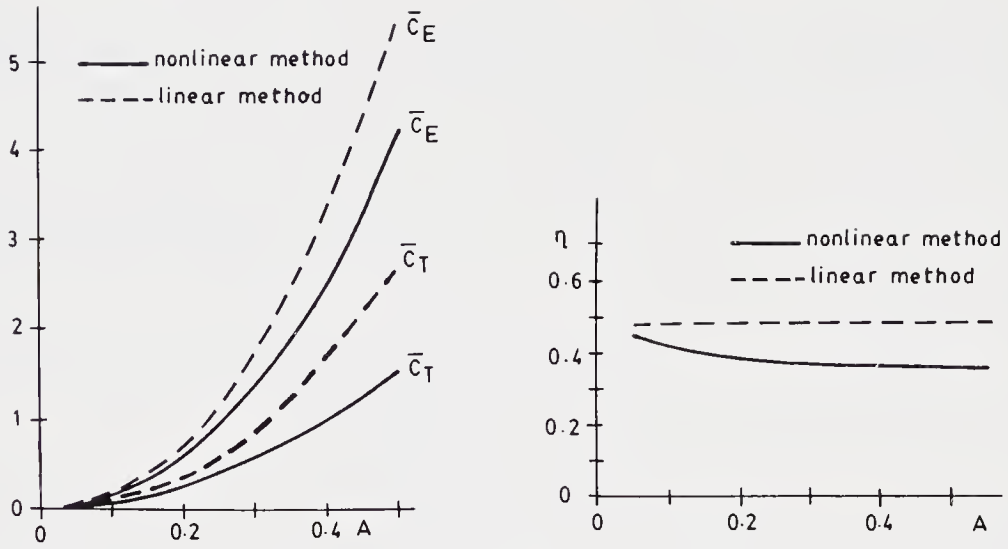

Figure 3. Comparison of linear and nonlinear results including effects of finite amplitude and wake evolution, $a(x) = Ax^2$, $\omega = 2\pi$, $k = \pi$.

6. Discussion of nonlinear effects

Three nonlinear factors will be considered here, namely the nonlinear boundary condition owing to the large amplitude of the waving plate, the nonlinear evolution of wake vortex layer and the nonlinear effect of wall to a closely moving undulatory plate.

A nonlinear theory of the 2-D waving plate is developed to estimate the deviations of swimming performance from the results of linear waving plate theory, considering the effects of large amplitude and wake evolution (Zhuang *et al* 1990). Linear and nonlinear calculations were carried out for a series of amplitudes, A, ranging from 0·05 to 0·5 for amplitude function Ax^2 (i.e. $m = 2$). The calculated results for $\bar{C}_T$, $\bar{C}_E$ and η are shown in figure 3. It is shown that when $A \geqslant 0.1$, the deviations between nonlinear and linear results are very apparent, that is, the linearized approximation overestimates all the $\bar{C}_T$, $\bar{C}_E$ and η. Even in the small amplitude case, the nonlinear effect of wake evolution is very important and should be taken into consideration, as shown in figure 4.

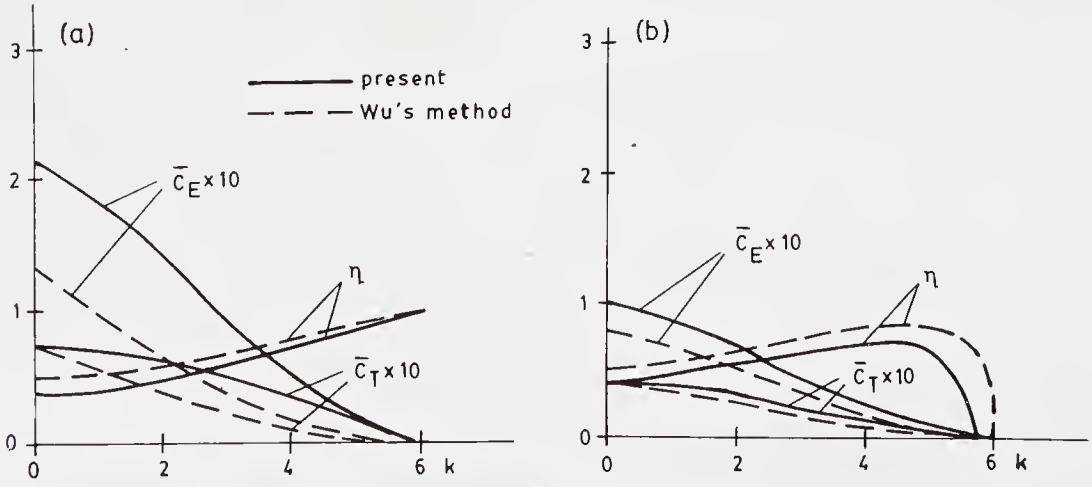

Figure 4. Comparison of linear and nonlinear results, including wake evolution effect only. (**a**) $a(x) = 0{\cdot}05$; (**b**) $a(x) = 0{\cdot}05x$.

Besides, the wall effect has been studied, using the linear 3-D waving plate theory (Cheng *et al* 1991c) and the nonlinear 2-D waving plate theory (Zhuang *et al* 1990). It has been concluded that the wall effects on the unsteady hydrodynamic forces become notable as the distance decreases to a value of the order of the plate chord length. The mean values of $\bar{C}_T$ and $\bar{C}_E$, as well as their varying amplitudes, for the case of small amplitude, increase very sharply as the waving plate approaches the wall. On the other hand, the wall effect on the averaged lift is such that, as the distance decreases, the force first acts as a suction, then becomes repulsive. But the wall effect on η is small.

7. Accelerated swimming performance

The accelerated swimming performance of a 3-D rectangular waving plate with constant amplitude is studied by linear 3-D waving plate theory (Tong & Wang 1991). All nondimensional quantities and energetic coefficients are normalized with the instantaneous forward variable speed $U(t)$. Several of them are introduced herein for interpreting their meaning.

(a) Reduced frequency $\omega = \omega^* L/U(t)$ means that for keeping ω unchanged in the accelerated swimming process, the dimensional circular frequency ω^* should be increased at the same rate as $U(t)$.
(b) Nondimensional phase velocity $c = \omega/k = \omega^*/k^* U(t) = c^*/U(t)$, where ω^*, k^*, c^* denote corresponding dimensional quantitics of ω, k, c, has the meaning that if c is kept constant in the acceleration process, and if k^* is unchanged, then the dimensional ω^* or c^* should be changed at the same rate as $U(t)$.
(c) Thrust coefficient $C_T = 2T/\rho U(t)^2 S$ means that if C_T is kept constant, the thrust force T has to increase with the square of $U(t)$.
(d) Nondimensional time $t = t^* U(t)/L$ is proportional to both dimensional time t^* and $U(t)$.

The main findings in this problem are as follows.

(1) The curves of C_T and C_E versus t of a rectangular waving plate with constant amplitude in the accelerated motion are qualitatively analogous to these curves of the plate in the constant speed motion, if nondimensional phase velocity c or reduced frequency ω is kept constant and equal in both cases, as shown in figure 5. There exist positive C_T and C_E only when $c > 1$. Further, when c is increasing, the mean values of C_T and C_E increase, but the value of η decreases.
(2) From the observations of fishes in accelerated swimming, their waving frequency ω^* is increasing in proportion to the increasing speed $U(t)$ roughly. This means that

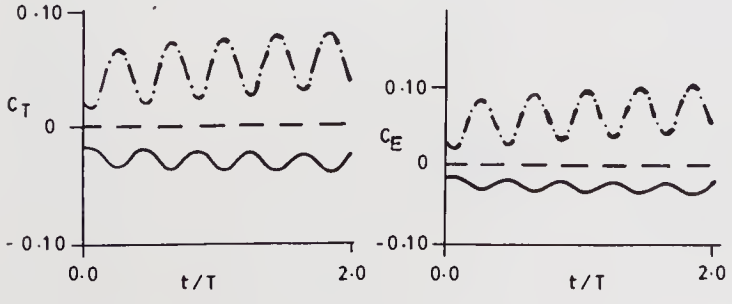

Figure 5. C_T and C_E versus t for a waving plate ($A_0 = 0{\cdot}05$, $AR = 1$, $a = 1$) with values of $c = 1{\cdot}33$ (—·—·—), $1{\cdot}0$ (------), $0{\cdot}89$ (———).

fishes intend to keep constant c and to have in some degree 'steady' swimming performance.

(3) The instantaneous energetic coefficients are independent of the forward acceleration.

(4) A decrease of the plate aspect ratio causes a decrease of mean C_T and C_E, but has almost no influence on η.

This research work was supported by the National Natural Science Foundation of China. The authors are very much indebted to Professor T Y Wu of Caltech for his valuable suggestions and instructive discussions on the research topic.

References

Ahmadi A R, Widnall S E 1986 Energetics and optimum motion of oscillating lifting surfaces of finite span. *J. Fluid Mech.* 162: 261–282

Cheng H K, Murillo L E 1984 Lunate-tail propulsion as a problem of curved lifting line in unsteady flow. Part 1. Asymptotic theory. *J. Fluid Mech.* 143: 327–350

Cheng J Y 1988 *Hydrodynamic study on aquatic animals' swimming*, Ph D dissertation, University of Science and Technology of China (in Chinese)

Cheng J Y, Zhuang L X, Tong B G 1989 Swimming performance analysis for anguilliform propulsion. *J. Hydrodyn. (Engl. Ed.)* 4: 89–102

Cheng J Y, Zhuang L X, Tong B G 1991a Numerical calculation of propulsive characteristics of fish's swimming. *Acta Aerodyn. Sin.* 9: 94–103 (in Chinese)

Cheng J Y, Zhuang L X, Tong B G 1991b Analysis of three dimensional waving plate swimming. *J. Fluid Mech.* 232: 341–356

Cheng J Y, Zhuang L X, Tong B G 1991c The effects of spanwise deformation and closeness to the ground on the swimming of waving plates. *J. China Univ. Sci. Technol.* 21: 423–427 (in Chinese)

Chopra M G, Kambe T 1977 Hydromechanics of lunate-tail swimming propulsion. *J. Fluid Mech.* 79: 49–60

Karpouzian G, Spedding G, Cheng H K 1990 Lunate-tail propulsion. Part 2. Performance analysis. *J. Fluid Mech.* 210: 329–351

Lan C E 1979 The unsteady quasi-vortex-lattice method with application to animal propulsion. *J. Fluid Mech.* 93: 747–765

Lighthill M J 1975 *Mathematical biofluiddynamics* (Philadelphia: SIAM)

Tong B G, Wang A P 1991 A numerical study on the acceleration of a three-dimensional waving plate. *Acta Aerodyn. Sin.* 9: 285–293 (in Chinese)

Webb P W 1971 The swimming energetics of trout. *J. Exp. Biol.* 55: 484–520

Wu T Y 1961 Swimming of a waving plate. *J. Fluid Mech.* 10: 321–344

Wu T Y 1971 Hydromechanics of swimming propulsion. *J. Fluid Mech.* 46: 521–568

Yates G T 1983 Hydromechanics of body and caudal fin propulsion. In *Fish biomechanics* (eds) P W Webb, D Weihs (New York: Prager)

Zhuang L X, Shida Y, Takami H 1990 Two-dimensional unsteady flow around a waving plate in wall effects. *Fluid Dyn. Res.* 5: 321–336

Author Index

Adams M S
see Drummond J P 269
Adenji-Fashola A 295, 296
Ahmadi A R 352
Ames Report 331
Amsden A A 66, 86
Anderson K A 65
Aoki K 346
Aoki T
see Matsuo K 334
Arie M 320
Armaly B P 100
Armfield S W 290, 294, 296
Ashurst W T 111, 177
see Meiron D I 112

Babenko V V 20
Bagust K 303
Bain J G 290, 301
Baines N C 92
Bakos R J 269
Balakrishnan N 55
Bar-Yoseph P 295
Barnes F H
see Ross J A 20, 29, 34
Barry M D J 20
Basu A
see Melander M V 153
Batchelor G K 130, 167
Beam R M 64
Bearman P W
see Obasaju E D 316, 323
Ben-Dor G 327, 330, 333, 335, 340
Bensen T J
see Kunik W G 269
Berger E 174
Bertolotti F P 20, 34
Birkhoff G 330
Bouard R 316, 321, 323
Bouthier M 20
Bradbury L J S 320
Bray K N C 296
Braza M 316, 323
Bridges J 110
Bridges T J 20
Brown G L 110
Burns J C
see Ross J A 20, 29, 34

Carpenter L H 317–319
Carpenter M H
see Drummond J P 269
Carr L W 208, 209
Caughey D A 65
Cercignani C 346
Chakravarthy S R 44, 65, 73, 100
Champagne F H 110
Chang J L C 66
Chang K S
see Chyu W J 210
Chapman G T 187–189, 194, 200, 205
Chassaing P
see Braza M 316, 323
Chaussee O S 65, 81
Chein R 320
Chen C P 295, 296
Cheng H K 352
see Karpouzian G 352
Cheng J Y 351, 353–355, 359
Chetverushkin B N 38
Chien K Y 71
Chinitz W
see Bakos R J 269
Cho N–H 290, 296, 301
see Armfield S W 290, 294, 296
Choi Y D 296
Chong M S 265
Chopra M G 352, 357
Chorin A J 66, 165, 177
Chung J N 320
Chung M K 296
Chung T J 269–271, 281
Chyu W J 210
Correa S M
see Shyy W 66
Courant R 327, 330, 337, 339
Coutanceau M 316, 321, 323
Croisille J P 38
Cross M 289
Crow S C 110, 111
Crowe C T 291, 292, 294

Daiguji H 63, 65, 92, 93, 95
see Ikohagi T 100
see Shin B R 66, 96, 99, 104
Dallmann U 205
Dass A K 51
Davis R T 219
Davis S S
see Chyu W J 210
DeFrain P D
see Pasterkamp H 16
Delorme P 38
Demirdzic I 66
Denton J D 64
Deshpande M D 346, 348
Deshpande S M 37–39, 41–44, 50, 51, 54, 55, 57, 58
Dewey J M 327, 330
Dey J 20
di Giacinto M 292, 294
Dodge P R 66
Dosanjh D 128
Douglas J 223
Drummond J P 269
Durst F
see Armaly B P 100
Dwyer D S 269

Elghobashi S
see Modaress D 296
Elizarova T G 38
Emery J C 99
Erdos J I
see Bakos R J 269
Erlebacher G 121–123, 128
Erwin J R
see Emery J C 99

Fasel H 19, 20, 34
Feiereisen W 121
Felix A R
see Emery J C 99
Ferziger J
see Feiereisen W 121
see Shariff K 120
Fletcher C A J 289, 290, 295–297, 299–301, 303
see Armfield S W 290, 294, 296
see Cho N–H 290, 301
Francis M S 208
Friedrichs K O 327, 330, 337, 339

Fujii K 65

Gaster M 20, 25, 26, 28–31, 34
Gatski T B 210
Ghia K N 207–209, 223, 224, 264, 265
see Huang Y 210
see Osswald G A 208–211, 216, 219, 221, 222, 224
Ghia U 207, 209
see Ghia K N 208, 209, 223, 224, 264, 265
see Huang Y 210
see Osswald G A 208–211, 216, 219, 221, 222, 224
Ghoniem A F 166
Ghosh A K
see Deshpande S M 58
Gibson C H
see Ashurst W T 177
Glass I I 333, 334
Glaz H 333
Gnoffo P A 269
Gosman A D
see Demirdzic I 66
Graham J M R
see Obasaju E D 316, 323
Greene J M 156
Gresho P M 210
Gunn J E 223
Guo L
see Ling G C 323
Gustafson K 208

Han T-Y 190, 195
Hankey W L
see Ghia K N 209
Harlow F H 66, 86
Harradine D M 269
Harrington S
see Wang K C 190, 194
Harten A 64, 65
Hartwich P M 66
Helin H E 208
see Walker J M 225, 232, 233, 240, 241, 246, 247
Herbert T
see Bertolotti F P 20, 34
Herrig L J
see Emery J C 99
Hertz 346
Hiramoto M 6, 14
Hodge J K
see Ghia K N 209
Hosokawa I 177
Hu C H 66
see Wang K C 190, 194
Huang Y 210
Humphrey J A C 295
Husain H 112
see Bridges J 110
Hussain F 109–112, 114, 118, 150, 154, 156, 157, 159, 167, 177
see Bridges J 110
see Melander M V 153
see Stanaway S 120
Hussaini M
see Erlebacher G 121–123, 128

Ikohagi T 100
see Shin B R 66, 96, 99, 104
Ikui T
see Matsuo K 334
Ishii H 166, 167, 170, 174, 177
see Kiya M 167, 168, 170
Issa R I
see Demirdzic I 66

Jimenez J 177
Johnson J P
see Kim J 101
Johnson T A 196

Kachanov Yu S 20
Kambe T 352, 357
Kaniel S 38
Karki K C 66
Karo T 174
Karpouzian G 352
Kerr R M
see Ashurst W T 177
Kerr R N 114
Kerstein A R
see Ashurst W T 177
Keulegan C H 317–319
Kida S 157
Kim J 66, 101
Kim S E 190, 202
Kim Y M 269
Kino O M 166
Kiris C
see Rogers S E 66
Kitamura M
see Kiya M 167, 168, 170
Kitchen A K 292, 295
Kiya M 163, 166–168, 170, 177, 320
Kline S J 110
see Kim J 101
Knight B
see Cross M 289
Knudsen M 346
Kondoh T 100
Konzelmann U 19, 20, 34
Kozlov L F 20
Kozlov V V
see Kachanov Yu S 20
Kraman S S
see Pasterkamp H 16
Kreiss H
see Erlebacher G 121–123, 128
Krishnamurthy R
see Deshpande S M 50
Kulkarni P S
see Deshpande S M 50
Kumar A 269
Kunik W G 269
Kuwahara K
see Matida Y 216
see Shirayama S 165
Kwak D
see Chang J L C 66
see Rogers S E 66
see Rosenfeld M 66

Lan C E 352
Lang J D 208
Launder B E 71
Lee S 121, 128
Lele S
see Lee S 121, 128
Leonard A 111, 164, 165, 167, 177, 182
see Shariff K 120
Lerner P 208
Lesieur M 144
Levchenko V Ya
see Kachanov Yu S 20
Lian W 318, 319
Lighthill M J 2, 187, 352
Ling G C 315, 316, 319, 321, 323
Ling G P
see Ling G C 319, 321, 323
Liu C H 316
Lundgren T S 111, 152, 177
Luo C M 316
Lyman J L
see Harradine D M 269

Ma H Y
see Ling G C 323
MacCormack R W 64
Mandal J C 43, 44, 46
see Deshpande S M 58
Mandella M 128
Marble F E 345, 346
Markatos N C
see Cross M 289
Mathur J S 46
Matida Y 216
Matsumura M 163
Matsuo K 334
Matsuoka Y
see Ouwa Y 14

Matthaeus W 122, 123
Maxwell J C 344
McAllister K W 209
McCandless R S 269
see Gnoffo P A 269
McWilliams J C 154
see Melander M V 132, 154
Mehta U B 210, 233, 240–243
Meiburg E 111
Meiron D I 112
Melander M V 109, 118, 132, 153, 154, 157, 159
Melville W K 296
Mendez R
see Shirayama S 165
Minh H H
see Braza M 316, 323
Modaress D 296
Moffatt H K 144
Moin P 66
see Lee S 121, 128
Mongia H C 294
Morris P J 20
Morton K W 41
Moses H E 145
Mostafa A A 294
Motohashi Y
see Daiguji H 65
Murillo L E 352

Nagano Y 100
Nagarathinam M
see Deshpande S M 50
Nakamura Y 66
Nakaya H 174
Narasimha R 110
Nayfeh A H 20
Newcomb W A 156
Ng W F
see Kunik W G 269
Northam G B 269

Obasaju E D 316, 323
Ohe T
see Kiya M 167, 168, 170
Okubo M 316, 325
Oldenborg R C
see Harradine D M 269
Oldfield M L G
see Baines N C 92
Ongoren A 316
Onishi Y 345
Orszag S A
see Meiron D I 112
Osher S 44, 65, 73, 100
Oshima S
see Okubo M 316, 325
Osswald G A 207–211, 213, 216, 219, 221, 222, 224
see Ghia K N 208, 209, 223, 224, 264, 265
Ouwa Y 14

Pao Y P 346
Parthasarathy R N 201
Passot T 121
Pasterkamp H 16
Patankar S V 66
Patel V C 185, 190, 195
see Parthasarathy R N 201
Peake D J 187
Peraire J
see Zienkiewicz O C 271, 273
Peretra J C F
see Armaly B P 100
Peric M
see Demirdzic I 66
Perry A E 265
Perthame B 38
Piva R
see di Giacinto M 292, 294
Platfoot R A 291
Pouquet A 121
Pourahmadi F 295
Powell K G 57
Prabhu A
see Dey J 20
Prahl J M
see Strazisar A J 20
Pulliam T H 65, 81
Pullin D I 38
Pulsonetti M V
see Bakos R J 269

Raghurama Rao S V 54, 55, 57, 58
Raul R 39, 41
Reichenbach H 327, 328
Reshotko E
see Strazisar A J 20
Reynolds W
see Feiereisen W 121
Reynolds W D
see Kline S J 110
Richards C W
see Cross M 289
Rietz R D 38
Riggins D W
see Drummond J P 269
Rizkalla O
see Bakos R J 269
Roache P J 210
Rockwell D 316
Rodi W 296
Roe P L 38, 299
Rogers S E 66
see Chang J L C 66
Rohling T C 221
Rosenfeld M 66
Roshko A 110
Ross J A 20, 29, 34
Ross M A
see Ross J A 20, 29, 34
Ross M A S 20
Runstadler P W
see Kline S J 110

Sabetta F
see di Giacinto M 292, 294
Saito T
see Sasoh A 330, 331
Sakao F 1, 6, 14
see Ouwa Y 14
Salari K 210
Sankar N L 210, 233, 243
Saric W S 20
Sarkar S
see Erlebacher G 121–123, 128
Sarpkaya T 316
Sasoh A 330, 331
Schneider G E 300
Scholz D
see Berger E 174
Schonung D
see Armaly B P 100
Schott G L
see Harradine D M 269
Schraub F A
see Kline S J 110
Schreiber H A
see Tweedt D L 92
Schubauer G B 20
Schumm M
see Berger E 174
Schwarz K 111
Sekar S
see Deshpande S M 50
Sen P K 19, 20, 29, 30, 33
Sethian J A 164
Shang J S 210, 241
Shankar P N 343, 345, 346, 348
Shariff K 120
see Stanaway S 120
Shelley M J
see Meiron D I 112
Shida Y
see Zhuang L X 358, 359
Shin B R 63, 66, 96, 99, 104
see Ikohagi T 100
Shirayama S 165
Shyy W 66
Siggia E D 156, 182
Simons J P
see Baines N C 92

Sinha P K
see Deshpande S M 50
Sirviente A I
see Parthasarathy R N 201
Skramstad H K 20
Smith F T 19, 34
Spalart P R
see Bertolotti F P 20, 34
Spalding D B 71
Spedding G
see Karpouzian G 352
Speziale C G 210
Srinivas K
see Cho N–H 290, 301
Stalker R J 269
Stanaway S 120
Starken H
see Tweedt D L 92
Steger J L 64, 82, 298
Stone H 300
Strazisar A J 20
Strickland J H
see Walker J M 225, 232, 233, 240, 241, 246, 247
Stuart J T 26
Szmelter J
see Zienkiewicz O C 271, 273

Ta Phuoc Loc 323
Takaki R 111, 114
Takami H
see Matida Y 216
see Zhuang L X 358, 359
Takaoka M 157
Takayama K 327, 328, 340
see Sasoh A 330, 331
Takemoto Y 66
Tamangno J
see Bakos R J 269
Tamura Y 65
Tan H
see Modaress D 296
Tassa Y 210, 233, 243
Taylor A
see Kunik W G 269
Theerthamalai P 51
Thomas J L
see Anderson K A 65
Tobak M 187
Tong B G 351, 359
see Cheng J Y 353–355, 359
Tong S S
see Shyy W 66
Toyoda K 167, 168
see Kiya M 167, 168, 170
Tsinober A 144
Tumen D
see Dey J 20
Tweedt D L 92

Van de Vooren A I 20
Van Dyke M 151
Van Leer B 38, 57
Van Stijn T L 20
Vashist T K 20, 29, 30, 33
Verma R 26, 31
Villedieu 38
Vinokur M
see Rosenfeld M 66
Virk D 109
Visbal M R 208, 210, 241

Walker J D A 208
Walker J M 225, 232, 233, 240, 241, 246, 247
Wang A P 359
Wang K C 187, 190, 194
Wang Y P
see Ling G C 319, 321, 323
Warming R F 64, 82
Watanabe H H
see Harradine D M 269
Weatherill N P 46
Webb P W 355
Weeks T 128
Welch J E 66, 86
Werle H 190, 233, 240
Whitfield D L
see Anderson K A 65
Whitham G B 331
Williamson C H K 316, 325
Winckelmans G 165, 167, 182
Windall S E 168, 352
Wodicka G R
see Pasterkamp H 16
Wright J M
see Baines N C 92
Wu T Y 352
Wu Z B 323
see Ling G C 323
Wyss W 208

Yamamoto K 177
Yamamoto S 65, 92, 93, 95
see Daiguji H 65
see Shin B R 66
Yamane R
see Okubo M 316, 325
Yang J 207, 216, 217, 223
see Ghia K N 209, 223, 224, 264, 265
Yang R J
see Chang J L C 66
Yates G T 355
Yates L A 187–189, 194, 200, 205
Yee H C 65
see Gnoffo P A 269
Yenenko N N 80
Yokota J W 65
Yoon W S 269–271, 277, 281

Zabusky N
see Shariff K 120
Zabusky N J
see Melander M V 132, 154
Zank G 122, 123
Zedan M 300
Zhou H C
see Wang K C 190, 194
Zhuang L X 351, 358, 359
see Cheng J Y 353–355, 359
Zienkiewicz O C 271, 273

Subject Index

Active control
Analysis and control of dynamic stall phenomenon using Navier–Stokes formulation involving vorticity, stream function and circulation 207
Aerodynamic sound
Modelling aerodynamic sound in the airways of a human body: A possible diagnostic tool 1

Bluff body
Numerical study of bluff body flow structures 315
Boltzmann equation
Boltzmann schemes for continuum gas dynamics 37
Boundary-layer
Some recent developments in the theory of boundary layer stability 19

Chemically reacting flows
Turbulence/shock wave interactions in chemically reacting flows 269
Coal classification
Gas particle industrial flow simulation using RANSTAD 289
Coherent structure/small scale turbulence coupling
New studies in vortex dynamics: Incompressible and compressible vortex reconnection, core dynamics and coupling between large and small scales 109
Coherent structures
New studies in vortex dynamics: Incompressible and compressible vortex reconnection, core dynamics and coupling between large and small scales 109
Simulating three-dimensional vortex motion by a vortex blob method 163
Compressible flow
Some numerical schemes using curvilinear coordinate grids for incompressible and compressible Navier–Stokes equations 63
Compressible vortex dynamics
New studies in vortex dynamics: Incompressible and compressible vortex reconnection, core dynamics and coupling between large and small scales 109
Computational fluid dynamics
Boltzmann schemes for continuum gas dynamics 37
Some numerical schemes using curvilinear coordinate grids for incompressible and compressible Navier–Stokes equations 63
Gas particle industrial flow simulation using RANSTAD 289
Core dynamics
New studies in vortex dynamics: Incompressible and compressible vortex reconnection, core dynamics and coupling between large and small scales 109
Curvilinear coordinates
Some numerical schemes using curvilinear coordinate grids for incompressible and compressible Navier–Stokes equations 63

Diagnostics
Modelling aerodynamic sound in the airways of a human body: A possible diagnostic tool 1
Dynamic stall phenomenon
Analysis and control of dynamic stall phenomenon using Navier–Stokes formulation involving vorticity, stream function and circulation 207

Energetics
The hydrodynamic analysis of fish propulsion performance and its morphological adaptation 351
Eulerian particulate model
Gas particle industrial flow simulation using RANSTAD 289

Finite element formulations
Turbulence/shock wave interactions in chemically reacting flows 269
Flat-plate
Some recent developments in the theory of boundary layer stability 19
Flow visualization
Three-dimensional flow separation 185
Fluid mechanics
The fluid mechanics of phase change 343

Gas dynamics
Boltzmann schemes for continuum gas dynamics 37
Gas particle flows
Gas particle industrial flow simulation using RANSTAD 289

Helical wave decomposition
New studies in vortex dynamics: Incompressible

and compressible vortex reconnection, core dynamics and coupling between large and small scales 109

Hybrid method
Numerical study of bluff body flow structures 315

Hydrodynamics
The hydrodynamic analysis of fish propulsion performance and its morphological adaptation 351

Incompressible flow
Some numerical schemes using curvilinear coordinate grids for incompressible and compressible Navier–Stokes equations 63

Kinematic and dynamic complications
Three-dimensional flow separation 185
Kinetic schemes for Euler equation
Boltzmann schemes for continuum gas dynamics 37

Large-scale/small-scale interaction
New studies in vortex dynamics: Incompressible and compressible vortex reconnection, core dynamics and coupling between large and small scales 109

Mach reflection
State-of-the-art in research on Mach reflection of shock waves 327
Molecular gas dynamics
The fluid mechanics of phase change 343
Morphology
The hydrodynamic analysis of fish propulsion performance and its morphological adaptation 351

Navier–Stokes analysis
Analysis and control of dynamic stall phenomenon using Navier–Stokes formulation involving vorticity, stream function and circulation 207
Navier–Stokes equations
Some numerical schemes using curvilinear coordinate grids for incompressible and compressible Navier–Stokes equations 63
Near wake evolution
Numerical study of bluff body flow structures 315
Non-circular jets
Simulating three-dimensional vortex motion by a vortex blob method 163
Non-parallel effects
Some recent developments in the theory of boundary layer stability 19
Numerical schemes
Some numerical schemes using curvilinear coordinate grids for incompressible and compressible Navier–Stokes equations 63
Numerical simulation
Simulating three-dimensional vortex motion by a vortex blob method 163

Phase change
The fluid mechanics of phase change 343
Propulsion
The hydrodynamic analysis of fish propulsion performance and its morphological adaptation 351

Regular reflection
State-of-the-art in research on Mach reflection of shock waves 327
Robust numerical schemes
Boltzmann schemes for continuum gas dynamics 37

Soft wall
Modelling aerodynamic sound in the airways of a human body: A possible diagnostic tool 1
Stability
Some recent developments in the theory of boundary layer stability 19
Supersonic combustion
Turbulence/shock wave interactions in chemically reacting flows 269
Swimming
The hydrodynamic analysis of fish propulsion performance and its morphological adaptation 351

Temperature inversion
The fluid mechanics of phase change 343
Temperature jumps
The fluid mechanics of phase change 343
Three-dimensional evolution
Numerical study of bluff body flow structures 315
Three-dimensional flow separation
Three-dimensional flow separation 185
Turbulence
Simulating three-dimensional vortex motion by a vortex blob method 163
Turbulence model
Gas particle industrial flow simulation using RANSTAD 289
Turbulence/shock wave interactions
Turbulence/shock wave interactions in chemically reacting flows 269
Turbulent shear flows
Simulating three-dimensional vortex motion by a vortex blob method 163
Turbulent structure
Numerical study of bluff body flow structures 315

Turbulent wakes
Simulating three-dimensional vortex motion by a vortex blob method 163

Unsteady incompressible flow
Analysis and control of dynamic stall phenomenon using Navier–Stokes formulation involving vorticity, stream function and circulation 207

Unsteady flow
The hydrodynamic analysis of fish propulsion performance and its morphological adaptation 351

Von Neuman–Mach reflection
State-of-the-art in research on Mach reflection of shock waves 327

Vortex dynamics
New studies in vortex dynamics: Incompressible and compressible vortex reconnection, core dynamics, and coupling between large and small scales 109
Simulating three-dimensional vortex motion by a vortex bolb method 163

Vortex method
Simulating three-dimensional vortex motion by a vortex bolb method 163

Vortex reconnection
New studies in vortex dynamics: Incompressible and compressible vortex reconnection, core dynamics and coupling between large and small scales 109

Vortex rings
Simulating three-dimensional vortex motion by a vortex blob method 163

Vorticity, stream function and circulation formulation
Analysis and control of dynamic stall phenomenon using Navier–Stokes formulation involving vorticity, stream function and circulation 207

ACADEMY PUBLICATIONS IN ENGINEERING SCIENCES

Volume 1. The Aryabhata Project (eds U R Rao, K Kasturirangan)

Volume 2. Computer Simulation (eds N Seshagiri, R Narasimha)

Volume 3. Rural Technology (ed. A K N Reddy)

Volume 4. Alloy Design (eds S Ranganathan, V S Arunachalam, R W Cahn)

. . . written by eminent scientists of India and abroad . . . Academy deserves all praise in bringing out these [papers]

Powder Metall. Assoc. India, Newslett.

Volume 5. Surveys in Fluid Mechanics (eds R Narasimha, S M Deshpande)

An informal and stimulating publication . . . (provides) a survey of many important topics in Fluid Mechanics . . . All the papers are of excellent technical content and most are very well written. Many include lengthy reference lists, which are as useful as the body of the paper . . . The publishing quality is very good . . .

IEEE J. Ocean Eng.

. . . The general level (of papers) is high . . . Several are likely to have wide appeal . . .

J. Fluid Mech.

Volume 6. Wood Heat for Cooking (eds K Krishna Prasad, P Verhaart)

. . . interesting and stimulating account of technical thinking on the wood stove problem up to date . . . excellent collection of valuable and thought-provoking investigations.

Rev. Projector (India)

Volume 7. Remote Sensing (eds B L Deekshatulu, Y S Rajan)

. . . Several contributions are specifically addressing topics of national interest, however, the majority of the papers is of general interest for a wide community. The book can serve not only as an inventory of the Indian activities, but also as a textbook on techniques and applications of remote sensing.

Photogrammetria

. . . particularly refreshing . . .

Int. J. Remote Sensing

Volume 8. Water Resources Systems Planning (eds M C Chaturvedi, P Rogers)

. . . well got up and very well printed . . . forms a valuable addition to our limited literature on Water Resources of India.

Curr. Sci.

Volume 9. Reactions and Reaction Engineering (eds R A Mashelkar, R Kumar)

. . . eighteen portraits of some major frontiers of research in CRE by a Micro-Who's Who of contemporary CRE researchers . . . good mix of theory and experiment that will provide many a good read for the specialist as well as the generalist researcher . . . "must-buy" for all research libraries, corporate or personal that contain CRE titles.

Can. J. Chem. Eng.

Volume 10. Reliability and Fault-Tolerance Issues in Real-Time Systems (ed. N Viswanadham)

. . . should help the reader to obtain a global view of the design of real-time systems with specifications in reliability and fault tolerance.

IEEE Control Syst. Mag.

Volume 11. Composite Materials and Structures (ed. K A V Pandalai)

. . . will surely find its place in libraries dealing with applied research.

Bull. Electrochem.

Volume 12. Developments in Fluid Mechanics and Space Technology (eds R Narasimha, A P J Abdul Kalam)

Volume 13. Advanced Ceramics (ed. E C Subbarao)

. . . presents a comprehensive view of advanced ceramics . . . should be of interest to students, research scientists, development engineers and to those engaged in the modern ceramic industry.

Ind. Ceram.

. . . most of the chapters put stress not only on the science, but also on the technological aspects.

Trans. Indian Ceram. Soc.

Volume 14. Modelling and Control of Stochastic Systems (eds N Viswanadham, V S Borkar)

Volume 15. Parallel and Real-Time Distributed Computing (ed. R K Shyamasundar)